



HAL
open science

Multi-scale compressible turbulence in astrophysical plasmas viewed through theoretical, numerical and observational methods

Renaud Ferrand

► **To cite this version:**

Renaud Ferrand. Multi-scale compressible turbulence in astrophysical plasmas viewed through theoretical, numerical and observational methods. Earth and Planetary Astrophysics [astro-ph.EP]. Université Paris-Saclay, 2021. English. NNT : 2021UPASP086 . tel-03545797

HAL Id: tel-03545797

<https://theses.hal.science/tel-03545797>

Submitted on 27 Jan 2022

HAL is a multi-disciplinary open access archive for the deposit and dissemination of scientific research documents, whether they are published or not. The documents may come from teaching and research institutions in France or abroad, or from public or private research centers.

L'archive ouverte pluridisciplinaire **HAL**, est destinée au dépôt et à la diffusion de documents scientifiques de niveau recherche, publiés ou non, émanant des établissements d'enseignement et de recherche français ou étrangers, des laboratoires publics ou privés.

Multi-scale compressible turbulence in astrophysical
plasmas viewed through theoretical, numerical and
observational methods

*Turbulence multi-échelles compressible dans les
plasmas astrophysiques: une approche théorique,
numérique et observationnelle*

Thèse de doctorat de l'université Paris-Saclay

École doctorale n° 127, Astronomie et Astrophysique d'Ile de France

Spécialité de doctorat: Astronomie et astrophysique

Unité de recherche: Université Paris-Saclay, CNRS, École polytechnique, LPP,
91128, Palaiseau, France

Réfèrent: Faculté des sciences d'Orsay

**Thèse présentée et soutenue à Palaiseau,
le 1er octobre 2021, par**

Renaud Ferrand

Composition du jury:

Alain Abergel Professeur, Université Paris-Saclay	Président
William Matthaeus Professeur, University of Delaware, Newark	Rapporteur & Examineur
Luca Sorriso-Valvo Chercheur, CNR, Istituto per la Scienza e Tecnologia dei Plasmi, Bari	Rapporteur & Examineur
Aurélie Marchaudon Directrice de recherches, CNRS, Institut de Recherche en Astrophysique et Planétologie, Université Paul Sabatier, Toulouse	Examinatrice
Patrick Hennebelle Directeur de recherches, Commissariat à l'énergie atomique et aux éner- gies alternatives, Université Paris-Saclay	Examineur
Robert Wicks Maître de conférences, Northumbria University, Newcastle	Examineur

Direction de la thèse:

Fouad Sahraoui Directeur de recherches, CNRS, École polytechnique	Directeur de thèse
Sébastien Galtier Professeur des universités, Université Paris-Saclay	Co-directeur de thèse

Remerciements

Il n'y a encore pas si longtemps de cela (quand bien même ça me paraît être une éternité maintenant) la vue du Soleil ne m'évoquait pas grand-chose d'exceptionnel, si ce n'est chaleur et lumière, les vacances d'été, et une formule bien connue des initiés : *Praise the Sun*. Trois ans plus tard, c'est un maelstrom de mots et d'émotions qui m'assaille quand j'y pense, ainsi qu'à tous ces moments de joie, de doute, de triomphe et de déprime qui ont empli mon long séjour au LPP. Alors que j'apporte le point final à cet ouvrage, je repense à tous ceux qui m'ont aidé et soutenu, ceux qui ont été là pour moi ces trois dernières années, et sans qui rien de tout ça n'aurait été possible.

Alors naturellement, commençons par le commencement, ceux sans qui cette thèse n'aurait littéralement jamais eu lieu. Un grand merci à mes directeurs de thèse Fouad et Sébastien pour leur pédagogie, leur disponibilité et leurs innombrables conseils. Merci à eux de m'avoir proposé de travailler avec eux alors que je n'étais qu'un petit master 2 errant au hasard à la recherche d'un stage, et pour m'avoir guidé d'une main de maître pendant ces trois longues années. Merci à eux d'avoir toujours été à l'écoute, de m'avoir aidé à relativiser dans les moments difficiles, et de m'avoir enseigné tout ce que je sais aujourd'hui sur la turbulence plasma et le vent solaire. Certaines discussions techniques auront apporté leur lot de défis et d'incompréhensions, mais finalement on a toujours réussi à s'en sortir et à se retrouver sur la même longueur d'onde, et les succès en découlant n'en furent que plus satisfaisants ! Ces moments où je passais voir Fouad 5 minutes en coup de vent en sachant pertinemment que j'y serai encore une heure plus tard me manqueront à l'avenir. Merci à eux aussi pour les bons moments en marge du travail, les voyages, le tourisme, les bars et les restos, quand bien même ils se firent rares avec le début de la crise sanitaire.

Je remercie également les multiples collaborateurs avec qui j'ai travaillé au cours de ma thèse : Nahuel Andrés tout d'abord, auprès de qui j'ai commencé ma thèse et qui m'a appris à utiliser tous les outils relatifs aux simulations GHOST, au calcul de lois exactes, et qui m'a grandement facilité l'étude des données satellite MMS. Je remercie aussi le reste de la team argentine de l'IAFE, et notamment Pablo Mininni, Pablo Dmitruk et Daniel Gómez pour les inputs sur GHOST et le vent solaire et l'organisation du meeting à Buenos Aires. La team niçoise ensuite, Dimitri Laveder, Thierry Passot et Pierre-Louis Sulem pour nous avoir fourni les données CGL et LF, pour tout leur travail sur ce beau projet et pour m'avoir permis de présenter un poster au workshop Waves côte d'azur. Un grand merci enfin à Christoph Federrath pour m'avoir donné l'occasion unique d'étudier ses énormes simulations du milieu interstellaire et m'avoir aidé à les manipuler, et à Ralph Klessen pour le support informatique et pour m'avoir donné accès aux serveurs du LRZ. Ce n'était pas directement le sujet central de ma thèse, mais l'occasion était vraiment trop belle pour passer à côté et les résultats furent au rendez-vous !

Bien sûr, une thèse ne serait pas grand chose sans quiconque pour juger objectivement de la valeur du travail accompli. En ce sens, je remercie chaleureusement Alain Abergel pour avoir accepté la présidence de mon jury de thèse, ainsi que l'ensemble des membres le constituant: William Matthaeus et Luca Sorriso-Valvo pour avoir accepté d'endosser le rôle de rapporteurs, et Aurélie Marchaudon, Patrick Hennebelle et Robert Wicks pour avoir bien voulu être les examinateurs de mon travail de thèse.

Un grand merci également à l'ensemble du LPP pour m'avoir accueilli pour ces trois années. Merci à Marilyne Bazin, Cherifa Ighoud et Catherine Jegu pour l'aide et le soutien avec les nombreuses questions administratives rencontrées, et à Edouard Bouchet pour avoir organisé mon arrivée au labo et mis en place mon contrat d'après-thèse (et par la même m'avoir évité le traquenard d'une soutenance en août). Merci à Pierre Morel et Anne Bourdon pour avoir accepté de faire partie de mon comité de suivi, pour leur bienveillance et leur disponibilité. Merci également à Pauline, qui prend la relève en tant que doctorante de Fouad et sans qui on n'aurait probablement jamais réussi à comprendre à 100% les subtilités du code que j'utilise depuis le début de ma thèse !

N'oublions pas cependant que la thèse ne se résume pas qu'à du travail h24, et en ce sens je remercie Nicolas Aunai, Alexis Jeandet, Philip Deegan, Nadjirou Ba ainsi que Bayane pour avoir partagé mes pauses déjeuner et m'avoir fait oublier mes soucis une petite heure chaque jour, et bien sûr merci à Gautier Nguyen, camarade de l'X et compagnon d'infortune perdu comme moi dans les méandres de l'administration balbutiante d'IPParis et de Paris Saclay, pour le soutien mutuel et les soirées jeux ou escape game ! Plus largement, j'aimerais également remercier Pauline, Kosta, Clothilde, Gaëtan et Ramy pour la courte mais mémorable aventure Doc'Union, les quelques soirées qu'on a pu organiser et le week-end des doctorants restent parmi les meilleurs souvenirs de ma thèse ! De même, merci à Alexandra Béhus, Audrey Lemaréchal et Élodie Lelaidier, qui m'ont épaulé pour les demandes de bourse de thèse, de missions d'enseignement et durant le début de ma thèse, et pour le soutien apporté à Doc'Union avant qu'elle ne succombe aux multiples confinements. J'aimerais enfin dire merci à Ronan Modolo, qui m'a aidé à découvrir les bons coins de Buenos Aires et m'a notamment indiqué un ou deux restos fort sympathiques (promis un jour je trouverai un moyen de te rendre ta carte de tram) !

Fort heureusement ma vie ces dernière années ne s'est pas limitée à mon petit bureau du 412, car à un moment la seule compagnie des fouines qui rôdent dans le plafond (et que je salue bien bas) m'aurait parue bien dérisoire. Aussi, je tiens à remercier tous ceux qui, de l'extérieur, m'ont apporté leur soutien jusqu'au bout de cette aventure. Un très grand merci à famille : à mes parents, ma sœur et mes grand-parents pour leur soutien constant et inconditionnel, à ma belle-famille, et bien entendu à Séverine qui a toujours été là pour moi dans les moments difficiles, notamment pendant les trois confinements qu'elle a partagé avec moi. Tous ont toujours cru en moi et m'ont aidé à avancer depuis toujours, et je ne serai pas arrivé si loin sans leur soutien.

Un grand merci également à l'ensemble de la RI : à Raphaël, Charlotte, Ivan et Auriane. Merci de m'avoir soutenu et aidé à relativiser les difficultés rencontrées. Merci pour toutes ces soirées en ligne passées à rendre les abeilles heureuses ou à protéger la Terre des fourmis géantes, pour les soirées jeu de rôle passées à saccager le Nouveau Monde, et pour les soirées et week-end IRL rendus trop rares par la pandémie, mais toujours accueillis avec le plus grand bonheur ; autant de moments calme et de détente qui m'auront permis d'aller toujours de l'avant. Et merci à Jean Patrick, que sa curiosité sans limite a amené à me poser des questions beaucoup trop pointues sur mon travail, qui m'ont régulièrement fait réaliser combien je n'étais vraiment pas au point sur certains sujets !

Je tiens aussi à remercier mes anciens et nouveaux amis de l'X (mais pas que) qui m'ont aidé à sortir la tête de mon travail ces trois années de thèse. Merci à toute la communauté Faërix, les vieux comme les jeunes, pour les pauses jeux de société au local et les sushis tradis, les week-ends ski et les RRX. Merci également à la communauté BJR 2014 / Navets pour les innombrables soirées passées à se détendre (ou pas ?) sur League of Legends, les watch party et les sorties ciné, mais aussi pour leur expertise algorithmique qui m'aura appris pas mal de choses en programmation !

Pour finir, j'ai une pensée pour ces enseignants qui m'ont permis d'arriver là où je suis aujourd'hui. Merci à mes profs de prépa, et plus particulièrement à Catherine Jaulent, Frédéric Picco et Denis Favennec qui à l'époque ont cru en moi, m'ont poussé à donner le meilleur de moi-même, et dont la dévotion et la pédagogie m'ont finalement permis d'intégrer l'X que je convoitais tant. Et enfin, merci à Roland Lehoucq et Frédéric Daigne, dont le cours de physique stellaire à l'X a fait basculer mon avenir dans le monde merveilleux de l'astrophysique !

Abstract

The [Solar Wind \(SW\)](#) is a turbulent plasma emitted by the Sun that is in constant interaction with our planet's magnetic field. It stands as a colossal natural laboratory that boasts extremely rich physics, most of it still remaining to be fully understood. The sole study of the turbulent phenomena at work at the multiple scales of the [SW](#) represents a full-fledged challenge, and a great opportunity to hone our understanding of plasma turbulence in general. Numerous satellite missions were sent throughout the years to make *in situ* measurements directly within the [SW](#) or its incursions in Earth's magnetosphere, and a vast array of theoretical and computational methods was developed to allow for the analysis of the resulting data. Specifically, the questions surrounding turbulence energy dissipation in the [SW](#) constitute a key field of study that is still today an open area of investigation.

In this thesis, we present a step by step approach of the study of [SW](#) turbulence, from the early theoretical work that makes the foundations of future applied studies to their application to [Direct Numerical Simulation \(DNS\)](#) data, and the final analysis of *in situ* satellite data. The theoretical work, which is focused on the mathematical derivation of so-called exact laws pertaining to Hall [Magnetohydrodynamics \(MHD\)](#) plasma models, yields new, improved tools for estimating the turbulence cascade rate at [MHD](#) and sub-ion scales and investigating both incompressible and compressible plasma turbulence. The applied calculations are made with a parallelized Python code adaptable to the computation of a wide range of exact law models in 3D periodic datasets.

The theoretical and numerical methods developed as the first part of this thesis are then used to compute the energy cascade rates for a large array of [DNSs](#) of different fluid models and presenting varied physics. For part of these [DNSs](#), the study of the cascade rates provides us with a detailed understanding of how our theoretical models intrinsically work, in order to contextualize the results obtained in subsequent investigations of [DNS](#) or satellite data. It notably shows that the different exact laws for a given plasma model provide matching values of the cascade rate, even if the turbulence is not perfectly stationary.

The other part of these [DNSs](#) aims at shedding light on some physical effects governing specific turbulent media, such as the [SW](#). Through these, it is shown that the energy cascade rate, albeit being derived from a fluid plasma description, is able to quantitatively represent the heating due to kinetic Landau damping. This conclusion would now have to be extended to a wider array of kinetic dissipative processes in the quest of truly legitimating the study of [SW](#) energy dissipation through the fluid energy cascade rate. On another note we also present, through the analysis of massive compressible hydrodynamic supersonic [DNSs](#) of the [Interstellar Medium \(ISM\)](#), new evidences of the existence of two turbulent regimes in supersonic media, whose interplay may have an important role in the stabilization of star-forming interstellar filaments in dense regions of the [ISM](#).

The insights brought by the study of these turbulent [DNS](#) datasets is finally put to contribution in the analysis of real data measured by the [Magnetospheric Multiscale mission \(MMS\)](#) in the magnetosheath. Using exact laws for compressible Hall [MHD](#) turbulence, we study the behavior of the turbulence energy cascade at large and small scales, and investigate the computational methods usually used for calculating 3D vector fields derivatives on a tetrahedral satellite formation, generalized from the curlometer technique. Through these studies we find that the approximate calculations made with the curlometer lead to potentially important errors, a conclusion that is further evidenced by the use of a virtual spacecraft in [DNS](#) data that allows us to test this method in a controlled environment. These limitations call for the development of new data treatment methods or better ways to compute 3D derivatives on spacecraft data, which may help designing future multi-spacecraft missions.

Résumé

Le vent solaire est un plasma turbulent émis par le Soleil et en interaction constante avec le champ magnétique de notre planète. Il s'apparente à un colossal laboratoire naturel, pourvu d'une incroyable richesse physique, et dont toutes les subtilités ne sont pas encore comprises. La seule étude des phénomènes turbulents à l'œuvre à toutes les échelles du vent solaire représente un défi à part entière, ainsi qu'une belle occasion d'affiner notre compréhension générale des plasmas turbulents. Au fil des années, quantité de satellites furent envoyés prendre des mesures directement dans le vent solaire ou la magnétosphère terrestre, et une large gamme de méthodes théoriques et numériques fut mise en place pour permettre l'analyse des données ainsi obtenues. Plus spécifiquement, les questions qui entourent la dissipation d'énergie turbulente dans le vent solaire forment une problématique importante qui est encore, de nos jours, un domaine d'étude ouvert.

Dans cette thèse, nous présentons une approche complète de l'étude de la turbulence dans le vent solaire, allant des travaux théoriques initiaux visant à poser les fondations de futures études à l'application de ces outils à des données de simulation numériques directes et des données satellites. L'étude théorique, qui se concentre sur le calcul de lois exactes en magnétohydrodynamique (MHD) Hall, aboutit à l'obtention de nouveaux outils performants permettant d'estimer le taux de cascade d'énergie aux échelles MHD et sub-ioniques et d'étudier la turbulence dans des plasmas incompressibles comme compressibles. En pratique, le calcul des lois est effectué sur des cubes de données 3D périodiques au moyen d'un code Python parallélisé, adaptable à des lois obtenues pour une grande variété de modèles.

Les outils théoriques et numériques ainsi développés sont ensuite utilisés pour calculer les taux de cascade d'énergie dans d'une vaste gamme de simulations numériques directes, effectuées pour différents modèles fluides et incluant des effets physiques variés. Une partie de ces simulations permet d'étoffer notre compréhension du fonctionnement intrinsèque des modèles théoriques obtenus plus tôt, et ainsi de mieux comprendre leurs résultats lorsque appliqués à l'étude d'autres ensembles de données. Nous montrons notamment que les différentes lois exactes, pour un modèle donné, donnent des résultats équivalents même si la turbulence étudiée n'est pas parfaitement stationnaire.

Les autres simulations visent à identifier certains comportements et phénomènes physiques à l'œuvre dans des milieux turbulents spécifiques, tels que le vent solaire. Leur étude montre que le taux de cascade d'énergie, bien qu'il soit obtenu dans le cadre d'un modèle fluide, parvient à rendre compte quantitativement du chauffage dû à l'amortissement Landau. Cette conclusion, qui devra par la suite être étendue à différents processus de dissipation cinétiques, est un premier pas vers la légitimation de l'emploi du taux de cascade dans l'étude de la dissipation d'énergie dans le vent solaire. Dans un autre contexte, nous étudions également des données issues d'une gigantesque simulation hydrodynamique supersonique du milieu interstellaire (MIS). Cette étude révèle de nouvelles preuves de l'existence d'une turbulence à deux régimes dans les milieux fortement supersoniques, et qui pourrait contribuer à la formation de filaments interstellaires, structures denses du MIS dans lesquelles se forment des étoiles.

Les connaissances acquises dans l'analyse de ces données de simulation sont finalement mises à contribution pour étudier des données satellites mesurées dans la magnétogaine par la mission Magnetospheric MultiScale (MMS). Grâce aux lois exactes pour la MHD Hall compressible, nous étudions le comportement du taux de cascade d'énergie à grande et petite échelle, et initiions une étude poussée du fonctionnement du « curlometer », une méthode numérique permettant de calculer des dérivées 3D de champs de vecteurs sur la base d'une formation de satellites tétraédrique. Ces études montrent que les calculs approchés effectués avec des méthodes dérivées du curlometer présentent des erreurs parfois importantes, une conclusion appuyée par des tests additionnels effectués sur des données de simulations via l'emploi de satellites virtuels. Les problèmes ainsi mis à jour soulignent le besoin de concevoir de nouvelles méthodes de calcul des dérivées 3D sur de telles données. Ces considérations pourraient aider à concevoir et préparer de futures missions multi-satellites.

Contents

Contents	vii
1 Introduction	1
1.1 Theory of collisionless plasmas	1
1.1.1 What is a plasma ?	1
1.1.2 Kinetic and fluid description of a plasma	2
1.1.3 The equations of MHD	4
1.2 From space to astrophysical plasmas	6
1.2.1 The Solar Wind: a turbulence laboratory	6
1.2.2 The Interstellar Medium and star-forming regions	8
1.3 Theory of turbulence	10
1.3.1 Basics of turbulence	10
1.3.2 The zeroth law of turbulence	11
1.3.3 Spectral approach of turbulence	12
1.4 Overview of the thesis	14
2 Exact laws in Hall MHD turbulence	17
2.1 Introduction	17
2.2 Exact law in the incompressible Hall MHD model	18
2.2.1 Description of the model	18
2.2.2 Calculation of the dynamical equation	19
2.2.3 From the dynamical equation to the exact law	21
2.2.4 Equivalence of IHMHD exact laws	22
2.3 Exact law in compressible models	24
2.3.1 Description of the compressible Hall MHD model	24
2.3.2 Calculation of a compressible dynamical equation	25
2.3.3 From the dynamical equation to the exact law	28
2.3.4 Limit cases and alternative compressible laws	30
2.4 Conclusion	30
3 Methodology: laws computation and numerical implementation	33
3.1 Introduction	33
3.2 Numerical calculation of exact laws	33
3.2.1 Generic framework	33
3.2.2 Isotropy hypothesis: 3D increments	35
3.2.3 Axisymmetry hypothesis: 3D increments	36
3.2.4 Axisymmetry hypothesis: 2D increments	37
3.3 Implementation of the numerical methods	38
3.3.1 Main steps of the calculation	38
3.3.2 Parallelization paradigm	39
3.3.3 Memory constraints	40
3.4 Conclusion	41

4	Understanding plasma turbulence through DNS data analysis	43
4.1	Introduction	43
4.2	Numerical test of IHMHD exact laws	44
4.2.1	Convergence of exact laws and model choice	44
4.2.2	Influence of the mean magnetic field	46
4.2.3	Summary of the study on the IHMHD laws	47
4.3	In-depth study with generalized CHMHD exact laws	47
4.3.1	Context of the study	47
4.3.2	Presentation of the data	48
4.3.3	Calculation of law F21	50
4.3.4	Non-stationary CHMHD laws	54
4.3.5	Summary of the GHOST study	60
4.4	Application to Landau-fluid simulations	61
4.4.1	Context of the study	61
4.4.2	Theory of CGL and LF models	62
4.4.3	Description of the numerical code	62
4.4.4	Evaluation of the exact law and dissipations	65
4.4.5	Methods of calculation of the hyperdissipation	66
4.4.6	Energy cascade in presence of Landau damping	71
4.4.7	Calculation of the heating due to Landau damping	74
4.4.8	Summary: relations between fluid and kinetic models	77
4.5	Supersonic CHD turbulence	78
4.5.1	Context of the study	78
4.5.2	Framework and presentation of the data	79
4.5.3	Calculation of the energy cascade rate	80
4.5.4	Filamentary structures and locality of turbulence	82
4.5.5	Insights into a two-regimes turbulence	86
4.5.6	Summary and link to the ISM	87
4.6	Conclusion	88
5	Application to Virtual spacecraft and MMS data in Earth's magnetosheath	91
5.1	Introduction	91
5.2	Working with <i>in situ</i> data	92
5.2.1	Space-time ambiguity and Taylor hypothesis	92
5.2.2	Calculation of 3D divergences: the curlometer / gradiometer	93
5.3	MMS data analysis	94
5.3.1	Context and presentation of the data	94
5.3.2	Selection of the time intervals	95
5.3.3	Results	97
5.4	Gradiometer: evaluation and limitations of the method	101
5.4.1	Quality factor of the gradiometer	101
5.4.2	Causes of error of the gradiometer	105
5.5	Simulated MMS fly-by	106
5.5.1	Description of the method	106
5.5.2	General precision of the gradiometer	109
5.5.3	Reaction of the gradiometer to non-linearity	111
5.6	Conclusion	113
6	Conclusions and perspectives	115
6.1	Summary of the thesis	115
6.2	Tools for turbulence analysis	116
6.2.1	Derivation of exact laws	116
6.2.2	Numerical implementation of the exact laws	116

6.3	Studying turbulent flows through DNSs	117
6.3.1	In-depth analysis of exact laws	117
6.3.2	Relation between the fluid cascade and kinetic dissipation	118
6.3.3	Supersonic CHD turbulence in the ISM	118
6.4	MMS <i>in situ</i> data analysis	119
6.4.1	Selection and exploitation of the data	119
6.4.2	Investigation of the gradiometer	120
6.5	Final words and perspectives	121
A	List of Acronyms	133
B	Papers published and in preparation	135

Chapter 1

Introduction

1.1 Theory of collisionless plasmas

1.1.1 What is a plasma ?

For most people, the matter that forms our universe is categorized in three classical states: solids, liquids and gas. Yet, these states of matter that are the stage of our whole lives, the ground we walk on and the air we breathe, only represent a tiny 0.01% of the entire visible universe. The remaining 99.9%, from lightning strikes to the most distant stars and nebulae, exist in a fourth state of matter: they are plasmas.

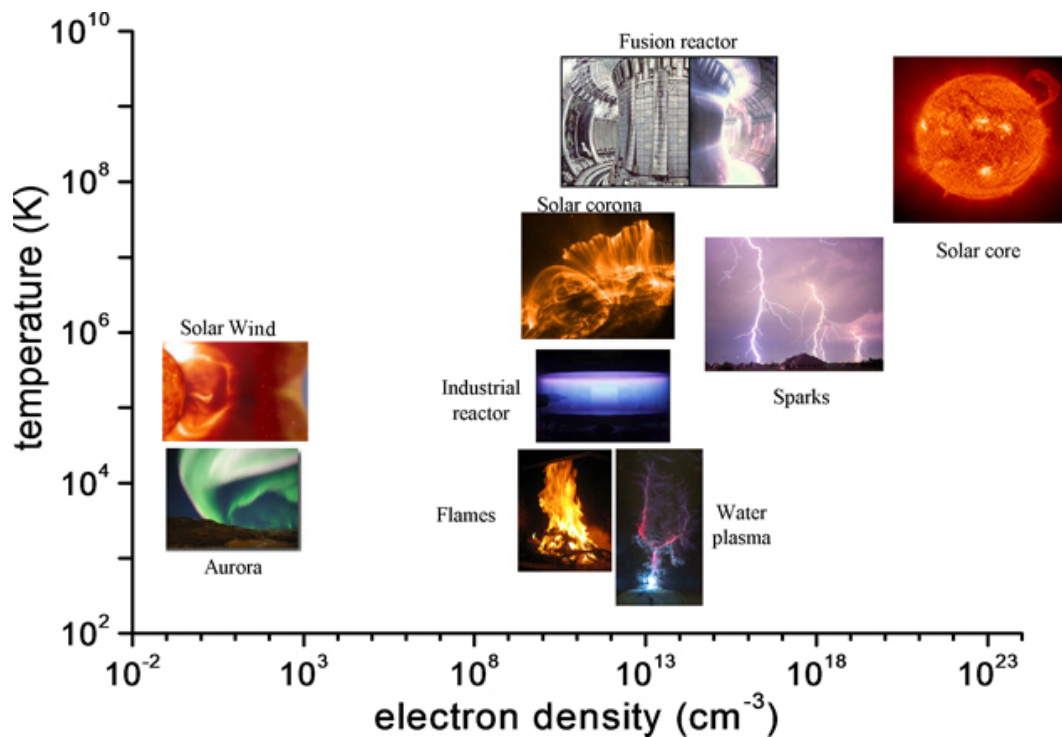


Figure 1.1: Classification of natural and laboratory plasmas in a logarithmic diagram charges density/temperature (credits: Laboratoire de Physique des Plasmas).

A plasma is a form of partially ionized gas that is usually obtained by either heating a neutral gas or putting it in a strong electromagnetic field, so that ions and electrons can detach from neutral particles and roam in the gas. This allows the medium to become an electric conductor, whereas a neutral gas would have remained an insulator. Macroscopically, a plasma does not differ much from a neutral gas as it tends to retain a global neutrality of charges: it usually contains as many positive charges as negative ones. However, microscopic portions of the plasma can show large differences in charges densities, leading to a variety

of effects that make plasmas behave very differently from neutral gas. This particularity is referred to as *quasi-neutrality*.

Plasmas can be classified under different archetypes depending on their degree of ionization and the interactions between the particles they are made of. One can distinguish, among other types, collisional plasmas from non-collisional ones. For the first category the motion of charged particles is dictated by the macroscopic electromagnetic field, but also by its interaction with neighboring particles through the Coulomb forces. In this situation their movements will be correlated to some extent and representative of the global behavior of the plasma. Non-collisional plasmas, on the other hand, are diluted plasmas in which charged particles have little to no interaction between each-others. Due to this, each particle will have its own behavior, that can be totally different from the global movement of the plasma. It is this category of plasmas that we will be studying in the entirety of this work.

As the behavior of a non-collisional plasma changes depending on whether we look at the whole medium or at individual particles, several models exist to describe and study such a plasma. Of course following the individual movement of each of the numerous charged particles is out of the question, so we usually take a semi-global or a global approach. The kinetic approach consists in looking at an ensemble of particles, whose velocities are distributed according to their distribution function f , and studying the evolution of this distribution function over time. The fluid approach discards the individuality of particles to study the macroscopic behavior of the plasma by considering the different moments of the distribution function f . The lowest order (simplest) of such fluid description is called **MHD**. It provides less information *a priori* than the kinetic approach on the inner behavior of the plasma, such as energy whereabouts of charged particles, but is usually easier to manipulate. In particular, the fluid description provides relatively simple means to handle other complex physical phenomena such as plasma turbulence, of which we will speak in more details in the last section of this chapter.

1.1.2 Kinetic and fluid description of a plasma

In the kinetic description of a plasma we study the time evolution of the distribution functions $f_s(\mathbf{r}, \mathbf{v}, t)$, which represents the amount of particles of species "s" (electrons or any kind of ions) contained within an infinitesimal six-dimensional volume $d\mathbf{r}d\mathbf{v}$ in phase space at position (\mathbf{r}, \mathbf{v}) . The time evolution of this distribution function is given in the collisionless limit by the Vlasov equation:

$$\frac{\partial}{\partial t} f_s + \mathbf{v} \cdot \nabla f_s + \frac{q_s}{m_s} (\mathbf{E} + \mathbf{v} \times \mathbf{B}) \cdot \frac{\partial}{\partial \mathbf{v}} f_s = 0, \quad (1.1)$$

where q_s and m_s are the particles' charge and mass, \mathbf{E} and \mathbf{B} are the electric and magnetic fields, and ∇ denotes the 3D vectorial derivative operator $(\partial_x, \partial_y, \partial_z)$. Note that considering particle collisions would lead to add a non-zero collisions term $(\partial_t f)_{coll}$ to the right-hand side of (1.1): the resulting equation is known as the Boltzmann equation. To solve this equation one needs to get the expressions of \mathbf{E} and \mathbf{B} , which is made possible thanks to Maxwell equations:

$$\text{Maxwell-Gauss: } \nabla \cdot \mathbf{E} = \frac{\rho_e}{\epsilon_0}, \quad (1.2)$$

$$\text{Maxwell-Gauss for } \mathbf{B}: \nabla \cdot \mathbf{B} = 0, \quad (1.3)$$

$$\text{Maxwell-Faraday: } \nabla \times \mathbf{E} = -\frac{\partial \mathbf{B}}{\partial t}, \quad (1.4)$$

$$\text{Maxwell-Ampère: } \nabla \times \mathbf{B} = \mu_0 \mathbf{J} + \mu_0 \epsilon_0 \frac{\partial \mathbf{E}}{\partial t}, \quad (1.5)$$

where ρ_e is the charge density, \mathbf{J} the current density, ϵ_0 the vacuum dielectric permittivity and μ_0 the vacuum magnetic permeability. In practice the second term of the right-hand side of Ampère equation is often neglected in the non-relativistic and quasi-neutrality limits

(Sahraoui et al., 2003), so only equations (1.3) to (1.5) are necessary to close the system with Vlasov equation, provided one has an expression for the current \mathbf{J} . It can be obtained by averaging the infinitesimal current given by the distribution function over particle velocities:

$$\mathbf{J} = \sum_s \iiint q_s f_s \mathbf{v} d\mathbf{v}. \quad (1.6)$$

This kind of relation is akin to what are called moments equations.

Aside from the kinetic representation detailed above, plasmas can also be described through a global, fluid representation. This description is in fact obtained by an integration of the kinetic model using what we call the *moments* of Vlasov equation. From the distribution function f one can obtain various physical quantities, the so-called moments, by an integration over particles velocities, just as we did to derive the current density in the kinetic model (1.6). The zeroth and first order moments give the particle density n_s and the mean velocity \mathbf{u}_s :

$$n_s = \iiint f_s d\mathbf{v}, \quad (1.7)$$

$$\mathbf{u}_s = \frac{1}{n_s} \iiint f_s \mathbf{v} d\mathbf{v}. \quad (1.8)$$

The mean velocity allows for the calculation of further moments, typically the pressure tensor \mathbf{P}_s and the heat fluxes tensor \mathbf{Q}_s , which are respectively the second and third order moments:

$$\mathbf{P}_s = m_s \iiint (\mathbf{v} - \mathbf{u}_s)^2 f_s m_s d\mathbf{v}, \quad (1.9)$$

$$\mathbf{Q}_s = \frac{1}{2} m_s \iiint (\mathbf{v} - \mathbf{u}_s)^3 f_s \mathbf{v} d\mathbf{v}. \quad (1.10)$$

To obtain the equations describing the evolution of these moments, and that form the MHD model (as well as any other, more complete fluid representation of plasmas) we multiply Vlasov equation (1.1) by the corresponding order of particle velocity and proceed to the integration. At order zero (i.e. we only integrate on speed) we have, recalling that in phase space \mathbf{r} and \mathbf{v} are independent:

$$\begin{aligned} & \frac{\partial}{\partial t} \iiint f_s d\mathbf{v} + \nabla \cdot \iiint \mathbf{v} f_s d\mathbf{v} + \frac{q_s}{m_s} \iiint (\mathbf{E} + \mathbf{v} \times \mathbf{B}) \cdot \frac{\partial}{\partial \mathbf{v}} f_s d\mathbf{v} = 0 \\ \Leftrightarrow & \frac{\partial}{\partial t} (m_s n_s) + \nabla \cdot (m_s n_s \mathbf{u}_s) \\ & + q_s \iiint \frac{\partial}{\partial \mathbf{v}} (\mathbf{E} f_s) d\mathbf{v} + \iiint \frac{\partial}{\partial \mathbf{v}} \cdot (f_s \mathbf{v} \times \mathbf{B}) d\mathbf{v} - \iiint f_s \frac{\partial}{\partial \mathbf{v}} \cdot (\mathbf{v} \times \mathbf{B}) d\mathbf{v} = 0. \end{aligned} \quad (1.11)$$

One can then show that all three terms of the bottom line are equal to zero. Indeed, using Ostrogradski theorem we have:

$$\iiint \frac{\partial}{\partial \mathbf{v}} (\mathbf{E} f_s) d\mathbf{v} = \lim_{R \rightarrow \infty} \oint_{\mathcal{S}_R} f_s \mathbf{E} \cdot d\mathbf{S}, \quad (1.12)$$

where \mathcal{S}_R denotes a sphere of radius R . As the surface element $d\mathbf{S}$ scales as R^2 and f_s as something that tends to zero "quicker" than R^2 tends to infinity (typically, a Maxwellian that behaves like e^{-R^2}), then the limit will tend to zero, which means that the 3D integral is equal to zero. A similar reasoning shows that the second term is also equal to zero. Finally, for the third one, a simple cartesian decomposition of $\frac{\partial}{\partial \mathbf{v}} \cdot (\mathbf{v} \times \mathbf{B})$ is enough to see right away that the term is null. Consequently, we are left with the equation:

$$\frac{\partial}{\partial t} (m_s n_s) + \nabla \cdot (m_s n_s \mathbf{u}_s) = 0, \quad (1.13)$$

which is akin to the well known continuity equation of hydrodynamics, albeit for a single species s .

Similarly, an equation for the first order moment can be obtained by multiplying (1.1) by \mathbf{v} and taking the 3D integral. In this case, the calculation leads to the following equation:

$$n_s m_s \left(\frac{\partial}{\partial t} \mathbf{u}_s + \mathbf{u}_s \cdot \nabla \mathbf{u}_s \right) = -\nabla \cdot \mathbf{P}_s + n_s q_s (\mathbf{E} + \mathbf{u}_s \times \mathbf{B}), \quad (1.14)$$

which corresponds to Navier-Stokes equation for a single species in presence of electromagnetic forces. Note that the right-hand-side of this equation will change to reflect the forces truly acting on the plasma: if one were to take collisions into account, and thus use the Boltzmann equation instead of Vlasov equation, an additional term would be added to reflect the contribution of viscous forces. This is what will be done below to derive the [MHD](#) equations.

Other equations can also be derived for higher order moments and, just as we can already observe for the two equations derived above, they depend on moments of inferior and immediately superior orders too. Consequently, the resulting system of equation, no matter the maximum order we choose to calculate the moments at, cannot be solved as each equation added to the system introduces a new variable. Closing the system thus requires fixing a desired order, and using a closure equation to connect the maximum order variable to the lower order ones. For example the [MHD](#) equations that we derive below, and that consists of only the zeroth and first order moments equations, need to be closed with an equation on the pressure tensor \mathbf{P} . The most classical closures for this model are the isothermal one $P = c_s^2 \rho$ (with c_s^2 the speed of sound), which is the closure we will consider in all the theoretical calculations led in this thesis, and the polytropic one $P = K \rho^\gamma$ for a constant K and a polytropic index γ . Both assume a scalar pressure. Other closures exist such as the [Chew, Goldenberg, Low \(CGL\)](#) closure, that considers an axi-symmetric pressure tensor ([Chew et al., 1956](#)), or closures making use of heat fluxes or higher order moments such as the normal closure (see for instance the review in [Hunana et al. \(2019\)](#)).

Note that, although the fluid plasma description is unable to describe kinetic effects, it is still possible to emulate some of them through the choice of a specific closure. This is notably the case of the [Landau fluid \(LF\)](#) closures, closed either at third or fourth order moments ([Hammett and Perkins, 1990](#); [Snyder et al., 1997](#); [Passot and Sulem, 2007](#)), that lead to fluid models able to transcribe the effects of kinetic Landau damping. The nature of this closure, along with the [CGL](#) one, will be explained in more details in chapter 4.

1.1.3 The equations of MHD

The equations of [MHD](#), that describe the movement of a conductive fluid in an electromagnetic field, can be obtained by the combination of equations (1.13), (1.14) and Maxwell equations. These first two equations only stand for an individual species of electrons or ions, but one can obtain a more general version by considering a mono-fluid model (i.e. all species behave as a single fluid). We consider the most simplistic model of a fluid formed of only H^+ ions and electrons, labeled as species "i" and "e" respectively, which will be the type of plasma considered in most of this work. Defining the mass density $\rho = m_i n_i + m_e n_e$, the charge density $\rho_c = q_i n_i + q_e n_e$ and the fluid velocity $\mathbf{u} = (m_i n_i \mathbf{u}_i + m_e n_e \mathbf{u}_e) / \rho$, and summing equations (1.13) for both species, we get:

$$\frac{\partial}{\partial t} \rho + \nabla \cdot (\rho \mathbf{u}) = 0. \quad (1.15)$$

Similarly, summing equations (1.14) for both species yields:

$$\rho \left(\frac{\partial}{\partial t} \mathbf{u} + \mathbf{u} \cdot \nabla \mathbf{u} \right) = -\nabla \cdot \mathbf{P} + \rho_c (\mathbf{E} + \mathbf{u} \times \mathbf{B}). \quad (1.16)$$

The property of quasi neutrality mentioned earlier can be put into equations in the following way: the charges are distributed so that $\rho_c \sim 0$, while still allowing for a current to exist as $\rho_c \mathbf{u} \sim \mathbf{J} = en(\mathbf{u}_i - \mathbf{u}_e)$. If we introduce viscosity forces with a viscosity coefficient ν in the system and consider a simple scalar pressure, (1.16) becomes:

$$\rho \left(\frac{\partial}{\partial t} \mathbf{u} + \mathbf{u} \cdot \nabla \mathbf{u} \right) = -\nabla P + \mathbf{J} \times \mathbf{B} + \nu (\Delta \mathbf{u} + \frac{1}{3} \nabla (\nabla \cdot \mathbf{u})). \quad (1.17)$$

Now we need to add to this system an equation describing the time evolution of the magnetic field. Maxwell-Faraday equation (1.4) already proposes a dynamical equation for \mathbf{B} as a function of \mathbf{E} . One can get rid of the electric field by using Ohm's law. In its simplest form, inside a solid conductor, this law connects the current density to the electric field through the conductivity σ as:

$$\mathbf{J} = \sigma \mathbf{E}. \quad (1.18)$$

Here we are in presence of a conductive fluid whose movement in the global magnetic field will contribute to current density through induction. This contribution will be reflected in Ohm's law by the addition of a term $\mathbf{u} \times \mathbf{B}$, which leads to models of resistive MHD. Various more specific effects can be taken into account to further refine this law. In this work we will essentially make use of the *Hall effect*: in presence of a magnetic field perpendicular to the current density, Lorentz forces create a local asymmetry of charge distribution, creating a feedback loop that influences the current density. This effect is especially important as it allows the final model to describe (at least partially) the small scales of the plasma, typically around and below the ion characteristic scale. Other effects such as electron pressure and electron inertia can be considered. The generalized Ohm's law can thus be written as:

$$\mathbf{J} = \sigma \left(\mathbf{E} + \mathbf{u} \times \mathbf{B} - \frac{1}{nq_e} \mathbf{J} \times \mathbf{B} + \frac{1}{nq_e} \nabla P_e + \frac{m_e}{nq_e^2} \frac{\partial \mathbf{J}}{\partial t} \right), \quad (1.19)$$

where terms appearing in the right-hand-side respectively represent the aforementioned effects. In this section, and the vast majority of our studies, we will stop at the Hall effect which is enough to describe the first order (ion) small scale behavior of the plasma. This leads to the following expression for the electric field:

$$\mathbf{E} = \frac{1}{\sigma} \mathbf{J} - \mathbf{u} \times \mathbf{B} + \frac{1}{nq_e} \mathbf{J} \times \mathbf{B}. \quad (1.20)$$

The limit $\sigma \rightarrow \infty$ (i.e. $1/\sigma \simeq 0$) is often considered for the generalized Ohm's law, which leads to non-resistive models called *Ideal MHD* and *Hall MHD* (depending on whether we keep the Hall term or not). Note that, in section 4.4, the LF model also takes into account electron pressure. Other more specific models exist, such as the *Electron Magnetohydrodynamics (EMHD)* model in which electrons are assumed to move in almost immobile ions and that is suitable to describe high frequency fluctuations, and that will be studied in chapter 4.

Now that we have an equation linking \mathbf{E} to the other variables of the system, we can make use of Ampère and Faraday equations to derive the induction equation and get rid of the electric field \mathbf{E} :

$$\begin{aligned} \frac{\partial \mathbf{B}}{\partial t} &= -\nabla \times \mathbf{E} = -\frac{1}{\sigma \mu_0} \nabla \times (\nabla \times \mathbf{B}) + \nabla \times (\mathbf{u} \times \mathbf{B}) - \nabla \times \left(\frac{\mathbf{J}}{nq_e} \times \mathbf{B} \right) \\ &= \nabla \times (\mathbf{u} \times \mathbf{B}) - \nabla \times \left(\frac{\mathbf{J}}{nq_e} \times \mathbf{B} \right) + \eta \Delta \mathbf{B}, \end{aligned} \quad (1.21)$$

where $\eta = 1/(\sigma \mu_0)$ is the coefficient of electric resistivity. Putting all equations together, we

finally obtain the equations of Hall MHD for a compressible plasma:

$$\frac{\partial}{\partial t}\rho + \nabla \cdot (\rho\mathbf{u}) = 0, \quad (1.22)$$

$$\rho \left(\frac{\partial}{\partial t}\mathbf{u} + \mathbf{u} \cdot \nabla\mathbf{u} \right) = -\nabla P + \mathbf{J} \times \mathbf{B} + \nu(\Delta\mathbf{u} + \frac{1}{3}\nabla(\nabla \cdot \mathbf{u})), \quad (1.23)$$

$$\frac{\partial\mathbf{B}}{\partial t} = \nabla \times (\mathbf{u} \times \mathbf{B}) - \nabla \times \left(\frac{\mathbf{J}}{nq_e} \times \mathbf{B} \right) + \eta\Delta\mathbf{B}, \quad (1.24)$$

$$\nabla \cdot \mathbf{B} = 0. \quad (1.25)$$

Another version of this set of equations can be obtained for an incompressible plasma by considering the limit of a constant density $\rho = \rho_0$, usually taken equal to unity for the sake of simplicity. The corresponding equations can be found in chapter 2, where both the compressible and incompressible models will be used extensively to derive equations pertaining to turbulent movements of the plasma.

1.2 From space to astrophysical plasmas

1.2.1 The Solar Wind: a turbulence laboratory

As we mentioned in the previous section, plasmas are omnipresent in the universe, appearing under a variety of conditions, with each their own properties and specific behavior. Here we will focus on two astrophysical media that will be studied in more details in the subsequent chapters: the SW and the ISM.

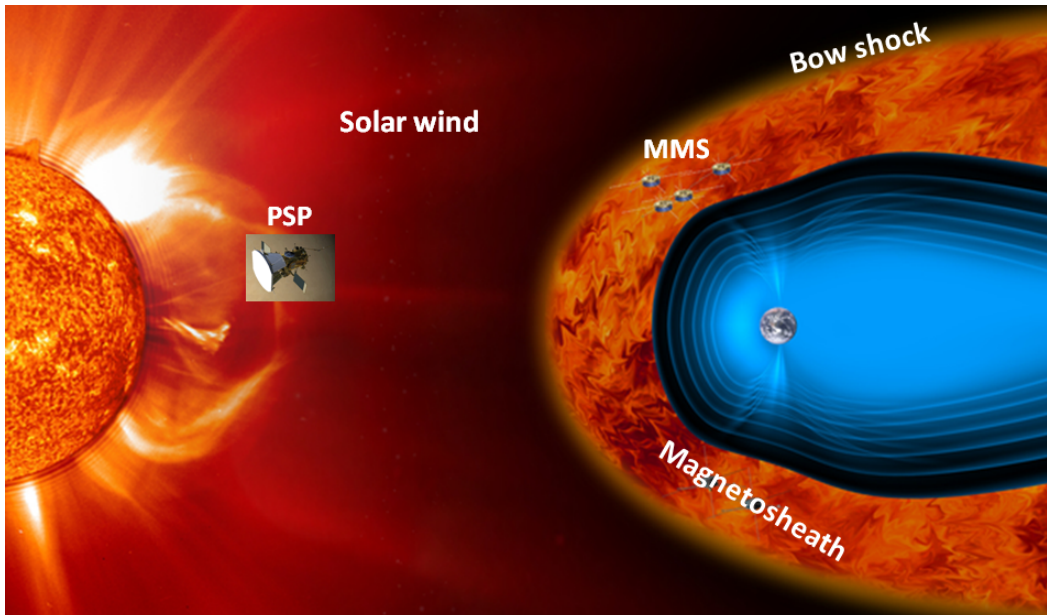


Figure 1.2: Artist representation of the interaction between the SW and Earth's magnetic field. Specific regions of the Sun-Earth couple are labeled, and MMS and Parker Solar Probe (PSP) are sketched in their respective target regions. Credits: ESA

The SW is a flow of charged particles, mainly constituted of electrons, protons (H^+ ions) and α particles (${}^4He^{2+}$ ions), which is identified as a non-collisional plasma. Two categories of SW are usually identified: the slow SW, produced by magnetic loops around the Sun's equator and crossing the solar system at average speeds of $\sim 300km/s$, and the fast SW, which mostly originates from open field lines around magnetic poles of the sun and is usually accelerated towards $\sim 700km/s$ (Rouillard et al., 2009; Pinto, R. F. et al., 2016). More occasional events such as coronal mass ejections, blobs of matter ejected during solar

flares following the break of large magnetic loops on the surface of the solar corona, are also part of the Sun-Earth ecosystem. This plasma boasts incredibly rich physics and has the major advantage of being very close to our planet (at least on an astronomical scale). It is thus accessible to *in-situ* measurements, and has been the target of several satellite missions aiming at gathering data directly from inside the **SW** and neighboring regions such as the Earth's magnetosphere. Missions targeting specifically the sun and the **SW** date back to the old Pioneer missions in the 1960s, followed in the 1970s by [National Aeronautics and Space Administration \(NASA\)](#)'s Helios and Voyager missions, then in the 1990s by the joint [NASA/European Space Agency \(ESA\)](#) Ulysses and [NASA](#)'s Wind and [Advanced Composition Explorer \(ACE\)](#). These have been complemented in the 21st century by missions like [Solar Terrestrial Relations Observatory \(STEREO\)](#) or the more recent [NASA](#)'s [PSP](#) mission and [ESA](#)'s Solar Orbiter.

Due to the intricate interactions between the **SW** and Earth's magnetic field the zone of contact between these two media, known as the *magnetosheath*, has also been the target of several specifically designed missions aiming at investigating the interaction between the **SW** and the magnetosphere along with fundamental processes such as magnetic reconnection, particle acceleration and turbulence. Magnetosheath turbulence is thus often studied jointly to the **SW**, as these missions bring valuable data through instruments optimized for near-Earth regions. Magnetospheric research includes missions such as the joint mission Cluster II or [NASA](#)'s [MMS](#) that have the particularity of being constituted of four satellites flying in a tetrahedral formation, which is a valuable asset for studying the physics governing the magnetosheath and the **SW** as it allows for a local 3D mapping of the structures and spatial gradients. This notably allows for the calculation of 3D spatial derivatives on the data, for instance to estimate the electric current through the curl of \mathbf{B} using a method called *curlometer technique* ([Dunlop et al., 1988, 2002](#)). This method, along with associated ones allowing for the calculation of spatial gradients or divergences, will be investigated in chapter 5.

Beyond the scientific curiosity for the massive near-Earth laboratory that is the **SW**, more grounded reasons have also motivated the study of this neighboring plasma along the past decades. Indeed, the speed and energy of the particles that form the **SW**, especially the ones emitted during powerful solar events (such as some coronal mass ejections, as we mentioned earlier) can pose a threat to the multiple satellites that orbit our planet or to astronauts sent on space vessels. The Earth itself is mostly protected by its magnetic field which acts as a shield against the charged particles of the **SW** yet, in rare cases, exceptional solar events can damage even ground installations. The Carrington solar flare of 1859 for instance, which was the most powerful geomagnetic storm ever registered, provoked massive damages in the telegraph systems, even throwing sparks from pylons and shocking some operators, and formed bright northern auroras at latitudes as low as Cuba. Should an event of this magnitude happen again today, it could cause extended blackouts and damage satellites and electrical systems all around the world. Considering these potential threats, understanding the physics governing solar activity and cycles, the **SW**, and its interactions with Earth's magnetic field may help predicting dangerous solar events and protecting sensitive equipments. These considerations are encompassed in a field of study called *Space Weather*, whose importance has grown significantly with our extended modern usage of satellites and communications.

Through the years, the numerous missions sent gathering data in the **SW** raised lots of questions. An historical problem that stemmed from such observations involves the way the **SW** cools down as it travels through the solar system. Adiabatic cooling models for the **SW** predicted the temperature to decrease as a power law with the radial distance to the Sun, with a scaling neighboring $-4/3$. However, anomalies were found in the temperature profile ([Marsch et al., 1982](#); [Gazis et al., 1994](#)) until, in 1995, [Richardson et al. \(1995\)](#) showed that the temperature profile of the **SW** as registered by Voyager 2 could not match an adiabatic cooling at all (see figure 1.3). Various explanations were proposed to understand this anomalous

cooling, mainly revolving around heating processes inside the SW that would be able to slow down its cooling. One major candidate is the influence of pickup ions [Matthaeus et al. \(1999\)](#); [Isenberg et al. \(2003\)](#): neutral ions of the ISM that wander the heliosphere and can be ionized through their interaction with the SW, leading to a heating of the medium. Another key explanation lies in the turbulent nature of the SW: the dissipation of turbulent energy inside the SW would lead to the heating of the particles ([Verma et al., 1995](#); [Matthaeus et al., 1999](#); [Vasquez et al., 2007](#); [Sahraoui et al., 2009](#); [He et al., 2015](#); [Woodham et al., 2018](#)) (see also reviews from [Bruno and Carbone \(2013\)](#)). The heating problem has been investigated using various approaches, notably that of exact laws that will be further developed in this thesis ([Podesta et al., 2007](#); [Sorriso-Valvo et al., 2007](#); [MacBride et al., 2008](#); [Marino et al., 2008](#); [Carbone et al., 2009](#); [Smith et al., 2009](#); [Stawarz et al., 2009](#); [Osman et al., 2011](#); [Coburn et al., 2015](#); [Banerjee et al., 2016](#); [Hadid et al., 2017](#)) including, most recently, the ones presented in chapter 5 of this thesis through the analysis of data gathered by MMS around the Earth's magnetosphere.

Now, one should note that we are faced with a perplexing contradiction. Historically, SW turbulence has been extensively studied through the use of fluid plasma models that are easier to handle (we will describe the corresponding theory in next section, and then chapter 2). In the meantime, we mentioned the non-collisional nature of the SW, which means that energy dissipation can be driven only through kinetic processes. And as we explained in the previous section, fluid models are not able to describe the kinetic mechanisms at work in the plasma, *a priori*. This paradox is at the heart of one of the major studies presented in chapter 4, and of the key results presented there in an attempt to reconcile the kinetic and fluid descriptions of a non-collisional plasma.

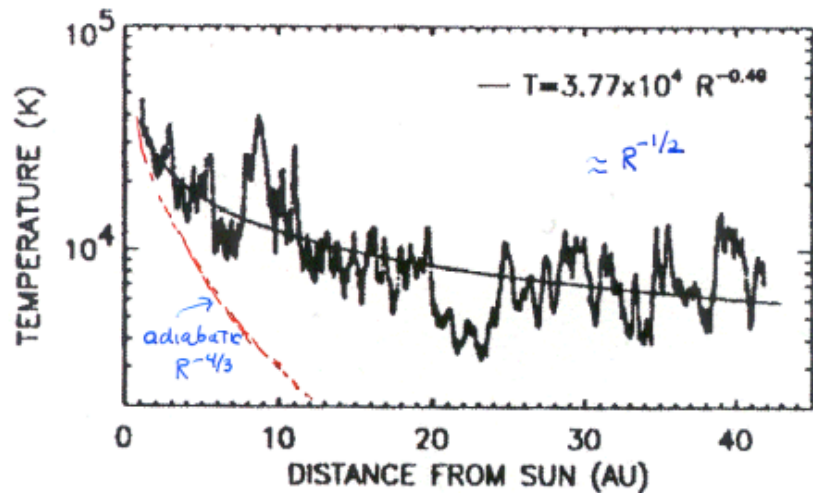


Figure 1.3: As presented in [Richardson et al. \(1995\)](#), Log of the 50-day running average of the plasma temperature from Voyager 2 versus radial distance. The red curve was added to provide an element of comparison with a possible adiabatic cooling.

1.2.2 The Interstellar Medium and star-forming regions

The various media that occupy the interior of a galaxy can be roughly separated in three categories: stars and all that is related to them (pulsars, winds, supernovae...), planets, and everything else that is not a planet nor a star. This "everything else" is usually known as the ISM. It is a blend of cosmic dusts and various types of gas (atomic or molecular, ionized or neutral), with usually a ratio of around 1% dust for 99% gas. The gas share a similar constitution with the SW, with a majority of hydrogen and helium atoms, albeit not always in ion form. Depending on the region of space and the celestial bodies neighboring the ISM, it can take the form of hot diluted plasmas or of colder, denser molecular clouds ([Hennebelle](#)

and Falgarone, 2012).

The ISM plays a major role in the stellar life cycle, as the densest clouds of the ISM are known to be the seat of star formation, such as the Orion complex or the massive Cygnus X region (see figure 1.4). Although the precise details of star formation are not fully understood yet, the general consensus is that within dense molecular clouds form elongated, tubular structures known as *interstellar filaments* that are believed to be a keystone of star formation (Balsara et al., 2001): the accretion along filaments, and especially around filaments crossings (Myers, 2011), would bring enough matter to pre-stellar cores to make them gravitationally unstable and force their collapse and eventual ignition. The main reason behind the formation and properties of these interstellar filaments is thought to be a strongly compressible turbulent activity. It is still unclear to what extent the presence of a magnetic field influences the behavior of turbulence in star-forming regions (McKee and Ostriker, 2007; Federrath, 2016), yet Hydrodynamics (HD) turbulence is often used to try to understand the creation of filaments (Mac Low and Klessen, 2004; Federrath et al., 2010), which proves to be a challenging task due to the usually strongly supersonic nature of these regions of the ISM.

The study on ISM simulations led in chapter 4 of this thesis only considers a Compressible Hydrodynamic (CHD) model, disregarding the influence of a magnetic field, which is not directly in line with the plasma thematic of my PhD. However, it represents a great opportunity to apply the tools developed in this thesis to a massive supersonic 10048³ dataset and see how it can help us better understand supersonic CHD turbulence. This study allowed us to obtain interesting results and shed more light on the relation between interstellar filaments and supersonic turbulence.

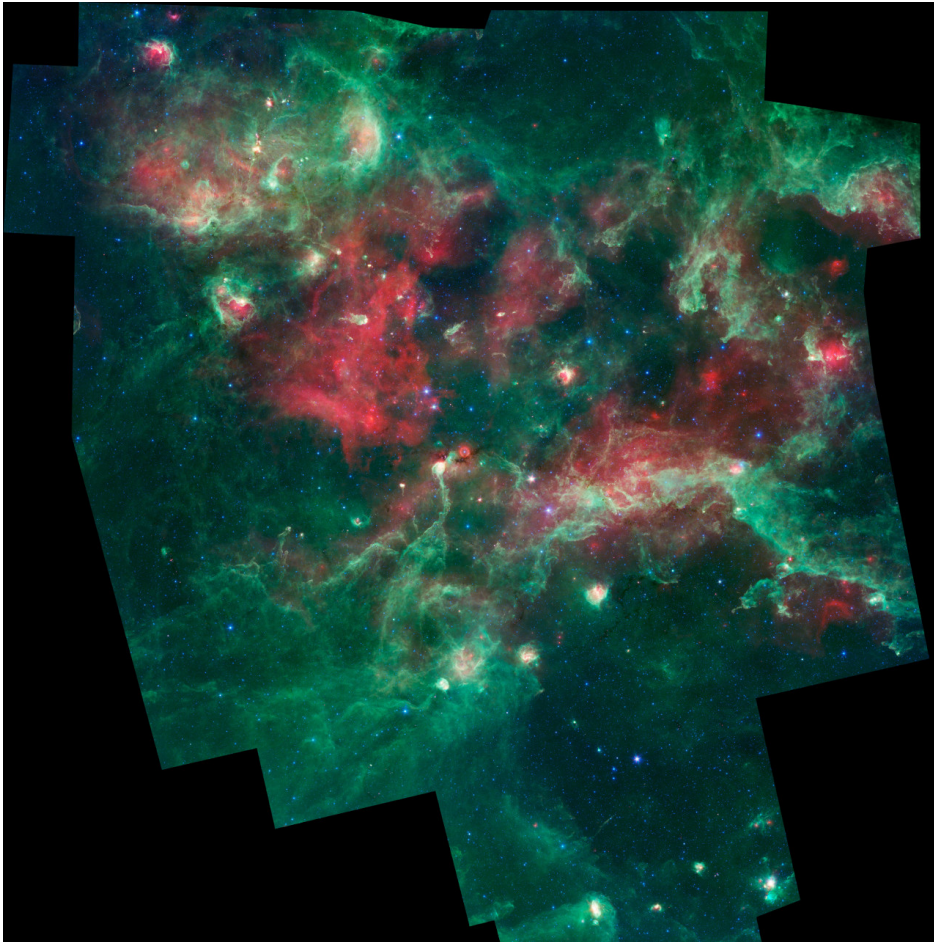


Figure 1.4: Images of the star forming region Cygnus X located in Cygnus constellation, 1.4kpc away from our solar system, taken by the Infrared Array Camera on board of Spitzer space telescope. Credits: NASA/JPL-Caltech/Harvard-Smithsonia CfA.

1.3 Theory of turbulence

1.3.1 Basics of turbulence

In previous section, we mentioned several times the turbulent nature of both the [SW](#) and the [ISM](#). For those who already traveled on board of a plane, the word may sound familiar. For all the others, probably the simplest way to picture a turbulent flow is to look at a flowing river: as long as the path of water is void of obstacles and the river bed even, the water flows smoothly and keeps a clear surface. But should the water travel through a section where rocks emerge from the surface or with a shallower, uneven bed, the flow will be disturbed past the obstacle by the creation of small whirlpools that will eventually vanish as the water keeps moving forward. These whirlpools are an expression of turbulence.



(a) Photo of turbulent motions in a river.

(b) [GHOST](#) simulated plasma turbulence.

Figure 1.5: Examples of turbulent flows observed in a flowing river and in a simulated plasma. Note the differences on the surface of the water before and after crossing the rock lines in the photo. The simulated picture is extracted from the compressible plasma datasets analyzed in chapter 4 and obtained with the [GHOST](#) suite.

More generally speaking, turbulence in fluid mechanics is a non-linear phenomenon that is characterized by the creation of vortices in fluids with a low enough viscosity. This phenomenon is present in a wide variety of natural media such as water bodies, air masses or, as we already mentioned them, astrophysical flows and plasmas, but also in artificial plasmas such as the ones generated in fusion reactors. Despite turbulent phenomena being so widely observed, understanding the dynamics of turbulent flows remains one of the most challenging problems of classical physics. The main obstacle is that turbulence is a chaotic physical process, which means that the slightest change in the initial conditions of a turbulent system is enough to render it totally unpredictable.

Due to its chaotic nature, turbulence is often studied through statistical methods that help regaining a certain degree of predictability. We will also consider in the entirety of this thesis that all studied turbulent flows obey two important assumptions : statistical homogeneity, i.e. invariance of the statistics of the turbulent flow through a translation in space, and statistical stationarity, i.e. invariance of the statistics of the turbulent flow through a translation in time. The first hypothesis is generally assumed to be verified in astrophysical plasmas (due to their large size we usually never reach the "edge" of the plasma), as long as we do not cross specific localized structures such as shocks and discontinuities. The second one is usually guaranteed by a balance between the energy injected and dissipated for a fully developed turbulence, which puts the system in a stationary state. Instead of considering and studying a physical variable \mathbf{X} , we will usually work with its ensemble average $\langle \mathbf{X} \rangle$ instead. The ensemble average

is a tool originating from statistical physics that represents the average of the variable over a large number of realizations. However, under the aforementioned hypothesis of statistical homogeneity the ensemble average can be identified to a classical space average based on the ergodic theorem. This identification will be made in all the studies presented here.

1.3.2 The zeroth law of turbulence

We mentioned earlier that turbulence forms in fluids of low viscosity. It is thus interesting to define the quantity known as the *Reynolds number*: it is a dimensionless quantity inversely proportional to the viscosity and that quantifies the turbulent nature of the system. It is defined as:

$$R_e = \frac{UL}{\nu}, \quad (1.26)$$

where U and L are respectively the characteristic velocity and scale of the turbulent system. A flow with a low Reynolds number (and thus a high viscosity or a small L) will behave as what is called a *laminar* flow, with sheets of water flowing parallel to one another, whereas a flow with a high Reynolds number (and consequently a low viscosity or a large L , more pertinent in an astrophysical context) will behave as a turbulent flow and lead to the creation of vortices. In the case of a plasma a similar quantity, the magnetic Reynolds number, can be defined for magnetic diffusivity:

$$R_m = \frac{UL}{\eta}. \quad (1.27)$$

These considerations on viscosity and Reynolds number lead us to mention one of the most important properties of a turbulent medium. In the simplest case of a freely decaying incompressible HD turbulence, it can be shown that the energy evolves as:

$$\frac{\partial \langle E \rangle}{\partial t} = \frac{1}{2} \frac{\partial \langle \mathbf{u}^2 \rangle}{\partial t} = \nu \langle \mathbf{u} \cdot \Delta \mathbf{u} \rangle = -\nu \langle (\nabla \times \mathbf{u})^2 \rangle. \quad (1.28)$$

A derivation of this relation is shown in chapter 2 for the [Incompressible Hall Magnetohydrodynamic \(IHMHD\)](#) model, and leads to the similar equation (2.20). The natural consequence of equation (1.28) is that in the limit of an infinite Reynolds number, so when viscosity tends to zero, the energy dissipation rate is expected to tend to zero as well. And yet, it does not: when the viscosity goes to zero, the mean dissipation rate reaches a constant value ε , independent of the viscosity:

$$\lim_{\nu \rightarrow 0} \frac{\partial \langle E \rangle}{\partial t} = -\varepsilon < 0. \quad (1.29)$$

This property is often called the *zeroth law of turbulence*, and is at the basis of the concept of *turbulent energy cascade*. It can be observed in figure 1.6a that shows the time evolution of the energy dissipation rate depending on the Reynolds number: one can see that for large values of R_E , the energy dissipation rate tends to a non-zero limit.

Looking back at equation (1.28), the only possible way to have a non-zero limit for the energy dissipation rate is that the square vorticity $(\nabla \times \mathbf{u})^2$ increases towards infinity at the same speed as ν tends to zero. Physically speaking, this means that smaller and smaller vortices are created in the turbulent medium as the viscosity decreases. Thus in practice, for a very high Reynolds number, the energy contained in vortices of a given scale will be transferred to vortices of smaller scale, without loss due to the absence of viscous effects on any large enough vortex, and the process will repeat until the resulting vortices are small enough for viscous dissipation to finally kick in. This process of turbulent energy cascading towards small scales is known as an *inertial cascade*, and the scales that bear the cascade are called the *inertial range*. The turbulent energy cascades from a scale to another at a rate ε that is usually called the *energy cascade rate*, and that remains constant throughout the entire inertial range. A depiction of this phenomenon is shown in figure 1.6b.

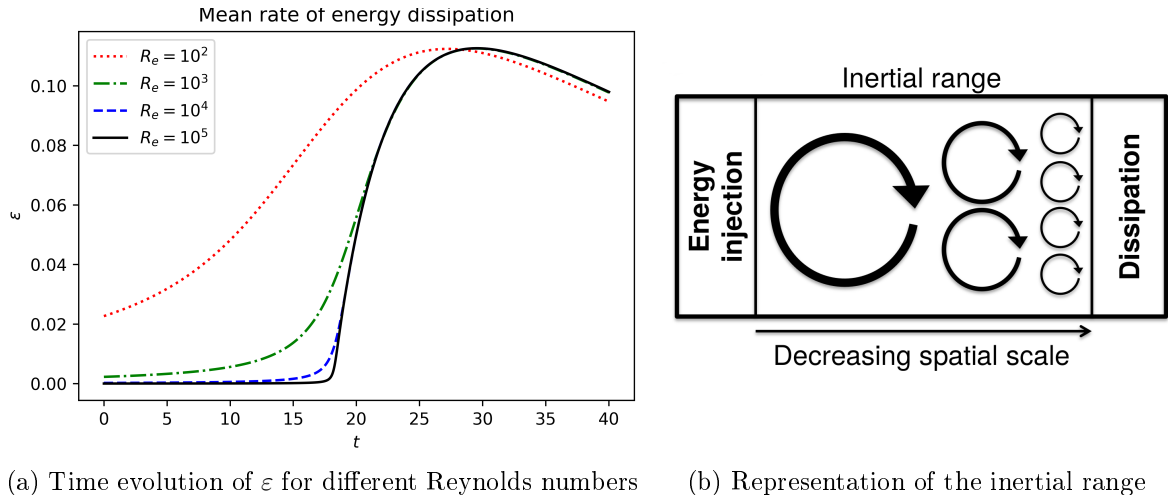


Figure 1.6: Illustration of the zeroth law of turbulence and of the concept of turbulent cascade. Note that simulations whose results are shown in the left panel are in free decay, hence the behavior of ε : it rises to a maximum corresponding to a fully developed turbulence, then decay as the energy is slowly dissipated.

The energy cascade rate ε can be estimated through equations involving the structure functions of physical variables and that are known as *exact laws*. It was [Kolmogorov \(1941\)](#) who paved the way with his 4/5th exact law for incompressible [HD](#):

$$-\frac{4}{5}\varepsilon\ell = \left\langle [\mathbf{u}(\mathbf{r} + \boldsymbol{\ell}) - \mathbf{u}(\mathbf{r})]^3 \right\rangle \quad (1.30)$$

Subsequently, different exact laws have been derived through the years for a variety of fluid models such as [CHD](#) ([Galtier and Banerjee, 2011](#); [Banerjee and Galtier, 2014](#)), (in)compressible [MHD](#) ([Politano and Pouquet, 1998](#); [Banerjee and Galtier, 2013](#); [Andrés and Sahraoui, 2017](#)) and finally (in)compressible Hall [MHD](#) ([Galtier, 2008](#); [Banerjee and Galtier, 2017](#); [Hellinger et al., 2018](#); [Andrés et al., 2018](#)), for which we derived the evolution equations at the beginning of this chapter. These laws are computed by averaging over the entire studied domain; similar versions holding for just a local averaging in spacetime were also obtained thanks to the theory of distributions ([Duchon and Robert, 2000](#); [Eyink, 2002](#)), but these laws are outside of the scope of this thesis. A vast majority of the work presented in this thesis consists in calculating and applying exact laws to a variety of fluid and plasma simulations in order to unravel fundamental properties of turbulence.

1.3.3 Spectral approach of turbulence

Thus far, we primarily gave an introduction to turbulence in real space. However, turbulence is also often studied in Fourier space through the analysis of kinetic and magnetic energy spectra. Thus, we define in Fourier space the spectral energy density as:

$$E(\mathbf{k}) = \frac{1}{2} \langle |\hat{\mathbf{u}}(\mathbf{k})|^2 \rangle, \quad (1.31)$$

where $\hat{\mathbf{u}}$ is the Fourier transform of the velocity field \mathbf{u} and \mathbf{k} is the wave vector corresponding to the spatial scale ℓ . This quantity represents the amount of energy contained in an infinitesimal volume $d\mathbf{k}$ at position \mathbf{k} in Fourier space. A similar quantity can be defined for the magnetic field:

$$E_m(\mathbf{k}) = \frac{1}{2} \langle |\hat{\mathbf{B}}(\mathbf{k})|^2 \rangle. \quad (1.32)$$

In practice, the energy density is usually integrated, assuming isotropy, for a constant value of $||\mathbf{k}|| = k$ (note that we use spherical coordinates here):

$$E(k) = \iint \frac{1}{2} |\hat{\mathbf{u}}(\mathbf{k})|^2 dS = \int_{\phi=0}^{2\pi} \int_{\theta=0}^{\pi} \frac{1}{2} |\hat{\mathbf{u}}(k)|^2 k^2 \sin(\theta) d\theta d\phi = 2\pi k^2 |\hat{\mathbf{u}}(k)|^2, \quad (1.33)$$

where $k = 2\pi/\ell$. $E(k)$ now represents the amount of energy contained in the spectral band $[k, k + dk]$ and is the energy spectrum that is usually studied in turbulence.

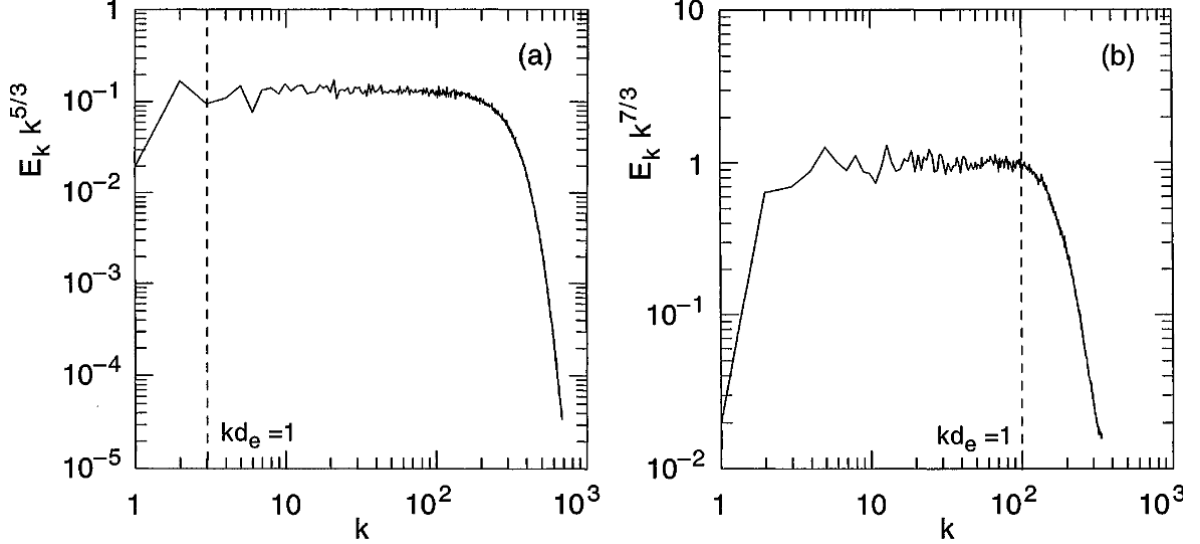


Figure 1.7: Compensated energy spectra from a 2D DNS of EMHD turbulence, as presented in Biskamp et al. (1996): (a) $k^{5/3} E_k$ for $d_e = 0.3$; (b) $k^{7/3} E_k$ for $d_e = 0.01$, where d_e is the electron inertial length.

One of the main reasons energy spectra are widely used in turbulence is that they tend to be easier to compute than exact laws while following precise behaviors in presence of turbulent motions. This is easily seen when considering Kolmogorov's law (1.30) with a simple dimensional analysis: indeed the law states that, in presence of a constant energy cascade rate ε (i.e. in the inertial range), $u^3 \propto \ell$. In Fourier space this becomes $u^3 \propto k^{-1}$ and so:

$$E(k) \propto \frac{u^2}{k} \propto k^{-5/3}. \quad (1.34)$$

A kinetic energy spectrum scaling as $k^{-5/3}$ is probably the most widely used marker of a Kolmogorov turbulent cascade. Note that this spectrum only stands for simple MHD: turbulence driven by Hall MHD will have, at small (sub-ion) scales, a theoretical scaling of $k^{-7/3}$. Figures 1.7 and 1.8 summarize these turbulent scalings over a broad range of frequencies in DNS and real *in situ* data respectively. Note that time scales and frequencies are usually used for spacecraft data analysis instead of spatial scales and wave numbers. More explanations about this are given in the dedicated chapter 5.

In this thesis, we will rarely make use of energy spectra and will instead mainly work in real space. However, we will make use of spectra on two occasions. In chapter 4, energy spectra will be used to identify deviations from Kolmogorov turbulence in supersonic CHD simulations and characterize specific turbulent regimes. In chapter 5, energy spectra will be used as a key marker of the presence of a turbulent cascade to select which MMS burstmode events to study.

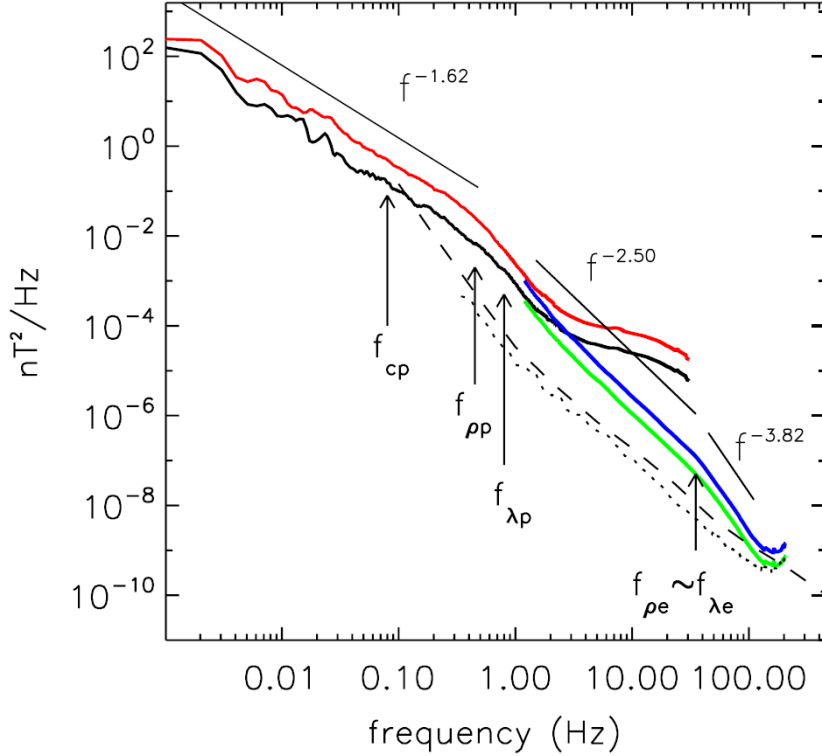


Figure 1.8: As presented in [Sahraoui et al. \(2009\)](#): parallel (black) and perpendicular (red) magnetic spectra of Cluster’s FGM data ($f < 33$ Hz) and STAFF-SC data (respectively, light line; green online and dark line; blue online); $1.5 < f < 225$ Hz). The STAFF-SC noise level as measured in the laboratory and in-flight are plotted as dashed and dotted lines, respectively. The straight black lines are power law fits to the spectra.

1.4 Overview of the thesis

This thesis aims at studying in details plasma turbulence through the use of exact laws derived for both the incompressible and compressible Hall MHD models. To this end, I provide a detailed derivation of the two corresponding exact laws in chapter 2, along with a discussion of the relation of these new exact laws to already existing ones. In order to apply these exact laws to DNS data, I conceived the general structure of a numerical code whose details and are explained in chapter 3. In this chapter I discuss the strengths, limitations and constraints of the code and provide a mathematical overview of the models used. Chapter 4 is then dedicated to all the studies led on the various simulated datasets at our disposal, and include:

- An EMHD study aiming at understanding the way IHMHD exact laws relate to each other, and gain a better understanding on how they react to the presence of a background magnetic field.
- A Compressible Hall Magnetohydrodynamic (CHMHD) study focused on the detailed analysis to the compressible exact law derived in chapter 2, and that provides more information on the behavior of its scale-dependent components and on the validity of the hypotheses leading to its derivation.
- A CHMHD, LF focused study in which we tackle the fundamental problem of bridging together the fluid and kinetic plasma descriptions, and show that predictions on the kinetic mechanisms at work in the plasma can be retrieved through the analysis of the fluid energy cascade.
- A CHD study led on a massive 10048^3 supersonic simulation that provides important insights into a two-regime turbulence at work in the ISM, with possible ties to the

existence of interstellar filaments.

Finally, I propose in chapter 5 a last study that makes use of the same exact laws applied, this time, to *in situ* data gathered by MMS in the Earth's magnetosphere. Thanks to the tetrahedral formation of the four satellites, one can compute all the fields divergences required for the calculation of the compressible law by making use of gradients estimation techniques. In the meantime, I investigate the performances and limitations of this method thanks to artificial multi-spacecraft fly-by performed in our simulation data, commonly referred to as *virtual spacecraft data*.

Chapter 2

Exact laws in Hall MHD turbulence

2.1 Introduction

As stated in the previous chapter, exact laws are a statistical tool used to evaluate the turbulent energy cascading within the inertial range as a function of second or third-order structure functions of the turbulent fluctuations. The true strength of these laws, and the reason for their "exact" appellation is that no mathematical approximations such as asymptotic developments are required to obtain them. They only require a few classical assumptions on the nature of the system to be derived, typically statistical homogeneity, time stationarity and a high Reynolds number, and oftentimes assumptions pertaining to the spatial symmetries of the system such as isotropy or axi-symmetry (usually around the direction of the background magnetic field, if any).

The complexity of exact laws and the variables they depend on vary with the model used to describe the medium. The first one was obtained by [Kolmogorov \(1941\)](#) for an incompressible HD turbulence and is usually known as the 4/5th law (see equation (1.30)). It was obtained through tensorial calculation thanks to previous results from [von Kármán and Howarth \(1938\)](#) who obtained a dynamical equation for second-order correlation tensors, however this is not a widely represented method in recent derivations and is not the one used here. Instead we will use a direct calculation similar to the one first proposed by [Yaglom \(1949\)](#) and later refined by [Antonia et al. \(1997\)](#) that led, for the same model, to the slightly different 4/3rd law. This method aims at deriving the dynamic equation of a well-chosen correlator for the energy of the system which allows one, under the aforementioned assumptions, to obtain the desired exact law. I will develop in this chapter the theoretical derivation and properties of two exact laws, pertaining to the two models of three-dimensional, isothermal IHMHD and CHMHD.

Prior to presenting the theory of exact laws we introduce some notations and relations that all derivations have in common. These calculations rely on the key hypothesis of statistical homogeneity, which means that the system is supposed to be statistically invariant under a spatial translation. As a consequence, any correlation function between two points of the system \mathbf{r} and \mathbf{r}' will only depend on the relative distance between these points. Thus, we introduce the spatial increment $\boldsymbol{\ell} = \mathbf{r}' - \mathbf{r}$. To ease the calculations we define for any variable, e.g. the velocity field \mathbf{u} , the notations $\mathbf{u} \equiv \mathbf{u}(\mathbf{r})$ and $\mathbf{u}' \equiv \mathbf{u}(\mathbf{r}')$ (see Figure 2.1 for a visual representation). We also use the notations $\delta\mathbf{u} \equiv \mathbf{u}' - \mathbf{u}$ and $\bar{\delta}\mathbf{u} \equiv \frac{1}{2}(\mathbf{u}' + \mathbf{u})$.

The assumption of statistical homogeneity has important consequences on the relative derivative operator $\nabla_{\boldsymbol{\ell}}$, which represents derivation along the $\boldsymbol{\ell}$ variable. Let α and \mathbf{Y} be arbitrary scalar and vector fields, we have the following relations:

$$\langle \nabla \cdot (\alpha \mathbf{Y}') \rangle = - \nabla_{\boldsymbol{\ell}} \cdot \langle (\alpha \mathbf{Y}') \rangle, \quad (2.1)$$

$$\langle \nabla' \cdot (\alpha \mathbf{Y}') \rangle = \nabla_{\boldsymbol{\ell}} \cdot \langle (\alpha \mathbf{Y}') \rangle, \quad (2.2)$$

$$\nabla_{\boldsymbol{\ell}} \cdot \langle (\alpha \mathbf{Y}') \rangle = - \nabla_{\boldsymbol{\ell}} \cdot \langle (\alpha' \mathbf{Y}) \rangle \quad (2.3)$$

where ∇ and ∇' are respectively the derivative operators for the \mathbf{r} and \mathbf{r}' variables, and $\langle \rangle$ is

the spatial average introduced in chapter 1 for the study of turbulence. Note that ∇ and ∇' only apply to fields depending on \mathbf{r} and \mathbf{r}' respectively, which means that $\langle \nabla \cdot \mathbf{Y}' \rangle = 0$ and $\langle \nabla' \cdot \mathbf{Y} \rangle = 0$. An immediate consequence of this is that $\nabla_{\ell} \cdot \langle (\alpha \mathbf{Y}) \rangle = -\nabla'_{\ell} \cdot \langle (\alpha' \mathbf{Y}') \rangle = 0$.

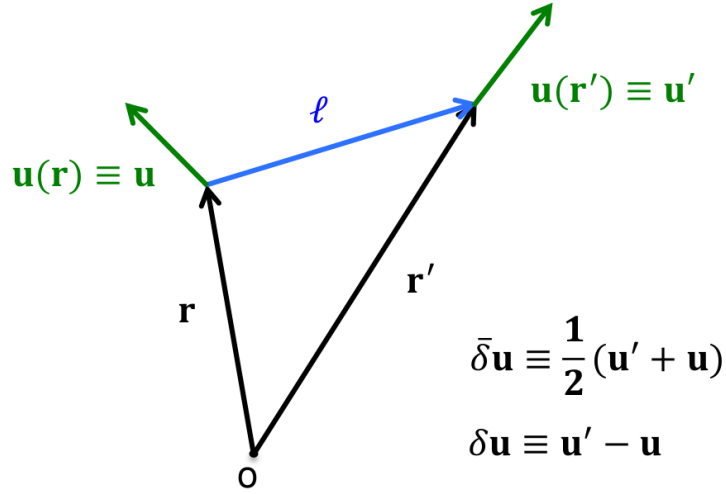


Figure 2.1: Visual representation of the relation between position vectors \mathbf{r} and \mathbf{r}' , connected by the increment ℓ . A reminder of the main notations is also given.

2.2 Exact law in the incompressible Hall MHD model

2.2.1 Description of the model

Now that these fundamental relations have been introduced we can start working on the derivation of the laws, starting from the simplest one, which is obtained for IHMHD. We (re)introduce the following notations: we note \mathbf{u} the velocity field, \mathbf{B} the magnetic field and $\mathbf{J} = \nabla \times \mathbf{B} / \mu_0$ the electric current; the mass density ρ_0 is taken constant and equal to unity. We use the Alfvén units for the magnetic field and the electric current, i.e. $\mathbf{b} = \mathbf{B} / \sqrt{\mu_0 \rho_0}$ and $\mathbf{j} = \nabla \times \mathbf{b}$. In the incompressible case we get the following velocity and induction equations,

$$\partial_t \mathbf{u} = -(\mathbf{u} \cdot \nabla) \mathbf{u} + (\mathbf{b} \cdot \nabla) \mathbf{b} - \nabla P + \mathbf{d}_\nu + \mathbf{f}, \quad (2.4)$$

$$\begin{aligned} \partial_t \mathbf{b} = & -(\mathbf{u} \cdot \nabla) \mathbf{b} + (\mathbf{b} \cdot \nabla) \mathbf{u} \\ & + d_i (\mathbf{j} \cdot \nabla) \mathbf{b} - d_i (\mathbf{b} \cdot \nabla) \mathbf{j} + \mathbf{d}_\eta, \end{aligned} \quad (2.5)$$

$$\nabla \cdot \mathbf{b} = 0, \quad (2.6)$$

$$\nabla \cdot \mathbf{u} = 0, \quad (2.7)$$

where $P = p + b^2/2$ is the total pressure and \mathbf{f} a stationary homogeneous external force acting only at large scales. $d_i \equiv c/\omega_{pi}$, where c is the speed of light and $\omega_{pi} = \sqrt{n_i q_e^2 / m_i \epsilon_0}$ the plasma ionic pulsation, is the ion inertial length, i.e. the scale at which the Hall term becomes effective in the generalized Ohm's law. The dissipation terms are

$$\mathbf{d}_\nu = \nu \Delta \mathbf{u}, \quad (2.8)$$

$$\mathbf{d}_\eta = \eta \Delta \mathbf{b}, \quad (2.9)$$

where ν is the kinematic viscosity and η the magnetic diffusivity. Note that using the relation $\langle \mathbf{X} \cdot \Delta \mathbf{X} \rangle = -\langle (\nabla \times \mathbf{X})^2 \rangle$, which is valid for any incompressible vector field \mathbf{X} , we have:

$$\langle \mathbf{u} \cdot \mathbf{d}_\nu \rangle + \langle \mathbf{b} \cdot \mathbf{d}_\eta \rangle = -\nu \langle \omega^2 \rangle - \eta \langle \mathbf{j}^2 \rangle, \quad (2.10)$$

with $\boldsymbol{\omega} = \nabla \times \mathbf{u}$ the vorticity, which gives the expression of the mean rate of total energy dissipation.

2.2.2 Calculation of the dynamical equation

In order to retrieve the exact law from equations (2.4)-(2.7) we need to search for a dynamical equation for a well-chosen structure function or correlation function. Three different laws already exist in IHMHD (Galtier, 2008; Banerjee and Galtier, 2017; Hellinger et al., 2018), stemming from the analysis of different functions, yet relying on the same underlying assumptions. On the one hand, the laws obtained by Galtier (2008) (hereafter G08) and Banerjee and Galtier (2017) (hereafter BG17) are derived from the dynamical analysis of the two-points correlator,

$$\langle R_E \rangle = \left\langle \frac{\mathbf{u} \cdot \mathbf{u}' + \mathbf{b} \cdot \mathbf{b}'}{2} \right\rangle. \quad (2.11)$$

On the other hand, the law derived by Hellinger et al. (2018), as well as the one derived here (Ferrand et al., 2019), stem from the evolution equation of the second order structure function

$$\langle S \rangle = \langle |\mathbf{u}' - \mathbf{u}|^2 + |\mathbf{b}' - \mathbf{b}|^2 \rangle, \quad (2.12)$$

which is linked to expression (2.11) through the relation

$$\langle S/4 \rangle = \langle E^{tot} \rangle - \langle R_E \rangle, \quad (2.13)$$

where the total energy is defined as $E^{tot} = u^2/2 + b^2/2$. Using equations (2.4)-(2.7) we can calculate the various components of $\partial_t \langle S \rangle$. Taking $\partial_t \langle \mathbf{u} \cdot \mathbf{u}' \rangle$ as an example we get:

$$\begin{aligned} \partial_t \langle \mathbf{u} \cdot \mathbf{u}' \rangle &= \mathbf{u} \cdot [-(\mathbf{u}' \cdot \nabla')\mathbf{u}' + (\mathbf{b}' \cdot \nabla')\mathbf{b}' - \nabla' P'] + \mathbf{u}' \cdot [-(\mathbf{u} \cdot \nabla)\mathbf{u} + (\mathbf{b} \cdot \nabla)\mathbf{b} - \nabla P] \\ &\quad + \mathbf{u}' \cdot \mathbf{d}_\nu + \mathbf{u} \cdot \mathbf{d}'_\nu + \mathbf{u}' \cdot \mathbf{f} + \mathbf{u} \cdot \mathbf{f}' \\ &= -\nabla' \cdot [(\mathbf{u} \cdot \mathbf{u}')\mathbf{u}' - (\mathbf{u} \cdot \mathbf{b}')\mathbf{b}' + P'\mathbf{u}] - \nabla \cdot [(\mathbf{u} \cdot \mathbf{u}')\mathbf{u} - (\mathbf{u}' \cdot \mathbf{b})\mathbf{b} + P\mathbf{u}] \\ &\quad + \mathbf{u}' \cdot \mathbf{d}_\nu + \mathbf{u} \cdot \mathbf{d}'_\nu + \mathbf{u}' \cdot \mathbf{f} + \mathbf{u} \cdot \mathbf{f}'. \end{aligned} \quad (2.14)$$

Similarly we obtain for all other components:

$$\begin{aligned} \partial_t \langle \mathbf{b} \cdot \mathbf{b}' \rangle &= -\nabla' \cdot [(\mathbf{b} \cdot \mathbf{b}')\mathbf{u}' - (\mathbf{b} \cdot \mathbf{u}')\mathbf{b}' - d_i(\mathbf{b} \cdot \mathbf{b}')\mathbf{j}' + d_i(\mathbf{b} \cdot \mathbf{j}')\mathbf{b}'] \\ &\quad - \nabla \cdot [(\mathbf{b}' \cdot \mathbf{b})\mathbf{u} - (\mathbf{b}' \cdot \mathbf{u})\mathbf{b} - d_i(\mathbf{b}' \cdot \mathbf{b})\mathbf{j} + d_i(\mathbf{b}' \cdot \mathbf{j})\mathbf{b}] \\ &\quad + \mathbf{b}' \cdot \mathbf{d}_\eta + \mathbf{b} \cdot \mathbf{d}'_\eta, \end{aligned} \quad (2.15)$$

$$\partial_t \langle \mathbf{u}^2 \rangle = -\nabla \cdot [(\mathbf{u} \cdot \mathbf{u})\mathbf{u}] + 2\mathbf{u} \cdot (\mathbf{b} \cdot \nabla)\mathbf{b} - 2\mathbf{u} \cdot \nabla P + 2\mathbf{u} \cdot \mathbf{d}_\nu + 2\mathbf{u} \cdot \mathbf{f}, \quad (2.16)$$

$$\begin{aligned} \partial_t \langle \mathbf{b}^2 \rangle &= -\nabla \cdot [(\mathbf{b} \cdot \mathbf{b})\mathbf{u}] + 2\mathbf{b} \cdot (\mathbf{b} \cdot \nabla)\mathbf{u} \\ &\quad + d_i \nabla \cdot [(\mathbf{b} \cdot \mathbf{b})\mathbf{j}] - 2d_i \mathbf{b} \cdot (\mathbf{b} \cdot \nabla)\mathbf{j} + 2\mathbf{b} \cdot \mathbf{d}_\eta. \end{aligned} \quad (2.17)$$

Expressions for $\partial_t \langle \mathbf{u}^2 \rangle$ and $\partial_t \langle \mathbf{b}^2 \rangle$ are obtained by taking all variables in Eqs. (2.16)–(2.17) at point \mathbf{r} instead of \mathbf{r}' , which comes down to replacing them by their primed notations. Taking spatial averages and using relations (2.1)–(2.2) along with the incompressibility equation (2.7) the contribution of the pressure terms cancels out:

$$\begin{aligned} \langle \mathbf{u} \cdot \nabla P \rangle &= \langle \nabla \cdot (P\mathbf{u}) \rangle = -\langle \nabla' \cdot (P\mathbf{u}) \rangle = 0, \\ \langle \nabla' \cdot (P'\mathbf{u}) \rangle &= -\langle \nabla \cdot (P'\mathbf{u}) \rangle = 0. \end{aligned}$$

By remarking that,

$$\begin{aligned} \langle \mathbf{u} \cdot (\mathbf{b} \cdot \nabla)\mathbf{b} \rangle &= -\langle \mathbf{b} \cdot (\mathbf{b} \cdot \nabla)\mathbf{u} \rangle, \\ \langle \mathbf{b} \cdot (\mathbf{b} \cdot \nabla)\mathbf{j} \rangle &= -\langle \mathbf{j} \cdot (\mathbf{b} \cdot \nabla)\mathbf{b} \rangle, \end{aligned}$$

a combination of Eq. (2.14) to (2.17) leads to,

$$\begin{aligned}
\partial_t \langle S \rangle = & 2\nabla_\ell \cdot \langle (\mathbf{u} \cdot \mathbf{u}') \delta \mathbf{u} + (\mathbf{b} \cdot \mathbf{b}') \delta \mathbf{u} - (\mathbf{u} \cdot \mathbf{b}') \delta \mathbf{b} - (\mathbf{b} \cdot \mathbf{u}') \delta \mathbf{b} \rangle \\
& + 2d_i \nabla_\ell \cdot \langle -(\mathbf{b} \cdot \mathbf{b}') \delta \mathbf{j} + (\mathbf{b} \cdot \mathbf{j}') \mathbf{b}' - (\mathbf{b}' \cdot \mathbf{j}) \mathbf{b} \rangle \\
& + 2d_i \langle \mathbf{j} \cdot (\mathbf{b} \cdot \nabla) \mathbf{b} + \mathbf{j}' \cdot (\mathbf{b}' \cdot \nabla') \mathbf{b}' \rangle \\
& + 4 \langle \mathbf{u} \cdot \mathbf{d}_\nu \rangle - 2 \langle \mathbf{u} \cdot \mathbf{d}'_\nu \rangle - 2 \langle \mathbf{u}' \cdot \mathbf{d}_\nu \rangle + 4 \langle \mathbf{b} \cdot \mathbf{d}_\eta \rangle - 2 \langle \mathbf{b} \cdot \mathbf{d}'_\eta \rangle - 2 \langle \mathbf{b}' \cdot \mathbf{d}_\eta \rangle \\
& + 4 \langle \mathbf{u} \cdot \mathbf{f} \rangle - 2 \langle \mathbf{u} \cdot \mathbf{f}' \rangle - 2 \langle \mathbf{u}' \cdot \mathbf{f} \rangle. \tag{2.18}
\end{aligned}$$

Using relations (2.16)–(2.17) one can derive the equation of energy conservation (Galtier, 2016). Indeed, using relations (2.1)–(2.3) along with vectorial relations $\nabla \times (\mathbf{X} \times \mathbf{Y}) = \mathbf{X}(\nabla \cdot \mathbf{Y}) - \mathbf{Y}(\nabla \cdot \mathbf{X}) + (\mathbf{Y} \cdot \nabla) \mathbf{X} - (\mathbf{X} \cdot \nabla) \mathbf{Y}$ and $\nabla \cdot (\mathbf{X} \times \mathbf{Y}) = \mathbf{Y} \cdot \nabla \times \mathbf{X} - \mathbf{X} \cdot \nabla \times \mathbf{Y}$, we show that:

$$\begin{aligned}
\langle \mathbf{b} \cdot (\mathbf{b} \cdot \nabla) \mathbf{j} \rangle &= \langle \mathbf{b} \cdot [(\mathbf{j} \cdot \nabla) \mathbf{b} + \nabla \times (\mathbf{j} \times \mathbf{b})] \rangle \\
&= -\frac{1}{2} \nabla_\ell \cdot \langle (\mathbf{b} \cdot \mathbf{b}) \mathbf{j} \rangle - \nabla_\ell \cdot \langle (\mathbf{j} \times \mathbf{b}) \times \mathbf{b} \rangle + \langle (\mathbf{j} \times \mathbf{b}) \cdot \mathbf{j} \rangle \\
&= 0 \tag{2.19}
\end{aligned}$$

and we then immediately have:

$$\partial_t \langle E^{tot} \rangle = \langle \mathbf{u} \cdot \mathbf{d}_\nu \rangle + \langle \mathbf{b} \cdot \mathbf{d}_\eta \rangle + \langle \mathbf{u} \cdot \mathbf{f} \rangle. \tag{2.20}$$

With equalities $\nabla \cdot [(\mathbf{b} \cdot \mathbf{j}') \mathbf{b}] = \mathbf{j}' \cdot (\mathbf{b} \cdot \nabla) \mathbf{b}$ and $\nabla' \cdot [(\mathbf{b}' \cdot \mathbf{j}) \mathbf{b}'] = \mathbf{j} \cdot (\mathbf{b}' \cdot \nabla') \mathbf{b}'$ and equation (2.20) we can further simplify (2.18) to:

$$\begin{aligned}
\partial_t \langle S \rangle = & 4\partial_t \langle E^{tot} \rangle - \nabla_\ell \cdot \langle (\delta \mathbf{u} \cdot \delta \mathbf{u} + \delta \mathbf{b} \cdot \delta \mathbf{b}) \delta \mathbf{u} - 2(\delta \mathbf{u} \cdot \delta \mathbf{b}) \delta \mathbf{b} \rangle \\
& - d_i \nabla_\ell \cdot \langle -(\delta \mathbf{b} \cdot \delta \mathbf{b}) \delta \mathbf{j} + 2(\delta \mathbf{b} \cdot \delta \mathbf{j}) \delta \mathbf{b} \rangle + 2d_i \langle \delta \mathbf{j} \cdot \delta [(\mathbf{b} \cdot \nabla) \mathbf{b}] \rangle \\
& - 2 \langle \mathbf{u} \cdot \mathbf{d}'_\nu \rangle - 2 \langle \mathbf{u}' \cdot \mathbf{d}_\nu \rangle - 2 \langle \mathbf{b} \cdot \mathbf{d}'_\eta \rangle - 2 \langle \mathbf{b}' \cdot \mathbf{d}_\eta \rangle - 2 \langle \mathbf{u} \cdot \mathbf{f}' \rangle - 2 \langle \mathbf{u}' \cdot \mathbf{f} \rangle. \tag{2.21}
\end{aligned}$$

Bringing another simplification to (2.21) will require a fair amount of calculation on the Hall terms. We adopt the same notation as Hellinger et al. (2018):

$$A = d_i \langle \delta \mathbf{j} \cdot \delta [(\mathbf{b} \cdot \nabla) \mathbf{b}] \rangle, \tag{2.22}$$

and making use of the vectorial relation $\nabla(\mathbf{X} \cdot \mathbf{X}) = 2\mathbf{X} \times (\nabla \times \mathbf{X}) + 2(\mathbf{X} \cdot \nabla) \mathbf{X}$ we rewrite it as:

$$A = d_i \left\langle \delta \mathbf{j} \cdot \delta \left[\frac{1}{2} \nabla(\mathbf{b} \cdot \mathbf{b}) + \mathbf{j} \times \mathbf{b} \right] \right\rangle. \tag{2.23}$$

Using relations (2.1)–(2.3) along with the fact that $\nabla \cdot \mathbf{j} = 0$, one can show that:

$$\langle \mathbf{j} \cdot \nabla(\mathbf{b} \cdot \mathbf{b}) \rangle = -\nabla_\ell \cdot \langle (\mathbf{b} \cdot \mathbf{b}) \mathbf{j} \rangle - \langle (\mathbf{b} \cdot \mathbf{b}) \nabla \cdot \mathbf{j} \rangle = 0, \tag{2.24}$$

$$\langle \mathbf{j}' \cdot \nabla(\mathbf{b} \cdot \mathbf{b}) \rangle = -\nabla_\ell \cdot \langle (\mathbf{b} \cdot \mathbf{b}) \mathbf{j}' \rangle = -\langle (\mathbf{b} \cdot \mathbf{b}) \nabla' \cdot \mathbf{j}' \rangle = 0, \tag{2.25}$$

and reduce A to

$$A = d_i \langle \delta \mathbf{j} \cdot \delta(\mathbf{j} \times \mathbf{b}) \rangle. \tag{2.26}$$

Now, with the relation $\nabla \cdot (\mathbf{X} \times \mathbf{Y}) = \mathbf{Y} \cdot (\nabla \times \mathbf{X}) - \mathbf{X} \cdot (\nabla \times \mathbf{Y})$ we show that:

$$\begin{aligned}
\langle (\mathbf{j} \times \mathbf{b}) \cdot \mathbf{j}' \rangle &= \langle (\mathbf{j} \times \mathbf{b}) \cdot (\nabla' \times \mathbf{b}') \rangle \\
&= -\langle \nabla' \cdot [(\mathbf{j} \times \mathbf{b}) \times \mathbf{b}'] \rangle \\
&= -\nabla_\ell \cdot \langle (\mathbf{j} \times \mathbf{b}) \times \mathbf{b}' \rangle, \tag{2.27}
\end{aligned}$$

$$\langle (\mathbf{j}' \times \mathbf{b}') \cdot \mathbf{j} \rangle = \nabla_\ell \cdot \langle (\mathbf{j}' \times \mathbf{b}') \times \mathbf{b} \rangle, \tag{2.28}$$

$$\langle (\mathbf{j}' \times \mathbf{b}') \cdot \mathbf{j}' \rangle = \langle (\mathbf{j} \times \mathbf{b}) \cdot \mathbf{j} \rangle = 0, \tag{2.29}$$

which leads to

$$A = d_i \nabla_{\ell} \cdot \langle (\mathbf{j} \times \mathbf{b}) \times \mathbf{b}' - (\mathbf{j}' \times \mathbf{b}') \times \mathbf{b} \rangle. \quad (2.30)$$

With identities on double cross products Eq. (2.30) can be cast as,

$$\begin{aligned} A &= d_i \nabla_{\ell} \cdot \langle (\mathbf{b}' \cdot \mathbf{j}) \mathbf{b} - (\mathbf{b}' \cdot \mathbf{b}) \mathbf{j} + (\mathbf{b} \cdot \mathbf{j}') \mathbf{b}' - (\mathbf{b} \cdot \mathbf{b}') \mathbf{j}' \rangle \\ &= \frac{1}{2} d_i \nabla_{\ell} \cdot \langle 2(\delta \mathbf{b} \cdot \delta \mathbf{j}) \delta \mathbf{b} - (\delta \mathbf{b} \cdot \delta \mathbf{b}) \delta \mathbf{j} \rangle - d_i \nabla_{\ell} \cdot \langle (\mathbf{b} \cdot \mathbf{j}') \mathbf{b} - (\mathbf{b}' \cdot \mathbf{j}) \mathbf{b}' \rangle \end{aligned} \quad (2.31)$$

$$\begin{aligned} &= \frac{1}{2} d_i \nabla_{\ell} \cdot \langle 2(\delta \mathbf{b} \cdot \delta \mathbf{j}) \delta \mathbf{b} - (\delta \mathbf{b} \cdot \delta \mathbf{b}) \delta \mathbf{j} \rangle + d_i \langle \mathbf{j}' \cdot [(\mathbf{b} \cdot \nabla) \mathbf{b}] + \mathbf{j} \cdot [(\mathbf{b}' \cdot \nabla') \mathbf{b}'] \rangle \\ &= \frac{1}{2} d_i \nabla_{\ell} \cdot \langle 2(\delta \mathbf{b} \cdot \delta \mathbf{j}) \delta \mathbf{b} - (\delta \mathbf{b} \cdot \delta \mathbf{b}) \delta \mathbf{j} \rangle - A, \end{aligned} \quad (2.32)$$

to finally obtain

$$2A = \frac{1}{2} d_i \nabla_{\ell} \cdot \langle 2(\delta \mathbf{b} \cdot \delta \mathbf{j}) \delta \mathbf{b} - (\delta \mathbf{b} \cdot \delta \mathbf{b}) \delta \mathbf{j} \rangle. \quad (2.33)$$

Thanks to (2.33) we can bring equation (2.21) to its simplest form:

$$\begin{aligned} \partial_t \langle S \rangle &= 4 \partial_t \langle E^{tot} \rangle - \nabla_{\ell} \cdot \langle (\delta \mathbf{u} \cdot \delta \mathbf{u} + \delta \mathbf{b} \cdot \delta \mathbf{b}) \delta \mathbf{u} - 2(\delta \mathbf{u} \cdot \delta \mathbf{b}) \delta \mathbf{b} \rangle \\ &\quad - \frac{1}{2} d_i \nabla_{\ell} \cdot \langle -(\delta \mathbf{b} \cdot \delta \mathbf{b}) \delta \mathbf{j} + 2(\delta \mathbf{b} \cdot \delta \mathbf{j}) \delta \mathbf{b} \rangle \\ &\quad - 2 \langle \mathbf{u} \cdot \mathbf{d}'_{\nu} \rangle - 2 \langle \mathbf{u}' \cdot \mathbf{d}_{\nu} \rangle - 2 \langle \mathbf{b} \cdot \mathbf{d}'_{\eta} \rangle - 2 \langle \mathbf{b}' \cdot \mathbf{d}_{\eta} \rangle - 2 \langle \mathbf{u} \cdot \mathbf{f}' \rangle - 2 \langle \mathbf{u}' \cdot \mathbf{f} \rangle. \end{aligned} \quad (2.34)$$

2.2.3 From the dynamical equation to the exact law

The final expression of the exact law for 3D IHMHD, valid in the inertial range, is obtained by using the stationarity assumption and the limit of a wide inertial range (i.e. limit large kinetic/magnetic Reynolds numbers). We define the mean rate of total energy injection as $\varepsilon = \langle \mathbf{u} \cdot \mathbf{f} \rangle$. Note that with equation (2.20), we can conclude that in the stationary regime the following relation for dissipation holds:

$$\langle \mathbf{u} \cdot \mathbf{d}_{\nu} + \mathbf{b} \cdot \mathbf{d}_{\eta} \rangle = -\varepsilon. \quad (2.35)$$

In the inertial range, far away from both the forcing and dissipation scales, some approximations can be made. On the one hand the forcing is assumed to act on large scales only, thus its spatial variations should remain small and cross-terms such as $\langle \mathbf{u} \cdot \mathbf{f}' \rangle$ are expected to behave like $\langle \mathbf{u} \cdot \mathbf{f} \rangle = \varepsilon$. On the other hand dissipation acts at small scales only, thus cross-terms like $\langle \mathbf{u} \cdot \mathbf{d}'_{\nu} \rangle$ or $\langle \mathbf{b} \cdot \mathbf{d}'_{\eta} \rangle$ will be uncorrelated and of null statistical mean. Then, using equation (2.35), the following simplifications arise:

$$\langle \mathbf{u} \cdot \mathbf{d}'_{\nu} \rangle \simeq \langle \mathbf{u}' \cdot \mathbf{d}_{\nu} \rangle \simeq \langle \mathbf{b} \cdot \mathbf{d}'_{\eta} \rangle \simeq \langle \mathbf{b}' \cdot \mathbf{d}_{\eta} \rangle \simeq 0, \quad (2.36)$$

$$\langle \mathbf{u} \cdot \mathbf{f}' \rangle \simeq \langle \mathbf{u}' \cdot \mathbf{f} \rangle \simeq \varepsilon. \quad (2.37)$$

We thus find the final expression:

$$-4\varepsilon = \nabla_{\ell} \cdot \left\langle (\delta \mathbf{u} \cdot \delta \mathbf{u} + \delta \mathbf{b} \cdot \delta \mathbf{b}) \delta \mathbf{u} - 2(\delta \mathbf{u} \cdot \delta \mathbf{b}) \delta \mathbf{b} + d_i (\delta \mathbf{b} \cdot \delta \mathbf{j}) \delta \mathbf{b} - \frac{1}{2} d_i (\delta \mathbf{b} \cdot \delta \mathbf{b}) \delta \mathbf{j} \right\rangle, \quad (2.38)$$

which can be written in a compact form as,

$$\boxed{-4\varepsilon = \nabla_{\ell} \cdot \left(\mathbf{Y} + \frac{1}{2} \mathbf{H} \right)}, \quad (2.39)$$

where

$$\mathbf{Y} = \langle (\delta \mathbf{u} \cdot \delta \mathbf{u} + \delta \mathbf{b} \cdot \delta \mathbf{b}) \delta \mathbf{u} - 2(\delta \mathbf{u} \cdot \delta \mathbf{b}) \delta \mathbf{b} \rangle, \quad (2.40)$$

$$\mathbf{H} = d_i \langle 2(\delta \mathbf{b} \cdot \delta \mathbf{j}) \delta \mathbf{b} - (\delta \mathbf{b} \cdot \delta \mathbf{b}) \delta \mathbf{j} \rangle. \quad (2.41)$$

Assuming isotropy, and due to the fact that ε is supposed to remain constant in the inertial range, we can also integrate expression (2.39) which leads to:

$$\boxed{-\frac{4}{3}\varepsilon\ell = Y_\ell + \frac{1}{2}H_\ell}, \quad (2.42)$$

where Y_ℓ and H_ℓ are the projections along the displacement direction ℓ .

Exact law (2.39), which will be referred to as **F19**, is the main result of this section and is closely related to the one proposed in **Hellinger et al. (2018)** except for the Hall term A which has been corrected and expressed as a function of \mathbf{H} . It has the double advantage of depending only on the product of increments of the physical fields (unlike the **G08** model) and of being expressed only as flux terms like a typical Yaglom-like equation, much like the laws of **Antonia et al. (1997)** and **Politano and Pouquet (1998)**. Note that, in the limit of ideal **MHD** ($d_i/L \rightarrow 0$ where L is the characteristic scale of turbulence) we recover the classic **MHD** law of **Politano and Pouquet (1998)**.

2.2.4 Equivalence of IHMHD exact laws

If we exclude the exact law from **Hellinger et al. (2018)** which is closely related to **F19** we have a total of three archetypes of exact law for the **IHMHD** model. Thus, it is important to verify whether all three of these are equivalent or not, and if they should provide the same values of ε . For the ideal **MHD** part of the law (2.40) the \mathbf{Y} term is exactly the same as the one from **Galtier (2008)**. **BG17 MHD** term reads:

$$2\varepsilon_{BG17}^{MHD} = \langle \delta(\mathbf{u} \times \boldsymbol{\omega}) \cdot \delta \mathbf{u} \rangle + \langle \delta(\mathbf{j} \times \mathbf{b}) \cdot \delta \mathbf{u} \rangle + \langle \delta(\mathbf{u} \times \mathbf{b}) \cdot \delta \mathbf{j} \rangle. \quad (2.43)$$

Each of all three terms of the left-hand side can be rewritten to fit in \mathbf{Y} . Indeed, we have:

$$\begin{aligned} \langle (\mathbf{u} \times \boldsymbol{\omega}) \cdot \mathbf{u}' + (\mathbf{u}' \times \boldsymbol{\omega}') \cdot \mathbf{u} \rangle &= \frac{1}{2} \langle [\nabla(\mathbf{u} \cdot \mathbf{u}) - (\mathbf{u} \cdot \nabla)\mathbf{u}] \cdot \mathbf{u}' + [\nabla'(\mathbf{u}' \cdot \mathbf{u}') - (\mathbf{u}' \cdot \nabla')\mathbf{u}'] \cdot \mathbf{u} \rangle \\ &= \frac{1}{2} \nabla_\ell \cdot \langle -(\mathbf{u} \cdot \mathbf{u})\mathbf{u}' + 2(\mathbf{u} \cdot \mathbf{u}')\mathbf{u} + (\mathbf{u}' \cdot \mathbf{u}')\mathbf{u} - 2(\mathbf{u} \cdot \mathbf{u}')\mathbf{u}' \rangle \\ &= \frac{1}{2} \nabla_\ell \cdot \langle +2(\mathbf{u} \cdot \mathbf{u}')\mathbf{u} - 2(\mathbf{u} \cdot \mathbf{u}')\mathbf{u}' \rangle \\ &= \frac{1}{2} \nabla_\ell \cdot \langle (\delta \mathbf{u} \cdot \delta \mathbf{u}) \delta \mathbf{u} \rangle, \end{aligned} \quad (2.44)$$

$$\langle (\mathbf{j} \times \mathbf{b}) \cdot \mathbf{u}' + (\mathbf{j}' \times \mathbf{b}') \cdot \mathbf{u} \rangle = \frac{1}{2} \nabla_\ell \cdot \langle -2(\mathbf{b} \cdot \mathbf{u}')\mathbf{b} + 2(\mathbf{b}' \cdot \mathbf{u})\mathbf{b}' \rangle, \quad (2.45)$$

$$\begin{aligned} \langle (\mathbf{u} \times \mathbf{b}) \cdot \mathbf{j}' + (\mathbf{u}' \times \mathbf{b}') \cdot \mathbf{j} \rangle &= \langle (\mathbf{b} \times \mathbf{j}') \cdot \mathbf{u} + (\mathbf{b}' \times \mathbf{j}) \cdot \mathbf{u}' \rangle \\ &= \frac{1}{2} \nabla_\ell \cdot \langle 2(\mathbf{b}' \cdot \mathbf{b})\mathbf{u} - 2(\mathbf{b}' \cdot \mathbf{u})\mathbf{b}' - 2(\mathbf{b} \cdot \mathbf{b}')\mathbf{u}' + 2(\mathbf{b} \cdot \mathbf{u}')\mathbf{b} \rangle \\ &= \frac{1}{2} \nabla_\ell \cdot \langle (\delta \mathbf{b} \cdot \delta \mathbf{b}) \delta \mathbf{u} + 2(\mathbf{b} \cdot \mathbf{u}')\mathbf{b}' - 2(\mathbf{b}' \cdot \mathbf{u})\mathbf{b} \rangle, \end{aligned} \quad (2.46)$$

and all other terms are either null or canceling each other. Putting relations (2.44)–(2.46) together we obtain:

$$\begin{aligned} 2\varepsilon_{BG17}^{MHD} &= -\frac{1}{2} \nabla_\ell \cdot \langle (\delta \mathbf{u} \cdot \delta \mathbf{u}) \delta \mathbf{u} + (\delta \mathbf{b} \cdot \delta \mathbf{b}) \delta \mathbf{u} - 2(\mathbf{b} \cdot \mathbf{u}')\mathbf{b} + 2(\mathbf{b}' \cdot \mathbf{u})\mathbf{b}' + 2(\mathbf{b} \cdot \mathbf{u}')\mathbf{b}' - 2(\mathbf{b}' \cdot \mathbf{u})\mathbf{b} \rangle \\ &= -\frac{1}{2} \nabla_\ell \cdot \langle (\delta \mathbf{u} \cdot \delta \mathbf{u}) \delta \mathbf{u} + (\delta \mathbf{b} \cdot \delta \mathbf{b}) \delta \mathbf{u} - 2(\delta \mathbf{u} \cdot \delta \mathbf{b}) \delta \mathbf{b} \rangle \\ &= -\frac{1}{2} \nabla_\ell \cdot \mathbf{Y} = 2\varepsilon_{F19}^{MHD}, \end{aligned} \quad (2.47)$$

which proves that the MHD components of laws BG17 and F19 are equivalent.

Obtaining similar relations for the Hall components is easier, as less terms are involved and most of the work has already been done in the previous subsection. Indeed, in G08, the law reads with our notation,

$$-4\varepsilon_{G08}^{Hall} = 4d_i \nabla_{\ell} \cdot \langle (\mathbf{j} \times \mathbf{b}) \times \delta \mathbf{b} \rangle. \quad (2.48)$$

We already showed with (2.33) that $\frac{1}{2} \nabla_{\ell} \cdot \mathbf{H} = 2A$. With Eq. (2.30) and the assumption of statistical homogeneity we have,

$$\begin{aligned} \frac{1}{2} \nabla_{\ell} \cdot \mathbf{H} &= 2d_i \nabla_{\ell} \cdot \langle (\mathbf{j} \times \mathbf{b}) \times \mathbf{b}' - (\mathbf{j}' \times \mathbf{b}') \times \mathbf{b} \rangle \\ &= 4d_i \nabla_{\ell} \cdot \langle (\mathbf{j} \times \mathbf{b}) \times \mathbf{b}' \rangle, \end{aligned} \quad (2.49)$$

which is sufficient to show that,

$$-4\varepsilon_{F19}^{Hall} = \frac{1}{2} \nabla_{\ell} \cdot \mathbf{H} = 4d_i \nabla_{\ell} \cdot \langle (\mathbf{j} \times \mathbf{b}) \times \delta \mathbf{b} \rangle = -4\varepsilon_{G08}^{Hall}, \quad (2.50)$$

proving the compatibility between G08 and F19.

Finally, the Hall term of BG17 is written:

$$2\varepsilon_{BG17}^{Hall} = -d_i \langle \delta(\mathbf{j} \times \mathbf{b}) \cdot \delta \mathbf{j} \rangle. \quad (2.51)$$

Using Eqs. (2.26) and (2.33) we immediately obtain:

$$-4\varepsilon_{F19}^{Hall} = \frac{1}{2} \nabla_{\ell} \cdot \mathbf{H} = 2d_i \langle \delta(\mathbf{j} \times \mathbf{b}) \cdot \delta \mathbf{j} \rangle = -4\varepsilon_{BG17}^{Hall}. \quad (2.52)$$

This achieves the proof of the mathematical equivalence of G08, BG17 and F19 under the hypotheses of the calculation. Note that this equivalence holds in a situation of perfect statistical homogeneity, thus it is necessary to test how it behaves in practice when studying real data, where this hypothesis may not be perfectly met. Such a test will be done on DNS data in chapter 4.

This diversity of exact laws gives more freedom to compute the energy cascade rate of IHMHD turbulence as it is possible to adapt the computation method to the data available. Indeed, BG17 is expected to converge quicker due to it being a function of second-order increments, is computationally cheaper to calculate due to not involving derivatives with respect to the increment, and should be free of any constraints of directionality with respect to the increment vector. However, it depends on the vorticity which can be problematic for studying *in situ* data, as the calculation of 3D spatial derivatives requires a multi-spacecraft mission. In this sense, F19 will prove to be better to compute the energy cascade rate from single satellite data (provided the current is available through particles velocity measurements).

It is interesting to observe that the introduction of a uniform magnetic field \mathbf{B}_0 (i.e. replacing \mathbf{b} by $\mathbf{b} + \mathbf{b}_0$, with $\mathbf{b}_0 = \mathbf{B}_0 / \sqrt{\mu_0 \rho_0}$) into the previous laws does not change their expression. This property is obvious for F19 which only depends on increments and for BG17 in which the \mathbf{b}_0 influence translates as $\langle \delta \mathbf{j} \cdot ((\delta \mathbf{j}) \times \mathbf{b}_0) \rangle = 0$. For G08 we have,

$$\begin{aligned} \varepsilon_{G08}^{Hall} &= 2 \nabla_{\ell} \cdot \langle (\mathbf{j} \times \mathbf{b}_0) \times \mathbf{b}' - (\mathbf{j}' \times \mathbf{b}_0) \times \mathbf{b} \rangle \\ &= -2 \langle (\mathbf{j} \times \mathbf{b}_0) \cdot \mathbf{j}' + (\mathbf{j}' \times \mathbf{b}_0) \cdot \mathbf{j} \rangle \\ &= 0. \end{aligned} \quad (2.53)$$

Consequently, a modification of the background magnetic field (and *a fortiori* not considering it in the calculation) should not change *directly* the value of the energy cascade rate. However, even in the absence of an explicit dependence in \mathbf{B}_0 , it is still expected to have an indirect impact on the energy cascade by the way it shapes the non-linear dynamics (Wan et al., 2012; Meyrand and Galtier, 2013). Note also that an explicit dependence in \mathbf{B}_0 appears when considering incompressible fourth-order correlation functions (as opposed to the third-order ones presented here) (Oughton et al., 2013). As we will see below the introduction of compressibility in the model lead to a different behavior, as the corresponding exact relations depend explicitly on \mathbf{B}_0 .

2.3 Exact law in compressible models

2.3.1 Description of the compressible Hall MHD model

In the previous section I presented for IHMHD the derivation of a new exact law with a typical Yaglom-like expression thanks to the use of a second-order structure function, different from the correlator used for past laws, to initiate the calculation. The same can be done for all other compressible models, however deriving an exact law while taking compressibility into account is a much more time-consuming and tedious operation than for an incompressible model, be it an HD or MHD one. Thus, I will only present the derivation of the law for the most complete model of (isothermal) CHMHD and use it as a basis to infer the laws in Compressible Magnetohydrodynamics (CMHD) and CHD (see Simon and Sahraoui (2021) for a more general derivation for isentropic flows that encompasses polytropic and isothermal closures, and for the related discussion about the thermodynamics behind exact laws).

To describe this model we consider the three-dimensional isothermal CHMHD equations (Galtier, 2016) that were presented in chapter 1, and that we slightly rewrite as:

$$\partial_t \rho + \nabla \cdot (\rho \mathbf{u}) = 0, \quad (2.54)$$

$$\rho(\partial_t \mathbf{u} + \mathbf{u} \cdot \nabla \mathbf{u}) = -\nabla P + \mathbf{J} \times \mathbf{B} + \mathbf{d}_\nu + \mathbf{f}, \quad (2.55)$$

$$\partial_t \mathbf{B} = \nabla \times (\mathbf{u} \times \mathbf{B}) - \lambda \nabla \times (\mathbf{J}_c \times \mathbf{B}) + \mathbf{d}_\eta, \quad (2.56)$$

$$\nabla \cdot \mathbf{B} = 0. \quad (2.57)$$

We use the same notations as before, with the addition of the no-longer-constant mass density ρ , the normalized current $\mathbf{J}_c = \mathbf{J}/\rho$, and $\lambda = m_i/q_e$ with m_i the ion mass and q_e the magnitude of the electron charge. This new term is connected to the previously used ion skin depth d_i through the relation $d_i = \lambda/\sqrt{\mu_0 \rho_0}$. The dissipation terms this time are:

$$\mathbf{d}_\nu = \nu \Delta \mathbf{u} + \frac{\nu}{3} \nabla \theta, \quad (2.58)$$

$$\mathbf{d}_\eta = \eta \Delta \mathbf{B}, \quad (2.59)$$

with $\theta = \nabla \cdot \mathbf{u}$ the dilatation. We use the isothermal closure $P = c_s^2 \rho$ with c_s the constant speed of sound. For this system, the equation of energy conservation reads:

$$\partial_t \langle E^{tot} \rangle = \langle \mathbf{u} \cdot \mathbf{d}_\nu \rangle + \frac{1}{\mu_0} \langle \mathbf{B} \cdot \mathbf{d}_\eta \rangle + \langle \mathbf{u} \cdot \mathbf{f} \rangle, \quad (2.60)$$

where $E^{tot} = \rho u^2/2 + B^2/(2\mu_0) + \rho e$ is the total energy and e the work component of internal energy (per unit mass). e can be expressed as a function of the density by assuming that the work reads $W = -PdV$, and by considering the usual definition of density $\rho = m/V$ (for units of mass m and volume V) which gives the relation:

$$dV = -\frac{m}{\rho^2} d\rho. \quad (2.61)$$

Thus, the expression of the work becomes:

$$W = -\frac{m c_s^2}{\rho} d\rho, \quad (2.62)$$

and by integrating and defining $e \equiv W/m$ we get the relation:

$$e = c_s^2 \ln\left(\frac{\rho}{\rho_0}\right) \quad (2.63)$$

This definition limits the variations of the internal energy to the work done by the pressure force, the heat component due to entropy variation being neglected (note that in incompressible turbulence the whole internal energy is conserved, see Simon and Sahraoui (2021) for a

detailed explanation). We define again the mean rate of total energy injection as $\varepsilon = \langle \mathbf{u} \cdot \mathbf{f} \rangle$. By using this quantity, equation (2.60) reduces in the stationary regime to:

$$\langle \mathbf{u} \cdot \mathbf{d}_\nu + \frac{1}{\mu_0} \mathbf{B} \cdot \mathbf{d}_\eta \rangle = -\varepsilon. \quad (2.64)$$

We can also obtain a relation similar to (2.10):

$$\langle \mathbf{u} \cdot \mathbf{d}_\nu \rangle + \frac{1}{\mu_0} \langle \mathbf{B} \cdot \mathbf{d}_\eta \rangle = -\nu \left\langle \omega^2 + \frac{4}{3} \theta^2 \right\rangle - \mu_0 \eta \langle \mathbf{J}^2 \rangle, \quad (2.65)$$

which once again gives the expression of the mean rate of total energy dissipation.

2.3.2 Calculation of a compressible dynamical equation

The previous CHMHD law derivation from Andrés et al. (2018) (hereafter A18) made use of a correlator for total energy as their starting point, namely:

$$\langle R_E \rangle = \left\langle \frac{\rho}{2} (\mathbf{u} \cdot \mathbf{u}' + \mathbf{v}_A \cdot \mathbf{v}'_A) + \rho e' \right\rangle, \quad (2.66)$$

where $\mathbf{v}_A = \mathbf{B} / \sqrt{\mu_0 \rho}$ is the Alfvén speed, this time normalized by the non-constant density. Following the idea of section 2.2 we choose to work with a mixed structure function for total fluctuating energy (i.e. changes of the energy between points \mathbf{r} and \mathbf{r}') instead:

$$\langle S \rangle = \left\langle \frac{1}{2} \bar{\delta} \rho |\delta \mathbf{u}|^2 + \frac{1}{2\mu_0} |\delta \mathbf{B}|^2 + \frac{1}{2} \delta \rho \delta e \right\rangle. \quad (2.67)$$

First of all, we note that for homogeneous turbulence we have the expressions:

$$\langle \bar{\delta} \rho |\delta \mathbf{u}|^2 \rangle = \langle \rho u^2 \rangle - 2 \langle \bar{\delta} \rho \mathbf{u} \cdot \mathbf{u}' \rangle + \frac{1}{2} \langle \rho u'^2 + \rho' u^2 \rangle, \quad (2.68)$$

$$\langle \delta \rho \delta e \rangle = 2 \langle \rho e \rangle - \langle \rho e' + \rho' e \rangle, \quad (2.69)$$

$$\langle |\delta \mathbf{B}|^2 \rangle = 2 \langle B^2 \rangle - 2 \langle \mathbf{B} \cdot \mathbf{B}' \rangle, \quad (2.70)$$

that lead to the relation:

$$\langle S \rangle = \langle E^{tot} \rangle - \langle \bar{\delta} \rho \mathbf{u} \cdot \mathbf{u}' + \mathbf{B} \cdot \mathbf{B}' + \rho e' + \rho' e \rangle + \frac{1}{4} \langle \rho u'^2 + \rho' u^2 + B^2 + B'^2 \rangle. \quad (2.71)$$

This relation is analogous to (2.13) in the IHMHD case: the second term of the right-hand side is a modified version of (2.66) using the magnetic field instead of the Alfvén speed, and an additional term featuring both the squared velocity and magnetic fields appears. In the incompressible limit ($\rho \rightarrow \rho_0 = 1$) (2.71) becomes:

$$\begin{aligned} \frac{1}{2} \langle |\delta \mathbf{u}|^2 + |\delta \mathbf{b}|^2 \rangle &= \langle E^{tot} \rangle - \langle \mathbf{u} \cdot \mathbf{u}' + \mathbf{b} \cdot \mathbf{b}' \rangle + \frac{1}{2} \langle u^2 + b^2 \rangle. \\ &= 2 \langle E^{tot} \rangle - \langle \mathbf{u} \cdot \mathbf{u}' + \mathbf{b} \cdot \mathbf{b}' \rangle, \end{aligned} \quad (2.72)$$

and we retrieve relation (2.13).

Using relations (2.1)–(2.3) we can once again compute $\partial_t \langle S \rangle$, starting with the following expressions:

$$\begin{aligned} \partial_t \langle \rho \mathbf{u} \cdot \mathbf{u}' \rangle &= \left\langle \rho \mathbf{u} \cdot \left(-\mathbf{u}' \cdot \nabla' \mathbf{u}' - \frac{1}{\rho'} \nabla' P' + \mathbf{J}'_c \times \mathbf{B}' \right) \right\rangle \\ &\quad + \langle \mathbf{u}' \cdot (-\nabla \cdot (\rho \mathbf{u} \mathbf{u}) - \nabla P + \mathbf{J} \times \mathbf{B}) \rangle + \left\langle \mathbf{u}' \cdot \mathbf{d}_\nu + \mathbf{u}' \cdot \mathbf{f} + \frac{\rho}{\rho'} \mathbf{u} \cdot (\mathbf{d}'_\nu + \mathbf{f}') \right\rangle \\ &= \nabla_\ell \cdot \langle -\rho (\mathbf{u} \cdot \mathbf{u}') \delta \mathbf{u} + P \mathbf{u}' - \rho e' \mathbf{u} \rangle + \langle \rho \theta' (\mathbf{u} \cdot \mathbf{u}') \rangle \\ &\quad + \langle \rho \mathbf{u} \cdot (\mathbf{J}'_c \times \mathbf{B}') + \mathbf{u}' \cdot (\mathbf{J} \times \mathbf{B}) \rangle \\ &\quad + \left\langle \mathbf{u}' \cdot \mathbf{d}_\nu + \mathbf{u}' \cdot \mathbf{f} + \frac{\rho}{\rho'} \mathbf{u} \cdot (\mathbf{d}'_\nu + \mathbf{f}') \right\rangle, \end{aligned} \quad (2.73)$$

$$\begin{aligned}
\partial_t \langle \mathbf{B} \cdot \mathbf{B}' \rangle &= \langle \mathbf{B} \cdot (\mathbf{B}' \cdot \nabla' \mathbf{u}' - \mathbf{u}' \cdot \nabla' \mathbf{B}' - \mathbf{B}' \theta') \rangle + \langle \mathbf{B}' \cdot (\mathbf{B} \cdot \nabla \mathbf{u} - \mathbf{u} \cdot \nabla \mathbf{B} - \mathbf{B} \theta) \rangle \\
&\quad - \lambda \langle \mathbf{B}' \cdot (\nabla \times (\mathbf{J}_c \times \mathbf{B})) + \mathbf{B} \cdot (\nabla' \times (\mathbf{J}'_c \times \mathbf{B}')) \rangle + \langle \mathbf{B}' \cdot \mathbf{d}_\eta + \mathbf{B} \cdot \mathbf{d}'_\eta \rangle \\
&= \langle \nabla' \cdot ((\mathbf{B} \cdot \mathbf{u}') \mathbf{B}') - \nabla' \cdot ((\mathbf{B} \cdot \mathbf{B}') \mathbf{u}') + \nabla \cdot ((\mathbf{B}' \cdot \mathbf{u}) \mathbf{B}) - \nabla \cdot ((\mathbf{B} \cdot \mathbf{B}') \mathbf{u}) \rangle \\
&\quad - \lambda \langle \nabla \cdot ((\mathbf{J}_c \cdot \mathbf{B}') \mathbf{B}) - (\mathbf{J}_c \cdot \nabla) (\mathbf{B} \cdot \mathbf{B}') - (\mathbf{B} \cdot \mathbf{B}') \nabla \cdot \mathbf{J}_c \rangle \\
&\quad - \lambda \langle \nabla' \cdot ((\mathbf{J}'_c \cdot \mathbf{B}) \mathbf{B}') - (\mathbf{J}'_c \cdot \nabla') (\mathbf{B} \cdot \mathbf{B}') - (\mathbf{B} \cdot \mathbf{B}') \nabla' \cdot \mathbf{J}'_c \rangle \\
&\quad + \langle \mathbf{B}' \cdot \mathbf{d}_\eta + \mathbf{B} \cdot \mathbf{d}'_\eta \rangle \\
&= \nabla_\ell \cdot \langle -(\mathbf{B} \cdot \mathbf{B}') \delta \mathbf{u} + (\mathbf{B} \cdot \mathbf{u}') \mathbf{B}' - (\mathbf{B}' \cdot \mathbf{u}) \mathbf{B} \rangle \\
&\quad - \lambda \nabla_\ell \cdot \langle -(\mathbf{B} \cdot \mathbf{B}') \delta \mathbf{J}_c + (\mathbf{J}'_c \cdot \mathbf{B}) \mathbf{B}' - (\mathbf{J}_c \cdot \mathbf{B}') \mathbf{B} \rangle \\
&\quad + \langle \mathbf{B}' \cdot \mathbf{d}_\eta + \mathbf{B} \cdot \mathbf{d}'_\eta \rangle, \tag{2.74}
\end{aligned}$$

$$\begin{aligned}
\partial_t \langle \rho u'^2 \rangle &= \langle 2\rho \mathbf{u}' \cdot \partial_t \mathbf{u}' + u'^2 \partial_t \rho \rangle \\
&= \left\langle -\mathbf{u}' \cdot \nabla' (\rho u'^2) - 2\frac{\rho}{\rho'} \mathbf{u}' \cdot \nabla' P' + 2\frac{\rho}{\rho'} \mathbf{u}' \cdot (\mathbf{J}' \times \mathbf{B}') \right\rangle \\
&\quad + \nabla_\ell \cdot \langle \rho u'^2 \mathbf{u} \rangle + \left\langle 2\frac{\rho}{\rho'} \mathbf{u}' \cdot (\mathbf{d}'_\nu + \mathbf{f}') \right\rangle \\
&= \nabla_\ell \cdot \langle -\rho u'^2 \mathbf{u}' + \rho u'^2 \mathbf{u} \rangle + \left\langle \rho u'^2 \theta' - 2\frac{\rho}{\rho'} \mathbf{u}' \cdot \nabla' P' + 2\frac{\rho}{\rho'} \mathbf{u}' \cdot (\mathbf{J}' \times \mathbf{B}') \right\rangle \\
&\quad + \left\langle 2\frac{\rho}{\rho'} \mathbf{u}' \cdot (\mathbf{d}'_\nu + \mathbf{f}') \right\rangle, \tag{2.75}
\end{aligned}$$

$$\partial_t \langle \rho e' \rangle = \nabla_\ell \cdot \langle -\rho e' \delta \mathbf{u} - P \mathbf{u}' \rangle + \langle \rho e' \theta' \rangle, \tag{2.76}$$

which, after being put together, give:

$$\begin{aligned}
\partial_t \langle S \rangle &= \partial_t \langle E^{tot} \rangle + \partial_t \langle \frac{B^2}{2\mu_0} \rangle \\
&\quad - \frac{1}{2} \nabla_\ell \cdot \left\langle -2\bar{\delta} \rho (\mathbf{u} \cdot \mathbf{u}') \delta \mathbf{u} - \rho e' \mathbf{u}' + \rho' e \mathbf{u} + \frac{1}{2} \rho u'^2 \mathbf{u}' - \frac{1}{2} \rho u'^2 \mathbf{u} - \frac{1}{2} \rho' u^2 \mathbf{u} + \frac{1}{2} \rho' u^2 \mathbf{u}' \right\rangle \\
&\quad - \frac{1}{2} \langle \rho \mathbf{u} \cdot (\mathbf{J}'_c \times \mathbf{B}') + \rho' \mathbf{u}' \cdot (\mathbf{J}_c \times \mathbf{B}) + \mathbf{u}' \cdot (\mathbf{J} \times \mathbf{B}) + \mathbf{u} \cdot (\mathbf{J}' \times \mathbf{B}') \rangle \\
&\quad + \frac{1}{4} \left\langle \rho u'^2 \theta' + \rho' u^2 \theta - 2\frac{\rho}{\rho'} \mathbf{u}' \cdot \nabla' P' - 2\frac{\rho'}{\rho} \mathbf{u} \cdot \nabla P + 2\frac{\rho}{\rho'} \mathbf{u}' \cdot (\mathbf{J}' \times \mathbf{B}') + 2\frac{\rho'}{\rho} \mathbf{u} \cdot (\mathbf{J} \times \mathbf{B}) \right\rangle \\
&\quad - \frac{1}{2} \langle (\rho \theta' + \rho' \theta) (\mathbf{u} \cdot \mathbf{u}') \rangle - \frac{1}{2} \langle \rho e' \theta' + \rho' e \theta \rangle \\
&\quad - \frac{1}{\mu_0} \nabla_\ell \cdot \langle -(\mathbf{B} \cdot \mathbf{B}') \delta \mathbf{u} + (\mathbf{B} \cdot \mathbf{u}') \mathbf{B}' - (\mathbf{B}' \cdot \mathbf{u}) \mathbf{B} \rangle \\
&\quad - \frac{\lambda}{\mu_0} \nabla_\ell \cdot \langle (\mathbf{B} \cdot \mathbf{B}') \delta \mathbf{J}_c - \lambda (\mathbf{J}'_c \cdot \mathbf{B}) \mathbf{B}' + \lambda (\mathbf{J}_c \cdot \mathbf{B}') \mathbf{B} \rangle \\
&\quad - \frac{1}{2} \left\langle \left(1 + \frac{\rho'}{\rho}\right) \mathbf{u}' \cdot (\mathbf{d}'_\nu + \mathbf{f}') + \left(1 + \frac{\rho}{\rho'}\right) \mathbf{u} \cdot (\mathbf{d}'_\nu + \mathbf{f}') \right\rangle \\
&\quad + \frac{1}{2} \left\langle \frac{\rho}{\rho'} \mathbf{u}' \cdot (\mathbf{d}'_\nu + \mathbf{f}') + \frac{\rho'}{\rho} \mathbf{u} \cdot (\mathbf{d}'_\nu + \mathbf{f}') \right\rangle - \frac{1}{\mu_0} \langle \mathbf{B}' \cdot \mathbf{d}_\eta + \mathbf{B} \cdot \mathbf{d}'_\eta \rangle. \tag{2.77}
\end{aligned}$$

We can simplify the previous expression by remarking that:

$$\begin{aligned}
\nabla_\ell \cdot \langle \bar{\delta} \rho |\delta \mathbf{u}|^2 \delta \mathbf{u} \rangle &= \nabla_\ell \cdot \left\langle -2\bar{\delta} \rho \mathbf{u} \cdot \mathbf{u}' \delta \mathbf{u} + \frac{1}{2} \rho u'^2 \mathbf{u}' - \frac{1}{2} \rho u'^2 \mathbf{u} + \frac{1}{2} \rho' u^2 \mathbf{u}' - \frac{1}{2} \rho' u^2 \mathbf{u} \right\rangle \\
&\quad + \left\langle \frac{1}{2} \rho u^2 \theta' + \frac{1}{2} \rho' u'^2 \theta \right\rangle, \tag{2.78}
\end{aligned}$$

$$\begin{aligned} \left\langle \frac{\rho}{\rho'} \mathbf{u}' \cdot \nabla' P' \right\rangle + \left\langle \frac{\rho'}{\rho} \mathbf{u} \cdot \nabla P \right\rangle &= \langle \rho \mathbf{u}' \cdot \nabla' e' + \rho' \mathbf{u} \cdot \nabla e \rangle \\ &= \nabla_{\ell} \cdot \langle \rho e' \mathbf{u}' - \rho' e \mathbf{u} \rangle - \langle \rho e' \theta' + \rho' e \theta \rangle, \end{aligned} \quad (2.79)$$

$$\nabla_{\ell} \cdot \langle (\delta \mathbf{u} \cdot \delta \mathbf{B}) \delta \mathbf{B} \rangle = \nabla_{\ell} \cdot \langle -(\mathbf{u}' \cdot \mathbf{B}) \mathbf{B}' + (\mathbf{u} \cdot \mathbf{B}') \mathbf{B} - (\mathbf{u} \cdot \mathbf{B}') \mathbf{B}' + (\mathbf{u}' \cdot \mathbf{B}) \mathbf{B} \rangle, \quad (2.80)$$

$$\nabla_{\ell} \cdot \langle |\delta \mathbf{B}|^2 \delta \mathbf{u} \rangle = \nabla_{\ell} \cdot \langle -2(\mathbf{B} \cdot \mathbf{B}') \delta \mathbf{u} + B^2 \mathbf{u}' - B'^2 \mathbf{u} \rangle, \quad (2.81)$$

$$\langle (\rho \theta' + \rho' \theta) |\delta \mathbf{u}|^2 \rangle = \langle -2(\rho \theta' + \rho' \theta)(\mathbf{u} \cdot \mathbf{u}') + \rho \theta' u'^2 + \rho \theta u^2 + \rho' \theta u'^2 + \rho' \theta u^2 \rangle, \quad (2.82)$$

$$\langle |\delta \mathbf{B}|^2 \delta \mathbf{J}_c \rangle = \langle B'^2 \delta \mathbf{J}_c + B^2 \delta \mathbf{J}_c - 2(\mathbf{B} \cdot \mathbf{B}') \delta \mathbf{J}_c \rangle, \quad (2.83)$$

$$\nabla_{\ell} \cdot \langle (\delta \mathbf{B} \cdot \delta \mathbf{J}_c) \delta \mathbf{B} \rangle = \nabla_{\ell} \cdot \langle -(\mathbf{B}' \cdot \mathbf{J}_c) \mathbf{B}' + (\mathbf{B}' \cdot \mathbf{J}_c) \mathbf{B} - (\mathbf{B} \cdot \mathbf{J}'_c) \mathbf{B}' + (\mathbf{B} \cdot \mathbf{J}'_c) \mathbf{B} \rangle. \quad (2.84)$$

Introducing the previous expressions into (2.77) gives:

$$\begin{aligned} \partial_t \langle S \rangle &= \partial_t \langle E^{tot} \rangle + \partial_t \left\langle \frac{B^2}{2\mu_0} \right\rangle - \frac{1}{2} \nabla_{\ell} \cdot \langle \bar{\delta} \rho |\delta \mathbf{u}|^2 \delta \mathbf{u} \rangle + \frac{1}{4} \langle (\rho \theta' + \rho' \theta) |\delta \mathbf{u}|^2 \rangle \\ &\quad - \frac{1}{2} \langle \rho \mathbf{u} \cdot (\mathbf{J}'_c \times \mathbf{B}') + \rho' \mathbf{u}' \cdot (\mathbf{J}_c \times \mathbf{B}) - \rho \mathbf{u}' \cdot (\mathbf{J}'_c \times \mathbf{B}') - \rho' \mathbf{u} \cdot (\mathbf{J}_c \times \mathbf{B}) \rangle \\ &\quad - \frac{1}{2} \langle \mathbf{u}' \cdot (\mathbf{J} \times \mathbf{B}) + \mathbf{u} \cdot (\mathbf{J}' \times \mathbf{B}') \rangle \\ &\quad - \frac{1}{2\mu_0} \nabla_{\ell} \cdot \langle |\delta \mathbf{B}|^2 \delta \mathbf{u} - 2(\delta \mathbf{u} \cdot \delta \mathbf{B}) \delta \mathbf{B} - B^2 \mathbf{u}' + B'^2 \mathbf{u} - 2(\mathbf{u} \cdot \mathbf{B}') \mathbf{B}' + 2(\mathbf{u}' \cdot \mathbf{B}) \mathbf{B} \rangle \\ &\quad + \frac{\lambda}{2\mu_0} \nabla_{\ell} \cdot \langle |\delta \mathbf{B}|^2 \delta \mathbf{J}_c - B'^2 \delta \mathbf{J}_c - B^2 \delta \mathbf{J}_c - 2(\delta \mathbf{B} \cdot \delta \mathbf{J}_c) \delta \mathbf{B} - 2(\mathbf{B}' \cdot \mathbf{J}_c) \mathbf{B}' + 2(\mathbf{B} \cdot \mathbf{J}'_c) \mathbf{B} \rangle \\ &\quad - \frac{1}{2} \left\langle \left(1 + \frac{\rho'}{\rho} \right) \mathbf{u}' \cdot (\mathbf{d}_{\nu} + \mathbf{f}) + \left(1 + \frac{\rho}{\rho'} \right) \mathbf{u} \cdot (\mathbf{d}'_{\nu} + \mathbf{f}') \right\rangle \\ &\quad + \frac{1}{2} \left\langle \frac{\rho}{\rho'} \mathbf{u}' \cdot (\mathbf{d}'_{\nu} + \mathbf{f}') + \frac{\rho'}{\rho} \mathbf{u} \cdot (\mathbf{d}_{\nu} + \mathbf{f}) \right\rangle - \frac{1}{\mu_0} \langle \mathbf{B}' \cdot \mathbf{d}_{\eta} + \mathbf{B} \cdot \mathbf{d}'_{\eta} \rangle. \end{aligned} \quad (2.85)$$

Using again the relation $\nabla(\mathbf{X} \cdot \mathbf{X}) = 2\mathbf{X} \times (\nabla \times \mathbf{X}) + 2(\mathbf{X} \cdot \nabla)\mathbf{X}$, we find the following expressions:

$$\begin{aligned} \langle \mathbf{u}' \cdot (\mathbf{J} \times \mathbf{B}) + \mathbf{u} \cdot (\mathbf{J}' \times \mathbf{B}') \rangle &= \frac{1}{\mu_0} \langle \mathbf{u}' \cdot ((\nabla \times \mathbf{B}) \times \mathbf{B}) + \mathbf{u} \cdot ((\nabla' \times \mathbf{B}') \times \mathbf{B}') \rangle \\ &= \nabla_{\ell} \cdot \left\langle \frac{B^2}{2} \mathbf{u}' - (\mathbf{B} \cdot \mathbf{u}') \mathbf{B} - \frac{B'^2}{2} \mathbf{u} + (\mathbf{B}' \cdot \mathbf{u}) \mathbf{B}' \right\rangle, \end{aligned} \quad (2.86)$$

$$\nabla_{\ell} \cdot \langle (\mathbf{B} \cdot \mathbf{J}'_c) \mathbf{B} \rangle = -\langle \mathbf{J}'_c \cdot ((\mathbf{B} \cdot \nabla) \mathbf{B}) \rangle = \nabla_{\ell} \cdot \left\langle \frac{B^2}{2} \mathbf{J}'_c \right\rangle + \mu_0 \langle \mathbf{J}'_c \cdot (\mathbf{B} \times \mathbf{J}) \rangle, \quad (2.87)$$

$$\nabla_{\ell} \cdot \langle (\mathbf{B}' \cdot \mathbf{J}_c) \mathbf{B}' \rangle = \langle \mathbf{J}_c \cdot ((\mathbf{B}' \cdot \nabla') \mathbf{B}') \rangle = \nabla_{\ell} \cdot \left\langle \frac{B'^2}{2} \mathbf{J}_c \right\rangle - \mu_0 \langle \mathbf{J}_c \cdot (\mathbf{B}' \times \mathbf{J}') \rangle. \quad (2.88)$$

The term $\partial_t \langle B^2/2\mu_0 \rangle$ can be dealt with easily by remarking that it is no other than the time derivative of magnetic energy $\partial_t \langle E^b \rangle$. Using Faraday equation (1.4) one can show that $\partial_t \langle E^b \rangle = \left\langle -\nabla \cdot \left(\mathbf{E} \times \frac{\mathbf{B}}{\mu_0} \right) - \mathbf{J} \cdot \mathbf{E} \right\rangle$ (note that \mathbf{E} is the electric field and should not be confused with the energy). Then the Ohm's law (1.20) and relation $\Delta \mathbf{X} = \nabla(\nabla \cdot \mathbf{X}) - \nabla \times \nabla \times \mathbf{X}$ lead to:

$$\begin{aligned} \partial_t \langle E^b \rangle &= - \left\langle \nabla \cdot \left[\left(\eta \mu_0 \mathbf{J} - \mathbf{u} \times \mathbf{B} + \frac{1}{ne} \mathbf{J} \times \mathbf{B} \right) \times \frac{\mathbf{B}}{\mu_0} \right] + \mathbf{J} \cdot \left(\eta \mu_0 \mathbf{J} - \mathbf{u} \times \mathbf{B} + \frac{1}{ne} \mathbf{J} \times \mathbf{B} \right) \right\rangle \\ &= \eta \langle \nabla \cdot (\mathbf{J} \times \mathbf{B}) \rangle - \eta \mu_0 \langle \mathbf{J} \cdot \mathbf{J} \rangle - \langle \mathbf{u} \cdot (\mathbf{J} \times \mathbf{B}) \rangle \\ &= \frac{1}{\mu_0} \langle \mathbf{B} \cdot \mathbf{d}_{\eta} \rangle - \langle \mathbf{u} \cdot (\mathbf{J} \times \mathbf{B}) \rangle. \end{aligned} \quad (2.89)$$

Thanks to these relations we find:

$$\begin{aligned}
\partial_t \langle S \rangle &= \partial_t \langle E^{tot} \rangle - \frac{1}{2} \nabla_{\ell} \cdot \langle \bar{\delta} \rho |\delta \mathbf{u}|^2 \delta \mathbf{u} \rangle + \frac{1}{4} \langle (\rho \theta' + \rho' \theta) |\delta \mathbf{u}|^2 \rangle \\
&- \frac{1}{2} \langle \rho \mathbf{u} \cdot (\mathbf{J}'_c \times \mathbf{B}') + \rho' \mathbf{u}' \cdot (\mathbf{J}_c \times \mathbf{B}) - \rho \mathbf{u}' \cdot (\mathbf{J}'_c \times \mathbf{B}') - \rho' \mathbf{u} \cdot (\mathbf{J}_c \times \mathbf{B}) + 2 \mathbf{u} \cdot (\mathbf{J} \times \mathbf{B}) \rangle \\
&- \frac{1}{2 \mu_0} \nabla_{\ell} \cdot \left\langle |\delta \mathbf{B}|^2 \delta \mathbf{u} - 2(\delta \mathbf{u} \cdot \delta \mathbf{B}) \delta \mathbf{B} - \frac{B^2}{2} \mathbf{u}' + \frac{B'^2}{2} \mathbf{u} - (\mathbf{u} \cdot \mathbf{B}') \mathbf{B}' + (\mathbf{u}' \cdot \mathbf{B}) \mathbf{B} \right\rangle \\
&- \frac{\lambda}{2 \mu_0} \nabla_{\ell} \cdot \langle -|\delta \mathbf{B}|^2 \delta \mathbf{J}_c + 2(\delta \mathbf{B} \cdot \delta \mathbf{J}_c) \delta \mathbf{B} \rangle + \lambda \langle \mathbf{J}_c \cdot (\mathbf{B}' \times \mathbf{J}') + \mathbf{J}'_c \cdot (\mathbf{B} \times \mathbf{J}) \rangle \\
&- \frac{1}{2} \left\langle \left(1 + \frac{\rho'}{\rho}\right) \mathbf{u}' \cdot (\mathbf{d}_{\nu} + \mathbf{f}) + \left(1 + \frac{\rho}{\rho'}\right) \mathbf{u} \cdot (\mathbf{d}'_{\nu} + \mathbf{f}') \right\rangle \\
&+ \frac{1}{2} \left\langle \frac{\rho}{\rho'} \mathbf{u}' \cdot (\mathbf{d}'_{\nu} + \mathbf{f}') + \frac{\rho'}{\rho} \mathbf{u} \cdot (\mathbf{d}_{\nu} + \mathbf{f}) \right\rangle - \frac{1}{\mu_0} \langle \mathbf{B}' \cdot \mathbf{d}_{\eta} + \mathbf{B} \cdot \mathbf{d}'_{\eta} - \mathbf{B} \cdot \mathbf{d}_{\eta} \rangle. \tag{2.90}
\end{aligned}$$

Finally, we introduce the relations:

$$\begin{aligned}
\langle 2 \delta \rho \delta \mathbf{u} \cdot \bar{\delta} (\mathbf{J}_c \times \mathbf{B}) \rangle &= \langle \rho' \mathbf{u}' \cdot (\mathbf{J}_c \times \mathbf{B}) + \rho' \mathbf{u}' \cdot (\mathbf{J}'_c \times \mathbf{B}') - \rho' \mathbf{u} \cdot (\mathbf{J}_c \times \mathbf{B}) \\
&- \rho' \mathbf{u} \cdot (\mathbf{J}'_c \times \mathbf{B}') - \rho \mathbf{u}' \cdot (\mathbf{J}_c \times \mathbf{B}) \\
&- \rho \mathbf{u}' \cdot (\mathbf{J}'_c \times \mathbf{B}') + \rho \mathbf{u} \cdot (\mathbf{J}_c \times \mathbf{B}) + \rho \mathbf{u} \cdot (\mathbf{J}'_c \times \mathbf{B}') \rangle, \tag{2.91}
\end{aligned}$$

$$\langle \delta (\mathbf{J} \times \mathbf{B}) \cdot \delta \mathbf{J}_c \rangle = \langle \mathbf{J}_c \cdot (\mathbf{B}' \times \mathbf{J}') + \mathbf{J}'_c \cdot (\mathbf{B} \times \mathbf{J}) \rangle, \tag{2.92}$$

to get:

$$\begin{aligned}
\partial_t \langle S \rangle &= \partial_t \langle E^{tot} \rangle - \frac{1}{2} \nabla_{\ell} \cdot \langle \bar{\delta} \rho |\delta \mathbf{u}|^2 \delta \mathbf{u} \rangle + \frac{1}{4} \langle (\rho \theta' + \rho' \theta) |\delta \mathbf{u}|^2 \rangle - \langle \delta \rho \delta \mathbf{u} \cdot \bar{\delta} (\mathbf{J}_c \times \mathbf{B}) \rangle \\
&- \frac{1}{2 \mu_0} \nabla_{\ell} \cdot \langle |\delta \mathbf{B}|^2 \delta \mathbf{u} - 2(\delta \mathbf{u} \cdot \delta \mathbf{B}) \delta \mathbf{B} - \lambda |\delta \mathbf{B}|^2 \delta \mathbf{J}_c + 2 \lambda (\delta \mathbf{B} \cdot \delta \mathbf{J}_c) \delta \mathbf{B} \rangle \\
&+ \lambda \langle \delta (\mathbf{J} \times \mathbf{B}) \cdot \delta \mathbf{J}_c \rangle \\
&- \frac{1}{2} \left\langle \left(1 + \frac{\rho'}{\rho}\right) \mathbf{u}' \cdot (\mathbf{d}_{\nu} + \mathbf{f}) + \left(1 + \frac{\rho}{\rho'}\right) \mathbf{u} \cdot (\mathbf{d}'_{\nu} + \mathbf{f}') \right\rangle \\
&+ \frac{1}{2} \left\langle \frac{\rho}{\rho'} \mathbf{u}' \cdot (\mathbf{d}'_{\nu} + \mathbf{f}') + \frac{\rho'}{\rho} \mathbf{u} \cdot (\mathbf{d}_{\nu} + \mathbf{f}) \right\rangle - \frac{1}{\mu_0} \langle \mathbf{B}' \cdot \mathbf{d}_{\eta} + \mathbf{B} \cdot \mathbf{d}'_{\eta} - \mathbf{B} \cdot \mathbf{d}_{\eta} \rangle. \tag{2.93}
\end{aligned}$$

2.3.3 From the dynamical equation to the exact law

Similarly to what has been done in section 2.2 we can approximate the forcing and dissipative terms by considering the energy cascade in the inertial range and in a stationary state. Considering the forcing to act at large scales, the dissipation at small ones and using equation (2.64), the following simplifications arise:

$$\frac{1}{\mu_0} \langle \mathbf{B}' \cdot \mathbf{d}_{\eta} + \mathbf{B} \cdot \mathbf{d}'_{\eta} \rangle \simeq 0, \tag{2.94}$$

$$-\frac{1}{2} \left\langle \left(1 + \frac{\rho'}{\rho}\right) \mathbf{u}' \cdot \mathbf{d}_{\nu} + \left(1 + \frac{\rho}{\rho'}\right) \mathbf{u} \cdot \mathbf{d}'_{\nu} \right\rangle \simeq 0, \tag{2.95}$$

$$-\frac{1}{2} \left\langle \left(1 + \frac{\rho'}{\rho}\right) \mathbf{u}' \cdot \mathbf{f} + \left(1 + \frac{\rho}{\rho'}\right) \mathbf{u} \cdot \mathbf{f}' \right\rangle \simeq -2\varepsilon, \tag{2.96}$$

$$\frac{1}{2} \left\langle \frac{\rho}{\rho'} \mathbf{u}' \cdot \mathbf{f}' + \frac{\rho'}{\rho} \mathbf{u} \cdot \mathbf{f} \right\rangle \simeq \varepsilon, \tag{2.97}$$

$$\frac{1}{2} \left\langle \frac{\rho}{\rho'} \mathbf{u}' \cdot \mathbf{d}'_{\nu} + \frac{\rho'}{\rho} \mathbf{u} \cdot \mathbf{d}_{\nu} \right\rangle + \frac{1}{\mu_0} \langle \mathbf{B} \cdot \mathbf{d}_{\eta} \rangle \simeq -\varepsilon. \tag{2.98}$$

This ultimately leads to the exact law for CHMHD turbulence :

$$\begin{aligned}
-4\varepsilon = & \nabla_{\ell} \cdot \left\langle \bar{\delta}\rho |\delta\mathbf{u}|^2 \delta\mathbf{u} + \frac{1}{\mu_0} |\delta\mathbf{B}|^2 \delta\mathbf{u} - \frac{2}{\mu_0} (\delta\mathbf{u} \cdot \delta\mathbf{B}) \delta\mathbf{B} \right\rangle \\
& + \frac{\lambda}{\mu_0} \nabla_{\ell} \cdot \langle 2(\delta\mathbf{B} \cdot \delta\mathbf{J}_c) \delta\mathbf{B} - |\delta\mathbf{B}|^2 \delta\mathbf{J}_c \rangle \\
& - \frac{1}{2} \langle (\rho\theta' + \rho'\theta) |\delta\mathbf{u}|^2 \rangle + 2 \langle \delta\rho \delta\mathbf{u} \cdot \bar{\delta}(\mathbf{J}_c \times \mathbf{B}) \rangle - 2\lambda \langle \delta(\mathbf{J} \times \mathbf{B}) \cdot \delta\mathbf{J}_c \rangle, \tag{2.99}
\end{aligned}$$

that we can rewrite in a compact form as:

$$\boxed{-4\varepsilon = \nabla_{\ell} \cdot (\mathbf{F}_{\text{MHD}} + \lambda \mathbf{F}_{\text{Hall}}) + S_{\text{MHD}} + \lambda S_{\text{Hall}}}, \tag{2.100}$$

where by definition:

$$\mathbf{F}_{\text{MHD}} = \left\langle \bar{\delta}\rho |\delta\mathbf{u}|^2 \delta\mathbf{u} + \frac{1}{\mu_0} |\delta\mathbf{B}|^2 \delta\mathbf{u} - \frac{2}{\mu_0} (\delta\mathbf{u} \cdot \delta\mathbf{B}) \delta\mathbf{B} \right\rangle, \tag{2.101}$$

$$\mathbf{F}_{\text{Hall}} = \frac{1}{\mu_0} \langle 2(\delta\mathbf{B} \cdot \delta\mathbf{J}_c) \delta\mathbf{B} - |\delta\mathbf{B}|^2 \delta\mathbf{J}_c \rangle, \tag{2.102}$$

$$S_{\text{MHD}} = -\frac{1}{2} \langle (\rho\theta' + \rho'\theta) |\delta\mathbf{u}|^2 \rangle + 2 \langle \delta\rho \delta\mathbf{u} \cdot \bar{\delta}(\mathbf{J}_c \times \mathbf{B}) \rangle, \tag{2.103}$$

$$S_{\text{Hall}} = -2 \langle \delta(\mathbf{J} \times \mathbf{B}) \cdot \delta\mathbf{J}_c \rangle. \tag{2.104}$$

Equation (2.100), which will be referred to as F21, contains two Yaglom-like flux terms covering both MHD and Hall scales (\mathbf{F}_{MHD} and \mathbf{F}_{Hall} , respectively) with an overall shape strongly reminiscent of the incompressible law F19 derived in section 2.2, a similarity not observed with A18 due to the different forms of the correlators used in the two derivations. Additionally, two non-flux terms S_{MHD} and S_{Hall} complement the equation: S_{MHD} appears to be a mix of a pure source/sink component function of the dilatation θ and of a local mean component, whereas S_{Hall} consists of a single non-flux component. Although these last two components are not *stricto sensu* "source" terms (as they do not depend on the divergence of a field) we will usually designate them as such to separate them from the Yaglom-like fluxes. Note that, interestingly, the Hall source term is reminiscent of the Hall term from BG17 instead of the one from F19, which is another evidence of the close connections between these two incompressible laws.

The fact that only S_{MHD} depends on the divergence of a field (through the dilatation) is an important improvement over A18, in which all source terms are functions of such divergences. The precise evaluation of the divergence of a field is difficult when dealing with space plasmas data because it requires a three-dimensional mapping of the system to be computed, which in turn calls for multi-spacecraft data (we will return to this matter in chapter 5). Thus, F21 represents an advance for the analysis of space plasma turbulence as the Hall part of the law, which is the most important one when studying compressible plasma turbulence at small scales, can here be fully calculated.

Just like F19, F21 is Galilean invariant: changes on the mean velocity field will not have any impact on the value of the energy cascade rate. However, unlike its incompressible counterpart, the compressible law shows an explicit dependence on a mean background magnetic field \mathbf{B}_0 if it is initially present. When replacing \mathbf{B} by $\mathbf{B} + \mathbf{B}_0$ a new term appears in the right-hand side of (2.100) which reads:

$$S_{\mathbf{B}_0} = 2\mathbf{B}_0 \cdot \langle \delta\rho (\delta\mathbf{u} \times \bar{\delta}\mathbf{J}_c) \rangle - 2\lambda \mathbf{B}_0 \cdot \langle \delta\mathbf{J}_c \times \delta\mathbf{J} \rangle. \tag{2.105}$$

We see that these new terms goes to zero in the incompressible limit, so we retrieve the behavior already observed for F19. The background magnetic field is thus expected to reshape the overall dynamics with more influence than for a purely incompressible turbulent plasma.

2.3.4 Limit cases and alternative compressible laws

From F21 one can retrieve other equations for various simpler models. We mentioned earlier strong similitudes between F21 and the incompressible laws. It is possible to retrieve F19 by taking the incompressible limit $\rho \rightarrow \rho_0$ and renormalizing (2.100) by the density, which leads to considering the normalized variables $\bar{\varepsilon} = \varepsilon/\rho_0$, $\mathbf{b} = \mathbf{B}/\sqrt{\mu_0\rho_0}$ and the ion skin depth $d_i = \lambda/\sqrt{\mu_0\rho_0}$. It is immediate to see that, under this limit, $\mathbf{F}_{\text{MHD}} \rightarrow \mathbf{Y}$ and $S_{\text{MHD}} \rightarrow 0$ (as $\theta \rightarrow 0$). The case of the two Hall terms is less straightforward as neither tends to zero. However, we do find that the sum of the flux and source is:

$$\nabla_{\ell} \cdot \mathbf{F}_{\text{Hall}} + S_{\text{Hall}} = \nabla_{\ell} \cdot \mathbf{H} - 2A = \frac{1}{2} \nabla_{\ell} \cdot \mathbf{H}, \quad (2.106)$$

as was demonstrated in section 2.2. With this we indeed retrieve equation (2.39):

$$-4\bar{\varepsilon} = \nabla_{\ell} \cdot (\mathbf{Y} + \frac{1}{2}\mathbf{H}). \quad (2.107)$$

While the previous limit merely serves as a validation of F21 with regard to F19, new results can also be obtained by considering other limits. Indeed, one can consider the CMHD limit of equation (2.100) by taking $d_i/L \rightarrow 0$. This is simply akin to removing the Hall components of the law, which yields:

$$\boxed{-4\varepsilon^{\text{CMHD}} = \nabla_{\ell} \cdot \left\langle \bar{\delta}\rho |\delta\mathbf{u}|^2 \delta\mathbf{u} + \frac{1}{\mu_0} |\delta\mathbf{B}|^2 \delta\mathbf{u} - \frac{2}{\mu_0} (\delta\mathbf{u} \cdot \delta\mathbf{B}) \delta\mathbf{B} \right\rangle - \frac{1}{2} \langle (\rho\theta' + \rho'\theta) |\delta\mathbf{u}|^2 \rangle + 2 \langle \delta\rho \delta\mathbf{u} \cdot \bar{\delta}(\mathbf{J}_c \times \mathbf{B}) \rangle.} \quad (2.108)$$

In a similar fashion, the limit of CHD can be obtained by taking $\mathbf{B} \rightarrow 0$ (and $\lambda \rightarrow 0$, although this limit is implicitly included in the other). One immediately finds the relation:

$$\boxed{-4\varepsilon^{\text{CHD}} = \nabla_{\ell} \cdot \langle \bar{\delta}\rho |\delta\mathbf{u}|^2 \delta\mathbf{u} \rangle - \frac{1}{2} \langle (\rho\theta' + \rho'\theta) |\delta\mathbf{u}|^2 \rangle = \nabla_{\ell} \cdot \mathbf{F} + S.} \quad (2.109)$$

This compact exact law allows for an efficient analysis of highly compressible turbulent flow where magnetic forces are absent or negligible. The simplicity of both the flux and the source makes it easier to interpret the results and understand the physical processes at work in such a medium. In particular we will make use of it in chapter 4 to study the behavior of supersonic turbulence in the ISM.

2.4 Conclusion

In this chapter I explained in more detail what exact laws are: equations that allow one to estimate the energy cascade rate of a turbulent cascade with minimal approximations of statistical homogeneity, time stationarity and large Reynolds number. I detailed the framework and the general method for deriving exact laws for a given fluid or plasma model, and introduced important notations and properties pertaining to the use of increment vectors.

I provided the complete, step-by-step derivation of a new exact law in IHMHD, obtained through the manipulation of a dynamical equation for a well-chosen second-order structure function (2.12), which was already proposed by Hellinger et al. (2018). This derivation led to a simple, Yaglom-like expression for the energy cascade rate (2.39), a formulation quite different from the already existing laws G08 (Galtier, 2008) and BG17 (Banerjee and Galtier, 2017). Nevertheless I proved that these 3 laws, despite stemming from different premises and taking different forms, are mathematically equivalent under the aforementioned assumptions. This allows one to choose which law to use depending on the data and the objective: BG17 is

expected to converge quicker and lift some constraints of directionality in the system, whereas [F19](#) will be more efficient to study data from single-spacecraft missions.

I also proposed a lengthy derivation for the more complex model of [CHMHD](#), although with a bit less details in some intermediate calculations. This allowed us to obtain a much simpler exact law ([2.100](#)) than the one already derived by [Andrés et al. \(2018\)](#), featuring only 9 separate terms instead of the previous 35. Furthermore this new law has a lesser emphasis on source terms and divergences of vector fields (with only two of these terms), which greatly simplify its computation, especially on single satellite data since it does not require computing many vector fields derivatives. Taking the limits of [CMHD](#) and [CHD](#) yielded two simplified laws, removing the need for a specific calculation in each of these models.

These two laws are also theorized to behave differently in presence of a background magnetic field. In the case of [IHMHD](#) the mean field has no direct impact on the computed energy cascade rate, aside from its underlying effect on the turbulence dynamics. Results will not change if it is not included in the calculation and one can remove it safely beforehand if necessary. However, both source terms of [F21](#) show a direct dependence on the mean magnetic field, which is thus expected to have a greater impact on the shape and amplitude of these terms. These assumptions will be verified on [DNS](#) data in [chapter 4](#).

All these exact laws, and more specifically the ones for [IHMHD](#), [CHD](#) and [CHMHD](#) models, will be put to the test and used in [chapter 4](#) to analyze [DNS](#) data obtained from various codes and physical models. We will see on this occasion that the compactness of these laws is an important asset for simplifying the physical interpretation of the results.

All the results presented in this chapter are published in two papers: [Ferrand, Galtier, Sahraoui, Meyrand, Andrés, and Banerjee \(2019\)](#) [*Astrophysical Journal* **881**] for the derivation of the [IHMHD](#) law [F19](#), and [Ferrand, Galtier, and Sahraoui \(2021a\)](#) [*Journal of Plasma Physics* **87**] for the [CHMHD](#) exact law [F21](#). The former also contains numerical results presented in [chapter 4](#) of this thesis.

Chapter 3

Methodology: laws computation and numerical implementation

3.1 Introduction

Now that most of the theoretical work has been done, and that new laws have been derived in chapter 2, we need a way to apply these equations to either real data or DNS data. When computing exact laws on one dimensional data measured by satellites, the time average on increment values (equivalent to a spatial average under the Taylor hypothesis, on which we will come back at the beginning of chapter 5) can only be done directly on the single line of data used, so the method of calculation in itself is rather straightforward. The case of 3D DNS data analysis is much more complicated however, as it offers the possibility to compute the laws with a much better accuracy than in *in situ* data. Computing an exact law on such a dataset requires having strong enough statistics for a given increment vector ℓ , by taking an average over as many pairs of points as possible, but also considering enough different sizes and directions for said vector to obtain a broad and accurate representation of the turbulent cascade. This "double average" is a very costly process which requires using parallel computing to reduce the execution to a reasonable execution time. The numerical code also needs to be optimized in memory usage to prepare for future works on larger datasets.

In light of these remarks, this chapter will aim at explaining in details the methods chosen to compute the exact laws in a generic 3D DNS dataset. I will provide a mathematical description of these methods for the different models studied and explain the numerical implementation and parallelization. Once this protocol has been established, its limitations and potential ways to improve the overall performances in the future will be discussed. A note of warning: this chapter is a purely technical one and features no discussion on physics whatsoever. Yet, the topics presented here need to be discussed to understand some difficulties and a very few of the results presented in chapter 4. Readers that would prefer to avoid this kind of discussion are advised to jump directly to the next chapter, and would understand almost all the physical results presented there.

3.2 Numerical calculation of exact laws

3.2.1 Generic framework

The numerical code I designed to compute the energy cascade rate in DNS data was written in Python for convenience and to easily adjust it on the fly. It requires all three components of the velocity and the magnetic field (or the potential vector if the magnetic field is not readily available), and for compressible models the density scalar field, to compute the energy cascade rate. These data must be laid on a 3D regular grid and be periodic in all three directions of space. This allows one to use the maximum amount of pairs of points to average on even for

large modulus of the increment vector.

As was stated before, the calculation of the exact law requires averaging over as much pairs of points as possible in the physical space, connected by a broad variety of increment vectors probing all directions of space, to obtain the most accurate estimate of the energy cascade rate. Various methods exist, such as randomly generating pairs of points $(\mathbf{r}, \mathbf{r}')$ and binning afterwards on the corresponding increments $\boldsymbol{\ell} = \mathbf{r}' - \mathbf{r}$, or selecting increments of evenly spaced directions and sizes and defining \mathbf{r}' from \mathbf{r} and $\boldsymbol{\ell}$. The problem of the first method is that it gives little to no control on the direction and size of the increments used in the study, whereas the second method requires a 3D interpolation of all vector fields (a costly and lengthy process) as, for most increment vectors, position $\mathbf{r}' = \mathbf{r} + \boldsymbol{\ell}$ will not lie on a grid point.

The method I chose for my code is an alternative to the second option, and is inspired by the work of Taylor et al. (2003). Instead of selecting increments of regularly sampled directions and interpolating when the pair of points do not lie on grid points, I specifically choose the increment vectors so that they always lead from a grid point to another one. To do so I define a "base vector", for instance $\boldsymbol{\ell} = (1, 0, 1)$ in units of the grid resolution. For any position $\mathbf{r} = (x, y, z)$ of a grid point, the corresponding $\mathbf{r}' = (x + 1, y + 0, z + 1)$ will obviously lie on a grid point too, so the correlations for all pairs of points defined this way can be readily calculated without any interpolation. I then take all possible multiples of this base vector: $\boldsymbol{\ell} = (n, 0, n)$ for any positive integer n . This defines a direction for the increment in which I will have all the required information to compute the scale-dependent exact law (see figure 3.1 for a visual representation).

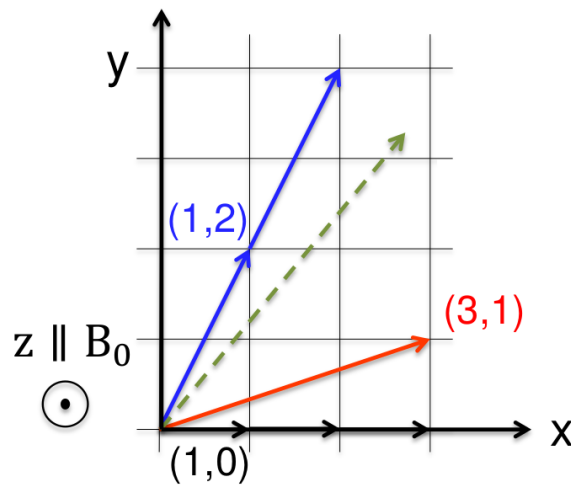


Figure 3.1: 2D representation of the selection method for increment vectors. Vectors obtained by taking an increment vector $((1,0)$ in black, $(1,2)$ in blue, $(3,1)$ in red) and its multiples always fall on grid points. An arbitrary increment vector not landing on a grid point (example in green) will require an interpolation.

By carefully selecting the base vectors we can obtain a set of well distributed directions, and along each direction (defined by a given base vector) compute the exact law at discrete scales equal to the norm of the various multiples of the corresponding base vector. For a given increment, all the spatial averages are obtained by summing over the whole simulation domain, so that the spatial average of any function $\xi(\mathbf{r}, \boldsymbol{\ell})$ is given by:

$$\langle \xi \rangle (\boldsymbol{\ell}) = \sum_{\mathbf{r}} \frac{\xi(\mathbf{r}, \boldsymbol{\ell})}{N_X N_Y N_Z}, \quad (3.1)$$

where (N_X, N_Y, N_Z) are the dimensions of the numerical grid. This average is sufficient to compute all source terms of the laws, however for flux terms of the form $\nabla_{\boldsymbol{\ell}} \cdot \langle \mathbf{F} \rangle$ the average

$\langle \mathbf{F} \rangle$ will have to be evaluated in several directions in order to compute the derivative. Thus, in a given direction, only $\langle \mathbf{F} \rangle$ will be computed and the derivative will be applied *a posteriori*. Note that this process only gives the value of the exact law at discrete scales that depend on the direction, so a 1D interpolation is required to retrieve the values at any given scale and average the law over multiple directions. The ensemble of chosen base vectors depends on the data we want to study, the underlying plasma model, and the hypotheses we make on the symmetries of the system.

3.2.2 Isotropy hypothesis: 3D increments

In HD models, or MHD simulations when there is no background magnetic field, it is appropriate to consider the system to be isotropic, as no privileged direction appears. In this situation we naturally adopt a spherical coordinates system, in which $\boldsymbol{\ell}$ is defined as $\boldsymbol{\ell} = (\ell, \phi, \theta)$. Thanks to the isotropy hypothesis the derivative operator $\nabla_{\boldsymbol{\ell}}$ appearing in the calculation of flux terms reduces to $\nabla_{\boldsymbol{\ell}} \cdot \langle \mathbf{F} \rangle = \frac{1}{\ell^2} \partial_{\ell} [\ell^2 \langle F_{\ell} \rangle_{\phi, \theta}(\ell)]$, where $\langle F_{\ell} \rangle_{\phi, \theta}$ represents the non-weighted average of $\langle F_{\ell} \rangle$ (in the space of increments) over ϕ and θ . Thus, we only have to compute the projection of the vectorial flux \mathbf{F} on the direction of $\boldsymbol{\ell}$, which writes:

$$\langle F_{\ell} \rangle(\ell, \phi, \theta) = \langle \cos(\phi) \sin(\theta) F_x + \sin(\phi) \sin(\theta) F_y + \cos(\theta) F_z \rangle. \quad (3.2)$$

These projections are then averaged at fixed ℓ :

$$\langle F_{\ell} \rangle_{\phi, \theta}(\ell) = \sum_{\phi, \theta} \frac{\langle F_{\ell} \rangle(\ell, \phi, \theta)}{n_{dir}}, \quad (3.3)$$

where n_{dir} is the number of different directions taken for $\boldsymbol{\ell}$, equivalent to the number of different base vectors retained.

In this situation the chosen increment vectors need to probe all directions of space as evenly as possible, while maintaining a good resolution on the calculation. This means that we need to take as many base vectors as possible while limiting their norm. Indeed, in a direction defined by a base vector $\boldsymbol{\ell}$ the minimum scale at which we can make use of the interpolation is $\|\boldsymbol{\ell}\| = \ell$: taking large base vectors brings no information at the smallest scales of the turbulence which, in the case of Hall MHD, is where most of the Hall-driven physics is expected to occur. For the case of a 3D Isotropic computation I thus chose the same set described by Taylor et al. (2003): I took vectors (1,0,0), (1,1,0), (1,1,1), (2,1,0), (2,1,1), (2,2,1), (3,1,0), and (3,1,1), all vectors defined by permutations of the sign and index of their coordinates, and removed all opposed vectors. This yields the following set:

$$\begin{aligned} \boldsymbol{\ell}_{base} \in \{ & (1, 0, 0), (1, 1, 0), (1, 1, 1), (2, 1, 0), (2, 1, 1), (2, 2, 1), (3, 1, 0), (3, 1, 1), (0, 1, 0), (0, 0, 1), \\ & (0, 1, 1), (1, 0, 1), (-1, 1, 0), (-1, 1, 1), (1, 1, -1), (1, 2, 0), (0, 2, 1), (0, 1, 2), (2, 0, 1), \\ & (1, 0, 2), (-2, 1, 0), (-1, 2, 0), (1, 2, 1), (1, 1, 2), (-2, 1, 1), (2, 1, -1), (-1, 2, 1), (1, 2, -1), \\ & (-1, 1, 2), (1, 1, -2), (1, 2, 2), (2, 1, 2), (-2, 2, 1), (2, 2, -1), (-1, 2, 2), (1, 2, -2), \\ & (-2, 1, 2), (2, 1, -2), (1, 3, 0), (0, 3, 1), (0, 1, 3), (3, 0, 1), (1, 0, 3), (-3, 1, 0), (-1, 3, 0), \\ & (1, 3, 1), (1, 1, 3), (-3, 1, 1), (3, 1, -1), (-1, 3, 1), (1, 3, -1), (-1, 1, 3), (1, 1, -3), \\ & (0, 1, -1), (1, 0, -1), (-1, 1, -1), (0, 2, -1), (0, 1, -2), (2, 0, -1), (1, 0, -2), (-2, 1, -1), \\ & (-1, 2, -1), (-1, 1, -2), (-2, 2, -1), (-1, 2, -2), (-2, 1, -2), (0, 3, -1), (0, 1, -3), \\ & (3, 0, -1), (1, 0, -3), (-3, 1, -1), (-1, 3, -1), (-1, 1, -3) \}, \end{aligned} \quad (3.4)$$

which is constituted of $n_{dir} = 73$ vectors of norms at most $\sqrt{11}$ (i.e. slightly more than three times the grid resolution) probing half of the space. The reason the other 73 opposed vectors are removed is because all exact laws are invariant under the transformation $\boldsymbol{\ell} \rightarrow -\boldsymbol{\ell}$, so considering these additional vectors would only provide redundant information. This set has been successfully used before (Taylor et al., 2003; Andr es et al., 2018) and was shown to be well-enough distributed spatially to give a reliable representation of the 3D energy cascade.

3.2.3 Axisymmetry hypothesis: 3D increments

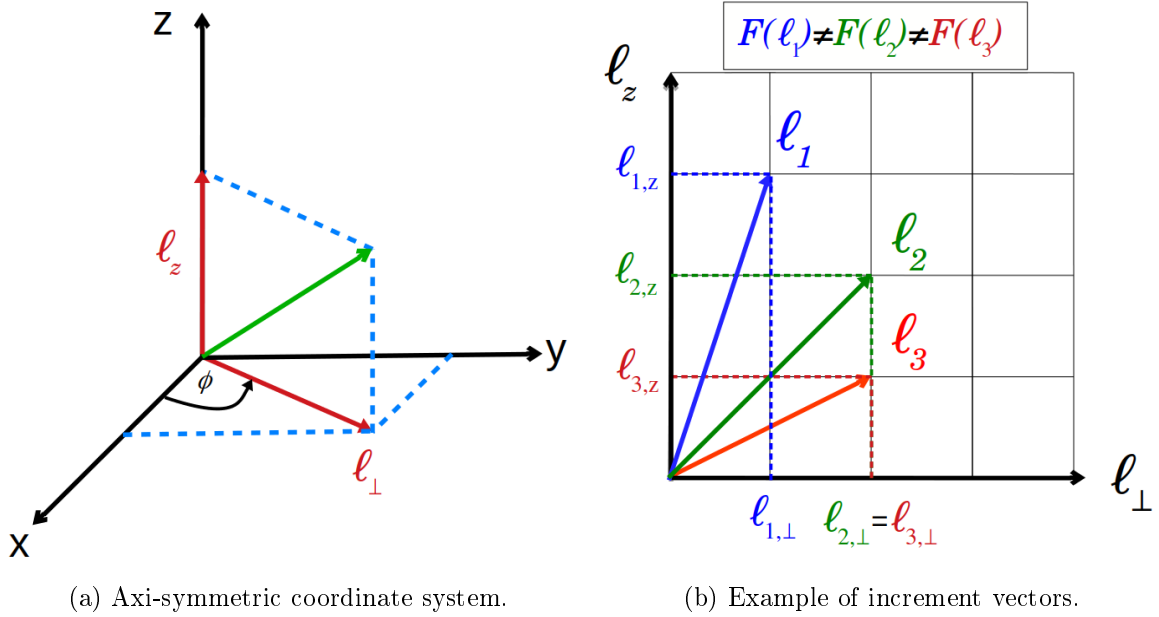


Figure 3.2: Representation of the coordinate system used to describe increments in the axi-symmetric case, and examples of increment vectors (projected on a 2D plane for a simplified representation). Note that several increment vectors can share the same orthogonal component and still differ by their parallel component: exact laws computed for such increments are averaged, and their contributions are attributed to the common orthogonal component ℓ_{\perp} . Be aware that, even if two increment vectors share the same orthogonal component, the respective flux contributions are not identical *a priori* !

For simulations where a strong enough background magnetic field is present the cascading modes are expected to be located predominantly in the plane orthogonal to \mathbf{B}_0 . Consequently, we will usually prefer to the isotropy assumption a symmetry of revolution around \mathbf{B}_0 (usually chosen to be the z -axis). In this case we adopt cylindrical coordinates: the increment vector is defined as $\ell = (\ell_{\perp}, \phi, \ell_z)$ and the derivative operator becomes $\nabla_{\ell} \cdot \langle \mathbf{F} \rangle = \frac{1}{\ell_{\perp}} \partial_{\ell_{\perp}} [\ell_{\perp} \langle F_{\ell_{\perp}} \rangle_{\phi}(\ell_{\perp}, \ell_z)] + \partial_{\ell_z} \langle F_{\ell_z} \rangle_{\phi}(\ell_{\perp}, \ell_z)$. However, the discrete choice of directions adopted here makes it impossible to effectively compute $\partial_{\ell_z} \langle F_{\ell_z} \rangle_{\phi}(\ell_{\perp}, \ell_z)$ at arbitrary values of (ℓ_{\perp}, ℓ_z) without resorting to multi-dimensional interpolation on irregular grids, bringing lots of additional calculations and more imprecision to the results. Consequently, we will only study transfers in transverse directions by considering the flux averaged in the z direction, i.e. the average of the fluxes calculated for increments with a fixed ℓ_{\perp} and a variable ℓ_z (see figure 3.2). The derivative operator is thus reduced to: $\nabla_{\ell} \cdot \langle \mathbf{F} \rangle = \frac{1}{\ell_{\perp}} \partial_{\ell_{\perp}} [\ell_{\perp} \langle F_{\ell_{\perp}} \rangle_{\phi, \ell_z}(\ell_{\perp})]$. We compute the projection of \mathbf{F} on the direction of ℓ_{\perp} as:

$$\langle F_{\ell_{\perp}} \rangle(\ell_{\perp}, \phi, \ell_z) = \langle \cos(\phi)F_x + \sin(\phi)F_y \rangle, \quad (3.5)$$

and take the average over all directions:

$$\langle F_{\ell_{\perp}} \rangle_{\phi, \ell_z}(\ell_{\perp}) = \sum_{\phi, \ell_z} \frac{\langle F_{\ell_{\perp}} \rangle(\ell_{\perp}, \phi, \ell_z)}{n_{dir}}. \quad (3.6)$$

The selection of the set of vectors is a bit trickier for this model due to data periodicity. Indeed, we need to choose the base vectors so that their multiples will reach values of ℓ_{\perp} large enough to gather information at all pertinent scales. Typically, as the datasets are periodic, the maximum useful scale is of half the simulation domain. Any larger increments would in fact correspond to smaller ones, and thus any calculation done at such large scales would be ill defined (see figure 3.3). Thus, the parallel coordinate ℓ_z should never be taken larger than

half the simulation domain either as it would give a contribution corresponding to a different, smaller increment and alter the calculation of the exact law. In summary, for a dataset of size L , we need to use only increment vectors whose component ℓ_\perp spans the entire interval $[0, L/2]$, and so that $\ell_z \leq L/2$. Due to these limitations, we only keep base vectors that verify the property $\ell_\perp \geq \ell_z$, which will ensure that these conditions are verified. Following this remark, I chose to take the same set of vectors (3.4) as in the isotropic case and removed all vectors not verifying this property, which gives a set of $n_{dir} = 57$ directions:

$$\begin{aligned} \ell_{base} \in \{ & (1, 0, 0), (1, 1, 0), (1, 1, 1), (2, 1, 0), (2, 1, 1), (2, 2, 1), (3, 1, 0), (3, 1, 1), (0, 1, 0), (0, 1, 1), \\ & (1, 0, 1), (-1, 1, 0), (-1, 1, 1), (1, 1, -1), (1, 2, 0), (0, 2, 1), (2, 0, 1), (-2, 1, 0), (-1, 2, 0), \\ & (1, 2, 1), (-2, 1, 1), (2, 1, -1), (-1, 2, 1), (1, 2, -1), (1, 2, 2), (2, 1, 2), (-2, 2, 1), (2, 2, -1), \\ & (-1, 2, 2), (1, 2, -2), (-2, 1, 2), (2, 1, -2), (1, 3, 0), (0, 3, 1), (0, 1, 3), (3, 0, 1), (-3, 1, 0), \\ & (-1, 3, 0), (1, 3, 1), (-3, 1, 1), (3, 1, -1), (-1, 3, 1), (1, 3, -1), (0, 1, -1), (1, 0, -1), \\ & (-1, 1, -1), (0, 2, -1), (2, 0, -1), (-2, 1, -1), (-1, 2, -1), (-2, 2, -1), (-1, 2, -2), \\ & (-2, 1, -2), (0, 3, -1), (3, 0, -1), (-3, 1, -1), (-1, 3, -1) \}. \end{aligned} \quad (3.7)$$

Note that, by disregarding parallel fluxes, axi-symmetric models may miss a small portion of the cascade. Due to this limitation the isotropic decomposition may sometimes yield slightly better results even in presence of background magnetic field, as we will see in chapter 4.

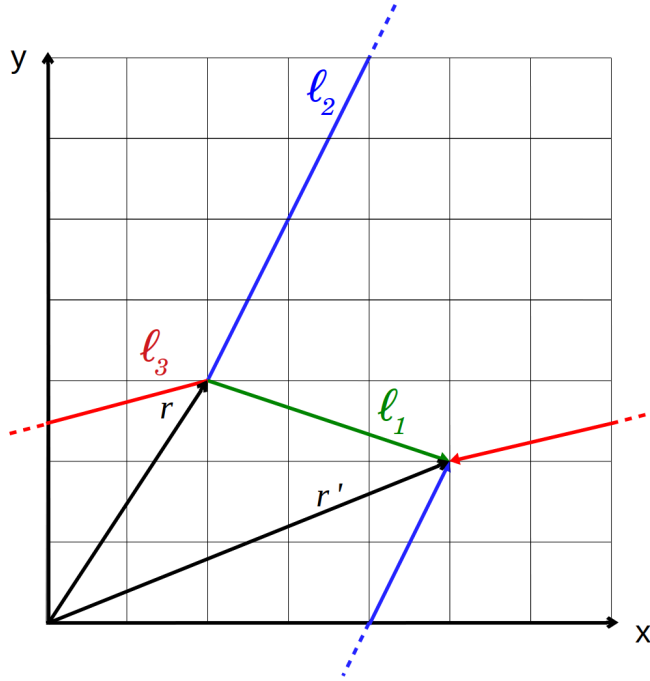


Figure 3.3: Due to the periodicity of the data, the two points \mathbf{r} and \mathbf{r}' can be connected by the green increment ℓ_1 , the blue one ℓ_2 or the red one ℓ_3 (among others), but the green one is the only one that has a norm inferior to half the size of the simulation domain. The values of the exact laws calculated with either increment will be the same, as points \mathbf{r} and \mathbf{r}' are left unchanged. Consequently, using increments whose size exceeds half the size of the simulation domain will yield results that should be attributed to a totally different, smaller increment vector, and as such the related calculations are ill defined.

3.2.4 Axisymmetry hypothesis: 2D increments

The case of an axisymmetric dataset can also be treated through a simpler 2D selection of increment vectors by only considering vectors in the plane orthogonal to \mathbf{B}_0 . This basically

means that we only consider increments for which $\ell_z = 0$. Here again the derivative operator will read $\nabla_{\boldsymbol{\ell}} \cdot \langle \mathbf{F} \rangle = \frac{1}{\ell_{\perp}} \partial_{\ell_{\perp}} [\ell_{\perp} \langle F_{\ell_{\perp}} \rangle_{\phi}(\ell_{\perp})]$ and the expressions for $\langle F_{\ell_{\perp}} \rangle_{\phi}$ remain unchanged. The set of base vectors in this case is chosen similarly to the one used by [Imazio and Mininni \(2017\)](#) and [Andrés et al. \(2018\)](#), which is a reduction of (3.4) where all vectors with $\ell_z \neq 0$ are removed. It consists of the 12 base vectors:

$$\begin{aligned} \boldsymbol{\ell}_{base} \in \{ & (1, 0, 0), (1, 1, 0), (2, 1, 0), (3, 1, 0), (0, 1, 0), (-1, 1, 0), (1, 2, 0), \\ & (-2, 1, 0), (-1, 2, 0), (1, 3, 0), (-3, 1, 0), (-1, 3, 0) \}. \end{aligned} \quad (3.8)$$

This set naturally gives less precise results due to the weaker statistics provided by these 12 directions, but the overall trends observed in the exact laws should not be radically different between this model and the 3D one. This method has the advantage of being way faster to run on simulation data, as the bi-directionality of the study allows for a more efficient parallelization of the numerical code (we will give more details on this topic in the following section). It was used for the tests on [IHMHD](#) exact laws, which required less precision to yield meaningful results, and for most early tests led on various simulations data in order to gather first insights and prepare for the more detailed (and costly) calculation that came after.

3.3 Implementation of the numerical methods

3.3.1 Main steps of the calculation

Whatever the model chosen to make the calculation of the exact laws, the structure of the code remains the same. The program is written in Python and makes a notable use of the libraries Numpy for array manipulation, Numexpr for realizing efficient array operations and scipy for data interpolation. Additional libraries were used to open the data (h5py) and allow for the parallelization of the code (mpi4py).

The program first loads all the necessary data (at most all three components of the velocity and magnetic fields and the density) and computes all the other fields required to the calculation. This goes from just computing the current from the magnetic field in the [IHMHD](#) case, to computing all fields divergences, the pressure, the internal energy etc. for [CHMHD](#). The end goal is that all individual vectorial and scalar fields appearing in the computation are readily available and can be put together to calculate the various structure functions forming the laws. The derivative of any scalar field is obtained by applying a 5-point stencil central differences method to every point of the field in the desired direction:

$$f'(x) \approx \frac{-f(x+2h) + 8f(x+h) - 8f(x-h) + f(x-2h)}{12h}, \quad (3.9)$$

taking advantage of the periodicity to avoid boundary effects.

Once all variables have been calculated at all points of the grid, the exact laws are computed through two nested loops: one on the base vectors, and another on the multiples of the currently used base vector. The end point of this second loop is determined by the number of multiples of the base vector it is necessary to take to obtain an increment of half the size of the simulation domain. Variables evaluated at point \mathbf{r} are stored in the base array, and data evaluated at point $\mathbf{r}' = \boldsymbol{\ell} + \mathbf{r}$ are obtained by shifting the array in all three directions according to the Cartesian coordinates of $\boldsymbol{\ell}$. For each iteration the terms of the exact laws are computed at all points through array calculation with the Numexpr module, which allows for a very fast evaluation of array expressions thanks to cache optimization and reduced memory access. These calculations give the scale-dependent variations of all terms of the laws in all specified directions.

Finally, once all mono-directional structure functions have been computed, we proceed for each of those to a 1D interpolation using cubic splines, a piecewise cubic polynomial which is twice continuously differentiable, in order to obtain the values of the functions for

scales between the ones they were first evaluated at. Results from all directions are then averaged according to the chosen model. This program thus provides the twice averaged scale-dependent values of each separate term of the exact laws, and can be easily modified to compute other kinds of structure functions or consider different sets of vectors.

3.3.2 Parallelization paradigm

The first implementations of the program required around an hour to compute the [CMHD](#) exact law components on a small 256^3 dataset with only the 2D increments. Considering [CHMHD](#) would take even more time due to the presence of more terms to compute and that larger data cubes would have to be studied after, the need to optimize the code to reduce the execution time rapidly arose. The first attempts at a "naive" parallelization, consisting on parallelizing the directions loop (and so computing the terms for several directions simultaneously) only managed to cut the execution time in half at best, and so did not yield satisfying results.

The method I finally chose to implement consists in a [Message Passing Interface \(MPI\)](#) parallelization that divides the data itself and distributes it evenly between all processors. The idea is to write the code as a function of the rank of the processors (i.e. its ID number) so that each processor interprets the instructions differently and only executes a part of the total work. However, when working with [MPI](#), each processor possesses its own memory, that is not shared with the others. This requires sending the relevant data to each processor so they can proceed with the calculations, and regrouping the final results at the end of the execution. Of course, one cannot simply send all the data used to each processor as the memory usage will be multiplied by the total number of processors (which will most certainly trigger a memory error). Thus, a bit of memory management is required to do things right.

First, a single processor opens the base data and computes all the additional arrays. For each of these arrays, the base processor sends only a slice of the data (usually cut along the mean magnetic field axis, by default the z-axis) to every other processor (see figure 3.4). This ensures that, at any given time, the memory allocated to store n variables corresponds to at most (n+1) data cubes (n cubes for the variables and an additional empty one scattered between processors destined to receive the data sent). The initial data cubes are ultimately deleted so that the base processor too only keeps the slice it needs.

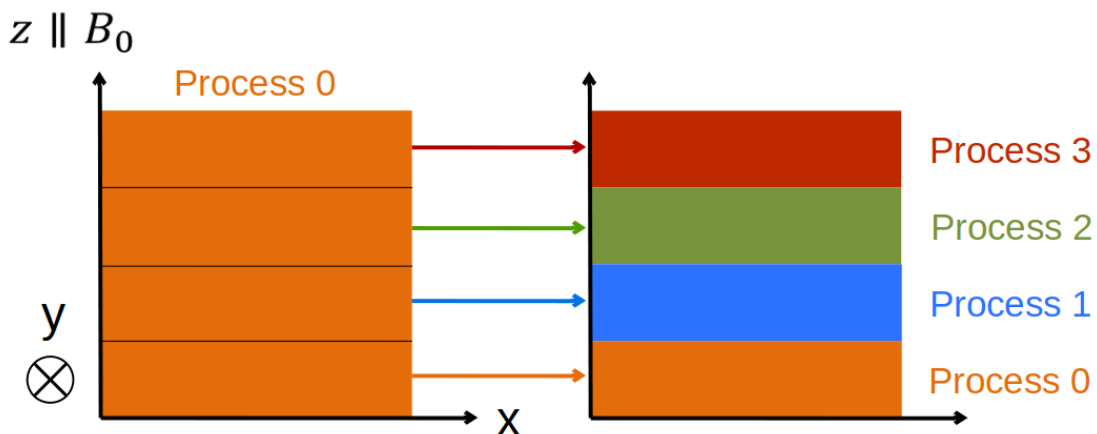


Figure 3.4: Visual representation of the data distribution between processors. All data, initially held by the base processor 0, is cut along the z-axis then distributed to other processors, which will work individually on its own part.

Once the data transfer is done, each processor will compute the scale-dependent structure functions for its own part of the data. Here the method differs slightly depending on the vector set adopted: if we use the 2D set, all increment vectors lie in the (xy) plane. As the

data slices are cut along the z-axis, all pair of points will be contained in a given slice, so each processor is self-sufficient and can make all the calculations without communicating with the others. However, in the case of a 3D vector set, all increment vectors with a non-zero l_z component will lead outside of the slice from some positions \mathbf{r} , so the processor will need to communicate with the other ones to retrieve the data at the shifted positions \mathbf{r}' . This unfortunately introduces an additional communication cost that slows down the execution of the program.

After all the calculations have been done, the results from all processors are reduced and summed in the base processor which will complete the execution by itself by computing the cubic splines and averaging over directions. With this method of parallelization I was able to cut the computation time by a significant amount, as shown in figure 3.5. This benchmarking was led on a small 256^3 CHMHD dataset. It compares the execution speed of the program for 1, 2, 4, 8, 16 and 32 processors on two decompositions, the 2D one and an adapted 3D one reduced to 12 vectors so that both compute the same number of directions. With no parallelization (i.e. one processor) both models show similar execution times, which is coherent as they proceed to roughly the same amount of calculations. For two processors or more however the 2D model shows more improvements than the 3D one, especially when using a large number of processors, going from $\sim 4000s$ to $\sim 100s$ whereas the 3D models only improves towards $\sim 400s$ and shows even worse results for 32 processors. This clearly shows the limitation imposed by the constant communications between processors imposed by the 3D models: parallelization is less efficient and using too many processors ultimately makes the communication cost overshadow the improvements on the calculations. This behavior tends to become less noticeable as the size of the datasets increases: for 512^3 it is still worth to go as far as using 64 processors to lead a full 3D computation.

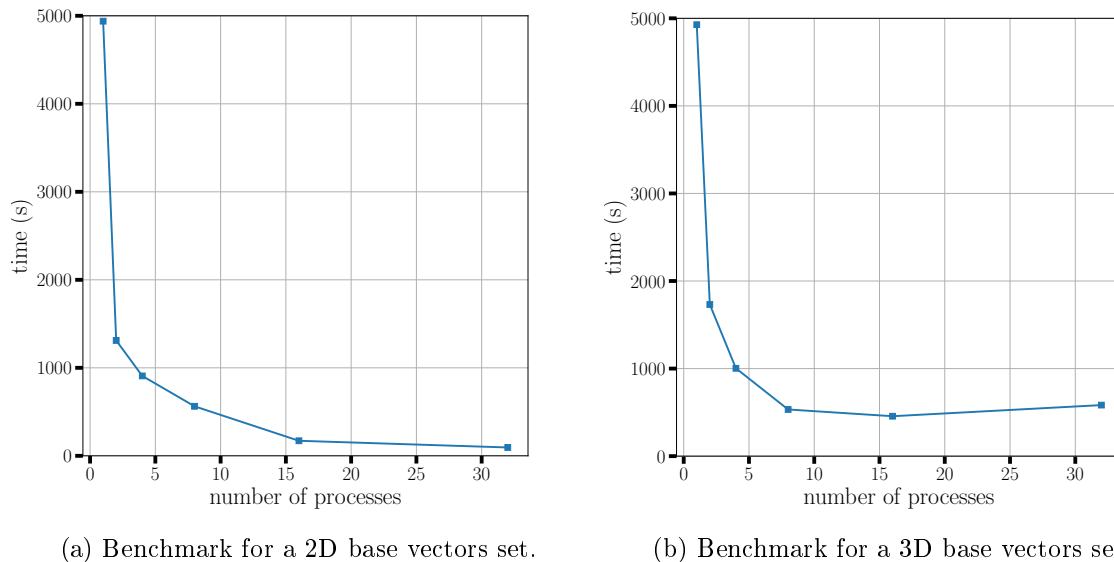


Figure 3.5: Benchmark on the efficiency of the parallelization of the program for both 2D and 3D base vectors sets led on a 256^3 CHMHD simulation. The 2D set is the 12 vectors one depicted in section 3.2.4, and the 3D one is a 12 vectors set obtained from the one depicted in section 3.2.3 by keeping only vectors whose coordinates are 0 or ± 1 .

3.3.3 Memory constraints

Due to the size of the data cubes used in the calculations, memory usage can quickly become a limiting factor. This is especially true for the data used in the CHD study of ISM simulations that will be detailed in chapter 4, as the cubes on which the calculations were made are

of resolution 2512^3 . This means that for single precision floats, only the 4 initial cubes representing the density and the velocity field already take 254 Gb of memory, which is unrealistic in the scope of simple data analysis. This kind of problem called for an improvement of the program in order to keep instantaneous memory usage at a reasonable level.

The method I used in most of my studies simply consists in analyzing only a part of the data at once, by loading and working on a slice of the total dataset, again cut along the z-axis. To compute the derivatives I also had to load two small additional slices above and below the main studied slice, and which will be discarded once the derivatives calculation is done. Of course this method only works for the 2D base vectors decomposition, as using increment vectors with a non-zero ℓ_z component would create pairs of points for which \mathbf{r}' lies outside of the loaded data. Nevertheless it was sufficient to lead the study of the largest datasets, for which the computation time was a determining limiting factor anyways.

Other options were thought of to reduce memory usage, notably saving all the derivatives and other additional arrays as hdf5 datasets (exactly like the base arrays) and having all processors open their own instance of the files. Each processor would then store two arrays of coordinates for \mathbf{r} and \mathbf{r}' instead of the data arrays, and use them to load on the fly the part of the data required for the calculation. Theoretically, this could both reduce the memory usage, as portions of the large data arrays are only loaded punctually, and improve the execution time when using 3D base vectors decompositions, as processors would have access to any part of the data and would not have to communicate between one another anymore. However, opening a file several times in several processors simultaneously proved to be more difficult than expected, and as the program worked fine as is I did not take more time to investigate such possibilities.

3.4 Conclusion

In this chapter, I present the general theory adopted to compute the exact laws in a 3D periodic dataset. In order to avoid costly 3D interpolations, I adopt the angle averaging technique described by [Taylor et al. \(2003\)](#), that express all the increment vectors the laws are averaged on as multiples of pre-selected base vectors. Two main sets of base vectors are discussed, one to be used on axi-symmetric simulations (i.e. mostly simulations featuring a non-zero background magnetic field) and another one more suited for the analysis of isotropic datasets. The first one however has the drawback of discarding fluxes in the direction of the mean magnetic field, which could give slightly incomplete results.

The program is parallelized using [MPI](#) to make each processor work on an individual slice of the data, cut along the direction of the background magnetic field (or by default the z-direction). This parallelization allowed for vast improvements, cutting the execution time by a factor of hundreds when analyzing a 256^3 dataset with only transverse increment vectors. When also using non-transverse increments however, the overhead cost induced by the communications between processors can exceed the benefits of parallelization when working with too many processors. Note however that this situation is not encountered for datasets of resolution 512^3 , as they are usually analyzed using a maximum of 64 processors, which is not enough in this case to induce prohibitive communication costs.

Currently the program is lacking an efficient way to save memory for the study of large datasets, as the method proposed in this chapter only works when working with transverse increments only. To continue using this program in the future it may be useful to find another way to economize memory, for instance by storing all relevant data cubes on hard drive memory and letting each processor access a specific part of the files, provided the continuous data reading would not increase the computation time too much.

Chapter 4

Understanding plasma turbulence through DNS data analysis

4.1 Introduction

In previous chapters I presented the derivation of exact laws for a variety of flow and plasma models, and the elaboration of a method and a numerical program to apply them to either [DNS](#) or *in-situ* data. In this chapter, these tools will be used to study the behavior of turbulence in different models and physical contexts through the analysis of various [DNS](#) datasets. A total of four studies are presented which are summarized below:

- In the first of these studies, I applied the protocol developed in chapter [3](#) to compute the incompressible exact laws [G08](#), [BG17](#) and [F19](#) on an [EMHD](#) dataset simulated by Romain Meyrand ([Meyrand and Galtier, 2013](#)). This study aims at confirming numerically the equivalence between the three laws, understanding the potential limits of this equivalence, and investigating the influence of a background magnetic field on the turbulence.
- The second of these studies started with a similar goal as the first one: investigating the relationship between the two compressible laws [A18](#) and [F21](#), and along the way getting a better understanding of how the different components of [F21](#) relate to one another, similarly to what was done in [Andrés et al. \(2018\)](#) for law [A18](#). To this end I used the [Geophysical High-Order Suite for Turbulence \(GHOST\)](#) code to simulate three [CHMHD](#) runs with varied parameters, and calculated the exact laws on them. Other problematics arose during the study concerning the decaying nature of turbulence of these runs, which led me to compute and analyze generalized versions of the exact laws valid without the stationarity hypothesis.
- The third study is more physics-oriented than the previous two, and aims at tackling a fundamental problem of space plasma turbulence analysis: is the *fluid* turbulent cascade rate estimated with exact laws in simulations and spacecraft observations representative of the actual *kinetic* dissipation in media such as the [SW](#) ? This question is all but trivial, as a fluid plasma model does not take into account any kinetic effect, which are supposed to be the main energy dissipation channels in non-collisional plasmas. This question is tackled through a collaborative work with Dimitri Laveder, Thierry Passot and Pierre-Louis Sulem who, following inputs that we provided, ran an ensemble of eight simulations of [CHMHD](#) turbulence with [CGL](#) and [LF](#) closures, featuring the presence (or absence) of various intensities of Landau damping. I then analyzed those simulation data and computed the energy cascade rates on these datasets with exact law [F19](#), compared their behaviors between the simulations, and attempted to estimate separately the energy dissipation to understand to what extent the fluid cascade rate

would be able to feel Landau dissipation. The direct estimation of the dissipation due to Landau damping brought the final evidence needed to quantitatively correlate the energy cascade to the kinetic dissipation.

- The fourth and final study presented in this chapter focuses onto a different medium than the SW that is at the heart of most of this thesis. In this study I make use of the CHD limit of the CHMHD law F21 to study a DNS dataset for supersonic CHD turbulence of an unparalleled resolution of $10,048^3$ grid points (Federrath et al., 2016; Federrath et al., 2021), simulated by Christoph Federrath. The in-depth analysis I led by studying the turbulent cascade within high-density, localized structures formed in these datasets is a way to see how turbulence exact laws can provide us with useful information susceptible to explain the general behavior of supersonic media such as the ISM, where the turbulent sonic Mach number M_S can reach very high values ($M_S > 10$).

Below we develop four sections, each dedicated to one of these studies, in which we provide more details on the context and draw the conclusions specifically related to each one of them. Note that, in all visual representations of the scale-dependent energy cascade rates the following formalism is systematically adopted: plain lines represent positive values, and dashed lines represent negative values.

4.2 Numerical test of IHMHD exact laws

The objective of this first study is twofold: on the one hand, it is the occasion to use the code developed in chapter 3 to compute the exact laws, to learn to handle it properly, and to check how the two base vectors decompositions introduced in chapter 3 influence the results obtained. On the other hand, it also aims at verifying how the three incompressible laws relate to one another, and how they react to the presence of a background magnetic field, two topics that were already mentioned and investigated theoretically in chapter 2.

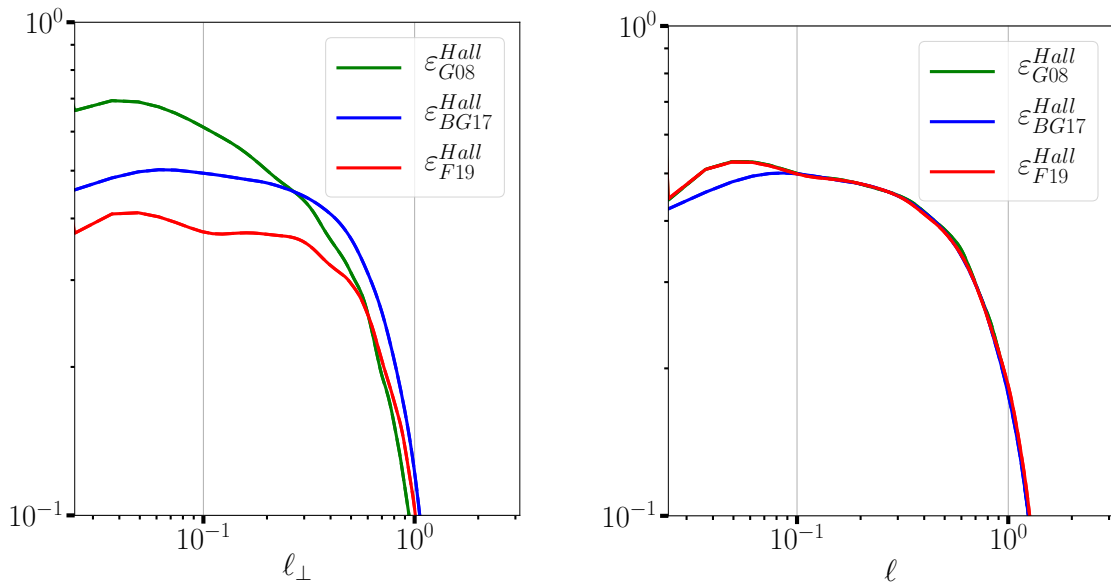
4.2.1 Convergence of exact laws and model choice

Thanks to the program detailed in the previous chapter I make the first round of tests on the various exact laws derived in chapter 2. For IHMHD laws most of the new materials (compared to existing laws) concern the Hall part of the exact law, so the study will only focus on this part. To this end I use a 3D DNS of incompressible EMHD turbulence (which corresponds to equation (2.6) with $\mathbf{u} = 0$). This dataset was obtained by using a modified version of the Solver for TURbulent flows with periodic BOundary conditions (TURBO) code (Teaca et al., 2009) in which the Hall effect has been implemented to solve the EMHD equations in a triply periodic box. A pseudo-spectral algorithm is used to perform the spatial discretization on a grid with a resolution of 512^3 collocation points (see Meyrand and Galtier (2013) for further details). A mean guide field \mathbf{B}_0 of magnitude unity is introduced along the z-axis, and a large-scale forcing is applied which enforces a constant rate of energy injection with no helicity. The system is evolved until a stationary state is reached such that $\mathbf{B}_{rms} \sim \mathbf{B}_0$. We removed the amount of ideal invariants that is injected into the system by the forcing mechanism by means of magnetic hyperdiffusivity $\eta_3 \Delta^3$ with $\eta_3 = 10e^{-11}$, which replaces the standard diffusivity d_ν normally present in (2.6). The final data consists of three periodic cubes giving the three components of the magnetic field in each grid point.

As stated before two numerical schemes are available to lead the data analysis, both bearing their own advantages and disadvantages. When studying a dataset with no mean magnetic field (supposed to be isotropic) the 3D isotropic model is a candidate of choice, however for datasets with a non-zero mean field the choice is way less obvious. The axisymmetric decomposition will fit to the real symmetries of the system, but as we neglected the contribution from fluxes parallel to the mean field (the F_{ℓ_z} component) we will lack

some information which could prove to be non-negligible. On the other hand the isotropic decomposition does not neglect any flux contribution, thus it is interesting to see if it yields good results even if the dataset is not isotropic. This last goal is particularly relevant to *SW in situ* data analysis since an isotropic model is often used despite the presence of a background mean field and the axi-symmetric nature of *SW* turbulence (Wicks et al., 2012). All in all, which decomposition to choose may depend on the dataset and needs to be tested beforehand.

Among the three incompressible laws available, *BG17* has an important feature the other two do not have: it is fully expressed as non-flux terms whose calculation does not depend on the numerical scheme used. This non-directionality makes *BG17* a good reference for testing which model is best suited for analyzing a dataset: as all three laws are mathematically equivalent, differences between them should only arise from numerical limitations on either the dataset itself (if hypotheses such as statistical homogeneity are not truly met) or the method used to analyze it. Thus, the method that shows the least discrepancies between the *IHMHD* laws would be deemed most suited for the study.



(a) Computation with the axisymmetric method. (b) Computation with the isotropic method.

Figure 4.1: Hall components of the *IHMHD* exact laws calculated with the 3D isotropic base vector decomposition and the 3D axisymmetric one. In the right panel all lines overlap for $\ell \gtrsim 10^{-1}$

We apply the two 3D methods to the *EMHD* dataset and summarize the results in Fig. 4.1. We notice right away a difference between the two models for both *G08* and *F19*, however for *BG17* the differences are, as expected, much more subtle. This corroborates the previous assumption that *BG17* is a good reference for the energy cascade rate as it depends less on the symmetries of the system. Here, despite the mean magnetic field being non-zero the equivalence seems to really hold only for the isotropic method, in which the three laws fit remarkably well. This indicates that the isotropic method is the more pertinent one to study this dataset, and thus that parallel fluxes (that are neglected by the axi-symmetric model) are important and must be taken into account. Consequently, only this method will be used to analyze the *EMHD* data. From Fig. 4.1 we can also roughly estimate the scales of the inertial range to go from 0.05 to 0.3.

Note that the laws still separate at the smallest scales of the system ($\ell \leq 0.1$). This could be due to imprecisions from the discrete derivative operator used to compute *G08* and *F19*, or to the increasing influence of dissipation as we reach the dissipative scales. This may also be the consequence of a lack of statistics to have a full convergence on the third order laws

G08 and F19 (whereas BG17 is second order), but such theory is difficult to verify as it would require analyzing (and thus simulating) larger datasets.

4.2.2 Influence of the mean magnetic field

In chapter 2 we mentioned that IHMHD exact laws were not directly dependent on the presence of the mean magnetic field. For BG17 and F19 this result is immediate and is a direct consequence of vectorial calculus. For G08 however it requires a few manipulations that make use of the hypothesis of statistical homogeneity. Due to this it is necessary to test this property numerically, as we did for the laws equivalence, to ensure that it holds in a practical situation.

To this end I computed the energy cascade rate of all three laws on the EMHD dataset after removing the mean magnetic field and keeping only the fluctuations. This was done by averaging the magnetic field component along the guide field axis (here the z axis) and subtracting this value from that component (the other components both bear negligible mean fields). In Fig. 4.2 I represent the ratio of the cascade rate calculated without mean field over the one calculated with the full mean field. One can see that computing the energy cascade rate with or without the mean guide field leads to the same result for both BG17 and F19, as expected. For G08 however the two cascade rates show some differences, even though the contribution of \mathbf{B}_0 reduces to zero theoretically. The difference is, however, relatively small in the inertial range (less than 0.5%). The sudden increase of the ratio at large and small scale is due to the presence of the dissipation and the forcing respectively: in these regions the hypotheses of the laws derivation are no longer met.

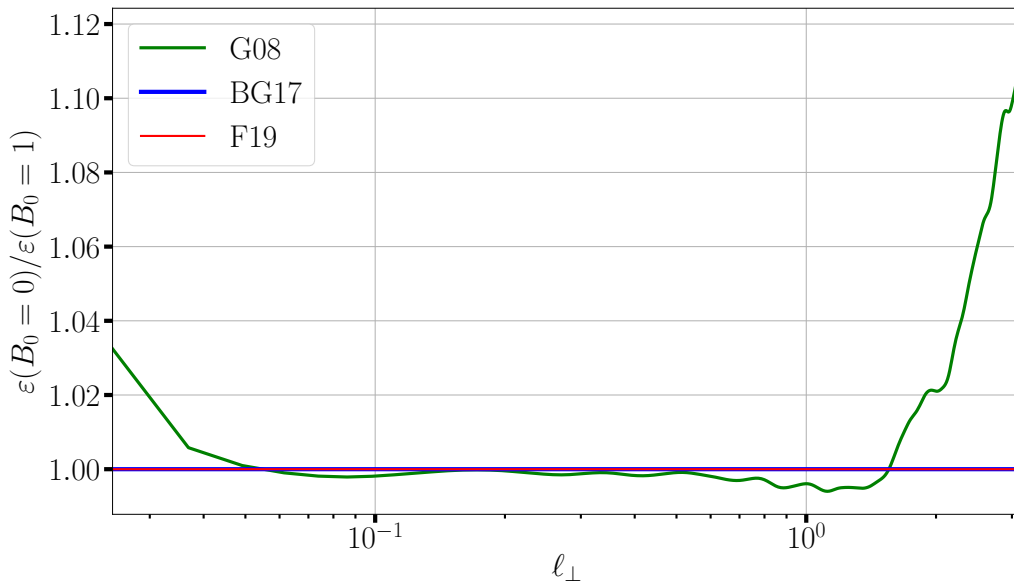


Figure 4.2: Ratios of ε_{Hall} computed from the data cubes where the guide field $\mathbf{b}_0 = 1$ is removed and from the data cubes where it is not. The values obtained with F19 and BG17 overlap.

This behavior is most probably a consequence of a non perfect homogeneity of the system, which is expected to be the case of all datasets to some extent. This test shows the limitations we must be aware of when analyzing data, be it DNS data or *in-situ* data, as the hypotheses used to derive tools such as exact laws may not always be met in practice. In our case it may be safer to remove the mean field beforehand when using incompressible laws in order to avoid possible errors. This is especially true when studying *in-situ* data in which the hypotheses are expected to be much more loosely met than in controlled DNS data.

4.2.3 Summary of the study on the IHMHD laws

Through the study led in this section, we showed that the equivalence between the three incompressible exact laws that was demonstrated in chapter 2 still holds in practice when computing the energy cascade rates with the protocol described in chapter 3. This already supposes that we choose the most suited base vector decomposition, which is not as straightforward as one could think in the first place. Indeed, despite the axi-symmetric nature of the EMHD datasets presented here, the isotropic decomposition was found to provide the best results, suggesting that the parallel fluxes that are discarded in the axi-symmetric decompositions may bear non-negligible contributions. Choosing the right decomposition can be done by looking at which one yields a better matching between exact laws, a method that will be used again in next section.

Through this study, it was also possible to show that the presence of a background magnetic field does not influence directly the values obtained for the exact laws, except for G08 that shows a slight sensitivity to this parameter. This may be due to a non-perfect statistical homogeneity of the datasets, with the consequence that the terms of G08 depending on \mathbf{B}_0 will not cancel each other out correctly.

4.3 In-depth study with generalized CHMHD exact laws

4.3.1 Context of the study

Incompressible exact laws have been used extensively in past years to analyze turbulence from *in situ* data (Sorriso-Valvo et al., 2007; MacBride et al., 2008; Stawarz et al., 2009; Osman et al., 2011). Thus, the recent derivation of exact laws for CHMHD comes as a natural and fitting extension to these studies. However, compressible exact laws such as the ones derived in section 2 often take the form of intricate combinations of varied mathematical expressions. The different terms they are made of require access to various physical variables, some of which cannot be computed in certain situations: for example one cannot compute the so-called source terms (i.e. terms depending on 3D field derivatives such as $\nabla \cdot \mathbf{u}$) from single-spacecraft *in situ* data, as a minimum of four spacecraft is required to obtain a 3D mapping of the vector fields. This is the main reason why some recent compressible studies on satellite data neglect the unobtainable compressible terms (Banerjee et al., 2016; Hadid et al., 2018).

Considering these limitations it is important to determine whether the terms being omitted are significant or not. Thankfully, the application of CHMHD law A18 to DNS data simulated with the GHOST code has shown that purely compressible terms (the so-called source terms) have no meaningful influence on the overall dynamics (Andrés et al., 2018), justifying these components being neglected in other studies. Such specific numerical analysis of exact laws are important, as they allow for testing the behavior and boundaries of these equations within a fully controllable environment, and thus to pinpoint important, specific details susceptible to ease subsequent studies on more complex datasets, such as SW real data analysis.

Similarly to previous section, this section will be dedicated to extensive testing of the CHMHD law F21 and its comparison with law A18. We aim at verifying to what extent the two laws provide matching results and how the various components of F21 behave individually. We also test how the exact laws react when used to analyze non-forced (and so non-stationary) simulations, which will require considering more general versions of the exact laws. Note that the work presented in this section was still ongoing during the writing of this manuscript. Thus, the paper summarizing this study and that can be found at the end of appendix B contains additional comments and findings.

4.3.2 Presentation of the data

To obtain the datasets used in this study, I used the pseudo-spectral code **GHOST** (Gómez et al., 2005; Mininni et al., 2011) along with a module for numerically solving the **CHMHD** equations (2.54)-(2.57). I ran three simulations for almost two years on the supercomputer Occigen based in France, each parallelized on 360 CPUs through **MPI**. The three simulations were ran in a cubic periodic box of spatial resolution of $N = 1024$ grid points in all three directions, and all simulations use dimensionless viscosity and magnetic diffusivity of $\nu = \eta = 3.0 \times 10^{-4}$. The specificity of these simulations is that they do not feature any forcing: instead, they are set to an initial state and the flow is left to evolve and decay. The setup of the initial state is provided by the **GHOST** library: it is built from a superposition of harmonic modes with random phases whose energy in Fourier space is put between two spheres of radius k_{down} and k_{up} , following the idea of Pouquet and Patterson (1978). The presence of a background magnetic field \mathbf{B}_0 and the value of the Mach number M_S vary between simulations, which allows us to evaluate the influence of these parameters on the dynamics of the system. All aforementioned parameters are reported in Table 4.1.

Run	$ \mathbf{B}_0 $	Resolution	$\nu = \eta$	d_i/L_0	M_S	k_{down}	k_{up}
I	2	1024^3	3.0×10^{-4}	0.02	0.25	1	3
II	0	1024^3	3.0×10^{-4}	0.02	0.25	1	3
III	0	1024^3	3.0×10^{-4}	0.02	0.5	1	3

Table 4.1: List of **CHMHD** runs and their relevant parameters. $L_0 = 2\pi$ denotes the side length of the simulation box.

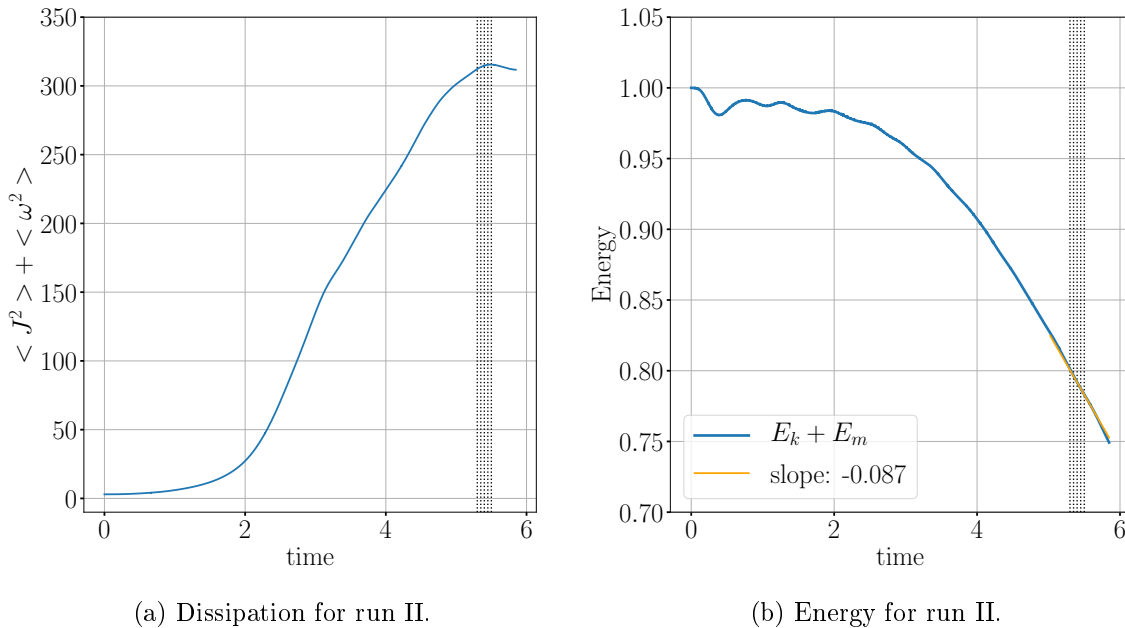


Figure 4.3: Incompressible dissipation and fluctuations of the kinetic and magnetic energies as a function of time for run II. The vertical dotted lines represent the 5 times selected to compute the exact laws. A linear fit is made on these 5 times and gives the average energy dissipation rate around these moments.

Due to the runs being in free decay, instead of looking for a stationary regime we must wait for the simulations to reach a maximum of dissipation, indicating that turbulence has had enough time to fully develop, and lead our study on times selected around this moment (see Figure 4.3). Around the selected times the sum of the kinetic and magnetic energies of the system, $E_k + E_m = \rho u^2/2 + B^2/(2\mu_0)$ is expected to be decreasing steadily, which is observed here in the case of run II. I thus used 5 snapshots at turnover times [5.3,5.35,5.4,5.45,5.5] to

lead this study. Note that, as the energy is steadily decreasing, one can estimate the energy dissipation rate thanks to a simple linear fit. Thus for run II the dissipation rate should amount to roughly -0.087 . Run III has time series (not shown) that are very similar to run II: again 5 times were retained for the analysis, for turnover times $[5.6, 5.65, 5.7, 5.75, 5.8]$, and the energy dissipation rate is also estimated at -0.087 .

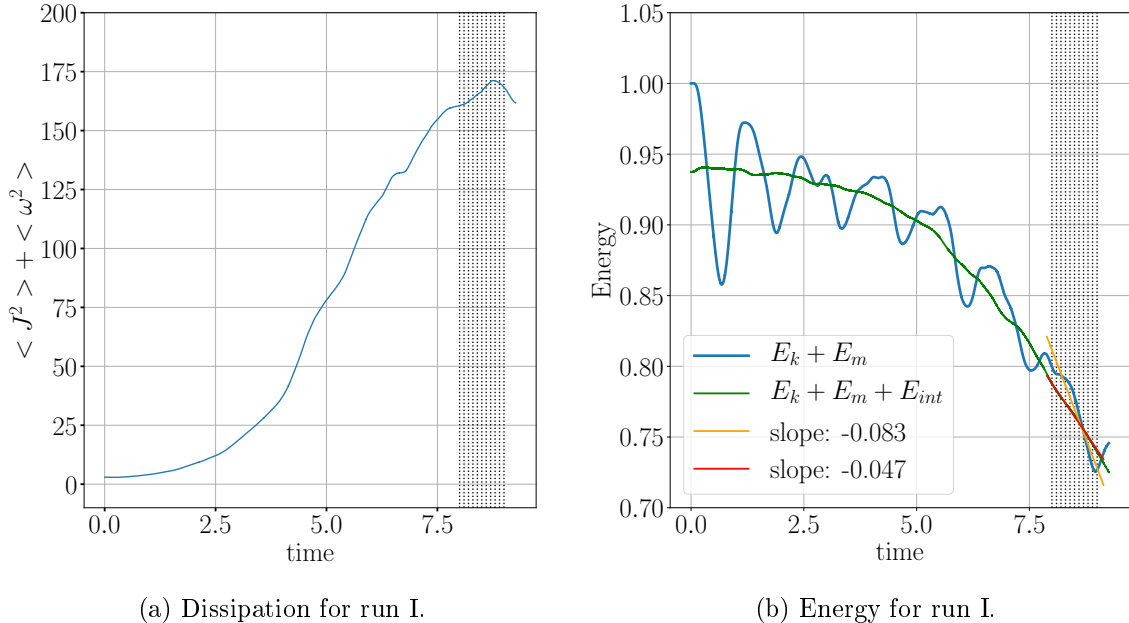


Figure 4.4: Incompressible dissipation and fluctuations of the kinetic, magnetic and internal energies as a function of time for run I. The vertical dotted lines represent the 11 times selected to compute the exact laws. The orange line represent a linear fit made on the 11 selected times for kinetic and magnetic energies, and the red line a similar fit for total energy.

The case of run I, presented in figure 4.4, is a bit more complicated as energy is a lot more fluctuating. These oscillations match the fluctuations of internal energy and are thus thought to be a consequence of exchanges between the kinetic plus magnetic energy and internal energy, as was recently reported by Yang et al. (2021). For this run, it was necessary to select more snapshots over a larger period of time, and to average all the resulting calculations in time to obtain exploitable results despite the oscillations. For this run, the study is thus led on 11 snapshots turnover times $[8, 8.1, 8.2, 8.3, 8.4, 8.5, 8.6, 8.7, 8.8, 8.9, 9]$. We can again estimate the energy dissipation rate through a linear fit on the times studied: this leads to a dissipation rate of around -0.083 when considering only $E_k + E_m$, and -0.047 when considering the total energy. The latter should be more representative of the dissipation in the system, as it is not influenced by the reversible exchanges between $E_k + E_m$ and E_{int} . To confirm this, I used another method to estimate this dissipation rate: similarly to equation (1.28) we can write:

$$\partial_t \langle E^{tot} \rangle = -\nu \langle \omega^2 \rangle - \eta \langle \mathbf{J}^2 \rangle. \quad (4.1)$$

Using the mean value taken by the dissipation displayed in figure 4.4a, at the times considered for run I, we obtain an estimate for the energy dissipation rate of -0.05 which matches the estimate obtained with the linear fit on total energy.

Aside from the fluctuations observed in the evolution of energy in run I, the presence of a mean magnetic field in this simulation also has an influence on the general shape of turbulence, as stated earlier. Contrary to runs with no mean field, which do not have an obvious privileged direction, current sheets and turbulent structures will be oriented by this background magnetic field in run I. This effect is readily visible in the 2D plots of the current density shown in figures 4.5 and 4.6: for run I current sheets oriented along the z-axis are visible, while no privileged direction appears in plane (xy). For run II, this phenomenon is

not observed in any direction. The current cuts for run III are not shown here but present the same behavior as run II. Like in previous section, the asymmetry presented by run I will influence the choice of the numerical method when calculating exact laws, as will be discussed hereafter.

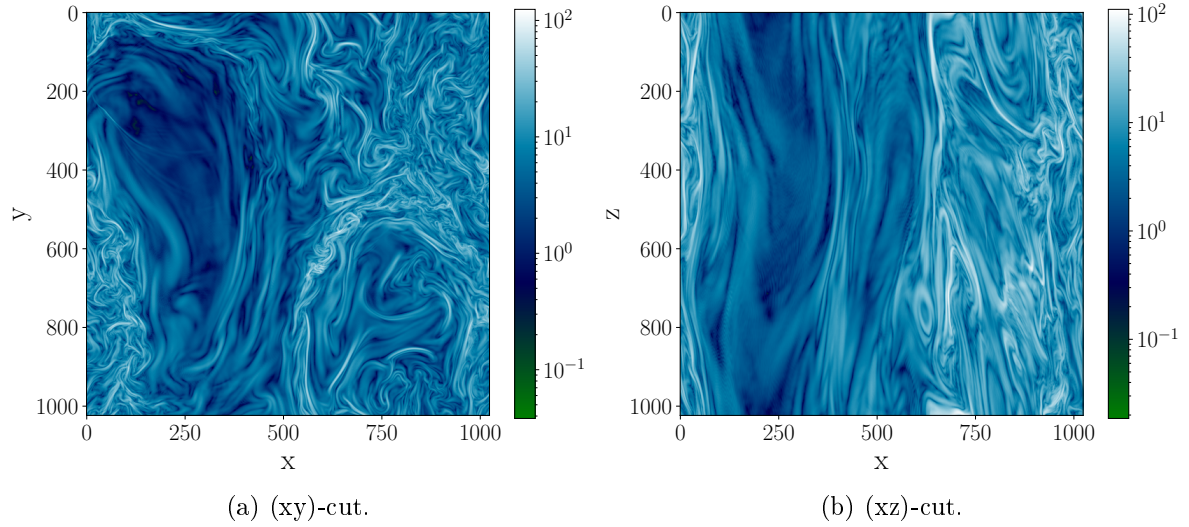


Figure 4.5: (xy)-cut and (xz)-cut of the current density for run I, taken respectively at positions $z = 512$ and $y = 512$.

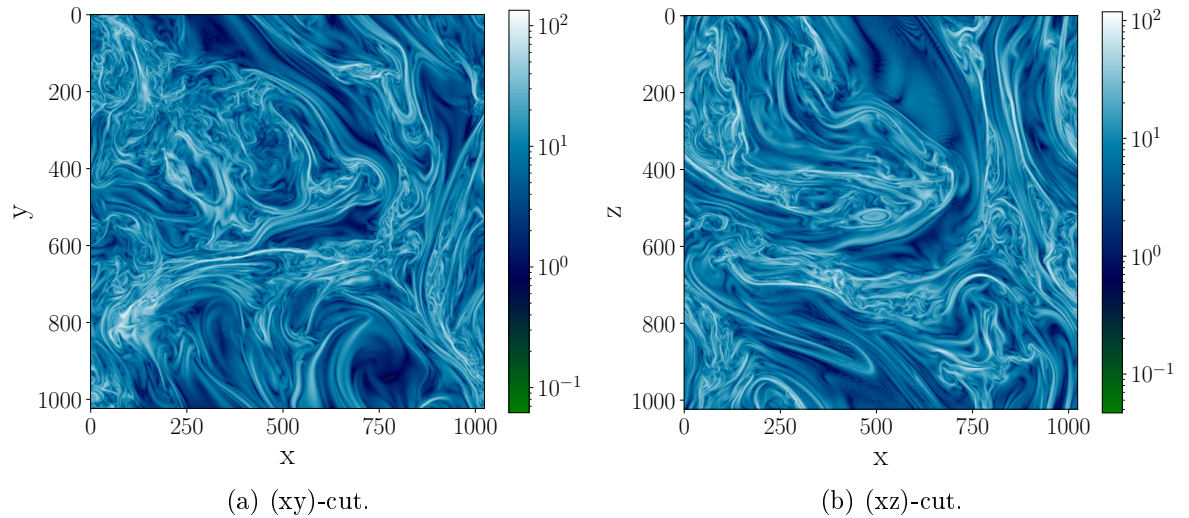


Figure 4.6: Same as figure 4.5 for run II.

4.3.3 Calculation of law F21

First of all, we study the general behavior of exact law F21 and how it relates to the other compressible law A18. To compute the laws I used the numerical schemes described in chapter 3. For runs II and III it is straightforward to use the 3D isotropic base vector set, however the case of run I is subject to caution: in previous section it appeared that using the isotropic version yielded better results, despite the simulation not being isotropic. Here I present a test similar to the one shown in figure 4.1: I computed both exact laws with the 3D isotropic and axi-symmetric vector sets to see for which vector set the two laws match better. The two computations are shown in figure 4.7. The MHD components of the laws match equally for both methods, however the Hall components show a better matching for the isotropic vector

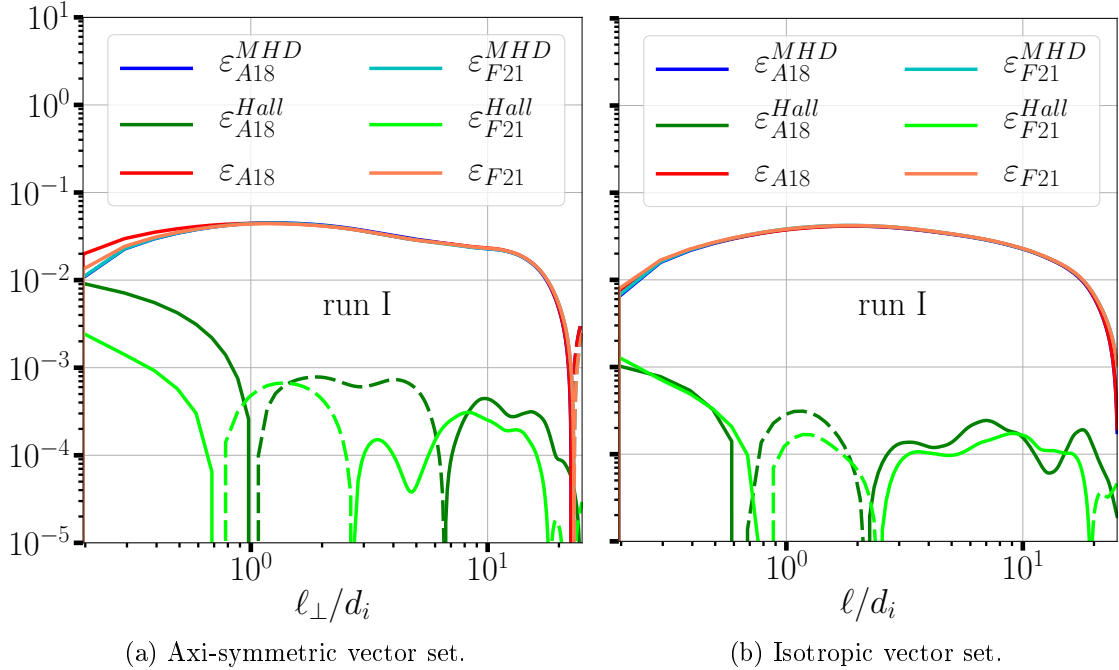


Figure 4.7: Energy cascade rate calculated with laws A18 and F21 for run I, using either the 3D axi-symmetric base vectors set or the isotropic one. The blue, cyan, red and orange lines overlap at most scales.

set than for the axi-symmetric one, similarly to the EMHD run analyzed in previous section. Consequently, I also used the isotropic decomposition to study all datasets from run I.

Figure 4.8 shows the same comparisons between the two laws for runs II and III, also computed with the isotropic vector set. We see a very good matching between the two laws for both runs. These results confirm that the two compressible exact laws indeed represent the same energy cascade rate. Note that the matching on the Hall term is not as good as it was for the EMHD dataset that made use of incompressible laws. This is a consequence of the fact that these compressible laws require having large statistics and probing the turbulence in a lot of directions to yield the same results: earlier calculations that were made using reduced base vector sets (isotropic sets of 13 vectors with components equal to $-1, 0$ or 1) led to worse matchings for the Hall component, as seen in figure 4.9. This highlights the needs for strong statistics to efficiently study the turbulence cascade rate, an important point to which we will return when studying MMS data in chapter 5.

Following the comparison of the exact laws, we focus our study on the detailed analysis of law F21. We use the notations introduced in chapter 2, with equations (2.101)–(2.104), and split the term S_{MHD} into two (recall here that $\theta = \nabla \cdot \mathbf{u}$):

$$S_{\text{MHD}}^{\theta} = -\frac{1}{2} \langle (\rho\theta' + \rho'\theta) |\delta\mathbf{u}|^2 \rangle, \quad (4.2)$$

$$S_{\text{MHD}}^{\mathbf{B}} = 2 \langle \delta\rho \delta\mathbf{u} \cdot \bar{\delta}(\mathbf{J}_c \times \mathbf{B}) \rangle. \quad (4.3)$$

In figure 4.10 we display the scale-dependent energy cascade rate and its individual components, computed with the isotropic base vector set for the three runs. For the MHD part of the law, a clear dominance of the flux term F_{MHD} can be seen at all scales. The two source components both remain negligible in comparison to the flux one at MHD and near ion scales, similarly to what was observed for law A18 (Andrés et al., 2018). As we will see below, the amplitude of these source terms is smaller than the error supposedly induced by the non-stationarity of the runs, and as such their changes in behavior from one run to another can probably be attributed to statistical effects.

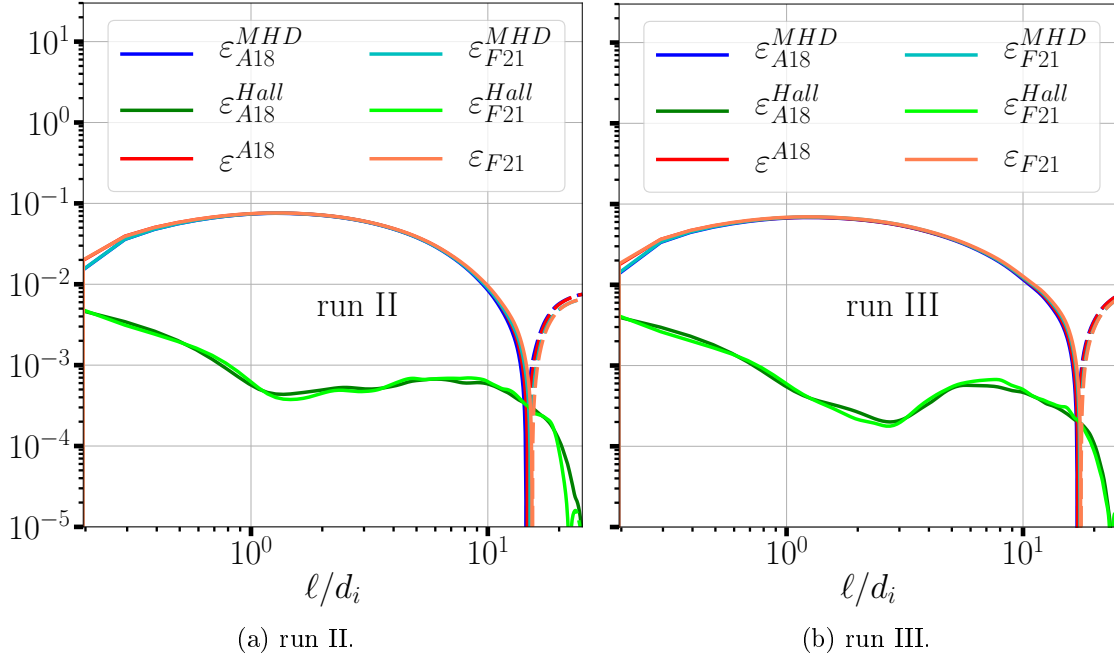


Figure 4.8: Energy cascade rate calculated with laws A18 and F21 for runs II and III, using 3D isotropic base vectors set. The blue, cyan, red and orange lines overlap at most scales.

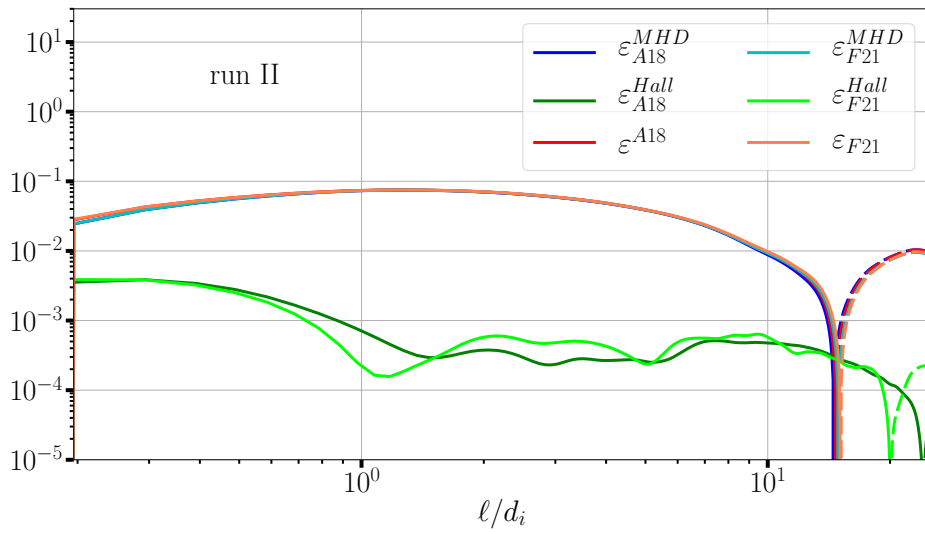


Figure 4.9: Same as figure 4.8a with a reduced isotropic vector set of 13 vectors, used during early tests to speed up the calculations.

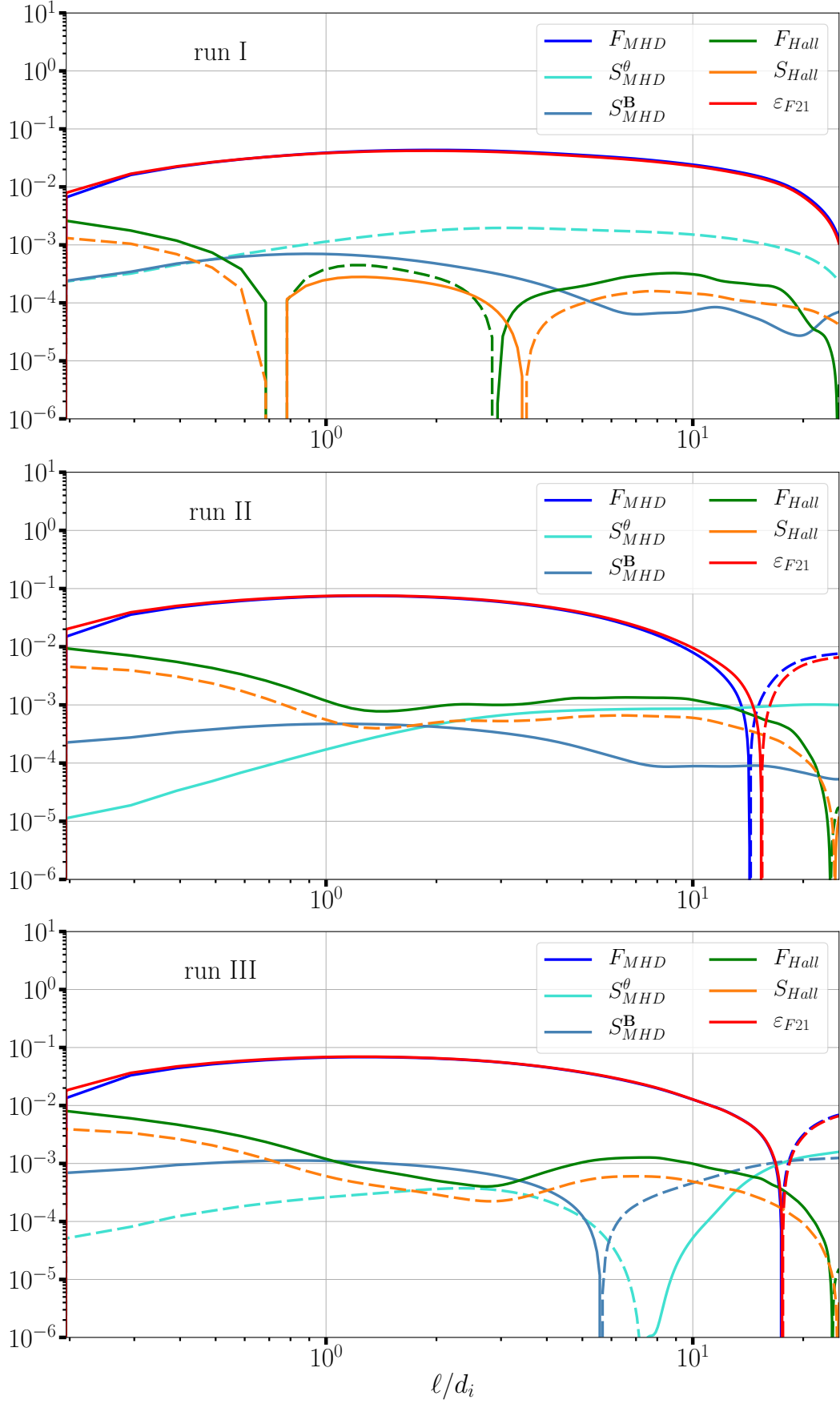


Figure 4.10: Total energy cascade rate and its individual components computed with F21 for all three runs.

The behavior of the Hall components is more constant between the three runs. In every case, the Hall flux term F_{Hall} is roughly equal to $-2S_{\text{Hall}}$, a particularity that is inherited by their likeness to the incompressible terms \mathbf{H} and $-2A$ respectively, and that were shown in chapter 2 to be related as $\frac{1}{2}\nabla \cdot \mathbf{H} = 2A$. Thus the relation between F_{Hall} and S_{Hall} is to be expected for weakly compressible runs, and it appears that this behavior persists in more compressible cases such as run III. Aside from this observation, the Hall part of the law does not dominate even at the smallest scales of the simulation domain, in contrast to what we will see in the next study about LF simulations. The main reason for this is the low value of d_i that was selected to run these simulations: in order to increase the resolution to 1024^3 , it appeared necessary to reduce this parameter so that the simulation would compute successfully. The high resolution and large statistics obtained at the cost of a less developed Hall dynamics make these runs more suited to a theoretical investigation of the exact laws than to a physical interpretation of the Hall effect in turbulence, which will again be more addressed in next study.

If we look at the total energy cascade rate resulting from these calculations we observe that it does not vary much over a decade, yet it cannot be qualified of constant, as we would expect for an inertial cascade. The most probable reason to this is the weak Hall effect mentioned above, which makes it so that dissipation starts acting before the Hall effect can start driving the cascade on its own. We will not see this behavior in the following DNS studies as they make use of hyperdissipation, contrary to the data presented here: instead of dissipating energy through the second derivatives presented in equations (2.58) and (2.59), hyperdissipation terms of higher derivation order are used (e.g. $d_\nu = \nu\Delta^4\mathbf{u}$). These terms push the dissipation back to even smaller scales, allowing for the turbulence cascade to develop over a broader range of scales. I tried to implement hyperdissipation in the GHOST code, but once the change was done I could not find a set of parameters that would allow the code to run successfully, and values always ended up overflowing. It would probably have required a more thorough modification of the code to work properly, so I ultimately had to put this idea aside.

A last remark can be done, regarding the estimates for the energy dissipation rate proposed in figures 4.3 and 4.4. Using a linear fit on the energy evolution, I estimated this dissipation rate to be around -0.087 for both run II and run III. The energy cascade rate indeed reaches similar values at intermediate, MHD scales, suggesting that this cascade rate is representative of the energy dissipated in the system. This matching does not extend to small scales due to dissipation starting to take energy away from the turbulent cascade. For run I I obtained two estimates for the energy dissipation rate: one around -0.083 obtained through a linear fit similar to runs II and III and that matches the local variation of energy, and one around -0.05 obtained from the mean value of $-\nu\langle\omega^2\rangle - \eta\langle\mathbf{J}^2\rangle$ and that is best suited to follow the global evolution of energy, disregarding the oscillations. In figure 4.10 the energy cascade rate for run I lies around 0.05 at intermediate scales, which would suggest that the energy cascade rate is able to transcribe the global dynamics of the system, disregarding the reversible exchanges with the internal energy. Note that the reduction of the cascade rate in presence of a mean magnetic field has already been observed before (Andrés et al., 2018).

4.3.4 Non-stationary CHMHD laws

Switching from a forced turbulence model to a free decay model, like the one used to compute the simulations presented in this section, invalidates the stationarity hypothesis used to derive the final expression of the compressible exact laws. Indeed, this assumption is tied to the forcing and allowed us to remove the time-derivatives of the structure functions from the equations, and to approximate both the forcing and the dissipation to the energy cascade rate. In a free decay model, the stationarity assumption (and its implications) does not stand anymore, and one could then wonder if the exact laws are still valid. Thus it is advisable to return to a more general expression of the exact laws, prior to applying the simplifications

stemming from the stationarity and the presence of the forcing.

For [F21](#) we will simply use equation [\(2.93\)](#) that we rewrite under the compact form:

$$\boxed{2\varepsilon_{F21} + \partial_t \langle E^{tot} \rangle - \partial_t \langle S \rangle + \mathcal{D}_{F21} + \mathcal{D}_{F21}^{loc} + \mathcal{F}_{F21} + \mathcal{F}_{F21}^{loc} = 0,} \quad (4.4)$$

where we define the dissipative terms:

$$\mathcal{D}_{F21} \equiv -\frac{1}{2} \left\langle \left(1 + \frac{\rho'}{\rho}\right) \mathbf{u}' \cdot \mathbf{d}_\nu + \left(1 + \frac{\rho}{\rho'}\right) \mathbf{u} \cdot \mathbf{d}'_\nu \right\rangle - \frac{1}{\mu_0} \langle \mathbf{B}' \cdot \mathbf{d}_\eta + \mathbf{B} \cdot \mathbf{d}'_\eta \rangle, \quad (4.5)$$

$$\mathcal{D}_{F21}^{loc} \equiv \frac{1}{2} \left\langle \frac{\rho}{\rho'} \mathbf{u}' \cdot \mathbf{d}'_\nu + \frac{\rho'}{\rho} \mathbf{u} \cdot \mathbf{d}_\nu \right\rangle + \frac{1}{2\mu_0} \langle \mathbf{B} \cdot \mathbf{d}_\eta + \mathbf{B}' \cdot \mathbf{d}'_\eta \rangle, \quad (4.6)$$

and the forcing terms:

$$\mathcal{F}_{F21} \equiv -\frac{1}{2} \left\langle \left(1 + \frac{\rho'}{\rho}\right) \mathbf{u}' \cdot \mathbf{f} + \left(1 + \frac{\rho}{\rho'}\right) \mathbf{u} \cdot \mathbf{f}' \right\rangle, \quad (4.7)$$

$$\mathcal{F}_{F21}^{loc} \equiv \frac{1}{2} \left\langle \frac{\rho}{\rho'} \mathbf{u}' \cdot \mathbf{f}' + \frac{\rho'}{\rho} \mathbf{u} \cdot \mathbf{f} \right\rangle, \quad (4.8)$$

and where ε_{F21} is the cascade rate whose expression is given by equation [\(2.99\)](#). The superscript *loc* for the forcing and dissipation is used to designate terms that are computed locally, with variables taken in a single point \mathbf{r} or \mathbf{r}' (excluding the density ratios, that would remain close to 1 in weakly compressible turbulence). For the datasets presented here the forcing terms \mathcal{F}_{F21} and \mathcal{F}_{F21}^{loc} will be equal to zero.

For exact law [A18](#) we need to provide more details as the law was not derived in this thesis. It can be obtained through the same overall method as [F21](#), but the three-dimensional [CHMHD](#) equations make use of the Alfvén speed $\mathbf{v}_A \equiv \mathbf{B}/\sqrt{\mu_0\rho}$ instead of the magnetic field:

$$\partial_t \rho = -\nabla \cdot (\rho \mathbf{u}), \quad (4.9)$$

$$\partial_t \mathbf{u} = -\mathbf{u} \cdot \nabla \mathbf{u} + \mathbf{v}_A \cdot \nabla \mathbf{v}_A - \frac{1}{\rho} \nabla (P + P_M) - \mathbf{v}_A \cdot (\nabla \cdot \mathbf{v}_A) + \mathbf{d}_\nu + \mathbf{f}, \quad (4.10)$$

$$\partial_t \mathbf{v}_A = -(\mathbf{u} - \lambda \mathbf{J}_c) \cdot \nabla \mathbf{v}_A + \mathbf{v}_A \cdot \nabla (\mathbf{u} - \lambda \mathbf{J}_c) - \frac{\mathbf{v}_A}{2} (\nabla \cdot \mathbf{v} - \lambda \nabla \cdot \mathbf{J}_c) + \frac{\mathbf{d}_\eta}{\sqrt{\rho}}, \quad (4.11)$$

$$\mathbf{v}_A \cdot \nabla \rho = -2\rho (\nabla \cdot \mathbf{v}_A), \quad (4.12)$$

$$\mathbf{J}_c \cdot \nabla \rho = -\rho (\nabla \cdot \mathbf{J}_c), \quad (4.13)$$

where $P_M \equiv \rho v_A^2/2$ is the magnetic pressure. This system is also closed with an isothermal closure. The calculation of the dynamical equation $\partial_t \langle R'_E + R_E \rangle$ ultimately leads, after calculations similar to the ones presented in section [2.3](#), to the exact law:

$$\boxed{-2\varepsilon_{A18} = \frac{1}{2} \nabla_\ell \cdot (\mathbf{F}^{\text{MHD}} + d_i \mathbf{F}^{\text{HMHD}}) + (S^{\text{MHD}} + d_i S^{\text{HMHD}}) + S_H^{\text{MHD}} + M_\beta^{\text{MHD}}} \quad (4.14)$$

where the [MHD](#) terms read:

$$\mathbf{F}^{\text{MHD}} = \langle [(\delta(\rho \mathbf{u}) \cdot \delta \mathbf{u} + \delta(\rho \mathbf{v}_A) \cdot \delta \mathbf{v}_A + 2\delta e \delta \rho)] \delta \mathbf{u} - [\delta(\rho \mathbf{u}) \cdot \delta \mathbf{v}_A + \delta \mathbf{u} \cdot \delta(\rho \mathbf{v}_A)] \delta \mathbf{v}_A \rangle \quad (4.15)$$

$$S^{\text{MHD}} = \left\langle [R'_E - \frac{1}{2}(R'_B + R_B)](\nabla \cdot \mathbf{v}) + [R_E - \frac{1}{2}(R_B + R'_B)](\nabla' \cdot \mathbf{v}') \right\rangle \\ + \left\langle [(R_H - R'_H) - \bar{\rho}(\mathbf{u}' \cdot \mathbf{v}_A)](\nabla \cdot \mathbf{v}_A) + [(R'_H - R_H) - \bar{\rho}(\mathbf{u} \cdot \mathbf{v}'_A)](\nabla' \cdot \mathbf{v}'_A) \right\rangle \quad (4.16)$$

$$S_H^{\text{MHD}} = \left\langle \left[\frac{P'_M - P'}{2} - E^{tot'} \right] (\nabla \cdot \mathbf{v}) + \left[\frac{P_M - P}{2} - E^{tot} \right] (\nabla' \cdot \mathbf{v}') \right\rangle \\ + \langle H'(\nabla \cdot \mathbf{v}_A) + H(\nabla' \cdot \mathbf{v}'_A) \rangle \\ + \frac{1}{2} \left\langle \left(e' + \frac{v_A'^2}{2} \right) [\nabla \cdot (\rho \mathbf{u})] + \left(e + \frac{v_A^2}{2} \right) [\nabla' \cdot (\rho' \mathbf{u}')] \right\rangle \quad (4.17)$$

$$M_\beta^{\text{MHD}} = \frac{1}{2} \left\langle \beta^{-1'} \nabla' \cdot (e' \rho \mathbf{u}) + \beta^{-1} \nabla \cdot (e \rho' \mathbf{u}') \right\rangle \quad (4.18)$$

and the Hall terms:

$$\mathbf{F}^{\text{HMHD}} = 2[(\overline{\rho \mathbf{J}_c \times \mathbf{v}_A}) \times \delta \mathbf{v}_A - \delta(\mathbf{J}_c \times \mathbf{v}_A) \times \overline{\rho \mathbf{v}_A}] \quad (4.19)$$

$$\begin{aligned} S^{\text{HMHD}} &= \left\langle \delta \rho \frac{\mathbf{J}_c \cdot \mathbf{v}'_A}{2} (\nabla \cdot \mathbf{v}_A) - \delta \rho \frac{\mathbf{J}'_c \cdot \mathbf{v}_A}{2} (\nabla' \cdot \mathbf{v}'_A) \right\rangle \\ &+ \left\langle \frac{R_B - R'_B}{2} (\nabla \cdot \mathbf{J}_c) + \frac{R'_B - R_B}{2} (\nabla' \cdot \mathbf{J}'_c) \right\rangle \end{aligned} \quad (4.20)$$

with the cross helicity $H \equiv \rho(\mathbf{u} \cdot \mathbf{v}_A)$, its two-points correlator $R_H \equiv \rho(\mathbf{u} \cdot \mathbf{v}'_A + \mathbf{v}_A \cdot \mathbf{u}')/2$, the correlator for magnetic energy $R_B \equiv \rho \mathbf{v}_A \cdot \mathbf{v}'_A/2$ and $\beta^{-1} \equiv v_A^2/2c_s^2$. Just like equation (2.99), this law is obtained under the assumptions of statistical homogeneity, time stationarity and infinite Reynolds number. An expression similar to (2.93) that does not make use of the stationarity assumption is also reported in Andrés et al. (2018), and can here again be written under a compact form:

$$\boxed{2\varepsilon_{A18} + \partial_t \langle R_E + R'_E \rangle + \mathcal{D}_{A18} + \mathcal{F}_{A18} = 0.} \quad (4.21)$$

The dissipative term \mathcal{D}_{A18} is not explicitly given in Andrés et al. (2018) but is easy to calculate. Just like \mathcal{D}_{F21} it is made of a dissipation component given by terms like $\partial_t \langle \rho \mathbf{u} \cdot \mathbf{u}' \rangle$ and Navier-Stokes equation, and a diffusion component given by terms of the form $\partial_t \langle \rho \mathbf{v}_A \cdot \mathbf{v}'_A \rangle$ and the induction equation. The component stemming from the velocity field and Navier-Stokes equation is the same as in (4.5), as both originate from the same time derivative and the dissipative term of Navier-Stokes is the same in the two models. The component originating from the magnetic field and induction equation is different however, and takes the form of:

$$\begin{aligned} \partial_t \left\langle \frac{1}{2} (\rho + \rho') \mathbf{v}_A \cdot \mathbf{v}'_A \right\rangle &\rightarrow \frac{1}{2} \left\langle \rho \mathbf{v}_A \cdot \frac{\mathbf{d}'_\eta}{\sqrt{\rho'}} + \rho \mathbf{v}'_A \cdot \frac{\mathbf{d}_\eta}{\sqrt{\rho}} + \rho' \mathbf{v}_A \cdot \frac{\mathbf{d}'_\eta}{\sqrt{\rho'}} + \rho' \mathbf{v}'_A \cdot \frac{\mathbf{d}_\eta}{\sqrt{\rho}} \right\rangle, \\ &\rightarrow \frac{1}{2} \left\langle \left(\frac{\sqrt{\rho}}{\sqrt{\rho'}} + \frac{\sqrt{\rho'}}{\sqrt{\rho}} \right) (\mathbf{B} \cdot \mathbf{d}'_\eta + \mathbf{B}' \cdot \mathbf{d}_\eta) \right\rangle, \end{aligned} \quad (4.22)$$

which ultimately leads to

$$\begin{aligned} \mathcal{D}_{A18} &= -\frac{1}{2} \left\langle \left(1 + \frac{\rho'}{\rho} \right) \mathbf{u}' \cdot \mathbf{d}_\nu + \left(1 + \frac{\rho}{\rho'} \right) \mathbf{u} \cdot \mathbf{d}'_\nu \right\rangle \\ &- \frac{1}{2} \left\langle \left(\frac{\sqrt{\rho}}{\sqrt{\rho'}} + \frac{\sqrt{\rho'}}{\sqrt{\rho}} \right) (\mathbf{B} \cdot \mathbf{d}'_\eta + \mathbf{B}' \cdot \mathbf{d}_\eta) \right\rangle. \end{aligned} \quad (4.23)$$

Note that the non approximated version of A18 does not have any equivalent to $\mathcal{D}_{F21}^{\text{loc}}$. Indeed, the structure function of F21, $\langle S \rangle$, can be developed into cross terms such as $\langle \mathbf{B} \cdot \mathbf{B}' \rangle$ and same-point terms like $\langle \mathbf{B} \cdot \mathbf{B} \rangle$. Local terms originate from the latter, that have no equivalent in the correlator used to derive A18. Similarly, the forcing term \mathcal{F}_{A18} is the same as the one for law F21:

$$\mathcal{F}_{A18} = -\frac{1}{2} \left\langle \left(1 + \frac{\rho'}{\rho} \right) \mathbf{u}' \cdot \mathbf{f} + \left(1 + \frac{\rho}{\rho'} \right) \mathbf{u} \cdot \mathbf{f}' \right\rangle. \quad (4.24)$$

This term is also equal to zero for the datasets studied here.

Using the same code skeleton and integration method used to compute the terms of the exact laws, I calculated the new terms $\langle S \rangle$, $\langle R_E + R'_E \rangle$, $\langle E_{\text{tot}} \rangle$, \mathcal{D}_{F21} , $\mathcal{D}_{F21}^{\text{loc}}$ and \mathcal{D}_{A18} for all snapshots of the three runs. Time derivatives were all calculated over five snapshots with the same five-points stencil (3.9) used to compute the spatial derivatives in the datasets. For runs II and III, the derivatives make use of the 5 snapshots retained and all other terms are calculated on the middle one, respectively at times 5.4 and 5.7. Averaging these terms over

the five snapshots was found to bring no change to the results. For run I, I calculated all possible time derivatives using the 11 snapshots, for a total of 7 (one using times 8 to 8.4, one using times 8.1 to 8.5 etc.), and computed their time average. For all other terms I computed the time average over all 11 snapshots. Figure 4.11 and 4.12 present all individual terms of laws A18 and F21 respectively obtained for the three runs, along with the sum of these terms which is displayed in black.

We start by looking at results obtained with A18, displayed in figure 4.11. Both run II and run III show very similar behaviors. The term $\partial_t \langle R_E + R'_E \rangle$ reaches at intermediate and small scales an almost constant value corresponding to twice the energy dissipation rate reported earlier, which is consistent with the fact that at small enough scales $\partial_t \langle R_E + R'_E \rangle \rightarrow \partial_t \langle 2E_{tot} \rangle$. We can observe that $2\varepsilon_{A18}$ follows the same trend as $\partial_t \langle R_E + R'_E \rangle$, albeit with an opposed sign, at all scales except the smallest ones where dissipation is not negligible anymore. Yet, the full sum of all terms (theoretically equal to zero) remains low even at these small scales, which suggests that the rise of the dissipation amounts for twice the decrease of the energy cascade rate. At dissipative scales, expression (4.23) can be approximated to:

$$\begin{aligned} \mathcal{D}_{A18} &\simeq -\frac{1}{2} \left\langle \left(1 + \frac{\rho}{\rho'}\right) \mathbf{u} \cdot \mathbf{d}_\nu + \left(1 + \frac{\rho}{\rho'}\right) \mathbf{u} \cdot \mathbf{d}_\nu + \left(\frac{\sqrt{\rho}}{\sqrt{\rho'}} + \frac{\sqrt{\rho'}}{\sqrt{\rho}}\right) (\mathbf{B} \cdot \mathbf{d}_\eta + \mathbf{B} \cdot \mathbf{d}_\eta) \right\rangle. \\ &= -\frac{1}{2} \langle 2\mathbf{u} \cdot \mathbf{d}_\nu + 2\mathbf{u} \cdot \mathbf{d}_\nu + 2\mathbf{B} \cdot \mathbf{d}_\eta + 2\mathbf{B} \cdot \mathbf{d}_\eta \rangle = 2\varepsilon_{A18}, \end{aligned} \quad (4.25)$$

which is indeed what is observed here for runs II and III, corroborating the correlation between energy dissipation and energy cascade. In the scope of the non-stationary exact law, the term $\partial_t \langle R_E + R'_E \rangle$ can be interpreted as a scale-dependent reservoir of energy, taking the role of the forcing absent from these free decay runs. At a given scale, it represents the energy available to be either transferred by the cascade, or dissipated at small scales. The terms $2\varepsilon_{A18}$ and \mathcal{D}_{A18} thus describe the balance between cascade and dissipation in the whereabouts of this reservoir of energy.

For run I the relations between the terms remain pretty consistent with what is observed for runs II and III, except for a notable gap between the amplitude of $\partial_t \langle R_E + R'_E \rangle$ and the amplitude of the sum $2\varepsilon_{A18} + \mathcal{D}_{A18}$: these quantities are not compensating each other as they are supposed to, but instead $\partial_t \langle R_E + R'_E \rangle$ is overall higher. Yet, the difference between them remains constant, as indicated by the black curve. The energy cascade rate for this run, as stated before, matches the estimate obtained for the dissipation rate at -0.05 , whereas $\partial_t \langle R_E + R'_E \rangle$ appears to be closer to (twice) the linear fit estimate of -0.083 . This is further evidenced by the difference curve, that has an amplitude of ~ -0.06 to ~ -0.07 corresponding to twice the difference between the two estimates (remember that the difference is calculated between terms that supposedly amount for $2\varepsilon_{A18}$). Thus, we can argue that the energy cascade rate is able to transcribe the general dynamics of the system and of energy evolution, bypassing the oscillations, whereas $\partial_t \langle R_E + R'_E \rangle$ is perturbed by the fluctuations of energy at the considered times. With this interpretation, the sum of all terms is not equal to zero, but rather represents the error induced in the calculations of time derivatives by the fluctuations of energy.

We now look at the results obtained with F21, displayed in figure 4.12. Again the behaviors of runs II and III are pretty similar, and differ from the one of run I. Here there are more terms that need to be analyzed. First, we notice that both the energy cascade rate and the dissipative term \mathcal{D}_{F21} are the same as for law A18. This was already observed before for the energy cascade rate, and the likeness of \mathcal{D}_{A18} and \mathcal{D}_{F21} can be seen in their respective expressions, that only differ by the addition of factors $\sqrt{\rho}/\sqrt{\rho'}$ and $\sqrt{\rho'}/\sqrt{\rho}$ on the magnetic dissipation. This result suggests that, even for the more compressible run III, these factors remain close to unity.

One can note that \mathcal{D}_{F21}^{loc} remains constant in ℓ for all simulations despite containing the scale dependent terms ρ/ρ' and ρ'/ρ , even for run III. This can be explained by the fact that ρ'/ρ remains close to unity, as already stated, but also by a domination of the magnetic,

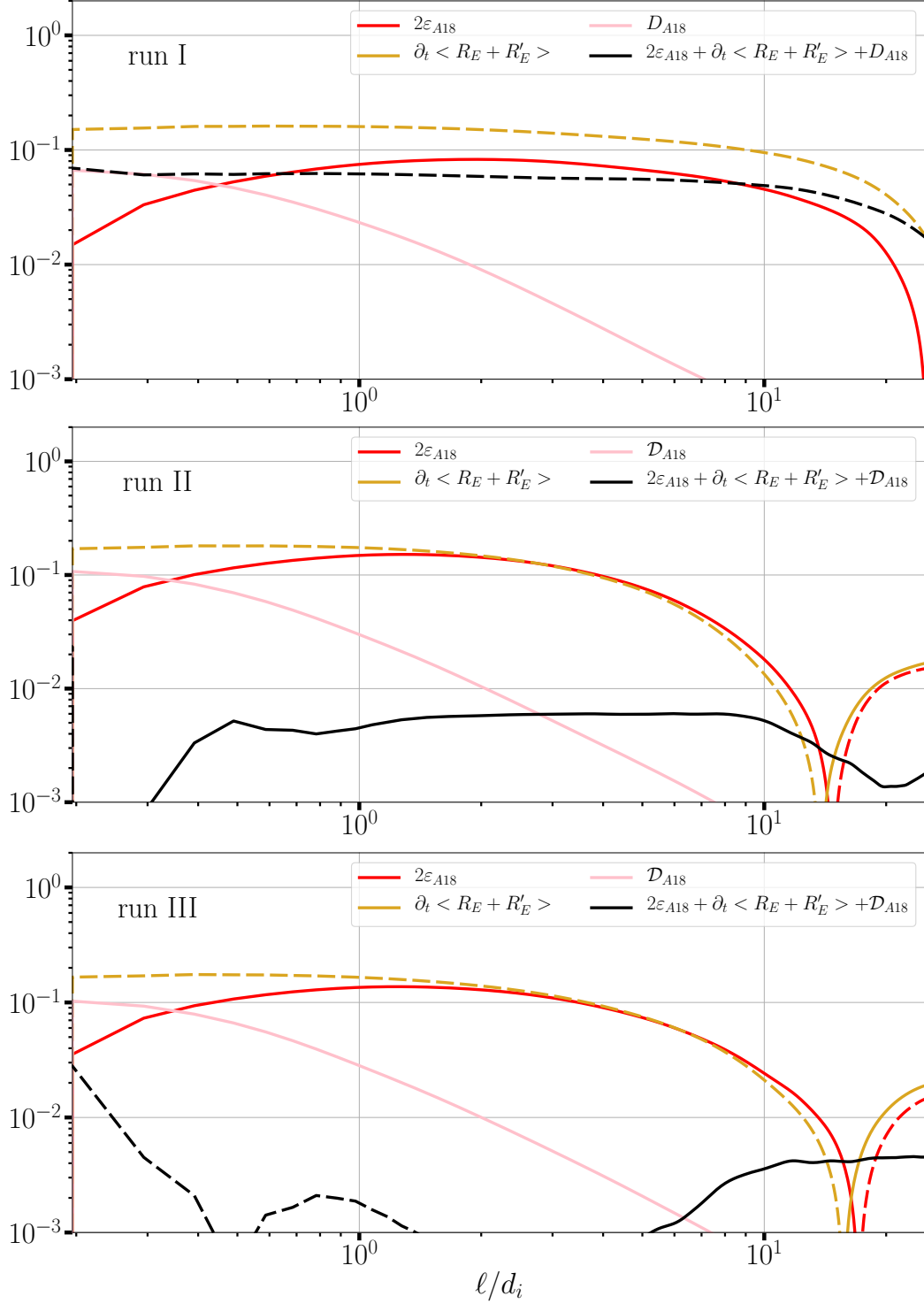


Figure 4.11: Terms of the general equation (4.21) along with their sum (black) for the three **GHOST** runs.

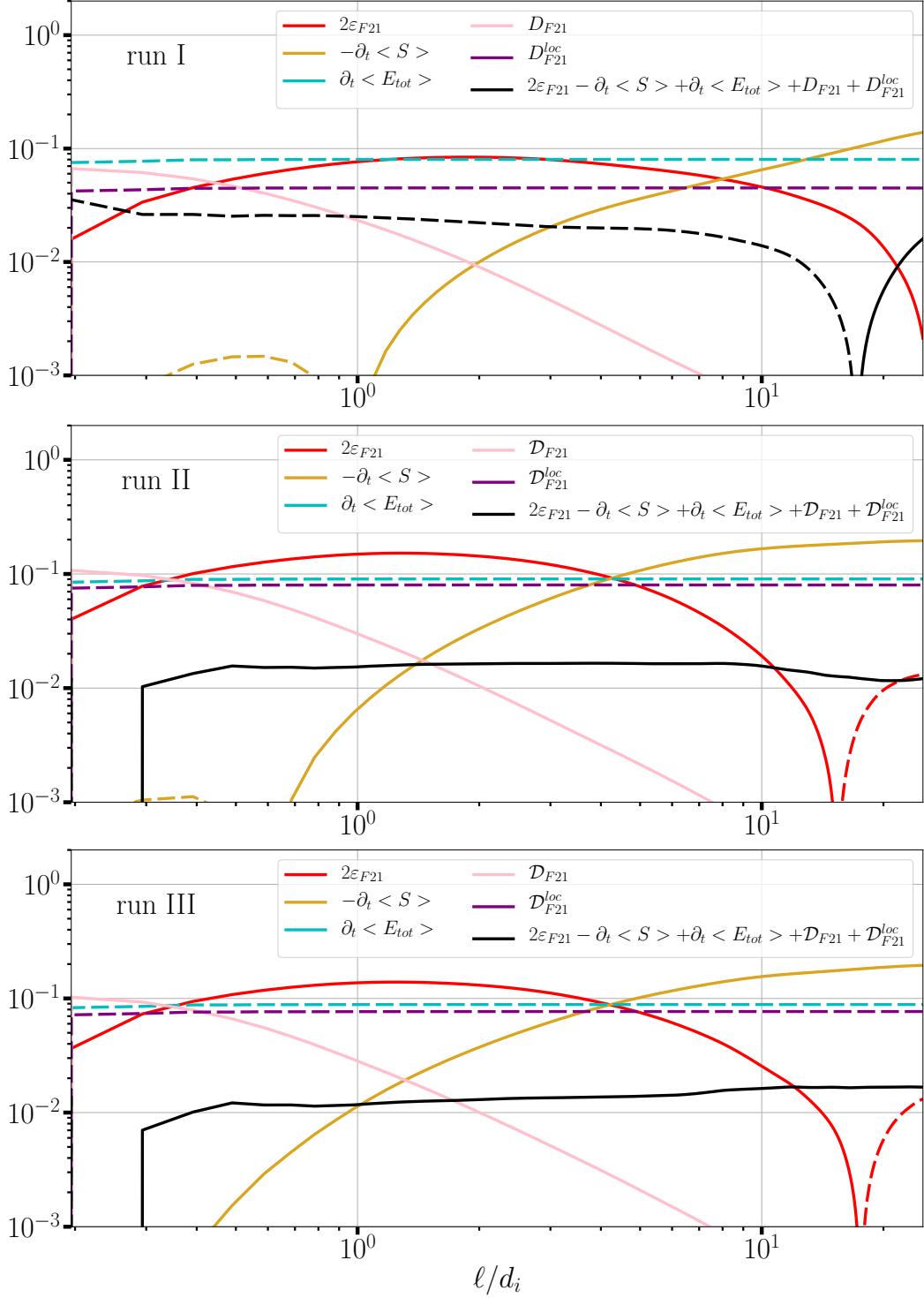


Figure 4.12: Terms of the general equation (4.4) along with their sum (black) for the three **GHOST** runs.

non-scale dependent part of the dissipation, a phenomenon that is also observed in the LF runs studied in next section. In runs II and III, \mathcal{D}_{F21}^{loc} and $\partial_t \langle E_{tot} \rangle$ are almost equal, which is explained by the fact that $\mathcal{D}_{F21}^{loc} \sim -\varepsilon_{F21}$ in the limit of $\rho \sim \rho'$ (or of dominant magnetic dissipation), which is indeed verified by comparing this term to the energy cascade rate. The small gap between \mathcal{D}_{F21}^{loc} and $\partial_t \langle E_{tot} \rangle$ can be attributed to the fact that the latter also takes internal energy into account (no fluctuations of energy are observed on these runs that could explain the gap otherwise).

For run I however we observe a large difference between these terms with \mathcal{D}_{F21}^{loc} lying closer to ε_{F21} , and $\partial_t \langle E_{tot} \rangle$ being similar to its values in other runs and of the same order as the local estimate of dissipation obtained previously with a linear fit on the energy (around -0.083). Here we witness the same discrepancy observed for A18 between quantities related to instantaneous turbulence and time derivatives for the energy or correlation functions. The former do not feel the oscillations and show the global behavior of the system, and the latter are influenced by the time fluctuations of the system. Similarly to what was obtained for A18, the error for F21 is representative of the difference between the estimates of the dissipation rate, this time by taking an almost constant value of ~ -0.03 at small and intermediate scales, which is consistent with the fact that the error at these scales stems only from $\partial_t \langle E_{tot} \rangle$ that should amount to one time the dissipation rate.

Interpreting the balance between the terms of the non-stationary F21 law is more subtle than for A18. Recall that, from equation (2.71), we can write a relation connecting $\langle S \rangle$, $\partial_t \langle E_{tot} \rangle$ and a modified correlation function $\langle \tilde{R}_E \rangle = \langle 0.5\rho\mathbf{u} \cdot \mathbf{u}' + \mathbf{B} \cdot \mathbf{B}' + \rho e' \rangle$. If ρ and ρ' are similar enough, said relation can be derived in time and written as:

$$\partial_t \langle S \rangle = \partial_t \langle E^{tot} \rangle - \partial_t \langle \tilde{R}_E + \tilde{R}'_E \rangle + \partial_t \langle E_k + E_m \rangle, \quad (4.26)$$

with the kinetic and magnetic energies $E_k = 0.5|\rho\mathbf{u}|^2$ and $E_m = 0.5|\mathbf{B}|^2$ respectively. The third term of the right-hand side corresponds to local kinetic and magnetic energy dissipations, which are akin to term \mathcal{D}_{F21}^{loc} . Consequently, the ensemble of terms $-\partial_t \langle S \rangle + \partial_t \langle E^{tot} \rangle + \mathcal{D}_{F21}^{loc}$ can be interpreted as a reservoir of energy similar to $\partial_t \langle R_E + R'_E \rangle$ for law A18. Again, the shapes of $2\varepsilon_{F21}$ and \mathcal{D}_{F21} will dictate whether this energy cascades or is dissipated at a given scale.

4.3.5 Summary of the GHOST study

In this section we present an in-depth study of exact laws A18 and F21 on simulations in a state of free energy decay. These simulations allowed us to confirm that the two laws provide the same results for both the MHD and the Hall components of the energy cascade rate. The energy cascade rates obtained match the energy dissipation rates estimated on the basis of the time evolution of the energy or the average dissipation, suggesting that the energy transferred by the cascade corresponds to the energy dissipated at small scales. The specific analysis of F21 showed that the MHD source term, similarly to A18, remains negligible at all scales in comparison to the flux one. However, this behavior is not reproduced by the Hall part of the law: the Hall flux term is roughly equal to minus two times the source one, showing a trend similar to their incompressible counterparts. The terms of the law seem to be weakly influenced by compression, as they show few differences between run II and run III of respective Mach numbers 0.25 and 0.5. The presence of a background magnetic field in run I reduces the overall amplitude of the cascade.

The exact laws are then rewritten and studied without the usual assumption of time stationarity, that requires a large scale forcing to balance out the dissipation. Through this in-depth study we see that the full exact laws remain valid in the absence of an external forcing, albeit with a change in the interpretation. Indeed, instead of a constant flow of energy fueling the turbulence from the large scales, the turbulent cascade seems to draw from a local pool of energy destined to either continue cascading or be dissipated. In the special case of run I,

fluctuations appear on the time evolution of energy, probably due to the introduction of waves in the system due to \mathbf{B}_0 . Because of these fluctuations a discrepancy is observed between the time derivatives and the remaining terms: the former seem sensitive to the fluctuations, whereas the latter only depict the global trend of the evolution of the system. The error induced by this discrepancy is, for both laws, tied to the difference between estimates of the dissipation rates obtained by taking into account these fluctuations or not. These differences are very likely to have appeared due to insufficient time statistics when studying run I. If the run were pushed further in time and more snapshots were taken to cover several periods of the time fluctuations, this error should ultimately be reduced. However, this would require spending much more time than is currently affordable on this particular aspect of the thesis.

In any case, the study led here brings several information and results that will be useful for subsequent studies. Knowing the individual behaviors of the terms forming F21 is an important asset to analyze and physically interpret results obtained from more specific studies on DNS or *in situ* data, such as those of MMS that will be worked on in chapter 5. This work also shows the correlation between the turbulence energy cascade rate and the energy dissipation, and as such is a first step towards the more complete study presented in the next section, which aims at connecting again cascade and dissipation in presence of kinetic effects, namely Landau damping.

4.4 Application to Landau-fluid simulations

4.4.1 Context of the study

As we explained in chapter 1, turbulence is known to play an important role in some physical processes at work within the SW, notably with its non-adiabatic expansion (Richardson et al., 1995). This turbulence has been extensively studied with exact laws (Smith et al., 2006; Podesta et al., 2007; MacBride et al., 2008; Marino et al., 2008; Smith et al., 2009; Stawarz et al., 2009; Osman et al., 2011; Coburn et al., 2015; Hadid et al., 2017): the estimated cascade rate was interpreted as the turbulence energy dissipation rate, and hence used to quantify the amount of plasma heating due to turbulence (Sorriso-Valvo et al., 2007; Carbone et al., 2009; Banerjee et al., 2016). However, the weakly collisional nature of the SW makes it so that, in such plasmas, classical viscous and/or resistive effects are absent, and dissipation is expected to occur via kinetic effects (e.g., Landau and cyclotron resonances) (Leamon et al., 1998; Sahraoui et al., 2009; Sahraoui et al., 2010; He et al., 2015; Woodham et al., 2018; Chen et al., 2019) that are not described by the typical fluid models under which all exact laws are derived. Hence the fundamental question already stated earlier: is it possible for the *fluid* turbulence energy cascade rate to provide an estimate of the actual *kinetic* dissipation in non-collisional (astrophysical) plasmas ?

To investigate this question, we take advantage of the weak compressibility of the runs and use the IHMHD exact law F19 derived in chapter 2 to investigate the fundamental question of the correlation between the (fluid) turbulent cascade rate and the kinetic dissipation occurring in a given medium. This question directly impacts the use of fluid models to interpret part of in-situ spacecraft observations in the near-Earth space and the theoretical (fluid vs. kinetic) modeling of weakly collisional plasmas. Previous studies based on 2D hybrid particle-in-cell simulations already investigated the behavior of exact laws in presence of kinetic effects (Hellinger et al., 2018; Bandyopadhyay et al., 2020; Vásconez et al., 2021), but none was able to quantitatively prove the existence of a relation between the cascade rate and kinetic dissipation. The 3D LF models used in this section give the possibility to isolate the influence of electron and ion Landau damping, neglecting all the other kinetic effects and allowing for an in-depth, quantitative analysis of the possible correlations between the energy cascade and Landau damping.

4.4.2 Theory of CGL and LF models

In this study we make use of simulations obtained with two models: the **CGL** model and the **LF** model, based on the same general **CMHD** model presented in chapter 1 but using different closures. The **CGL** model refers to a closure with anisotropic ion pressure whose axi-symmetric components parallel and perpendicular to the local magnetic field obey the following nonlinear dynamical equations, where the heat fluxes are neglected:

$$\frac{d}{dt} \left(\frac{p_{\parallel} |B|^2}{\rho^3} \right) = 0 ; \quad \frac{d}{dt} \left(\frac{p_{\perp}}{\rho |B|} \right) = 0. \quad (4.27)$$

Here p_{\perp} and p_{\parallel} are the components of the pressure tensor $\mathbf{P} = p_{\perp} \mathbf{I} + (p_{\parallel} - p_{\perp}) \widehat{\mathbf{b}} \widehat{\mathbf{b}}$, \mathbf{I} is the unit tensor and $\widehat{\mathbf{b}} = \mathbf{B}/|B|$ the unit vector aligned with the magnetic field. The time derivative operator reads $d/dt = \partial/\partial t + \mathbf{u} \cdot \nabla$. This closure is also known as the bi-adiabatic approximation and was introduced by Chew, Goldenberg and Low ([Chew et al., 1956](#)) (hence the acronym). Note that in our case this closure only applies to the ions: the electrons are still assumed isothermal. This model does not contains built-in kinetic dissipation, thus in our **CGL** simulations all energy dissipation occurs through artificial hyperdissipation (see the description of the code in next subsection).

Differently, the LF model retains the nonlinear dynamics of the parallel and perpendicular pressures and heat fluxes for both the ions and the electrons through equations:

$$\frac{d}{dt} \ln \left(\frac{p_{\parallel} |B|^2}{\rho^3} \right) = -\frac{2c}{|B|} \widehat{\mathbf{b}} \cdot \nabla \times \mathbf{E} - \frac{1}{p_{\parallel}} \left(-2q_{\perp} \nabla \cdot \widehat{\mathbf{b}} + \nabla \cdot (q_{\parallel} \widehat{\mathbf{b}}) \right) \quad (4.28)$$

$$\frac{d}{dt} \ln \left(\frac{p_{\perp}}{\rho |B|} \right) = \frac{c}{|B|} \widehat{\mathbf{b}} \cdot \nabla \times \mathbf{E} - \frac{1}{p_{\perp}} \left(q_{\perp} \nabla \cdot \widehat{\mathbf{b}} + \nabla \cdot (q_{\perp} \widehat{\mathbf{b}}) \right). \quad (4.29)$$

Here, \mathbf{E} is the electric field as we already defined it through Ohm's law (1.20) in Hall **MHD**, but also takes into account the term for electron pressure that was neglected before. q_{\parallel} and q_{\perp} are the longitudinal and transverse heat fluxes obtained from the integration of the model closed at the level of the fourth-order moments, with a closure consistent with the low-frequency linear kinetic theory ([Snyder et al., 1997](#)). The main assumption for modeling Landau damping (and thus closing the fluid hierarchy) is that, up to the distortion of the magnetic field lines, Landau damping keeps the same form as in the linear regime. This allows for building the appropriate closure based on the linear expression of Landau damping, which is easier to determine. In this model, as we will show below, the heat fluxes are essentially driven by Landau damping, and only a small fraction of dissipation originates from the heat fluxes present in the quasi-normal closure (i.e., a fluid closure at the fourth order that would not include Landau damping, see [Hunana et al. \(2019\)](#)). Thus, the comparison of this model and the **CGL** one, which contains no heat fluxes, should help highlighting the influence of kinetic dissipation (and more specifically Landau damping) on the energy cascade.

4.4.3 Description of the numerical code

The simulations were ran using a numerical code that solves all fluid equations for density, velocity, magnetic field, pressures and heat fluxes (when applicable) in Fourier space. The simulations are run in triply periodic boxes of various resolutions and are performed using a desaliased spectral code (at 2/3 of the maximum wavenumber) with a third-order Runge-Kutta scheme for time stepping. The specific modeling of Landau damping involves a Hilbert transform along the distorted magnetic field lines which leads to Landau dissipation, and whose approximation in the numerical code is discussed in [Passot et al. \(2014\)](#). In both **CGL** and **LF** models, finite ion and electron Larmor radius corrections are neglected, thus reducing the kinetic effects to the sole Landau damping. The Ohm's law includes the Hall term and

the electron pressure contribution. In all the simulations, $\beta_i = 1$ and the ion and electron pressures are taken isotropic and equal initially.

Turbulence is forced with counter-propagating [Kinetic Alfvén Waves \(KAWs\)](#) making an angle θ with the ambient magnetic field, at transverse wavenumbers $k_{\perp,f}$ corresponding to the largest scales of the simulation domain. Note that the simulation domains are elongated in the longitudinal direction (along the mean magnetic field direction): the ratio of the longitudinal to transverse box sizes is given by $\tan(\theta)$. The amplitudes of the forcing waves obey a Langevin equation, with an oscillation frequency given by the [KAW](#) linear dispersion relation ([TenBarge et al., 2014](#)). We also introduce two thresholds in order to constrain the sum of perpendicular kinetic and magnetic energies to stay within a certain range: above the maximum threshold the forcing stops and energy is left to decay, and below the minimum threshold the forcing resumes. Aside from Landau damping, small-scale dissipation is ensured by hyperviscosity and hyperdiffusivity terms in the velocity and induction equations that replace the terms \mathbf{d}_ν and \mathbf{d}_η introduced in chapter 2. These are of the form $\mathbf{d}_\nu = \nu(\Delta_\perp + \alpha\partial_z^2)^4\mathbf{u}$ and $\mathbf{d}_\eta = \eta(\Delta_\perp + \alpha\partial_z^2)^4\mathbf{b}$, with α being an anisotropy coefficient.

Run	$k_{\perp,f}d_i$	Resolution	θ	$\nu = \eta$	α
CGL1	0.045	512^3	83°	7.35×10^{-8}	80
CGL2	0.045	512^3	75°	7.35×10^{-8}	10
CGL3	0.5	$512^2 \times 1024$	75°	10^{-14}	2.5
CGL4	0.011	1024^3	75°	3×10^{-3}	5
LF1	0.045	512^3	83°	7.35×10^{-8}	1
LF2	0.045	512^3	75°	7.35×10^{-8}	1
LF3	0.5	432^3	75°	7×10^{-14}	1.5
LF4	0.011	512^3	75°	3×10^{-3}	2

Table 4.2: List of runs and their relevant parameters, where CGLx and LFx refer to HMHD-CGL and LF simulations, respectively. $\tan(\theta)$ corresponds to the ratio of the longitudinal to transverse box sizes.

A total of eight runs are performed: four with the [CGL](#) model, and the other four with the [LF](#) model. All of their relevant parameters are summarized in Table 4.2. These runs feature various forcing wavenumbers which allow us to draw a broad picture of the turbulence across about 3 decades in scale. Two different propagation angles for the driving [KAWs](#) of each LF simulation were chosen to reflect different levels of Landau damping ([Kobayashi et al., 2017](#)). Indeed one can see in Fig. 4.13, which compares the linear dispersion relation and damping rate of the [KAWs](#), that the propagation angle has an influence on the magnitude of Landau damping: the higher the angle, the lower the damping rate at a given scale ([Sahraoui et al., 2012](#)).

Finally, we proceed to an energy balance check to verify that energy is conserved in our simulations. Let $\mathcal{E}_{\text{tot}}(t) = \rho\mathbf{u}^2/2 + \rho\mathbf{b}^2/2 + \rho e$ be the total energy of the system at time t , $\mathcal{I}_t(t)$ the injection rate due to the external forcing on the perpendicular velocity components, and $\mathcal{D}_h(t)$ the total dissipation rate due to the hyperviscous and hyperdiffusive terms. Since Landau damping only transfers turbulent energy to internal energy through heating, it does not affect the total energy balance and thus total energy conservation reads:

$$\frac{d}{dt}\mathcal{E}_{\text{tot}}(t) = \mathcal{I}_t(t) - \mathcal{D}_h(t). \quad (4.30)$$

Denoting by \mathcal{E}_{int} and \mathcal{E}_{\parallel} the parts of the total energy associated with the pressure components (internal energy) and the parallel velocity and magnetic field components entering the kinetic and magnetic parts, we can write

$$\frac{d}{dt}\mathcal{E}_{\text{tot}}(t) - \frac{d}{dt}\mathcal{E}_{\text{int}}(t) - \frac{d}{dt}\mathcal{E}_{\parallel}(t) \equiv \frac{d}{dt}\mathcal{E}_{\perp}(t) \approx 0, \quad (4.31)$$

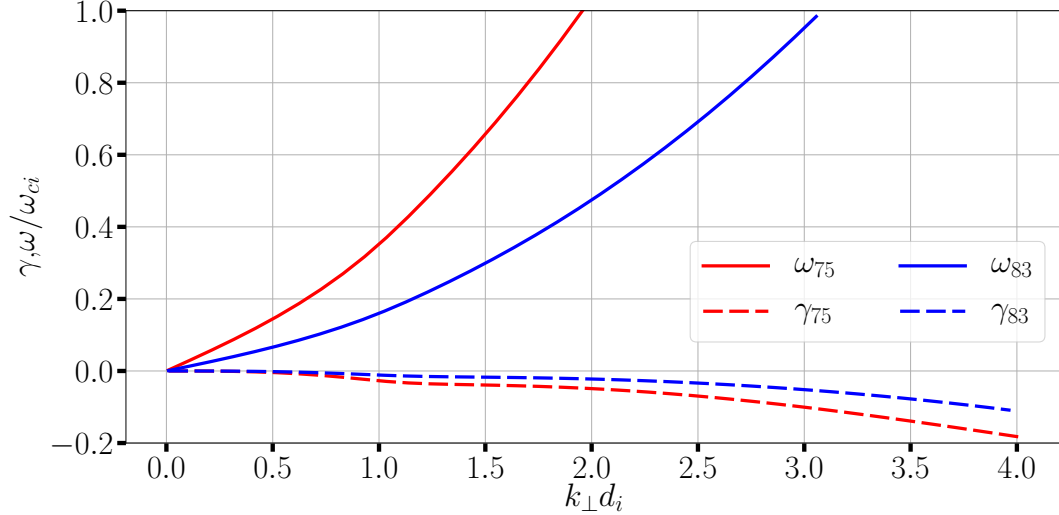


Figure 4.13: Linear dispersion relation (ω) and damping rate (γ) of KAWs for the LF model at the two propagation angles $\theta = 83^\circ$ and 75° used in driving the simulations ($\beta_i = 1$, $T_i = T_e$, d_i denotes the ion Larmor radius and ω_{ci} the ion gyrofrequency).

where \mathcal{E}_\perp is the sum of the perpendicular kinetic and magnetic energies, a quantity bound to remain nearly constant by the forcing procedure described above.

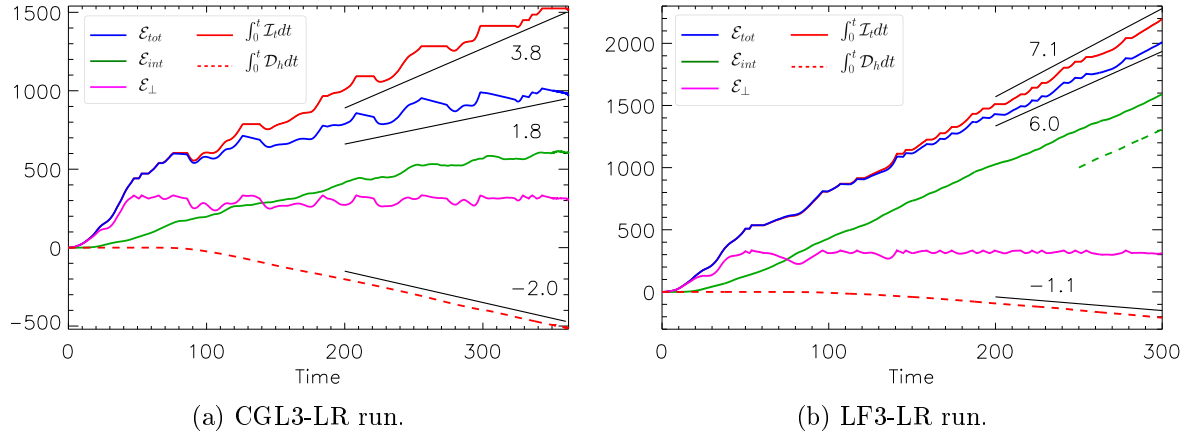


Figure 4.14: Low resolution runs of CGL3 and LF3: Time evolution of the total energy injected in the system $\int_0^t \mathcal{I}_t dt$ (solid red line), total energy \mathcal{E}_{tot} (solid blue), internal energy \mathcal{E}_{int} (solid green), perpendicular energy \mathcal{E}_\perp (solid magenta, roughly constant) and the time integrated hyperdissipation $\int_0^t \mathcal{D}_h dt$ (dashed red). The piece of dashed green curve (right) starting at $t = 250$, whose vertical position is arbitrary, displays the heating due to heat fluxes, which is consistent with the increase of internal energy.

Because of computational constraints the time evolution of the different energy components is computed for low resolution (LR) simulations analog of runs CGL3 and LF3 (injection and dissipation rates needed to perform this extra study were not output at a high-enough frequency in the simulations presented in this section). From the results displayed in Figure 4.14 it is obvious that the time evolution of total energy (blue), injection (red) and hyperdissipation (dashed red), whose slopes are reported in the plots, is consistent with the energy conservation equation (4.30). Moreover, one can see the driving procedure at play in keeping the perpendicular energy \mathcal{E}_\perp roughly constant. Its time stationarity is in practice reached when the hyperdissipation rate has reached a constant value. When comparing CGL3-LR with LF3-LR, one notices that run LF3-LR requires a larger injection rate to maintain the same level of turbulence on the magnetic and perpendicular velocity than in run CGL3-LR,

since Landau damping efficiently converts a part of the injected energy into internal energy. This is evidenced by the dashed green curve in Fig. 4.14b, which shows that the increase of the internal energy is consistent with the heating by heat fluxes. Moreover, the hyperdissipation rate is lower on run LF3-LR, suggesting that part of the cascading energy is taken by Landau damping.

4.4.4 Evaluation of the exact law and dissipations

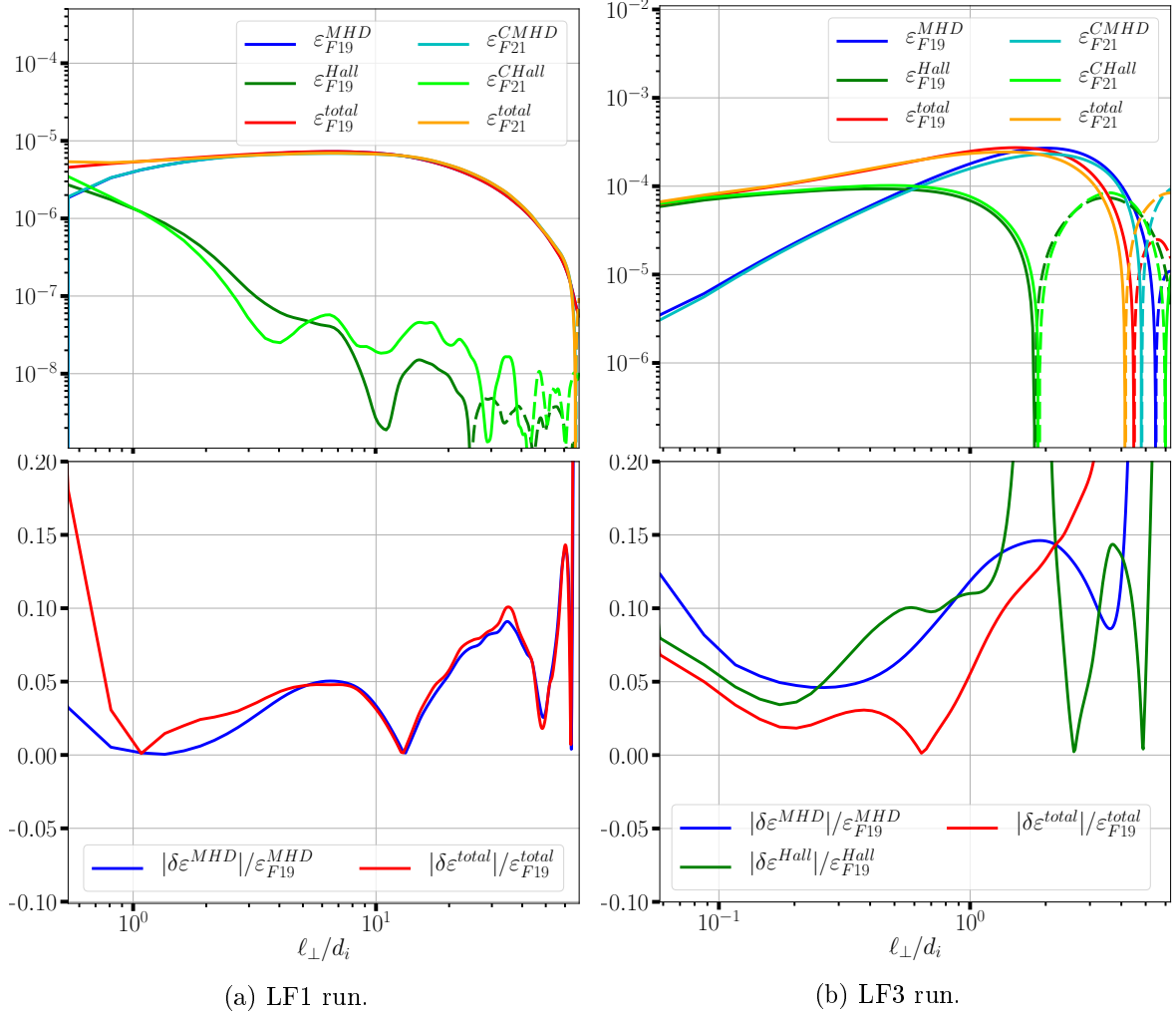


Figure 4.15: Comparison of the IHMHD model F19 and the CHMHD model F21 for runs LF1 and LF3. The top panels show a visual comparison of the total cascade rate and its two components for F19 and F21 (in dark and bright lines respectively). The bottom panels show the relative difference between the two models as $|\varepsilon_{F21} - \varepsilon_{F19}|/|\varepsilon_{F19}|$. Note that the Hall component is absent from the bottom panel for run LF1: this is because it is negligible in the inertial range and more sensitive to errors due to its low amplitude. Thus, it brings no information on the discrepancy between the two models.

To study these CGL and LF datasets I chose to use the IHMHD law F19 presented in section 2.2:

$$\varepsilon = \varepsilon^{MHD} + \varepsilon^{Hall} = -\frac{1}{4} \nabla \ell \cdot \mathbf{Y} - \frac{1}{8} \nabla \ell \cdot \mathbf{H}. \quad (4.32)$$

I chose to use an incompressible law because the datasets are weakly compressible (with a Mach number $M_S = 1/\sqrt{2}$) in order to simplify the analysis and accelerate the computation. As shown in Figure 4.15, the full CHMHD exact law F21 was also used, and only a slight change ($\lesssim 10\%$ in the inertial range) in the cascade rate was found with respect to the estimate

from the incompressible model. This justifies the use of an incompressible law on our datasets. The calculation was done with the 3D anisotropic vector decomposition described in section 3.2.3 due to the axi-symmetric nature of these simulations, and this decomposition proved to be in good agreement with the theoretical equivalence between the three IHMHD laws demonstrated in chapter 2 (and already discussed in section 4.2), as shown in figure 4.16. A deviation can be observed for law G08 in run LF3 (see figure 4.16b), that may be the result of the lower resolution of run LF3, yet the equivalence between the two other laws holds very well. Thus, we consider this decomposition as a valid model to study the present datasets.

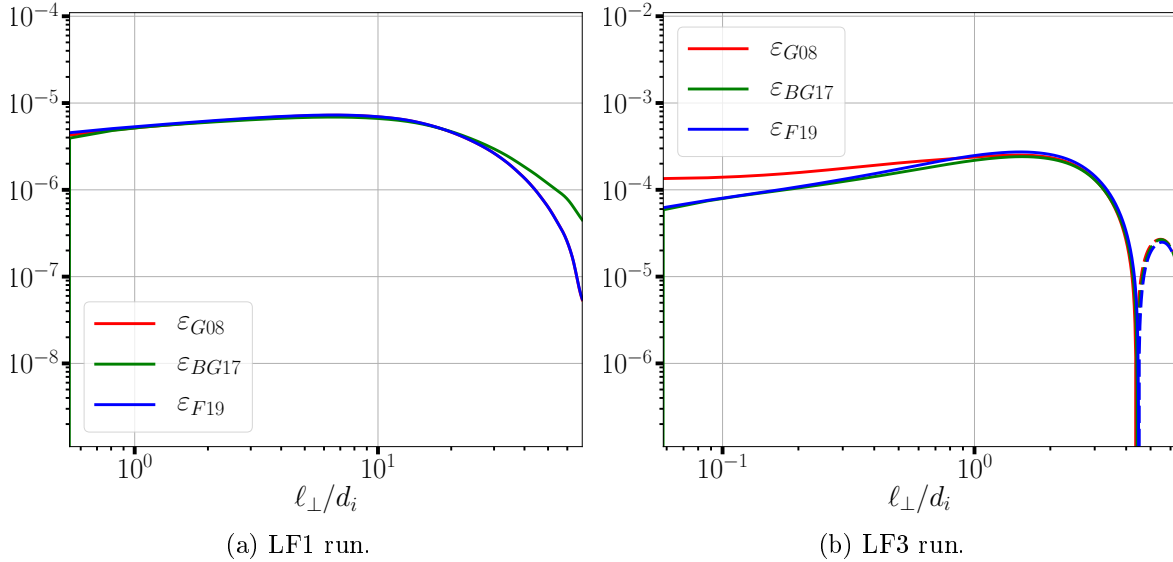


Figure 4.16: Comparison of the three IHMHD models G08, BG17 and F19 for runs LF1 and LF3.

As mentioned in previous subsection the spectral code was desaliased at $2/3$ of the maximum wavenumber. In practice, this means that all information computed with the exact law for scales smaller than $3/2$ of the grid separation is polluted by the numerical scheme and must not be taken into account. Usually I do not compute the value of the exact law at grid separation as the computation method used leads to weaker statistics at this scale, and only start the calculations at twice the separation, so the calculations lie outside the desaliasing range. Nevertheless, to get the most complete picture possible of the turbulence, values below the minimum calculated scale are extrapolated using a cubic spline constructed on all available data points. This allows the calculated cascade rates to reach the desaliasing scale and to be fully compared to the hyperdissipation (that naturally reaches this scale as it is computed in Fourier space).

4.4.5 Methods of calculation of the hyperdissipation

In the first iterations of this study I calculated the hyperdissipative terms as they appear in the fluid exact law. According to equation (2.34), the dissipative terms of the cascade (outside of the inertial range where they would otherwise be negligible) read:

$$\varepsilon^{diss}(\ell_{\perp}) = -\frac{1}{2} \langle \mathbf{u} \cdot \mathbf{d}'_{\perp, \nu} + \mathbf{u}' \cdot \mathbf{d}_{\perp, \nu} \rangle - \frac{1}{2} \langle \mathbf{b} \cdot \mathbf{d}'_{\perp, \eta} + \mathbf{b}' \cdot \mathbf{d}_{\perp, \eta} \rangle, \quad (4.33)$$

where $\mathbf{d}_{\perp, \nu} = \nu \Delta_{\perp}^4 \mathbf{u}$ and $\mathbf{d}_{\perp, \eta} = \eta \Delta_{\perp}^4 \mathbf{b}$ are the transverse hyperviscosity and hyperdiffusivity. I calculated this dissipation in the same way I usually compute all the other terms of the exact law, through an average on both space and increment vectors. The calculation of the eighth derivative can be done either in real space or in Fourier space, and both methods were found to give the same results. The resulting dissipation is shown in figure 4.17a. Aside from the huge gap in amplitude between the dissipation and the energy cascade rate (which should be

matching at small scales) the dissipation appears to be roughly following a scaling of $\sim \ell_{\perp}^{-2}$ around intermediate scales. This behavior is unexpected as the hyperdissipation takes the form of an eighth derivative: this should introduce a factor of k_{\perp}^8 in Fourier space, so one would expect a steep scaling of around $\sim \ell_{\perp}^{-7}$ in real space instead of the observed $\sim \ell_{\perp}^{-2}$ one. We suspect this discrepancy to be the result of a saturation of the scaling, a mathematic limitation preventing the slope from becoming steeper than $\sim \ell_{\perp}^{-2}$.

Such a saturation was already found for structure functions, e.g. $SF_2(\ell) = \langle |\delta \mathbf{u}|^2 \rangle$, which can be obtained mathematically (see [Cho and Lazarian \(2009\)](#)). Indeed, one can show that the second-order structure function associated to a spectrum of slope k^{-m} will scale as:

$$SF_2(\ell) \propto \begin{cases} \ell^{m-1}, & \text{if } m < 3 \\ \ell^2, & \text{if } m > 3. \end{cases} \quad (4.34)$$

Consequently, a function that has a power-law spectrum equal to, or steeper than, k^{-3} has its structure function that is ill-defined and should bear no physical meaning. Here a similar problem seems to be occurring, but on the correlation function instead of the structure function. We did not manage to find a mathematical proof of this saturation, but it was observed empirically by computing the correlation function

$$R(\ell) = \int_0^{\infty} \frac{\sin(k\ell)}{k\ell} E_k(k) dk \quad (4.35)$$

for artificial spectra E_k of fixed slopes. As one can see in figure 4.17b, we observed that if the spectrum becomes steeper than k^1 then the slope of the associated correlation function reaches an asymptotic value of ℓ^{-2} . In the case of our hyperdissipation the spectrum associated to e.g. $\langle \mathbf{u} \cdot \mathbf{d}'_{\perp, \nu} \rangle$ is $k_{\perp}^8 |\hat{\mathbf{u}}|^2$, whose scaling is roughly $k_{\perp}^8 k_{\perp}^{-5/3} \sim k_{\perp}^6$, way above k_{\perp}^1 , hence the observed behavior.

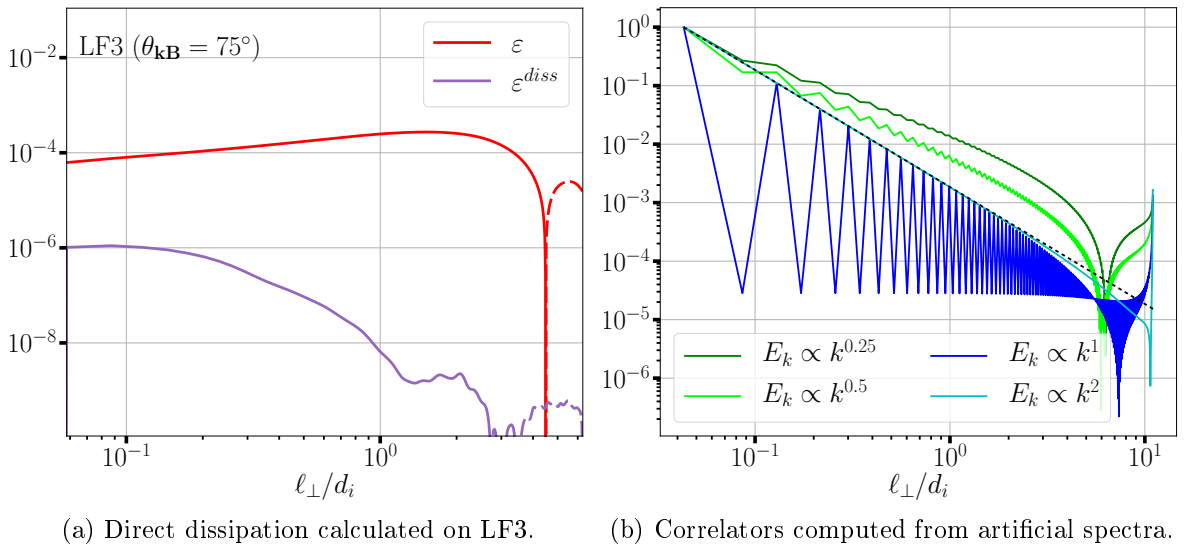


Figure 4.17: Left: Total energy cascade rate and dissipation directly calculated from equation (4.33). The scaling of the dissipation results from a saturation on the slope of the associated spectrum. This is evidenced empirically by the figure on the right, that shows correlation functions (in real space) calculated from artificial spectra, defined as perfect power-laws of various scalings: the correlation functions saturate at a slope of ℓ_{\perp}^{-2} , represented by the black dashed line.

Since it is not possible to retrieve a correct scaling for dissipation in real space through a direct calculation of the dissipative term, I searched for a way to apply this scaling in real space after making the calculations and averages on the simulation domain. Assuming statistical homogeneity Δ_{\perp} obeys the usual relations $\langle \Delta'_{\perp} \mathbf{u} \rangle = \langle \Delta_{\perp} \mathbf{u}' \rangle = 0$ and $\langle \Delta'_{\perp} (\mathbf{u} \cdot \mathbf{u}') \rangle =$

$\langle \Delta_{\perp}(\mathbf{u} \cdot \mathbf{u}') \rangle = \Delta_{\perp, \ell} \langle \mathbf{u} \cdot \mathbf{u}' \rangle$. With these relations we can write:

$$\varepsilon^{diss} = \frac{1}{2} \langle \nu \Delta_{\perp}^4 |\delta \mathbf{u}|^2 + \eta \Delta_{\perp}^4 |\delta \mathbf{b}|^2 \rangle = \frac{1}{2} \Delta_{\perp, \ell_{\perp}}^4 \langle \nu |\delta \mathbf{u}|^2 + \eta |\delta \mathbf{b}|^2 \rangle. \quad (4.36)$$

Thus, one can compute the energy dissipation from hyperviscosity and hyperdiffusivity by taking the fourth power two-dimensional Laplacian of the transverse second-order structure functions for \mathbf{u} and \mathbf{b} . These structure functions can be calculated in the same way as the energy cascade rate, and we check afterwards that their scaling is lower than 2 (see figure 4.18 for an example on run LF3), indicating that they are not in the state of saturation described by relation (4.34). Note that the other simulations are not affected by this problem either since the corresponding energy spectra are shallower than k_{\perp}^{-3} . I then needed to find a way to compute the operator Δ_{\perp}^4 , where $\Delta_{\perp} = \frac{\partial^2}{\partial \ell_{\perp}^2} + \frac{1}{\ell_{\perp}} \frac{\partial}{\partial \ell_{\perp}}$, with enough precision to ensure a correct result, which was the most difficult part of this method. I investigated two methods to make this calculation.

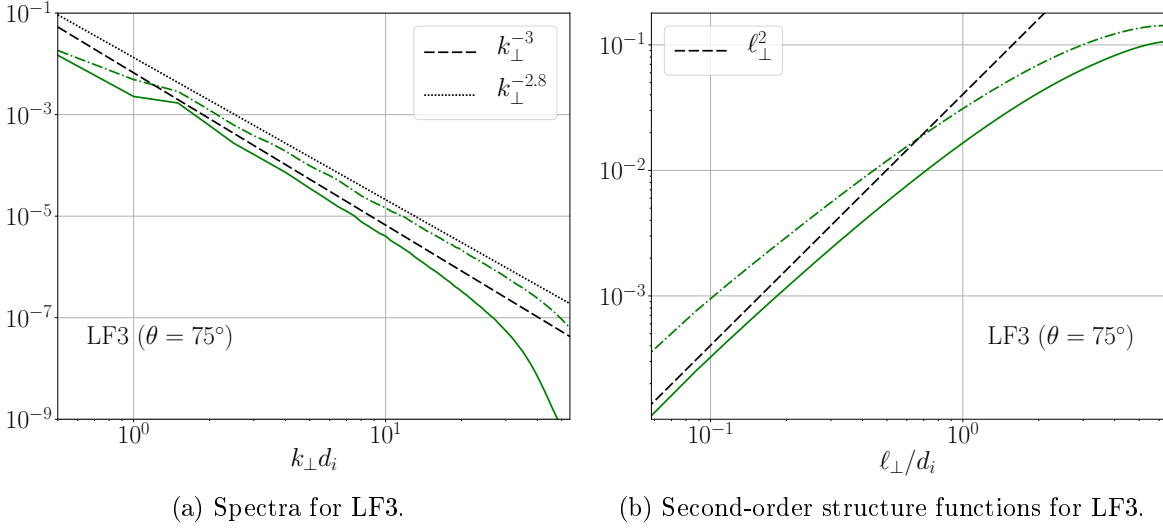


Figure 4.18: Kinetic (plain lines) and magnetic (dashed-dotted lines) energy spectra and corresponding second-order structure functions for simulation LF3, found to be the run with the steepest spectra among all our simulations. The dashed and dotted black lines show the reference for various scalings.

The first attempt to obtain a numerical scheme able to compute an eighth derivative made use of compact finite differences (see [Lele \(1992\)](#)). Considering a 1D array representing a function f , and whose points are labeled as $[f_0, \dots, f_i, \dots, f_{N-1}]$, the method of compact finite differences consists in using relations connecting, for a given point i , f'_i to the values and derivatives of its neighboring points. Applying these relations to each point i leads to a system of N equations whose variables are the derivatives at the N points of the array. Such relations exist for the first and second derivatives, which would allow us to compute Δ_{\perp}^4 by applying the derivation scheme four times. However, one needs to be careful to the precision of the numerical scheme: indeed, for a second-order scheme of precision $O(h^{\alpha})$, 3 subsequent applications of the same scheme will lead to a final precision of $O(h^{\alpha-6})$. Consequently, if one wants to retain a total precision of at least $O(h^2)$, both the first and second order schemes must be of precision at least $O(h^8)$. Luckily, [Lele \(1992\)](#) provides relations that match this requirement. For the first derivative, the relations read:

$$\beta f'_{i-2} + \alpha f'_{i-1} + f'_i + \alpha f'_{i+1} + \beta f'_{i+2} = a \frac{f_{i+1} - f_{i-1}}{2h} + b \frac{f_{i+2} - f_{i-2}}{4h},$$

$$\alpha = \frac{4}{9}, \quad \beta = \frac{1}{36}, \quad a = \frac{40}{27}, \quad b = \frac{25}{54}, \quad (4.37)$$

and for the second derivative:

$$\begin{aligned} & \beta f''_{i-2} + \alpha f''_{i-1} + f''_i + \alpha f''_{i+1} + \beta f''_{i+2} \\ &= a \frac{f_{i+1} - 2f_i + f_{i-1}}{h^2} + b \frac{f_{i+2} - 2f_i + f_{i-2}}{4h^2} + c \frac{f_{i+3} - 2f_i + f_{i-3}}{9h^2}, \end{aligned} \quad (4.38)$$

$$\alpha = \frac{334}{899}, \quad \beta = \frac{43}{1798}, \quad a = \frac{1065}{1798}, \quad b = \frac{1038}{899}, \quad c = \frac{79}{1798}. \quad (4.39)$$

Here h denotes the constant separation between two points. Those two schemes have respective precisions of $O(h^8)$ and $O(h^{10})$, and thus match our criterion.

In our case, the 1D structure functions we want to derive are not periodic. Consequently, as the two schemes presented above establish a relation between a point and, at most, its six neighbors (three on each side) they cannot be used on the first and last three points of the array. For these points, a specific boundary scheme needs to be used. Such schemes are also described by [Lele \(1992\)](#) but none has a high enough precision, thus I had to derive new ones. Let us start with the first derivative, for which we consider the general equation:

$$f'_i + \alpha f'_{i+1} + \beta f'_{i+2} = \frac{1}{h}(af_i + bf_{i+1} + cf_{i+2} + df_{i+3} + ef_{i+4} + ff_{i+5} + gf_{i+6}). \quad (4.40)$$

To find the values of the coefficients we develop this expression as a Taylor series in point i . The Taylor series in i of f_{i+k} for example is given by:

$$\sum_{n=0}^{\infty} \frac{f_i^{(n)}}{n!} (kh)^n = f_i + \frac{f'_i}{1!} (kh) + \frac{f''_i}{2!} (kh)^2 + \frac{f'''_i}{3!} (kh)^3 + \frac{f_i^{(4)}}{4!} (kh)^4 + \dots \quad (4.41)$$

The 9 relations necessary to solve this system of 9 variables are obtained by setting the first 9 Taylor coefficients of the general equation to zero. This leads to the following system:

$$\begin{cases} a + b + c + d + e + f + g = 0 \\ -(\alpha + \beta) + b + 2c + 3d + 4e + 5f + 6g = 1 \\ -n(\alpha + 2^{n-1}\beta) + b + 2^n c + 3^n d + 4^n e + 5^n f + 6^n g = 0, \quad n = 2..8, \end{cases} \quad (4.42)$$

whose resolution leads to the coefficients:

$$\alpha = 12, \quad \beta = 15, \quad a = \frac{-79}{20}, \quad b = \frac{-77}{5}, \quad c = \frac{55}{4}, \quad d = \frac{20}{3}, \quad e = \frac{-5}{4}, \quad f = \frac{1}{5}, \quad g = \frac{-1}{60}. \quad (4.43)$$

The final truncation error is given by the first non-zero coefficient, which is here proportional to $h^8 f^{(9)}$, and corresponds to a precision $O(h^8)$. For the second derivative I used the same method: I considered the general equation

$$f''_i + \alpha f''_{i+1} + \beta f''_{i+2} = \frac{1}{h}(af_i + bf_{i+1} + cf_{i+2} + df_{i+3} + ef_{i+4} + ff_{i+5} + gf_{i+6} + jf_{i+7}), \quad (4.44)$$

which leads to a system of 10 equations:

$$\begin{cases} a + b + c + d + e + f + g + j = 0 \\ b + 2c + 3d + 4e + 5f + 6g + 7j = 0 \\ -2(\alpha + 2\beta) + b + 2^2 c + 3^2 d + 4^2 e + 5^2 f + 6^2 g + 7^2 j = 2 \\ -n(n-1)(\alpha + 2^{n-1}\beta) + b + 2^n c + 3^n d + 4^n e + 5^n f + 6^n g + 7^n j = 0, \quad n = 3..9. \end{cases} \quad (4.45)$$

Solving this system gives the following coefficients

$$\begin{aligned} \alpha &= \frac{18922}{563}, \quad \beta = \frac{65943}{563}, \quad a = \frac{2186893}{101340}, \quad b = \frac{526369}{5067}, \quad c = \frac{-3296517}{11260}, \\ d &= \frac{1940803}{10134}, \quad e = \frac{-583529}{20268}, \quad f = \frac{14802}{2815}, \quad g = \frac{-14839}{20268}, \quad h = \frac{2659}{50670}, \end{aligned} \quad (4.46)$$

and the truncation error is again $O(h^8)$.

The second method I used to compute the eighth derivative of the structure function is to proceed analytically: assuming that the structure functions behaves roughly as a power-law, we can fit them point-by-point with a piecewise power-law approximation and take the analytical derivative for each part of said approximate function. It is straightforward to show that, for $n \geq 1$, the n -th Laplacian derivative (i.e., Δ_{\perp}^n) of a power-law function $f(\ell_{\perp}) = \beta \ell_{\perp}^{\alpha}$ (with α and β two arbitrary constants) yields:

$$\Delta_{\perp, \ell_{\perp}}^n f(\ell_{\perp}) = \beta \ell_{\perp}^{(\alpha-2n)} \prod_{p=0}^{n-1} (\alpha - 2p)^2 \quad (4.47)$$

which yields for $n = 4$:

$$\Delta_{\perp, \ell_{\perp}}^4 f(\ell_{\perp}) = \beta [\alpha(\alpha - 2)(\alpha - 4)(\alpha - 6)]^2 \ell_{\perp}^{\alpha-8} \quad (4.48)$$

The dissipation function $\varepsilon_{analytical}^{diss}(\ell_{\perp})$ is ultimately obtained by reconnecting the eighth derivatives of each part of the piecewise power-law approximation.

Results for both methods are displayed in figure 4.19. Despite all my efforts it was not possible to obtain a fully consistent dissipation with any numerical scheme, even with the high-precision compact finite differences schemes derived above. I believe the successive use of a second-order scheme brings a lot more errors in the calculation than what the first theoretical estimations suggested. A way to circumvent this problem would have been to develop the fourth Laplacian in a sum of first to eighth linear derivatives, and develop a numerical scheme directly for each order of derivation; but it would have been far too much work (if it were only possible to obtain) when other possibly more efficient methods had yet to be tested. The analytical derivative however shows both a scaling compatible with the order of derivation and a rough matching with the cascade rate at small scales. Note however that, as a eighth derivative, this calculation remains extremely sensitive to minor fluctuations in the slope of the power-law approximations, and thus the dissipation given by this method has to be taken with caution.

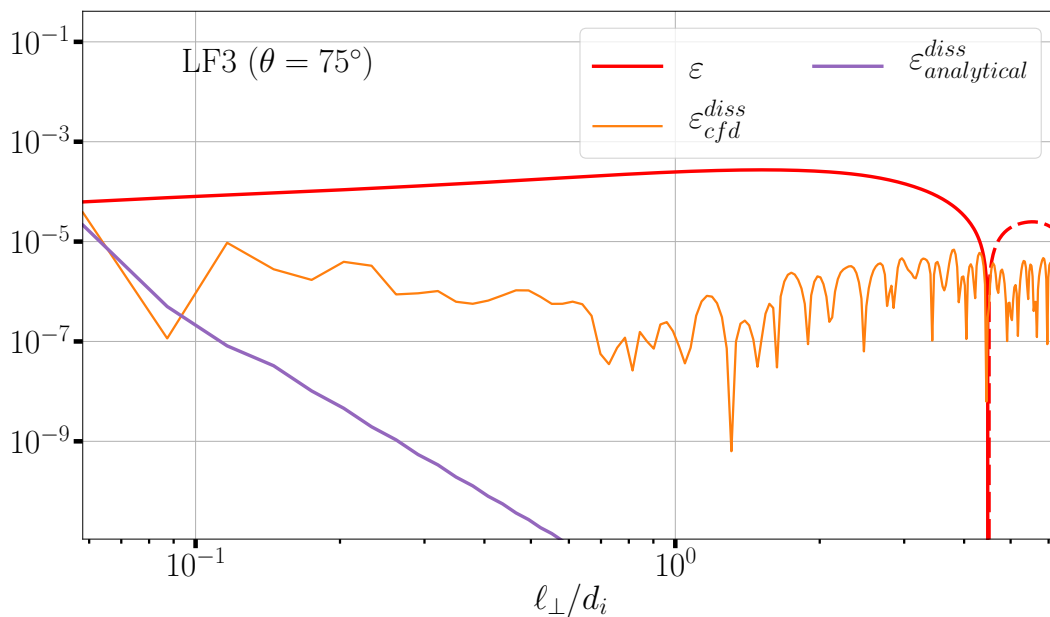


Figure 4.19: Total energy cascade rate and dissipation calculated with either compact finite differences schemes (orange) or a piecewise analytical derivative (purple) for run LF3.

Ultimately, during the review process of the paper summarizing this study, it appeared that calculating the dissipative terms through their expression from the exact law was not the

best way to do given our objective of reconciling kinetic dissipation and fluid energy cascade. Indeed, through this method, we calculate both the cascade rate and the dissipation within the same fluid model. A more robust method to demonstrate the link between kinetic Landau damping and fluid cascade rate is to calculate the hyperdissipation and the Landau damping directly from the simulations, independently of the exact law, and check if all quantities match together. Consequently, transverse hyperdissipation and hyperdiffusivity were computed in Fourier space as

$$\varepsilon^{diss}(\ell_{\perp}) = \int_0^{k_{\perp}} dk'_{\perp} \int k'^8_{\perp} (\eta |\mathbf{b}(\mathbf{k}')|^2 + \nu |\mathbf{v}(\mathbf{k}')|^2) k'_{\perp} d\theta' dk'_z \quad (4.49)$$

where we use $\ell_{\perp} = \pi/k_{\perp}$. This direct inversion from k_{\perp} to ℓ_{\perp} allows one to avoid the saturation due to the steepness of the spectrum. Note that, similarly to the energy cascade rate, the longitudinal contribution of the dissipation is not taken into account but the transverse one is still integrated over parallel wavenumbers. The evaluation of Landau damping being much more complicated, it will be tackled in a subsequent section.

4.4.6 Energy cascade in presence of Landau damping

Using the methods described above, we computed the MHD and Hall components of the incompressible energy cascade rate and the hyperdissipation for all eight simulations. We start with the study of the four simulations forced at intermediate scales: as runs CGL1 / LF1 are forced with a propagation angle $\theta = 83^{\circ}$ and runs CGL2 / LF2 with $\theta = 75^{\circ}$, these runs allow one to qualitatively evaluate the behavior of the turbulence cascade depending on the presence and magnitude of Landau damping. Results are reported in Fig. 4.20.

First and foremost, we point out that the total energy cascade rate ε is almost constant for more than one decade of scales, except for run LF2 that shows a drop in the cascade at small scales, demonstrating the existence of a clear inertial range. This large inertial range contrasts with the energy cascade rates evaluated in section 4.3 that did not show a truly constant ε . This large inertial range, as stated in previous section, is a consequence of hyperdissipation: as most of energy dissipation is pushed to the smallest possible scales, the cascade is allowed to continue at scales where natural, physical dissipation would have damped it already. The constancy of the cascade rate is a consequence of the interplay between the MHD and Hall components, which behave similarly in all four simulations: the MHD part of the law is constant and dominant at most scales (except large scales, affected by the forcing) and starts decreasing towards small scales. The mostly negligible Hall component starts rising up at sub-ion scales, then dominates the MHD part at about the ion inertial length.

The comparison of CGL and LF runs shows that the presence of Landau damping appears to alter the shape of the energy cascade at all scales of the system. Indeed, for run LF1 that only features a weak Landau damping the energy cascade varies less steeply at intermediate to large scales. The effect of Landau damping is much more prominent for LF2, where the damping is more intense, and which shows a stronger decrease in the energy cascade rate around small scales. The overall amplitude of the LF2 cascade also seems to be lower than its CGL2 counterpart, in contrast with runs forced at $\theta = 83^{\circ}$ for which the amplitudes of CGL1 and LF1 cascades are roughly the same.

To emphasize the effect of Landau damping on the cascade rate, we show in Fig. 4.21 a comparison of the cascade rates calculated for the LF simulations with $\theta = 75^{\circ}$ and $\theta = 83^{\circ}$ normalized by the corresponding ones from the CGL simulations. We observe a stronger decrease (by up to a factor 5) in the amplitude of the ratio at small scales for CGL2-LF2 simulations, i.e. for the strongest Landau damping ($\theta = 75^{\circ}$), than for runs with $\theta = 83^{\circ}$ for which the ratio $\varepsilon_{LF1}/\varepsilon_{CGL1}$ remains nearly constant at all scales. This result clearly establishes a correlation between the enhancement of Landau damping at kinetic scales and the decline of the energy cascade rate at the same scales. The fact that the estimated dissipation rate matches the cascade rate at the smallest scale of the simulation box for runs CGL1 and

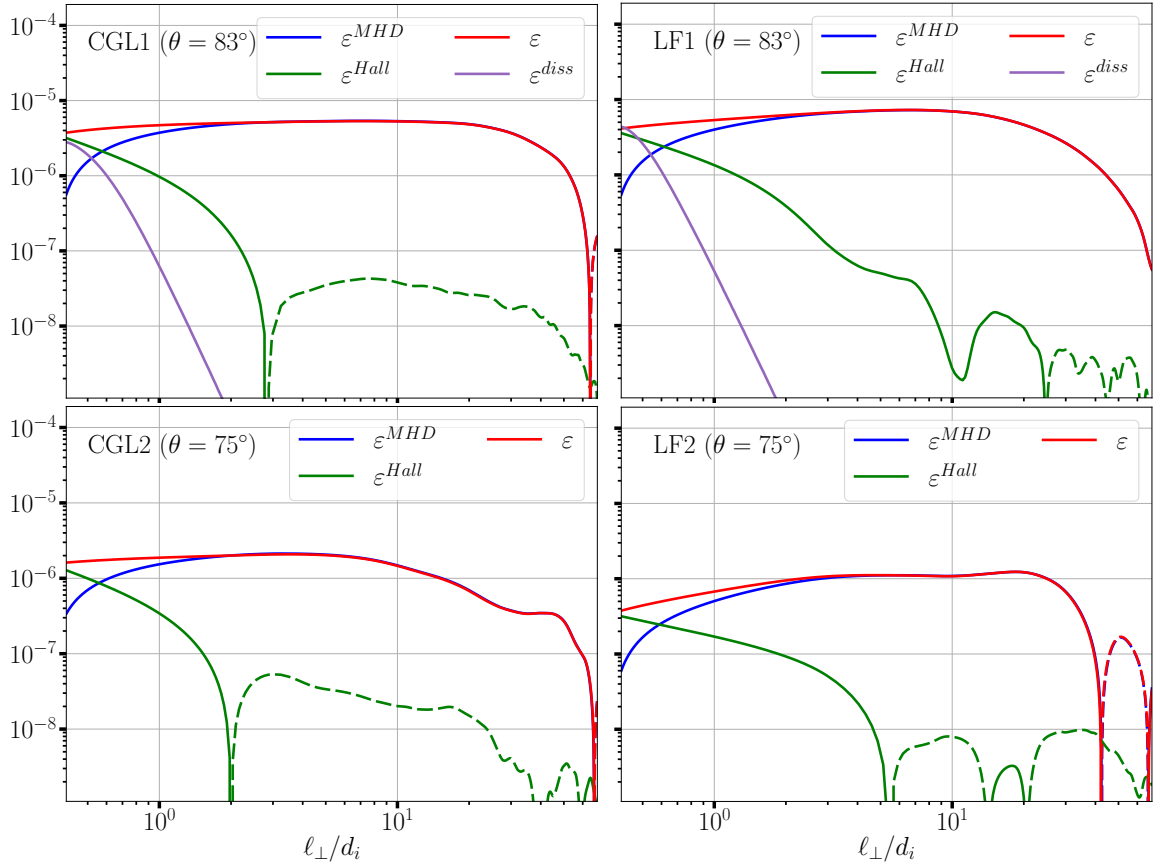


Figure 4.20: Energy cascade rate ε and its **MHD** and Hall components computed for runs CGL1 (top left), LF1 (top right), CGL2 (bottom left) and LF2 (bottom right). For runs CGL1 and LF1 the transverse hyperdissipation is also displayed. Plain lines represent positive values and dashed lines negative values.

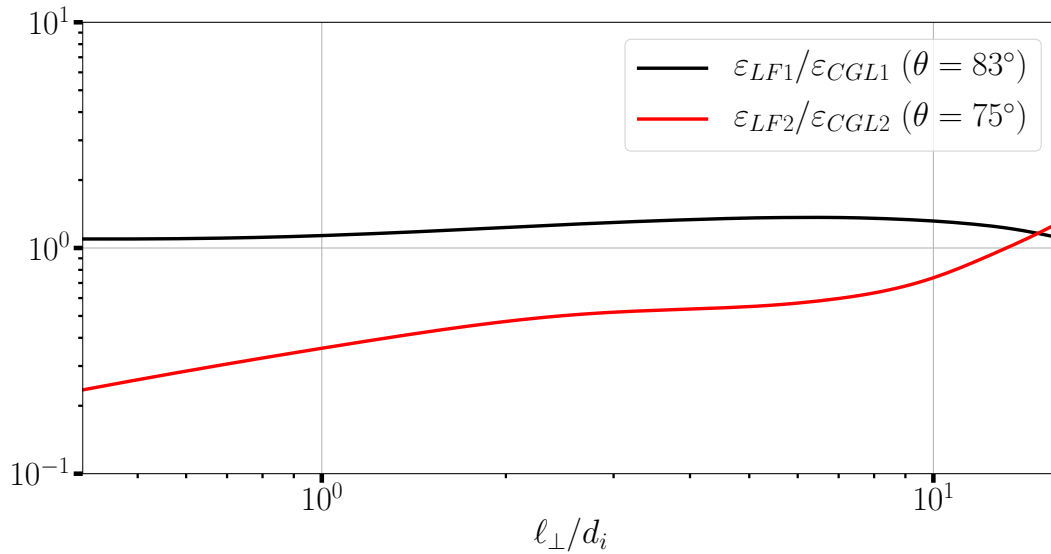


Figure 4.21: Ratios of the energy cascade rate computed for **LF** simulations over the one for **CGL** simulations for a driving wave angle $\theta = 83^\circ$ (black) and $\theta = 75^\circ$ (red).

LF1 (figure 4.20) further indicates that the cascade rate at small scales reflects the actual dissipation in the simulation.

To provide a stronger evidence of the interplay between Landau damping and the energy cascade rate at the sub-ion scales, we complement our study with the cascade rates estimated from simulations forced at even smaller scales (LF3 and CGL3) with $\theta = 75^\circ$ and reported in Fig. 4.22. Note that run LF3 contains Landau damping on both ions and electrons whereas runs LF1 and LF2, forced at a larger scale, only featured ion Landau damping. Unlike the previous runs, run LF3 exhibits a strong decrease in ε^{MHD} partially compensated by a quick rising of the Hall component, giving no clear inertial range. This contrasts with run CGL3 which still behaves similarly to previous simulations forced at intermediate scales. This effect may be attributed to the fact that dissipation via Landau damping reaches high levels at the sub-ion scales of LF3 (scales that are not reached by the previous simulations), whereas CGL3 contains no physical process able to dissipate energy other than the hyperviscosity and hyperdiffusivity, which are bound to act only at the smallest scales of the simulation domain.

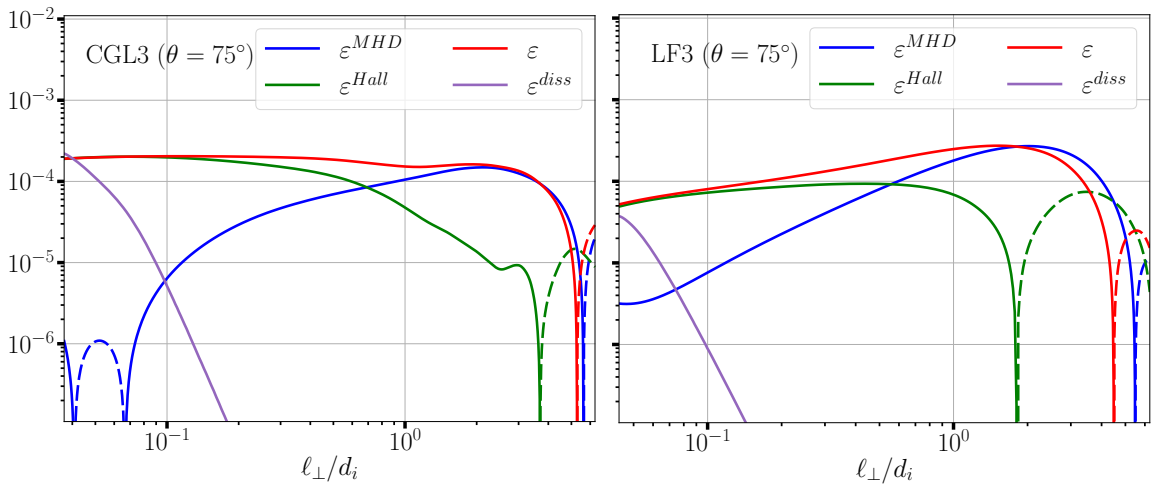


Figure 4.22: Energy cascade rate ε , its MHD and Hall components and transverse hyperdissipation computed for runs CGL3 and LF3.

One can notice sudden changes of sign at large scales in some components of the estimated cascade rates in Figs. 4.20 and 4.22: these are likely due to the proximity of the forcing. As the form of the exact law used here is valid only in the inertial range, far enough from the forcing, observing unphysical behavior at large scales is not unexpected. Other changes of sign are observed at small scales for the MHD component of run CGL3, and can be attributed to numerical errors in the calculation of ε^{MHD} given its very small magnitude at those scales. In any case, ε^{MHD} is negligible at these scales so the overall cascade rate and the conclusions drawn from it are not affected by this oddity.

To obtain a full picture as to how Landau damping affects the energy cascade rate, we also performed simulations forced at large scales and for $\theta = 75^\circ$, namely LF4 and CGL4, whose cascade rates are displayed in figure 4.23. These runs allow for extending the study towards large scales and see how the cascade rate behaves in comparison to runs forced at smaller scales. To this purpose, we combine all the runs CGL2-3-4 and LF2-3-4 to reconstruct a multi-scale energy cascade rate over nearly three decades of scale. As the simulations were run at different scales, the amplitude of the forcing had to be changed to ensure that each simulation reaches a fully turbulent state. Therefore, we renormalized the cascade rate ε obtained from the different simulations to match the one of intermediate runs CGL2 and LF2 (which were left unchanged), while taking care to discard the smallest scales of intermediate and large scale forcing cascade rates to ensure that hyperviscosity would not be present at intermediate scales of the reconstructed energy cascade. This simple renormalization provides a visual overview of how Landau damping affects the cascade at different scales. Figure 4.24

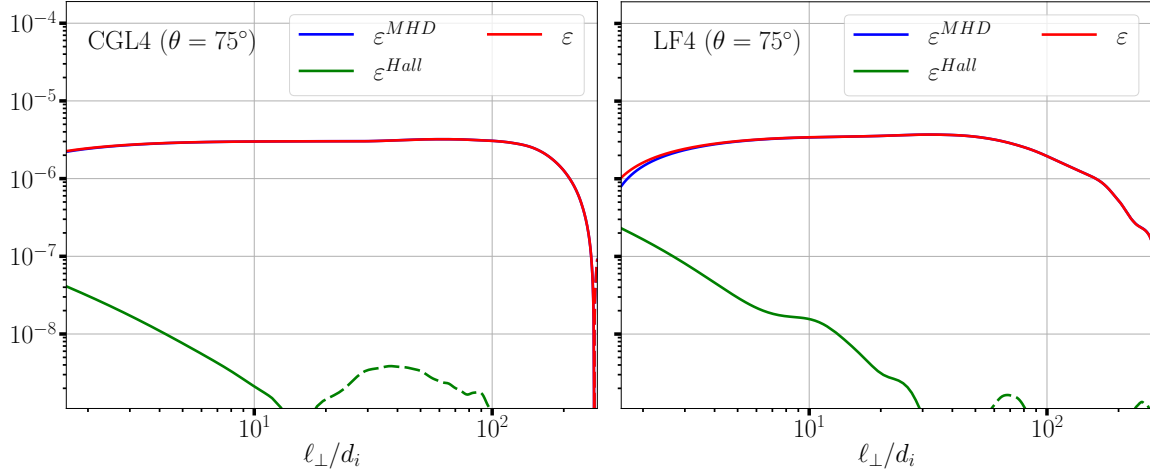


Figure 4.23: Energy cascade rate ε and its **MHD** and Hall components computed for runs CGL4 and LF4.

shows the full energy cascade rate for **CGL** and **LF** runs for the driving wave angle $\theta = 75^\circ$ (the slight irregularity observed for the **CGL** cascade rate around the transition between CGL2 and CGL3 is the result of an insufficient overlap of the scales spanned by the two simulations, which complicated the renormalization procedure). The **CGL** runs exhibit an almost constant energy cascade rate over two and a half decades, whereas ε_{LF} decreases steadily over scales and reaches its minimum value at the smallest ones. This confirms that the behavior already observed in figure 4.21 remains valid over a broader range of scales: Landau damping seems to drain energy from the turbulent cascade as we reach to the sub-ion scales of the system. An important point is now to verify if the amount of energy handed to internal energy through Landau damping matches the decrease of the cascade rate, which requires additional theoretical work.

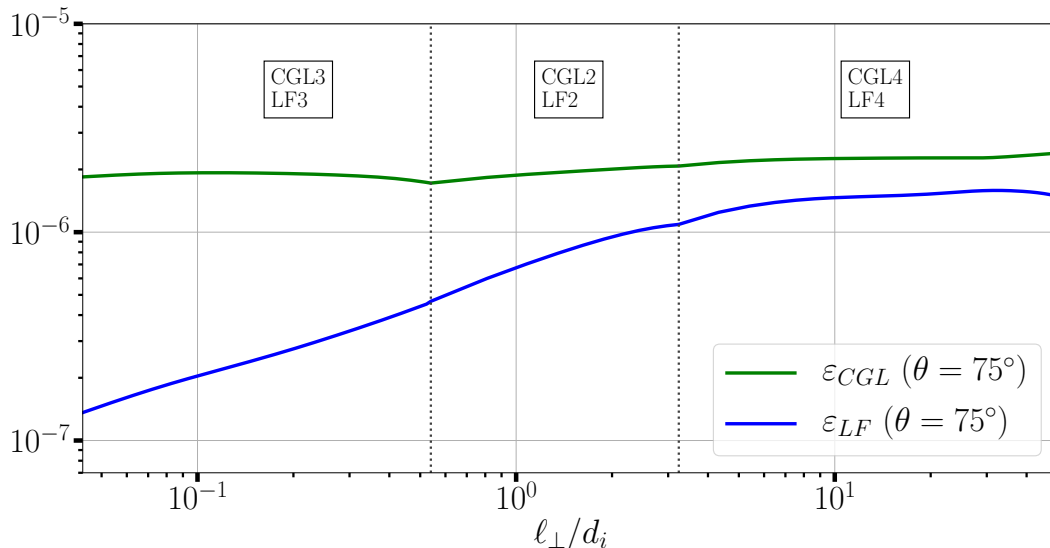


Figure 4.24: Energy cascade rates reconstructed with CGL2-3-4 runs and LF2-3-4 runs. The ranges spanned by each simulation are delimited by the black dotted lines.

4.4.7 Calculation of the heating due to Landau damping

From equations (4.28) and (4.29) describing the **LF** model, one can derive an expression for the heating rate induced by Landau damping. To this end we define the parallel, perpendicular

and total entropies per unit mass

$$s_{\parallel} = \frac{c_V}{3} \ln\left(\frac{p_{\parallel}|B|^2}{\rho^3}\right), \quad s_{\perp} = \frac{2c_V}{3} \ln\left(\frac{p_{\perp}}{\rho|B|}\right), \quad s = s_{\parallel} + s_{\perp} = \frac{c_V}{3} \ln\left(\frac{p_{\parallel}p_{\perp}^2}{\rho^5}\right), \quad (4.50)$$

where c_V is the specific heat at constant volume. Denoting by e the internal energy per unit mass, the internal energy per unit volume reads $E \equiv \rho e = p_{\perp} + \frac{1}{2}p_{\parallel} = \frac{3}{2}nT$ where $T = \frac{1}{3}(2T_{\perp} + T_{\parallel})$. From $e = c_V T$, one gets $c_V = \frac{3}{2m}$ (note that the Boltzmann constant is already included in the definition of temperature). From equations (4.28) and (4.29), we can conclude that the rates of change of the parallel and perpendicular entropies per unit mass (s_{\parallel}^p and s_{\perp}^p respectively) associated with a production (or destruction) and excluding transport or exchanges between the parallel and perpendicular directions (see e.g. Hazeltine et al. (2013)), are given by

$$\frac{d}{dt}s_{\parallel}^p = \frac{1}{\rho T_{\parallel}} q_{\perp} \nabla \cdot \hat{\mathbf{b}} - \frac{q_{\parallel}}{2\rho T_{\parallel}} (\hat{\mathbf{b}} \cdot \nabla) \ln T_{\parallel} \quad (4.51)$$

$$\frac{d}{dt}s_{\perp}^p = -\frac{1}{\rho T_{\perp}} q_{\perp} \nabla \cdot \hat{\mathbf{b}} - \frac{q_{\perp}}{\rho T_{\perp}} (\hat{\mathbf{b}} \cdot \nabla) \ln T_{\perp}. \quad (4.52)$$

The associated rates of heat production per unit mass are related by $dQ_{\parallel}/dt = T_{\parallel} ds_{\parallel}^p/dt$ and $dQ_{\perp}/dt = T_{\perp} ds_{\perp}^p/dt$. We thus get, for the total heat production $Q = Q_{\parallel} + Q_{\perp}$

$$\partial_t(\rho Q) + \nabla \cdot (\rho Q \mathbf{u}) = -\frac{q_{\parallel}}{2} (\hat{\mathbf{b}} \cdot \nabla) \ln T_{\parallel} - q_{\perp} (\hat{\mathbf{b}} \cdot \nabla) \ln T_{\perp}, \quad (4.53)$$

and the global heating is therefore given by

$$H = - \int \left(\frac{q_{\parallel}}{2} (\hat{\mathbf{b}} \cdot \nabla) \ln T_{\parallel} + q_{\perp} (\hat{\mathbf{b}} \cdot \nabla) \ln T_{\perp} \right) d^3x. \quad (4.54)$$

Finally, we can define a spectral density for the heating rate H in the form

$$H(\mathbf{k}) = -\frac{1}{2} \left(\frac{1}{2} \mathcal{F}\{q_{\parallel}\}(-\mathbf{k}) \mathcal{F}\left\{(\hat{\mathbf{b}} \cdot \nabla) \ln T_{\parallel}\right\}(\mathbf{k}) + \mathcal{F}\{q_{\perp}\}(-\mathbf{k}) \mathcal{F}\left\{(\hat{\mathbf{b}} \cdot \nabla) \ln T_{\perp}\right\}(\mathbf{k}) + c.c. \right) \quad (4.55)$$

where \mathcal{F} denotes the Fourier transform and *c.c.* the complex conjugate of the expression in the right-hand side.

An important remark can be made here: this heating rate takes into account the Landau damping on all the waves present in the simulations, including the magnetosonic waves. At this level, it appears difficult to separate the contributions of the KAWs, which are the only cascading modes described by the exact law, and to evaluate their dissipation by Landau damping. Nevertheless these magnetosonic waves get dissipated at large scales, thus at small enough scales the estimated heating rate mostly results from Landau damping of KAWs and it becomes possible to compare it to the cascading energy. This particularity is also the reason why Landau damping appears to be acting at all scales in all the results presented above, even in simulations forced at large scales.

The fact that Landau damping is present at all scales in the simulation can be seen by estimating the spectral density of total heating rate at a given wavenumber k_{\perp} , $D_L(k_{\perp}) = \int k_{\perp} H(\mathbf{k}) dk_z d\theta$, where $H(\mathbf{k})$ is the sum of the spectral densities given by equation (4.55) for both the ions and the electrons. This spectral density is represented in figure 4.25 along with the densities of hyperdissipation and hyperdiffusivity. One clearly sees that the heating rate due to the presence of heat fluxes dominates hyper-dissipation over a broad range of scales due to the dissipation of KAWs and magnetosonic modes, the two becoming comparable only at the smallest scales (note that the magnetic hyper-dissipation dominates at small scales over the kinetic one).

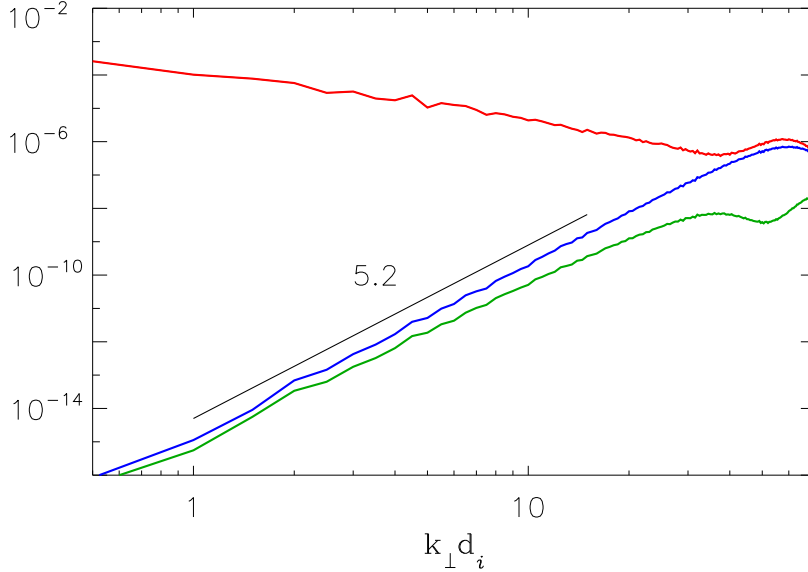


Figure 4.25: Spectral densities of the heating rate $D_L(k_\perp)$ (red) and of the magnetic (blue) and kinetic (green) hyper-dissipation as functions of the transverse wavenumber k_\perp for run LF3. Note that the 5.2 exponent is consistent with a -2.8 exponent for the magnetic energy spectrum (see figure 4.18a), considering the k_\perp^8 factor on hyperdissipation.

In order to derive a relation connecting the energy cascade to Landau dissipation, we write the equation of conservation of the energy $\mathcal{E}_\perp(t)$ of the (quasi-incompressible) **KAWs**:

$$\frac{d}{dt}\mathcal{E}_\perp(t) = \mathcal{I}^C(t) - \mathcal{D}_L^C(t) - \mathcal{D}_h^C(t), \quad (4.56)$$

where \mathcal{I}^C is the part of the injection rate that contributes to the **KAWs** cascade (the other part being transferred to the magnetosonic modes which are dominantly dissipated at large scales), while \mathcal{D}_L^C and \mathcal{D}_h^C are the parts of the Landau and hyperviscous (and hyperdiffusive) dissipations that affect the cascading modes. Using cylindrical coordinates and assuming time stationarity, one can write the integrated energy balance at each Fourier mode as (adopting roman scripts for spectral densities):

$$\epsilon(k_\perp) = \int_0^{k_\perp} \{I^C(k'_\perp) - D_L^C(k'_\perp) - D_h^C(k'_\perp)\} dk'_\perp. \quad (4.57)$$

Considering two wavenumbers $k_{\perp 1}$ and $k_{\perp 2}$ large enough so that the forcing (which is concentrated at large scales) leads to $\int_0^{k_{\perp 1,2}} I^C(k'_\perp) dk'_\perp = \mathcal{I}^C$, yet small enough for hyperviscous dissipation to be negligible, one obtains:

$$\epsilon(k_{\perp 1}) - \epsilon(k_{\perp 2}) = \int_{k_{\perp 1}}^{k_{\perp 2}} D_L^C(k'_\perp) dk'_\perp \lesssim \int_{k_{\perp 1}}^{k_{\perp 2}} D_L(k'_\perp) dk'_\perp. \quad (4.58)$$

The inequality draws closer to an equality for values of k_\perp large enough so that all magnetosonic modes have been dissipated.

Equation (4.58) can be used to estimate a correction to the energy cascade rate which would take into account the energy lost due to Landau damping. We do so for run LF3: using this equation we add to the transfer rate the cumulative Landau dissipation between an arbitrarily chosen scale (chosen however to be not too large nor too small) and the running (smaller) scale l_\perp . Two of these resulting corrected rates ϵ^{corr} are shown in Fig. 4.26. They appear to be almost constant, and as such they behave very similarly to the transfer rate of run CGL3 (Fig. 4.22). The slight increase of ϵ^{corr} towards small scales probably reflects the (weak) contribution of some remaining magnetosonic waves to the calculated Landau

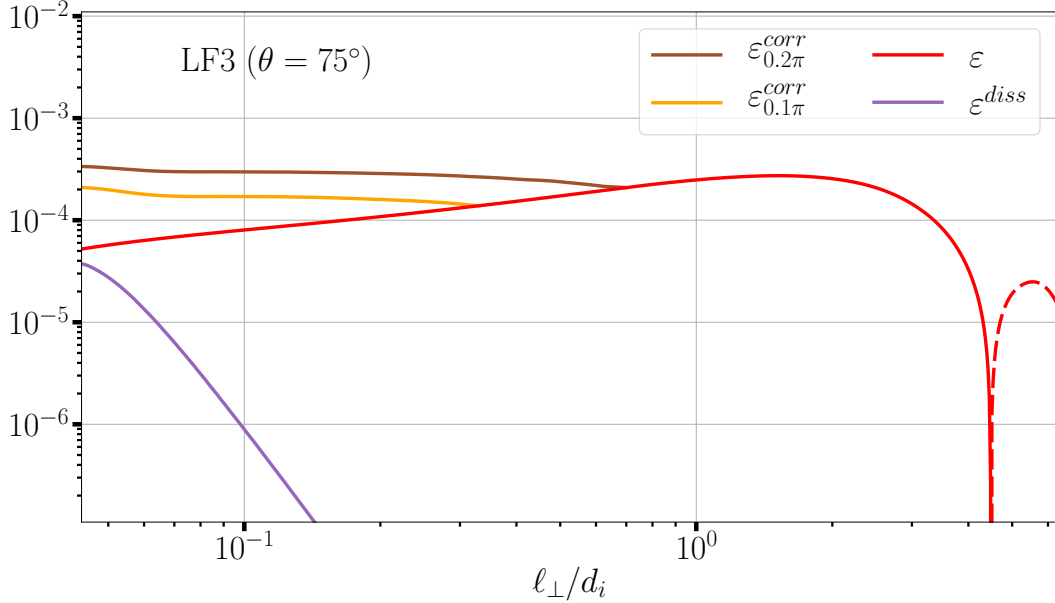


Figure 4.26: Energy cascade rate ε (red) and transverse hyperdissipation (violet) for run LF3. The orange and brown curves show the same ε corrected by Landau damping integrated between ℓ_{\perp} and a reference scale $\ell_{\perp} = 0.1\pi d_i$ and $\ell_{\perp} = 0.2\pi d_i$ respectively, following equation (4.58).

damping. This clearly demonstrates that the energy lost along the cascade due to Landau damping is well captured by the decline of the (fluid) cascade rate at the corresponding scales.

A complementary estimate of energy dissipation can be done in Fourier space by also taking into account hyperdissipation. Indeed, assuming stationarity, one can also derive that

$$\epsilon(k_{\perp}) = \mathcal{I}^C - \mathcal{D}_L^C + \int_{k_{\perp}}^{\infty} D_L^C(k'_{\perp}) dk'_{\perp} - \int_0^{k_{\perp}} D_h^C(k'_{\perp}) dk'_{\perp} = \int_{k_{\perp}}^{\infty} \{D_h^C(k'_{\perp}) + D_L^C(k'_{\perp})\} dk'_{\perp}. \quad (4.59)$$

Equation (4.59) indicates that, as expected, the rate of energy transfer at the wavenumber k_{\perp} identifies with the sum of the rates of Landau and hyperdissipation beyond this wavenumber. One can compare the second right-hand-side term of this equation to the energy cascade rate $\epsilon(k_{\perp})$ obtained from the IHMHD exact law, as displayed in figure 4.27. The difference between the two curves, which is especially significant at large scales, is due to the fact that the estimation of the dissipation includes the Landau damping of magnetosonic modes, whereas the cascade rate considers only incompressible modes. At smaller scales however, where magnetosonic modes have already been dissipated, the dissipation and cascade rates decreases parallel to each other: this indicates that, at scales not yet affected by hyperdissipation, the decay of $\epsilon(k_{\perp})$ in a spectral interval identifies with Landau dissipation within this interval.

4.4.8 Summary: relations between fluid and kinetic models

This study tackles a fundamental question about the ability of fluid exact laws to reflect the presence of kinetic (Landau) damping. By constructing multi-scale energy cascade and dissipation rates using the HMHD model on a variety of turbulence simulations bearing different intensities of Landau damping, we showed that the presence of Landau damping at small (kinetic) scales is reflected by the steady decline of the energy cascade rate at the same scales. This decay of the cascade rate at the sub-ion scales is consistent with 2D hybrid PIC simulations and observational data in the magnetosheath and solar wind measured by the Magnetospheric Multiscale (MMS) mission (Hellinger et al., 2018; Bandyopadhyay et al., 2020).

We detail the methods of calculation for both the hyperdissipation and Landau dissipation along with the underlying theory, while shedding light on possible problems and limitations

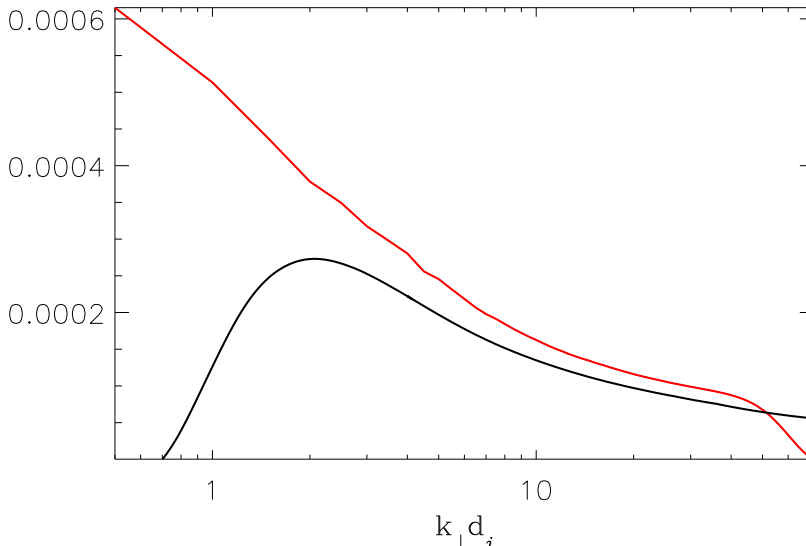


Figure 4.27: Energy cascade rate $\epsilon(k_{\perp})$ (black line) together with Landau and hyper-dissipation (red line) computed with equation (4.59) for run LF3.

of broader interest that can arise when studying spectra or structure functions, such as the problem of structure function saturation. By calculating individually the energy cascade rate, the hyperdissipation and the heat fluxes induced by Landau damping, we showed that the loss of energy along the cascade towards sub-ion scales corresponds to the amount of energy dissipated by Landau damping. The remaining energy of the cascading KAWs is correctly caught by hyperdissipation around the smallest scale of the simulation, ensuring the stationarity on transverse energy.

By demonstrating the ability of a fluid exact law to provide a correct estimate of kinetic dissipation in the sub-ion range of numerical simulations, this work provides a means to evaluate the amount of energy that is dissipated into particle heating: the decline of the cascade rate allows one to evaluate the kinetic dissipation as a function of scale. Although the DNSs studied here are quite specific (the runs are forced with KAWs and Landau damping is obtained with a linear model) the cascade rate and Landau damping are undoubtedly correlated in the study presented here. These results should help solving (at least partially) a long-standing problem in astrophysical plasmas about energy partition between ions and electrons (Kawazura et al., 2019), which are generally heated at different scales. It is however important to stress that, even if the oversimplified (yet fully nonlinear) fluid models of turbulence can provide good estimates of the amount of energy that is dissipated into particle heating, they do not specify how this dissipation occurs. Additional analyses led on DNS data featuring different kinds of dissipative effects may bring some answers to this problem. The analysis of *in situ* data could also shed some light on this question, which is one of the objectives of chapter 5.

4.5 Supersonic CHD turbulence

4.5.1 Context of the study

The last study presented in this chapter is an extension to highly supersonic turbulence of the work presented in this thesis. Highly supersonic CHD turbulence only applies to a handful of physical systems, yet understanding the physics governing them is essential to understand large scale astrophysical processes such as star formation, in which turbulence is known to play a key role (Heyer and Brunt, 2004; McKee and Ostriker, 2007; Federrath and Klessen, 2012; Hennebelle and Falgarone, 2012; Padoan et al., 2014; Orkisz et al., 2017). Notably, past

numerical simulations of the ISM performed in the framework of compressible (isothermal) HD (Vazquez-Semadeni, 1994; Passot and Vázquez-Semadeni, 1998; Kritsuk et al., 2007; Federrath et al., 2010; Federrath, 2013) have shown the presence of filaments that resemble the structures observed in the ISM (Arzoumanian et al., 2011; Federrath, 2016) and in which most pre-stellar cores appear to form.

The new CHD exact law derived from F21 allows us to clearly identify the different contributions to the turbulent cascade and to better understand how it reacts to the compression of the medium. It will be complemented by an in-depth analysis of the shapes formed by the interplay between compression and classical turbulence and a spectral study. The main goal is to understand where and how the turbulence mainly acts in a highly compressible medium, and why its presence is able to give form to filamentary structures that may, ultimately, be fit for star formation.

4.5.2 Framework and presentation of the data

In this section we study an ensemble of CHD datasets for supersonic turbulence computed with the objective of simulating ISM turbulence. While some simulations for molecular clouds and star forming regions include a magnetic field in order to study MHD turbulence (Nakamura and Li, 2008; Federrath, 2016), the choice was made here to consider only an HD model and push the resolution and compression to very high values. This simulation was run with a grid resolution of $10,048^3$ points and an integral Mach number of 4, the Mach number being defined as $M_S = \sigma_v/c_s$ where σ_v is the velocity dispersion at the main forcing scale $L/2$ and L is the simulation side length.

The simulation was performed using a modified version of the FLASH code (Fryxell et al., 2000; Dubey et al., 2008; Federrath et al., 2020), which solves the isothermal CHD equations in a triply periodic box. Following the methods described in Federrath et al. (2010) the simulation uses a naturally mixed driving ($\zeta = 0.5$) with an Ornstein-Uhlenbeck process acting on large scales. The forcing amplitude is a paraboloid spanning $k = 1..3$, peaking at $k = 2$ and reaching zero at both $k = 1$ and $k = 3$, where the wavenumber k is in units of $2\pi/L$. Thus, the forcing only acts directly on scales larger than $L/3$ which are well above the ones we consider in this study. The data used consists of 7 snapshots of the $10,048^3$ simulation down-sampled at a resolution of $2,512^3$ of the density and the three components of the velocity field, taken at 2, 3, 4, 5, 6, 7 and 8 turbulence turnover times T . The down-sampling was necessary due to limitations on the download time, storage space, memory usage and computation times that quickly appeared to be prohibitively large. Nevertheless it was shown by Federrath et al. (2021) that such a down-sampling did not harm the precision of the results nor the conclusions in the case of the calculation of the scale-dependent Mach number, whose calculation method is close to the one of an exact law as both take the form of mean second or third order moments. The key factor is that the simulations were run at very high resolution in the first place, which allows for some effects unseen at lower resolutions to develop. Fig. 4.28 shows through the root mean square (rms) Mach number and minimum and maximum densities that statistics for both velocity and density have converged after 2 turnover times, indicating that the simulation has reached a state of fully developed turbulence (Federrath et al., 2009), hence the use in this study of snapshots for times $t \geq 2T$.

I analyzed those datasets with the CHD exact law (2.109) derived in chapter 2. Due to their size I faced important limitations in terms of computation time and especially memory. To circumvent these limitations I only made the computation along the three directions x, y and z, generated by base vectors (1,0,0), (0,1,0) and (0,0,1) respectively, instead of using one of the base vectors set described in chapter 3. This allowed to retain an isotropic computation while drastically reducing the total number of operations. The loss of the statistics usually brought by the multiple directions used to analyze 512^3 datasets is compensated by the much larger sample of spatial points included in the average (2512^3). Moreover, computing the exact laws only along the three axes of the simulation domain allows for saving memory through

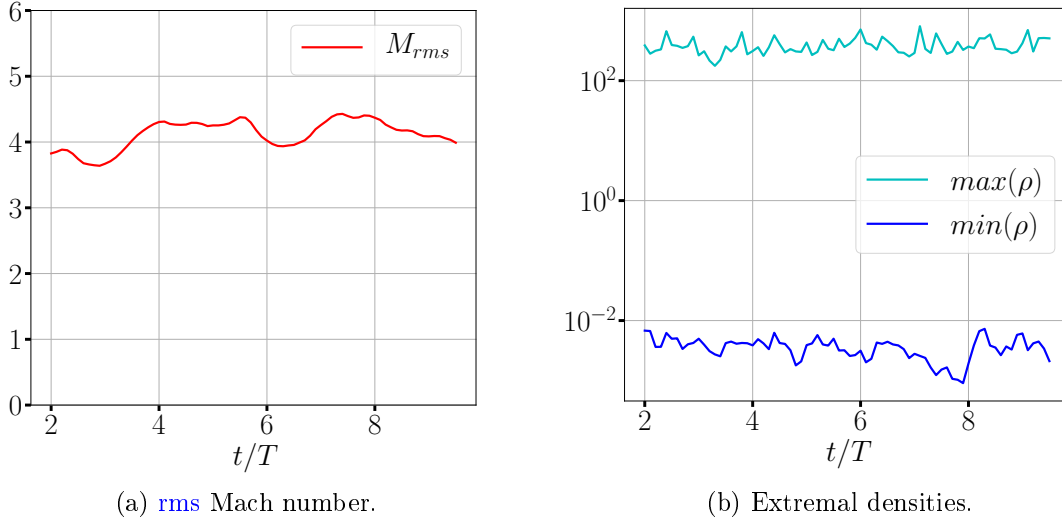


Figure 4.28: rms Mach number M_{rms} and maximum and minimum density as functions of time (normalized to the turnover time T).

the method described in chapter 3, by partitioning the data along the z -axis (to compute the law in directions x and y) and then along the y -axis (to compute the law in direction z)

4.5.3 Calculation of the energy cascade rate

The exact law $-4\varepsilon = \nabla_{\ell} \cdot \mathbf{F} + S$, where $\nabla_{\ell} \cdot \mathbf{F} = \nabla_{\ell} \cdot \langle \bar{\delta\rho} |\delta\mathbf{u}|^2 \delta\mathbf{u} \rangle$ and $S = -\frac{1}{2} \langle (\rho\theta' + \rho'\theta) |\delta\mathbf{u}|^2 \rangle$, can be interpreted as if we had an effective cascade driven only by the flux term $-4\varepsilon_{\text{eff}} \equiv \nabla_{\ell} \cdot \mathbf{F}$ (such that $\varepsilon_{\text{eff}} = \varepsilon + S/4$), which is the term that represents energy exchanges between turbulent structures of different sizes. It involves the usual energy cascade rate (ε) known in incompressible theory and a new purely compressible component (the source S) that reflects the contraction and dilatation of the turbulent structures. The sign of S is directly given by the sign of the dilatation: when the flow is mainly in a phase of dilatation ($\theta > 0$) the source is negative, whereas in a phase of compression ($\theta < 0$) the source is positive. Thus, if we assume that the effective cascade driven by the flux term is direct (i.e., $\varepsilon_{\text{eff}} > 0$) then a dilatation (compression) will tend to oppose (sustain) the effective energy cascade, preventing (enforcing) the formation of smaller structures. Furthermore, the dilatation of the structures ($S < 0$) can annihilate the cascade to small scales (if $\varepsilon = -S/4$) or even reverse it (if $\varepsilon + S/4 < 0$) in extreme cases, leading to the formation of large-scale structures via an inverse cascade, as we will see throughout this study.

For each snapshot I computed the two terms $\nabla_{\ell} \cdot \mathbf{F}$ and S of the exact law as functions of ℓ , and the signals obtained for all 7 different turnover times are eventually averaged to obtain the result displayed in Fig. 4.29. A first and immediate observation is that the energy cascade rate ε is approximately constant over more than a decade, which shows the existence of an inertial range. This observation indicates that the assumptions made to derive the law are well satisfied on these scales of the simulation. Note that this large inertial range, similarly to the results obtained in section 4.4, contrasts with the results obtained in section 4.3 on **GHOST** datasets. A large inertial range was allowed to develop in this case because the code does not feature any *physical* dissipation (i.e. dissipation through viscous terms such as \mathbf{d}_{ν} , as presented in chapter 2), but instead makes use of numerical dissipation that discards the energy around the smallest scales of the simulation domain only. This allows the energy to cascade to the very smallest scales, thus extending the scales spanned by the inertial range, similarly to the use of hyperviscosity and hyperdiffusivity in previous section.

Second, we see that the contribution of the flux term is significantly higher than ε which

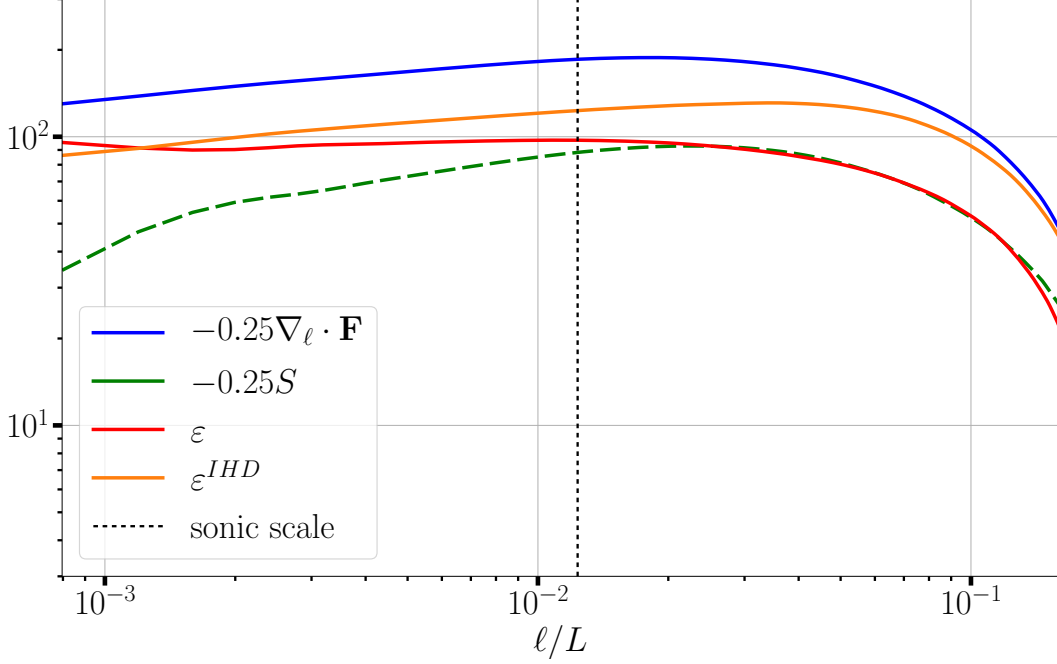


Figure 4.29: Normalized flux term $-\nabla_\ell \cdot \mathbf{F}/4$ (blue) and normalized source $-S/4$ (green). The total energy cascade rate ε (red), which corresponds to the mean rate of energy injection/dissipation, is then deduced from the exact law (2.109). For comparison, we show the same quantity ε^{IHD} (orange) computed from the exact four-third incompressible law F19 (2.39). Solid lines represent positive values and dashed lines negative values. The vertical dotted line corresponds to the sonic scale $\ell_s \simeq 0.01235L$ (i.e. the scale where the scale-dependent Mach number is $M_S(\ell_s/L) = 1$) measured in Federrath et al. (2021). Increments are normalized to the side length L of the simulation domain.

means that the source brings a correction with an opposite sign, which is confirmed by the green dashed curve. Considering the distinction between ε and ε_{eff} introduced above, one can see that $\varepsilon < \varepsilon_{\text{eff}}$ with a non-negligible contribution from the source: in this case the source appears to strengthen the effective cascade, so the supersonic nature of the medium acts "in favor of" the turbulence. This behavior contrasts with the one reported from DNSs of subsonic (compressible) MHD turbulence, where the overall contribution of the non-flux terms was found to be negligible with respect to the flux term (see section 4.3 and Andrés et al. (2018)), and which would yield $\varepsilon \sim \varepsilon_{\text{eff}}$.

Note that the incompressible cascade rate ε^{IHD} , computed with law F19, lies between ε and ε_{eff} : it does not contain the compressible flux modifications that ε_{eff} has, and does not benefit from the compressible correction brought by the source. More importantly, it does not behave like the characteristic constant energy flux usually seen in less compressible (*a fortiori* incompressible) flows (Kadomtsev and Petviashvili, 1973; Passot et al., 1988). Thus, we argue that variations of ε^{IHD} in the inertial range, as observed in this situation, may point towards the presence of non-negligible compressible effects. In space plasma data, where it is not always possible to measure precisely the source terms (Hadid et al., 2017; Andrés et al., 2019), variations of ε^{IMHD} at MHD scales could prove to be a simple diagnostic to detect strong compressible effects in the turbulence. At smaller scales, this diagnostic requires one to be more cautious as we showed in section 4.4 that variations of ε^{IMHD} can also be the result of energy dissipation.

Another remark can be made about the exact law: given the high resolution of the simulation one would expect the energy cascade rate to form a steady plateau over more than one decade. This small inertial range may be attributed to two possible effects not included in our exact law: i) non-local effects due to the large-scale forcing; ii) additional local dissipation (in the supersonic range) through shocks/discontinuities (Duchon and Robert, 2000; Saw et al., 2016; Galtier, 2018), since our exact law assumes smoothness of the turbulent fields. This

shortcoming calls for a new theory of compressible HD turbulence where such singular fields and non local effects due to large scale forcing can be accounted for, and which would be very relevant to supersonic turbulence, yet such a theory is not considered in this thesis and left to future studies.

4.5.4 Filamentary structures and locality of turbulence

I further investigated the properties of this supersonic simulation in order to understand the origin of the source contribution and its influence on turbulence. As we have seen above, the source term is globally positive (thus inducing a negative contribution to ε), which reflects the dominance of compression in the medium. Therefore, we can look directly to the data to try to identify how coherent structures form and which ones may have an important influence on the source term. To this end I searched in a given snapshot for the grid point of minimal dilatation θ (so of maximum contraction of the fluid) and selected the three slices of data (cut along planes (xy), (yz) and (xz)) intersecting at this point. I then computed both the density-dilatation $\rho\theta$ and the modulus of the vorticity $|\omega|$ in each of these slices, normalized to their mean value averaged on the whole slice. It is thought that the density-dilatation and the vorticity highlight the turbulence structures better than the previously used quantities θ and ρ (Kritsuk et al., 2007; Federrath et al., 2010), which are less relevant to investigate the physics involved in the generalized Kolmogorov law.

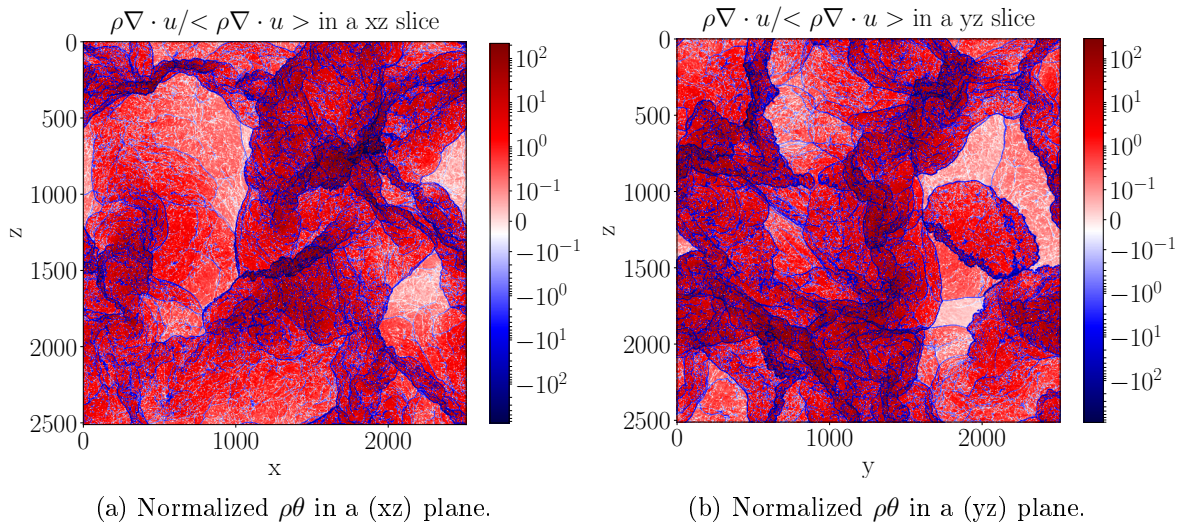


Figure 4.30: Normalized density-dilatation $\rho\theta$ in (xz) and (yz) planes at 6 turnover times. The amplitude and sign of the fields are given by the color bars.

Figures 4.30 to 4.33 show the (xy) slices obtained for $\rho\theta$ and $|\omega|$, along with a zoom on a specific turbulent structure. These cuts reveal the existence of various regions exhibiting different behaviors. Some extended *blank* regions show almost no density-dilatation (bright regions of figures 4.30 and 4.32) nor vorticity (black regions of figures 4.31 and 4.33). Those regions seem almost void of structures and thus are expected not to bring any significant contribution to the energy cascade rate. We also see turbulent filamentary structures (elongated dark red structures for $\rho\theta$) in which both $|\theta|$ and $|\omega|$ are up to several orders of magnitude higher than in the rest of the plane. A zoom on one of these structures is shown in figures 4.32 and 4.33. These structures are typically delimited by very thin boundaries of strong contraction (dark blue lines for $\rho\theta$) in which a high turbulent activity with many vorticity tubes is observed. The regions featuring high density-dilatation are expected to drive most of the (average) source term.

To test these assumptions, I selected a turbulent structure and a blank region in which I computed both terms of the exact law, represented in figure 4.34. To do so, I cut a trapezoid

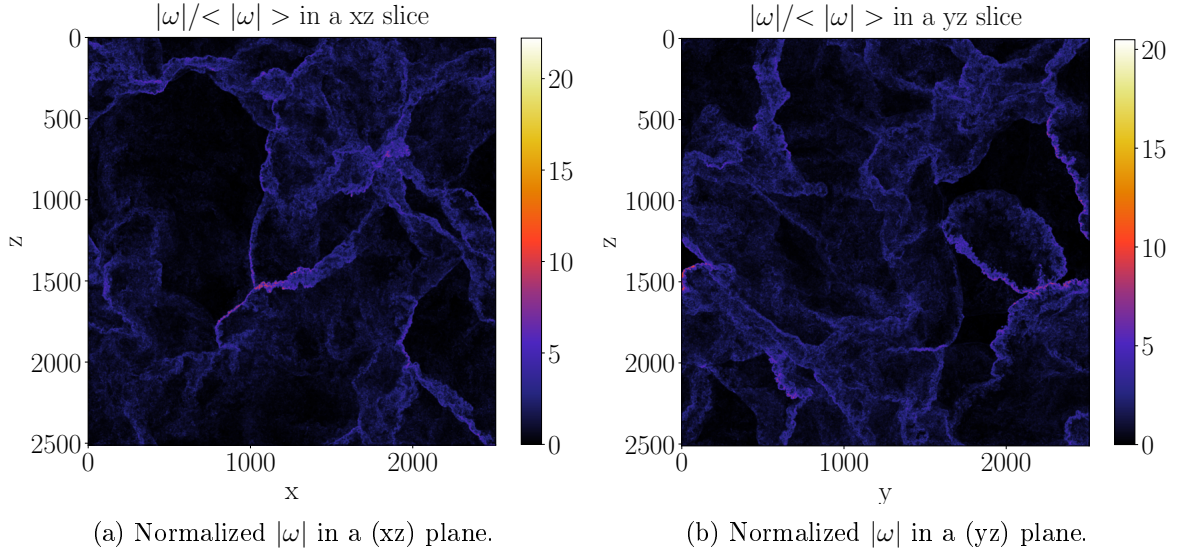


Figure 4.31: Normalized modulus of the vorticity $|\omega|$ in (xz) and (yz) planes at 6 turnover times. The amplitude of the fields is given by the color bars.

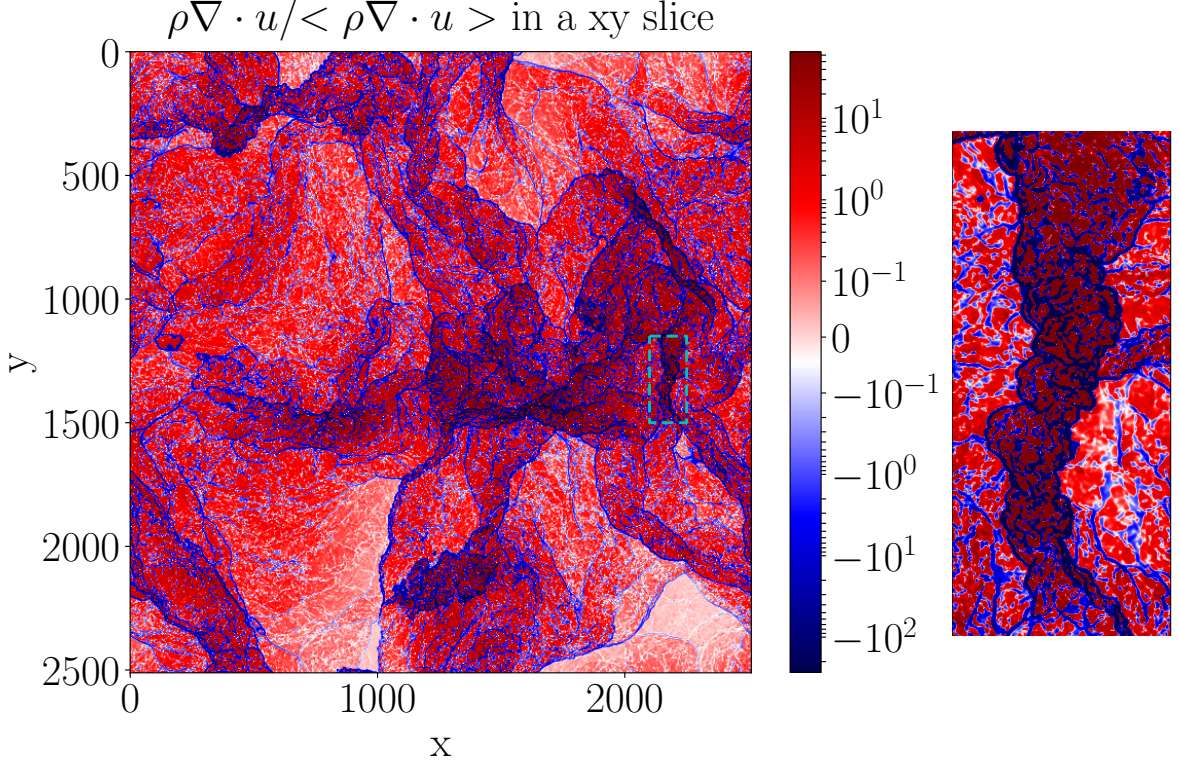


Figure 4.32: Normalized density-dilatation $\rho \nabla \cdot u$ in a (xy) plane at 6 turnover times. The amplitude and sign of the fields are given by the color bars. The region enclosed in the dashed cyan box is zoomed in and shown on the right.

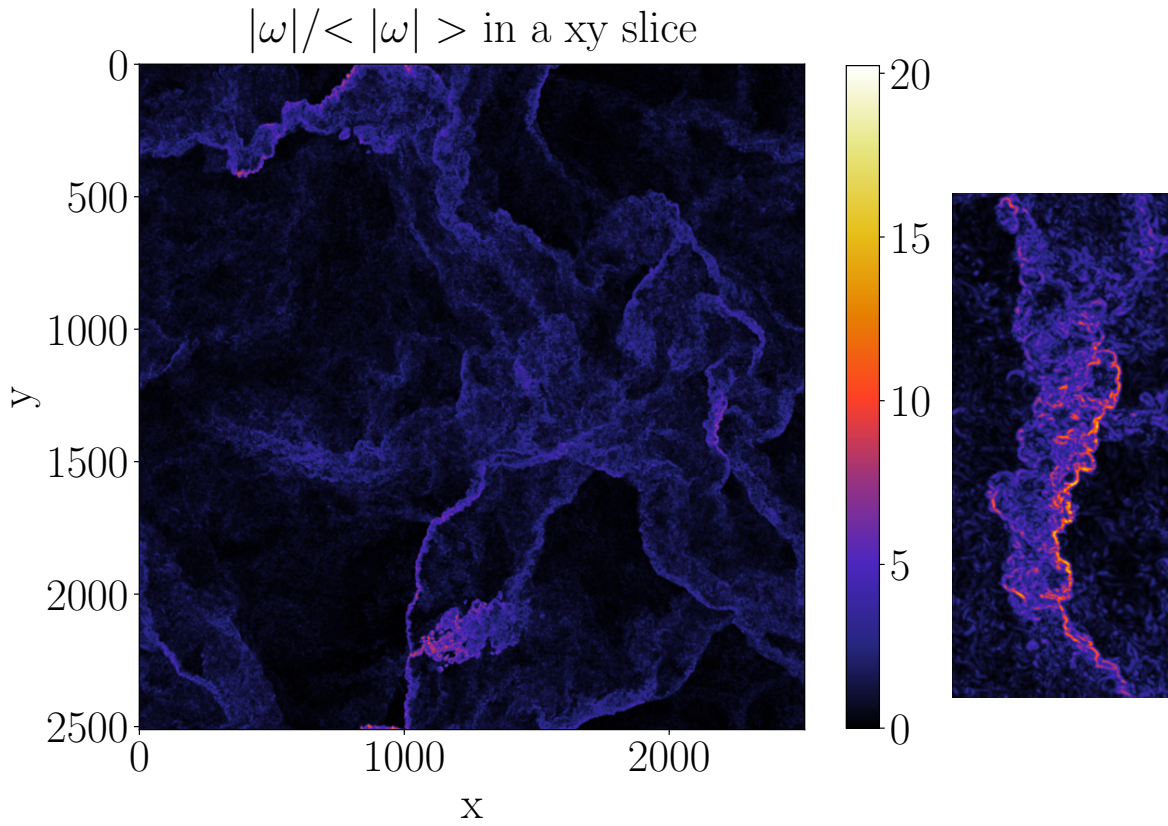


Figure 4.33: Normalized modulus of the vorticity $|\omega|$ in a (xy) plane at 6 turnover times. The amplitude of the fields is given by the color bars. The region enclosed in the dashed cyan box is zoomed in and shown on the right.

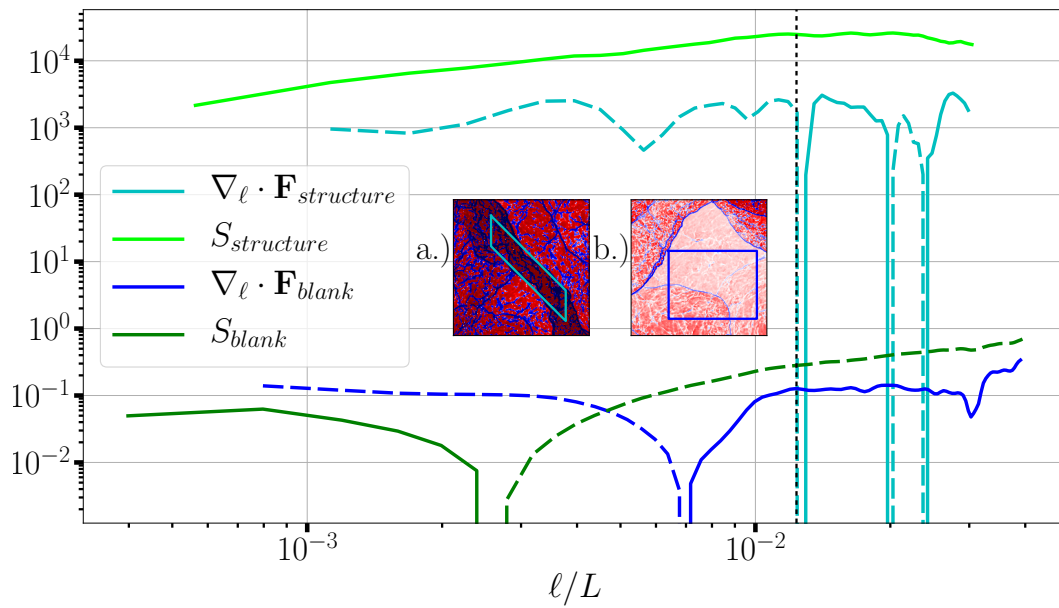


Figure 4.34: Flux and source terms computed in a single turbulent (filamentary) structure (bright lines) and a single blank zone (dark lines); Insets a.) and b.) show respectively the turbulent structure and the blank zone in which the statistics are made. Both regions are extracted from the (xy) cut shown in figure 4.32.

in each of those regions (see both insets of figure 4.34) and computed the exact law along its longest side, in order to retain enough statistics for the result to be meaningful. Because these selected regions are not periodic anymore, the maximum scale I can calculate the law on through this method is roughly half the trapezoid length: this is enough to reach the sonic scale, and studying larger scales would start bringing the statistics down too much. The resulting law components confirm our previous hypotheses: the flux and source terms computed on the blank zone have similar amplitudes and are around three orders of magnitude below the total components averaged on the entire simulation domain that are shown in figure 4.29. On the contrary, law components computed along the turbulent structure exhibit very strong amplitudes, with the source being an order of magnitude above the flux. As expected, these structures contain strong turbulent activity.

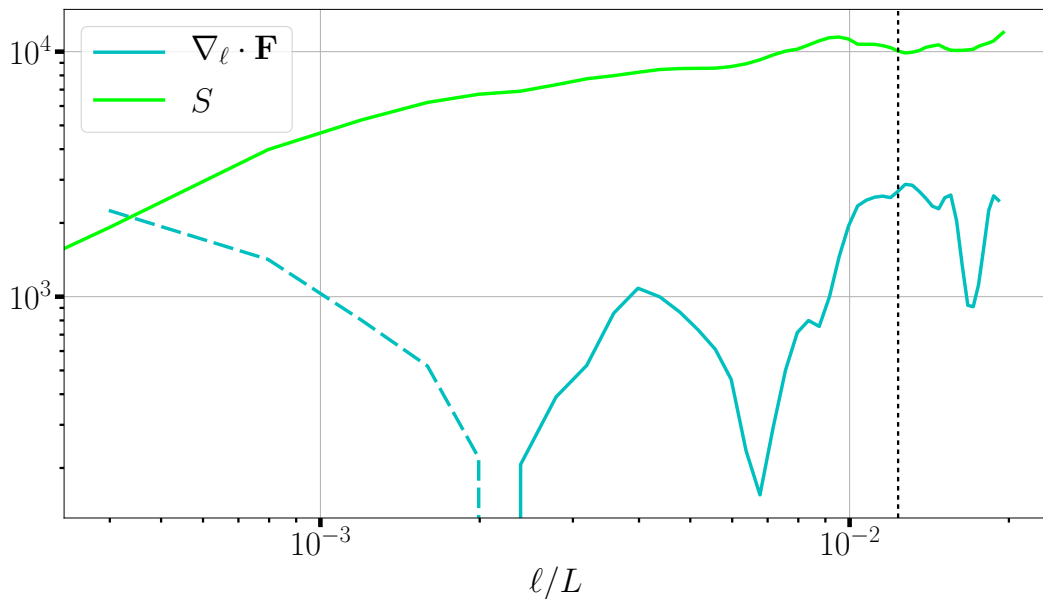


Figure 4.35: Flux and source terms averaged over 14 filamentary structures from different snapshots. The sonic scale is given by the vertical dotted lines.

All the blank regions I studied showed a similar behavior, displaying very weak turbulent activity. Consequently, I decided to focus the study on the filamentary structures by selecting a sample of these regions in different snapshots. I retained 14 structures in which the mean density was at least 5 times higher than the average density on the whole domain, and again computed the source and flux term for increments along the main orientation of the filamentary structures. The results obtained were then averaged over the selected samples, and are displayed in figure 4.35. We observe a similar trend to the previous individual computation: the source is dominant, positive and increases with the scale until it reaches approximately the sonic scale. The flux term does not have a constant sign but remains negligible with respect to the source at most scales.

The energy cascade was computed in other regions that were not blank zones nor turbulent structures, but no recurring pattern could be identified for the flux or source terms. This leads us to believe that the filamentary structures, which feature high amplitude cascade components and a mostly positive source term, drive most of the turbulence in this simulation. What is interesting here is that those filamentary structures appear to have a limited width: the ones showing high levels of vorticity rarely exceed a width of at most the sonic scale. This coincides with the total energy cascade rate of figure 4.29 that is roughly constant at small scales, but start decreasing above the sonic scale and does not show anymore a behavior typical of an inertial cascade. This correlation led me to investigate the possible existence of several scale-dependent regimes for the turbulence.

4.5.5 Insights into a two-regimes turbulence

To get a better idea of the overall scale repartition of the flux and the source, I took their absolute values before performing their statistical averages. Therefore, we define $\tilde{\mathbf{F}} = \langle \bar{\delta\rho}(\delta\mathbf{u})^2|\delta\mathbf{u}| \rangle$ and $\tilde{S} = \frac{1}{2} \langle |\rho\theta' + \rho'\theta|(\delta\mathbf{u})^2 \rangle$ and compute them on the entire simulation domain at a given time. These two quantities represent the total activity due to the flux and the source respectively, disregarding the sign of the local contributions and so the direction of the resulting turbulent cascade (direct or inverse). Note that these results should not necessarily comply to any theoretical prediction brought by the exact law (such as a constant cascade rate or any form of scaling), as the terms computed here are not the ones forming the exact law *per se*. Yet, the non-signed quantities have the advantage of converging faster than their signed counterpart, and can lend some information about the mechanisms dominating on different scales. The results are reported in Fig. 4.36.

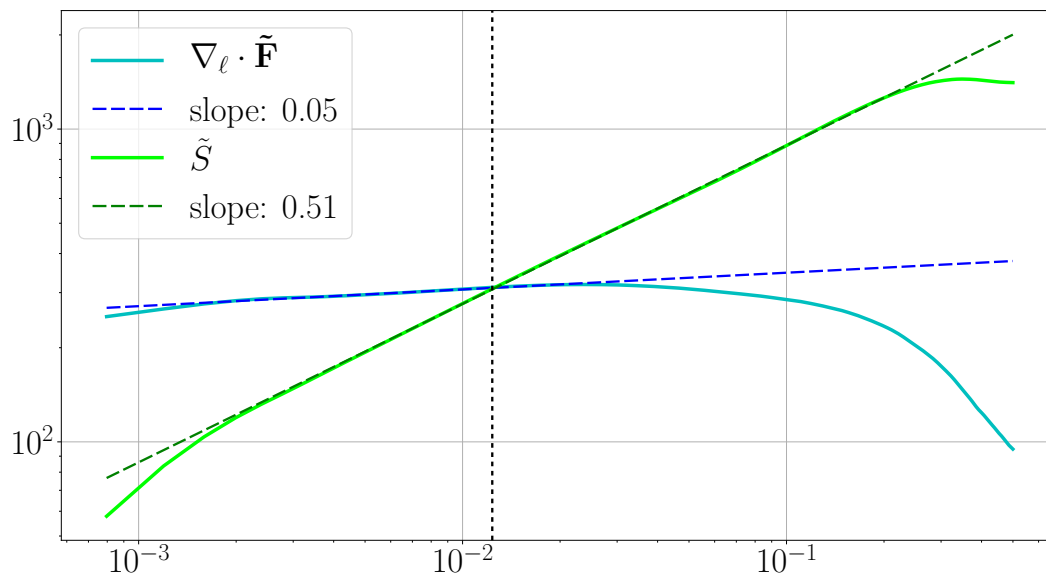


Figure 4.36: Modified flux $\nabla \cdot \tilde{\mathbf{F}}$ and source \tilde{S} computed in the entire simulation domain at time corresponding to 6 turnover times. A comparison is made with the scalings $\ell^{0.05}$ and $\ell^{0.51}$.

We immediately distinguish two regimes on this figure, separated by the sonic scale: a small scale, subsonic regime dominated by the modified flux, and a large scale, supersonic regime dominated by the modified source. Note, as was stated above, that this does not contradict the results of figure 4.29 where the flux term still dominates at large scales: the modified source is merely a representation of the absolute values of the source throughout the simulation domain. In practice, the non modified source is lower because most of the local contributions actually cancel each others.

In the subsonic regime the modified flux exhibits a plateau on small scales, as expected for a subsonic turbulent cascade mainly driven by the flux. This means that most of the energy transiting in either direction through these scales is transferred by a flux-driven process. A transition appears around the sonic scale above which the flux starts to drop: this behavior can be attributed to the dominance of the compressible source activity on supersonic scales, and interpreted as a shift from a "classical" turbulent cascade to a different, compression-driven model of turbulence.

In this other large scale regime, the dominant modified source follows a clear power-law $\tilde{S} \sim \ell^{1/2}$. A simple dimensional analysis yields $\delta u \sim \ell^{1/2}$ (note that we do not include the density appearing in the expression of S as it appears as a local average and not as a pure fluctuating quantity). This scaling is actually compatible with the one reported in Federrath et al. (2020) on supersonic scales using the second-order structure function (which

is positive definite and therefore comparable to our calculation using absolute values), while a classical (incompressible) scaling $\delta u \sim \ell^{1/3}$ was approximately found on subsonic scales. This supersonic scaling is dimensionally compatible with a velocity spectrum $E^u \sim k^{-2}$, which is often attributed to a purely compressible (Burgers), shocks-driven turbulence (Kadomtsev and Petviashvili, 1973; Passot et al., 1988; Frisch, 1995).

To support this observation, I complemented the analysis led in real space by studying the behavior of turbulence in the spectral domain and computed the 3D isotropic power spectrum of \mathbf{u} as defined by equation (1.33). This power spectrum, reported in Fig. 4.37, brings additional evidence of the existence of the two regimes. It shows a break around the sonic scale of the system, corresponding to the onset of the decline of the energy cascade rate in the real space. The small wavenumber (large scale) regime shows a spectral slope of around -1.97 which is compatible with the compressible Burgers prediction discussed above, and the large wavenumber (small scale) regime a slope of around -1.54. This slope can be interpreted as the predicted scaling $-3/2$ for weak acoustic turbulence (Zakharov and Sagdeev, 1970; L'vov et al., 1997), which would suggest that this regime is indeed closer to classical (compressible) turbulence than the supersonic one, as already suggested by the quasi-constant modified flux. Note that, if we assume that the cascade rate computed here is representative of (if not identical to) the energy dissipation rate in the system, the observation that cascade/dissipation rate peaks near the sonic scale (Fig. 4.35), where turbulence appears to transition from shock-like (k^{-2}) to fluctuation/wave-like ($k^{-3/2}$) dominated regimes, would be an indication of strong shock dissipation around the sonic scale.

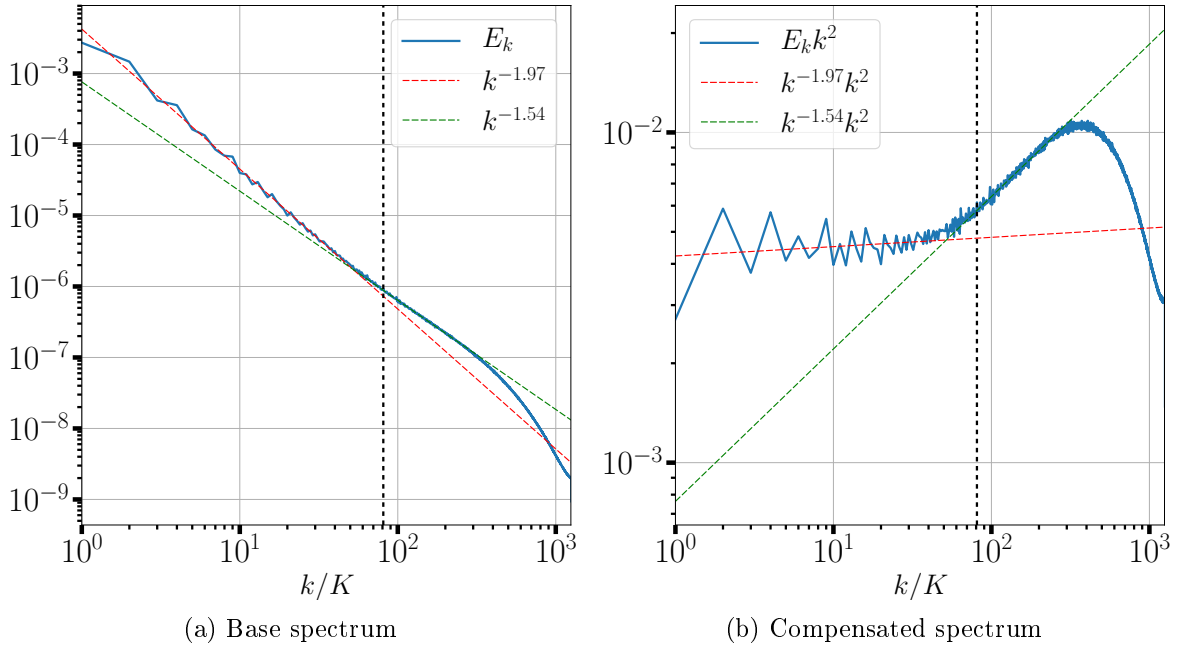


Figure 4.37: Spectrum for the velocity field \mathbf{u} and spectrum compensated by k^2 . Two linear fits are made before and after crossing the sonic wave number k_{ℓ_s} (dotted vertical line), and are represented by the red and green dashed lines respectively. Wavenumbers are normalized to $K = 2\pi/L$ (see also (Federrath et al., 2021)).

4.5.6 Summary and link to the ISM

Using the new exact law (2.109) on a high-resolution dataset for supersonic CHD turbulence, I found multiple evidences of a two-regime turbulence. The small, subsonic scales show all the characteristics of a "traditional", conservative (and possibly acoustic) turbulent cascade driven by both the flux and source terms of the exact law. This cascade appears to be concentrated in filamentary structures, which is corroborated by the high levels of vorticity

they contain and by local computations of the law, showing high amplitudes of the cascade. At intermediate, transonic scales both the flux and the source contributions reach a peak. We thus suggest that the energy cascade in supersonic HD turbulence reaches its maximum efficiency (i.e. ε_{eff} is maximal) around the transition from the subsonic to supersonic regimes. Then, on supersonic scales, the exact law shows a decrease in the energy cascade rate ε which is no longer constant, whereas compressible effects start dominating the dynamics, leaning towards a more shock-driven, Burgers-like compressible regime as evidenced by the k^2 spectral scaling.

This transition from a highly compressible regime at supersonic scales to a subsonic turbulent conservative cascade echoes to other studies that were led on similar media. For instance, similar conclusions were drawn by [Aluie et al. \(2012\)](#) who reported for subsonic and transonic simulations that pressure-dilatation (which is equivalent to density-dilatation for an isothermal model) acts essentially on large scales, whereas at small scales, below a transitional “conversion” scale range localized at sub-sonic scales, a turbulent cascade appears in which kinetic energy behaves like an invariant. This study shed a new light onto those findings using a different approach that helps better understand how various mechanisms shape supersonic turbulence.

The conclusions reached in this section also allow us to gain deep insight into supersonic ISM turbulence. The filamentary structures observed in the ISM seem to be characterized by a universal thickness of the order of the sonic scale ([Arzoumanian et al., 2011](#); [Federrath, 2016](#)). Their shape is supposed to be mainly due to CHD turbulence and to be little affected by other factors such as gravity or magnetic fields ([Federrath, 2016](#); [Ntormousi et al., 2016](#)). These studies associated with the results presented here suggest that this universality could be explained by the existence of the two distinct regimes reported here: i) a supersonic regime dominated by shock-like structures where the energy cascade rate ε is not constant; ii) a subsonic regime with a lower and mainly constant ε where vortices (and acoustic waves) are produced and in which a classic conservative cascade is formed. In between, the transonic scales where turbulence reaches its peak of effective energy transfer would correspond to the size of the filaments. Our interpretation is thus that filaments are shaped by the smallest scale of the supersonic regime, which is the sonic scale, while the weaker subsonic cascade produces vorticity tubes on smaller scales.

Applications of the law to more complete simulations, featuring for instance gravitational forces or magnetic fields, would help refine this interpretation and may provide new clues on the interplay between ISM turbulence and the problem of star formation ([Mac Low and Klessen, 2004](#); [Hennebelle and Falgarone, 2012](#); [Padoan et al., 2014](#)). For example, [Orkisz et al. \(2017\)](#) were able for the first time to observationally derive the fractions of momentum density contained in the solenoidal and compressive modes of turbulence, in the Orion B molecular cloud where the mean Mach number is ~ 6 . They showed that the compressive modes are dominant in regions with a high star formation rate (as predicted in [Federrath and Klessen \(2012\)](#)). According to the analysis led in this section the source term is the dominant component of compressible turbulence inside filaments. Future work that would directly link the formalism of exact laws (and thus the source and flux terms) to the star formation rate could significantly advance our understanding of how turbulence controls the formation of structures on different scales in the ISM.

4.6 Conclusion

Throughout this chapter I presented an ensemble of applications of the various exact laws to different DNS datasets. These studies aim either at investigating the behavior of the exact laws in order to better understand the relationships between their various components, or at studying data presenting specific physical properties to see how these effects are represented by the energy cascade rate. This kind of study allows for developing tools and gathering

knowledge that will be useful for subsequent analyses of more complete datasets, be it simulated datasets or *in situ* data measured by satellite missions. The knowledge acquired on the behavior of exact laws will be put to use in next chapter to analyze **MMS** data, and investigate the numerical techniques used for the treatment of the multi-spacecraft data. The physical knowledge acquired especially on the correlation between the energy cascade rate and kinetic dissipation will also be, at short to medium term, at the center of another study aiming at identifying the presence of dissipation mechanisms in **MMS** data.

The results presented in the four sections of this chapter led to the publication or proposal of a total of four papers:

- The **EMHD** study presented in section 4.2 are published in **Ferrand, Galtier, Sahraoui, Meyrand, Andrés, and Banerjee (2019)** [*Astrophysical Journal* **881**], along with the derivation of law **F19** already provided in chapter 2.
- A paper by Ferrand, Sahraoui, Galtier, Andrés, Minnini and Dmitruk is currently being finalized to summarize the results of the **GHOST** study presented in section 4.3.
- A paper by **Ferrand, Sahraoui, Laveder, Passot, Sulem, and Galtier (2021b)** [*Astrophysical Journal*] that contains the results presented in section 4.4 on the relation between fluid cascade and kinetic dissipation was recently accepted.
- The study on the supersonic **DNS** of the **ISM** presented in section 4.5 led to a paper by **Ferrand, Galtier, Sahraoui, and Federrath (2020)** [*Astrophysical Journal* **904**].

Chapter 5

Application to Virtual spacecraft and MMS data in Earth's magnetosheath

5.1 Introduction

In the previous chapter I presented a variety of studies and results for simulated turbulence in various models and situations. One of the main, common goals of such studies is to isolate and understand the consequences of specific physical effects or parameters on plasma turbulence in order to allow for a more precise subsequent analysis of real life, natural turbulent media. Although we have limited information and no control on the physical phenomena at work in natural plasmas, we can piece together the various individual models obtained through DNS data analysis to try to understand which effects drive the behavior of these turbulent media.

As was already explained in chapter 1, the SW and the magnetosheath are valuable objects of study due to their (relative) accessibility and the richness of their underlying physics. Numerous satellite missions were launched to gather data in the SW and the magnetosheath, in the hope of honing our understanding of these astrophysical plasmas. Through these missions it was notably possible to show that these media are inherently turbulent, which was evidenced by various reports of a $k^{-5/3}$ magnetic spectrum characteristic of Alfvénic turbulence (Matthaeus and Goldstein, 1982; Bale et al., 2005; Narita et al., 2010). This turbulent nature, which is thought to be a major cause of the non-adiabatic cooling of the SW (Richardson et al., 1995; Matthaeus et al., 1999; Sahraoui et al., 2009; He et al., 2015; Woodham et al., 2018) due to turbulence energy dissipation, has been largely investigated through the use of turbulence exact laws and the analysis of the energy cascade rate (Smith et al., 2006; Sorriso-Valvo et al., 2007; Vasquez et al., 2007; MacBride et al., 2008; Coburn et al., 2015; Hadid et al., 2017; Bandyopadhyay et al., 2020), a method that now finds a new justification through the LF study presented in chapter 4. Recent multi-spacecraft missions such as Cluster and MMS along with new developments in turbulence theory allowed for the calculation of compressible exact laws within the magnetosheath, which is more compressible than the SW. A first study was led at MHD scales using Themis and Cluster data (Hadid et al., 2018) that showed the importance of taking compressibility into account in the magnetosheath. This conclusion was then extended to Hall scales by computing the full compressible exact law A18 on MMS data: in Andrés et al. (2019) we showed that the Hall energy cascade was largely influenced by even low levels of compression.

The study presented in this chapter started as a direct continuation of the work that we started in Andrés et al. (2019), with the objective of investigating further the cascade rate calculated on MMS data and trying to understand better the relation between energy cascade and kinetic dissipation, in light of the results regarding the ability of the cascade rate to reflect Landau damping that are presented in chapter 4 section 4.4. To this end I extended the set of events initially used in Andrés et al. (2019) by selecting new time intervals and calculated the full compressible laws, making use of a computational method called the gradiometer,

that will be explained and studied in details below, to compute all 3D derivatives. Yet, with the first results I obtained I noticed a problem in the calculation of the purely compressible terms (the so-called *source terms*) of the exact laws, that appeared to be much higher than expected. Thus, the focus finally shifted on understanding the reasons for this anomaly through a more thorough study of compressible exact laws on multi-spacecraft data, and an in-depth investigation of the numerical methods used in their calculation. In the scope of this investigation, I will present a study focused on the gradiometer, aiming at estimating the limitations of the method in the specific context of exact laws calculation. To this end the performances of the gradiometer will be tested in the more comfortable setting of [DNSs](#) by simulating a virtual satellite fly-by in a [CHMHD](#) simulation domain.

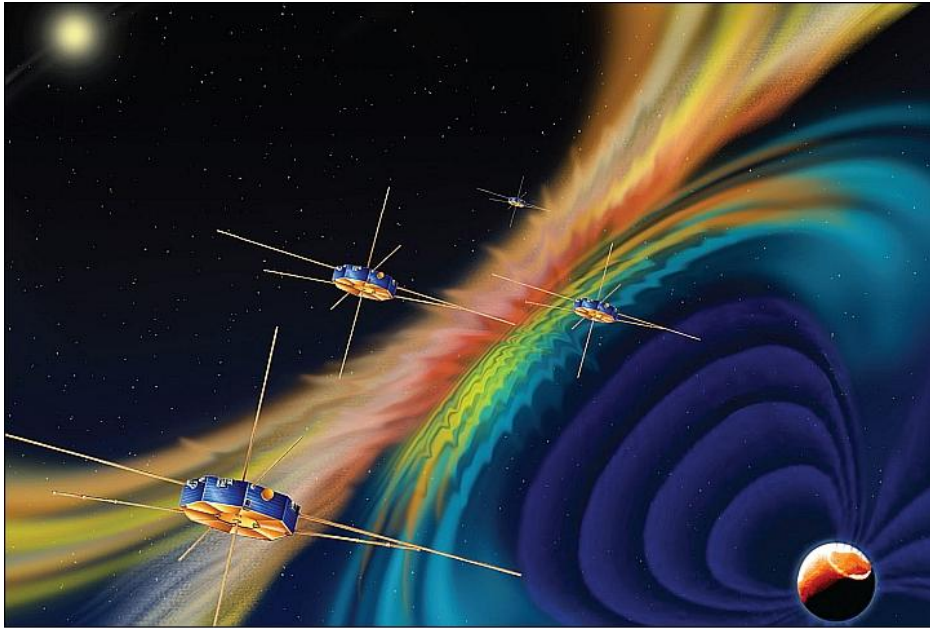


Figure 5.1: Artist's rendition of the MMS mission in Earth's magnetosphere (image credit: [NASA](#), Southwest Research Institute).

5.2 Working with *in situ* data

5.2.1 Space-time ambiguity and Taylor hypothesis

When analyzing satellite data one has to be mindful of some specific aspects that differ from 3D [DNS](#) data analysis. The most important one is the space-time ambiguity that comes with the way satellite data are measured. Indeed, when studying [DNS](#) data as we did in the previous chapters, we usually work at a fixed time and compute correlations on pairs of points, which ultimately leads to a scale-dependent representation of the exact laws. If necessary one can also make the same calculations for other times to ensure that the run is stationary: in this case the simulation domain (i.e. the "portion of space" studied) remains the same, but the plasma it contains has evolved with time: Alfvén waves for instance will have propagated according to their dispersion relation $\omega_A = \mathbf{k} \cdot \mathbf{v}_A$.

For satellite data however things are more complicated. Usually the [SW](#) moves much faster than the satellites (in the [Geocentric Solar Ecliptic \(GSE\)](#) system), so for the sake of simplicity we will consider that [MMS](#) is immobile inside the moving [SW](#). The satellites measure data, in our case, every 150ms. Between two measurements the turbulence has of course evolved, but the portion of space studied by the satellite has changed too due to the movement of the wind. This spatio-temporal ambiguity is generally resolved by using the *Taylor frozen-in-flow approximation*: it consists in considering that the timescales of the turbulence itself are much

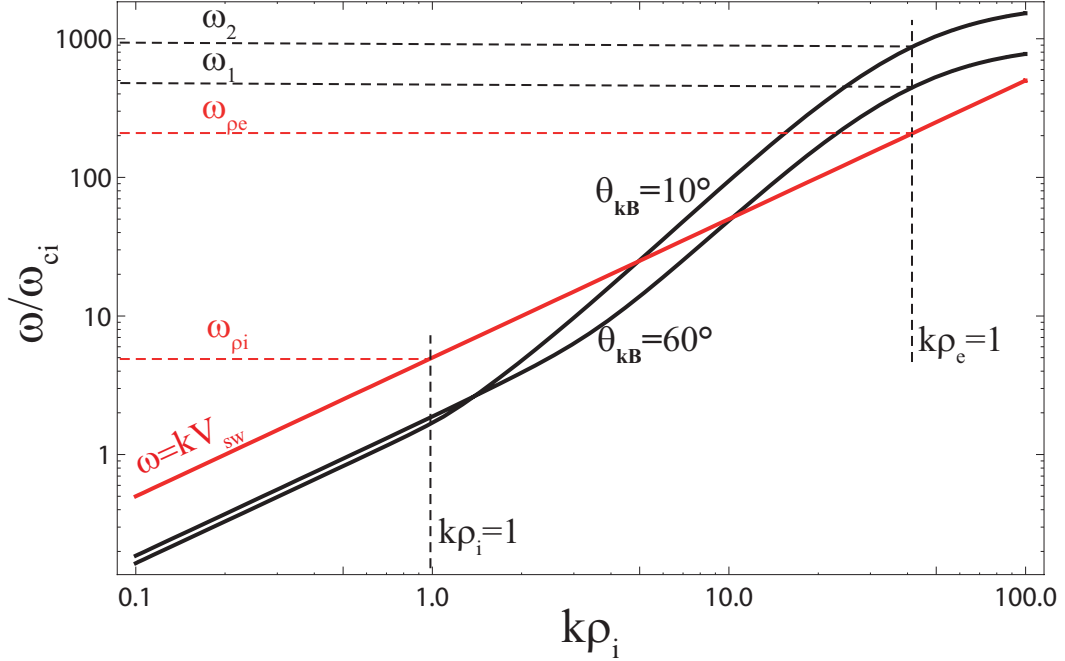


Figure 5.2: As presented in [Sahraoui et al. \(2012\)](#): frequency signatures of the ion and electron gyroscscales for a frozen-in flow approximation (red) and two whistler modes at two different angles of propagation ($T_i = T_e$), that would violate the Taylor hypothesis.

larger than the timescales of the advection of the wind, and so that the inner movements of the medium are negligible in comparison to the global movement of the flow.

In the specific case of a plasma, the Alfvén waves seen by the satellites that would normally follow the modified dispersion relation $\omega = \omega_A + \mathbf{k} \cdot \mathbf{V}_{SW} = \mathbf{k} \cdot \mathbf{v}_A + \mathbf{k} \cdot \mathbf{V}_{SW}$ (where \mathbf{V}_{SW} is the speed of the SW) will instead obey the simplified relation $\omega \simeq \mathbf{k} \cdot \mathbf{V}_{SW}$. This property is usually verified at MHD scales in the SW. At sub-ion and smaller scales however the Taylor hypothesis may be violated by the apparition of very fast modes such as whistler modes ([Howes et al., 2014](#); [Klein et al., 2014](#); [Huang and Sahraoui, 2019](#)), and may require a different, specific treatment ([Matthaeus et al., 2016](#)). Yet, as they usually appear as sporadic narrow-band emissions near the electron scales ([Lacombe et al., 2014](#); [Behar et al., 2020](#)), which are not addressed in this study, we assume here the Taylor hypothesis to hold.

In this study, the Taylor hypothesis also allows us to convert the time lag τ separating two measurements to a spatial lag $\ell = -\tau \mathbf{V}_{SW}$ corresponding to the distance traveled by the wind during this time frame. This relation allows for going back to spatial increments for the calculation of exact laws, just as we did until now for DNS data. Note that in this case we are restricted to using 1D increments, oriented in the general direction defined by the flow of the SW.

5.2.2 Calculation of 3D divergences: the curlometer / gradiometer

To compute the divergence terms appearing in both compressible exact laws [A18 \(4.14\)](#) and [F21 \(2.100\)](#) we make use of the tetrahedral formation of [MMS](#) and of an extension of the curlometer technique ([Dunlop et al., 1988, 2002](#)). This method initially makes use of Stokes theorem to calculate the current density on a given face of the tetrahedron, under the assumptions that this current density is constant on the considered face, meaning that the magnetic field evolves linearly between the satellites delimiting it. Let us number the satellites from 1 to 4, we define the position of satellite i as \mathbf{R}_i , the magnetic field it measures as \mathbf{B}_i , and the current density on the face delimited by satellites i , j and k as \mathbf{J}_{ijk} . Following the method proposed in [Dunlop et al. \(1988\)](#) we take satellite 1 as a reference and define for an arbitrary vectorial field \mathbf{X} : $\Delta \mathbf{X}_i = \mathbf{X}_i - \mathbf{X}_1$ for $i \in \{2, 3, 4\}$. Under the aforementioned hypotheses we

can derive the following relations:

$$\mu_0 \mathbf{J}_{1ij} \cdot (\Delta \mathbf{R}_i \times \Delta \mathbf{R}_j) = \Delta \mathbf{B}_i \cdot \Delta \mathbf{R}_j - \Delta \mathbf{B}_j \cdot \Delta \mathbf{R}_i, \quad (i, j) \in \{(2, 3), (2, 4), (3, 4)\}. \quad (5.1)$$

If we consider the current density to be constant and equal to \mathbf{J} on the entire tetrahedron volume, relations (5.1) form a system of three equations whose unknowns are the cartesian coordinates of \mathbf{J} . This is the core equation of the curlometer technique.

Similarly, using this time Ostrogradski theorem on the tetrahedron volume and assuming that $\nabla \cdot \mathbf{B}$ remains constant inside it, one can derive for $\nabla \cdot \mathbf{B}$:

$$\nabla \cdot \mathbf{B}(\Delta \mathbf{R}_i \cdot (\Delta \mathbf{R}_j \times \Delta \mathbf{R}_k)) = \Delta \mathbf{B}_i \cdot (\Delta \mathbf{R}_j \times \Delta \mathbf{R}_k) + \Delta \mathbf{B}_j \cdot (\Delta \mathbf{R}_k \times \Delta \mathbf{R}_i) + \Delta \mathbf{B}_k \cdot (\Delta \mathbf{R}_i \times \Delta \mathbf{R}_j). \quad (5.2)$$

Here the subscripts i , j and k can be taken in any order among satellites 2, 3 and 4. This equation was originally derived to provide means of calculating $\nabla \cdot \mathbf{B}$ as a test of the performances of the method, as we will see later in this chapter. Note that the equations written above are presented as they were originally derived, using the magnetic field and the current density, but they remain valid for any vectorial field \mathbf{X} and provide a means to estimate both $\nabla \times \mathbf{X}$ and $\nabla \cdot \mathbf{X}$.

To these equations we add an additional one allowing for the calculation of the three spatial gradients of a scalar field α , $\nabla \alpha$, obtained through a similar method as the divergence:

$$\nabla \alpha(\Delta \mathbf{R}_i \cdot (\Delta \mathbf{R}_j \times \Delta \mathbf{R}_k)) = \Delta \alpha_i(\Delta \mathbf{R}_j \times \Delta \mathbf{R}_k) + \Delta \alpha_j(\Delta \mathbf{R}_k \times \Delta \mathbf{R}_i) + \Delta \alpha_k(\Delta \mathbf{R}_i \times \Delta \mathbf{R}_j). \quad (5.3)$$

The projection of this equation in a cartesian basis gives three equations for the three components of the gradient of α . The three equation sets (5.1), (5.2) and (5.3) form an ensemble of numerical methods that will be referred to as the *gradiometer*, and will allow for the calculation of all the spatial derivatives necessary to the computation of exact laws in MMS data. Note that in the case of MMS we do not need to compute the curl of any vector field *a priori*, as the current density is already provided by measurements of particles velocities and densities from the *Fast Plasma Investigation (FPI)* sensors. However, as we will see below, calculating \mathbf{J} through the gradiometer will provide a good way to test the efficiency of this method by comparing the results to the ones directly measured by the instruments.

5.3 MMS data analysis

5.3.1 Context and presentation of the data

The study that is presented in this chapter makes use of data measured in the magnetosheath (see figure 1.2 from chapter 1) by MMS, which presents a double advantage: the magnetosheath is a more compressible medium than the SW, allowing for more efficiently investigating the influence of compression on exact laws, and the satellites offer multi-point, high frequency measurements that allow for a full calculation of CHMHD exact laws at sub-ionic scales. To compute the exact laws I made use of data gathered by two instruments, the *Fluxgate Magnetometer (FGM)* and the *FPI*, and focused on data measured in burst mode in order to have small enough time resolutions to probe sub-ion scales. In this case, the *FGM* measures the three components of the magnetic field with a time resolution of 10ms, whereas the *FPI* ion and electron sensors provide data on the velocity distribution functions, which allow for the calculation of particles densities, velocities, and temperatures as moments of these distribution functions, and have respective time resolutions of 150ms and 30ms. As we want to compute third-order moments as functions of the time lag, all the data used need to be evenly spaced in time. Thus, all the data had to be downsampled to the resolution of the *FPI* ion sensor that has the lowest resolution available of 150ms. In the context of the SW the characteristic ion time scales associated to the ion inertial length or Larmor radius usually lie around 1s, so this resolution indeed allows for the analysis of turbulence at sub-ion scales.

Using [MMS](#) burst mode data comes with a drawback however: the duration of the available time intervals will usually be quite short, with a majority being only a few minutes long, as the burst mode is mainly used for the quick passings of [MMS](#) in the thin magnetopause. The longest interval I worked with had a duration of a little less than one hour, and had to be cut anyway to fit the criteria of selection (see the selection protocol below). The short duration of these intervals make it difficult to study the [MHD](#) inertial range of the turbulent cascade (which is already hard to identify due to its small size) but they still allow for studying the sub-ion scales and the transition towards the [MHD](#) ones, which are the main goals of this study.

5.3.2 Selection of the time intervals

Prior to computing the exact laws, it was necessary to build a library of events to work on. This library was built by first looking at the set of 18 time intervals that were already selected and studied in [Andrés et al. \(2019\)](#) and filtering out some edge cases. This led to a first selection of 15 time intervals of duration 73s to 898s, each containing burstmode data for all four satellites. From this point, I had to search manually the entire burst mode database of [MMS](#) for time intervals that would match a certain number of criteria of varying importance:

- the first and most important criterion is the magnetic spectrum. As we looked for events featuring fully developed turbulence, I only retained time intervals in which the magnetic spectrum has a scaling visually close to $k^{-5/3}$ in the MHD and near ion frequencies, typically between -1.55 and -1.8 . All intervals not verifying this condition were immediately discarded ([Huang et al., 2017](#)).
- another criterion is on the angle θ_{VB} separating the velocity field and the magnetic field. As the value of this angle defines the direction in which we analyze the cascade, we ideally want to keep it roughly constant, so that the cascade is oriented in the same general direction throughout the entire time interval. I still retained some events with a non constant angle (as long as it is not heavily oscillating) that showed a very clear $k^{-5/3}$ energy spectrum.
- finally I looked at the density and magnetic field profiles to make sure that the time interval did not contain radically different regimes, or that the event did not correspond to the inner magnetosphere that is not the region we are interested in.

Two examples of times intervals, one accepted as a valid case and one rejected for various reasons, are shown in figure [5.3](#) for reference. For a chosen time interval in the initial burstmode events list, we display the time series for $|\mathbf{B}|$, n_i , θ_{VB} and density fluctuations $(n_i - \langle n_i \rangle) / \langle n_i \rangle$, along with the magnetic energy spectrum. The first three time series are complemented with overplots of brighter color corresponding to a centered running average performed on a window of size equal to a fourth of the total time interval. This is especially useful to easily check if θ_{VB} follows a constant trend or shows low frequency oscillations. With the magnetic spectrum are also plotted a reference power law $k^{-5/3}$, the mean Taylor-shifted ion inertial length on the interval $f_{d_i} = \langle |V_{SW}| / (2\pi d_i) \rangle$ and an automatic fit on the [MHD](#) range (on frequencies below f_{d_i}) that serves as a quick estimate of the spectral slope. Based on these plots, the acceptance (or rejection) of the interval was done by hand on a visual basis.

Through this selection process I ultimately built a set of 146 burstmode events of durations going from 73s to 1000s. For each event the times series for the position, magnetic field, current density and the ion and electron densities, velocities and parallel and perpendicular components of the temperature were saved for all four satellites. The current density was simply evaluated as $\mathbf{J} = q_e(n_i \mathbf{u}_i - n_e \mathbf{u}_e)$, which has the advantage of being a local measurement instead of a byproduct of the magnetic field through the gradiometer technique, which would likely have been a less precise estimate.

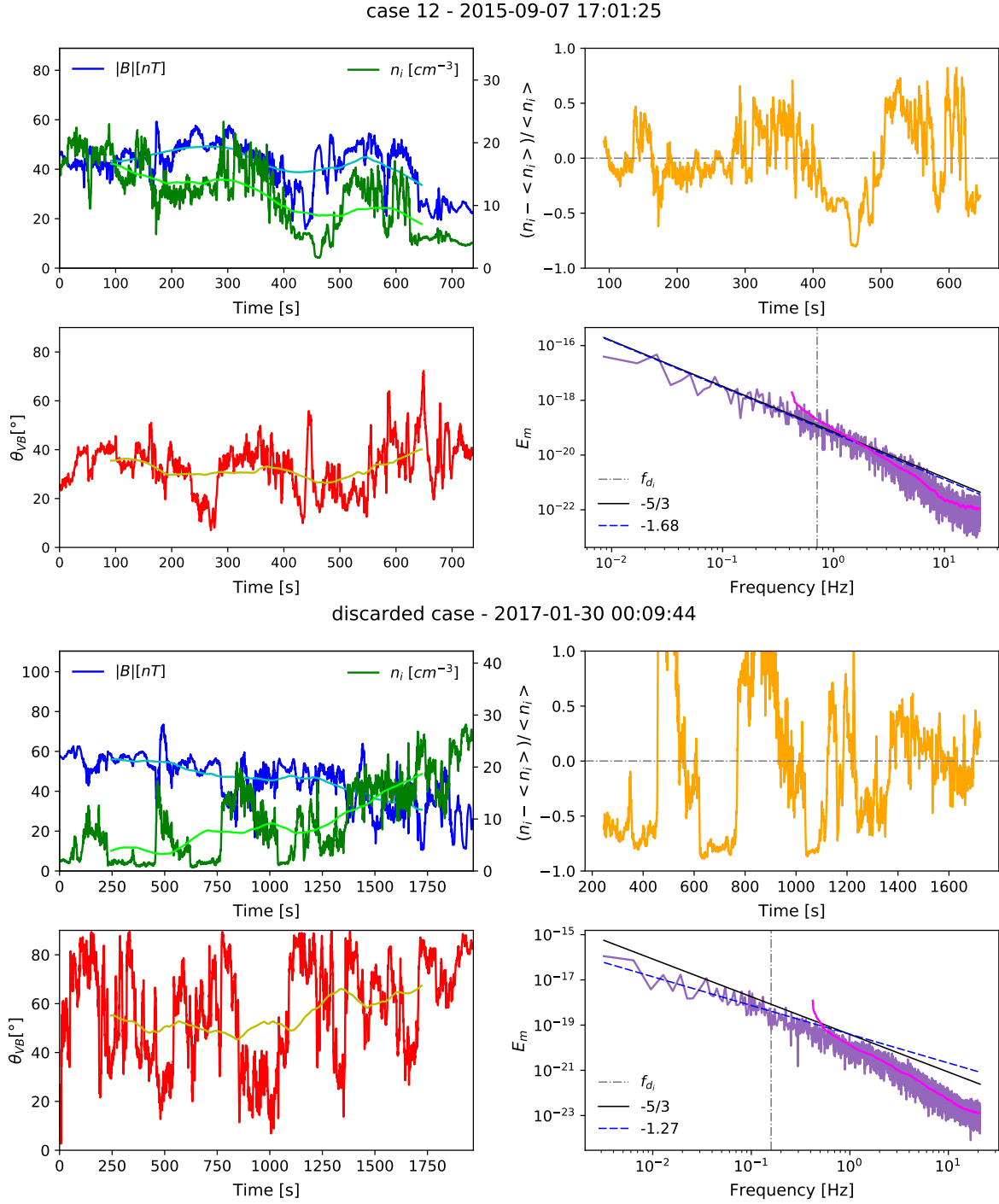


Figure 5.3: Top: Typical spectrum and time series corresponding to a valid case. The spectrum follows a clear $k^{-5/3}$ scaling, the angle θ_{VB} remains around 30° to 40° and neither the magnetic field nor the ion density show strong irregularities susceptible to be the result of shocks or of a change in the turbulent regime. This case was already presented in [Andrés et al. \(2019\)](#). Bottom: Typical spectrum and time series corresponding to a rejected case. The spectrum is too shallow, which is already enough to not consider this case, but we also see important and repeated variations in θ_{VB} that would also be a matter for rejection.

5.3.3 Results

For each selected case I then computed all terms of the compressible exact laws A18 and F21. For a given time interval, these laws are computed by averaging measured variables over the four satellites and calculating the mean spatial derivatives over the satellite formation. The mean values (over time) of the velocity and magnetic field are manually removed beforehand so that we can make sure they do not interfere with the calculations of the two laws, that have very different dependencies to the mean fields. Spatial averages for a separation ℓ , that correspond here to time averages at a given time lag τ , are calculated on all available pairs of measures separated by a time τ . The minimum time lag corresponds to the resolution of the data, i.e. 150ms, and the maximum time lag to the total duration of the interval. Note that, as the data is not periodic this time, taking a bigger time lag yields fewer pairs of points to average on, thus more fluctuations are expected to be seen for large values of τ as the statistics decrease. Fluxes are ultimately calculated by using an isotropy assumption due to the limited directional information available. Note that in this chapter we will disregard the sign of the total cascade rate and only represent its absolute value in the figures, as the poor statistics imposed by the context of the study are not sufficient to ensure meaningful interpretations on the direct or inverse nature of the energy cascade in the observations. This is not to be confused with the modified law we studied in section 4.5: here the exact laws we compute are the usual ones, and are simply represented in absolute values.

As stated in the introduction, we already initiated in Andrés et al. (2019) a similar work on the general influence of compressibility by making a comparison of incompressible law F19 with A18. In the work presented here, I focus on the in-depth study of both compressible laws and their relation to the gradiometer. Thus, each law is divided into four contributions: two MHD contributions and two Hall contributions, with in each case a part made only of terms depending on 3D divergences such as the dilatation $\nabla \cdot \mathbf{u}$, and another part made of the remaining terms (notably including the flux terms). The former will be referred to as *divergence-dependent terms*, the latter as *non divergence-dependent terms*. For F21 this division looks like this:

$$-4\varepsilon_{nodiv}^{MHD} = \nabla_{\ell} \cdot \left\langle \bar{\delta}\rho |\delta\mathbf{u}|^2 \delta\mathbf{u} + \frac{1}{\mu_0} |\delta\mathbf{B}|^2 \delta\mathbf{u} - \frac{2}{\mu_0} (\delta\mathbf{u} \cdot \delta\mathbf{B}) \delta\mathbf{B} \right\rangle + 2 \langle \delta\rho \delta\mathbf{u} \cdot \bar{\delta}(\mathbf{J}_c \times \mathbf{B}) \rangle, \quad (5.4)$$

$$-4\varepsilon_{div}^{MHD} = -\frac{1}{2} \langle (\rho(\nabla' \cdot \mathbf{u}') + \rho'(\nabla \cdot \mathbf{u})) |\delta\mathbf{u}|^2 \rangle, \quad (5.5)$$

$$-4\varepsilon_{nodiv}^{Hall} = \frac{1}{\mu_0} \nabla_{\ell} \cdot \langle 2(\delta\mathbf{B} \cdot \delta\mathbf{J}_c) \delta\mathbf{B} - |\delta\mathbf{B}|^2 \delta\mathbf{J}_c \rangle - 2 \langle \delta(\mathbf{J} \times \mathbf{B}) \cdot \delta\mathbf{J}_c \rangle, \quad (5.6)$$

with no Hall term depending on any divergence. For A18, using the notations introduced in Andrés et al. (2018), we have:

$$-4\varepsilon_{nodiv}^{MHD} = \nabla_{\ell} \cdot \mathbf{F}^{MHD}, \quad (5.7)$$

$$-4\varepsilon_{div}^{MHD} = 2S^{MHD} + 2S_H^{MHD} + 2M_{\beta}^{MHD}, \quad (5.8)$$

$$-4\varepsilon_{nodiv}^{Hall} = \nabla_{\ell} \cdot \mathbf{F}^{HMHD}, \quad (5.9)$$

$$-4\varepsilon_{div}^{Hall} = 2S^{HMHD}. \quad (5.10)$$

$$(5.11)$$

Note that for this law the divergence-dependent terms coincide with the terms usually labeled as "source terms". This is not exactly the case for F21 as some non-flux terms do not contain divergences, such as $\langle \delta(\mathbf{J} \times \mathbf{B}) \cdot \delta\mathbf{J}_c \rangle$. With this decomposition we distinguish the components of the cascade that only depend on directly measured quantities, and the components depending on 3D divergences that can only be obtained through the use of the gradiometer.

We display the results for two events that we already studied in Andrés et al. (2019), one weakly compressible and the other more compressible, in figures 5.4 and 5.5 respectively. An

immediate observation can be made: on both cases divergence-dependent terms are at best of the same order of magnitude as the other terms, and at worst orders of magnitude higher, which is not what was observed in simulations (see chapter 4 and [Andrés et al. \(2018\)](#)) nor was reported in [Andrés et al. \(2019\)](#). At this point an important statement has to be made: when I recalculated the so-called source terms reported in this letter, I found out that these terms had been mistakenly offset by a factor $1/V_{SW}$ due to an error in the conversion from spatial to time increments. This mistake made the source terms appear of way lower amplitude than they really are, which led them to be neglected. Note however that this does not invalidate the study that was led afterwards on the sole flux terms, nor the conclusions that were drawn from it. This mistake only questions the initial decision of ignoring the source terms, and we will show in this chapter that this decision is not invalidated due to important limitations on the gradiometer.

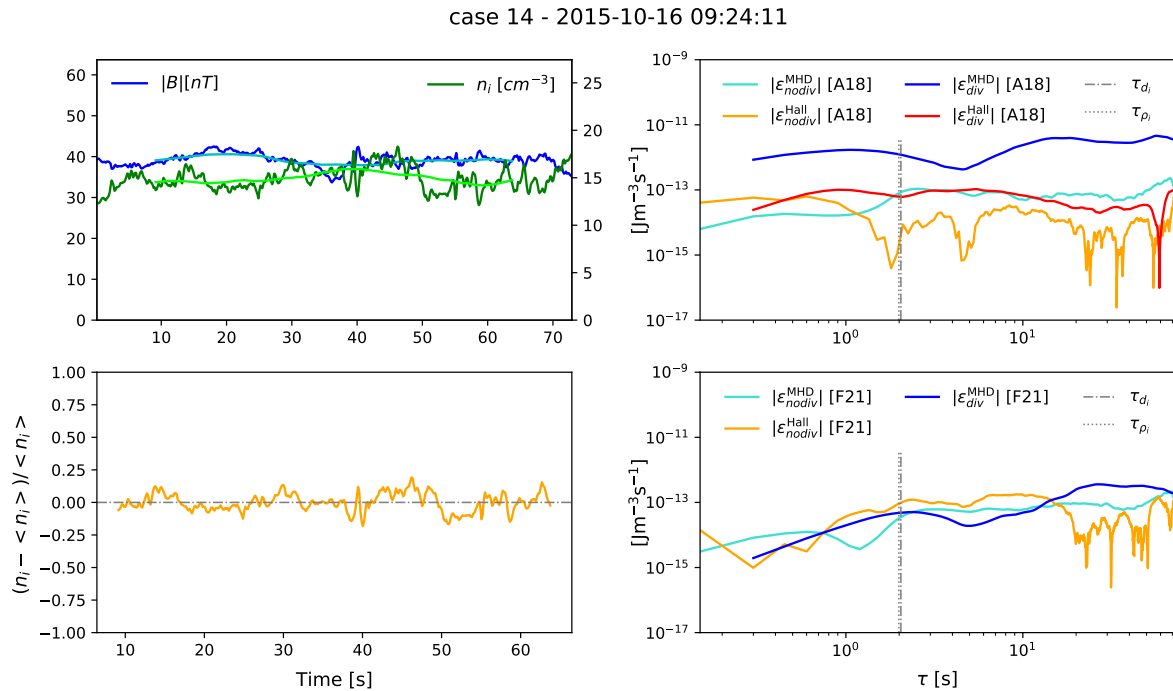


Figure 5.4: Left panels: time series for the magnetic field (blue), ion number density (green) and density fluctuations (orange). Right panels: contributions to the compressible cascade rates from **MHD** terms with (blue) and without (turquoise) divergences, and from Hall terms with (red) and without (orange) divergences. The dotted and dashed-dotted lines are the time lags corresponding to the ion larmor radius and ion inertial length respectively. Note that the red line is missing from the plot for law **F21**, due to the fact that this law contains no Hall term depending on a divergence. The point at smallest τ of divergence-dependent terms is missing due to the integration scheme applied to these terms. This event corresponds to the weakly compressible event studied in [Andrés et al. \(2019\)](#) and already presented in [Chen and Boldyrev \(2017\)](#).

Aside from the apparent dominance of divergence-dependent terms, we can pinpoint similarities between the two cases presented in details here. First, the values of $\varepsilon_{nodiv}^{MHD}$ obtained for the two laws appear to have similar behaviors across all time scales. This consistency is to be expected as both non divergence-dependent **MHD** terms share close expressions, with the exception of the non-flux term appearing in (5.4). For the Hall terms $\varepsilon_{nodiv}^{Hall}$ however these similarities vanish: **A18** shows a sub-dominant Hall term at **MHD** scales, but this term starts dominating at sub-ion scales, as we already noticed in [Andrés et al. \(2019\)](#). For **F21** the Hall term remains close to the **MHD** cascade rate at all scales and does not appear as dominant as with **A18** at sub-ion scales. The differences observed between the Hall cascade rates of the two laws contrast with observations made on **GHOST** simulations in chapter 4, where we showed that the **MHD** and Hall components were matching from one law to another. The

case 12 - 2015-09-07 17:01:25

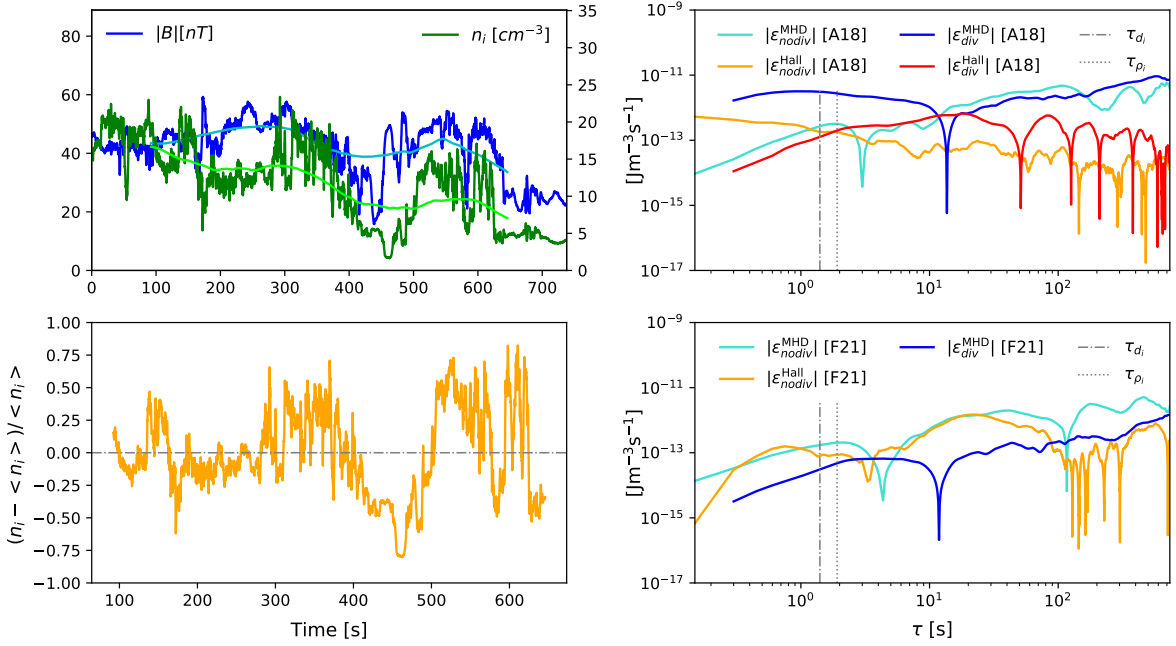


Figure 5.5: Same plot as figure 5.4 for a more compressible event, already presented in figure 5.3. This one corresponds to the weakly compressible event studied in Andrés et al. (2019).

discrepancies observed here may result from insufficient sample sizes or from the errors induced by the gradiometer, as the matching was demonstrated for the complete laws, including divergence-dependent terms.

These analyses are pushed further by calculating the mean ratios $|\epsilon_{div}^{MHD}|/|\epsilon_{nodiv}^{MHD}|$ and $|\epsilon_{div}^{Hall}|/|\epsilon_{nodiv}^{Hall}|$ for the two laws (when applicable) for all available cases. The mean values for the Hall and the MHD cascade rates are evaluated on specific time lag intervals taken respectively below and above τ_{d_i} , and that I had to select manually for each event due to the strong discrepancies observed among all cases. These intervals were chosen far away from the transition from the MHD to Hall regimes. The results, shown in figure 5.6, corroborate our previous conclusions: the dominance of the divergence-dependent term is much more prominent, and widely verified, for the MHD part of A18. For its Hall part and the MHD part of F21 however no evident domination of either divergence-dependent terms or the other terms is observed. This can be understood by recalling that ϵ_{div}^{MHD} in A18 is made of three large amplitude terms that usually cancel out each other (Andrés et al., 2018), whereas other divergence-dependent terms are only made of single terms that are negligible by themselves. Consequently, we can expect the former to reach much higher amplitudes here if its components are different enough for not canceling out.

Similar statistics can be drawn to verify whether the cascade rates evaluated by both laws generally coincide or not. Figure 5.7 shows that, as we observed on the individual cases presented in figures 5.4 and 5.5, the MHD energy cascade driven by non divergence-dependent terms is on average the same for the two laws. On the contrary, the Hall cascade appears on average to be overestimated by A18. A much more thorough study of individual components of the Hall terms of both laws, especially for F21 that is made of two separate flux and non-flux components, would be needed to explain these differences. I unfortunately did not have enough time to lead this study, but plan to investigate this matter after the end of this thesis. Instead, I decided to focus on trying to understand why divergence-dependent terms appear to be so strong even in presence of small density fluctuations: as this effect is more prominent for A18 MHD cascade rate, that contains more divergence terms, the gradiometer is suspected to be the main cause of this behavior.

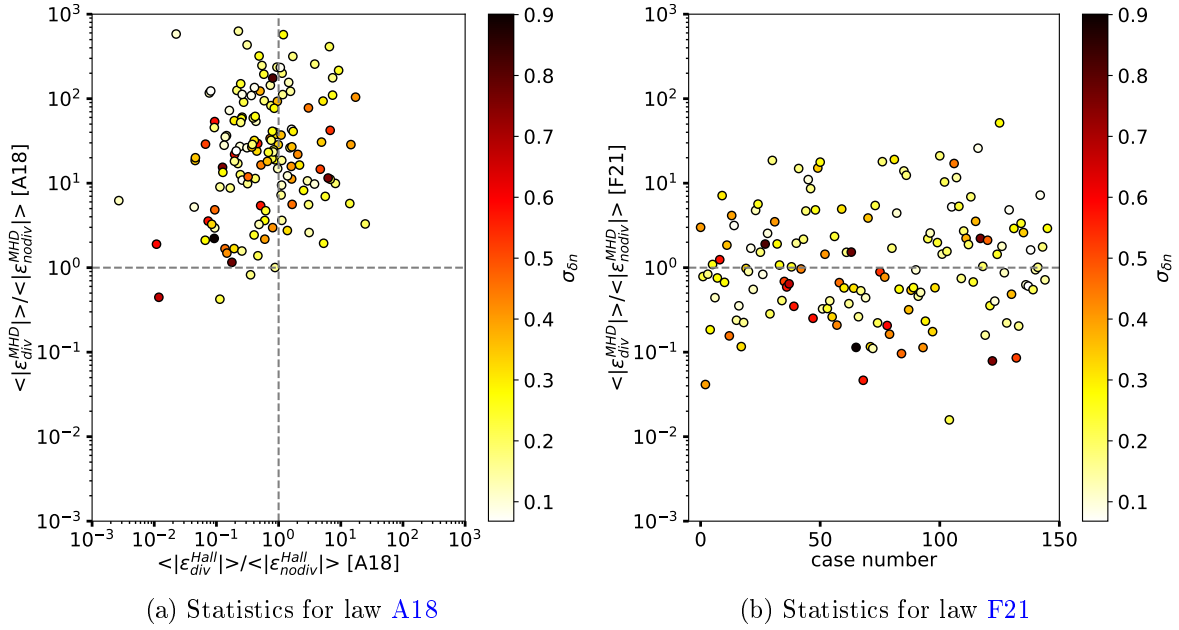


Figure 5.6: Statistics of the mean ratios $|\varepsilon_{div}^{MHD}|/|\varepsilon_{nodiv}^{MHD}|$ and $|\varepsilon_{div}^{Hall}|/|\varepsilon_{nodiv}^{Hall}|$ for laws **A18** and **F21**. Only the **MHD** case is shown for **F21** as it does not have divergence-dependent Hall terms. The colorbar shows the standard deviation $\sigma_{\delta n}$ of the time series of density fluctuations $(n_i - \langle n_i \rangle)/\langle n_i \rangle$, indicating the degree of compression of the event.

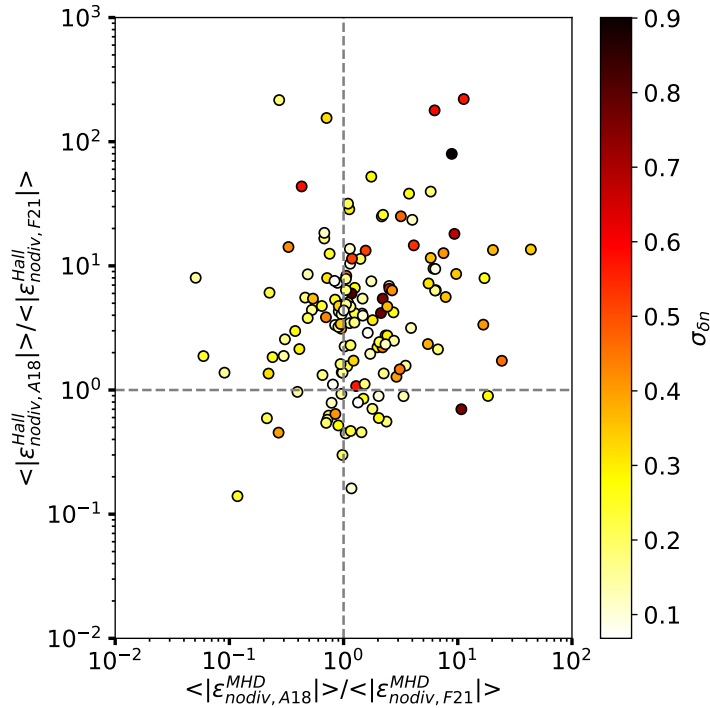


Figure 5.7: Statistics of the mean ratios of **A18** non divergence-dependent terms over the ones for **F21**. The colorbar is the same as in figure 5.6.

5.4 Gradiometer: evaluation and limitations of the method

5.4.1 Quality factor of the gradiometer

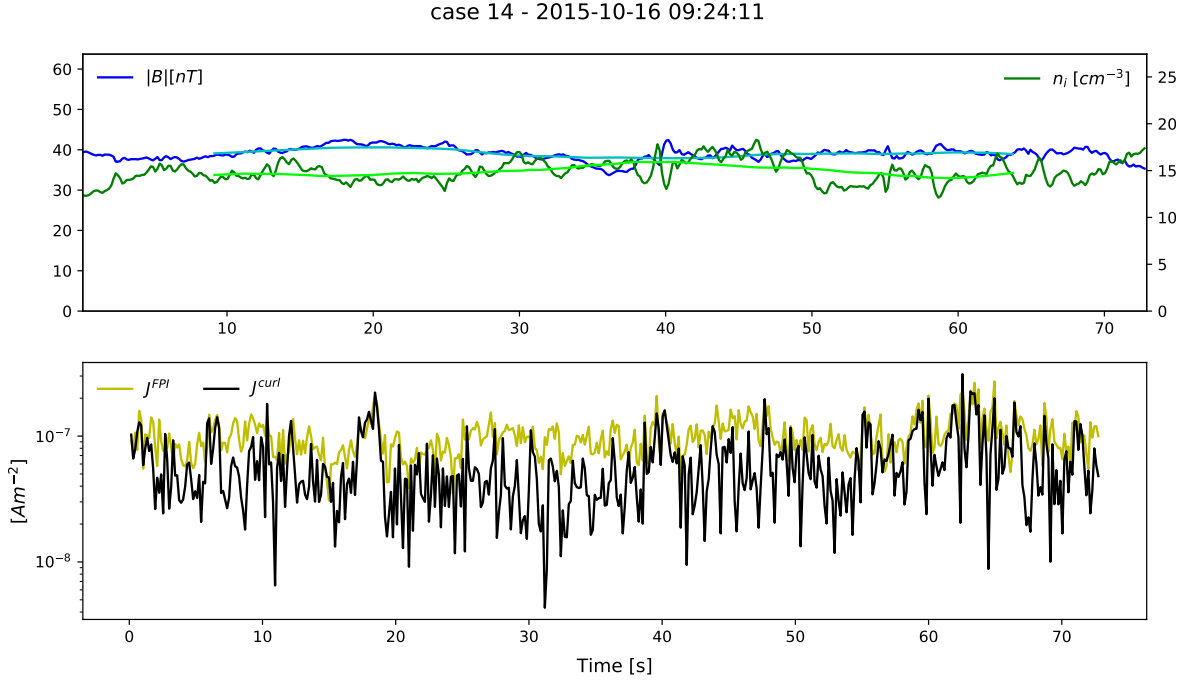


Figure 5.8: Time series for the magnetic field and ion density (top) and for the current density (bottom) measured by the FPI (yellow) and calculated by the gradiometer (black) on the weakly compressible case 14. All displayed variables are averaged over the four satellites.

I investigate here the performances of the gradiometer through, once again, single case studies and statistical studies on the entire set of events. To this end we need a parameter that would give a measure of the quality of the gradiometer’s estimate. Dunlop et al. (1988) proposed to use $|\nabla \cdot \mathbf{B}|/|\nabla \times \mathbf{B}|$. The idea behind this quantity is that $|\nabla \cdot \mathbf{B}|$ is supposed to be null, but is most probably not due to imprecisions on the gradiometer. By normalizing it by a similar quantity, namely $|\nabla \times \mathbf{B}|$ that is also calculated through the gradiometer, we obtain a dimensionless quality estimation of the gradiometer. However, $|\nabla \times \mathbf{B}|$ is also subject to variations by virtue of being a derivative, and so may not be the best normalization factor to represent to what extent $|\nabla \cdot \mathbf{B}|$ is close to zero. I thus introduced in these tests an alternative normalization by $\langle |\mathbf{B}| \rangle_{MMS} / \langle \Delta R \rangle_{MMS}$ where $\langle |\mathbf{B}| \rangle_{MMS}$ is the average magnetic field over the four satellites and $\langle \Delta R \rangle_{MMS}$ is the average separation between all four satellites. This allows for obtaining a dimensionless quantity free from perturbations brought by the use of additional derivatives. Finally, as we have access to a direct measurement of the current density, comparing this measured value to the one calculated with the gradiometer may be the best method to estimate the accuracy of this method. We will focus on this quality estimate in the subsequent study, and use it to check the performances of the other estimates that would be the only ones available whenever the current cannot be directly measured.

We display in figures 5.8 and 5.9 the time series for the current density computed with the gradiometer, and compare it to the average current density measured by the four satellites with the FPI. The ion density and magnetic field are also given for reference. On both the weakly compressible case and the more compressible one the current as calculated by the gradiometer appears to be underestimated in comparison to its real, measured value, a behavior that was already reported in previous studies (Perri et al., 2017). Moreover case 12, besides showing an increased amplitude of the current fluctuations, seems to show a larger gap between the two values of the current. However, it is not clear whether this behavior can

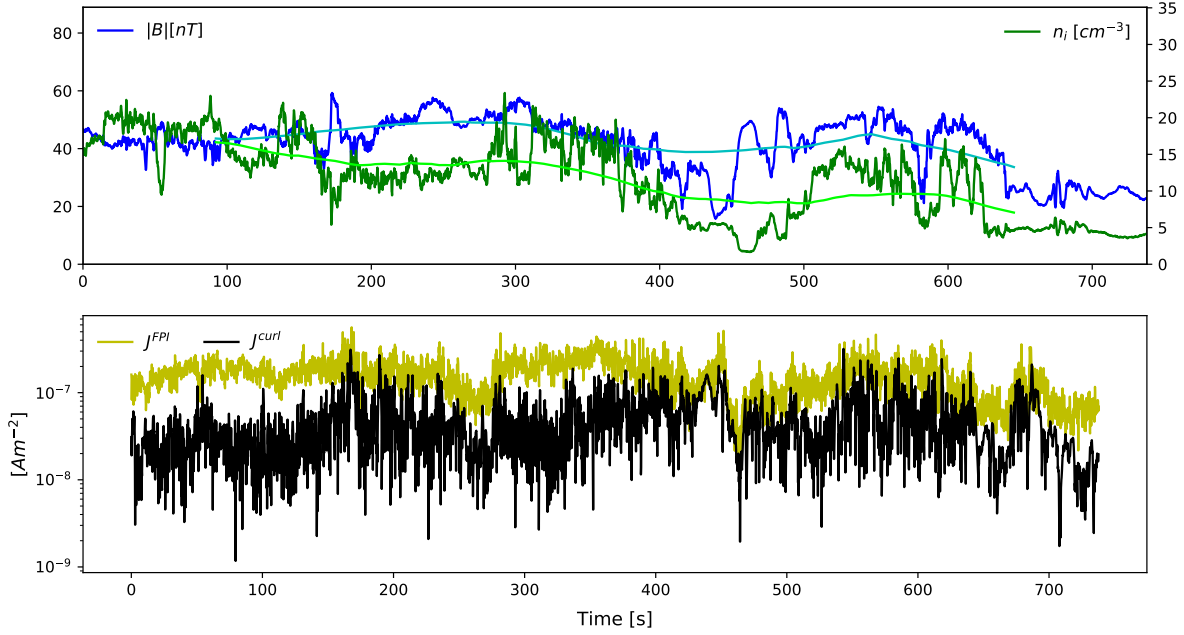


Figure 5.9: Same as figure 5.8 for the compressible case 12.

be attributed to the stronger compressibility. A statistical study reported in figure 5.10 shows that the error induced by the gradiometer is reflected by all three cartesian components of the current. No direction appears to be privileged: if the current estimate appears miscalculated, each of its component is individually miscalculated as well. This figure also indicates that the current can be underestimated by up to five times its real value, which would indicate important errors in the gradiometer estimates.

We also make a comparison between the quality estimate provided by the two calculations of the current with the other two estimates proposed earlier that make use of $\nabla \cdot \mathbf{B}$. We want to determine which one would be more suited to evaluate the precision of the gradiometer, taking the one for the current as a reference. In figure 5.11, one can see that the variable $|\nabla \cdot \mathbf{B}| / |\nabla \times \mathbf{B}|$ originally proposed by Dunlop et al. (1988) struggles to give a proper estimate of the quality of the gradiometer, except for its smallest values that are correctly correlated to a good matching of the current. The other variable, $\langle |\mathbf{B}| \rangle_{MMS} / \langle \Delta R \rangle_{MMS}$, spans a much larger range of values but also seems to offer a better correlation to the current estimate: the lowest values correspond to matching currents, and the highest ones to stronger current discrepancies. This estimate also gives birth to less artifacts. We thus argue that in situations where the current cannot be measured, and so where the currents ratio estimate is not available to measure the efficiency of the gradiometer, $\langle |\mathbf{B}| \rangle_{MMS} / \langle \Delta R \rangle_{MMS}$ could be a good candidate as a quality estimate of the method.

It is interesting to note that compressibility does not seem to play any role in the quality of the gradiometer approximation. The stronger differences in the two values of the current observed in figure 5.9 is thus an isolated behavior and cannot *a priori* be correlated to the stronger compressibility of this event. In any case, we undoubtedly see here that the estimates provided by the gradiometer are often off, in some cases of a significant factor. In itself this is not a major problem, but in the calculation of exact laws these estimates are multiplied to other terms that can exacerbate these errors to significant values. This is especially problematic as the cascade rates we compute are of low amplitude in the first place. To get a better idea of how these errors on the gradiometer translate in the calculation of the exact laws, I tried to derive a "lower bound" for this error: I computed for law A18 the terms depending on the divergence of the Alfvén speed by setting the density to a constant equal to its mean

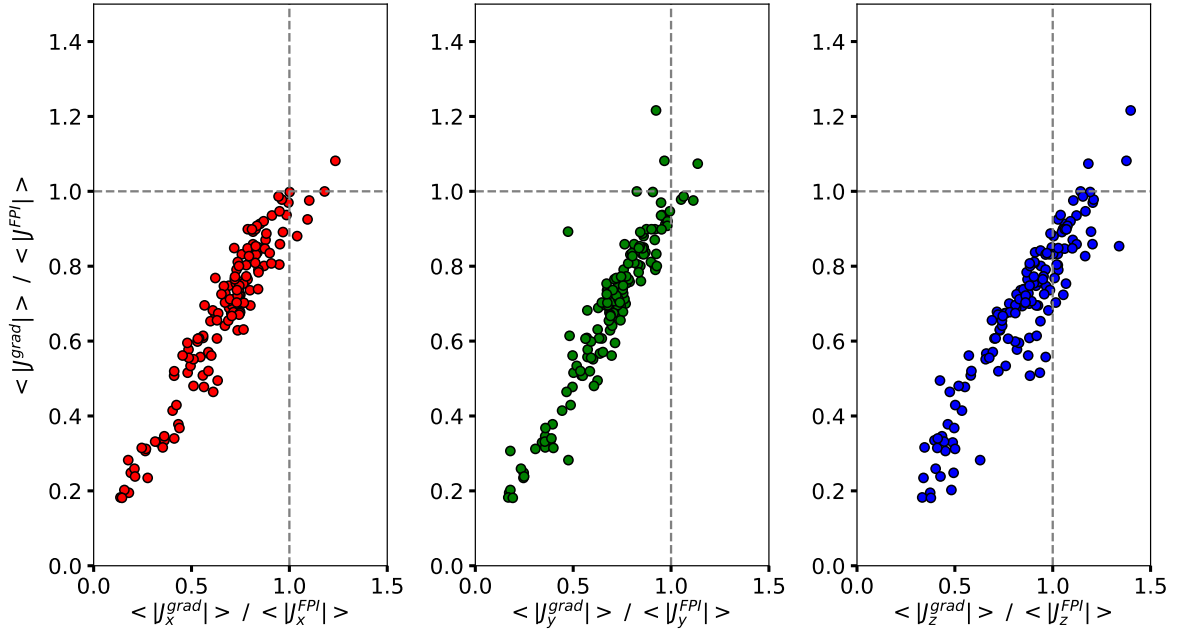


Figure 5.10: Statistical study of the ratios J^{grad}/J^{FPI} for the total current and each individual component of the current.

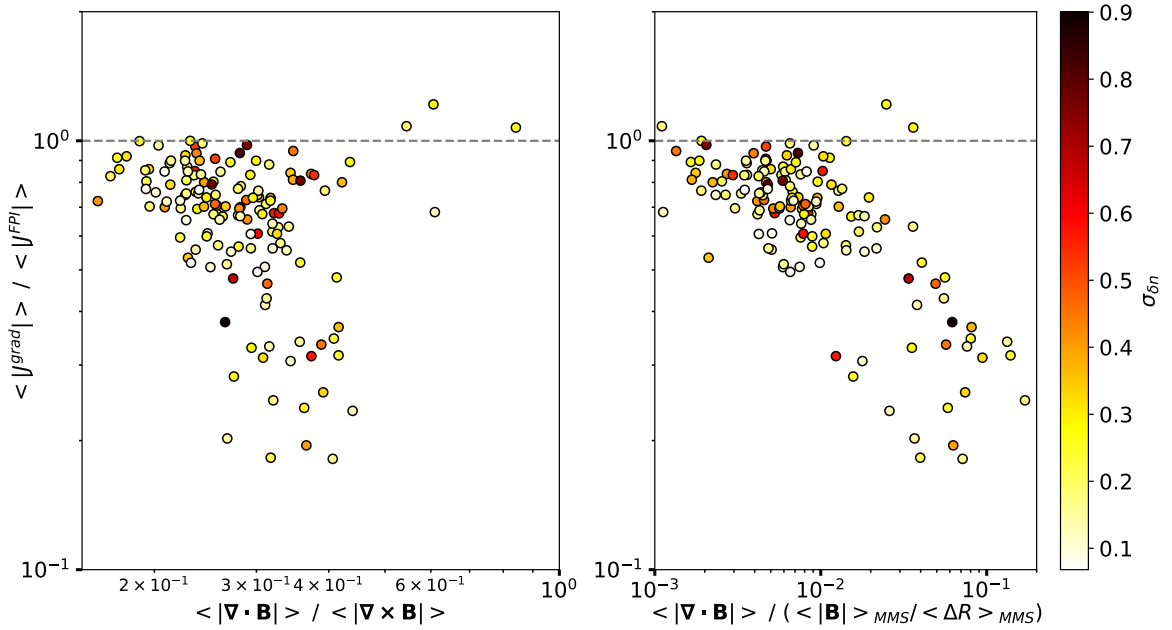


Figure 5.11: Statistical study of the ratios J^{grad}/J^{FPI} for the total current and of the two estimates of the gradiometer quality presented above, $\langle \nabla \cdot \mathbf{B} \rangle / \langle \nabla \times \mathbf{B} \rangle$ (left) and $\langle |\mathbf{B}| \rangle_{MMS} / \langle \Delta R \rangle_{MMS}$ (right). The color bar still represents the degree of compressibility of each event through the standard deviation of density fluctuations.

value. As a consequence the terms computed this way, denoted by ε_{floor} , should be equal to zero as multiples of $\nabla \cdot \mathbf{B}$. Of course they most probably will not be really equal to zero, but their amplitude will provide a lower bound on the amplitude below which we cannot reasonably trust the compressible terms.

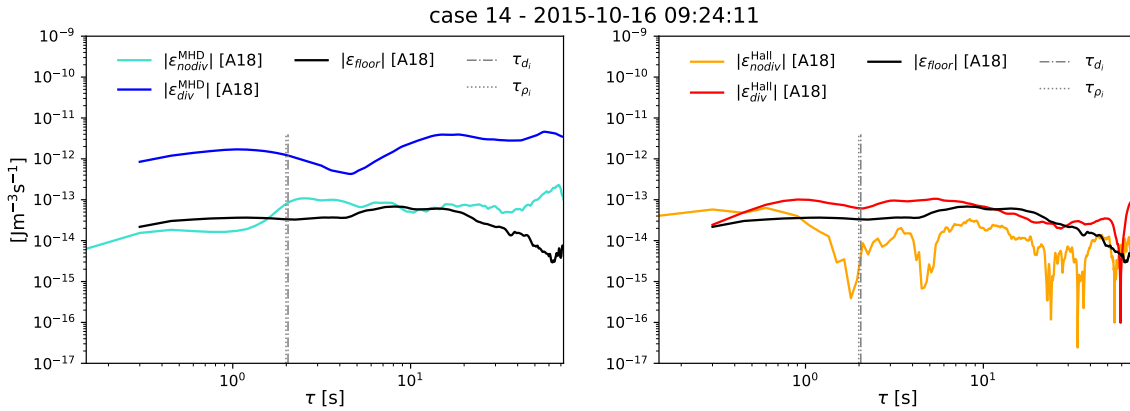


Figure 5.12: MHD (left) and Hall (right) components of the energy cascade for the weakly compressible event. The black curve represents the "floor" of the gradiometer: the values of terms depending on $\nabla \cdot \mathbf{v}_A$ computed with $\rho = \langle \rho \rangle = cte$. These terms are a lower bound of the error induced by the gradiometer.

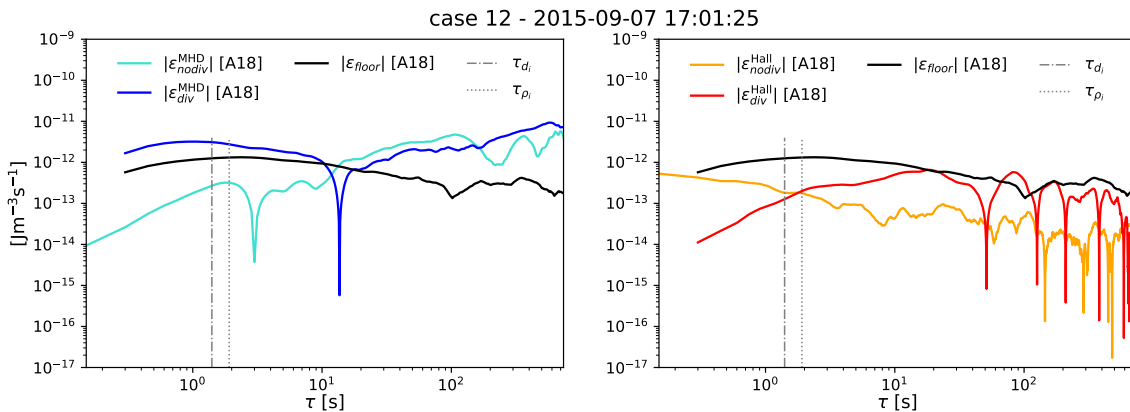


Figure 5.13: Same as figure 5.12 for the compressible event.

Figures 5.12 and 5.13 show the MHD and Hall cascade rates for our two reference cases along with the lower bound on the error of the gradiometer. An immediate remark can be made: these lower bounds are too high. For both cases this bound is of the same amplitude as the non divergence-dependent terms for the MHD cascade, and is even higher than the Hall cascade. The lower bound also has an amplitude similar to all divergence-dependent terms, except for the MHD ones in the weakly compressible event. This not only means that most of these source terms cannot be trusted, but that any divergence-dependent terms whose contribution would be equivalent to or lower than the traditional flux terms, as it is the case in the numerical studies, could not be trusted at all either. Note also that this only represents a lower bound on the error induced by the gradiometer: the true errors could be more important than this. From these results, we draw the conclusion that the gradiometer technique as currently used may not be suitable for estimating divergence-dependent components of the turbulence energy cascade rates in the context of MMS data analysis. Similarly, extreme care should be taken when working with similar multi-spacecraft missions that may be subject to the same limitations. The problems encountered here call for the development of new methods for estimating spatial divergences or at least for a better understanding of the causes of the errors observed on the gradiometer. This second aspect will be the main focus of the following

subsection, and of the next section of this chapter.

5.4.2 Causes of error of the gradiometer

We determined above that the gradiometer technique in its current form is too limited to allow for a precise study of the energy cascade rate in MMS data. We also concluded that compressibility is not responsible for bad gradiometer results. At this point, it would be interesting to understand what may be the origin of these errors. We have several candidates to explain the poor performance of the gradiometer: irregularities of the tetrahedral formation, non-linear evolution of the fields between the satellites, or a lack of statistics for the results to be believable. The regularity of the formation can be estimated with two mathematical parameters known as planarity and elongation of the tetrahedron. Robert (2000) defines these parameters using the ellipsoid created by the positions of the four satellites. If we note a , b and c the major, middle and minor semi-axis of the ellipsoid, then we define the elongation and planarity as:

$$E = 1 - (b/a) ; P = 1 - (c/b). \quad (5.12)$$

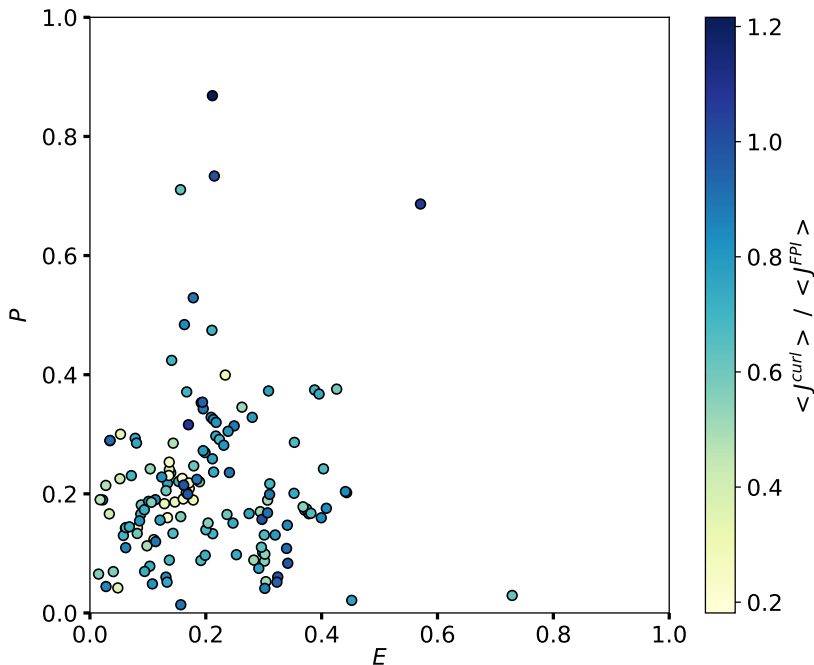


Figure 5.14: Statistics of the mean planarity and elongation of the selected events. The colorbar represents the current quality estimate of the gradiometer. We recall that the closer the value of this parameter is to 1, the better the quality of the gradiometer estimate is.

A perfectly regular tetrahedron would have $E = P = 0$ and its associated ellipsoid would be a sphere. A tetrahedron with $P \sim 1$ would correspond to a flat formation, with an associated ellipsoid described as a "pancake". On the other hand, a tetrahedron with $E \sim 1$ would correspond to an elongated formation with an ellipsoid described as a "cigar". Through these parameters it was shown by Yang et al. (2019), using Cluster data and 3D calculation techniques specifically designed for the magnetic field (different from the gradiometer), that these parameters only really disturb the estimate of the 3D fields for large values of E and P , typically $E \gtrsim 0.8$ and $P \gtrsim 0.8$. I calculated the mean planarity and elongation for the 146 events, and results are displayed in figure 5.14. No trend appears that would allow to correlate the planarity and elongation of MMS formation to the quality of the gradiometer. This may be tied to the fact that calculated values of E and P rarely exceed 0.5, far from the values reported by Yang et al. (2019) to actually have an effect on their 3D fields estimates. Thus, these parameters do not appear to be correlated to the imprecisions of the gradiometer.

One may note that a very few cases have large values of P or E , yet show a ratio close to unity, but these cases are statistically poorly significant so no reasonable conclusion can be drawn from them.

When investigating the influence of the non-linearity of the fields (i.e. spatial fluctuations of the fields between the satellites, or local perturbation affecting even a single spacecraft) we are faced with a problem: measures of the fields in-between the satellites are impossible to obtain. Consequently, I reused the "floor" terms presented in figures 5.12 and 5.13 and computed them again after smoothing the time series to attenuate the non-linearities at time scales corresponding to the mean satellite separation (transposed in time) τ_{sep} . I again used a running average, with a windows size that is a multiple of τ_{sep} . The results, displayed in figure 5.15, show that the floor terms decrease in amplitude as the size of the average window increases. It thus seems that smoothing the time series improves the precision of the gradiometer. This method is not applicable in practice as lowering the error significantly requires a strong smoothing, and we thus loose all information on the small scale energy cascade rate, where most dissipative processes happen. Such a smoothing would only be justified on scales up to τ_{sep} anyway, below which we do not have enough information. Nevertheless, this test tells us that the non-linearity of the fields between the satellites may be a major reason for the errors brought by the gradiometer technique.

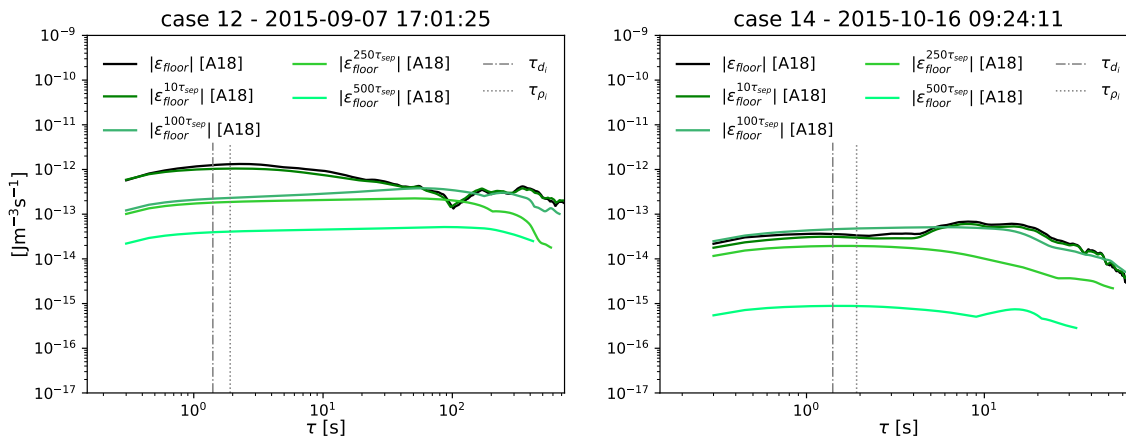


Figure 5.15: Lower bounds of the gradiometer error calculated on smoothed data from the compressible case (left) and the weakly compressible one (right). The smoothing is performed with a running average on a window of size 10, 100, 250 and 500 times the mean satellite separation (transposed in time space).

5.5 Simulated MMS fly-by

5.5.1 Description of the method

Considering the limitations imposed by the **MMS** data, it appears difficult to push the investigation further on this sole basis. To circumvent these limitations and better understand the results obtained for **MMS** data we can turn to simulated data, namely the **GHOST** 1024³ run II ($\mathbf{B}_0 = 0$, $M_S = 0.25$) already studied in chapter 4 (once again reduced to a resolution of 512³) to run additional tests in a more controlled environment. Using this **DNS**, I conceived a program simulating a virtual **MMS** fly-by within the datasets: starting from the center of the data cubes, I define the positions of four "virtual spacecraft" distributed in a perfectly regular tetrahedral formation, centered on a grid point that will serve as a reference. Then, the spacecraft are "launched" along the x-axis at a "speed" of one grid separation per step. This ensures that the center of the formation will remain on a grid point at each step, forming its general traveling path. For each step, the satellites "measure" the data at their respective

positions thanks to a 3D interpolation that was estimated beforehand on all available grid points. The data measured are all the usual fields ρ , \mathbf{u} and \mathbf{B} , but also all derivatives (such as $\nabla \cdot \mathbf{u}$, \mathbf{J} etc.) that are calculated the same way they were in chapter 4, using a finite differences scheme. This virtual fly-by will allow us to compare the usual derivative to the ones calculated using the gradiometer on the virtual formation. As a result, I obtained for each scalar and vector field four 1D series, one for each satellite, on which I then computed the exact laws just like for real [MMS](#) data.

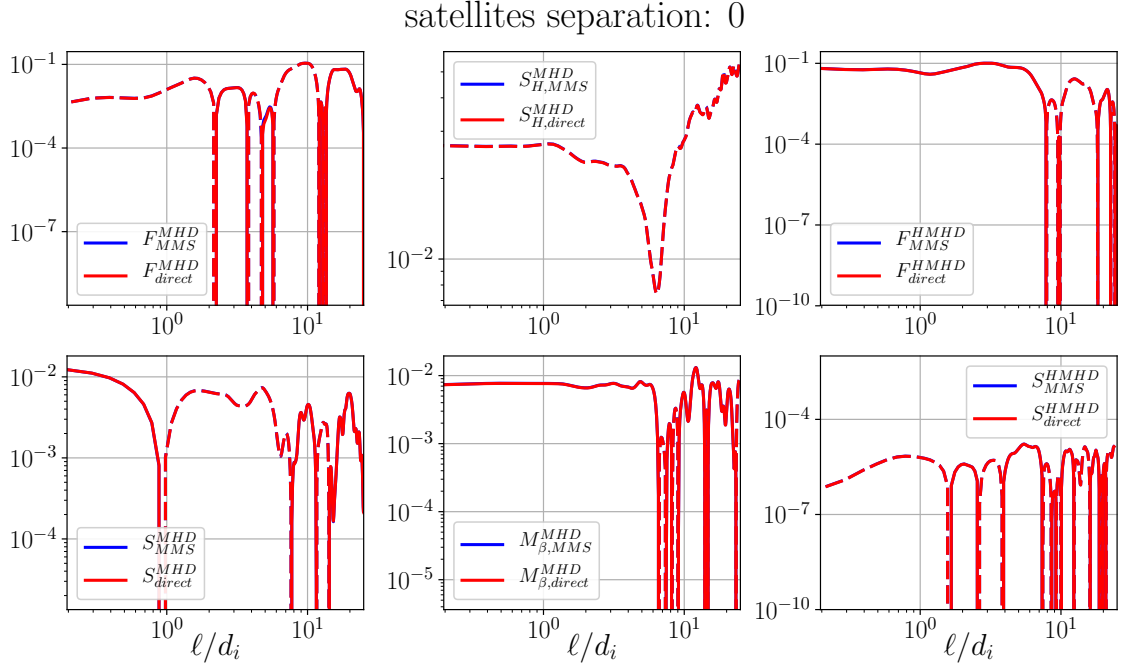


Figure 5.16: Individual terms of exact law [A18](#) calculated with the direct method (red), and using the artificial spacecraft without gradiometer (blue). We use for the different terms the same notations as [Andrés et al. \(2019\)](#), reminded in equations [\(4.15\)](#)–[\(4.20\)](#) in chapter 4. Here satellite separation is equal to zero: all satellites are on the same grid point.

In the meantime, the exact laws are computed on the data cube themselves, like in chapter 4, but only on the traveling path of the artificial formation. The laws obtained are thus mono-directional and averaged on a single line of points, and will serve as a reference to test the performances of the gradiometer in computing the laws for the artificial formation. Then, the various terms of exact law [A18](#) (the law that has the most divergence-dependent terms to use the gradiometer on) are calculated using the data measured by the satellites with two methods: by using the pre-computed divergences, and by computing them afterwards with the gradiometer. The first method allows us to compare the results obtained by computing the law on the grid points, and by computing it using the average values of the four interpolated points corresponding to the satellites around said grid points. This way, we can ensure that the interpolation and the average on the four spacecraft do not introduce important errors in the results before even calculating the gradiometer.

In figure [5.16](#) we display the results of the direct calculation and of the calculation with artificial [MMS](#) data without gradiometer for a formation with a separation equal to zero. This means that all satellites are always on a same point that corresponds to the central reference grid point. The purpose of this test is to verify that the artificial fly-by behaves as intended. As expected, both the direct calculation and the no-gradiometer one provide the same results, which tells us that the spacecraft formation "flies" as intended. Note that in this case the gradiometer terms are undefined.

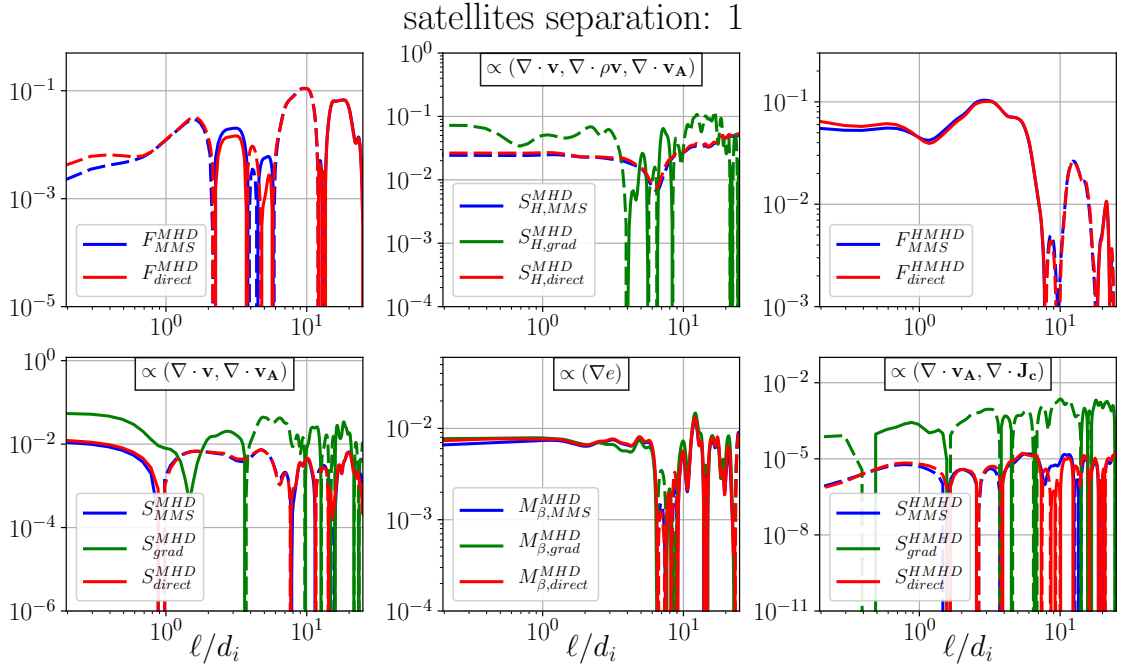


Figure 5.17: Individual terms of exact law A18 calculated with the direct method (red), artificial spacecraft without gradiometer (blue) and, when applicable, with the gradiometer (green). For each term calculated with the gradiometer, the spatial derivatives it depends on is reminded on top of the respective box. The satellite separation here is equal to one time the grid resolution.

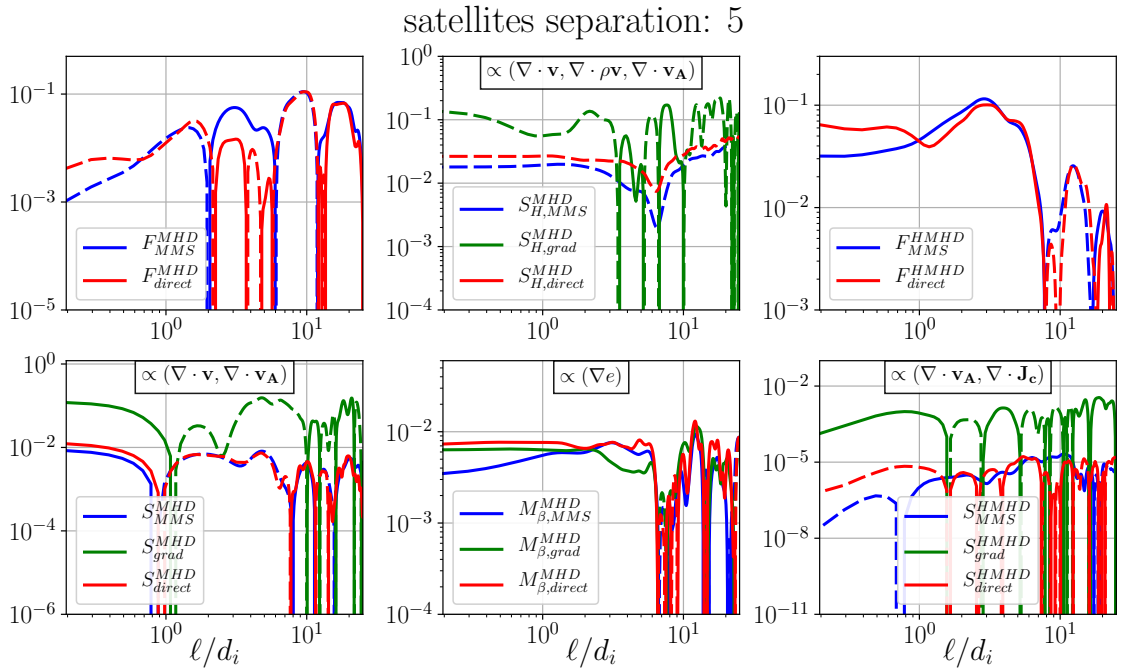


Figure 5.18: Same as figure 5.17 with a separation of 5 times the grid resolution.

5.5.2 General precision of the gradiometer

Now that we made sure that the artificial fly-by works correctly and that the reference can be trusted, we start increasing the separation between the satellites to see how it will affect the calculation of divergence-dependent terms when using the gradiometer. We display in figures 5.17 and 5.18 the results obtained with the three methods for a satellite separation equal to one time and five times the grid resolution respectively. As expected, the blue lines corresponding to the terms calculated with pre-computed divergences do not differ much from the reference, as the differences between the two methods only stem from the values used to compute the terms (central grid point for the red reference, average on the four satellites for the blue lines).

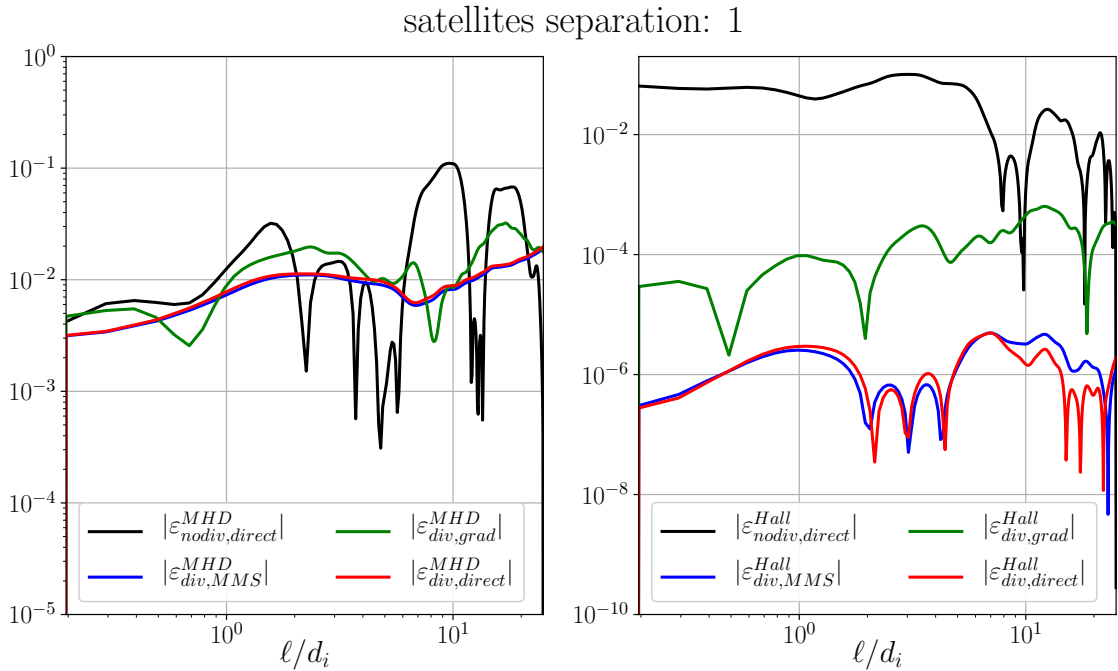


Figure 5.19: Energy cascade rates given by the reference flux terms (black) and the divergence-dependent terms in MHD (left) and Hall MHD (right). Divergence-dependent terms, are here again calculated with the direct method (red), with satellites data without gradiometer (blue) and using the gradiometer (green). Satellite separation is equal to one time the grid resolution.

Values obtained using the gradiometer show more differences even for a separation of one. For an increased separation of 5, the gradiometer ends up being an order of magnitude higher than the reference for the source and hybrid terms. These differences are even higher for the Hall source term, as it was already a low amplitude term and is thus more sensitive to errors. The case of the beta term M_β^{MHD} is interesting, as it shows a lesser sensitivity to satellite separation and the gradiometer seems to give much better results overall. This probably has to do with the fact that this term is the only one calculated using gradient terms instead of a real divergence, however why this version of the gradiometer seems to be more robust remains unclear. In any case, we clearly see in those two figures that satellite separation has a direct influence on the quality of the gradiometer estimate. It is possible that the scales at which the derivatives are calculated, which are dictated by the distance between MMS spacecraft, are too large in *in situ* data analysis and thus are partly responsible for the error induced by the gradiometer.

Besides investigating the individual terms of the exact law, we need to look at how the sum of the non divergence and divergence-dependent terms behaves relatively to each other. Indeed, nothing suggests that individual divergence-dependent terms should be negligible toward the flux terms, but it was proven that their sum is. Thus, again for a separation of one and

satellites separation: 5

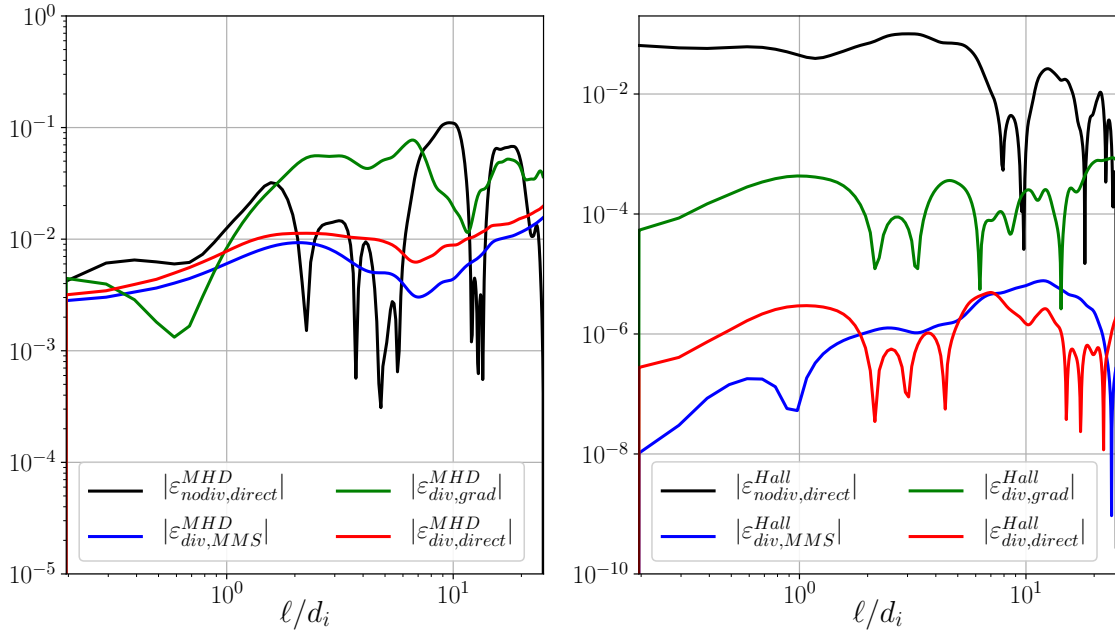


Figure 5.20: Same as figure 5.19 with a separation of 5 times the grid resolution.

satellites separation: 0, full spatial average

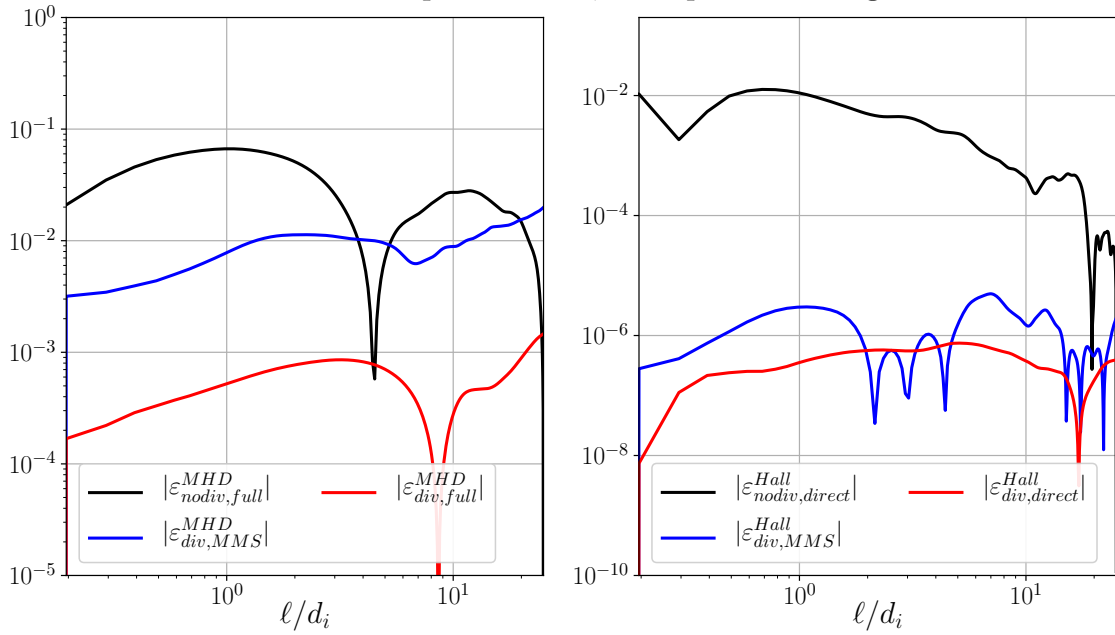


Figure 5.21: Same as figure 5.19 with a null separation (gradiometer terms are undefined). The reference terms in black and red were averaged on the entire simulation domain.

five times the grid resolution, we compare the corresponding cascade rates to obtain figures similar to the ones obtained for [MMS](#) data that were presented in previous section.

The partial cascade rates are displayed in figures [5.19](#) and [5.20](#). Overall the behaviors observed in previous figures [5.17](#) and [5.18](#) remain unchanged, except that the total sum of divergence-dependent terms calculated with the gradiometer seems to be slightly less sensitive to satellites separation. These plots however reveal a new problem: even for the reference calculation, that was made using the classical [DNS](#) computation method, the [MHD](#) divergence-dependent terms are absolutely not negligible. Yet, this is not incompatible with the results reported in [Andrés et al. \(2018\)](#) and chapter [4](#), as here the calculation is made using a single direction, and more importantly spatial averages on a single line of points, i.e. on 512 points instead of 512^3 . If we proceed to the same calculation for the reference plots using a spatial average on the whole simulation domain instead of this single line, we obtain the results shown in figure [5.21](#): the [MHD](#) divergence-dependent cascade is indeed negligible in comparison to the flux term. This flux term is also slightly higher than before.

These results have important implications regarding [MMS](#) data analysis, as they seem to suggest that the problems affecting the divergence-dependent terms that we encountered earlier may mostly be related to, in fact, an important lack of statistics. It is highly possible that the satellites just do not gather enough data to allow for a correct calculation of the divergence-dependent terms of the turbulent cascade, independently of the quality of gradiometer estimates.

5.5.3 Reaction of the gradiometer to non-linearity

As a final test, I investigated in more details the reaction of the gradiometer to non-linearities of the fields between the satellites. Neither [MMS](#) nor [DNS](#) data offer enough control on the non-linearities to quantitatively estimate their influence on the gradiometer. Thus, instead of reusing a simulated dataset, I created an artificial dataset linear in the three directions of space in which I can introduced a controlled noise, and proceeded to emulate a fly-by as I did in the [GHOST](#) dataset. To this end I first generated 128^3 3D linear components for the velocity field \mathbf{u} by assigning to the point in position $[x,y,z]$ the value $(1+x+y+z)$. Then, similarly to what was done before, I simulated an artificial [MMS](#) fly-by in the direction of the x-axis in the resulting dataset, and finally compared the precomputed derivatives to the ones obtained with the gradiometer (with a satellite separation of one time the grid resolution). For this perfectly linear dataset, we see in figure [5.22](#) that the gradiometer estimate of $\nabla \cdot \mathbf{u}$ is in excellent agreement with the derivatives computed with finite differences.

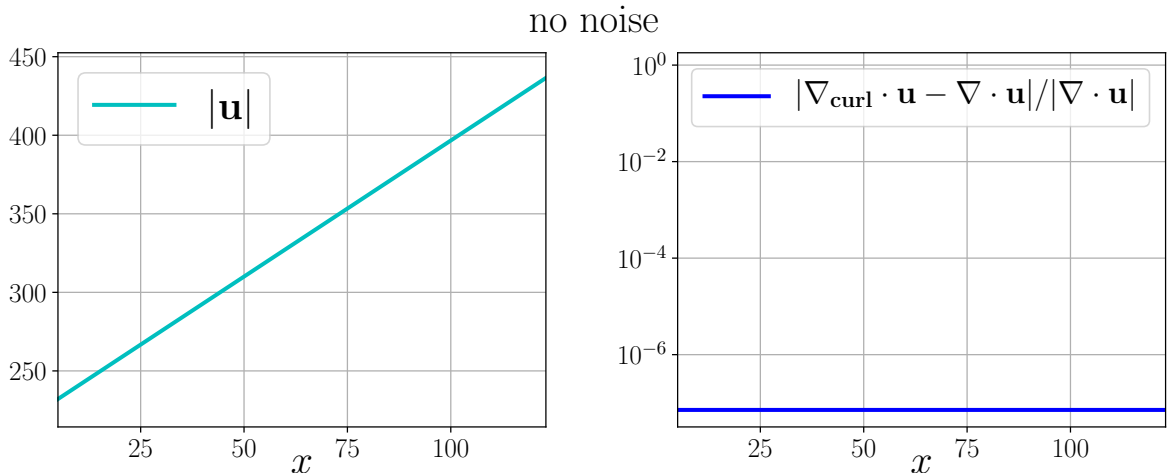


Figure 5.22: Velocity amplitude along the x-axis (left) and relative error on the calculation of $\nabla \cdot \mathbf{u}$ between the finite differences and the gradiometer (right). Here the velocity field is perfectly linear.

As mentioned above, I subsequently investigated the influence of non-linearities on this result by introducing some noise in the linear dataset. The noise is generated at each point of the dataset by using a continuous uniform distribution between zero and a given percent of the value taken by that point. I thus proceeded to the same comparison of divergences on datasets perturbed with noises generated by uniform distributions on $[0, 0.02|\mathbf{u}|]$ and $[0, 0.2|\mathbf{u}|]$, that would amount to an expected value of 1% and 10% of $|\mathbf{u}|$ respectively. Results are displayed respectively in figures 5.23 and 5.24. It appears that the average error induced by the gradiometer ends up being an order of magnitude higher than the expected value of the noise: an expected noise of 1% gives an average error of 28%, and an expected noise of 10% an average error of around 300%. For real MMS data the amplitude of the "noise" (i.e. of the non-linearities between satellites) is not accessible, but based on the high frequency fluctuations observed on the density or the magnetic field we can roughly estimate these non-linearities to be of the order of 10%. According to the results presented here, this could amount to significant errors on the calculation of the gradiometer, which could be further amplified in the calculation of the exact laws.

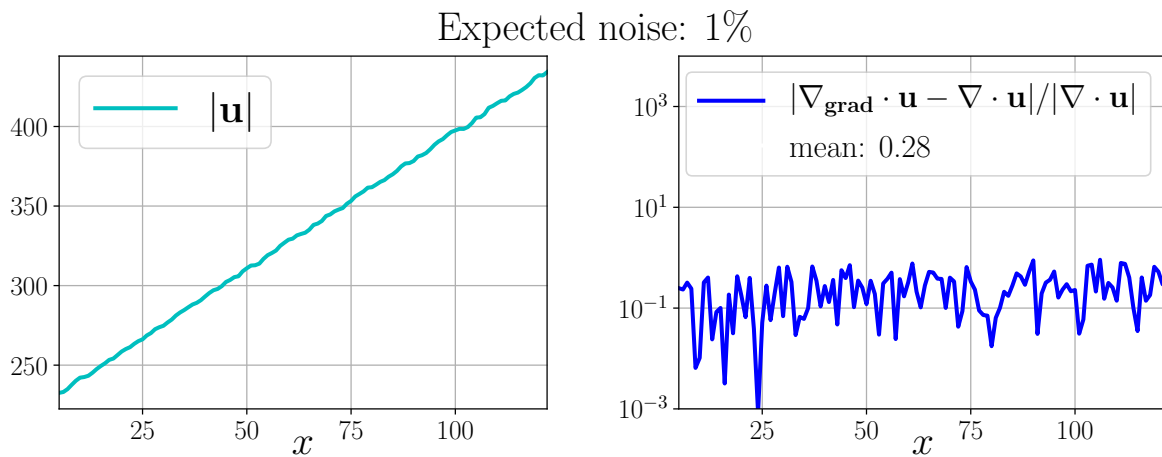


Figure 5.23: Same plots as in figure 5.22 but the velocity field has been perturbed with a noise generated by an uniform distribution of expectation 1% of $|\mathbf{u}|$. The mean value of the error is also displayed on the right panel.

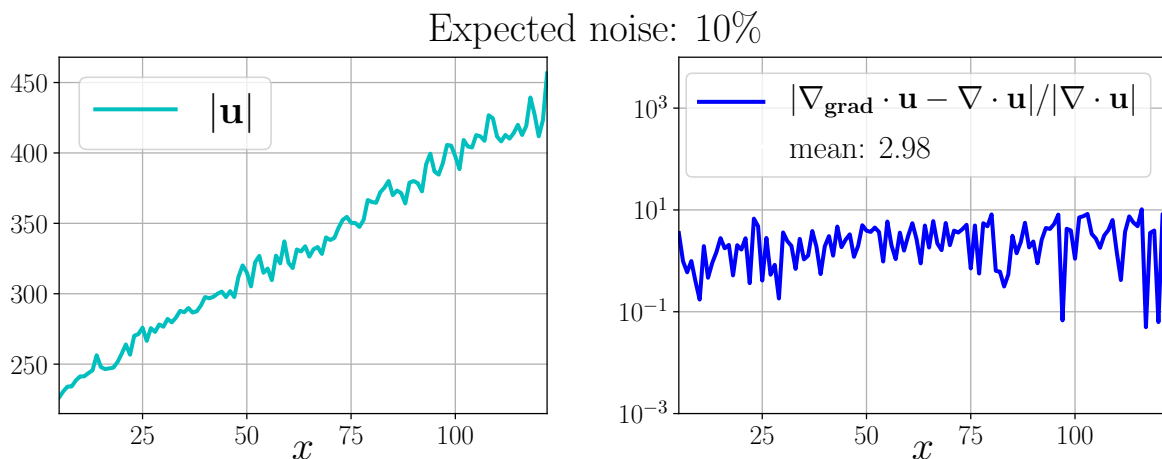


Figure 5.24: Same as in figure 5.23 for a noise generated by an uniform distribution of expectation 10% of $|\mathbf{u}|$.

Similarly to what was done for real MMS data we can smooth the vector fields measured by the satellite formation to reduce the importance of the non-linearities. I applied again a running average with a window size dependent on the separation between the satellites

(here taken equal to one grid resolution). Two tests were run, with a window of size 5 and a window of size 25. We notice that the stronger the smoothing, the more reduced are the errors induced by the gradiometer, which falls in line with the results obtained when smoothing [MMS](#) data. These tests suggest that, as expected, non-linearities of the fields have an impact on the performances of the gradiometer. Their effect, paired with the ones attributed to the weak statistics of the computation, are thus likely to be responsible for the poor results provided overall by the gradiometer in the calculation of the divergence-dependent terms of the turbulence exact laws for *in situ* data.

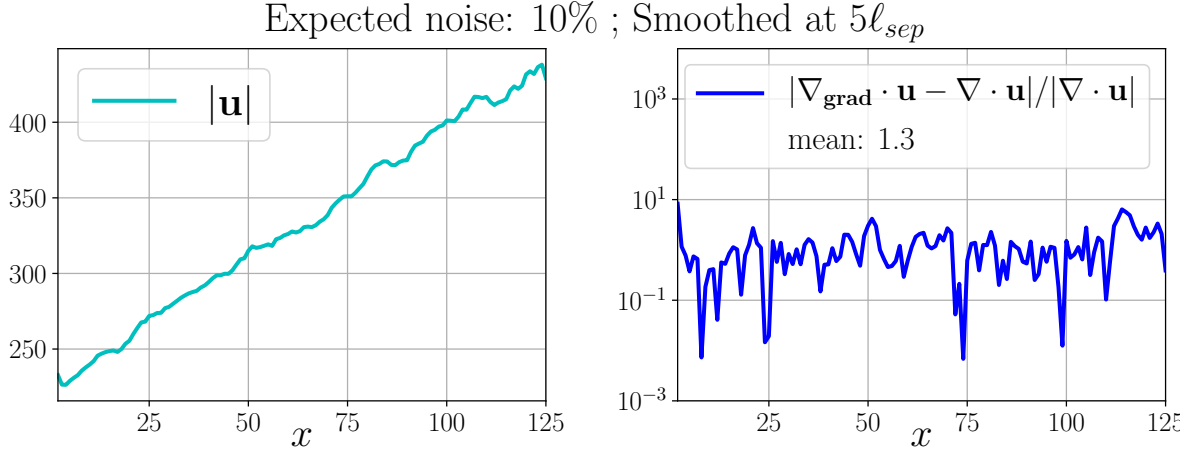


Figure 5.25: Same as in figure 5.24 with a smoothing on the vector fields measured by the virtual satellites through a running average of window of 5 times the satellites separation.

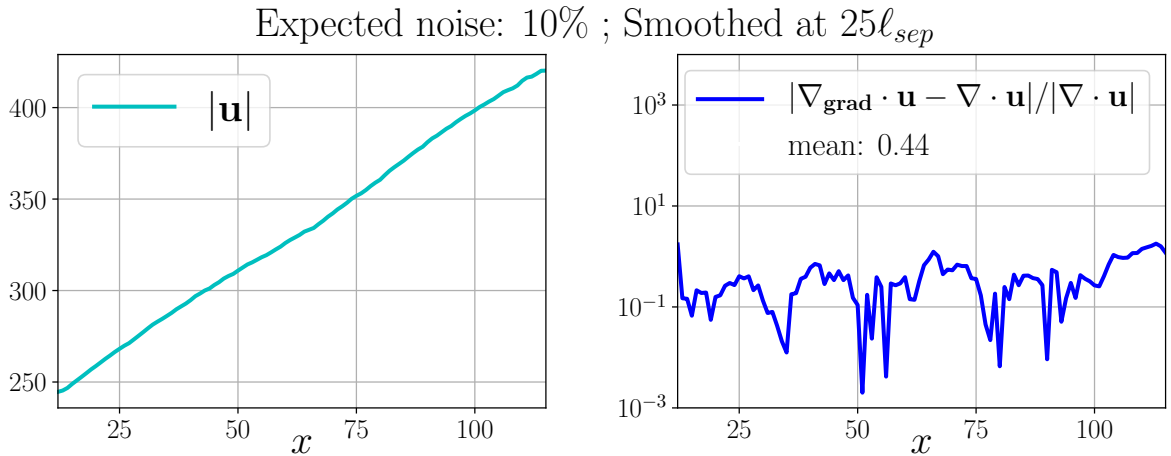


Figure 5.26: Same as in figure 5.24 with a smoothing on the vector fields measured by the virtual satellites through a running average of window of 25 times the satellites separation.

5.6 Conclusion

In this final study, led on *in situ* data gathered by [MMS](#), I proposed a detailed analysis of [MMS](#) data and of the numerical gradiometer techniques. To lead this study, I used [MMS](#) burstmode data to build an ensemble of suitable events to analyze, on which I applied the compressible exact laws [A18](#) and [F21](#). All terms depending on a divergence or gradients are calculated using values measured by the four spacecraft thanks to an extension of the curlometer technique ([Dunlop et al., 1988, 2002](#)) referred to as the gradiometer. It was found that divergence-dependent terms are overall non-negligible in comparison to the other terms, which differs from what was reported in [Andrés et al. \(2019\)](#) due to an error in the calculation. Yet, the

entire flux-based study reported in the aforementioned letter still remains valid, as the large amplitude of these divergence-dependent terms was found in this chapter to be originating from limitations of the gradiometer, and as such they may not be estimated reliably.

The observed limitation on the gradiometer prompted an in-depth study of this method. Through its detailed analysis it was possible to pinpoint two main causes for the potentially important errors: a lack of statistics in [MMS](#) observed events (that could be solved by averaging over very large time intervals), and a non-linearity of the fields between the satellites of [MMS](#) formation. While the lack of statistics is a problem that cannot be solved in current data, the non-linearity problem can be attenuated by smoothing the data measured by the satellites at the cost of losing information at small time scales, which can be problematic if studying turbulence energy dissipation and small scale cascade. Ultimately, introducing divergence-dependent terms in turbulent cascade studies for currently available data proves to be a full-fledged challenge, that would require a new form of data treatment or new methods for derivatives calculation. Note that, considering these limitations, exact law [F21](#) appears to be perfectly suited to the study of sub-ion turbulence in *in situ* data, as its Hall components do not feature any divergence-dependent term.

The conclusions drawn in this chapter may appear concerning, yet they bring important information on limitations one needs to remain aware of when working on space plasma turbulence with *in situ* data. More importantly, as we were able to pinpoint the possible causes of error as essentially originating from the geometry of [MMS](#) mission, the studies developed here bring new arguments in favor of newly designed multi-spacecraft missions such as Cross-scale or EIDOScope previously proposed at [ESA](#) ([Schwartz et al., 2009](#); [Vaivads et al., 2012](#)) or, more recently, [NASA](#)'s Helioswarm that should receive a final answer on its validation around the end of this year and [ESA](#)'s Debye ([Verscharen et al., 2021](#)). By increasing the number of satellites and positioning them to define multiple spatial scales, it is possible to increase both the statistics of turbulent studies (by increasing the number of "lines" on which the properties of the plasma are measured) and to improve the results of the gradiometer by providing multiple scales at which we could compute the divergences, as well as providing means to investigate non-linearities of the fields between the most distant satellites.

It would be interesting to complement the work presented here by additional studies, such as introducing perturbations on a single spacecraft to test how the gradiometer would react to a single satellite flying in a localized turbulent structure, or pushing further the analysis of non divergence-dependent cascade terms on [MMS](#) events. Such ideas are postponed to a near future.

The study presented in this final chapter follows initial results that were reported in [Andrés, Sahraoui, Galtier, Hadid, Ferrand, and Huang \(2019\)](#) [*Physical Review Letters* **123**]. It is currently being finalizing and should be published in an upcoming paper.

Chapter 6

Conclusions and perspectives

6.1 Summary of the thesis

The detailed study of the physics governing turbulent plasmas, and even turbulent flows in general, is still to this day a vast and active research field in physics. Encompassing hard theoretical work, numerical simulations calculation and analysis, experiments on artificial turbulent flows (in wind tunnels for example) and *in situ* satellite data analysis for turbulent astrophysical plasmas, the angles through which one can approach turbulence are numerous, and its applications are even more. The **SW** in itself has drawn lots of attention for many decades, by virtue of being a naturally turbulent plasma as well as an important laboratory for plasma data measurement, allowing for in-depth turbulence studies.

In this thesis I present a broad approach of **SW** plasma turbulence through a continuity of interconnected studies. I first handle the theoretical derivation of exact laws for **IHMHD** and **CHMHD** plasma models, complementing the toolbox that already existed for analyzing turbulent energy cascades. The theoretical calculations are then transposed into a numerical Python code, allowing for the practical study of both simulated and measured turbulent flows. The tools developed in the scope of this theoretical work are then applied to a variety of **DNS** data, based on different models and featuring various physical effects, with the aim of honing our understanding of either turbulent flows themselves, or of the exact laws used to study them. These **DNS** studies, led in a controlled environment, pave the way to the challenge of analyzing satellite data by providing important keys to interpret the results obtained on these *in situ* data. Through the intertwined studies made on simulated and measured turbulent plasmas, we can slowly unravel the physics governing complex turbulent media such as the **SW**, the magnetosheath or the **ISM**.

In this final chapter, I will return on each major step of this thesis and summarize the results obtained. It will also be the occasion to highlight both the strengths and weaknesses of the methods presented in previous chapters, and to pinpoint potential improvements that could be made in the future.

6.2 Tools for turbulence analysis

6.2.1 Derivation of exact laws

The first chapter of this thesis is dedicated to the hard mathematics. Throughout chapter 2, I propose a detailed mathematical derivation of two turbulence exact laws for the plasma models of IHMHD and isothermal CHMHD. Both exact laws are derived under the usual assumptions of statistical homogeneity, statistical stationarity, and large Reynolds numbers.

For the IHMHD model the new exact law F19 comes as the third of its kind, following exact laws G08 and BG17. Unlike the previous ones, this new law takes the form of a typical Yaglom-like flux of third-order moments, similarly to other laws for incompressible HD or MHD models (Antonia et al., 1997; Politano and Pouquet, 1998). The three IHMHD laws are proved to be mathematically equivalent under the aforementioned assumptions, allowing one to safely choose which one to use based on the data available. Typically, F19 can be readily calculated on satellite data provided that the current density is measured, and BG17 is free from directionality constraints by virtue of not being a flux term. All exact laws are also found to be mathematically independent on an eventual background magnetic field \mathbf{B}_0 , which means that the amplitude of the mean field will not change directly the values of the energy cascade rate, but can only influence it through the way it shapes the turbulent dynamics.

Exact law F21, derived for the isothermal CHMHD model, comes after the other law A18 derived by Andrés et al. (2018). It involves less components overall, which makes it easier to compute numerically, and its flux and Hall components are directly reminiscent of their IHMHD counterparts from BG17 and F19. However, contrary to the IHMHD case, this law remains dependent on the direct value of the background magnetic field. Also, no mathematical equivalence could be obtained between A18 and F21. Being derived for a CHMHD model, this law can be degraded by considering various limit cases such as IHMHD, MHD or CHD to obtain other laws pertaining to these respective models. One such law, obtained in the CHD limit, is later used to study a DNS dataset in chapter 4.

With three exact laws providing various advantages and points of view, we now have more than enough tools to lead basic studies on IHMHD turbulent cascades. For CHMHD however a lot of work still remains to be done. First of all, it would be interesting in further developments to try to find an analytical equivalence between A18 and F21 as was done for the IHMHD laws, or to unveil possible specific conditions that would lead to such a relation. Then, more generally one has to keep in mind that these laws only cover isothermal flows. It would be interesting to have access to similar exact laws for other models, such as ones using a CGL or a polytropic closure. Fortunately, with recent developments on generalized isentropic CHMHD exact laws (Simon and Sahraoui, 2021), the future of this aspect appears to be in good hands.

6.2.2 Numerical implementation of the exact laws

Following the derivation of exact laws, chapter 3 is dedicated to the development of a Python code able to calculate them on either DNS or satellite data. This chapter presents the general method adopted to select the increment vectors and scan various directions in the datasets, and discuss the technical implementation and limitations tied to the execution time and memory constraints.

In order to compute the exact laws in 3D periodic DNS datasets, we need to average the different terms spatially over a large number of pairs of points, connected by an increment vector ℓ . In the code I wrote, I first set a vector ℓ and then average on all available pairs in the datasets. The selection of the increments vector follows the angle-averaging technique developed by Taylor et al. (2003), where all increments are multiples of an initial set of base vectors defined spherically on the simulation grid. This ensures that for a point \mathbf{r} on the grid, the associated point $\mathbf{r}' = \mathbf{r} + \ell$ also lies on the grid, avoiding the needs for 3D data

interpolation. Once the calculation of the exact laws is done for each value of ℓ , the results are averaged using either an axi-symmetry (around the background magnetic field) or an isotropy assumption, depending on the data studied.

This method works especially well for datasets with no background magnetic field, as the isotropy hypothesis is usually well verified statistically. However, it faces some limitations for anisotropic data due to the irregular angular spacing of the increment vectors imposed by this method. Indeed, if we choose to compute the laws with the axi-symmetry assumption, fluxes can only be calculated along directions orthogonal to the background field only, averaging on the parallel direction, or inversely along directions parallel to the field only, averaging on orthogonal directions. In both cases, either the parallel or orthogonal flux variations have to be discarded. On the other hand, if we choose to use the isotropic decomposition we retain the entire flux dynamics, but the resulting average on increment vectors is ill defined as the data is not, *a priori*, isotropic. In the end, one needs to find for each given case which method gives the most plausible results.

The aforementioned limitations did not hinder too much the DNS data analyses presented in this thesis, as it was systematically possible to find a fitting method to calculate the exact laws. Nevertheless it appears important in the long term to have access to another method of calculation that could allow for the calculation of flux terms as a function of ℓ_{\perp} and ℓ_z simultaneously. This could be done by fully interpolating the datasets in 3D and working with increments defined on regular Cartesian coordinates. This would simplify the calculation of spatial derivatives, as increment vectors would be evenly spaced in all three Cartesian directions. Such a code would allow to see the relative importance of the transverse and parallel fluxes depending on the direction of the increment vector.

On a more technical note, chapter 3 also presents the parallelization and memory optimization techniques adopted in the numerical code. The parallelization was done by splitting the datasets in slices cut along the direction of the mean background field (or the z-axis otherwise), each CPU computing all terms of the laws on its own slice only. It is also possible to only open a part of the data at once to reduce memory usage. However, these methods are more limited when working with non-transverse increments as the overhead cost of communications between CPUs quickly add to the execution time. The code could maybe be improved further by giving to each CPU access to an external file containing the relevant parts of the data.

6.3 Studying turbulent flows through DNSs

6.3.1 In-depth analysis of exact laws

The theoretical and numerical methods developed in chapters 2 and 3 are used in chapter 4 to analyze 4 ensembles of datasets. The first two, simulated for models of EMHD and CHMHD, are used to lead an in-depth study of the incompressible and compressible exact laws respectively.

The EMHD datasets allow for a direct verification of how the Hall components of the three laws G08, BG17 and F21 relate to one another. It is found that the three laws are indeed equivalent, with a slight deviation on BG17 probably due to its different nature as a non-flux term. The influence of \mathbf{B}_0 is also investigated and laws BG17 and F21 are, as expected, found to be totally independent on the direct value of the background field. G08 however shows a slight dependence on the presence of \mathbf{B}_0 . This may suggest that this law is more sensitive to deviations from the hypotheses, especially the homogeneity one, in which case the terms depending on \mathbf{B}_0 would not cancel out properly.

The CHMHD datasets were simulated as part of this thesis using the GHOST code, and consist of three decaying datasets of various background magnetic fields and Mach numbers. Their study reveals that the MHD and Hall terms of compressible laws A18 and F21 provide equivalent results. The in-depth study of F21 shows that the MHD source term is negligible in

comparison to the flux one, and that the two Hall components differ from a -2 multiplicative factor, just as their incompressible counterparts. The total energy cascade rate is shown to be reduced in the run with a non-zero background magnetic field, indicating that as expected this background field influences the cascade rate through the way it alters the dynamics of the system.

The decaying nature of the three simulations led to investigating the behavior of the compressible laws in a more general form, disregarding the usual stationarity assumption. The resulting equations appear as a mixture of the usual terms of the laws, instantaneous dissipation terms and time derivatives of the energy of correlation functions. The study of these terms shows that the equation behaves as if energy was stored at each scale of the system and distributed between the cascade and dissipation mechanisms. An error residue, overall constant in scale, was observed when calculating this equation and corresponds to the error on the calculation of time derivatives. This error is amplified for the run with $B_0 \neq 0$ for which the energy shows important fluctuations: the error residue corresponds to the local fluctuation at the times considered.

Note that due to the small value of the ion inertial length d_i used in these simulations, the Hall effect remains low at all scales in the three runs. Thus, these datasets do not allow us to investigate in details the relations between the MHD and Hall cascade as we would have liked to. Running simulations, perhaps at a lower resolution, with an increased value of d_i and/or implementing hyperdissipation in GHOST could help solving this problem and expanding this study.

6.3.2 Relation between the fluid cascade and kinetic dissipation

The next study, presented in section 4.4, tackles the fundamental question of the relation between the fluid energy cascade rate and kinetic dissipation. It makes use of a set of CGL and LF simulations that feature a "toggleable" and adjustable ionic and electronic Landau damping, allowing for an analysis of the energy cascade rate depending on the presence and strength of kinetic damping. The datasets are forced at three different scales in order to offer information on the cascade over the largest possible range of scales.

These datasets are studied with the incompressible law F19 due to their weakly compressible nature. They reveal that Landau damping attenuates the energy cascade at all scales of the system, but more prominently at sub-ion scales. The hyperdissipation matches the remaining energy at dissipation scales, indicating that the energy cascade is indeed representative of the energy transitioning from the forcing range to the dissipative terms. The amount of thermal energy transferred by Landau damping at given scales was specifically calculated, and was found to match the amount of energy lost by the energy cascade over the same scales, proving that the fluid energy cascade rate was indeed able to estimate the amplitude of kinetic dissipation in the simulations.

This study is of high importance, as it brings new evidences legitimating the use of the energy cascade rate and exact laws when studying dissipation mechanisms in either DNS data or satellite data. However, this is only a first step, as we are still unable to separate the contributions to the loss of the cascade rate of the various dissipation mechanisms at work in complex media such as the SW. It would be very beneficial to lead similar studies on simulations featuring a larger array of kinetic mechanisms to see how each of them influences the energy cascade rate, how they compare to one another, and how they depend on the scales considered. This would hand us precious keys to better understand results obtained in natural turbulent media and allow for the identification of specific dissipative processes.

6.3.3 Supersonic CHD turbulence in the ISM

The last study led on DNS data, presented in section 4.5, makes use of massive 10048^3 CHD simulations run with the FLASH code and aim at understanding how turbulence shape highly

supersonic regions of the ISM, notably star forming regions. They are analyzed thanks to the CHD reduction of law F21.

The sole calculation of the energy cascade rate shows an important interplay between its positive flux and negative source components, the latter not being negligible anymore in contrast to what was found in less compressible cases for the CHMHD law for example. This interplay leads to a constant energy cascade rate at all subsonic scales, despite neither of the two components being constant individually. The signs and amplitude of these components can be interpreted by considering the flux as an effective cascade rate, similar to what is found in incompressible laws, that is then amplified or reduced by respectively a compression or a dilatation of the medium.

Taking a look at vorticity and density-dilatation cuts of the data cubes reveals the existence of elongated, filamentary structures of very high density, compression and turbulent activity. The application of the exact laws within these regions, and on outside regions for comparison, shows that most of the turbulent cascade is concentrated in these turbulent structures whose width is of the same order as the sonic scale measured in the system. These findings point towards the existence of two turbulent regimes in the simulation, which is confirmed by the evaluation of the kinetic spectrum and of absolute laws components: a supersonic, large scale regime driven by shocks through Burgers-like turbulence, and a small scale subsonic regime more akin to standard (acoustic) turbulence, featuring a scale-to-scale energy cascade. The break point lying around the sonic scale suggests that this duality of regimes play a role in the formation and stabilization of the observed turbulent structures and, in the context of the ISM, of interstellar filaments: dense regions of matter collapsing through the supersonic movements of the flow, and internally stabilized by the action compressible turbulence.

These CHD datasets already bring lots of information on the whereabouts of supersonic turbulence in the ISM, yet one could wonder how these results would be altered by the introduction of a magnetic field, and a transition towards a CMHD description of the medium. The main advantage of the run studied in this section is its unprecedented resolution, that would be difficult to reproduce for a more complex, magnetized model. Nevertheless, should the occasion to apply the laws to such datasets (even of reduced resolution) arise, it would bring a highly valuable addition to the conclusions exposed in this study.

6.4 MMS *in situ* data analysis

6.4.1 Selection and exploitation of the data

The final study presented in chapter 5 aims at analyzing satellite data measured by MMS in the Earth's magnetosheath, and investigating a numerical technique used for multi-spacecraft data analysis known as the curlometer technique, that we extend under the designation of gradiometer.

The events to be studied are selected among MMS burstmode measurements following several criteria: the magnetic spectrum must follow a Kolmogorov scaling of $-5/3$ in the MHD region, the angle between the velocity and magnetic fields must remain as constant as possible, and the time series for the magnetic field and particle density must show no clear evidence of sudden changes of regime (such as, for instance, the entry of the formation in the inner magnetosphere). The manual selection following these criteria led to building an ensemble of 146 events. Note that there is still room for expanding this events set: of the 1351 burstmode time series of minimal duration of 200s that I first downloaded, I only looked at the first 236 ones to select these 146 events, which already was a lengthy process.

Nevertheless, the application of the compressible exact laws to these 146 events already bring lots of information through a statistical study. By comparing terms depending or not on divergences or gradients of the vector fields we observe that divergence-dependent terms, calculated with the gradiometer, are either of the same order of magnitude as the other terms of largely dominant, contrasting sharply with results obtained on different DNS datasets that

all showed divergence-dependent terms to be negligible. This behavior is a lot more prominent for the so-called **MHD** source terms of law **A18**. The non divergence-dependent **MHD** terms of both laws were also found to be statistically matching, but not the Hall ones that seem to be underestimated by **F21**. An in-depth study specifically focused on the Hall terms would be required to try to understand this discrepancy better.

6.4.2 Investigation of the gradiometer

The high values obtained for divergence-dependent terms are thought to be originating from errors in the calculation of divergences with the gradiometer. This is evidenced by the fact that all components of the current density calculated with this technique are overall underestimated in comparison to the one measured by the **FPI**. The minimal error on the gradiometer is estimated by computing terms of **A18** that depend on $\nabla \cdot \mathbf{v}_A$ while setting the density to a constant value: in this case these terms should depend on $\nabla \cdot \mathbf{B} = 0$ instead, and their amplitude would provide a lower bound below which gradiometer estimates cannot be trusted. This lower bound is found to be of the same order of magnitude as the non divergence-dependent terms, and even of some divergence-dependent terms, indicating that these estimates should not be trusted at all in the calculation of the cascade rates presented in chapter 5.

Then, several possible causes of the poor performances of the gradiometer are investigated. The regularity of the tetrahedral satellite formation is shown to not be responsible for these performances, as only extreme deformations (that are not observed in the selected events) are expected to really have an influence on the gradiometer. A smoothing of the time series, performed with a running average on a window whose size is equal to several times the separation between satellites, is shown to improve the performances of the gradiometer by reducing the lower bound on the error. This result suggests that the gradiometer could be strongly affected by the non-linearity of the fields between the satellites.

In order to test this hypothesis, and investigate further the gradiometer, an artificial **MMS** fly-by is performed in one of the **GHOST** runs studied in section 4.3. The data measured by this virtual spacecraft are used to calculate the terms of **A18** exactly as they would be on real **MMS** data, and the results are compared to the terms obtained directly with the direct numerical calculation on the same trajectory as the virtual spacecraft. The quality of the gradiometer is seen to be degrading as the distance between the satellites increase. More surprisingly, the sum of all **MHD** divergence-dependent terms is never found to be negligible in comparison to the flux term, as it should normally be, even for the direct reference calculation. This odd behavior disappears if we proceed to a spatial average over the entire simulation domain instead of just the trajectory of the spacecraft, indicating that having strong statistics plays a much bigger role than expected in the correct calculation of exact laws.

Finally, as an ultimate test, the virtual spacecraft is launched in a handmade dataset linear in all directions of space, that thus meets all the prerequisites for the use of the gradiometer. The estimate from the gradiometer is found to be perfectly matching the direct calculation in this case. However, introducing noise in the dataset is shown to quickly degrade the performances, indicating that the hypothesis of linearity of the fields is important in the application of the gradiometer. Smoothing the noisy data, as was done on **MMS** data, allow for retrieving partly the good performances of the gradiometer, similarly to results obtained on the *in situ* data.

All of these tests on the gradiometer point towards a similar conclusion: the gradiometer may not be suited for the calculation of turbulence exact laws, or at least not for currently available data. Thus, exact law **F21** appears as a natural fit to study Hall turbulence from *in situ* data, its Hall part being made of no divergence-dependent term. The needs for increased spatial statistics and better linearity (or at least ways to measure the linearity) of the fields between the spacecraft, highlighted by the limitations on the gradiometer, are constraints that should be taken into account in the definition of future multi-spacecraft **SW** missions to allow for a more complete investigation of turbulence exact laws in astrophysical plasmas.

6.5 Final words and perspectives

The complete study of plasma turbulence developed through this thesis shed a new light on the analysis of natural turbulent plasmas from different points of view. By giving access to new theoretical exact laws, it provides new means to estimate the turbulent energy cascade rate in various media and allow for more adaptability depending on the constraints imposed by the available data. By delving into the sub-ion scales behavior of the turbulent cascade, it partly reconciles the kinetic and fluid descriptions of plasmas and paves the way to a better understanding of kinetic dissipation in the [SW](#). By revealing and understanding the weaknesses of numerical methods used in multi-spacecraft data analysis, it brings new arguments to plan the future of space plasmas investigation.

Of course much work remains to be done, either about theoretical developments and about our generalized understanding of the complex physics governing turbulent plasmas. Exact laws for turbulence would need to be adapted to more complete plasma descriptions, and need to be tested on more varied and complete [DNS](#) datasets to grasp fully their particularities and better formulate subsequent physical interpretations. The correlation found between Landau damping and the turbulence cascade rate is merely a first step in constructing a more complete picture of dissipation through the use of fluid models, that would make the in-depth understanding of plasma turbulence truly possible. Also, now that we thoroughly investigated what does not work in satellite data analysis, a natural follow up would be to see how we can make it work ! For all these future applications, we believe that the results presented in this thesis will prove to be valuable starting points or developments, that will hopefully set the first stones of meaningful advances in the study of astrophysical plasmas.

Bibliography

- Aluie, H., Li, S., and Li, H.: *Conservative cascade of kinetic energy in compressible turbulence*, *Astrophys. J. Lett.*, **751**, L29, <https://doi.org/10.1088/2041-8205/751/2/L29>, 2012. [88](#)
- Andrés, N. and Sahraoui, F.: *Alternative derivation of exact law for compressible and isothermal magnetohydrodynamics turbulence*, *Phys. Rev. E*, **96**, 053205, <https://doi.org/10.1103/PhysRevE.96.053205>, 2017. [12](#)
- Andrés, N., Galtier, S., and Sahraoui, F.: *Exact law for homogeneous compressible Hall magnetohydrodynamics turbulence*, *Phys. Rev. E*, **97**, 013204, <https://doi.org/10.1103/PhysRevE.97.013204>, 2018. [12](#), [25](#), [31](#), [56](#), [97](#), [116](#), [133](#)
- Andrés, N., Sahraoui, F., Galtier, S., Hadid, L., Dmitruk, P., and Mininni, P.: *Energy cascade rate in isothermal compressible magnetohydrodynamic turbulence*, *J. Plasma Phys.*, **84**, 1–21, <https://doi.org/10.1017/S0022377818000788>, 2018. [35](#), [38](#), [43](#), [47](#), [51](#), [54](#), [81](#), [98](#), [99](#), [111](#)
- Andrés, N., Sahraoui, F., Galtier, S., Hadid, L. Z., Ferrand, R., and Huang, S. Y.: *Energy Cascade Rate Measured in a Collisionless Space Plasma with MMS Data and Compressible Hall Magnetohydrodynamic Turbulence Theory*, *Phys. Rev. Lett.*, **123**, 245101, <https://doi.org/10.1103/PhysRevLett.123.245101>, 2019. [81](#), [91](#), [95](#), [96](#), [97](#), [98](#), [99](#), [107](#), [113](#), [114](#)
- Antonia, R., Ould-Rouis, M., Anselmet, F., and Zhu, Y.: *Analogy between predictions of Kolmogorov and Yaglom*, *J. Fluid Mech.*, **332**, 395–409, <https://doi.org/10.1017/S0022112096004090>, 1997. [17](#), [22](#), [116](#)
- Arzoumanian, D., André, Ph., Didelon, P., Könyves, V., Schneider, N., Men'shchikov, A., Sousbie, T., Zavagno, A., Bontemps, S., Di Francesco, J., Griffin, M., Hennemann, M., Hill, T., Kirk, J., Martin, P., Minier, V., Molinari, S., Motte, F., Peretto, N., Pezzuto, S., Spinoglio, L., Ward-Thompson, D., White, G., and Wilson, C. D.: *Characterizing interstellar filaments with Herschel in IC 5146*, *Astron. & Astrophys.*, **529**, L6, <https://doi.org/10.1051/0004-6361/201116596>, 2011. [79](#), [88](#)
- Bale, S. D., Kellogg, P. J., Mozer, F. S., Horbury, T. S., and Reme, H.: *Measurement of the Electric Fluctuation Spectrum of Magnetohydrodynamic Turbulence*, *Phys. Rev. Lett.*, **94**, 215002, <https://doi.org/10.1103/PhysRevLett.94.215002>, 2005. [91](#)
- Balsara, D., Ward-Thompson, D., and Crutcher, R.: *A turbulent MHD model for molecular clouds and a new method of accretion on to star-forming cores*, *Mon. Not. Roy. Astron. Soc.*, **327**, 715–720, <https://doi.org/10.1046/j.1365-8711.2001.04787.x>, 2001. [9](#)
- Bandyopadhyay, R., Sorriso-Valvo, L., Chasapis, A., Hellinger, P., Matthaeus, W., Verdini, A., Landi, S., Franci, L., Matteini, L., Giles, B., Gershman, D., Moore, T., Pollock, C., Russell, C., Strangeway, R., Torbert, R., and Burch, J. L.: *In Situ Observation of Hall Magnetohydrodynamic Cascade in Space Plasma*, *Phys. Rev. Lett.*, **124**, 225101, <https://doi.org/10.1103/PhysRevLett.124.225101>, 2020. [61](#), [77](#), [91](#)

- Banerjee, S. and Galtier, S.: *Exact relation with two-point correlation functions and phenomenological approach for compressible magnetohydrodynamic turbulence*, Phys. Rev. E, **87**, 013 019, <https://doi.org/10.1103/PhysRevE.87.013019>, 2013. [12](#)
- Banerjee, S. and Galtier, S.: *A Kolmogorov-like exact relation for compressible polytropic turbulence*, J. Fluid Mech., **742**, 230–242, <https://doi.org/10.1017/jfm.2013.657>, 2014. [12](#)
- Banerjee, S. and Galtier, S.: *An alternative formulation for exact scaling relations in hydrodynamic and magnetohydrodynamic turbulence*, J. Phys. A: Math. Theo., **50**, 015 501, <https://doi.org/10.1088/1751-8113/50/1/015501>, 2017. [12](#), [19](#), [30](#), [133](#)
- Banerjee, S., Hadid, L., Sahraoui, F., and Galtier, S.: *Scaling of compressible magnetohydrodynamic turbulence in the fast solar wind*, Astrophys. J. Lett., **829**, L27, <https://doi.org/10.3847/2041-8205/829/2/L27>, 2016. [8](#), [47](#), [61](#)
- Behar, E., Sahraoui, F., and Berčić, L.: *Resonant Whistler-Electron Interactions: MMS Observations Versus Test-Particle Simulation*, Journal of Geophysical Research: Space Physics, **125**, e2020JA028 040, <https://doi.org/10.1029/2020JA028040>, 2020. [93](#)
- Biskamp, D., Schwarz, E., and Drake, J. F.: *Two-Dimensional Electron Magnetohydrodynamic Turbulence*, Phys. Rev. Lett., **76**, 1264–1267, <https://doi.org/10.1103/PhysRevLett.76.1264>, 1996. [13](#)
- Bruno, R. and Carbone, V.: *The Solar Wind as a Turbulence Laboratory*, Living Rev. Solar Phys., **10**, 2, <https://doi.org/10.12942/lrsp-2013-2>, 2013. [8](#)
- Carbone, V., Marino, R., Sorriso-Valvo, L., Noullez, A., and Bruno, R.: *Scaling Laws of Turbulence and Heating of Fast Solar Wind: The Role of Density Fluctuations*, Phys. Rev. Lett., **103**, 061 102, <https://doi.org/10.1103/PhysRevLett.103.061102>, 2009. [8](#), [61](#)
- Chen, C. H. K. and Boldyrev, S.: *Nature of Kinetic Scale Turbulence in the Earth's Magnetosheath*, Astrophys. J., **842**, 122, <https://doi.org/10.3847/1538-4357/aa74e0>, 2017. [98](#)
- Chen, C. H. K., Klein, K. G., and Howes, G. G.: *Evidence for electron Landau damping in space plasma turbulence*, Nat. Commun., **10**, 740, <https://doi.org/10.1038/s41467-019-08435-3>, 2019. [61](#)
- Chew, G. F., Goldberger, M. L., and Low, F. E.: *The Boltzmann equation and the one-fluid hydromagnetic equations in the absence of particle collisions*, Proc. Roy. Soc. A, **236**, 112–118, <https://doi.org/10.1098/rspa.1956.0116>, 1956. [4](#), [62](#)
- Cho, J. and Lazarian, A.: *Simulations of Electron Magnetohydrodynamic Turbulence*, Astrophys. J., **701**, <https://doi.org/10.1088/0004-637X/701/1/236>, 2009. [67](#)
- Coburn, J., Forman, M., Smith, C., Vasquez, B., and Stawarz, J.: *Third-moment descriptions of the interplanetary turbulent cascade, intermittency and back transfer*, Philos. Trans. Roy. Soc. A, **373**, 20140 150, <https://doi.org/10.1098/rsta.2014.0150>, 2015. [8](#), [61](#), [91](#)
- Dubey, A., Fisher, R., Graziani, C., Jordan, G. C., I., Lamb, D. Q., Reid, L. B., Rich, P., Sheeler, D., Townsley, D., and Weide, K.: *Challenges of Extreme Computing using the FLASH code*, Astron. Soc. Pac. Conference series, **385**, 145, 2008. [79](#)
- Duchon, J. and Robert, R.: *Inertial energy dissipation for weak solutions of incompressible Euler and Navier-Stokes equations*, Nonlinearity, **13**, 249–255, <https://doi.org/10.1088/0951-7715/13/1/312>, 2000. [12](#), [81](#)
- Dunlop, M., Southwood, D., Glassmeier, K.-H., and Neubauer, F.: *Analysis of multipoint magnetometer data*, Adv. Space Res., **8**, 273–277, [https://doi.org/10.1016/0273-1177\(88\)90141-X](https://doi.org/10.1016/0273-1177(88)90141-X), 1988. [7](#), [93](#), [101](#), [102](#), [113](#)

- Dunlop, M. W., Balogh, A., Glassmeier, K.-H., and Robert, P.: *Four-point Cluster application of magnetic field analysis tools: The Curlometer*, J. Geophys. Res.: Space Phys., **107**, SMP 23–1–SMP 23–14, <https://doi.org/10.1029/2001JA005088>, 2002. [7](#), [93](#), [113](#)
- Eyink, G. L.: *Local 4/5-law and energy dissipation anomaly in turbulence*, Nonlinearity, **16**, 137–145, <https://doi.org/10.1088/0951-7715/16/1/309>, 2002. [12](#)
- Federrath, C.: *On the universality of supersonic turbulence*, Mon. Not. Roy. Astron. Soc., **436**, 1245–1257, <https://doi.org/10.1093/mnras/stt1644>, 2013. [79](#)
- Federrath, C.: *On the universality of interstellar filaments: theory meets simulations and observations*, Mon. Not. Roy. Astron. Soc., **457**, 375–388, <https://doi.org/10.1093/mnras/stv2880>, 2016. [9](#), [79](#), [88](#)
- Federrath, C. and Klessen, R. S.: *The star formation rate of turbulent magnetized clouds: comparing theory, simulations and observations*, Astrophys. J., **761**, 156, <https://doi.org/10.1088/0004-637x/761/2/156>, 2012. [78](#), [88](#)
- Federrath, C., Klessen, R. S., and Schmidt, W.: *The Fractal Density Structure in Supersonic Isothermal Turbulence: Solenoidal Versus Compressive Energy Injection*, Astrophys. J., **692**, 364–374, <https://doi.org/10.1088/0004-637X/692/1/364>, 2009. [79](#)
- Federrath, C., Roman-Duval, J., Klessen, R. S., Schmidt, W., and Mac Low, M.-M.: *Comparing the statistics of interstellar turbulence in simulations and observations. Solenoidal versus compressive turbulence forcing*, Astron. & Astrophys., **512**, A81, <https://doi.org/10.1051/0004-6361/200912437>, 2010. [9](#), [79](#), [82](#)
- Federrath, C., Klessen, R. S., Iapichino, L., and Hammer, N. J.: *The world’s largest turbulence simulations*, arXiv e-prints, arXiv:1607.00630, 2016. [44](#)
- Federrath, C., Klessen, R. S., Iapichino, L., and Beattie, J. R.: *The sonic scale revealed by the world’s largest supersonic turbulence simulation*, <https://doi.org/10.1038/s41550-020-01282-z>, 2020. [79](#), [86](#)
- Federrath, C., Klessen, R. S., Iapichino, L., and Beattie, J. R.: *The sonic scale of interstellar turbulence*, Nat. Astron., **5**, 365–371, <https://doi.org/10.1038/s41550-020-01282-z>, 2021. [44](#), [79](#), [81](#), [87](#)
- Ferrand, R., Galtier, S., Sahraoui, F., Meyrand, R., Andrés, N., and Banerjee, S.: *On Exact Laws in Incompressible Hall Magnetohydrodynamic Turbulence*, Astrophys. J., **881**, 50, <https://doi.org/10.3847/1538-4357/ab2be9>, 2019. [19](#), [31](#), [89](#), [133](#)
- Ferrand, R., Galtier, S., Sahraoui, F., and Federrath, C.: *Compressible Turbulence in the Interstellar Medium: New Insights from a High-resolution Supersonic Turbulence Simulation*, Astrophys. J., **904**, 160, <https://doi.org/10.3847/1538-4357/abb76e>, 2020. [89](#)
- Ferrand, R., Galtier, S., and Sahraoui, F.: *A compact exact law for compressible isothermal Hall magnetohydrodynamic turbulence*, J. Plasma Phys., **87**, 905870 220, <https://doi.org/10.1017/S0022377821000374>, 2021a. [31](#), [133](#)
- Ferrand, R., Sahraoui, F., Laveder, D., Passot, T., Sulem, P., and Galtier, S.: *Fluid energy cascade rate and kinetic damping: new insight from 3D Landau-fluid simulations*, Astrophys. J. (accepted), 2021b. [89](#)
- Frisch, U.: *Turbulence*, Cambridge University Press, <https://doi.org/10.1017/CBO9781139170666>, 1995. [87](#)

- Fryxell, B., Olson, K., Ricker, P., Timmes, F. X., Zingale, M., Lamb, D. Q., MacNeice, P., Rosner, R., Truran, J. W., and Tufo, H.: *FLASH: An Adaptive Mesh Hydrodynamics Code for Modeling Astrophysical Thermonuclear Flashes*, *Astrophys. J. Suppl.*, **131**, 273–334, <https://doi.org/10.1086/317361>, 2000. [79](#)
- Galtier, S.: *von Kármán-Howarth equations for Hall magnetohydrodynamic flows*, *Phys. Rev. E*, **77**, 015 302, <https://doi.org/10.1103/PhysRevE.77.015302>, 2008. [12](#), [19](#), [22](#), [30](#), [133](#)
- Galtier, S.: *Introduction to Modern Magnetohydrodynamics*, Cambridge University Press, <https://doi.org/10.1017/CBO9781316665961>, 2016. [20](#), [24](#)
- Galtier, S.: *On the origin of the energy dissipation anomaly in (Hall) magnetohydrodynamics*, *J. Phys. A: Math. Theo.*, **51**, 205 501, <https://doi.org/10.1088/1751-8121/aabbb5>, 2018. [81](#)
- Galtier, S. and Banerjee, S.: *Exact Relation for Correlation Functions in Compressible Isothermal Turbulence*, *Phys. Rev. Lett.*, **107**, 134 501, <https://doi.org/10.1103/PhysRevLett.107.134501>, 2011. [12](#)
- Gazis, P. R., Barnes, A., Mihalov, J. D., and Lazarus, A. J.: *Solar wind velocity and temperature in the outer heliosphere*, *J. Geophys. Res.: Space Phys.*, **99**, 6561–6573, <https://doi.org/10.1029/93JA03144>, 1994. [7](#)
- Gómez, D. O., Mininni, P. D., and Dmitruk, P.: *Parallel Simulations in Turbulent MHD*, *Phys. Scripta*, p. 123, <https://doi.org/10.1238/physica.topical.116a00123>, 2005. [48](#)
- Hadid, L., Sahraoui, F., and Galtier, S.: *Energy cascade rate in compressible fast and slow solar wind turbulence*, *Astrophys. J.*, **838**, 11, <https://doi.org/10.3847/1538-4357/aa603f>, 2017. [8](#), [61](#), [81](#), [91](#)
- Hadid, L. Z., Sahraoui, F., Galtier, S., and Huang, S. Y.: *Compressible Magnetohydrodynamic Turbulence in the Earth's Magnetosheath: Estimation of the Energy Cascade Rate Using in situ Spacecraft Data*, *Phys. Rev. Lett.*, **120**, 055 102, <https://doi.org/10.1103/PhysRevLett.120.055102>, 2018. [47](#), [91](#)
- Hammett, G. W. and Perkins, F. W.: *Fluid moment models for Landau damping with application to the ion-temperature-gradient instability*, *Phys. Rev. Lett.*, **64**, 3019–3022, <https://doi.org/10.1103/PhysRevLett.64.3019>, 1990. [4](#)
- Hazeltine, R. D., Mahajan, S. M., and Morrison, P. J.: *Local thermodynamics of a magnetized, anisotropic plasma*, *Phys. Plasmas*, **20**, 022506, <https://doi.org/10.1063/1.4793735>, 2013. [75](#)
- He, J., Wang, L., Tu, C., Marsch, E., and Zong, Q.: *Evidence of Landau and cyclotron resonance between protons and kinetic waves in solar wind turbulence*, *Astrophys. J. Lett.*, **800**, L31, <https://doi.org/10.1088/2041-8205/800/2/L31>, 2015. [8](#), [61](#), [91](#)
- Hellinger, P., Verdini, A., Landi, S., Franci, L., and Matteini, L.: *von Kármán-Howarth Equation for Hall Magnetohydrodynamics: Hybrid Simulations*, *Astrophys. J.*, **857**, L19, <https://doi.org/10.3847/2041-8213/aabc06>, 2018. [12](#), [19](#), [20](#), [22](#), [30](#), [61](#), [77](#)
- Hennebelle, P. and Falgarone, E.: *Turbulent molecular clouds*, *Astron. & Astrophys. Rev.*, **20**, <https://doi.org/10.1007/s00159-012-0055-y>, 2012. [8](#), [78](#), [88](#)
- Heyer, M. and Brunt, C.: *The Universality of Turbulence in Galactic Molecular Clouds*, *Astrophys. J.*, **615**, L45–L48, <https://doi.org/10.1086/425978>, 2004. [78](#)
- Howes, G. G., Klein, K. G., and TenBarge, J. M.: *Validity of the Taylor hypothesis for linear kinetic waves in the weakly collisional solar wind*, *Astrophys. J.*, **789**, 106, <https://doi.org/10.1088/0004-637x/789/2/106>, 2014. [93](#)

- Huang, S. Y. and Sahraoui, F.: *Testing of the Taylor Frozen-in-flow Hypothesis at Electron Scales in the Solar Wind Turbulence*, *Astrophys. J.*, **876**, 138, <https://doi.org/10.3847/1538-4357/ab17d3>, 2019. [93](#)
- Huang, S. Y., Hadid, L. Z., Sahraoui, F., Yuan, Z. G., and Deng, X. H.: *On the Existence of the Kolmogorov Inertial Range in the Terrestrial Magnetosheath Turbulence*, *Astrophys. J.*, **836**, L10, <https://doi.org/10.3847/2041-8213/836/1/110>, 2017. [95](#)
- Hunana, P., Tenerani, A., Zank, G. P., Khomenko, E., Goldstein, M. L., Webb, G. M., Cally, P. S., Collados, M., Velli, M., Adhikari, L., and et al.: *An introductory guide to fluid models with anisotropic temperatures. Part 1. CGL description and collisionless fluid hierarchy*, *J. Plasma Phys.*, **85**, 205850 602, <https://doi.org/10.1017/S0022377819000801>, 2019. [4](#), [62](#)
- Imazio, P. R. and Mininni, P. D.: *Passive scalars: Mixing, diffusion, and intermittency in helical and nonhelical rotating turbulence*, *Phys. Rev. E*, **95**, 033 103, <https://doi.org/10.1103/PhysRevE.95.033103>, 2017. [38](#)
- Isenberg, P. A., Smith, C. W., and Matthaeus, W. H.: *Turbulent Heating of the Distant Solar Wind by Interstellar Pickup Protons*, *Astrophys. J.*, **592**, 564–573, <https://doi.org/10.1086/375584>, 2003. [8](#)
- Kadomtsev, B. B. and Petviashvili, V. I.: *Acoustic Turbulence*, *Sov. Phys.–Doklady*, **18**, 115, 1973. [81](#), [87](#)
- Kawazura, Y., Barnes, M., and Schekochihin, A.: *Thermal disequilibrium of ions and electrons by collisionless plasma turbulence*, *Proc. Nat. Acad. Sci. USA*, **116**, 771–776, <https://doi.org/10.1073/pnas.1812491116>, 2019. [78](#)
- Klein, K. G., Howes, G. G., and TenBarge, J. M.: *The violation of the Taylor hypothesis in measurements of solar wind turbulence*, *Astrophys. J.*, **790**, L20, <https://doi.org/10.1088/2041-8205/790/2/120>, 2014. [93](#)
- Kobayashi, S., Sahraoui, F., Passot, T., Laveder, D., Sulem, P. L., Huang, S. Y., Henri, P., and Smets, R.: *Three-dimensional Simulations and Spacecraft Observations of Sub-ion Scale Turbulence in the Solar Wind: Influence of Landau Damping*, *Astrophys. J.*, **839**, 122, <https://doi.org/10.3847/1538-4357/aa67f2>, 2017. [63](#)
- Kolmogorov, A.: *Dissipation of energy in locally isotropic turbulence*, *Dokl. Akad. Nauk SSSR*, **32**, 16–18, <https://doi.org/10.1098/rspa.1991.0076>, 1941. [12](#), [17](#)
- Kritsuk, A. G., Norman, M. L., Padoan, P., and Wagner, R.: *The Statistics of Supersonic Isothermal Turbulence*, *Astrophys. J.*, **665**, 416–431, <https://doi.org/10.1086/519443>, 2007. [79](#), [82](#)
- Lacombe, C., Alexandrova, O., Matteini, L., Santolík, O., Cornilleau-Wehrlin, N., Mangeney, A., de Conchy, Y., and Maksimovic, M.: *Whistler mode waves and the electron heat flux in the solar wind: cluster observations.*, *Astrophys. J.*, **796**, 5, <https://doi.org/10.1088/0004-637x/796/1/5>, 2014. [93](#)
- Leamon, R. J., Smith, C. W., Ness, N. F., Matthaeus, W. H., and Wong, H. K.: *Observational constraints on the dynamics of the interplanetary magnetic field dissipation range*, *J. Geophys. Res.*, **103**, 4775, <https://doi.org/10.1029/97JA03394>, 1998. [61](#)
- Lele, S. K.: *Compact finite difference schemes with spectral-like resolution*, *J. Comp. Phys.*, **103**, 16–42, [https://doi.org/10.1016/0021-9991\(92\)90324-R](https://doi.org/10.1016/0021-9991(92)90324-R), 1992. [68](#), [69](#)
- L’vov, V. S., L’vov, Y., Newell, A. C., and Zakharov, V.: *Statistical description of acoustic turbulence*, *Phys. Rev. E*, **56**, 390–405, <https://doi.org/10.1103/PhysRevE.56.390>, 1997. [87](#)

- Mac Low, M.-M. and Klessen, R. S.: *Control of star formation by supersonic turbulence*, Rev. Mod. Phys., **76**, 125–194, <https://doi.org/10.1103/RevModPhys.76.125>, 2004. [9](#), [88](#)
- MacBride, B., Smith, C., and Forman, M.: *The Turbulent Cascade at 1 AU: Energy Transfer and the Third-Order Scaling for MHD*, Astrophys. J., **679**, 1644, <https://doi.org/10.1086/529575>, 2008. [8](#), [47](#), [61](#), [91](#)
- Marino, R., Sorriso-Valvo, L., Carbone, V., Noullez, A., Bruno, R., and Bavassano, B.: *Heating the Solar Wind by a Magnetohydrodynamic Turbulent Energy Cascade*, Astrophys. J., **677**, L71, <https://doi.org/10.1086/587957>, 2008. [8](#), [61](#)
- Marsch, E., Mühlhäuser, K.-H., Schwenn, R., Rosenbauer, H., Pilipp, W., and Neubauer, F. M.: *Solar wind protons: Three-dimensional velocity distributions and derived plasma parameters measured between 0.3 and 1 AU*, J. Geophys. Res.: Space Phys., **87**, 52–72, <https://doi.org/10.1029/JA087iA01p00052>, 1982. [7](#)
- Matthaeus, W. H. and Goldstein, M. L.: *Stationarity of magnetohydrodynamic fluctuations in the solar wind*, J. Geophys. Res.: Space Phys., **87**, 10 347–10 354, <https://doi.org/10.1029/JA087iA12p10347>, 1982. [91](#)
- Matthaeus, W. H., Zank, G. P., Smith, C. W., and Oughton, S.: *Turbulence, Spatial Transport, and Heating of the Solar Wind*, Phys. Rev. Lett., **82**, 3444–3447, <https://doi.org/10.1103/PhysRevLett.82.3444>, 1999. [8](#), [91](#)
- Matthaeus, W. H., Weygand, J. M., and Dasso, S.: *Ensemble Space-Time Correlation of Plasma Turbulence in the Solar Wind*, Phys. Rev. Lett., **116**, 245 101, <https://doi.org/10.1103/PhysRevLett.116.245101>, 2016. [93](#)
- McKee, C. F. and Ostriker, E. C.: *Theory of Star Formation*, Annu. Rev. Astron. Astrophys., **45**, 565–687, <https://doi.org/10.1146/annurev.astro.45.051806.110602>, 2007. [9](#), [78](#)
- Meyrand, R. and Galtier, S.: *Anomalous $k_{\perp}^{-8/3}$ Spectrum in Electron Magnetohydrodynamic Turbulence*, Phys. Rev. Lett., **111**, 264 501, <https://doi.org/10.1103/PhysRevLett.111.264501>, 2013. [23](#), [43](#), [44](#)
- Mininni, P. D., Rosenberg, D., Reddy, R., and Pouquet, A.: *A hybrid MPI–OpenMP scheme for scalable parallel pseudospectral computations for fluid turbulence*, Parallel Comput., **37**, 316–326, <https://doi.org/10.1016/j.parco.2011.05.004>, 2011. [48](#)
- Myers, P. C.: *Filamentary condensation in a young cluster*, Astrophys. J., **735**, 82, <https://doi.org/10.1088/0004-637x/735/2/82>, 2011. [9](#)
- Nakamura, F. and Li, Z.-Y.: *Magnetically Regulated Star Formation in Three Dimensions: The Case of the Taurus Molecular Cloud Complex*, Astrophys. J., **687**, 354–375, <https://doi.org/10.1086/591641>, 2008. [79](#)
- Narita, Y., Glassmeier, K.-H., Sahraoui, F., and Goldstein, M. L.: *Wave-Vector Dependence of Magnetic-Turbulence Spectra in the Solar Wind*, Phys. Rev. Lett., **104**, 171 101, <https://doi.org/10.1103/PhysRevLett.104.171101>, 2010. [91](#)
- Ntormousi, E., Hennebelle, P., André, P., and Masson, J.: *The effect of ambipolar diffusion on low-density molecular ISM filaments*, Astron. & Astrophys., **589**, A24, <https://doi.org/10.1051/0004-6361/201527400>, 2016. [88](#)
- Orkisz, J. H., Pety, J., Gerin, M., Bron, E., Guzmán, V. V., Bardeau, S., Goicoechea, J. R., Gratier, P., Le Petit, F., Levrier, F., Liszt, H., Öberg, K., Peretto, N., Roueff, E., Sievers, A., and Tremblin, P.: *Turbulence and star formation efficiency in molecular clouds: solenoidal versus compressive motions in Orion B*, Astron. & Astrophys., **599**, A99, <https://doi.org/10.1051/0004-6361/201629220>, 2017. [78](#), [88](#)

- Osman, K. T., Wan, M., Matthaeus, W. H., Weygand, J. M., and Dasso, S.: *Anisotropic Third-Moment Estimates of the Energy Cascade in Solar Wind Turbulence Using Multi-spacecraft Data*, Phys. Rev. Lett., **107**, 165 001, <https://doi.org/10.1103/PhysRevLett.107.165001>, 2011. [8](#), [47](#), [61](#)
- Oughton, S., Wan, M., Servidio, S., and Matthaeus, W.: *On the Origin of Anisotropy in Magnetohydrodynamic Turbulence: The Role of Higher-order Correlations*, Astrophys. J., **768**, 10, <https://doi.org/10.1088/0004-637X/768/1/10>, 2013. [23](#)
- Padoan, P., Federrath, C., Chabrier, G., Evans, N. J., I., Johnstone, D., Jørgensen, J. K., McKee, C. F., and Nordlund, Å.: *The Star Formation Rate of Molecular Clouds*, in: *Protostars and Planets VI*, edited by Beuther, H., Klessen, R. S., Dullemond, C. P., and Henning, T., p. 77, University of Arizona Press, https://doi.org/10.2458/azu_uapress_9780816531240-ch004, 2014. [78](#), [88](#)
- Passot, T. and Sulem, P. L.: *Collisionless magnetohydrodynamics with gyrokinetic effects*, Phys. Plasmas, **14**, 082 502, <https://doi.org/10.1063/1.2751601>, 2007. [4](#)
- Passot, T. and Vázquez-Semadeni, E.: *Density probability distribution in one-dimensional polytropic gas dynamics*, Phys. Rev. E, **58**, 4501–4510, <https://doi.org/10.1103/PhysRevE.58.4501>, 1998. [79](#)
- Passot, T., Pouquet, A., and Woodward, P.: *The plausibility of Kolmogorov-type spectra in molecular clouds*, Astron. & Astrophys., **197**, 228–234, 1988. [81](#), [87](#)
- Passot, T., Henri, P., Laveder, D., and Sulem, P.-L.: *Fluid simulations of ion scale plasmas with weakly distorted magnetic fields*, Euro. Phys. J. D, **68**, <https://doi.org/10.1140/epjd/e2014-50160-1>, 2014. [62](#)
- Perri, S., Valentini, F., Sorriso-Valvo, L., Reda, A., and Malara, F.: *On the estimation of the current density in space plasmas: Multi- versus single-point techniques*, Planetary and Space Science, **140**, 6–10, <https://doi.org/https://doi.org/10.1016/j.pss.2017.03.008>, 2017. [101](#)
- Pinto, R. F., Brun, A. S., and Rouillard, A. P.: *Flux-tube geometry and solar wind speed during an activity cycle*, Astron. & Astrophys., **592**, A65, <https://doi.org/10.1051/0004-6361/201628599>, 2016. [6](#)
- Podesta, J. J., Forman, M. A., and Smith, C. W.: *Anisotropic form of third-order moments and relationship to the cascade rate in axisymmetric magnetohydrodynamic turbulence*, Phys. Plasmas, **14**, 092 305, <https://doi.org/10.1063/1.2783224>, 2007. [8](#), [61](#)
- Politano, H. and Pouquet, A.: *von Kármán-Howarth equation for magnetohydrodynamics and its consequences on third-order longitudinal structure and correlation functions*, Phys. Rev. E, **57**, 21, <https://doi.org/10.1103/PhysRevE.57.R21>, 1998. [12](#), [22](#), [116](#)
- Pouquet, A. and Patterson, G. S.: *Numerical simulation of helical magnetohydrodynamic turbulence*, J. Fluid Mech., **85**, 305–323, <https://doi.org/10.1017/S0022112078000658>, 1978. [48](#)
- Richardson, J. D., Paularena, K. I., Lazarus, A. J., and Belcher, J. W.: *Radial evolution of the solar wind from IMP 8 to Voyager 2*, Geophys. Res. Lett., **22**, 325–328, <https://doi.org/10.1029/94GL03273>, 1995. [7](#), [8](#), [61](#), [91](#)
- Robert, P.: *Tetrahedron Geometric Factors and Accuracy of Current Density Determination*, in: *Cluster-II Workshop Multiscale / Multipoint Plasma Measurements*, edited by Harris, R. A., vol. 449 of *ESA Special Publication*, p. 259, 2000. [105](#)

- Rouillard, A., Savani, N., Davies, J., Lavraud, B., Forsyth, R., Morley, S., Opitz, A., Sheeley, N., Burlaga, L., Sauvaud, J.-A., Simunac, K., Luhmann, J., Galvin, A., Crothers, S., Davis, C., Harrison, R., Lockwood, M., Eyles, C., Bewsher, D., and Brown, D.: *A Multispacecraft Analysis of a Small-Scale Transient Entrained by Solar Wind Streams*, *Solar Phys.*, **256**, <https://doi.org/10.1007/s11207-009-9329-6>, 2009. **6**
- Sahraoui, F., Belmont, G., and Rezeau, L.: *Hamiltonian canonical formulation of Hall-magnetohydrodynamics: Toward an application to weak turbulence theory*, *Phys. Plasmas*, **10**, 1325–1337, <https://doi.org/10.1063/1.1564086>, 2003. **3**
- Sahraoui, F., Goldstein, M. L., Robert, P., and Khotyaintsev, Y. V.: *Evidence of a Cascade and Dissipation of Solar-Wind Turbulence at the Electron Gyroscale*, *Phys. Rev. Lett.*, **102**, 231 102, <https://doi.org/10.1103/PhysRevLett.102.231102>, 2009. **8, 14, 61, 91**
- Sahraoui, F., Goldstein, M. L., Belmont, G., Canu, P., and Rezeau, L.: *Three Dimensional Anisotropic k Spectra of Turbulence at Subproton Scales in the Solar Wind*, *Phys. Rev. Lett.*, **105**, 131 101, <https://doi.org/10.1103/PhysRevLett.105.131101>, 2010. **61**
- Sahraoui, F., Belmont, G., and Goldstein, M. L.: *New insight into short-wavelength solar wind fluctuations from Vlasov theory*, *Astrophys. J.*, **748**, 100, <https://doi.org/10.1088/0004-637X/748/2/100>, 2012. **63, 93**
- Saw, E. W., Kuzay, D., Faranda, D., Guittonneau, A., Daviaud, F., Wiertel-Gasquet, C., Padilla, V., and Dubrulle, B.: *Experimental characterization of extreme events of inertial dissipation in a turbulent swirling flow*, *Nat. Commun.*, **7**, 12 466, <https://doi.org/10.1038/ncomms12466>, 2016. **81**
- Schwartz, S., Horbury, T., Owen, C., Baumjohann, W., Nakamura, R., Canu, P., Roux, A., Sahraoui, F., Louarn, P., Sauvaud, J.-A., Pinçon, J.-L., Vaivads, A., Marcucci, M., Anastasiadis, A., Fujimoto, M., Escoubet, P., Taylor, M., Eckersley, S., Allouis, E., and Team, o.: *Cross-scale: Multi-scale coupling in space plasmas*, *Exper. Astron.*, **23**, 1001–1015, <https://doi.org/10.1007/s10686-008-9085-x>, 2009. **114**
- Simon, P. and Sahraoui, F.: *General exact law of compressible isentropic magnetohydrodynamic flows: theory and spacecraft observations in the solar wind*, <https://doi.org/10.3847/1538-4357/ac0337>, 2021. **24, 116**
- Smith, C. W., Hamilton, K., Vasquez, B. J., and Leamon, R. J.: *Dependence of the Dissipation Range Spectrum of Interplanetary Magnetic Fluctuations on the Rate of Energy Cascade*, *Astrophys. J. Lett.*, **645**, L85–L88, <https://doi.org/10.1086/506151>, 2006. **61, 91**
- Smith, C. W., Stawarz, J. E., Vasquez, B. J., Forman, M. A., and MacBride, B. T.: *Turbulent Cascade at 1 AU in High Cross-Helicity Flows*, *Phys. Rev. Lett.*, **103**, 201 101, <https://doi.org/10.1103/PhysRevLett.103.201101>, 2009. **8, 61**
- Snyder, P. B., Hammett, G. W., and Dorland, W.: *Landau fluid models of collisionless magnetohydrodynamics*, *Phys. Plasmas*, **4**, 3974–3985, <https://doi.org/10.1063/1.872517>, 1997. **4, 62**
- Sorriso-Valvo, L., Marino, R., Carbone, V., Noullez, A., Lepreti, F., Veltri, P., Bruno, R., Bavassano, B., and Pietropaolo, E.: *Observation of Inertial Energy Cascade in Interplanetary Space Plasma*, *Phys. Rev. Lett.*, **99**, 115 001, <https://doi.org/10.1103/PhysRevLett.99.115001>, 2007. **8, 47, 61, 91**
- Stawarz, J. E., Smith, C. W., Vasquez, B. J., Forman, M. A., and MacBride, B. T.: *The Turbulent Cascade and Proton Heating in the Solar Wind at 1 AU*, *Astrophys. J.*, **697**, 1119–1127, <https://doi.org/10.1088/0004-637X/697/2/1119>, 2009. **8, 47, 61**

- Taylor, M., Kurien, S., and Eyink, G.: *Recovering isotropic statistics in turbulence simulations: The Kolmogorov 4/5th law*, Phys. Rev. E, **68**, 026 310, <https://doi.org/10.1103/PhysRevE.68.026310>, 2003. [34](#), [35](#), [41](#), [116](#)
- Teaca, B., Verma, M. K., Knaepen, B., and Carati, D.: *Energy transfer in anisotropic magnetohydrodynamic turbulence*, Phys. Rev. E, **79**, 046 312, <https://doi.org/10.1103/PhysRevE.79.046312>, 2009. [44](#)
- TenBarge, J., Howes, G., Dorland, W., and Hammett, G.: *An oscillating Langevin antenna for driving plasma turbulence simulations*, Comp. Phys. Comm., **185**, 578–589, <https://doi.org/10.1016/j.cpc.2013.10.022>, 2014. [63](#)
- Vaivads, A., Andersson, G., Bale, S. D., Cully, C. M., De Keyser, J., Fujimoto, M., Grahn, S., Haaland, S., Ji, H., Khotyaintsev, Y. V., Lazarian, A., Lavraud, B., Mann, I. R., Nakamura, R., Nakamura, T. K. M., Narita, Y., Retinò, A., Sahraoui, F., Schekochihin, A., Schwartz, S. J., Shinohara, I., and Sorriso-Valvo, L.: *EIDOSCOPE: particle acceleration at plasma boundaries*, Exper. Astron., **33**, 491–527, <https://doi.org/10.1007/s10686-011-9233-6>, 2012. [114](#)
- Vásconez, C. L., Perrone, D., Marino, R., Laveder, D., Valentini, F., Servidio, S., Mininni, P., and Sorriso-Valvo, L.: *Local and global properties of energy transfer in models of plasma turbulence*, J. Plasma Phys., **87**, 825870 101, <https://doi.org/10.1017/S0022377820001567>, 2021. [61](#)
- Vasquez, B. J., Smith, C. W., Hamilton, K., MacBride, B. T., and Leamon, R. J.: *Evaluation of the turbulent energy cascade rates from the upper inertial range in the solar wind at 1 AU*, J. Geophys. Res., **112**, A07 101, <https://doi.org/10.1029/2007JA012305>, 2007. [8](#), [91](#)
- Vazquez-Semadeni, E.: *Hierarchical Structure in Nearly Pressureless Flows as a Consequence of Self-similar Statistics*, Astrophys. J., **423**, 681, <https://doi.org/10.1086/173847>, 1994. [79](#)
- Verma, M. K., Roberts, D. A., and Goldstein, M. L.: *Turbulent heating and temperature evolution in the solar wind plasma*, J. Geophys. Res., **100**, 19 839–19 850, <https://doi.org/10.1029/95JA01216>, 1995. [8](#)
- Verscharen, D., Wicks, R. T., Alexandrova, O., Bruno, R., Burgess, D., Chen, C. H. K., D’Amicis, R., De Keyser, J., de Wit, T. D., Franci, L., He, J., Henri, P., Kasahara, S., Khotyaintsev, Y., Klein, K. G., Lavraud, B., Maruca, B. A., Maksimovic, M., Plaschke, F., Poedts, S., Reynolds, C. S., Roberts, O., Sahraoui, F., Saito, S., Salem, C. S., Saur, J., Servidio, S., Stawarz, J. E., Štverák, Š., and Told, D.: *A Case for Electron-Astrophysics*, Exper. Astron., <https://doi.org/10.1007/s10686-021-09761-5>, 2021. [114](#)
- von Kármán, T. and Howarth, L.: *On the Statistical Theory of Isotropic Turbulence*, Proc. Roy. Soc. A, **164**, 195–215, <https://doi.org/10.1098/rspa.1938.0013>, 1938. [17](#)
- Wan, M., Oughton, S., Servidio, S., and Matthaeus, W. H.: *von Kármán self-preservation hypothesis for magnetohydrodynamic turbulence and its consequences for universality*, J. Fluid Mech., **697**, 296–315, <https://doi.org/10.1017/jfm.2012.61>, 2012. [23](#)
- Wicks, R. T., Forman, M. A., Horbury, T. S., and Oughton, S.: *power anisotropy in the magnetic field power spectral tensor of solar wind turbulence*, Astrophys. J., **746**, 103, <https://doi.org/10.1088/0004-637x/746/1/103>, 2012. [45](#)
- Woodham, L. D., Wicks, R. T., Verscharen, D., and Owen, C. J.: *The Role of Proton Cyclotron Resonance as a Dissipation Mechanism in Solar Wind Turbulence: A Statistical Study at Ion-kinetic Scales*, Astrophys. J., **856**, 49, <https://doi.org/10.3847/1538-4357/aab03d>, 2018. [8](#), [61](#), [91](#)

- Yaglom, A.: *On the local structure of a temperature field in a turbulent flow*, Dokl. Akad. Nauk SSSR, **69**, 743–746, 1949. [17](#)
- Yang, Y., Wan, M., Matthaeus, W. H., and Chen, S.: *Energy budget in decaying compressible MHD turbulence*, J. Fluid Mech., **916**, A4, <https://doi.org/10.1017/jfm.2021.199>, 2021. [49](#)
- Yang, Y.-Y., Shen, C., and Ji, Y.: *Strong southward and northward currents observed in the inner plasma sheet*, Ann. Geophys., **37**, 931–941, <https://doi.org/10.5194/angeo-37-931-2019>, 2019. [105](#)
- Zakharov, V. E. and Sagdeev, R. Z.: *Spectrum of Acoustic Turbulence*, Soviet Physics Doklady, **15**, 439, 1970. [87](#)

Appendix A

List of Acronyms

- A18** The **CHMHD** exact law derived by **Andrés et al. (2018)**. 25, 29, 43, 47, 51–53, 55–58, 61, 91, 93, 97–101, 103, 107–109, 114, 118, 119, 122
- BG17** The **IHMHD** exact law derived by **Banerjee and Galtier (2017)**. 19, 22, 23, 29, 30, 43, 45, 46, 67, 118, 119
- CGL** Chew, Goldenberg, Low. 4, 43, 62–64, 72, 74, 118, 120
- CHD** Compressible Hydrodynamic. 9, 12–14, 24, 30, 31, 40, 44, 79, 80, 87, 88, 118, 120, 121
- CHMHD** Compressible Hall Magnetohydrodynamic. 14, 17, 24, 25, 29, 31, 38–40, 43, 44, 47, 48, 55, 65, 66, 92, 94, 117–119, 121, 125
- CMHD** Compressible Magnetohydrodynamics. 24, 30, 31, 39, 62, 121
- DNS** Direct Numerical Simulation. v, 13, 14, 23, 31, 33, 43, 44, 46, 47, 53, 61, 78, 79, 82, 89, 91–93, 107, 110, 112, 117–121, 123
- EMHD** Electron Magnetohydrodynamics. 5, 13, 14, 43–47, 51, 89, 119
- ESA** European Space Agency. 7, 115
- F19** The **IHMHD** exact law (2.39) derived in section 2.2 and **Ferrand et al. (2019)**. 22, 23, 29–31, 43, 45, 46, 62, 64, 66, 67, 81, 82, 89, 97, 118, 120
- F21** The **CHMHD** exact law (2.100) derived in section 2.3 and **Ferrand et al. (2021a)**. 29–31, 43, 44, 47, 51, 52, 54–58, 61, 65, 66, 79, 93, 97–101, 114, 118, 119, 121, 122
- FGM** Fluxgate Magnetometer. 94
- FPI** Fast Plasma Investigation. 94, 101, 102, 122
- G08** The **IHMHD** exact law derived by **Galtier (2008)**. 19, 22, 23, 30, 43, 45–47, 65, 67, 118, 119
- GHOST** Geophysical High-Order Suite for Turbulence. 10, 43, 47, 48, 53, 59, 60, 81, 89, 98, 107, 112, 119, 120, 122
- HD** Hydrodynamics. 9, 11, 12, 17, 24, 35, 79, 88, 118
- IHMHD** Incompressible Hall Magnetohydrodynamic. 11, 14, 17, 18, 22–25, 30, 31, 38, 44–46, 62, 64–67, 78, 117, 118, 125

ISM Interstellar Medium. [v](#), [6](#), [8–10](#), [14](#), [30](#), [40](#), [44](#), [79](#), [88](#), [89](#), [117](#), [121](#)

KAW Kinetic Alfvén Wave. [63](#), [76](#), [78](#), [79](#)

LF Landau fluid. [4](#), [5](#), [14](#), [43](#), [53](#), [58](#), [62–64](#), [72](#), [74](#), [91](#), [120](#)

MHD Magnetohydrodynamics. [v](#), [2–6](#), [12–14](#), [22–24](#), [35](#), [51](#), [53](#), [58](#), [61](#), [62](#), [71–74](#), [79](#), [82](#), [91](#), [93](#), [95](#), [97–100](#), [104](#), [110](#), [118–122](#)

MMS Magnetospheric Multiscale mission. [v](#), [6–8](#), [13](#), [15](#), [52](#), [61](#), [89](#), [91–95](#), [105](#), [107](#), [108](#), [110](#), [112](#), [114](#), [115](#), [121](#), [122](#)

MPI Message Passing Interface. [39](#), [41](#), [48](#)

NASA National Aeronautics and Space Administration. [7](#), [92](#), [115](#)

PSP Parker Solar Probe. [6](#), [7](#)

rms root mean square. [80](#)

STEREO Solar Terrestrial Relations Observatory. [7](#)

SW Solar Wind. [v](#), [6–8](#), [10](#), [43–45](#), [47](#), [61](#), [91–94](#), [117](#), [120](#), [122](#), [123](#)




TURBO Solver for TURbulent flows with periodic BOundary conditions. [44](#)

Appendix B

Papers published and in preparation



On Exact Laws in Incompressible Hall Magnetohydrodynamic Turbulence

R. Ferrand¹, S. Galtier^{1,2} , F. Sahraoui¹, R. Meyrand¹, N. Andrés^{1,3} , and S. Banerjee⁴ 

¹ LPP/CNRS-Ecole polytechnique-Sorbonne Université-Université Paris-Sud-Observatoire de Paris, F-91128 Palaiseau, France; renaud.ferrand@lpp.polytechnique.fr

² Institut Universitaire de France, France

³ Instituto de Astronomía y Física del Espacio, UBA-CONICET, CC. 67, suc. 28, 1428, Buenos Aires, Argentina

⁴ Department of Physics, Indian Institute of Technology Kanpur, Kalyanpur 208016, Uttar Pradesh, India

Received 2019 May 10; revised 2019 June 20; accepted 2019 June 20; published 2019 August 12

Abstract

A comparison is made between several existing exact laws in incompressible Hall magnetohydrodynamic turbulence in order to show their equivalence, despite stemming from different mathematical derivations. Using statistical homogeneity, we revisit the law proposed by Hellinger et al. and show that it can be written, after being corrected by a multiplicative factor, in a more compact form implying only flux terms expressed as increments of the turbulent fields. The Hall contribution of this law is tested and compared to other exact laws derived by Galtier and Banerjee & Galtier using direct numerical simulations of three-dimensional electron MHD turbulence with a moderate mean magnetic field. We show that the studied laws are equivalent in the inertial range, thereby offering several choices on the formulation to use depending on the needs. The expressions that depend explicitly on a mean (guide) field may lead to residual errors in estimating the energy cascade rate; however, we demonstrate that this guide field can be removed from these laws after mathematical manipulation. Therefore, it is recommended to use an expression independent of the mean guide field to analyze numerical or in situ spacecraft data.

Key words: magnetohydrodynamics (MHD) – plasmas – solar wind – turbulence

1. Introduction

To date, understanding the dynamics of turbulent flows remains one of the most challenging problems of classical physics. As these systems are inherently chaotic they are generally studied by statistical means, thus requiring specific tools to be dealt with (Frisch 1995). The so-called exact laws are among the most important theoretical results of turbulence. The derivation of these statistical laws is based on the assumption of the existence of an inertial range where the physics is dominated by the nonlinear transfer from one scale to another. In a fully developed three-dimensional (3D) hydrodynamic turbulence of an incompressible fluid, kinetic energy is transferred from macroscopic length scales to the scale of molecular diffusion until it is eventually dissipated into thermal energy by viscous effects. The mean transfer rate of kinetic energy per unit volume, which is usually denoted by ε , is assumed to remain constant at each scale in the inertial range where both dissipation and forcing mechanisms are negligible. It is also equal to the average energy dissipation rate, which is expected to be independent of the viscosity in the limit of large Reynolds numbers. This property, often called the zeroth law of turbulence (Onsager 1949; Eyink 1994; Duchon & Robert 2000; Saint-Michel et al. 2014), is actually used to link the fluctuations of the velocity field to ε through exact laws.

The first and the most popular exact law is the so-called Kolmogorov’s four-fifths law, which was derived for incompressible turbulence (Kolmogorov 1941). It was first derived using tensorial calculus (Batchelor 1953), but a similar four-thirds law was computed more directly through the dynamical study of an appropriate two-point correlation function (Monin 1959; Antonia et al. 1997). Using these methods (with the generalized zeroth law of turbulence; Mininni & Pouquet 2009; Bandyopadhyay et al. 2018; Galtier 2018), new laws were derived for different plasma models such as incompressible MHD (IMHD; Politano & Pouquet 1998a) or

incompressible Hall magnetohydrodynamic (IHMHD; Galtier 2008). More recently, these results were extended to compressible (isothermal and polytropic) turbulence in hydrodynamics (CHD; Galtier & Banerjee 2011; Banerjee & Galtier 2014), and then to isothermal compressible MHD (CMHD; Banerjee & Galtier 2013; Andrés & Sahraoui 2017) and compressible HMHD (Andrés et al. 2018a). Using an alternative formulation (Banerjee & Galtier 2016, 2017), compressible exact relations were also derived for self-gravitating turbulence of both neutral and MHD fluids (Banerjee & Kritsuk 2017, 2018). Such laws were also derived for self-gravitating turbulence whose potential applications are the interstellar medium and star formation.

Since ε can be used as a proxy to evaluate the amount of energy available to be ultimately dissipated at small scales, exact laws are often used in collisionless astrophysical plasmas, such as the solar wind (SW), to evaluate the rate of plasma heating. Indeed, Richardson et al. (1995) have evidenced using *Voyager* data a slower decay of the (ion) temperature with the heliocentric distance in comparison with the prediction from the adiabatic expansion model (Matthaeus et al. 1999). Turbulence is proposed to explain this problem because it provides an efficient mechanism of energy dissipation through the nonlinear process of energy cascade from the MHD scales down to the sub-ion and electron scales, where the energy is eventually dissipated through some kinetic effects (Sahraoui et al. 2009, 2010; He et al. 2015). The energy cascade (or dissipation) rate was measured in both the SW (Podesta et al. 2007; Sorriso-Valvo et al. 2007; MacBride et al. 2008; Marino et al. 2008; Carbone et al. 2009; Smith et al. 2009; Stawarz et al. 2009; Osman et al. 2011; Coburn et al. 2015; Banerjee et al. 2016; Hadid et al. 2017) and the Earth’s magnetosheath (Hadid et al. 2018), and was shown to enlighten many aspects related to the dynamics of turbulent space plasmas.

Similarly to hydrodynamics, the case of IHMHD has driven some attention over the past 10 years with the derivation of

several exact laws (Galtier 2008; Banerjee & Galtier 2017; Hellinger et al. 2018). Although the underlying assumptions remain unchanged, these laws stem from the analysis of different statistical quantities. On the one hand, the laws given in Galtier (2008, hereafter G08) and Banerjee & Galtier (2017, hereafter BG17) are derived from the dynamical analysis of the two-point correlator:

$$\langle R_E \rangle = \left\langle \frac{\mathbf{v} \cdot \mathbf{v}' + \mathbf{b} \cdot \mathbf{b}'}{2} \right\rangle, \quad (1)$$

where $\langle \rangle$ is the ensemble average, \mathbf{v} and \mathbf{b} are the local velocity and Alfvén velocity fields, respectively, and the prime distinguishes values taken at points \mathbf{x} and \mathbf{x}' , respectively (see Section 2 for the definitions). However, the calculation was done differently in the two models (G08 and BG17) and yielded quite different expressions that cannot be trivially connected to each other. On the other hand, the law from Hellinger et al. (2018, hereafter H18) stems from the evolution equation of the second-order structure function

$$\langle S \rangle = \langle |\mathbf{v}' - \mathbf{v}|^2 + |\mathbf{b}' - \mathbf{b}|^2 \rangle, \quad (2)$$

which is linked to expression (1) through the relation $\langle S/4 \rangle = \langle E^{\text{tot}} \rangle - \langle R_E \rangle$ with $E^{\text{tot}} = (\mathbf{v}^2 + \mathbf{b}^2)/2$ the total energy. It is thus important to check whether or not these different laws are consistent with each other by providing the same energy cascade rate. Note that in the definition (2), $\langle S \rangle$ is independent of the (constant) mean fields \mathbf{v}_0 and \mathbf{b}_0 . We will return to this point in Section 5.

This paper aims at studying analytically and numerically the IHMHD exact laws and checking if they are mathematically equivalent despite stemming from a different logic of derivation. Following this goal, we expose in Section 2 a rigorous derivation of H18 and find a slight difference with the original paper. Furthermore, we provide a new, more compact form of that law that depends only on flux terms (hereafter F19). In Section 4 we give mathematical proof of the equivalence of the three laws F19, G08, and BG17. This equivalence is eventually tested in Section 5 with 3D direct numerical simulations (DNSs) of electron MHD (EMHD) turbulence. We also discuss the possible influence of a mean magnetic field on the exact laws and on the methods used to evaluate the energy cascade rate. The results are summarized and discussed in Section 6.

2. Derivation of H18

In this section we propose a step-by-step derivation of the H18 law based on the same premises as in the original paper, where the details were not given. Let \mathbf{B} represent the magnetic field and $\mathbf{J} = \nabla \times \mathbf{B}/\mu_0$ represent the electric current; the mass density ρ_0 is taken constant and equal to unity. We use the Alfvén units for the magnetic field and the electric current, i.e., $\mathbf{b} = \mathbf{B}/\sqrt{\mu_0\rho_0}$ and $\mathbf{j} = \nabla \times \mathbf{b}$. In the incompressible case (i.e., $\nabla \cdot \mathbf{v} = 0$) we get the following velocity and induction equations:

$$\begin{aligned} \partial_t \mathbf{v} &= -(\mathbf{v} \cdot \nabla) \mathbf{v} + (\mathbf{b} \cdot \nabla) \mathbf{b} - \nabla P + \mathbf{d}_\nu + \mathbf{f}, \\ \partial_t \mathbf{b} &= -(\mathbf{v} \cdot \nabla) \mathbf{b} + (\mathbf{b} \cdot \nabla) \mathbf{v} \end{aligned} \quad (3)$$

$$+ d_i (\mathbf{j} \cdot \nabla) \mathbf{b} - d_i (\mathbf{b} \cdot \nabla) \mathbf{j} + \mathbf{d}_\eta, \quad (4)$$

$$\nabla \cdot \mathbf{b} = 0, \quad (5)$$

where $P = p + b^2/2$ is the total pressure, d_i the ion inertial length, and \mathbf{f} a stationary homogeneous external force acting at large scales. The dissipation terms are

$$\mathbf{d}_\nu = \nu \Delta \mathbf{v}, \quad (6)$$

$$\mathbf{d}_\eta = \eta \Delta \mathbf{b}, \quad (7)$$

where ν is the kinematic viscosity and η the magnetic diffusivity. For this system the equation of total energy conservation writes (Galtier 2016)

$$\partial_t \langle E^{\text{tot}} \rangle = \langle \mathbf{v} \cdot \mathbf{d}_\nu \rangle + \langle \mathbf{b} \cdot \mathbf{d}_\eta \rangle + \langle \mathbf{v} \cdot \mathbf{f} \rangle, \quad (8)$$

where $\langle \rangle$ is an ensemble average, which is equivalent to a spatial average in homogeneous turbulence. We define the mean rate of total energy injection as $\varepsilon = \langle \mathbf{v} \cdot \mathbf{f} \rangle$. With this, we can conclude that in the stationary regime the following relation holds: $\langle \mathbf{v} \cdot \mathbf{d}_\nu + \mathbf{b} \cdot \mathbf{d}_\eta \rangle = -\varepsilon$. Note that using the relation $\langle \mathbf{X} \cdot \Delta \mathbf{X} \rangle = -\langle (\nabla \times \mathbf{X})^2 \rangle$, which is valid for any incompressible vector field \mathbf{X} , we also have

$$\langle \mathbf{v} \cdot \mathbf{d}_\nu \rangle + \langle \mathbf{b} \cdot \mathbf{d}_\eta \rangle = -\nu \langle \mathbf{w}^2 \rangle - \eta \langle \mathbf{j}^2 \rangle, \quad (9)$$

with $\mathbf{w} = \nabla \times \mathbf{v}$ the vorticity, which gives the expression of the mean rate of total energy dissipation.

Next, we consider a spatial increment ℓ connecting two points in space \mathbf{x} and \mathbf{x}' , as $\mathbf{x}' = \mathbf{x} + \ell$, and we define $\mathbf{v} \equiv \mathbf{v}(\mathbf{x})$ and $\mathbf{v}' \equiv \mathbf{v}(\mathbf{x}')$; the same notation is used for other variables. We also define the velocity increment $\delta \mathbf{v} \equiv \mathbf{v}' - \mathbf{v}$. We recall that under this formalism, we have for any entity A : $\partial_x A' = \partial_x A = 0$. We then search for a dynamical equation for expression (2), under the hypothesis of statistical homogeneity, which means that we have to calculate $\partial_t \langle S \rangle$. Using Equations (3)–(5) and the incompressibility of the flow we obtain

$$\begin{aligned} \partial_t \mathbf{v}^2 &= -\nabla \cdot [(\mathbf{v} \cdot \mathbf{v}) \mathbf{v}] + 2\mathbf{v} \cdot (\mathbf{b} \cdot \nabla) \mathbf{b} \\ &\quad - 2\mathbf{v} \cdot \nabla P + 2\mathbf{v} \cdot \mathbf{d}_\nu + 2\mathbf{v} \cdot \mathbf{f}, \end{aligned} \quad (10)$$

$$\begin{aligned} \partial_t \mathbf{b}^2 &= -\nabla \cdot [(\mathbf{b} \cdot \mathbf{b}) \mathbf{v}] + 2\mathbf{b} \cdot (\mathbf{b} \cdot \nabla) \mathbf{v} \\ &\quad + d_i \nabla \cdot [(\mathbf{b} \cdot \mathbf{b}) \mathbf{j}] - 2d_i \mathbf{b} \cdot (\mathbf{b} \cdot \nabla) \mathbf{j} + 2\mathbf{b} \cdot \mathbf{d}_\eta, \end{aligned} \quad (11)$$

$$\begin{aligned} \partial_t (\mathbf{v} \cdot \mathbf{v}') &= -\nabla' \cdot [(\mathbf{v} \cdot \mathbf{v}') \mathbf{v}' - (\mathbf{v} \cdot \mathbf{b}') \mathbf{b}' + P' \mathbf{v}] \\ &\quad - \nabla \cdot [(\mathbf{v} \cdot \mathbf{v}') \mathbf{v} - (\mathbf{v}' \cdot \mathbf{b}) \mathbf{b} + P \mathbf{v}'] \\ &\quad + \mathbf{v}' \cdot \mathbf{d}_\nu + \mathbf{v} \cdot \mathbf{d}'_\nu + \mathbf{v}' \cdot \mathbf{f} + \mathbf{v} \cdot \mathbf{f}', \end{aligned} \quad (12)$$

$$\begin{aligned} \partial_t (\mathbf{b} \cdot \mathbf{b}') &= \\ &\quad - \nabla' \cdot [(\mathbf{b} \cdot \mathbf{b}') \mathbf{v}' - (\mathbf{b} \cdot \mathbf{v}') \mathbf{b}' - d_i (\mathbf{b} \cdot \mathbf{b}') \mathbf{j}' \\ &\quad + d_i (\mathbf{b} \cdot \mathbf{j}') \mathbf{b}'] - \nabla \cdot [(\mathbf{b}' \cdot \mathbf{b}) \mathbf{v} - (\mathbf{b}' \cdot \mathbf{v}) \mathbf{b} \\ &\quad - d_i (\mathbf{b}' \cdot \mathbf{b}) \mathbf{j} + d_i (\mathbf{b}' \cdot \mathbf{j}) \mathbf{b}] + \mathbf{b}' \cdot \mathbf{d}_\eta + \mathbf{b} \cdot \mathbf{d}'_\eta, \end{aligned} \quad (13)$$

and similar equations as Equations (10)–(11) for the primed expressions. Below we will consider the ensemble average of the previous equations. We can use the relation $\langle \nabla' \cdot \rangle = -\langle \nabla \cdot \rangle = \nabla_\ell \cdot \langle \rangle$, where ∇_ℓ denotes the derivative operator along the increment ℓ , to suppress the pressure terms in Equations (10) and (12):

$$\langle \mathbf{v} \cdot \nabla P \rangle = \langle \nabla \cdot (P \mathbf{v}) \rangle = -\langle \nabla' \cdot (P \mathbf{v}) \rangle = 0,$$

$$\langle \nabla' \cdot (P' \mathbf{v}') \rangle = -\langle \nabla \cdot (P' \mathbf{v}') \rangle = 0.$$

By remarking that

$$\begin{aligned} \langle \mathbf{v} \cdot (\mathbf{b} \cdot \nabla) \mathbf{b} \rangle &= -\langle \mathbf{b} \cdot (\mathbf{b} \cdot \nabla) \mathbf{v} \rangle, \\ \langle \mathbf{b} \cdot (\mathbf{b} \cdot \nabla) \mathbf{j} \rangle &= -\langle \mathbf{j} \cdot (\mathbf{b} \cdot \nabla) \mathbf{b} \rangle, \end{aligned}$$

a combination of Equations (10)–(13) leads to

$$\begin{aligned} \partial_t \langle S \rangle &= \\ &2 \nabla_\ell \cdot \langle (\mathbf{v} \cdot \mathbf{v}') \delta \mathbf{v} + (\mathbf{b} \cdot \mathbf{b}') \delta \mathbf{v} \\ &\quad - (\mathbf{v} \cdot \mathbf{b}') \delta \mathbf{b} - (\mathbf{b} \cdot \mathbf{v}') \delta \mathbf{b} \rangle \\ &+ 2d_i \nabla_\ell \cdot \langle -(\mathbf{b} \cdot \mathbf{b}') \delta \mathbf{j} + (\mathbf{b} \cdot \mathbf{j}') \mathbf{b}' - (\mathbf{b}' \cdot \mathbf{j}) \mathbf{b} \rangle \\ &+ 2d_i \langle \mathbf{j} \cdot (\mathbf{b} \cdot \nabla) \mathbf{b} + \mathbf{j}' \cdot (\mathbf{b}' \cdot \nabla) \mathbf{b}' \rangle \\ &+ 4 \langle \mathbf{v} \cdot \mathbf{d}'_\nu \rangle - 2 \langle \mathbf{v} \cdot \mathbf{d}'_\nu \rangle - 2 \langle \mathbf{v}' \cdot \mathbf{d}_\nu \rangle + 4 \langle \mathbf{b} \cdot \mathbf{d}_\eta \rangle \\ &\quad - 2 \langle \mathbf{b} \cdot \mathbf{d}'_\eta \rangle - 2 \langle \mathbf{b}' \cdot \mathbf{d}_\eta \rangle + 4 \langle \mathbf{v} \cdot \mathbf{f} \rangle \\ &\quad - 2 \langle \mathbf{v} \cdot \mathbf{f}' \rangle - 2 \langle \mathbf{v}' \cdot \mathbf{f} \rangle. \end{aligned} \quad (14)$$

To further simplify expression (14) we can use the equalities $\nabla \cdot [(\mathbf{b} \cdot \mathbf{j}') \mathbf{b}] = \mathbf{j}' \cdot (\mathbf{b} \cdot \nabla) \mathbf{b}$ and $\nabla' \cdot [(\mathbf{b}' \cdot \mathbf{j}) \mathbf{b}'] = \mathbf{j} \cdot (\mathbf{b}' \cdot \nabla) \mathbf{b}'$ and relation (8). We then obtain

$$\begin{aligned} \partial_t \langle S \rangle &= -\nabla_\ell \cdot \langle (\delta \mathbf{v} \cdot \delta \mathbf{v} + \delta \mathbf{b} \cdot \delta \mathbf{b}) \delta \mathbf{v} - 2(\delta \mathbf{v} \cdot \delta \mathbf{b}) \delta \mathbf{b} \\ &\quad - d_i (\delta \mathbf{b} \cdot \delta \mathbf{b}) \delta \mathbf{j} + 2d_i (\delta \mathbf{b} \cdot \delta \mathbf{j}) \delta \mathbf{b} \rangle \\ &+ 2d_i \langle \delta \mathbf{j} \cdot \delta [(\mathbf{b} \cdot \nabla) \mathbf{b}] \rangle \\ &+ 4\partial_t \langle E^{\text{tot}} \rangle - 2 \langle \mathbf{v} \cdot \mathbf{d}'_\nu \rangle - 2 \langle \mathbf{v}' \cdot \mathbf{d}_\nu \rangle \\ &\quad - 2 \langle \mathbf{b} \cdot \mathbf{d}'_\eta \rangle - 2 \langle \mathbf{b}' \cdot \mathbf{d}_\eta \rangle - 2 \langle \mathbf{v} \cdot \mathbf{f}' \rangle - 2 \langle \mathbf{v}' \cdot \mathbf{f} \rangle. \end{aligned} \quad (15)$$

It is interesting to note at this level that expression (15) is fully compatible with the limit $\ell \rightarrow 0$ since in this case each term of the first line tends to 0, and in the second line we have an exact compensation between the first term and the others by means of Equation (8)

The final expression of the exact law for 3D IHMHD, valid in the inertial range, is obtained by using the stationarity assumption and the limit of a wide inertial range (i.e., large kinetic/magnetic Reynolds numbers limit) for which

$$\langle \mathbf{v} \cdot \mathbf{d}'_\nu \rangle \simeq \langle \mathbf{v}' \cdot \mathbf{d}_\nu \rangle \simeq \langle \mathbf{b} \cdot \mathbf{d}'_\eta \rangle \simeq \langle \mathbf{b}' \cdot \mathbf{d}_\eta \rangle \simeq 0, \quad (16)$$

and also (with the properties of the external force)

$$\langle \mathbf{v} \cdot \mathbf{f}' \rangle \simeq \langle \mathbf{v}' \cdot \mathbf{f} \rangle \simeq \varepsilon. \quad (17)$$

We find the expression

$$\begin{aligned} -4\varepsilon &= \nabla_\ell \cdot \langle (\delta \mathbf{v} \cdot \delta \mathbf{v} + \delta \mathbf{b} \cdot \delta \mathbf{b}) \delta \mathbf{v} - 2(\delta \mathbf{v} \cdot \delta \mathbf{b}) \delta \mathbf{b} \\ &\quad - d_i (\delta \mathbf{b} \cdot \delta \mathbf{b}) \delta \mathbf{j} + 2d_i (\delta \mathbf{b} \cdot \delta \mathbf{j}) \delta \mathbf{b} \rangle \\ &\quad - 2d_i \langle \delta \mathbf{j} \cdot \delta [(\mathbf{b} \cdot \nabla) \mathbf{b}] \rangle. \end{aligned} \quad (18)$$

This law can be written in a compact form as

$$-4\varepsilon = \nabla_\ell \cdot (\mathbf{Y} + \mathbf{H}) - 2A, \quad (19)$$

where

$$\mathbf{Y} = \langle (\delta \mathbf{v} \cdot \delta \mathbf{v} + \delta \mathbf{b} \cdot \delta \mathbf{b}) \delta \mathbf{v} - 2(\delta \mathbf{v} \cdot \delta \mathbf{b}) \delta \mathbf{b} \rangle, \quad (20)$$

$$\mathbf{H} = d_i \langle 2(\delta \mathbf{b} \cdot \delta \mathbf{j}) \delta \mathbf{b} - (\delta \mathbf{b} \cdot \delta \mathbf{b}) \delta \mathbf{j} \rangle, \quad (21)$$

$$A = d_i \langle \delta \mathbf{j} \cdot \delta [(\mathbf{b} \cdot \nabla) \mathbf{b}] \rangle. \quad (22)$$

Here the contribution of the Hall effect is split into a flux \mathbf{H} and a corrective term A . In the limit $d_i \rightarrow 0$ we recover the classic

MHD law of Politano & Pouquet (1998a). Note that Equation (19) is the same as the one proposed in Hellinger et al. (2018), except for the corrective term A , which is multiplied here by a -2 factor (instead of 1). Assuming isotropy we can integrate expression (19), which leads to

$$-\frac{4}{3}\varepsilon\ell = Y_\ell + H_\ell - 2I_A, \quad (23)$$

where Y_ℓ and H_ℓ are the projections along the displacement direction ℓ , respectively, and $I_A = (1/\ell^2) \int_0^\ell r^2 A dr$.

Because the corrective term A can prove to be difficult to compute in spacecraft data due to the term $\delta[(\mathbf{b} \cdot \nabla)\mathbf{b}]$, we will see in the next section that H18 law can be improved and written using a simpler and more compact formulation involving only the \mathbf{H} term.

3. Alternative Formulation of the Corrected H18

To improve the corrected H18 law we need to do some calculations on the term A . Using the fact that $\nabla(\mathbf{X} \cdot \mathbf{X}) = 2\mathbf{X} \times (\nabla \times \mathbf{X}) + 2(\mathbf{X} \cdot \nabla)\mathbf{X}$ and following a logic of calculation similar to Banerjee & Kritsuk (2018), we have

$$A = d_i \left\langle \delta \mathbf{j} \cdot \delta \left[\frac{1}{2} \nabla(\mathbf{b} \cdot \mathbf{b}) + \mathbf{j} \times \mathbf{b} \right] \right\rangle, \quad (24)$$

and, using derivative properties along with $\nabla \cdot \mathbf{j} = 0$, this equation reduces to

$$A = d_i \langle \delta \mathbf{j} \cdot \delta(\mathbf{j} \times \mathbf{b}) \rangle. \quad (25)$$

Now, with the relation $\nabla \cdot (\mathbf{X} \times \mathbf{Y}) = \mathbf{Y} \cdot (\nabla \times \mathbf{X}) - \mathbf{X} \cdot (\nabla \times \mathbf{Y})$ we can write (following Banerjee & Galtier 2017)

$$\begin{aligned} \langle (\mathbf{j} \times \mathbf{b}) \cdot \mathbf{j}' \rangle &= \langle (\mathbf{j} \times \mathbf{b}) \cdot (\nabla' \times \mathbf{b}') \rangle \\ &= -\langle \nabla' \cdot [(\mathbf{j} \times \mathbf{b}) \times \mathbf{b}'] \rangle \\ &= -\nabla_\ell \cdot \langle (\mathbf{j} \times \mathbf{b}) \times \mathbf{b}' \rangle, \end{aligned} \quad (26)$$

$$\langle (\mathbf{j}' \times \mathbf{b}') \cdot \mathbf{j} \rangle = \nabla_\ell \cdot \langle (\mathbf{j}' \times \mathbf{b}') \times \mathbf{b} \rangle, \quad (27)$$

$$\langle (\mathbf{j}' \times \mathbf{b}') \cdot \mathbf{j}' \rangle = \langle (\mathbf{j} \times \mathbf{b}) \cdot \mathbf{j} \rangle = 0, \quad (28)$$

which leads to

$$A = d_i \nabla_\ell \cdot \langle (\mathbf{j} \times \mathbf{b}) \times \mathbf{b}' - (\mathbf{j}' \times \mathbf{b}') \times \mathbf{b} \rangle. \quad (29)$$

Using identities for a double cross product, Equation (29) can be cast as

$$\begin{aligned} A &= \frac{1}{2} d_i \nabla_\ell \cdot \langle 2(\delta \mathbf{b} \cdot \delta \mathbf{j}) \delta \mathbf{b} - (\delta \mathbf{b} \cdot \delta \mathbf{b}) \delta \mathbf{j} \rangle \\ &\quad - d_i \nabla_\ell \cdot \langle (\mathbf{b} \cdot \mathbf{j}') \mathbf{b} - (\mathbf{b}' \cdot \mathbf{j}) \mathbf{b}' \rangle \\ &= \frac{1}{2} \nabla_\ell \cdot \mathbf{H} \\ &\quad + d_i \langle \mathbf{j}' \cdot [(\mathbf{b} \cdot \nabla) \mathbf{b}] + \mathbf{j} \cdot [(\mathbf{b}' \cdot \nabla) \mathbf{b}'] \rangle \\ &= \frac{1}{2} \nabla_\ell \cdot \mathbf{H} - A, \end{aligned} \quad (30)$$

and we obtain

$$\nabla_\ell \cdot \mathbf{H} = 4A. \quad (31)$$

Injecting relation (31) into expression (19) we finally obtain the new formulation

$$-4\varepsilon = \nabla_\ell \cdot \left(\mathbf{Y} + \frac{1}{2} \mathbf{H} \right), \quad (32)$$

which can be reduced to the following expression in the isotropic case:

$$-\frac{4}{3}\varepsilon\ell = Y_\ell + \frac{1}{2}H_\ell. \quad (33)$$

This new formulation, which will be referred to as F19 hereafter, is one of the main results of this paper. It has the double advantage of depending only on the product of increments of the physical fields (unlike the G08 model) and of being expressed only as flux terms. This makes it easier to apply in particular to single spacecraft data (under the assumption of isotropy).

Below we will verify whether the law (32) derived above is compatible with the other IHMHD laws (G08 and BG17) in the inertial range. The testing will be focused on the Hall-induced terms \mathbf{H} and A , as the ideal MHD term \mathbf{Y} is exactly the same as the one from Politano & Pouquet (1998b) and, by extension, the same as the ideal MHD component of G08. We will first investigate this question at the mathematical level and then with DNSs of EMHD.

4. Equivalence of the Exact Laws

4.1. Compatibility between F19 and G08

Here we show the equivalence of F19 and G08 by keeping only the Hall contributions. In G08, the law reads with our notation

$$-4\varepsilon_{\text{Hall}} = 4d_i \nabla_\ell \cdot \langle (\mathbf{j} \times \mathbf{b}) \times \delta \mathbf{b} \rangle. \quad (34)$$

We already showed that $\nabla_\ell \cdot \mathbf{H} = 4A$. With Equation (29) we have

$$\begin{aligned} \frac{1}{2} \nabla_\ell \cdot \mathbf{H} &= 2d_i \nabla_\ell \cdot \langle (\mathbf{j} \times \mathbf{b}) \times \mathbf{b}' - (\mathbf{j}' \times \mathbf{b}') \times \mathbf{b} \rangle \\ &= 4d_i \nabla_\ell \cdot \langle (\mathbf{j} \times \mathbf{b}) \times \mathbf{b}' \rangle, \end{aligned} \quad (35)$$

which is enough to show that

$$\frac{1}{2} \nabla_\ell \cdot \mathbf{H} = 4d_i \nabla_\ell \cdot \langle (\mathbf{j} \times \mathbf{b}) \times \delta \mathbf{b} \rangle, \quad (36)$$

proving the compatibility.

4.2. Compatibility between G08 and BG17

Demonstrating the equivalence between the Hall terms of G08 and BG17 is even simpler. In the latter the Hall term is written

$$-4\varepsilon_{\text{Hall}} = 2d_i \langle \delta(\mathbf{j} \times \mathbf{b}) \cdot \delta \mathbf{j} \rangle. \quad (37)$$

Using Equations (25) and (31) we immediately obtain

$$\frac{1}{2} \nabla_\ell \cdot \mathbf{H} = 2d_i \langle \delta(\mathbf{j} \times \mathbf{b}) \cdot \delta \mathbf{j} \rangle, \quad (38)$$

and thus prove the equivalence.

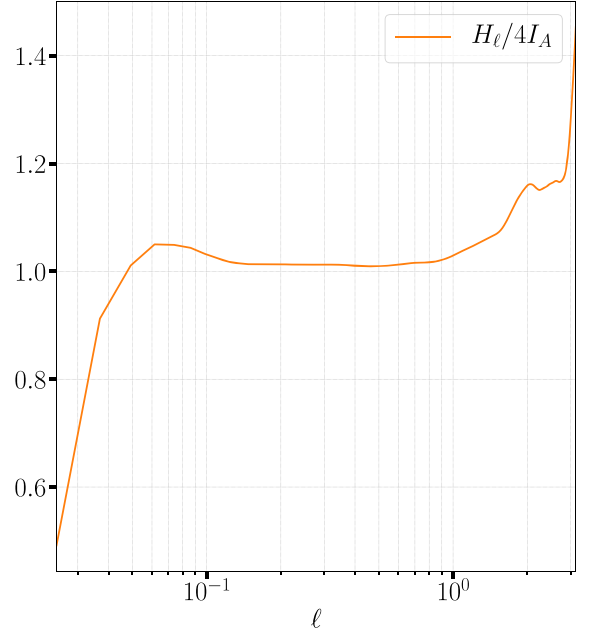


Figure 1. Ratio of H_ℓ to $4I_A$ of the F19 law.

5. Numerical Study

5.1. The Equivalence of the Models G08, BG17, and F19

In this section we will compare the G08, BG17, and F19 laws by using 3D DNSs of incompressible EMHD turbulence (Equations (4) with $\nu = 0$). We used a modified version of the TURBO code (Teaca et al. 2009) in which we have implemented the Hall effect (Meyrand & Galtier 2013). The EMHD equations are solved in a triply periodic box. A pseudospectral algorithm is used to perform the spatial discretization on a grid with a resolution of 512^3 collocation points (see Meyrand & Galtier 2013 for further details). A mean guide field \mathbf{b}_0 of magnitude unity is introduced along the z axis. A large-scale forcing is applied that enforces a constant rate of energy injection with no helicity. The system is evolved until a stationary state is reached such that $\mathbf{b}_{\text{rms}} \sim \mathbf{b}_0$. We removed the amount of ideal invariants that is injected into the system by the forcing mechanism by means of magnetic hyperdiffusivity $\eta_3 \Delta^3$ with $\eta_3 = 10e^{-11}$. The data consist of three periodic cubes giving the three components of the magnetic field in each grid point. The values of $\varepsilon_{\text{Hall}}$ are obtained by averaging the mixed field increments of the different exact laws over all the points of the data cubes and spherically integrating them, using for the increment vectors ℓ a set of specific directions in space defined by 73 base vectors as described in Taylor et al. (2003), and lengths going from a three point distance to half the size of the cubes (see also Andrés et al. 2018b).

First of all, we want to check numerically the new law F19 and, more precisely, the analytical relation found between H_ℓ and $4I_A$. In Figure 1 we represent $H_\ell/4I_A$, which shows differences mainly at large and small scales but not at intermediate scales where the inertial range is supposed to be. The differences observed are probably a consequence of the different nature of these two terms, being respectively a flux and an integrated term. The methods involved in the calculation being different, we can expect some minor differences. These should not alter the estimation of the energy cascade rate that is

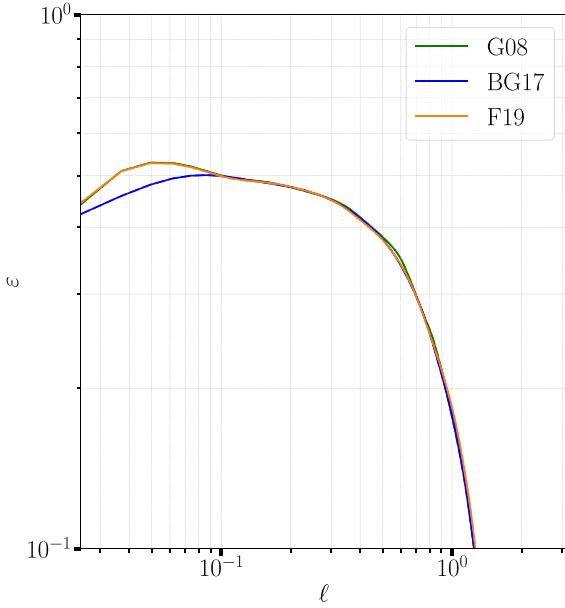


Figure 2. Energy cascade rates $\varepsilon_{\text{Hall}}$ computed with F19, G08, and BG17.

measured in the inertial range, i.e., for scales $\ell \leq 0.3$ (see below).

To compare the three energy cascade rates obtained with the different expressions we first note that the Hall term in the G08 model can be written as

$$\text{G08}_{\text{Hall}} = 2\nabla_{\ell} \cdot \langle (\mathbf{j} \times \mathbf{b}) \times \delta \mathbf{b} + (\mathbf{j}' \times \mathbf{b}') \times \delta \mathbf{b} \rangle.$$

This formulation is chosen (over other possible expressions) because it ensures a symmetry between \mathbf{x} and \mathbf{x}' as in the two other laws, F19 and BG17. One must also be careful when computing BG17, as this law gives the energy cascade rate as a function of a direct statistical mean and not a flux, and thus does not require an integration a priori. However, we need to keep in mind that ε is not, in fact, exactly constant in our data. Consequently, when we integrate F19 and G08, we compute in reality $(1/\ell^3) \int_0^{\ell} r^2 \varepsilon dr$ and not ε . To remain consistent between the three models, we need to use the nonintegrated forms of both F19 and G08 ((32), (34)). This is what will be done hereafter.

We computed the energy cascade rate from the three laws and obtained the results gathered in Figure 2. All three laws fit remarkably well with each other, however, with a slightly different behavior of BG17 model at scales $\ell \leq 0.1$. Using the nonintegrated forms of G08 and F19 required us to apply a discrete derivation to our results as we only compute the inner bracket of the flux terms, and we expect this operation to be responsible for the differences at small scales due to a lack of resolution in this range of scales. The inertial range induced by the Hall effect is not easy to pinpoint precisely, but can be roughly estimated as going from 0.05 to 0.3 in this simulation.

5.2. On the Role of \mathbf{b}_0

Finally, we tested the influence of a guide field \mathbf{b}_0 on the estimation of $\varepsilon_{\text{Hall}}$. Indeed, the introduction of a uniform magnetic field \mathbf{b}_0 into the previous laws does not change their expression. This is obvious for F19, which only depends on increments, and for BG17, in which the \mathbf{b}_0 influence translates

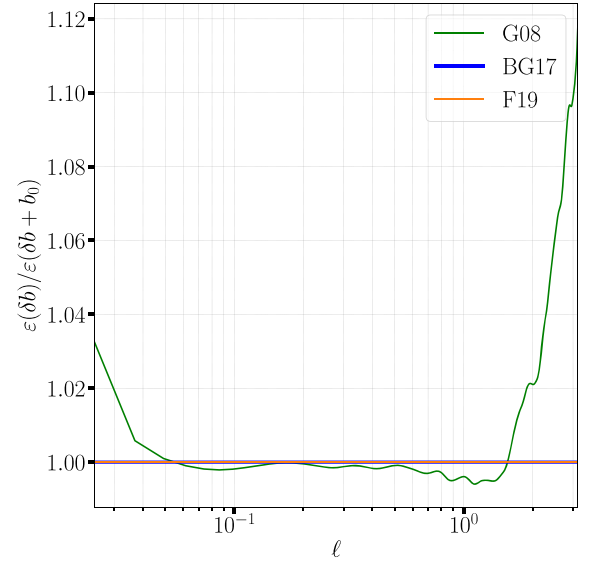


Figure 3. Ratios of $\varepsilon_{\text{Hall}}$ computed from the data cubes where the guide field \mathbf{b}_0 is removed and from the data cubes where it is not. The values obtained with F19 and BG17 overlap.

as $\langle \delta \mathbf{j} \cdot ((\delta \mathbf{j}) \times \mathbf{b}_0) \rangle = 0$. For G08 we have

$$\begin{aligned} \text{G08}_{\text{Hall}} &= 2\nabla_{\ell} \cdot \langle (\mathbf{j} \times \mathbf{b}_0) \times \mathbf{b}' - (\mathbf{j}' \times \mathbf{b}_0) \times \mathbf{b} \rangle \\ &= -2\langle (\mathbf{j} \times \mathbf{b}_0) \cdot \mathbf{j}' + (\mathbf{j}' \times \mathbf{b}_0) \cdot \mathbf{j} \rangle \\ &= 0. \end{aligned} \quad (39)$$

Thus, when computing ε taking \mathbf{b}_0 into account or not in the data should not affect the result. However, for practical reasons related to the numerical computation, \mathbf{b}_0 may have some influence on estimating ε as we show now.

Values of $\varepsilon_{\text{Hall}}$ computed only with the fluctuating magnetic fields were obtained by averaging the magnetic field component along the guide field axis (here the z axis) and subtracting this value from that component. In Figure 3 we see that computing the energy cascade rate with or without the mean guide field leads to the same result for all but G08, even though the contribution of \mathbf{b}_0 reduces to zero mathematically. The difference is, however, very small in the inertial range (less than 0.5%).

We believe this problem to be tied to the way we handle derivatives. F19 is formed of only increments and so does not involve \mathbf{b}_0 , unlike the models BG17 and G08 that contain a \mathbf{b}_0 contribution a priori, but whose contributions in fact reduce to zero. However, from these contributions, only the one in G08 comes from a flux term and so is preceded by a derivative. When we compute numerically the energy cascade rates we do not really calculate this derivative but rather use the approximation $\nabla_{\ell} \rightarrow 1/\ell$. Thus, we are making an approximation in the calculation and this may be the cause of the behavior shown in Figure 3. A similar remark was made in Hadid et al. (2017), which led us to this conclusion. It may also be worth mentioning that the validity of this approximation is tied to the validity of the hypotheses of isotropy and homogeneity, and the influence of \mathbf{b}_0 would probably be more important when using observational data where these hypotheses are harder to meet.

Based on these remarks and on the behavior of the three laws we conclude that, as expected, \mathbf{b}_0 does not contribute explicitly to the incompressible energy cascade rate and, in the purpose of

computing $\varepsilon_{\text{Hall}}$, that it should be removed from the simulation of the spacecraft data beforehand in order to minimize the possible numerical errors that it can generate. Note that this property does not mean that b_0 has no influence on the nonlinear dynamics (Galtier et al. 2000; Wan et al. 2012; Oughton et al. 2013): it is actually expected that the energy cascade rate $\varepsilon_{\text{Hall}}$ decreases with increasing b_0 , as shown recently with DNSs (Bandyopadhyay et al. 2018). It is worth mentioning that the situation is very different in compressible law (e.g., Banerjee & Galtier 2013) where the b_0 dependence is explicit and cannot a priori be ruled out (Hadid et al. 2017). However, recent developments suggest that its influence will not be significant as it mostly impacts the volumic contributions to the law, which appear to be small compared to the dominant flux terms (Andrés et al. 2018b).




6. Conclusion

The energy cascade rate ε is an essential tool for studying turbulent flows. Despite being sometimes hard to compute it can be theoretically calculated by several equivalent formulations. We showed here that the law (19), which is obtained using the same premises as proposed in Hellinger et al. (2018), can be written (when corrected) in a compact form with only a flux term (32). As shown numerically, this gives the same energy cascade rate in the inertial range as with the G08 and BG17 laws. This diversity of exact laws gives more freedom to compute the energy cascade rate of IHMHD turbulence as it is possible to adapt the computation method to the data available and their quality.

For instance, we showed that the presence of a mean guide field should not contribute explicitly to the energy cascade rate. This theoretical property is well verified with DNSs for BG17 and F19, but not for G08, which shows a dependence on b_0 that can be interpreted as residual errors due to the performed computation. Although this dependence remains small in the present paper, it is more important in spacecraft data analysis (N. Andrés 2019, private communication). Therefore, we advise using F19 or BG17 laws to compute the energy cascade rate as they are free from the errors induced by the presence of a mean guide field.

The authors acknowledge financial support from CNRS/CONICET Laboratoire International Associé (LIA) MAGNETO. N.A. is supported through a DIM-ACAV post-doctoral fellowship. S.B. acknowledges DST Inspire research grant.

ORCID iDs

S. Galtier  <https://orcid.org/0000-0001-8685-9497>
 N. Andrés  <https://orcid.org/0000-0002-1272-2778>
 S. Banerjee  <https://orcid.org/0000-0002-3746-0989>

References

Andrés, N., Galtier, S., & Sahraoui, F. 2018a, *PhRvE*, **97**, 013204

- Andrés, N., & Sahraoui, F. 2017, *PhRvE*, **96**, 053205
 Andrés, N., Sahraoui, F., Galtier, S., et al. 2018b, *JPhPh*, **84**, 905840404
 Antonia, R., Ould-Rouis, M., Anselmet, F., & Zhu, Y. 1997, *JFM*, **332**, 395
 Bandyopadhyay, R., Oughton, S., Wan, M., et al. 2018, *PhRvX*, **8**, 041052
 Banerjee, S., & Galtier, S. 2013, *PhRvE*, **87**, 013019
 Banerjee, S., & Galtier, S. 2014, *JFM*, **742**, 230
 Banerjee, S., & Galtier, S. 2016, *PhRvE*, **93**, 033120
 Banerjee, S., & Galtier, S. 2017, *JPhA*, **50**, 015501
 Banerjee, S., Hadid, L., Sahraoui, F., & Galtier, S. 2016, *ApJL*, **829**, L27
 Banerjee, S., & Kritsuk, A. G. 2017, *PhRvE*, **96**, 053116
 Banerjee, S., & Kritsuk, A. G. 2018, *PhRvE*, **97**, 023107
 Batchelor, G. 1953, *The Theory of Homogeneous Turbulence* (Cambridge: Cambridge Univ. Press)
 Carbone, V., Marino, R., Sorriso-Valvo, L., Noullez, A., & Bruno, R. 2009, *PhRvL*, **103**, 061102
 Coburn, J., Forman, M., Smith, C., Vasquez, B., & Stawarz, J. 2015, *RSPTA*, **373**, 20140150
 Duchon, J., & Robert, R. 2000, *Nonli*, **13**, 249
 Eyink, G. L. 1994, *PhyD*, **78**, 222
 Frisch, U. 1995, *Turbulence* (Cambridge: Cambridge Univ. Press)
 Galtier, S. 2008, *PhRvE*, **77**, 015302
 Galtier, S. 2016, *Introduction to Modern Magnetohydrodynamics* (Cambridge: Cambridge Univ. Press)
 Galtier, S. 2018, *JPhA*, **51**, 205501
 Galtier, S., & Banerjee, S. 2011, *PhRvL*, **107**, 134501
 Galtier, S., Nazarenko, S., Newell, A., & Pouquet, A. 2000, *JPhPh*, **63**, 447
 Hadid, L., Sahraoui, F., & Galtier, S. 2017, *ApJ*, **838**, 9
 Hadid, L. Z., Sahraoui, F., Galtier, S., & Huang, S. Y. 2018, *PhRvL*, **120**, 055102
 He, J., Wang, L., Tu, C., Marsch, E., & Zong, Q. 2015, *ApJL*, **800**, L31
 Hellinger, P., Verdini, A., Landi, S., Franci, L., & Matteini, L. 2018, *ApJL*, **857**, L19
 Kolmogorov, A. 1941, *DoSSR*, **32**, 16
 MacBride, B., Smith, C., & Forman, M. 2008, *ApJ*, **679**, 1644
 Marino, R., Sorriso-Valvo, L., Carbone, V., et al. 2008, *ApJL*, **677**, L71
 Matthaeus, W. H., Zank, G. P., Smith, C. W., & Oughton, S. 1999, *PhRvL*, **82**, 3444
 Meyrand, R., & Galtier, S. 2013, *PhRvL*, **111**, 264501
 Mininni, P. D., & Pouquet, A. 2009, *PhRvE*, **80**, 025401
 Monin, A. S. 1959, *Doklady Akademii Nauk SSSR*, **125**, 515
 Onsager, L. 1949, *NCim*, **6**, 279
 Osman, K. T., Wan, M., Matthaeus, W. H., Weygand, J. M., & Dasso, S. 2011, *PhRvL*, **107**, 165001
 Oughton, S., Wan, M., Servidio, S., & Matthaeus, W. H. 2013, *ApJ*, **768**, 10
 Podesta, J. J., Forman, M. A., & Smith, C. W. 2007, *PhPl*, **14**, 092305
 Politano, H., & Pouquet, A. 1998a, *PhRvE*, **57**, 21
 Politano, H., & Pouquet, A. 1998b, *GeoRL*, **25**, 273
 Richardson, J. D., Paularena, K. I., Lazarus, A. J., & Belcher, J. W. 1995, *GeoRL*, **22**, 325
 Sahraoui, F., Goldstein, M. L., Belmont, G., Canu, P., & Rezeau, L. 2010, *PhRvL*, **105**, 131101
 Sahraoui, F., Goldstein, M. L., Robert, P., & Khotyaintsev, Y. V. 2009, *PhRvL*, **102**, 231102
 Saint-Michel, B., Herbert, E., Salort, J., et al. 2014, *PhFI*, **26**, 125109
 Smith, C. W., Stawarz, J. E., Vasquez, B. J., Forman, M. A., & MacBride, B. T. 2009, *PhRvL*, **103**, 201101
 Sorriso-Valvo, L., Marino, R., Carbone, V., et al. 2007, *PhRvL*, **99**, 115001
 Stawarz, J. E., Smith, C. W., Vasquez, B. J., Forman, M. A., & MacBride, B. T. 2009, *ApJ*, **697**, 1119
 Taylor, M. A., Kurien, S., & Eyink, G. L. 2003, *PhRvE*, **68**, 026310
 Teaca, B., Verma, M. K., Knaepen, B., & Carati, D. 2009, *PhRvE*, **79**, 046312
 Wan, M., Oughton, S., Servidio, S., & Matthaeus, W. H. 2012, *JFM*, **697**, 296



Compressible Turbulence in the Interstellar Medium: New Insights from a High-resolution Supersonic Turbulence Simulation

R. Ferrand¹ , S. Galtier^{1,2} , F. Sahraoui¹, and C. Federrath³

¹Laboratoire de Physique des Plasmas, CNRS, École polytechnique, Université Paris-Saclay, Sorbonne Université, Observatoire de Paris-Meudon, F-91128 Palaiseau Cedex, France; renaud.ferrand@lpp.polytechnique.fr

²Institut Universitaire de France (IUF), France

³Research School of Astronomy and Astrophysics, Australian National University, Canberra, ACT 2611, Australia
Received 2020 July 10; revised 2020 September 8; accepted 2020 September 9; published 2020 November 30

Abstract

The role of supersonic turbulence in structuring the interstellar medium (ISM) remains an unsettled question. Here, this problem is investigated using a new exact law of compressible isothermal hydrodynamic turbulence, which involves two-point correlations in physical space. The new law is shown to have a compact expression that contains a single flux term reminiscent of the incompressible case and a source term with a simple expression whose sign is given by the divergence of the velocity. The law is then used to investigate the properties of such a turbulence at integral Mach number 4 produced by a massive numerical simulation with a grid resolution of $10,048^3$ points. The flux (resp. source) term was found to have positive (resp. negative) contribution to the total energy cascade rate, which is interpreted as a direct cascade amplified by compression, while their sum is constant in the inertial range. Using a local (in space) analysis it is shown that the source is mainly driven by filamentary structures in which the flux is negligible. Taking positive defined correlations reveals the existence of different turbulent regimes separated by the sonic scale, which determines the scale over which the nonnegligible source modifies the scaling of the flux. Our study provides new insight into the dynamics and structures of supersonic interstellar turbulence.

Unified Astronomy Thesaurus concepts: [Interstellar medium \(847\)](#); [Interstellar filaments \(842\)](#); [Hydrodynamical simulations \(767\)](#); [Hydrodynamics \(1963\)](#)

1. Introduction

Understanding turbulent space and astrophysical plasmas is an ongoing physical challenge that has drawn a lot of attention throughout recent years. As these plasmas are present in a wide range of astrophysical media, from the Earth's magnetosphere to distant star-forming clouds, being able to properly describe them would allow us to make significant progress in understanding the physics controlling the shape and evolution of these media. Among these recent findings, it has been shown that the introduction of compressibility in magnetohydrodynamic (MHD) and Hall-MHD models of space plasmas leads to a higher estimate of the mean dissipation rate of total energy (used as a proxy for measuring plasma heating; Banerjee et al. 2016; Hadid et al. 2017; Andrés et al. 2019) compared to the incompressible case (Sorriso-Valvo et al. 2007). For the interstellar medium (ISM) where observations indicate that turbulence is supersonic (Wilson et al. 1970; Elmegreen & Scalo 2004; Heyer & Brunt 2004; Padoan et al. 2014; Krumholz & Federrath 2019), numerical simulations performed in the framework of compressible (isothermal) HD (Vázquez-Semadeni 1994; Passot & Vázquez-Semadeni 1998; Kritsuk et al. 2007; Federrath et al. 2010; Federrath 2013) have shown the presence of filaments that resemble the structures observed in the ISM (Arzoumanian et al. 2011; Federrath 2016). It was found that incompressible predictions can be restored in some cases if one considers the density-weighted fluid velocity $\rho^{1/3}\mathbf{u}$ instead of the simple velocity \mathbf{u} (Kritsuk et al. 2007; Schmidt et al. 2008), a behavior that can be understood dimensionally with an exact law (Galtier & Banerjee 2011).

What makes this kind of study difficult is that the mechanisms governing fluid turbulence are still not fully

understood. Due to its chaotic nature, the favored way of studying turbulence is to resort to a statistical approach allowing for the use of specific tools (Frisch 1995), such as exact laws. Kolmogorov was among the pioneers in this field with his so-called four-fifths law (Kolmogorov 1941), an exact relation for homogeneous incompressible isotropic hydrodynamic (HD) turbulence that paved the way to new advances in the study of nonlinear physics. This statistical law allows one to express the mean rate of kinetic energy transfer per unit volume as a function of a two-point third-order longitudinal structure function in the limit of a high Reynolds number. In the wake of Kolmogorov's work, several other exact laws were derived for HD (Monin 1959; Antonia et al. 1997), quasi-geostrophic flows (Lindborg 2007), thin elastic plates (Dering & Krstulovic 2018), or plasmas (Politano & Pouquet 1998; Galtier 2008; Meyrand & Galtier 2010; Yoshimatsu 2012; Ferrand et al. 2019). The influence of compressibility being important for the description of space and astrophysical plasmas, efforts have been made during recent years to derive exact laws for compressible turbulence in HD (Galtier & Banerjee 2011; Banerjee & Kritsuk 2017; Lindborg 2019) and magnetohydrodynamics (MHD; Banerjee & Galtier 2013; Galtier 2016; Andrés & Sahraoui 2017; Andrés et al. 2018; Banerjee & Kritsuk 2018).

In the quest for exact laws for compressible turbulence, the complexity may increase significantly (Banerjee & Galtier 2013; Andrés et al. 2018). It is therefore relevant to ask whether it is possible to find a compact form of these laws that reveals the most salient feature of turbulence. Ferrand et al. (2019) recently showed that several different—yet equivalent—exact laws can be derived for Hall MHD, with some being more compact and easier to compute and interpret. Following

the same method, it is the first main goal of this paper to demonstrate that such a compact form—called hereafter the generalized Kolmogorov law—exists in isothermal compressible HD turbulence. In the second part, this new relation is used to study such a turbulence, at integral Mach number 4, using a massive numerical simulation with a grid resolution of 10, 048³ points (Federrath et al. 2016a, 2020). We proceed to a global computation of the law on the whole system and to a local computation along filamentary structures. Our analysis reveals supersonic turbulence properties that can be used to better understand ISM turbulence and star formation (Heyer & Brunt 2004; McKee & Ostriker 2007; Arzoumanian et al. 2011; Federrath & Klessen 2012; Padoan et al. 2014; Orkisz et al. 2017).

Section 2 contains the main steps of the derivation of the new exact law for compressible HD turbulence, along with a first theoretical interpretation. In Section 3 we apply this model to our numerical simulation and expose the results obtained. These results are discussed in Section 4 and we give an overall conclusion in Section 5 in the context of ISM turbulence and star formation.

2. Generalized Kolmogorov Law

Our analysis is based on the compressible HD equations

$$\partial_t \rho + \nabla \cdot (\rho \mathbf{u}) = 0, \quad (1)$$

$$\partial_t (\rho \mathbf{u}) + \nabla \cdot (\rho \mathbf{u} \mathbf{u}) = -\nabla P + \mathbf{d} + \mathbf{f}, \quad (2)$$

where ρ is the density, P is the pressure, $\mathbf{d} \equiv \mu \Delta \mathbf{u} + (\mu/3) \nabla \theta$ is the dissipation, $\theta \equiv \nabla \cdot \mathbf{u}$ is the dilatation, μ is the coefficient of viscosity, and \mathbf{f} is a stationary homogeneous external force assumed to act on large scales. The system is closed with the isothermal equation of state $P = c_s^2 \rho$ with c_s being the sound speed, assumed to be constant (in practice, we only use the density in the numerical code and set $c_s = 1$). The energy equation takes the form

$$\partial_t \langle E \rangle = \langle \mathbf{u} \cdot \mathbf{d} \rangle + \langle \mathbf{u} \cdot \mathbf{f} \rangle, \quad (3)$$

with $\langle \rangle$ an ensemble average, $E = \rho u^2/2 + \rho e$ the total energy, $e = c_s^2 \ln(\rho/\rho_0)$ the internal energy ($\rho_0 = \langle \rho \rangle$ is the average density), $\langle \mathbf{u} \cdot \mathbf{f} \rangle = \varepsilon$ the mean rate of total energy injection into the system, and $\langle \mathbf{u} \cdot \mathbf{d} \rangle = -\mu \langle (\nabla \times \mathbf{u})^2 \rangle - \frac{4}{3} \mu \langle \theta^2 \rangle$.

We define ℓ the spatial increment connecting two points \mathbf{x} and \mathbf{x}' as $\mathbf{x}' = \mathbf{x} + \ell$ and, for any given field ξ , $\xi(\mathbf{x}) \equiv \xi$, and $\xi(\mathbf{x}') \equiv \xi'$. We follow the same idea as Hellinger et al. (2018) and Ferrand et al. (2019) and search for a dynamical equation of a structure function for the fluctuating energy:

$$\langle \mathcal{S} \rangle = \langle \bar{\delta} \rho (\delta \mathbf{u})^2 + \delta \rho \delta e \rangle, \quad (4)$$

where for any given field ξ , $\delta \xi \equiv \xi' - \xi$ and $\bar{\delta} \xi \equiv (\xi + \xi')/2$. The use of this structure function represents the main difference between this approach and the one of Galtier & Banerjee (2011). Developing \mathcal{S} leads to

$$\begin{aligned} \langle \mathcal{S} \rangle &= 2 \langle E \rangle - 2 \langle \bar{\delta} \rho \mathbf{u} \cdot \mathbf{u}' \rangle - \langle \rho' e + \rho e' \rangle \\ &+ \frac{1}{2} \langle \rho u'^2 + \rho' u^2 \rangle. \end{aligned} \quad (5)$$

Therefore, finding the temporal evolution of \mathcal{S} is akin to finding the temporal evolution of every term on the RHS of Equation (5).

The rest of the derivation is similar to the one given in Galtier & Banerjee (2011). Most of the terms have been derived in Galtier & Banerjee (2011); therefore, we only give the details for the calculation of the new term $\langle \rho u'^2 \rangle$ (from which the symmetric contribution can be obtained immediately). We obtain the following expressions:

$$\begin{aligned} \partial_t \langle \rho \mathbf{u} \cdot \mathbf{u}' \rangle &= \nabla_\ell \cdot \langle -\rho (\mathbf{u} \cdot \mathbf{u}') \delta \mathbf{u} \\ &+ P \mathbf{u}' - \rho e' \mathbf{u} \rangle + \langle \rho \theta' (\mathbf{u} \cdot \mathbf{u}') \rangle \\ &+ \langle \mathbf{u}' \cdot \mathbf{d} + \mathbf{u}' \cdot \mathbf{f} + \frac{\rho}{\rho'} \mathbf{u} \cdot (\mathbf{d}' + \mathbf{f}') \rangle, \end{aligned} \quad (6)$$

$$\partial_t \langle \rho e' \rangle = \nabla_\ell \cdot \langle -\rho e' \delta \mathbf{u} - P \mathbf{u}' \rangle + \langle \rho e' \theta' \rangle, \quad (7)$$

$$\begin{aligned} \partial_t \langle \rho u'^2 \rangle &= \langle 2 \rho \mathbf{u}' \cdot \partial_t \mathbf{u}' + u'^2 \partial_t \rho \rangle \\ &= \left\langle -\mathbf{u}' \cdot \nabla' (\rho u'^2) - 2 \frac{\rho}{\rho'} \mathbf{u}' \cdot \nabla' P' \right\rangle \\ &+ \nabla_\ell \cdot \langle \rho u'^2 \mathbf{u}' \rangle + \left\langle 2 \frac{\rho}{\rho'} \mathbf{u}' \cdot \mathbf{d}' + 2 \frac{\rho}{\rho'} \mathbf{u}' \cdot \mathbf{f}' \right\rangle \\ &= \nabla_\ell \cdot \langle -\rho u'^2 \mathbf{u}' + \rho u'^2 \mathbf{u}' \rangle + \left\langle \rho u'^2 \theta' - 2 \frac{\rho}{\rho'} \mathbf{u}' \cdot \nabla' P' \right\rangle \\ &+ \left\langle 2 \frac{\rho}{\rho'} \mathbf{u}' \cdot \mathbf{d}' + 2 \frac{\rho}{\rho'} \mathbf{u}' \cdot \mathbf{f}' \right\rangle, \end{aligned} \quad (8)$$

where ∇_ℓ is the derivative along the ℓ direction. The combination of the different contributions gives after simplification,

$$\begin{aligned} \partial_t \langle \mathcal{S} \rangle &= 2 \partial_t \langle E \rangle - \nabla_\ell \cdot \langle \bar{\delta} \rho (\delta \mathbf{u})^2 \delta \mathbf{u} \rangle \\ &+ \frac{1}{2} \langle (\rho \theta' + \rho' \theta) (\delta \mathbf{u})^2 \rangle - F - D, \end{aligned} \quad (9)$$

with, by definition,

$$\begin{aligned} F \equiv \left\langle \mathbf{u} \cdot \mathbf{f}' + \mathbf{u}' \cdot \mathbf{f} + \frac{\rho}{\rho'} \mathbf{u} \cdot \mathbf{f}' + \frac{\rho'}{\rho} \mathbf{u}' \cdot \mathbf{f} \right. \\ \left. - \frac{\rho'}{\rho} \mathbf{u} \cdot \mathbf{f} - \frac{\rho}{\rho'} \mathbf{u}' \cdot \mathbf{f}' \right\rangle, \end{aligned} \quad (10)$$

$$\begin{aligned} D \equiv \left\langle \mathbf{u} \cdot \mathbf{d}' + \mathbf{u}' \cdot \mathbf{d} + \frac{\rho}{\rho'} \mathbf{u} \cdot \mathbf{d}' + \frac{\rho'}{\rho} \mathbf{u}' \cdot \mathbf{d} \right. \\ \left. - \frac{\rho'}{\rho} \mathbf{u} \cdot \mathbf{d} - \frac{\rho}{\rho'} \mathbf{u}' \cdot \mathbf{d}' \right\rangle. \end{aligned} \quad (11)$$

The stationarity assumption leads to the cancellation of the term on the LHS and the energy term on the RHS of Equation (9). In this situation, all the energy injected by the forcing must necessarily be dissipated at the same rate ε , so that we have the relationship $\varepsilon = \langle \mathbf{u} \cdot \mathbf{f} \rangle = -\langle \mathbf{u} \cdot \mathbf{d} \rangle$. The content of the forcing and dissipative terms F and D can then be broken down into three parts: first, since the forcing is assumed to act on large scales only, its variations across the simulation domain should remain small. Thus, forcing cross-terms like $\mathbf{u} \cdot \mathbf{f}'$ are expected to behave like $\mathbf{u} \cdot \mathbf{f} = \varepsilon$ so we may write (see Kritsuk

et al. 2013)

$$\left\langle \mathbf{u} \cdot \mathbf{f}' + \mathbf{u}' \cdot \mathbf{f} + \frac{\rho}{\rho'} \mathbf{u} \cdot \mathbf{f}' + \frac{\rho'}{\rho} \mathbf{u}' \cdot \mathbf{f} \right\rangle \simeq 4\varepsilon. \quad (12)$$

Second, the stationarity assumption states that mean forcing and dissipation should balance each other with $\mathbf{u} \cdot \mathbf{f} = -\mathbf{u} \cdot \mathbf{d} = \varepsilon$, leading to

$$\left\langle \frac{\rho'}{\rho} \mathbf{u} \cdot \mathbf{f} + \frac{\rho}{\rho'} \mathbf{u}' \cdot \mathbf{f}' + \frac{\rho'}{\rho} \mathbf{u} \cdot \mathbf{d} + \frac{\rho}{\rho'} \mathbf{u}' \cdot \mathbf{d}' \right\rangle \simeq 0. \quad (13)$$

Third, as the dissipation is assumed to act on small scales only dissipative cross-terms such as $\mathbf{u} \cdot \mathbf{d}'$ are expected to be uncorrelated and of null statistical mean, hence (limit of small μ)

$$\left\langle \mathbf{u} \cdot \mathbf{d}' + \mathbf{u}' \cdot \mathbf{d} + \frac{\rho}{\rho'} \mathbf{u} \cdot \mathbf{d}' + \frac{\rho'}{\rho} \mathbf{u}' \cdot \mathbf{d} \right\rangle \simeq 0. \quad (14)$$

With these different estimates, the generalized Kolmogorov law for three-dimensional compressible isothermal turbulence reads

$$-4\varepsilon = \nabla_{\ell} \cdot \langle \bar{\delta}\rho(\delta\mathbf{u})^2 \delta\mathbf{u} \rangle - \frac{1}{2} \langle (\rho\theta' + \rho'\theta)(\delta\mathbf{u})^2 \rangle. \quad (15)$$

Expression (15) is the first main result of this paper. This compact law is valid for homogeneous—but not necessarily isotropic—turbulence. As explained above, to derive this expression we have assumed the existence of an inertial range where the forcing and the dissipation are negligible (Frisch 1995; Aluie 2011). The expression found is much simpler than the one proposed in Galtier & Banerjee (2011) because (i) the flux, $\mathbf{F} \equiv \langle \bar{\delta}\rho(\delta\mathbf{u})^2 \delta\mathbf{u} \rangle$, is constructed as a single term that resembles its incompressible version (that we recover by taking $\bar{\delta}\rho = \rho_0$, with ρ_0 a constant mass density), and (ii) the source is simply written as $S \equiv -(1/2) \langle (\rho\theta' + \rho'\theta)(\delta\mathbf{u})^2 \rangle$. It is a purely compressible term, which goes to zero when the incompressible limit is taken; then, we recover the original form of the well-known four-thirds law (Antonia et al. 1997). The sign of S is directly given by the sign of the dilatation: when the flow is mainly in a phase of dilatation ($\theta > 0$) the source is negative, whereas in a phase of compression ($\theta < 0$) the source is positive. We can also see that the source tends to zero on small scales along with the $(\delta\mathbf{u})^2$ factor, as $(\rho\theta' + \rho'\theta)$ remains finite as ℓ goes to zero. This contrasts with the flux term that can still have a nontrivial contribution because of the ℓ -derivative introducing a $1/\ell$ scaling. A natural scale below which the source would be negligible is the sonic scale, i.e., the scale where the turbulence transitions from supersonic to subsonic (Federrath et al. 2010, 2020). Finally, note that expression (15) is Galilean invariant as the primitive Equations (1)–(2).

The generalized Kolmogorov law can be interpreted as if we had an effective cascade driven only by the flux term $-4\varepsilon_{\text{eff}} \equiv \nabla_{\ell} \cdot \mathbf{F}$ (such that $\varepsilon_{\text{eff}} = \varepsilon + S/4$) that involves the usual energy injection/dissipation rate (ε) known in incompressible theory and a new purely compressible component (source) that reflects contraction and dilatation of the turbulent structures. If we assume that the cascade driven by the flux term is direct (i.e., $\varepsilon_{\text{eff}} > 0$) then a dilatation (compression) will

tend to oppose (sustain) the energy cascade, preventing (enforcing) the formation of smaller structures. Furthermore, the dilatation of the structures ($S < 0$) can annihilate the cascade to small scales (if $\varepsilon = -S/4$) or even reverse it (if $\varepsilon + S/4 < 0$) leading to the formation of large-scale structures via an inverse cascade. Note, however, that if S is scale dependent then compressible turbulence is not characterized by constant energy flux solutions as in incompressible theory (Kadomtsev & Petviashvili 1973; Passot et al. 1988). As we will see below, the numerical simulation will be very useful to go further in our interpretation.

3. Numerical Simulation

In this section the exact law (15) derived above is used to investigate supersonic turbulence produced by a massive numerical simulation with a grid resolution of 10, 048³ points and at Mach number 4. The Mach number is defined as $\mathcal{M} = \sigma_v/c_s$ with σ_v the velocity dispersion at the main forcing scale $L/2$ and L the simulation side length. The simulation was performed using a modified version of the FLASH code (Fryxell et al. 2000; Dubey et al. 2008; Federrath et al. 2020), solving the isothermal compressible HD equations in a triply periodic box. Following the methods in Federrath et al. (2010) the simulation uses a naturally mixed driving ($\zeta = 0.5$) with an Ornstein–Uhlenbeck process acting on large scales. The forcing amplitude is a paraboloid spanning $k = 1..3$, peaking at $k = 2$ and reaching zero at both $k = 1$ and $k = 3$, where the wavenumber k is in units of $2\pi/L$. Thus, the forcing acts on scales larger than $L/3$, which are well above the ones we study in this paper. The data used here are seven snapshots of the 10, 048³ simulation, sampled at a resolution of 2, 512³, of the density and the three components of the velocity field, taken at 2, 3, 4, 5, 6, 7, and 8 turbulence turnover times T (downsampling the data eases its handling without affecting the results reported in this paper). Figure 1 shows through rms Mach number and minimum and maximum densities that statistics for both velocity and density have converged after two turnover times, indicating that the simulation has reached a statistically stationary state (Federrath et al. 2009), hence the use of snapshots for times $t \geq 2T$.

For each snapshot the two terms of the exact law are computed along the three main axes x , y , and z , and then averaged spatially over the full box. The four signals obtained for different turnover times were eventually averaged to obtain the result displayed in Figure 2. First, we see that the mean rate of energy injection/dissipation ε (in red) is approximately constant over more than a decade. This observation indicates that the assumptions made to derive the law are satisfied on these scales of the simulation. The changes in ε observed on larger scales will be discussed in the next section in light of subsequent observations. Second, we see that the contribution of the flux term (in blue) is significantly higher than ε , which means that the source (in green) brings a correction to its contribution with an opposite sign, which is confirmed by the green dashed curve. For a better interpretation we can make a distinction between ε and ε_{eff} introduced above, i.e., the energy transferred between scales through the usual (incompressible) turbulence cascade driven by the flux term, in which case we have $\varepsilon = \varepsilon_{\text{eff}}$. Here, we see that $\varepsilon < \varepsilon_{\text{eff}}$ with a nonnegligible contribution from the source. This behavior contrasts with the one reported from direct numerical simulations of subsonic (compressible) MHD turbulence, where the overall

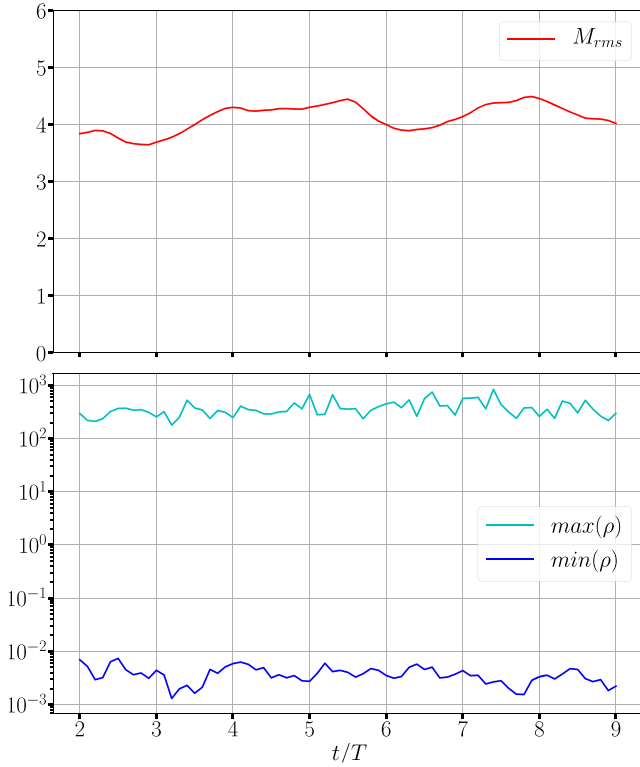


Figure 1. rms Mach number (top), maximum and minimum density (bottom) as functions of time (normalized to the turnover time T).

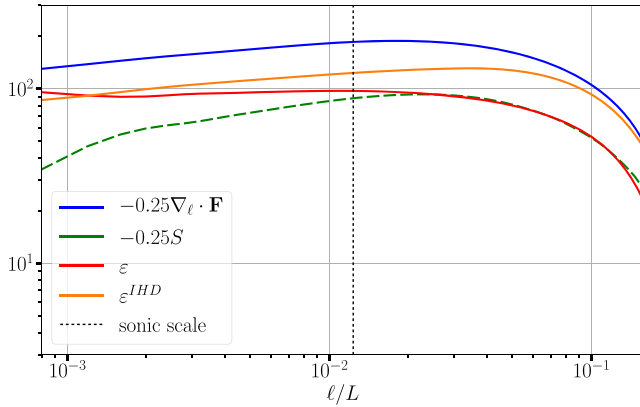


Figure 2. Normalized flux term, $-\nabla_{\ell} \cdot \mathbf{F}/4$ (blue), and normalized source $-S/4$ (green). The mean rate of energy injection/dissipation ε (red) is then deduced from the exact law (15). For comparison, we show the same quantity ε^{IHD} (orange) computed from the exact four-thirds incompressible law. Solid lines represent positive values and dashed lines represent negative values. The vertical dotted line corresponds to the sonic scale measured in Federrath et al. (2020). Increments are normalized to the side length L of the simulation domain.

contribution of the nonflux terms was found to be negligible with respect to the flux term (Andres et al. 2018). Note that in space plasma data, where it is not always possible to precisely measure the source (Hadid et al. 2017; Andrés et al. 2019), the variation of ε^{IHD} in the inertial range may indicate the presence of nonnegligible compressible effects, especially in media where density fluctuations are high (Hadid et al. 2018).

We further investigate the properties of this supersonic simulation in order to understand the origin of the source contribution and its influence on turbulence. As we have seen

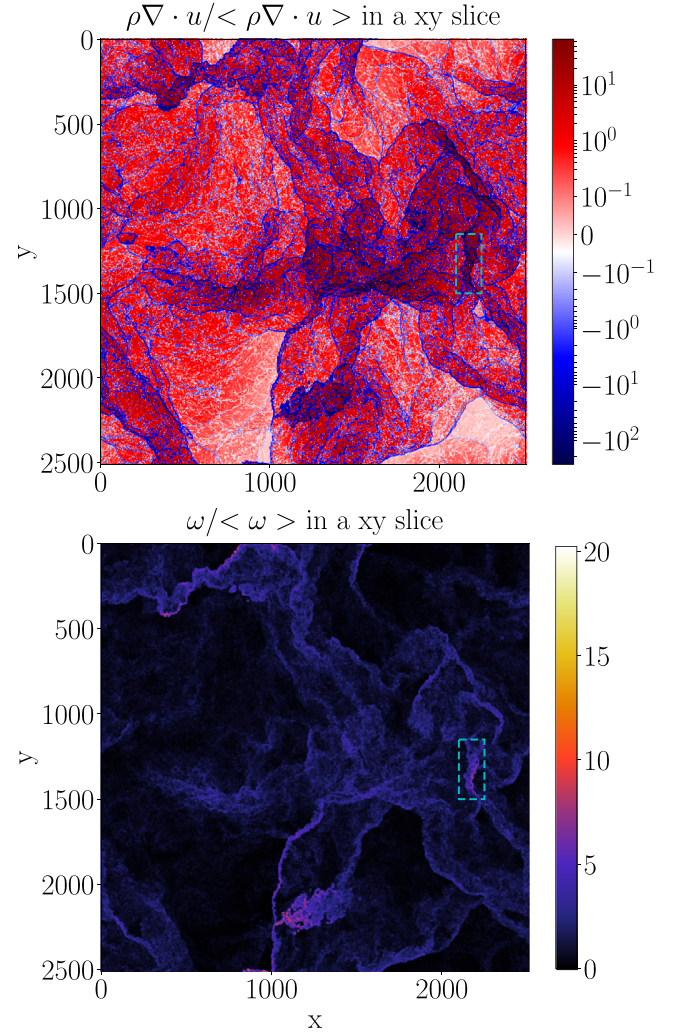


Figure 3. Density-dilatation $\rho\theta$ (top) and modulus of the vorticity $|\omega|$ (bottom) in a (xy) plane at six turnover times. The amplitude and sign of the fields are given by the color bars. The regions enclosed in the dashed cyan boxes are shown in Figure 4.

above, the source is globally positive, which reflects the dominance of compression. Therefore, for a given snapshot we searched for the grid point of minimal dilatation θ (maximum contraction of the fluid). In Figure 3 we show a slice of the data cube containing this point in the (yz) plane (other slices along (xy) or (xz) containing this point give a similar qualitative behavior). More precisely, we show the density-dilatation (top) and the modulus of the vorticity $\mathbf{w} = \nabla \times \mathbf{u}$ (bottom). These cuts reveal the existence of turbulent filamentary structures (elongated dark red structures for $\rho\theta$) in which both $|\theta|$ and $|\mathbf{w}|$ are up to several orders of magnitude higher than in the rest of the plane. A zoom on such structures is shown in Figure 4. These structures are typically delimited by very thin boundaries of strong contraction (dark blue lines for $\rho\theta$) in which a high turbulent activity with many vorticity tubes is observed. It is thought that the density-dilatation and the vorticity highlight the turbulence better than the previously used quantities θ and ρ (Kritsuk et al. 2007; Federrath et al. 2010), which are less relevant to investigate the physics involved in the generalized Kolmogorov law.

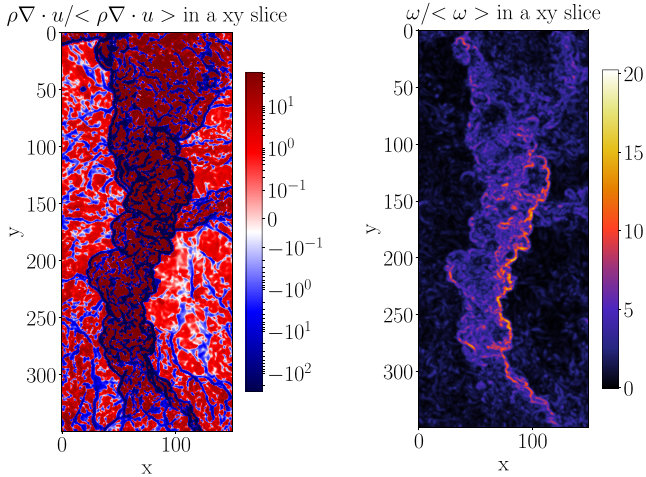


Figure 4. Zoom of the density-dilatation $\rho\theta$ (left) and modulus of the vorticity $|\omega|$ (right) of the regions enclosed in the dashed cyan box of Figure 3. The amplitude and sign of the fields are given by the color bars.

Regions with high density-dilatation are expected to drive most of the (average) source term. We therefore selected a sample of these regions (filaments) in which the mean density was high, and computed the source and flux term for increments along the main orientation of the filamentary structure. The results obtained were then averaged over the selected samples. In Figure 5 we show the result for a given filamentary structure and a “blank” region of weaker activity (top), and an average over eight filamentary structures (bottom). For all these filaments we observe a similar trend: the source is dominant, positive, and increases with spatial lag of the increments until it reaches approximately the sonic scale $\ell_s \simeq 0.01235L$, the scale where the scale-dependent Mach number is $\mathcal{M}(\ell_s/L) = 1$ (see Federrath et al. 2020 for the original determination of ℓ_s in these simulations). The flux term does not have a constant sign but remains negligible with respect to the source on most scales. We note that, because of the sample size effect, the interpretation of the largest scales of the structures are subject to caution. A comparison with a blank region gives a quite different result: the values of both the flux and the source terms are up to five orders of magnitude lower than their counterparts in filamentary structures. One should note that we only evaluate here the specific contribution of small pieces of the flow. Consequently one would not expect to retrieve any form of theoretical scaling predicted by the exact law, which would only apply to the full statistical average on the whole simulation domain.

We complement our analysis by taking the absolute value of the flux and the source before performing their statistical averages. Therefore, we define $\tilde{\mathbf{F}} = \langle \delta\rho(\delta\mathbf{u})^2|\delta\mathbf{u}| \rangle$ and $\tilde{S} = \frac{1}{2} \langle |\rho\theta' + \rho'\theta|(\delta\mathbf{u})^2 \rangle$ and compute them on the entire simulation domain at a given time. These two quantities represent the total activity due to the flux and the source, respectively, disregarding the sign of the local contributions and thus the direction of the resulting turbulent cascade (direct or inverse). Note that, again, these results do not have to comply to any theoretical prediction brought by the exact law, as the terms computed here are not the ones forming the exact law per se. Yet, the nonsigned quantities have the advantage of converging faster than their signed counterpart, and can lend some information about the mechanisms dominating on

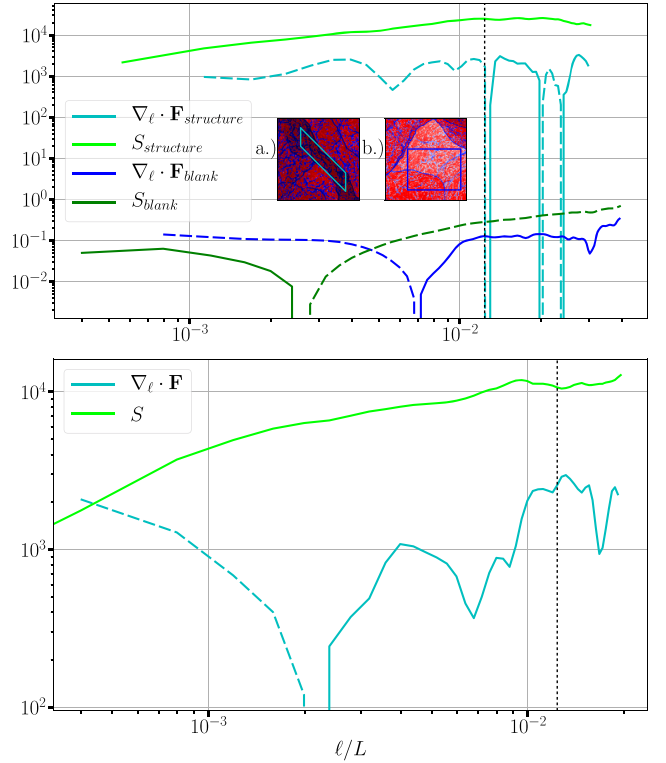


Figure 5. Top: flux term and source computed in a single turbulent (filamentary) structure and a single blank zone. Insets (a) and (b) show, respectively, the turbulent structure and the blank zone in which the statistics are made. Bottom: same type of plots averaged over eight filamentary structures from different snapshots. The sonic scale is given by the vertical dotted lines.

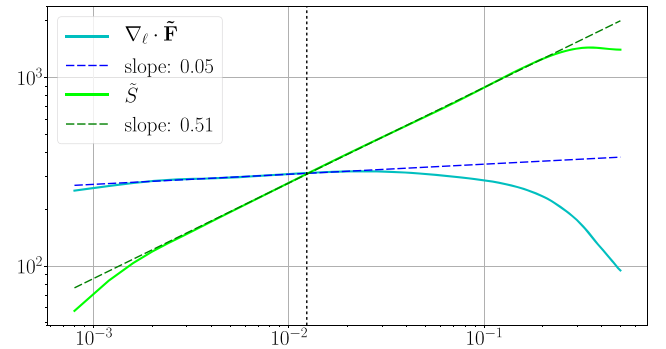


Figure 6. Modified flux $\nabla \cdot \tilde{\mathbf{F}}$ and source \tilde{S} computed in the entire simulation domain at time corresponding to six turnover times. A comparison is made with the scalings $\ell^{0.05}$ and $\ell^{0.51}$.

different scales. The results are reported in Figure 6. First, a clear power law $\tilde{S} \sim \ell^{1/2}$ emerges over two decades for the compressible source. By dimensionally equalizing the flux term and the source, we find $\delta u \sim \ell^{1/2}$ (we do not include the density that appears as a local average and not as a pure fluctuating quantity). This scaling is actually compatible with the one reported in Federrath et al. (2020) on supersonic scales using the second-order structure function (which is positive definite and therefore comparable to our calculation using absolute values), while a classical (incompressible) scaling $\delta u \sim \ell^{1/3}$ was approximately found on subsonic scales. Note that the supersonic law is dimensionally compatible with the

velocity spectrum $E^u \sim k^{-2}$, a scaling often attributed to a purely compressible (Burgers) turbulence (Frisch 1995; Federrath 2013). In the framework of the generalized Kolmogorov law we see, however, that the change of slope reported previously can find a precise origin: it marks a transition toward a regime/scale where the absolute activity of the source becomes nonnegligible. Second, we see that the modified flux exhibits a plateau on small scales, as expected for a subsonic turbulent cascade mainly driven by the flux, which means that most of the energy transiting in either direction through these scales is transferred by a flux-driven process. A transition appears around the sonic scale above which the flux starts to drop: this behavior can be attributed to the dominance of the compressible source activity on supersonic scales.

4. Discussion

Based on a single simulation, realized, however, at an unprecedented spatial resolution, some conclusions can be drawn. By directly applying the new exact law derived analytically to the data we found that the amplitude of the source in the turbulent filamentary structures (Figure 5) is much higher (up to two orders of magnitude) than when it is computed on the whole simulation (Figure 2). As the overall turbulent activity is less intense in the other regions we can conclude that these filaments drive the global behavior of S . On the contrary, it has been impossible to identify a recurring behavior in specific parts of the system for the flux term as we did for the source. At intermediate, transonic scales both the flux and the source contributions reach a peak. Furthermore the sign of S in both the global and local computations is positive, leading to a value of ε_{eff} higher than ε , which is fixed externally by the forcing. We thus suggest that the energy cascade in supersonic HD turbulence reaches its maximum efficiency (i.e., ε_{eff} is maximal) around the transition from the subsonic to supersonic regimes. This efficiency decreases with scales such that ε_{eff} tends to be closer to ε on subsonic scales, where S becomes subdominant. On supersonic scales, however, the exact law shows a decrease in the energy cascade rate ε , which is no longer constant. The law being exact under several assumptions means that at least one of them is not verified. For example, we cannot exclude a nonlocal effect of the forcing that would modify the scaling law mostly on large scales. An anomalous dissipation on supersonic scales originating from the irregularities of the fields, which is not accounted for in our theory, could also contribute to the energy budget (Duchon & Robert 2000; Saw et al. 2016; Galtier 2018). On the other hand, Figure 6 shows that the total, nonsigned activity of the compressible source grows higher than that of the flux: this suggests that density-dilatation acts strongly on supersonic scales, but in such a way that local contributions of opposite signs cancel each other out in the scope of the exact law. This strong compressible activity, coupled to the flux activity becoming nonconstant at supersonic scales, suggests a transition between two regimes around the sonic scale: a subsonic turbulent cascade driven by both the compressible flux and the source, and a highly compressible regime at supersonic scales that does not feature a conservative cascade. The vorticity distribution shown in Figure 3 reinforces this interpretation since stronger vorticity is only observed inside the small-scale turbulent structures. Similar conclusions were drawn by Aluie et al. (2012) who reported for subsonic and transonic simulations that pressure-dilatation acts essentially on

large scales, whereas at small scales, below a transitional “conversion” scale range, a conservative cascade appears. Here we shed a new light onto those findings using a different approach that helps better understand how various mechanisms shape supersonic turbulence.

A spectral analysis of the velocity field \mathbf{u} (not shown in this paper) reveals the existence of two distinct power-law scalings, separated roughly by the sonic scale. On supersonic scales the scaling is close to k^{-2} , which is usually attributed to Burgers turbulence (Kadomtsev & Petviashvili 1973; Passot et al. 1988; Frisch 1995); on subsonic scales the scaling becomes close to $k^{-3/2}$, which is compatible with a theory of weak acoustic turbulence (Zakharov & Sagdeev 1970; L’vov et al. 1997). This provides other evidence of the existence of two distinct regimes at supersonic and subsonic scales: a more shock-driven compressible regime and a (possibly acoustic) turbulent regime. If we assume that the cascade rate computed here is representative of (if not identical to) the energy dissipation rate in the system, the observation that cascade/dissipation rate peaks near the sonic scale (Figure 5), where turbulence transitions from shock-like (k^{-2}) to fluctuation/vortex-like ($k^{-3/2}$) dominated regimes would be an indication of strong shock dissipation at that scale.

It is interesting to note that using a model of acoustic turbulence with weak shocks at Mach number close to unity, Lindborg (2019) reported that a scaling relation similar to the incompressible Kolmogorov law could be retrieved for a modified energy cascade rate. In the framework of said model, our scaling relation (15) still holds considering a similar modified energy cascade rate. This remark, along with the previous one, means that subsonic turbulence could be composed of a mixture of weak shocks, acoustic waves, and vortices.

A final remark can be made about the exact law: given the high resolution of the simulation one would expect the energy cascade rate to form a steady plateau over more than one decade. This small inertial range may be attributed to two possible effects not included in our exact law (15): (i) nonlocal effects due to the large-scale forcing and (ii) additional local dissipation (in the supersonic range) through shocks/discontinuities (Duchon & Robert 2000; Saw et al. 2016; Galtier 2018), since our exact law assumes smoothness of the turbulent fields. This shortcoming calls for a new theory of compressible HD turbulence where such singular fields and nonlocal effects due to large-scale forcing can be accounted for, and which would be very relevant to supersonic turbulence. In addition, it would be interesting to investigate the question of intermittency in supersonic turbulence by evaluating separately the contributions of the flux and the source. Such theories are beyond the scope of this paper and are left to future studies.

5. Conclusion

The theory developed in this paper and applied to high-resolution numerical simulations allows us to gain deep insight into supersonic ISM turbulence. The filamentary structures observed in the ISM seem to be characterized by a universal thickness of the order of the sonic scale (Arzoumanian et al. 2011; Federrath et al. 2016b). Their shape is supposed to be mainly due to HD turbulence and to be little affected by other factors such as gravity or magnetic fields (Federrath et al. 2016b; Ntormousi et al. 2016). These studies associated with our work suggest that this universality could be explained by

the existence of the two distinct regimes reported here: (i) a supersonic regime dominated by shock-like structures where the energy cascade rate ε is not constant; (ii) a subsonic regime with a lower and mainly constant ε , where vortices (and acoustic waves) are produced and in which a classic conservative cascade is formed. In between, the transonic scales where turbulence reaches its peak of effective energy transfer would correspond to the size of the filaments. Our interpretation is thus that filaments are stuck on the smallest scale of the supersonic regime, which is the sonic scale, while the weaker subsonic cascade produces vorticity tubes on smaller scales.

Applications of the law to more complete simulations, featuring for instance gravitational forces or magnetic fields, would help refine this interpretation and may provide new clues on the interplay between ISM turbulence and the problem of star formation (mac Low & Klessen 2004; Hennebelle & Falgarone 2012; Padoan et al. 2014). For example, Orkisz et al. (2017) were able for the first time to observationally derive the fractions of momentum density contained in the solenoidal and compressive modes of turbulence. It was in the Orion B molecular cloud where the mean Mach number was ~ 6 . They showed that the compressive modes are dominant in regions with a high star formation rate (as predicted in Federrath & Klessen 2012). According to our analysis the source term is the dominant component of compressible turbulence inside filaments. Future work that would directly link the formalism of exact laws (and thus the source and flux terms) to the star formation rate could significantly advance our understanding of how turbulence controls the formation of structures on different scales in the ISM.

We thank the anonymous referee for valuable suggestions, which helped to improve this work. C.F. acknowledges funding provided by the Australian Research Council (Discovery Project DP170100603 and Future Fellowship FT180100495), and the Australia-Germany Joint Research Cooperation Scheme (UA-DAAD). We further acknowledge high-performance computing resources provided by the Leibniz Rechenzentrum and the Gauss Centre for Supercomputing (grants pr32lo, pr48pi, and GCS Large-scale project 10391), the Australian National Computational Infrastructure (grant ek9) in the framework of the National Computational Merit Allocation Scheme and the ANU Merit Allocation Scheme. The simulation software FLASH was in part developed by the DOE-supported Flash Center for Computational Science at the University of Chicago.

ORCID iDs

R. Ferrand  <https://orcid.org/0000-0002-0044-3405>
 S. Galtier  <https://orcid.org/0000-0001-8685-9497>
 C. Federrath  <https://orcid.org/0000-0002-0706-2306>

References

Aluie, H. 2011, *PhRvL*, **106**, 174502
 Aluie, H., Li, S., & Li, H. 2012, *ApJL*, **751**, L29

Andrés, N., Galtier, S., & Sahraoui, F. 2018, *PhRvE*, **97**, 013204
 Andrés, N., & Sahraoui, F. 2017, *PhRvE*, **96**, 053205
 Andrés, N., Sahraoui, F., Galtier, S., et al. 2018, *JPhPh*, **84**, 905840404
 Andrés, N., Sahraoui, F., Galtier, S., et al. 2019, *PhRvL*, **123**, 245101
 Antonia, R., Ould-Rouis, M., Anselmet, F., & Zhu, Y. 1997, *JFM*, **332**, 395
 Arzoumanian, D., André, Ph., Didelon, P., et al. 2011, *A&A*, **529**, L6
 Banerjee, S., & Galtier, S. 2013, *PhRvE*, **87**, 013019
 Banerjee, S., Hadid, L., Sahraoui, F., & Galtier, S. 2016, *ApJL*, **829**, L27
 Banerjee, S., & Kritsuk, A. 2017, *PhRvE*, **96**, 053116
 Banerjee, S., & Kritsuk, A. 2018, *PhRvE*, **97**, 023107
 Dubey, A., Fisher, R., Graziani, C., et al. 2008, in ASP Conf. Ser. 385, Numerical Modeling of Space Plasma Flows: Astronom 2007, ed. N. V. Pogorelov, E. Audit, & G. Zank (San Francisco, CA: ASP), **145**
 Duchon, J., & Robert, R. 2000, *Nonli*, **13**, 249
 During, G., & Krstulovic, G. 2018, *PhRvE*, **97**, 020201
 Elmegreen, B. G., & Scalo, J. 2004, *ARA&A*, **42**, 211
 Federrath, C. 2013, *MNRAS*, **436**, 1245
 Federrath, C. 2016, *MNRAS*, **457**, 375
 Federrath, C., & Klessen, R. S. 2012, *ApJ*, **761**, 156
 Federrath, C., Klessen, R. S., Iapichino, L., & Beattie, J. R. 2020, *NatAs*, submitted (arXiv:2011.06238)
 Federrath, C., Klessen, R. S., Iapichino, L., & Hammer, N. J. 2016a, arXiv:1607.00630
 Federrath, C., Klessen, R. S., & Schmidt, W. 2009, *ApJ*, **692**, 364
 Federrath, C., Rathborne, J. M., Longmore, S. N., et al. 2016b, *ApJ*, **832**, 143
 Federrath, C., Roman-Duval, J., Klessen, R. S., Schmidt, W., & mac Low, M.-M. 2010, *A&A*, **512**, A81
 Ferrand, R., Galtier, S., Sahraoui, F., et al. 2019, *ApJ*, **881**, 50
 Frisch, U. 1995, *Turbulence* (Cambridge: Cambridge Univ. Press)
 Fryxell, B., Olson, K., Ricker, P., et al. 2000, *ApJS*, **131**, 273
 Galtier, S. 2008, *PhRvE*, **77**, 015302
 Galtier, S. 2016, *Introduction to Modern Magnetohydrodynamics* (Cambridge: Cambridge Univ. Press)
 Galtier, S. 2018, *JPhA*, **51**, 205501
 Galtier, S., & Banerjee, S. 2011, *PhRvL*, **107**, 134501
 Hadid, L., Sahraoui, F., & Galtier, S. 2017, *ApJ*, **838**, 9
 Hadid, L. Z., Sahraoui, F., Galtier, S., & Huang, S. Y. 2018, *PhRvL*, **120**, 055102
 Hellinger, P., Verdini, A., Landi, S., Franci, L., & Matteini, L. 2018, *ApJL*, **857**, L19
 Hennebelle, P., & Falgarone, E. 2012, *A&ARv*, **20**, 55
 Heyer, M., & Brunt, C. 2004, *ApJL*, **615**, L45
 Kadomtsev, B. B., & Petviashvili, V. I. 1973, *SPhD*, **18**, 115
 Kolmogorov, A. 1941, *Dokl. Akad. Nauk SSSR*, **32**, 16
 Kritsuk, A. G., Norman, M. L., Padoan, P., & Wagner, R. 2007, *ApJ*, **665**, 416
 Kritsuk, A. G., Wagner, R., & Norman, M. L. 2013, *JFM*, **729**, 1
 Krumholz, M. R., & Federrath, C. 2019, *FrASS*, **6**, 7
 Lindborg, E. 2007, *JFM*, **572**, 255
 Lindborg, E. 2019, *JFM*, **874**, R2
 Lindborg, E. 2019, *JFM*, **874**, R2
 L'vov, V. S., L'vov, Y., Newell, A. C., & Zakharov, V. 1997, *PhRvE*, **56**, 390
 mac Low, M.-M., & Klessen, R. S. 2004, *RvMP*, **76**, 125
 McKee, C. F., & Ostriker, E. C. 2007, *ARA&A*, **45**, 565
 Meyrand, R., & Galtier, S. 2010, *ApJ*, **721**, 1421
 Monin, A. S. 1959, *SPhD*, **4**, 271
 Ntormousi, E., Hennebelle, P., André, P., & Masson, J. 2016, *A&A*, **589**, A24
 Orkisz, J. H., Pety, J., Gerin, M., et al. 2017, *A&A*, **599**, A99
 Padoan, P., Federrath, C., Chabrier, G., et al. 2014, in *Protostars and Planets VI*, ed. H. Beuther et al. (Tucson, AZ: Univ. Arizona Press), **77**
 Passot, T., Pouquet, A., & Woodward, P. 1988, *A&A*, **197**, 228
 Passot, T., & Vázquez-Semadeni, E. 1998, *PhRvE*, **58**, 4501
 Politano, H., & Pouquet, A. 1998, *PhRvE*, **57**, R21
 Saw, E. W., Kuzay, D., Faranda, D., et al. 2016, *NatCo*, **7**, 12466
 Schmidt, W., Federrath, C., & Klessen, R. 2008, *PhRvL*, **101**, 194505
 Sorriso-Valvo, L., Marino, R., Carbone, V., et al. 2007, *PhRvL*, **99**, 115001
 Vázquez-Semadeni, E. 1994, *ApJ*, **423**, 681
 Wilson, R. W., Jefferts, K. B., & Penzias, A. A. 1970, *ApJL*, **161**, L43
 Yoshimatsu, K. 2012, *PhRvE*, **85**, 066313
 Zakharov, V. E., & Sagdeev, R. Z. 1970, *SPhD*, **15**, 439

A compact exact law for compressible isothermal Hall magnetohydrodynamic turbulence

Renaud Ferrand ^{1,†}, Sébastien Galtier ^{1,2} and Fouad Sahraoui¹

¹Laboratoire de Physique des Plasmas, École polytechnique, CNRS, Sorbonne Université, Université Paris-Saclay, Observatoire de Paris, F-91128 Palaiseau Cedex, France

²Institut Universitaire de France, 75005 Paris, France

(Received 17 December 2020; revised 22 March 2021; accepted 22 March 2021)

Using mixed second-order structure functions, a compact exact law is derived for isothermal compressible Hall magnetohydrodynamic turbulence with the assumptions of statistical homogeneity, time stationarity and infinite kinetic/magnetic Reynolds numbers. The resulting law is written as the sum of a Yaglom-like flux term, with an overall expression strongly reminiscent of the incompressible law, and a pure compressible source. Being mainly a function of the increments, the compact law is Galilean invariant but is dependent on the background magnetic field if one is present. Only the magnetohydrodynamic source term requires multi-spacecraft data to be estimated whereas the other components, which include those introduced by the Hall term, can be fully computed with single-spacecraft data using the Taylor hypothesis. These properties make this compact law more appropriate for analysing both numerical simulations and *in situ* data gathered in space plasmas, in particular when only single-spacecraft data are available.

Key words: plasma nonlinear phenomena, space plasma physics

1. Introduction

Although having already been studied extensively in several areas of physics, turbulent flows are not yet fully understood because the nonlinear nature of the problem makes it difficult to derive fundamental laws. Most of these laws take the form of exact relations, mathematical expressions that relate the energy cascade rate to a third-order correlation function of the fields under the assumptions of statistical homogeneity, stationarity and high Reynolds numbers. A well-known result is the four-fifths law derived using a tensorial method by Kolmogorov (1941) for incompressible hydrodynamic turbulence, and the four-thirds law derived in a modern way through the use of a two-point correlation function only (Monin 1959; Antonia *et al.* 1997). Following this simpler derivation, other fundamental laws were derived for plasma models such as incompressible magnetohydrodynamics (IMHD) (Politano & Pouquet 1998), which allowed for the study of astrophysical turbulent plasmas such as the solar wind (Sorriso-Valvo *et al.* 2007; MacBride, Smith & Forman 2008; Marino *et al.* 2008; Stawarz *et al.* 2009; Osman *et al.* 2011; Galtier 2012). This plasma model was then refined by adding the Hall effect

† Email address for correspondence: renaud.ferrand@lpp.polytechnique.fr

(IHMHD) (Galtier 2008; Banerjee & Galtier 2017; Hellinger *et al.* 2018; Ferrand *et al.* 2019) as a way of describing near and sub-ion scales, which are not described by ideal MHD, and allow for multi-scale studies of space plasmas (Bandyopadhyay *et al.* 2020).

In addition to the incompressible models, exact laws have also been derived that take compressibility into account both for non-magnetized fluids (Galtier & Banerjee 2011; Banerjee & Galtier 2014; Banerjee & Kritsuk 2017; Ferrand *et al.* 2020) and magnetized plasmas (Banerjee & Galtier 2013; Andrés & Sahraoui 2017; Andrés, Galtier & Sahraoui 2018; Banerjee & Kritsuk 2018). The use of a compressible description of astrophysical flows is relevant for the solar wind (Banerjee *et al.* 2016; Hadid, Sahraoui & Galtier 2017) but also for highly compressible media, such as the interstellar medium, where supersonic turbulence is expected to play a key role in star-forming structures (Kritsuk *et al.* 2007; Arzoumanian *et al.* 2011; Kritsuk, Wagner & Norman 2013; Federrath 2016). It is also relevant to study the sub-ion scales of a subsonic turbulent plasma. Indeed, while the influence of compressibility at MHD scales has already been demonstrated in turbulent flows of the magnetosheath of the Earth (Hadid *et al.* 2018), it was recently shown that small density fluctuations can significantly enhance the compressible cascade rate, with respect to its incompressible estimate at sub-ion scales, even when the two cascade rates coincide at the large (MHD) scales (Andrés *et al.* 2019).

For a given model, the expression of the law is not unique. This is the case with incompressible hydrodynamics, where both the four-fifths and the four-thirds laws exist and were derived by different methods. Likewise, there is a tensorial derivation in IMHD that yields a four-fifths-like law (Yoshimatsu 2012) that is different from that derived by Politano & Pouquet (1998), and four different laws have been derived in IHMHD (Ferrand *et al.* 2019). In particular, it was shown in the latter study that using the appropriate structure function allows one to derive a simplified expression of the exact law. Owing to the size and complexity of the law already available for the compressible isothermal Hall MHD (CHMHD) model (Andrés *et al.* 2018), which will hereinafter be called the A18 law, we aim to apply a similar method to that used by Ferrand *et al.* (2019) (hereafter F19) to derive a CHMHD law with an expression that is significantly simpler. Deriving such a compact expression could ease the subsequent *in situ* data analysis by simplifying the computation and obtaining a more precise estimate of the heating rate.

In § 2, we present our derivation based on the three-dimensional isothermal CHMHD equations. We then discuss the new exact law in detail in § 3 and compare it with the previous law and its incompressible counterpart. We finally provide the conclusion of the study in § 4.

2. Derivation of the compact CHMHD law

2.1. Compressible Hall MHD equations

Hall MHD is a model often used in astrophysics in the context of cold and dense regions of protoplanetary discs (Kunz & Lesur 2013), crusts of neutron stars (Gourgouliatos & Cumming 2014), fast magnetic reconnection (Bhattacharjee 2004), high-frequency waves and turbulence in magnetospheric physics (Belmont & Rezeau 2001; Sahraoui *et al.* 2003; Sahraoui, Galtier & Belmont 2007) and in the solar wind (Galtier 2006), and laboratory experiments such as the Madison Plasma Dynamo (Cooper *et al.* 2014) or the Wisconsin Plasma Astrophysics Laboratory (Forest *et al.* 2015) experiments. In the context of weakly collisional plasmas, the limits of the validity of Hall MHD have been discussed in the literature (e.g. Howes 2009).

In this paper, we shall consider three-dimensional compressible isothermal Hall MHD, for which the equations are (Galtier 2016)

$$\partial_t \rho + \nabla \cdot (\rho \mathbf{u}) = 0, \quad (2.1)$$

$$\rho(\partial_t \mathbf{u} + \mathbf{u} \cdot \nabla \mathbf{u}) = -\nabla P + \mathbf{J} \times \mathbf{B} + \mathbf{d}_v + \mathbf{f}, \quad (2.2)$$

$$\partial_t \mathbf{B} = \nabla \times (\mathbf{u} \times \mathbf{B}) - \lambda \nabla \times (\mathbf{J}_c \times \mathbf{B}) + \mathbf{d}_\eta, \quad (2.3)$$

$$\nabla \cdot \mathbf{B} = 0, \quad (2.4)$$

where ρ is the mass density, \mathbf{u} is the velocity, P is the pressure, \mathbf{B} is the magnetic field, $\mathbf{J} = (\nabla \times \mathbf{B})/\mu_0$ is the current density, \mathbf{f} is a stationary homogeneous external force acting at large scales, $\mathbf{J}_c = \mathbf{J}/\rho$ is the normalized current, and $\lambda = m_i/q_e$ with m_i is the ion mass and q_e is the magnitude of the electron charge. The dissipation terms are

$$\mathbf{d}_v = \nu \Delta \mathbf{u} + \frac{\nu}{3} \nabla \theta, \quad (2.5)$$

$$\mathbf{d}_\eta = \eta \Delta \mathbf{B}, \quad (2.6)$$

with $\theta = \nabla \cdot \mathbf{u}$ is the dilatation, ν is the dynamic viscosity and η is the magnetic diffusivity. We use the isothermal closure $P = c_s^2 \rho$, where c_s is the speed of sound constant.

We introduce the spatial increment ℓ connecting two points \mathbf{x} and \mathbf{x}' in the physical space as $\mathbf{x}' = \mathbf{x} + \ell$ and we define, for any given field ξ , $\xi = \xi(\mathbf{x})$ and $\xi' = \xi(\mathbf{x}')$. We also define the field increment $\delta \xi = \xi' - \xi$ and the mean value $\bar{\delta \xi} = (\xi + \xi')/2$. For this system, the equation of energy conservation reads as

$$\partial_t \langle E^{\text{tot}} \rangle = \langle \mathbf{u} \cdot \mathbf{d}_v \rangle + \frac{1}{\mu_0} \langle \mathbf{B} \cdot \mathbf{d}_\eta \rangle + \langle \mathbf{u} \cdot \mathbf{f} \rangle, \quad (2.7)$$

where $\langle \rangle$ is an ensemble average, $E^{\text{tot}} = \rho u^2/2 + B^2/(2\mu_0) + \rho e$ is the total energy and $e = c_s^2 \ln(\rho/\rho_0)$ is the work component of internal energy ($\rho_0 = \langle \rho \rangle$ is the average density). Note that this definition limits the variations of the internal energy to the work done by the pressure force, the heat component owing to entropy variation being neglected (like in the case of incompressible turbulence). Thus, the total energy is conserved. We define the mean rate of total energy injection as $\varepsilon = \langle \mathbf{u} \cdot \mathbf{f} \rangle$. By using this quantity, (2.7) reduces in the stationary regime to

$$\left\langle \mathbf{u} \cdot \mathbf{d}_v + \frac{1}{\mu_0} \mathbf{B} \cdot \mathbf{d}_\eta \right\rangle = -\varepsilon. \quad (2.8)$$

Note that we also have the relation

$$\langle \mathbf{u} \cdot \mathbf{d}_v \rangle + \frac{1}{\mu_0} \langle \mathbf{B} \cdot \mathbf{d}_\eta \rangle = -\nu \left\langle \mathbf{w}^2 + \frac{4}{3} \theta^2 \right\rangle - \mu_0 \eta \langle \mathbf{J}^2 \rangle, \quad (2.9)$$

where $\mathbf{w} = \nabla \times \mathbf{u}$ is the vorticity, which gives the expression of the mean rate of total energy dissipation.

2.2. Two-point correlators

Next, we shall derive analytically a dynamical equation for the following mixed structure functions

$$\langle S \rangle = \left\langle \frac{1}{2} \bar{\delta \rho} |\delta \mathbf{u}|^2 + \frac{1}{2\mu_0} |\delta \mathbf{B}|^2 + \frac{1}{2} \delta \rho \delta e \right\rangle. \quad (2.10)$$

First, we note that for homogeneous turbulence, we have the relations

$$\langle \bar{\delta}\rho|\delta\mathbf{u}|^2 \rangle = \langle \rho u^2 \rangle - 2\langle \bar{\delta}\rho\mathbf{u} \cdot \mathbf{u}' \rangle + \frac{1}{2}\langle \rho u'^2 + \rho' u^2 \rangle, \quad (2.11)$$

$$\langle \delta\rho\delta e \rangle = 2\langle \rho e \rangle - \langle \rho e' + \rho' e \rangle, \quad (2.12)$$

$$\langle |\delta\mathbf{B}|^2 \rangle = 2\langle B^2 \rangle - 2\langle \mathbf{B} \cdot \mathbf{B}' \rangle. \quad (2.13)$$

We recall that, under our formalism, we have for any entity A the relation $\partial_x A' = \partial_x A = 0$. We also have the relation $\langle \nabla' \cdot \rangle = -\langle \nabla \cdot \rangle = \nabla_\ell \cdot \langle \rangle$, where ∇_ℓ denotes the derivative operator along the increment ℓ . Using these relations, we obtain from (2.1)–(2.4) the following expressions

$$\begin{aligned} \partial_t \langle \rho\mathbf{u} \cdot \mathbf{u}' \rangle &= \left\langle \rho\mathbf{u} \cdot \left(-\mathbf{u}' \cdot \nabla' \mathbf{u}' - \frac{1}{\rho'} \nabla' P' + \mathbf{J}'_c \times \mathbf{B}' \right) \right\rangle \\ &\quad + \langle \mathbf{u}' \cdot (-\nabla \cdot (\rho\mathbf{u}\mathbf{u}) - \nabla P + \mathbf{J} \times \mathbf{B}) \rangle + \left\langle \mathbf{u}' \cdot \mathbf{d}_v + \mathbf{u}' \cdot \mathbf{f} + \frac{\rho}{\rho'} \mathbf{u} \cdot (\mathbf{d}'_v + \mathbf{f}') \right\rangle \\ &= \nabla_\ell \cdot \langle -\rho(\mathbf{u} \cdot \mathbf{u}')\delta\mathbf{u} + P\mathbf{u}' - \rho e'\mathbf{u} \rangle + \langle \rho\theta'(\mathbf{u} \cdot \mathbf{u}') \rangle \\ &\quad + \langle \rho\mathbf{u} \cdot (\mathbf{J}'_c \times \mathbf{B}') + \mathbf{u}' \cdot (\mathbf{J} \times \mathbf{B}) \rangle \\ &\quad + \left\langle \mathbf{u}' \cdot \mathbf{d}_v + \mathbf{u}' \cdot \mathbf{f} + \frac{\rho}{\rho'} \mathbf{u} \cdot (\mathbf{d}'_v + \mathbf{f}') \right\rangle, \end{aligned} \quad (2.14)$$

$$\begin{aligned} \partial_t \langle \rho u'^2 \rangle &= \langle 2\rho\mathbf{u}' \cdot \partial_t \mathbf{u}' + u'^2 \partial_t \rho \rangle \\ &= \left\langle -\mathbf{u}' \cdot \nabla' (\rho u'^2) - 2\frac{\rho}{\rho'} \mathbf{u}' \cdot \nabla' P' + 2\frac{\rho}{\rho'} \mathbf{u}' \cdot (\mathbf{J}' \times \mathbf{B}') \right\rangle \\ &\quad + \nabla_\ell \cdot \langle \rho u'^2 \mathbf{u} \rangle + \left\langle 2\frac{\rho}{\rho'} \mathbf{u}' \cdot (\mathbf{d}'_v + \mathbf{f}') \right\rangle \\ &= \nabla_\ell \cdot \langle -\rho u'^2 \mathbf{u}' + \rho u'^2 \mathbf{u} \rangle + \left\langle \rho u'^2 \theta' - 2\frac{\rho}{\rho'} \mathbf{u}' \cdot \nabla' P' + 2\frac{\rho}{\rho'} \mathbf{u}' \cdot (\mathbf{J}' \times \mathbf{B}') \right\rangle \\ &\quad + \left\langle 2\frac{\rho}{\rho'} \mathbf{u}' \cdot (\mathbf{d}'_v + \mathbf{f}') \right\rangle, \end{aligned} \quad (2.15)$$

$$\partial_t \langle \rho e' \rangle = \nabla_\ell \cdot \langle -\rho e' \delta\mathbf{u} - P\mathbf{u}' \rangle + \langle \rho e' \theta' \rangle, \quad (2.16)$$

$$\begin{aligned} \partial_t \langle \mathbf{B} \cdot \mathbf{B}' \rangle &= \langle \mathbf{B} \cdot (\mathbf{B}' \cdot \nabla' \mathbf{u}' - \mathbf{u}' \cdot \nabla' \mathbf{B}' - \mathbf{B}' \theta') \rangle + \langle \mathbf{B}' \cdot (\mathbf{B} \cdot \nabla \mathbf{u} - \mathbf{u} \cdot \nabla \mathbf{B} - \mathbf{B}\theta) \rangle \\ &\quad - \lambda \langle \mathbf{B}' \cdot (\nabla \times (\mathbf{J}_c \times \mathbf{B})) + \mathbf{B} \cdot (\nabla' \times (\mathbf{J}'_c \times \mathbf{B}')) \rangle + \langle \mathbf{B}' \cdot \mathbf{d}_\eta + \mathbf{B} \cdot \mathbf{d}'_\eta \rangle \\ &= \langle \nabla' \cdot ((\mathbf{B} \cdot \mathbf{u}')\mathbf{B}') - \nabla' \cdot ((\mathbf{B} \cdot \mathbf{B}')\mathbf{u}') + \nabla \cdot ((\mathbf{B}' \cdot \mathbf{u})\mathbf{B}) - \nabla \cdot ((\mathbf{B} \cdot \mathbf{B}')\mathbf{u}) \rangle \\ &\quad - \lambda \langle \nabla \cdot ((\mathbf{J}_c \cdot \mathbf{B}')\mathbf{B}) - (\mathbf{J}_c \cdot \nabla)(\mathbf{B} \cdot \mathbf{B}') - (\mathbf{B} \cdot \mathbf{B}')\nabla \cdot \mathbf{J}_c \rangle \\ &\quad - \lambda \langle \nabla' \cdot ((\mathbf{J}'_c \cdot \mathbf{B})\mathbf{B}') - (\mathbf{J}'_c \cdot \nabla')(\mathbf{B} \cdot \mathbf{B}') - (\mathbf{B} \cdot \mathbf{B}')\nabla' \cdot \mathbf{J}'_c \rangle \\ &\quad + \langle \mathbf{B}' \cdot \mathbf{d}_\eta + \mathbf{B} \cdot \mathbf{d}'_\eta \rangle \\ &= \nabla_\ell \cdot \langle -(\mathbf{B} \cdot \mathbf{B}')\delta\mathbf{u} + (\mathbf{B} \cdot \mathbf{u}')\mathbf{B}' - (\mathbf{B}' \cdot \mathbf{u})\mathbf{B} \rangle \\ &\quad - \lambda \nabla_\ell \cdot \langle -(\mathbf{B} \cdot \mathbf{B}')\delta\mathbf{J}_c + (\mathbf{J}'_c \cdot \mathbf{B})\mathbf{B}' - (\mathbf{J}_c \cdot \mathbf{B}')\mathbf{B} \rangle \\ &\quad + \langle \mathbf{B}' \cdot \mathbf{d}_\eta + \mathbf{B} \cdot \mathbf{d}'_\eta \rangle. \end{aligned} \quad (2.17)$$

From these relations, we find

$$\begin{aligned}
 \partial_t \langle S \rangle &= \partial_t \langle E^{\text{tot}} \rangle + \partial_t \langle E^b \rangle \\
 &- \frac{1}{2} \nabla_\ell \cdot \left\langle -2\bar{\delta}\rho(\mathbf{u} \cdot \mathbf{u}')\delta\mathbf{u} - \rho e' \mathbf{u}' + \rho' e \mathbf{u} + \frac{1}{2}\rho u^2 \mathbf{u}' \right. \\
 &- \left. \frac{1}{2}\rho u^2 \mathbf{u} - \frac{1}{2}\rho' u^2 \mathbf{u} + \frac{1}{2}\rho' u^2 \mathbf{u}' \right\rangle \\
 &- \frac{1}{2} \langle \rho \mathbf{u} \cdot (\mathbf{J}'_c \times \mathbf{B}') + \rho' \mathbf{u}' \cdot (\mathbf{J}_c \times \mathbf{B}) + \mathbf{u}' \cdot (\mathbf{J} \times \mathbf{B}) + \mathbf{u} \cdot (\mathbf{J}' \times \mathbf{B}') \rangle \\
 &+ \frac{1}{4} \left\langle \rho u^2 \theta' + \rho' u^2 \theta - 2\frac{\rho}{\rho'} \mathbf{u}' \cdot \nabla' P' - 2\frac{\rho'}{\rho} \mathbf{u} \cdot \nabla P \right. \\
 &+ \left. 2\frac{\rho}{\rho'} \mathbf{u}' \cdot (\mathbf{J}' \times \mathbf{B}') + 2\frac{\rho'}{\rho} \mathbf{u} \cdot (\mathbf{J} \times \mathbf{B}) \right\rangle \\
 &- \frac{1}{2} \langle (\rho\theta' + \rho'\theta)(\mathbf{u} \cdot \mathbf{u}') \rangle - \frac{1}{2} \langle \rho e' \theta' + \rho' e \theta \rangle \\
 &- \frac{1}{\mu_0} \nabla_\ell \cdot \langle -(\mathbf{B} \cdot \mathbf{B}')\delta\mathbf{u} + (\mathbf{B} \cdot \mathbf{u}')\mathbf{B}' - (\mathbf{B}' \cdot \mathbf{u})\mathbf{B} \rangle \\
 &- \frac{\lambda}{\mu_0} \nabla_\ell \cdot \langle (\mathbf{B} \cdot \mathbf{B}')\delta\mathbf{J}_c - \lambda(\mathbf{J}'_c \cdot \mathbf{B})\mathbf{B}' + \lambda(\mathbf{J}_c \cdot \mathbf{B}')\mathbf{B} \rangle \\
 &- \frac{1}{2} \left\langle \left(1 + \frac{\rho'}{\rho}\right) \mathbf{u}' \cdot (\mathbf{d}_v + \mathbf{f}) + \left(1 + \frac{\rho}{\rho'}\right) \mathbf{u} \cdot (\mathbf{d}'_v + \mathbf{f}') \right\rangle \\
 &+ \frac{1}{2} \left\langle \frac{\rho}{\rho'} \mathbf{u}' \cdot (\mathbf{d}'_v + \mathbf{f}') + \frac{\rho'}{\rho} \mathbf{u} \cdot (\mathbf{d}_v + \mathbf{f}) \right\rangle - \frac{1}{\mu_0} \langle \mathbf{B}' \cdot \mathbf{d}_\eta + \mathbf{B} \cdot \mathbf{d}'_\eta \rangle. \tag{2.18}
 \end{aligned}$$

We can simplify the previous expression by stating that

$$\begin{aligned}
 \nabla_\ell \cdot \langle \bar{\delta}\rho|\delta\mathbf{u}|^2\delta\mathbf{u} \rangle &= \nabla_\ell \cdot \langle -2\bar{\delta}\rho\mathbf{u} \cdot \mathbf{u}'\delta\mathbf{u} + \frac{1}{2}\rho u^2 \mathbf{u}' - \frac{1}{2}\rho u^2 \mathbf{u} + \frac{1}{2}\rho' u^2 \mathbf{u}' - \frac{1}{2}\rho' u^2 \mathbf{u} \rangle \\
 &+ \langle \frac{1}{2}\rho u^2 \theta' + \frac{1}{2}\rho' u^2 \theta \rangle, \tag{2.19}
 \end{aligned}$$

$$\begin{aligned}
 \left\langle \frac{\rho}{\rho'} \mathbf{u}' \cdot \nabla' P' \right\rangle + \left\langle \frac{\rho'}{\rho} \mathbf{u} \cdot \nabla P \right\rangle &= \langle \rho \mathbf{u}' \cdot \nabla' e' + \rho' \mathbf{u} \cdot \nabla e \rangle \\
 &= \nabla_\ell \cdot \langle \rho e' \mathbf{u}' - \rho' e \mathbf{u} \rangle - \langle \rho e' \theta' + \rho' e \theta \rangle, \tag{2.20}
 \end{aligned}$$

$$\nabla_\ell \cdot \langle (\delta\mathbf{u} \cdot \delta\mathbf{B})\delta\mathbf{B} \rangle = \nabla_\ell \cdot \langle -(\mathbf{u}' \cdot \mathbf{B})\mathbf{B}' + (\mathbf{u} \cdot \mathbf{B}')\mathbf{B} - (\mathbf{u} \cdot \mathbf{B}')\mathbf{B}' + (\mathbf{u}' \cdot \mathbf{B})\mathbf{B} \rangle, \tag{2.21}$$

$$\nabla_\ell \cdot \langle |\delta\mathbf{B}|^2\delta\mathbf{u} \rangle = \nabla_\ell \cdot \langle -2(\mathbf{B} \cdot \mathbf{B}')\delta\mathbf{u} + \mathbf{B}^2 \mathbf{u}' - \mathbf{B}'^2 \mathbf{u} \rangle, \tag{2.22}$$

$$\langle (\rho\theta' + \rho'\theta)|\delta\mathbf{u}|^2 \rangle = \langle -2(\rho\theta' + \rho'\theta)(\mathbf{u} \cdot \mathbf{u}') + \rho\theta' u^2 + \rho\theta' u^2 + \rho'\theta u^2 + \rho'\theta u^2 \rangle, \tag{2.23}$$

$$\langle |\delta\mathbf{B}|^2\delta\mathbf{J}_c \rangle = \langle \mathbf{B}^2\delta\mathbf{J}_c + \mathbf{B}'^2\delta\mathbf{J}_c - 2(\mathbf{B} \cdot \mathbf{B}')\delta\mathbf{J}_c \rangle, \tag{2.24}$$

$$\nabla_\ell \cdot \langle (\delta\mathbf{B} \cdot \delta\mathbf{J}_c)\delta\mathbf{B} \rangle = \nabla_\ell \cdot \langle -(\mathbf{B}' \cdot \mathbf{J}_c)\mathbf{B}' + (\mathbf{B}' \cdot \mathbf{J}_c)\mathbf{B} - (\mathbf{B} \cdot \mathbf{J}'_c)\mathbf{B}' + (\mathbf{B} \cdot \mathbf{J}'_c)\mathbf{B} \rangle. \tag{2.25}$$

The introduction of these expressions into (2.18) gives

$$\begin{aligned}
\partial_t \langle S \rangle &= \partial_t \langle E^{\text{tot}} \rangle + \partial_t \langle E^b \rangle - \frac{1}{2} \nabla_\ell \cdot \langle \bar{\delta} \rho |\delta \mathbf{u}|^2 \delta \mathbf{u} \rangle + \frac{1}{4} \langle (\rho \theta' + \rho' \theta) |\delta \mathbf{u}|^2 \rangle \\
&\quad - \frac{1}{2} \langle \rho \mathbf{u} \cdot (\mathbf{J}'_c \times \mathbf{B}') + \rho' \mathbf{u}' \cdot (\mathbf{J}_c \times \mathbf{B}) - \rho \mathbf{u}' \cdot (\mathbf{J}'_c \times \mathbf{B}') - \rho' \mathbf{u} \cdot (\mathbf{J}_c \times \mathbf{B}) \rangle \\
&\quad - \frac{1}{2} \langle \mathbf{u}' \cdot (\mathbf{J} \times \mathbf{B}) + \mathbf{u} \cdot (\mathbf{J}' \times \mathbf{B}') \rangle \\
&\quad - \frac{1}{2\mu_0} \nabla_\ell \cdot \langle |\delta \mathbf{B}|^2 \delta \mathbf{u} - 2(\delta \mathbf{u} \cdot \delta \mathbf{B}) \delta \mathbf{B} - B^2 \mathbf{u}' + B'^2 \mathbf{u} - 2(\mathbf{u} \cdot \mathbf{B}') \mathbf{B}' + 2(\mathbf{u}' \cdot \mathbf{B}) \mathbf{B} \rangle \\
&\quad + \frac{\lambda}{2\mu_0} \nabla_\ell \cdot \langle |\delta \mathbf{B}|^2 \delta \mathbf{J}_c - B'^2 \delta \mathbf{J}_c - B^2 \delta \mathbf{J}_c - 2(\delta \mathbf{B} \cdot \delta \mathbf{J}_c) \delta \mathbf{B} \\
&\quad - 2(\mathbf{B}' \cdot \mathbf{J}_c) \mathbf{B}' + 2(\mathbf{B} \cdot \mathbf{J}'_c) \mathbf{B} \rangle \\
&\quad - \frac{1}{2} \left\langle \left(1 + \frac{\rho'}{\rho}\right) \mathbf{u}' \cdot (\mathbf{d}_v + \mathbf{f}) + \left(1 + \frac{\rho}{\rho'}\right) \mathbf{u} \cdot (\mathbf{d}'_v + \mathbf{f}') \right\rangle \\
&\quad + \frac{1}{2} \left\langle \frac{\rho}{\rho'} \mathbf{u}' \cdot (\mathbf{d}'_v + \mathbf{f}') + \frac{\rho'}{\rho} \mathbf{u} \cdot (\mathbf{d}_v + \mathbf{f}) \right\rangle - \frac{1}{\mu_0} \langle \mathbf{B}' \cdot \mathbf{d}_\eta + \mathbf{B} \cdot \mathbf{d}'_\eta \rangle. \tag{2.26}
\end{aligned}$$

As we have, for any vector field \mathbf{X} , the relation $\nabla(\mathbf{X} \cdot \mathbf{X}) = 2\mathbf{X} \times (\nabla \times \mathbf{X}) + 2(\mathbf{X} \cdot \nabla)\mathbf{X}$, we find the following expressions

$$\begin{aligned}
\langle \mathbf{u}' \cdot (\mathbf{J} \times \mathbf{B}) + \mathbf{u} \cdot (\mathbf{J}' \times \mathbf{B}') \rangle &= \frac{1}{\mu_0} \langle \mathbf{u}' \cdot ((\nabla \times \mathbf{B}) \times \mathbf{B}) + \mathbf{u} \cdot ((\nabla' \times \mathbf{B}') \times \mathbf{B}') \rangle \\
&= \nabla_\ell \cdot \left\langle \frac{B^2}{2} \mathbf{u}' - (\mathbf{B} \cdot \mathbf{u}') \mathbf{B} - \frac{B'^2}{2} \mathbf{u} + (\mathbf{B}' \cdot \mathbf{u}) \mathbf{B}' \right\rangle, \tag{2.27}
\end{aligned}$$

$$\nabla_\ell \cdot \langle (\mathbf{B} \cdot \mathbf{J}'_c) \mathbf{B} \rangle = -\langle \mathbf{J}'_c \cdot ((\mathbf{B} \cdot \nabla) \mathbf{B}) \rangle = \nabla_\ell \cdot \left\langle \frac{B^2}{2} \mathbf{J}'_c \right\rangle + \mu_0 \langle \mathbf{J}'_c \cdot (\mathbf{B} \times \mathbf{J}) \rangle, \tag{2.28}$$

$$\nabla_\ell \cdot \langle (\mathbf{B}' \cdot \mathbf{J}_c) \mathbf{B}' \rangle = \langle \mathbf{J}_c \cdot ((\mathbf{B}' \cdot \nabla') \mathbf{B}') \rangle = \nabla_\ell \cdot \left\langle \frac{B'^2}{2} \mathbf{J}_c \right\rangle - \mu_0 \langle \mathbf{J}_c \cdot (\mathbf{B}' \times \mathbf{J}') \rangle. \tag{2.29}$$

By stating that

$$\partial_t \langle E^b \rangle = - \left\langle \mathbf{J} \cdot \left(\eta \mu_0 \mathbf{J} - \mathbf{u} \times \mathbf{B} + \frac{1}{ne} \mathbf{J} \times \mathbf{B} \right) \right\rangle = \frac{1}{\mu_0} \langle \mathbf{B} \cdot \mathbf{d}_\eta \rangle - \langle \mathbf{u} \cdot (\mathbf{J} \times \mathbf{B}) \rangle, \tag{2.30}$$

we find

$$\begin{aligned}
\partial_t \langle S \rangle &= \partial_t \langle E^{\text{tot}} \rangle - \frac{1}{2} \nabla_\ell \cdot \langle \bar{\delta} \rho |\delta \mathbf{u}|^2 \delta \mathbf{u} \rangle + \frac{1}{4} \langle (\rho \theta' + \rho' \theta) |\delta \mathbf{u}|^2 \rangle \\
&\quad - \frac{1}{2} \langle \rho \mathbf{u} \cdot (\mathbf{J}'_c \times \mathbf{B}') \rangle \\
&\quad + \rho' \mathbf{u}' \cdot (\mathbf{J}_c \times \mathbf{B}) - \rho \mathbf{u}' \cdot (\mathbf{J}'_c \times \mathbf{B}') - \rho' \mathbf{u} \cdot (\mathbf{J}_c \times \mathbf{B}) + 2\mathbf{u} \cdot (\mathbf{J} \times \mathbf{B})
\end{aligned}$$

$$\begin{aligned}
 & -\frac{1}{2\mu_0} \nabla_\ell \cdot \left\langle |\delta \mathbf{B}|^2 \delta \mathbf{u} - 2(\delta \mathbf{u} \cdot \delta \mathbf{B}) \delta \mathbf{B} - \frac{B^2}{2} \mathbf{u}' + \frac{B'^2}{2} \mathbf{u} - (\mathbf{u} \cdot \mathbf{B}') \mathbf{B}' + (\mathbf{u}' \cdot \mathbf{B}) \mathbf{B} \right\rangle \\
 & -\frac{\lambda}{2\mu_0} \nabla_\ell \cdot \left\langle -|\delta \mathbf{B}|^2 \delta \mathbf{J}_c + 2(\delta \mathbf{B} \cdot \delta \mathbf{J}_c) \delta \mathbf{B} + \lambda(\mathbf{J}_c \cdot (\mathbf{B}' \times \mathbf{J}') + \mathbf{J}'_c \cdot (\mathbf{B} \times \mathbf{J})) \right\rangle \\
 & -\frac{1}{2} \left\langle \left(1 + \frac{\rho'}{\rho}\right) \mathbf{u}' \cdot (\mathbf{d}_v + \mathbf{f}) + \left(1 + \frac{\rho}{\rho'}\right) \mathbf{u} \cdot (\mathbf{d}'_v + \mathbf{f}') \right\rangle \\
 & + \frac{1}{2} \left\langle \frac{\rho}{\rho'} \mathbf{u}' \cdot (\mathbf{d}'_v + \mathbf{f}') + \frac{\rho'}{\rho} \mathbf{u} \cdot (\mathbf{d}_v + \mathbf{f}) \right\rangle - \frac{1}{\mu_0} \langle \mathbf{B}' \cdot \mathbf{d}_\eta + \mathbf{B} \cdot \mathbf{d}'_\eta - \mathbf{B} \cdot \mathbf{d}_\eta \rangle.
 \end{aligned} \tag{2.31}$$

Finally, we introduce the relations

$$\begin{aligned}
 \langle 2\delta\rho\delta\mathbf{u} \cdot \bar{\delta}(\mathbf{J}_c \times \mathbf{B}) \rangle &= \langle \rho' \mathbf{u}' \cdot (\mathbf{J}_c \times \mathbf{B}) + \rho' \mathbf{u}' \cdot (\mathbf{J}'_c \times \mathbf{B}') - \rho' \mathbf{u} \cdot (\mathbf{J}_c \times \mathbf{B}) \\
 &\quad - \rho' \mathbf{u} \cdot (\mathbf{J}'_c \times \mathbf{B}') - \rho \mathbf{u}' \cdot (\mathbf{J}_c \times \mathbf{B}) \\
 &\quad - \rho \mathbf{u}' \cdot (\mathbf{J}'_c \times \mathbf{B}') + \rho \mathbf{u} \cdot (\mathbf{J}_c \times \mathbf{B}) + \rho \mathbf{u} \cdot (\mathbf{J}'_c \times \mathbf{B}') \rangle,
 \end{aligned} \tag{2.32}$$

$$\langle \delta(\mathbf{J} \times \mathbf{B}) \cdot \delta \mathbf{J}_c \rangle = \langle \mathbf{J}_c \cdot (\mathbf{B}' \times \mathbf{J}') + \mathbf{J}'_c \cdot (\mathbf{B} \times \mathbf{J}) \rangle, \tag{2.33}$$

to obtain

$$\begin{aligned}
 \partial_t \langle S \rangle &= \partial_t \langle E^{\text{tot}} \rangle - \frac{1}{2} \nabla_\ell \cdot \langle \bar{\delta} \rho |\delta \mathbf{u}|^2 \delta \mathbf{u} \rangle + \frac{1}{4} \langle (\rho \theta' + \rho' \theta) |\delta \mathbf{u}|^2 \rangle - \langle \delta \rho \delta \mathbf{u} \cdot \bar{\delta}(\mathbf{J}_c \times \mathbf{B}) \rangle \\
 &\quad - \frac{1}{2\mu_0} \nabla_\ell \cdot \left\langle |\delta \mathbf{B}|^2 \delta \mathbf{u} - 2(\delta \mathbf{u} \cdot \delta \mathbf{B}) \delta \mathbf{B} - \lambda |\delta \mathbf{B}|^2 \delta \mathbf{J}_c + 2\lambda (\delta \mathbf{B} \cdot \delta \mathbf{J}_c) \delta \mathbf{B} \right\rangle \\
 &\quad + \lambda \langle \delta(\mathbf{J} \times \mathbf{B}) \cdot \delta \mathbf{J}_c \rangle \\
 &\quad - \frac{1}{2} \left\langle \left(1 + \frac{\rho'}{\rho}\right) \mathbf{u}' \cdot (\mathbf{d}_v + \mathbf{f}) + \left(1 + \frac{\rho}{\rho'}\right) \mathbf{u} \cdot (\mathbf{d}'_v + \mathbf{f}') \right\rangle \\
 &\quad + \frac{1}{2} \left\langle \frac{\rho}{\rho'} \mathbf{u}' \cdot (\mathbf{d}'_v + \mathbf{f}') + \frac{\rho'}{\rho} \mathbf{u} \cdot (\mathbf{d}_v + \mathbf{f}) \right\rangle - \frac{1}{\mu_0} \langle \mathbf{B}' \cdot \mathbf{d}_\eta + \mathbf{B} \cdot \mathbf{d}'_\eta - \mathbf{B} \cdot \mathbf{d}_\eta \rangle.
 \end{aligned} \tag{2.34}$$

2.3. Locality of interaction

In the inertial range and in a stationary state (the zeroth law of turbulence is used), we can simplify the expressions for the forcing and dissipative terms. The forcing is assumed to act on large scales only, thus its spatial variations should remain small and cross-terms such as $\mathbf{u} \cdot \mathbf{f}'$ are expected to behave like $\mathbf{u} \cdot \mathbf{f} = \varepsilon$. However, dissipation acts at small scales only, thus cross-terms like $\mathbf{u} \cdot \mathbf{d}'_v$ or $\mathbf{B} \cdot \mathbf{d}'_\eta$ will be uncorrelated and of null statistical mean. Then, using (2.8), the following simplifications can be made

$$\langle \mathbf{B}' \cdot \mathbf{d}_\eta + \mathbf{B} \cdot \mathbf{d}'_\eta \rangle \simeq 0, \tag{2.35}$$

$$-\frac{1}{2} \left\langle \left(1 + \frac{\rho'}{\rho}\right) \mathbf{u}' \cdot \mathbf{d}_v + \left(1 + \frac{\rho}{\rho'}\right) \mathbf{u} \cdot \mathbf{d}'_v \right\rangle \simeq 0, \tag{2.36}$$

$$-\frac{1}{2} \left\langle \left(1 + \frac{\rho'}{\rho}\right) \mathbf{u}' \cdot \mathbf{f} + \left(1 + \frac{\rho}{\rho'}\right) \mathbf{u} \cdot \mathbf{f}' \right\rangle \simeq -2\varepsilon, \tag{2.37}$$

$$\frac{1}{2} \left\langle \frac{\rho}{\rho'} \mathbf{u}' \cdot \mathbf{f}' + \frac{\rho'}{\rho} \mathbf{u} \cdot \mathbf{f} \right\rangle \simeq \varepsilon, \quad (2.38)$$

$$\frac{1}{2} \left\langle \frac{\rho}{\rho'} \mathbf{u}' \cdot \mathbf{d}'_v + \frac{\rho'}{\rho} \mathbf{u} \cdot \mathbf{d}_v \right\rangle + \frac{1}{\mu_0} \langle \mathbf{B} \cdot \mathbf{d}_\eta \rangle \simeq -\varepsilon. \quad (2.39)$$

Finally, the exact law for CHMHD turbulence reads as

$$\begin{aligned} -4\varepsilon = & \nabla_\ell \cdot \left\langle \bar{\delta}\rho |\delta\mathbf{u}|^2 \delta\mathbf{u} + \frac{1}{\mu_0} |\delta\mathbf{B}|^2 \delta\mathbf{u} - \frac{2}{\mu_0} (\delta\mathbf{u} \cdot \delta\mathbf{B}) \delta\mathbf{B} \right\rangle \\ & + \frac{\lambda}{\mu_0} \nabla_\ell \cdot \left\langle 2(\delta\mathbf{B} \cdot \delta\mathbf{J}_c) \delta\mathbf{B} - |\delta\mathbf{B}|^2 \delta\mathbf{J}_c \right\rangle \\ & - \frac{1}{2} \langle (\rho\theta' + \rho'\theta) |\delta\mathbf{u}|^2 \rangle + 2 \langle \delta\rho \delta\mathbf{u} \cdot \bar{\delta}(\mathbf{J}_c \times \mathbf{B}) \rangle - 2\lambda \langle \delta(\mathbf{J} \times \mathbf{B}) \cdot \delta\mathbf{J}_c \rangle. \end{aligned} \quad (2.40)$$

One can remark that the stationarity assumption used here implies neglect of the time derivatives of S and E^{tot} in (2.34), which are related, but not identical, to their counterparts in A18. Consequently, it might be useful to test, through direct numerical simulations, the convergence between the two laws and how this might be impacted by the stationarity assumption.

3. Discussion

Relation (2.40) is the main result of the paper. A comparison with the previous A18 law shows a drastic reduction in the number of terms (from 35 to 9). The present compact law can be written in the form

$$-4\varepsilon = \nabla_\ell \cdot (\mathbf{F}_{\text{MHD}} + \lambda \mathbf{F}_{\text{Hall}}) + S_{\text{MHD}} + \lambda S_{\text{Hall}}, \quad (3.1)$$

where, by definition,

$$\mathbf{F}_{\text{MHD}} = \left\langle \bar{\delta}\rho |\delta\mathbf{u}|^2 \delta\mathbf{u} + \frac{1}{\mu_0} |\delta\mathbf{B}|^2 \delta\mathbf{u} - \frac{2}{\mu_0} (\delta\mathbf{u} \cdot \delta\mathbf{B}) \delta\mathbf{B} \right\rangle, \quad (3.2)$$

$$\mathbf{F}_{\text{Hall}} = \frac{1}{\mu_0} \left\langle 2(\delta\mathbf{B} \cdot \delta\mathbf{J}_c) \delta\mathbf{B} - |\delta\mathbf{B}|^2 \delta\mathbf{J}_c \right\rangle, \quad (3.3)$$

$$S_{\text{MHD}} = -\frac{1}{2} \langle (\rho\theta' + \rho'\theta) |\delta\mathbf{u}|^2 \rangle + 2 \langle \delta\rho \delta\mathbf{u} \cdot \bar{\delta}(\mathbf{J}_c \times \mathbf{B}) \rangle, \quad (3.4)$$

$$S_{\text{Hall}} = -2 \langle \delta(\mathbf{J} \times \mathbf{B}) \cdot \delta\mathbf{J}_c \rangle. \quad (3.5)$$

The CHMHD law (2.40) contains two Yaglom-like flux terms that cover both the MHD and Hall scales (\mathbf{F}_{MHD} and \mathbf{F}_{Hall} , respectively) with an overall shape strongly reminiscent of the incompressible law, a situation not observed with the A18 law (Andrés *et al.* 2018). It is possible to recover the incompressible law in the associated limit after a renormalization by the mass density (and by taking $\rho \rightarrow \rho_0$). To do so, we need to use the mean rate of the total energy dissipation per unit of mass ($\bar{\varepsilon} = \varepsilon/\rho_0$) and the Alfvén units for the magnetic field ($\mathbf{b} = \mathbf{B}/\sqrt{\mu_0\rho_0}$). We also need to replace λ with the ion skin depth d_i , which has the relation $d_i = \lambda/\sqrt{\mu_0\rho_0}$. Similar to the flux, the two source terms cover both the MHD and Hall scales (S_{MHD} and S_{Hall} , respectively). In the incompressible limit, it is straightforward to show that S_{MHD} tends to zero, as this term is compressible by nature, so that only \mathbf{F}_{MHD}

remains at the MHD scale. At the Hall scale, a few lines of calculation are required, where we find that the sum of the flux and source is

$$\nabla_\ell \cdot \mathbf{F}_{\text{Hall}} + S_{\text{Hall}} = \frac{1}{2} \nabla_\ell \cdot \mathbf{F}_{\text{Hall}} = d_i \nabla_\ell \cdot \langle (\delta \mathbf{b} \cdot \delta \mathbf{J}) \delta \mathbf{b} - \frac{1}{2} |\delta \mathbf{b}|^2 \delta \mathbf{J} \rangle, \quad (3.6)$$

as was demonstrated by Ferrand *et al.* (2019), which ultimately leads to the incompressible Hall MHD exact relation

$$-4\bar{\varepsilon} = \nabla_\ell \cdot \langle |\delta \mathbf{u}|^2 \delta \mathbf{u} + |\delta \mathbf{b}|^2 \delta \mathbf{u} - 2(\delta \mathbf{u} \cdot \delta \mathbf{b}) \delta \mathbf{b} + d_i [(\delta \mathbf{b} \cdot \delta \mathbf{J}) \delta \mathbf{b} - \frac{1}{2} |\delta \mathbf{b}|^2 \delta \mathbf{J}] \rangle. \quad (3.7)$$

Unlike the A18 law, the new expression (2.40) does not depend explicitly on the (work part of the) internal energy. We also note that only the source S_{MHD} exhibits the divergence of a field (through the dilatation), whereas most of the source terms in the A18 law have such a dependence. As the precise evaluation of the divergence of a field is difficult when dealing with space plasma data because it requires a three-dimensional mapping of the system to be computed, which in turn calls for multi-spacecraft data, we conclude that the new law represents an important advance for the analysis of space plasma turbulence. This comment is particularly true considering that the entire Hall part of the law, which is the most important part when studying compressible plasma turbulence at small scales, can here be fully calculated. As the MHD source has been shown to have little influence on the energy cascade (Andrés *et al.* 2018), not being able to compute S_{MHD} for single-spacecraft missions should not significantly alter the estimation of the energy cascade rate. One should note however that this statement assumes that a direct measurement of the current is available (through ion and electron moments). If not, then multiple spacecraft are still required to compute the current as the curl of the magnetic field.

As expected, the compact law is Galilean invariant; however, and unlike the incompressible HMHD law (3.7), the compressible expression shows an explicit dependence on a mean background magnetic field \mathbf{B}_0 if one is initially present. In this case, a new term appears on the right-hand side of (3.1), which reads

$$\begin{aligned} S_{\mathbf{B}_0} &= 2\mathbf{B}_0 \cdot \langle \delta \rho (\delta \mathbf{u} \times \bar{\delta} \mathbf{J}_c) \rangle - 2\lambda \mathbf{B}_0 \cdot \langle \delta \rho (\delta \mathbf{J}_c \times \bar{\delta} \mathbf{J}_c) \rangle \\ &\simeq -2\mathbf{B}_0 \cdot \langle \delta \rho (\delta \mathbf{u}_e \times \bar{\delta} \mathbf{u}_e) \rangle, \end{aligned} \quad (3.8)$$

where the second line corresponds to the small-scale limit (where the assumption $\mathbf{J}_c \propto \mathbf{u}_e$ is used, where \mathbf{u}_e is the electron velocity). We see that this term goes trivially to zero in the incompressible limit. Note that, even in the absence of an explicit dependence in \mathbf{B}_0 , this term is still expected to have an impact on the energy cascade by the way it shapes the nonlinear dynamics (Wan *et al.* 2012; Meyrand & Galtier 2013; Oughton *et al.* 2013).

4. Conclusions

In this paper, we have detailed the derivation of a new exact law for three-dimensional compressible isothermal Hall MHD turbulence. This law stems from the analysis of mixed second-order structure functions for energy increments under the assumptions of statistical homogeneity, time stationarity and infinite kinetic/magnetic Reynolds numbers. The law is a function of the plasma velocity, the magnetic field and the plasma density. It can depend explicitly on a uniform magnetic field but it is Galilean invariant. The strength of this new law is its size, as it has only 9 terms instead of the 35 terms in the previous A18 law (Andrés *et al.* 2018), which makes it much easier to manipulate. Furthermore, this law has the advantage of being almost fully applicable to single-spacecraft data (assuming the Taylor hypothesis), except for the MHD source term S_{MHD} that requires a

three-dimensional mapping of the velocity field. This property will certainly allow for a more complete analysis of the new data from the recent NASA Parker Solar Probe (Bandyopadhyay *et al.* 2020), as well as the ESA Solar Orbiter mission, which should lead to a better understanding of the ion-scale turbulence in the solar wind turbulence.

Editor Steve Tobias thanks the referees for their advice in evaluating this article.

Funding

This research received no specific grant from any funding agency, commercial or not-for-profit sectors.

Declaration of interests

The authors report no conflict of interest.

REFERENCES

- ANDRÉS, N., GALTIER, S. & SAHRAOUI, F. 2018 Exact law for homogeneous compressible Hall magnetohydrodynamics turbulence. *Phys. Rev. E* **97**, 013204.
- ANDRÉS, N. & SAHRAOUI, F. 2017 Alternative derivation of exact law for compressible and isothermal magnetohydrodynamics turbulence. *Phys. Rev. E* **96** (5), 053205.
- ANDRÉS, N., SAHRAOUI, F., GALTIER, S., HADID, L. Z., DMITRUK, P. & MININNI, P. D. 2018 Energy cascade rate in isothermal compressible magnetohydrodynamic turbulence. *J. Plasma Phys.* **84** (4), 905840404.
- ANDRÉS, N., SAHRAOUI, F., GALTIER, S., HADID, L. Z., FERRAND, R. & HUANG, S. Y. 2019 Energy cascade rate measured in a collisionless space plasma with mms data and compressible hall magnetohydrodynamic turbulence theory. *Phys. Rev. Lett.* **123**, 245101.
- ANTONIA, R. A., OULD-ROUIS, M., ANSELMET, F. & ZHU, Y. 1997 Analogy between predictions of Kolmogorov and Yaglom. *J. Fluid Mech.* **332**, 395–409.
- ARZOUMANIAN, D., ANDRÉ, P., DIDELON, P., KÖNYVES, V., SCHNEIDER, N., MEN'SHCHIKOV, A., SOUSBIE, T., ZAVAGNO, A., BONTEMPS, S., DI FRANCESCO, J., *et al.* 2011 Characterizing interstellar filaments with herchel in ic 5146. *Astron. Astrophys.* **529**, L6.
- BANDYOPADHYAY, R., GOLDSTEIN, M. L., MARUCA, B. A., MATTHAEUS, W. H., PARASHAR, T. N., RUFFOLO, D., CHHIBER, R., USMANOV, A., CHASAPIS, A., QUDSI, R., *et al.* 2020 Enhanced energy transfer rate in solar wind turbulence observed near the sun from Parker solar probe. *Astrophys. J. Suppl.* **246** (2), 48.
- BANDYOPADHYAY, R., SORRISO-VALVO, L., CHASAPIS, A., HELLINGER, P., MATTHAEUS, W. H., VERDINI, A., LANDI, S., FRANCI, L., MATTEINI, L., GILES, B. L., *et al.* 2020 In situ observation of hall magnetohydrodynamic cascade in space plasma. *Phys. Rev. Lett.* **124** (22), 225101.
- BANERJEE, S. & GALTIER, S. 2013 Exact relation with two-point correlation functions and phenomenological approach for compressible magnetohydrodynamic turbulence. *Phys. Rev. E* **87** (1), 013019.
- BANERJEE, S. & GALTIER, S. 2014 A kolmogorov-like exact relation for compressible polytropic turbulence. *J. Fluid Mech.* **742**, 230–242.
- BANERJEE, S. & GALTIER, S. 2017 An alternative formulation for exact scaling relations in hydrodynamic and magnetohydrodynamic turbulence. *J. Phys. A* **50**, 015501.
- BANERJEE, S., HADID, L., SAHRAOUI, F. & GALTIER, S. 2016 Scaling of compressible magnetohydrodynamic turbulence in the fast solar wind. *Astrophys. J. Lett.* **829** (2), L27.
- BANERJEE, S. & KRITSUK, A. G. 2017 Exact relations for energy transfer in self-gravitating isothermal turbulence. *Phys. Rev. E* **96** (5), 053116.
- BANERJEE, S. & KRITSUK, A. G. 2018 Energy transfer in compressible magnetohydrodynamic turbulence for isothermal self-gravitating fluids. *Phys. Rev. E* **97** (2), 023107.
- BELMONT, G. & REZEAU, L. 2001 Magnetopause reconnection induced by magnetosheath hall-MHD fluctuations. *J. Geophys. Res.* **106**.

- BHATTACHARJEE, A. 2004 Impulsive magnetic reconnection in the earth's magnetotail and the solar corona. *Annu. Rev. Astron. Astrophys.* **42**, 365–384.
- COOPER, C. M., WALLACE, J., BROOKHART, M., CLARK, M., COLLINS, C., DING, W. X., FLANAGAN, K., KHALZOV, I., LI, Y., MILHONE, J., *et al.* 2014 The Madison plasma dynamo experiment: a facility for studying laboratory plasma astrophysics. *Phys. Plasmas* **21**.
- FEDERRATH, C. 2016 On the universality of interstellar filaments: theory meets simulations and observations. *MNRAS* **457** (1), 375–388.
- FERRAND, R., GALTIER, S., SAHRAOUI, F. & FEDERRATH, C. 2020 Compressible turbulence in the interstellar medium: new insights from a high-resolution supersonic turbulence simulation. *Astrophys. J.* **904** (2), 160.
- FERRAND, R., GALTIER, S., SAHRAOUI, F., MEYRAND, R., ANDRÉS, N. & BANERJEE, S. 2019 On exact laws in incompressible hall magnetohydrodynamic turbulence. *Astrophys. J.* **881** (1), 50.
- FOREST, C. B., FLANAGAN, K., BROOKHART, M., CLARK, M., COOPER, C. M., DÉLANGLES, V., EGEDAL, J., ENDRIZZI, D., KHALZOV, I. V., LI, H., *et al.* 2015 The Wisconsin plasma astrophysics laboratory. *J. Plasma Phys.* **81**, 345810501.
- GALTIER, S. 2006 Multi-scale turbulence in the inner solar wind. *J. Low Temp. Phys.* **145**, 59–74.
- GALTIER, S. 2008 von Kármán-Howarth equations for Hall magnetohydrodynamic flows. *Phys. Rev. E* **77** (1), 015302.
- GALTIER, S. 2012 Kolmogorov vectorial law for solar wind turbulence. *Astrophys. J.* **746**, 184.
- GALTIER, S. 2016 *Introduction to Modern Magnetohydrodynamics*. Cambridge University Press.
- GALTIER, S. & BANERJEE, S. 2011 Exact relation for correlation functions in compressible isothermal turbulence. *Phys. Rev. Lett.* **107** (13), 134501.
- GOURGOULIATOS, K. N. & CUMMING, A. 2014 Hall attractor in axially symmetric magnetic fields in neutron star crusts. *Phys. Rev. Lett.* **112**, 171101.
- HADID, L., SAHRAOUI, F. & GALTIER, S. 2017 Energy cascade rate in compressible fast and slow solar wind turbulence. *Astrophys. J.* **838**, 11.
- HADID, L. Z., SAHRAOUI, F., GALTIER, S. & HUANG, S. Y. 2018 Compressible magnetohydrodynamic turbulence in the earth's magnetosheath: estimation of the energy cascade rate using in situ spacecraft data. *Phys. Rev. Lett.* **120**, 055102.
- HELLINGER, P., VERDINI, A., LANDI, S., FRANCI, L. & MATTEINI, L. 2018 von Kármán-Howarth equation for hall magnetohydrodynamics: hybrid simulations. *Astrophys. J.* **857**, L19.
- HOWES, G. 2009 Limitations of Hall MHD as a model for turbulence in weakly collisional plasmas. *Nonlinear Process. Geophys.* **16**, 219–232.
- KOLMOGOROV, A. N. 1941 Dissipation of energy in locally isotropic turbulence. *Dokl. Akad. Nauk SSSR* **32**, 16–18.
- KRITSUK, A. G., NORMAN, M. L., PADOAN, P. & WAGNER, R. 2007 The statistics of supersonic isothermal turbulence. *Astrophys. J.* **665**, 416–431.
- KRITSUK, A. G., WAGNER, R. & NORMAN, M. L. 2013 Energy cascade and scaling in supersonic isothermal turbulence. *J. Fluid Mech.* **729**, 1.
- KUNZ, M. W. & LESUR, G. 2013 Magnetic self-organisation in Hall-dominated magnetorotational turbulence. *Mon. Not. R. Astron. Soc.* **2295**, 434.
- MACBRIDE, B. T., SMITH, C. W. & FORMAN, M. A. 2008 The turbulent cascade at 1 au: energy transfer and the third-order scaling for MHD. *Astrophys. J.* **679** (2), 1644.
- MARINO, R., SORRISO-VALVO, L., CARBONE, V., NOULLEZ, A., BRUNO, R. & BAVASSANO, B. 2008 Heating the solar wind by a magnetohydrodynamic turbulent energy cascade. *Astrophys. J.* **677**, L71.
- MEYRAND, R. & GALTIER, S. 2013 Anomalous $k_{\perp}^{-8/3}$ spectrum in electron magnetohydrodynamic turbulence. *Phys. Rev. Lett.* **111**, 264501.
- MONIN, A. S. 1959 On the theory of locally isotropic turbulence. *Dokl. Akad. Nauk SSSR* **125**, 515–518.
- OSMAN, K. T., WAN, M., MATTHAEUS, W. H., WEYGAND, J. M. & DASSO, S. 2011 Anisotropic third-moment estimates of the energy cascade in solar wind turbulence using multispacecraft data. *Phys. Rev. Lett.* **107** (16), 165001.
- OUGHTON, S., WAN, M., SERVIDIO, S. & MATTHAEUS, W. H. 2013 On the origin of anisotropy in magnetohydrodynamic turbulence: the role of higher-order correlations. *Astrophys. J.* **768**, 10.

- POLITANO, H. & POUQUET, A. 1998 Dynamical length scales for turbulent magnetized flows. *Geophys. Res. Lett.* **25**, 273–276.
- SAHRAOUI, F., GALTIER, S. & BELMONT, G. 2007 On waves in incompressible Hall magnetohydrodynamics. *J. Plasma Phys.* **73**, 723–730.
- SAHRAOUI, F., PINCON, J. L., BELMONT, G., REZEAU, L., CORNILLEAU-WEHRLIN, N., ROBERT, P., MELLUL, L., BOSQUED, J. M., BALOGH, A., CANU, P., *et al.* 2003 ULF wave identification in the magnetosheath: the k-filtering technique applied to Cluster II data. *J. Geophys. Res.* **108** (A9).
- SORRISO-VALVO, L., MARINO, R., CARBONE, V., NOULLEZ, A., LEPRETI, F., VELTRI, P., BRUNO, R., BAVASSANO, B. & PIETROPAOLO, E. 2007 Observation of inertial energy cascade in interplanetary space plasma. *Phys. Rev. Lett.* **99** (11), 115001.
- STAWARZ, J. E., SMITH, C. W., VASQUEZ, B. J., FORMAN, M. A. & MACBRIDE, B. T. 2009 The turbulent cascade and proton heating in the solar wind at 1 AU. *Astrophys. J.* **697**, 1119–1127.
- WAN, M., OUGHTON, S., SERVIDIO, S. & MATTHAEUS, W. H. 2012 von kármán self-preservation hypothesis for magnetohydrodynamic turbulence and its consequences for universality. *J. Fluid Mech.* **697**, 296–315.
- YOSHIMATSU, K. 2012 Examination of the four-fifths law for longitudinal third-order moments in incompressible magnetohydrodynamic turbulence in a periodic box. *Phys. Rev. E* **85**, 066313.

FLUID ENERGY CASCADE RATE AND KINETIC DAMPING: NEW INSIGHT FROM 3D LANDAU-FLUID SIMULATIONS

R. FERRAND¹, F. SAHRAOUI¹, D. LAVEDER², T. PASSOT², P.L. SULEM² AND S. GALTIER^{1,3}

¹ Laboratoire de Physique des Plasmas, CNRS, École polytechnique, Université Paris-Saclay, Sorbonne Université, Observatoire de Paris-Meudon, F-91128 Palaiseau Cedex, France

² Université Côte d’Azur, Observatoire de la Côte d’Azur, CNRS, Laboratoire J.L. Lagrange, Boulevard de l’Observatoire, CS 34229, 06304 Nice Cedex 4, France

and

³ Institut Universitaire de France (IUF)

(Dated: October 12, 2021)

ABSTRACT

Using an exact law for incompressible Hall magnetohydrodynamics (HMHD) turbulence, the energy cascade rate is computed from three-dimensional HMHD-CGL (bi-adiabatic ions and isothermal electrons) and Landau fluid (LF) numerical simulations that feature different intensities of Landau damping over a broad range of wavenumbers, typically $0.05 \lesssim k_{\perp} d_i \lesssim 100$. Using three sets of cross-scale simulations where turbulence is initiated at large, medium and small scales, the ability of the fluid energy cascade to “sense” the kinetic Landau damping at different scales is tested. The cascade rate estimated from the exact law and the dissipation calculated directly from the simulation are shown to reflect the role of Landau damping in dissipating energy at all scales, with an emphasis on the kinetic ones. This result provides new prospects on using exact laws for simplified fluid models to analyze dissipation in kinetic simulations and spacecraft observations, and new insights into theoretical description of collisionless magnetized plasmas.

1. INTRODUCTION

The understanding of turbulent astrophysical plasmas remains to date a challenging problem: their chaotic nature and the complexity of the mechanisms at work in such media impose limitations to the methods one can use to study them efficiently. Yet, enhancing our understanding of turbulent plasmas would provide the keys to solve a variety of problems related to energy dissipation, particle heating and acceleration. Examples of systems where these processes are crucial include the solar wind (SW) and planetary magnetospheres (Bruno & Carbone 2005; Matthaeus & Velli 2011; Goldstein et al. 1995; Sahraoui et al. 2020), accretion flows around compact objects (Balbus & Hawley 1998; Quataert & Gruzinov 1999) and fusion devices (Diamond et al. 2005; Garbet 2006; Fujisawa 2021). In the SW, the heating problem is reflected by the slow decline of ion tem-

perature (as function of the radial distance from the sun) in comparison with the prediction from the adiabatic expansion model of the wind (Richardson et al. 1995). Turbulence has long been proposed as a way to explain this behavior (Matthaeus et al. 1999), through scale-by-scale transfer of energy (i.e., cascade) toward small (kinetic) scales where dissipation is more effective (Schekochihin et al. 2009). A common tool used to estimate this energy dissipation is the formalism of exact law for fully developed turbulence first introduced by Kolmogorov (1941) to study incompressible neutral fluids. In this formalism, energy is assumed to be injected at large scales at a constant rate per unit volume ε , which is assumed to be equal to the rate of cascade to smaller scales and to the rate of dissipation at those scales. Assuming statistical homogeneity and stationarity of the turbulent fields, and the existence of an inertial range in which both forcing and dissipation mechanisms are negligible, the cascade rate ε must remain constant in the inertial range (Kolmogorov 1941; Monin

1959; Antonia et al. 1997). The formalism of exact law has been extended to (in)compressible magnetized plasmas within various approximations (Politano & Pouquet 1998; Galtier 2008; Banerjee & Galtier 2013; Andrés & Sahraoui 2017; Hellinger et al. 2018; Andrés et al. 2018; Ferrand et al. 2019).

Exact laws have been used successfully to measure the energy cascade rate in the SW (Smith et al. 2006; Podesta et al. 2007; Sorriso-Valvo et al. 2007; MacBride et al. 2008; Marino et al. 2008; Carbone et al. 2009; Smith et al. 2009; Stawarz et al. 2009; Osman et al. 2011; Coburn et al. 2015; Banerjee et al. 2016; Hadid et al. 2017) and terrestrial magnetosheath (Hadid et al. 2018; Andrés et al. 2019). In those studies, the estimated cascade rate was interpreted as the turbulence energy dissipation rate, and hence used to quantify the amount of plasma heating due to turbulence (Sorriso-Valvo et al. 2007; Carbone et al. 2009; Banerjee et al. 2016). However, as explained above, such an equivalence between injection, cascade and dissipation rates stems only from the hypothesis underlying exact laws derivation and cannot be demonstrated in spacecraft observations. Indeed, while in numerical simulations the injection, cascade and dissipation rates can generally be estimated separately and compared to each other as done in this paper, estimating (*irreversible*) dissipation from spacecraft observation is a challenge and, generally, only the cascade rate, which is directly linked to measurable quantities through the exact law, is accessible (Sorriso-Valvo et al. 2007; Hadid et al. 2017). Thus, in spacecraft data, interpreting the energy cascade rate as the actual dissipation rate is not straightforward. This is particularly true because of the weakly collisional nature of the SW: in such plasmas classical viscous and/or resistive effects are absent, and dissipation is expected to occur via kinetic effects (e.g., Landau and cyclotron resonances) (Leamon et al. 1998; Sahraoui et al. 2009; Sahraoui et al. 2010; He et al. 2015; Chen et al. 2019) that are not captured by usual fluid descriptions of plasmas. A fundamental question arises here: is the *fluid* turbulent cascade rate estimated in simulations and spacecraft observations of space plasmas representative of the actual *kinetic* dissipation in those media? It is the main goal of this paper to address this question, which impacts the use of fluid models to interpret part of in-situ spacecraft observations in the near-Earth space and the theoretical (fluid vs. kinetic) modeling of weakly collisional plasmas. In contrast with previous studies based on 2D hybrid particle-in-cell simulations (Hellinger et al. 2018;

Bandyopadhyay et al. 2020), the use of 3D LF models give the possibility to isolate the influence of electron and ion Landau damping, neglecting all the other kinetic effects, and is therefore very suited to address the question of interest here.

2. THEORETICAL MODEL

Although we are dealing with weakly compressible regimes we chose, for the sake of simplicity, to use here the exact law derived by Ferrand et al. (2019) for incompressible HMHD (see below about the use of more general compressible models). Starting from the incompressible HMHD equations, and under the usual assumptions of time stationarity, space homogeneity and infinite (kinetic and magnetic) Reynolds numbers, one can derive for the energy cascade rate in the inertial range the expression $\varepsilon = \varepsilon^{MHD} + \varepsilon^{Hall}$, with

$$\varepsilon^{MHD} = -\frac{1}{4}\nabla_{\ell} \cdot \langle (|\delta\mathbf{v}|^2 + |\delta\mathbf{b}|^2)\delta\mathbf{v} - 2(\delta\mathbf{v} \cdot \delta\mathbf{b})\delta\mathbf{b} \rangle, \quad (1)$$

$$\varepsilon^{Hall} = -\frac{1}{8}d_i\nabla_{\ell} \cdot \langle 2(\delta\mathbf{b} \cdot \delta\mathbf{j})\delta\mathbf{b} - |\delta\mathbf{b}|^2\delta\mathbf{j} \rangle, \quad (2)$$

where \mathbf{v} , $\mathbf{b} = \mathbf{B}/\sqrt{\mu_0\rho_0}$ and $\mathbf{j} = \nabla \times \mathbf{b}$ are the velocity, magnetic field and electric current in Alfvén units (ρ_0 is the constant mass density) and d_i is the ion inertial length. Fields are taken at points \mathbf{x} and \mathbf{x}' separated by a spatial increment $\boldsymbol{\ell} = \mathbf{x}' - \mathbf{x}$, and the notations $\mathbf{v} \equiv \mathbf{v}(\mathbf{x})$ and $\mathbf{v}' \equiv \mathbf{v}(\mathbf{x}')$ are adopted. We then define the increment operator δ as $\delta\mathbf{v} = \mathbf{v}' - \mathbf{v}$, and ∇_{ℓ} as the derivative operator with respect to the increment $\boldsymbol{\ell}$.

3. SIMULATION DATA

3.1. Presentation of the data

In this study, HMHD-CGL refers to a fluid model with anisotropic ion pressure whose gyrotropic components parallel and perpendicular to the local magnetic field obey nonlinear dynamical equations where the heat fluxes are neglected (bi-adiabatic approximation introduced by Chew, Goldenberg and Low (Chew et al. 1956), thus the acronym). The electrons are assumed isothermal. Differently, the LF model retains the nonlinear dynamics of the parallel and perpendicular pressures and heat fluxes for both the ions and electrons, and involves a closure at the level of the fourth-order moments, consistent with the low-frequency linear kinetic theory (Snyder et al. 1997; Passot & Sulem 2007). The main assumption for modeling Landau damping consists in retaining the imaginary contribution of the plasma response function in the closure relation which expresses the last

retained fluid moment of the hierarchy in terms of the lower ones. In Fourier space, this procedure generates factors of the form “ $i \operatorname{sgn}(k_z)$ ” which, in physical space, identifies with the Hilbert transform along the ambient magnetic field (Hammett & Perkins 1990; Hunana et al. 2019). It is then possible to generalize this formulation to take into account magnetic field line distortion, using the convolution form of the Hilbert transform (Snyder et al. 1997). Its approximation in the numerical code is discussed in Passot et al. (2014). In both models, finite ion and electron Larmor radius corrections are neglected, thus reducing the kinetic effects to Landau damping. The Ohm’s law includes the Hall term and the electron pressure contribution. Turbulence is forced with counter-propagating kinetic Alfvén waves (KAWs) making an angle θ with the ambient magnetic field, at the largest scales of the simulation domain. This corresponds to transverse wavenumbers $k_{\perp,f}$, whose values are summarized in Table 1. The amplitudes obey a Langevin equation, with an oscillation frequency given by the KAW linear dispersion relation (TenBarge et al. 2014). We also introduce two thresholds in order to constrain the sum of perpendicular kinetic and magnetic energies to stay within a certain range. Small-scale dissipation is ensured by the hyperviscosity and hyperdiffusivity terms in the velocity and induction equations, of the form $\mathbf{d}_\nu = \nu(\Delta_\perp + \alpha\partial_z^2)^4 \mathbf{v}$ and $\mathbf{d}_\eta = \eta(\Delta_\perp + \alpha\partial_z^2)^4 \mathbf{b}$, with α being an anisotropy coefficient.

In all the simulations, $\beta_i = 1$ and the ion and electron pressures are taken isotropic and equal initially. The other parameters are reported in Table 1. The simulations are performed using a desaliased spectral code (at 2/3 of the maximum wavenumber) with a third-order Runge-Kutta scheme for time stepping.

Two different propagation angles for the KAWs driven at the largest scale of each LF simulation were chosen, hence tuning Landau damping to two different levels (Kobayashi et al. 2017). This can be seen in Fig. 1 which compares the linear dispersion relation and damping rate of the KAWs: the higher the propagation angle, the lower the damping rate at a given scale. Note that, while changing the angle, we do not change the amplitude of the fluctuations at the driving scale (i.e., ω_{NL} remains constant), and so the nonlinear parameter $\chi = \omega_{NL}/\omega_L$ also varies: when the angle decreases, k_{\parallel} increases and so does ω_L , thus χ is reduced. As the ratio γ/ω_L is approximately constant for high oblique angles θ (e.g., Fig. 7 in Sahraoui et al. (2012)), the strength of the Landau damping relative to the cascade

Run	$k_{\perp,f}d_i$	Resolution	θ	$\nu = \eta$	α
CGL1	0.045	512^3	83°	7.35×10^{-8}	80
CGL2	0.045	512^3	75°	7.35×10^{-8}	10
CGL3	0.5	$512^2 \times 1024$	75°	10^{-14}	2.5
CGL4	0.011	1024^3	75°	3×10^{-3}	5
LF1	0.045	512^3	83°	7.35×10^{-8}	1
LF2	0.045	512^3	75°	7.35×10^{-8}	1
LF3	0.5	432^3	75°	7×10^{-14}	1.5
LF4	0.011	512^3	75°	3×10^{-3}	2

Table 1. List of runs and their relevant parameters, where CGLx and LFx refer to HMHD-CGL and LF simulations, respectively. The ratio of the longitudinal to transverse box sizes is given by $\tan(\theta)$.

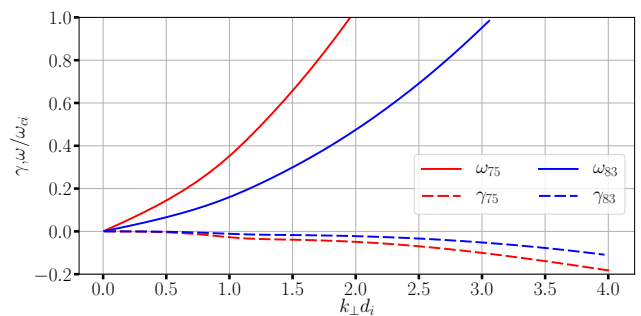


Figure 1. Frequency ω and damping rate γ (normalized by the ion gyrofrequency ω_{ci}) of KAWs versus the normalized transverse wavenumber $k_{\perp}d_i$ (where d_i refers to the ion inertial length) for the LF model at the two propagation angles $\theta = 83^\circ$ and 75° used in driving the simulations ($\beta_i = 1$, $T_i = T_e$).

rate $\gamma/\omega_{NL} = (1/\chi)(\gamma/\omega_L)$ thus increases as the angle decreases.

3.2. Energy balance and time stationarity

Let $\mathcal{E}_{\text{tot}}(t)$ be the total energy of the system at time t , $\mathcal{I}_t(t)$ the injection rate due to the external forcing on the perpendicular velocity components, and $\mathcal{D}_h(t)$ the total dissipation rate due to the hyperviscous and hyperdiffusive terms. Since Landau damping does not affect the total energy balance, total energy conservation implies

$$\frac{d}{dt}\mathcal{E}_{\text{tot}}(t) = \mathcal{I}_t(t) - \mathcal{D}_h(t). \quad (3)$$

Denoting by \mathcal{E}_{int} and \mathcal{E}_{\parallel} the parts of the total energy associated with the pressure components (internal energy) and the parallel velocity and magnetic field components entering the kinetic and magnetic parts, we can write

$$\frac{d}{dt}\mathcal{E}_{\text{tot}}(t) - \frac{d}{dt}\mathcal{E}_{\text{int}}(t) - \frac{d}{dt}\mathcal{E}_{\parallel}(t) \equiv \frac{d}{dt}\mathcal{E}_{\perp}(t) \approx 0, \quad (4)$$

where \mathcal{E}_\perp is the sum of the perpendicular kinetic and magnetic energies, a quantity bound to remain nearly constant by the forcing procedure.

Because of computational constraints, the time evolution of the different energy components is computed for low resolution (LR) simulations analogs of runs CGL3 and LF3 and shown in Fig. 2 (injection and dissipation rates needed to perform this extra study were not output at a high-enough frequency in the large-resolution simulations). From this figure it is conspicuous that the time evolution of total energy, injection and hyperdissipation is consistent with the energy conservation (3). Moreover, one can see the driving procedure at play in keeping the perpendicular energy \mathcal{E}_\perp roughly constant. Its time stationarity is in practice established when the hyperdissipation rate has reached a constant value. When comparing CGL3-LR with LF3-LR, one notices that run LF3-LR requires a larger injection rate to maintain the same level of turbulence on the magnetic and perpendicular velocity than in run CGL3-LR, since Landau damping efficiently converts a part of the injected energy into internal energy. This is evidenced by the dashed green curve in Fig. 2 (bottom), which shows that the increase of the internal energy is consistent with the heating by heat fluxes. Moreover, the hyperdissipation rate is lower on run LF3-LR, suggesting that part of the cascading energy is taken by Landau damping, as will be evidenced in next section.

4. CALCULATION OF THE ENERGY CASCADE RATE

Using Eqs. (1)-(2), we compute the transverse energy cascade rate for each simulation as a function of the perpendicular increment by averaging over all spatial positions in the simulation box and different increment vectors, at a time for which the simulations reached a stationary state. Increment vectors $\ell = (\ell_\perp, \ell_\parallel)$ are selected following the angle averaging method of Taylor et al. (2003), and only the increments forming an angle of at least 45° with the parallel direction are retained. As already mentioned, the exact law used is the one for incompressible HMHD, whereas the simulations are weakly compressible. A comparison (not shown) with a full compressible HMHD exact law (Andrés et al. 2018) only showed slight change ($\lesssim 10\%$ in the inertial range) of the cascade rate with respect to the current estimate from the incompressible model. The transverse cascade rate is then averaged over all increments of equal value of ℓ_\perp . The transverse hyperdissipation is computed in

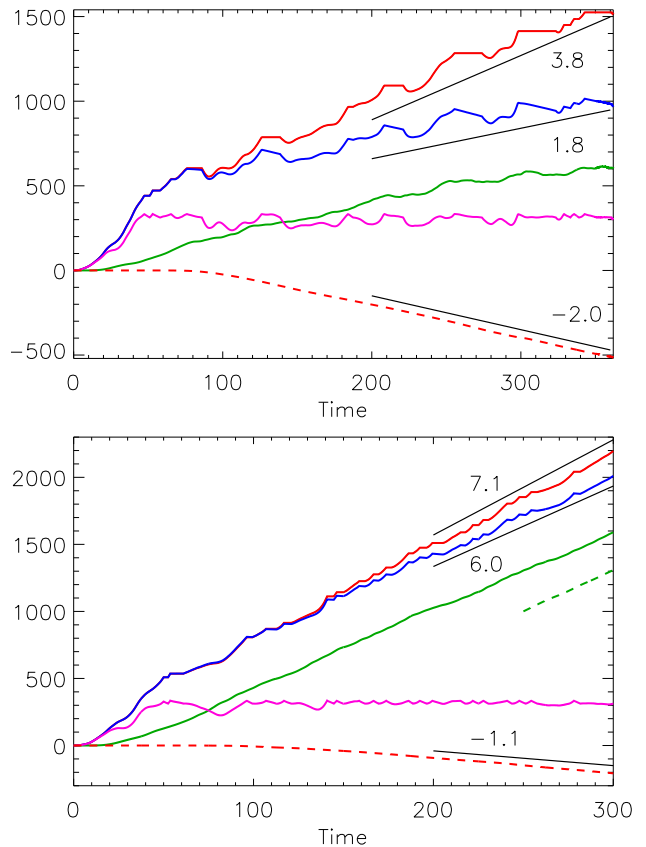


Figure 2. Low resolution runs of CGL3 (CGL3-LR, top) and LF3 (LF3-LR, bottom): Time evolution of the total energy injected in the system $\int_0^t \mathcal{I}_t dt$ (solid red line), total energy \mathcal{E}_{tot} (solid blue), internal energy \mathcal{E}_{int} (solid green), perpendicular energy \mathcal{E}_\perp (solid magenta, roughly constant) and the time integrated hyperdissipation $\int_0^t \mathcal{D}_h dt$ (dashed red). The piece of dashed green curve (right) starting at $t = 250$, whose vertical position is arbitrary, displays the heating due to heat fluxes, which is consistent with the increase of internal energy.

Fourier space as

$$\varepsilon^{\text{diss}}(\ell_\perp) = \int_0^{k_\perp} dk'_\perp \int k'^{\text{R}8}_\perp (\eta |\mathbf{b}(\mathbf{k}')|^2 + \nu |\mathbf{v}(\mathbf{k}')|^2) k'_\perp d\theta' dk'_z \quad (5)$$

where we use $\ell_\perp = \pi/k_\perp$.

For simulations forced at intermediate scales, whose results are reported in Fig. 3, the behavior of the MHD and Hall contributions to the energy cascade rate are similar, with the latter rising up at sub-ion scales, then dominating the former at about the ion inertial length. The total energy cascade rate is roughly constant on more than one decade of scales in the simulations with $\theta = 83^\circ$, in particular in CGL1, which demonstrates the existence of an inertial range. To highlight the effect of Landau damping on the cascade rate, we compare in Fig. 4 the cascade rates from the LF simulations with

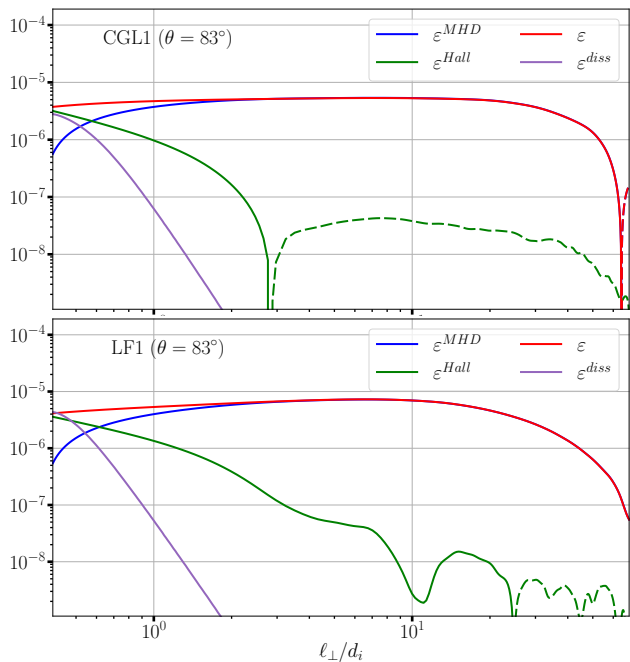


Figure 3. Energy cascade rate ε , its ideal MHD and Hall components together with the transverse hyperdissipation computed for runs CGL1 (top) and LF1 (bottom). Plain lines represent positive values and dashed lines negative values.

$\theta = 75^\circ$ and $\theta = 83^\circ$, normalized to the corresponding ones from the CGL simulations. We observe a stronger decrease (by up to a factor 5) in the normalized cascade rate at small scales for LF2 ($\theta = 75^\circ$), i.e. for the simulation with the strongest Landau damping, than for LF1 ($\theta = 83^\circ$) for which the normalized cascade rate remains nearly constant at all scales. This result clearly relates the enhancement of Landau damping at kinetic scales to the decline of the energy cascade rate at these scales. We note also the consistency between the (transverse) hyperdissipation and the cascade rate at the smallest scale of the simulation box (Fig. 3).

We complement our study with the cascade rates estimated from simulations forced at even smaller scales (LF3 and CGL3) with $\theta = 75^\circ$ and reported in Fig. 5. Simulation LF3 exhibits a strong decrease in ε^{MHD} partially compensated by a quick rising of the Hall component, giving no clear inertial range, in contrast to CGL3 which still behaves similarly to the simulations forced at intermediate scales. As shown below, this effect may be attributed to the fact that Landau dissipation reaches high levels at the sub-ion scales of LF3, whereas CGL3 contains no dissipation mechanisms other than hyper viscosity and diffusivity, which are bound to act only at the smallest scales. Note that the sudden changes of

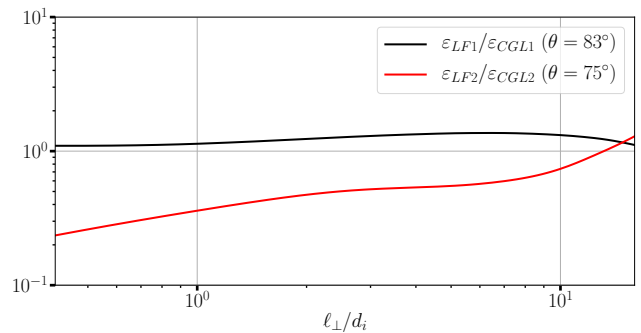


Figure 4. Ratios of the energy cascade rate computed for LF simulations over the one for CGL simulations for a driving wave angle $\theta = 83^\circ$ (black) and $\theta = 75^\circ$ (red).

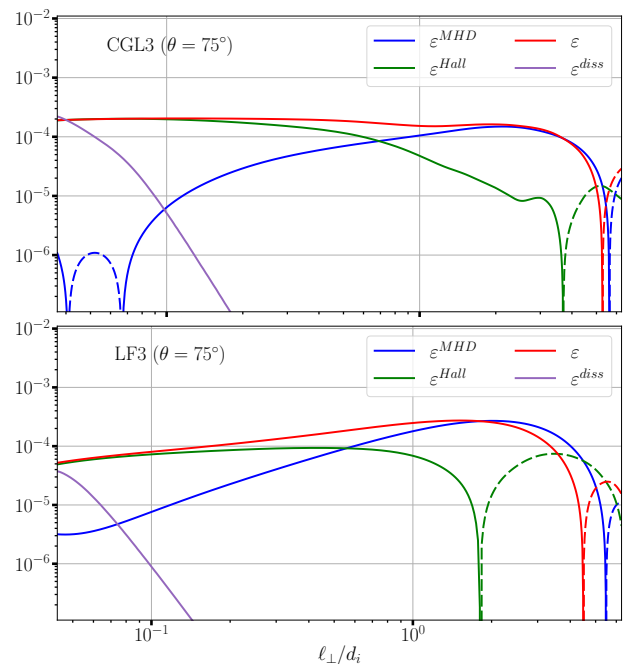


Figure 5. Same as in Fig. 3 for runs CGL3 (top) and LF3 (bottom).

sign observed at large scales in some components of the cascade rates in Figs. 3 and 5 are likely to be due to the proximity of the forcing. Those observed at small scales for the MHD component of run CGL3 would result from numerical errors in the calculation of ε^{MHD} given its very small magnitude at those scales.

To obtain a full picture as to how Landau damping affects the energy cascade rate, we performed simulations forced at large scales (LF4 and CGL4). Combining the runs CGL2-3-4 and LF2-3-4 we construct a multi-scale energy cascade rate over nearly three decades of scales that highlights the effect of Landau damping on it. As the simulations were run at different scales, the amplitude of the forcing was changed to ensure that each

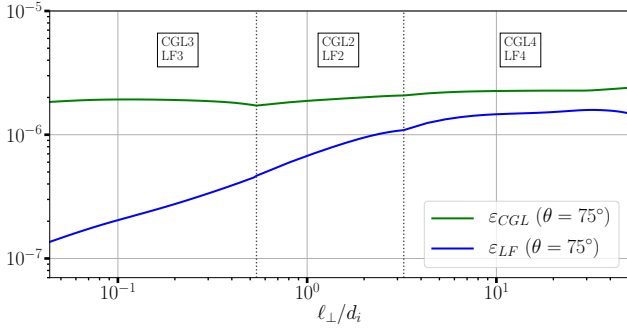


Figure 6. Energy cascade rates reconstructed with CGL2-3-4 runs and LF2-3-4 runs. The ranges spanned by each simulation are delimited by the black dotted lines. A slight irregularity is observed on the green curve at the transition between CGL2 and CGL3, which is caused by an insufficient overlap of the cascade rates at these scales.

simulation reaches a fully turbulent state. Therefore, we renormalized the cascade rate ε obtained from the different simulations to match the one of intermediate runs CGL2 and LF2, while taking care to discard the smallest scales of intermediate and large-scale forcing cascade rates to ensure that hyperviscosity is not acting at intermediate scales of the reconstructed energy cascade. Fig. 6 shows the full energy cascade rate for CGL and LF runs for the driving wave angle $\theta = 75^\circ$. CGL runs exhibit an almost constant energy cascade rate over two and a half decades of scales, whereas ε_{LF} decreases steadily over scales and reaches its minimum value at the smallest ones, confirming that the behavior already observed in Fig. 4 remains valid over a broader range of scales.

5. INFLUENCE OF LANDAU DISSIPATION

5.1. Heating due to heat fluxes

$$\partial_t(\rho s) + \nabla \cdot \left(\rho s \mathbf{u} + \left(\frac{q_{\perp}}{T_{\perp}} + \frac{q_{\parallel}}{2T_{\parallel}} \right) \hat{\mathbf{b}} \right) = \left(\frac{1}{T_{\parallel}} - \frac{1}{T_{\perp}} \right) q_{\perp} \nabla \cdot \hat{\mathbf{b}} - \left(\frac{q_{\perp}}{T_{\perp}} (\hat{\mathbf{b}} \cdot \nabla) \ln T_{\perp} + \frac{q_{\parallel}}{2T_{\parallel}} (\hat{\mathbf{b}} \cdot \nabla) \ln T_{\parallel} \right). \quad (10)$$

From the form of the right hand side of Eqs. (6)-(7), we can conclude that the rates of change of the parallel and perpendicular entropies per unit mass (s_{\parallel}^p and s_{\perp}^p respectively) associated with a production (or destruction) and excluding transport or exchanges between the parallel and perpendicular directions (see e.g. [Hazeltine](#)

in the wake of the previous results an important question arises : can the drop in the energy cascade rate for LF runs be directly connected to Landau damping? For this purpose, we calculate the heating due to heat fluxes in presence of Landau damping. For each species, the pressure equations with the Hall term and the gyrotopropic heat fluxes read

$$\frac{d}{dt} \ln \left(\frac{p_{\parallel} |B|^2}{\rho^3} \right) = -\frac{2c}{|B|} \hat{\mathbf{b}} \cdot \nabla \times \mathbf{E}_H - \frac{1}{p_{\parallel}} \left(-2q_{\perp} \nabla \cdot \hat{\mathbf{b}} + \nabla \cdot (q_{\parallel} \hat{\mathbf{b}}) \right), \quad (6)$$

$$\frac{d}{dt} \ln \left(\frac{p_{\perp}}{\rho |B|} \right) = \frac{c}{|B|} \hat{\mathbf{b}} \cdot \nabla \times \mathbf{E}_H - \frac{1}{p_{\perp}} \left(q_{\perp} \nabla \cdot \hat{\mathbf{b}} + \nabla \cdot (q_{\perp} \hat{\mathbf{b}}) \right). \quad (7)$$

We define the parallel, perpendicular and total entropies per unit mass

$$s_{\parallel} = \frac{c_V}{3} \ln \left(\frac{p_{\parallel} |B|^2}{\rho^3} \right), \quad s_{\perp} = \frac{2c_V}{3} \ln \left(\frac{p_{\perp}}{\rho |B|} \right), \quad (8)$$

$$s = s_{\parallel} + s_{\perp} = \frac{c_V}{3} \ln \left(\frac{p_{\parallel} p_{\perp}^2}{\rho^5} \right), \quad (9)$$

where c_V is the specific heat at constant volume. Denoting by e the internal energy per unit mass, the internal energy per unit volume reads $E \equiv \rho e = p_{\perp} + \frac{1}{2} p_{\parallel} = \frac{3}{2} nT$ where $T = \frac{1}{3} (2T_{\perp} + T_{\parallel})$. From $e = c_V T$, one gets $c_V = \frac{3}{2m}$ (the Boltzmann constant is included in the definition of temperature). The total entropy then obeys

[et al. \(2013\)](#)), are given by

$$\frac{d}{dt} s_{\parallel}^p = \frac{1}{\rho T_{\parallel}} q_{\perp} \nabla \cdot \hat{\mathbf{b}} - \frac{q_{\parallel}}{2\rho T_{\parallel}} (\hat{\mathbf{b}} \cdot \nabla) \ln T_{\parallel} \quad (11)$$

$$\frac{d}{dt} s_{\perp}^p = -\frac{1}{\rho T_{\perp}} q_{\perp} \nabla \cdot \hat{\mathbf{b}} - \frac{q_{\perp}}{\rho T_{\perp}} (\hat{\mathbf{b}} \cdot \nabla) \ln T_{\perp}. \quad (12)$$

The associated rates of heat production per unit mass are related by $dQ_{\parallel}/dt = T_{\parallel} ds_{\parallel}^p/dt$ and $dQ_{\perp}/dt = T_{\perp} ds_{\perp}^p/dt$. We thus get, for the total heat production

$$Q = Q_{\parallel} + Q_{\perp}$$

$$\partial_t(\rho Q) + \nabla \cdot (\rho Q \mathbf{u}) = -\frac{q_{\parallel}}{2} (\hat{\mathbf{b}} \cdot \nabla) \ln T_{\parallel} - q_{\perp} (\hat{\mathbf{b}} \cdot \nabla) \ln T_{\perp}. \quad (13)$$

The global heating is thus given by

$$H = - \int \left(\frac{q_{\parallel}}{2} (\hat{\mathbf{b}} \cdot \nabla) \ln T_{\parallel} + q_{\perp} (\hat{\mathbf{b}} \cdot \nabla) \ln T_{\perp} \right) d^3x, \quad (14)$$

$$H(\mathbf{k}) = -\frac{1}{2} \left(\frac{1}{2} \mathcal{F}\{q_{\parallel}\}(-\mathbf{k}) \mathcal{F}\{(\hat{\mathbf{b}} \cdot \nabla) \ln T_{\parallel}\}(\mathbf{k}) + \mathcal{F}\{q_{\perp}\}(-\mathbf{k}) \mathcal{F}\{(\hat{\mathbf{b}} \cdot \nabla) \ln T_{\perp}\}(\mathbf{k}) + c.c. \right) \quad (15)$$

where \mathcal{F} denotes the Fourier transform.

A few remarks can be made here:

1. In all the simulations we have performed, the volume integrated heat production is observed to be positive but its pointwise value can be negative in relatively small regions of space. This contrasts with the (semi)-collisional regime where the heat fluxes obey Fourier laws of the form $q = -\kappa(\hat{\mathbf{b}} \cdot \nabla)T$, making the heat production positive everywhere in space.

2. Inserting in Eq. (14) the quantities q_{\perp} and q_{\parallel} obtained by the integration of the dynamical equation for the heat fluxes results in taking into account in the heating rate contributions originating from the heat flux present when a quasi-normal closure is implemented (i.e. where the fourth-rank cumulants are taken equal to zero, thus making the Landau damping disappear). In the present simulations, this contribution does not exceed 15% of the total heating rate. In order to only deal with the heat flux originating from the Landau damping, it would be necessary to define a conserved entropy for the quasi-normal closure and evaluate its rate of change due to the introduction of Landau damping. This is left for future work as it is not straightforward.

3. More importantly, this heating rate takes into account the Landau damping on all the waves present in the simulations, including the magnetosonic waves. At this level, it appears difficult to separate the contributions of the KAW and to evaluate their dissipation by Landau damping. Nevertheless, these magnetosonic waves get dissipated at large scales, thus at small enough scales the estimated heating rate mostly results from Landau damping of KAWs and it becomes possible to compare it to the cascading energy. This particularity is also the reason why Landau damping appears to be acting at all scales in all the results presented above, even in simulations forced at large scales.

where q_{\parallel} and q_{\perp} are the heat fluxes obtained from the integration of the model closed at the level of the fourth-rank moments.

We can define a spectral density for the heating rate H (also referred to as co-spectrum) in the form

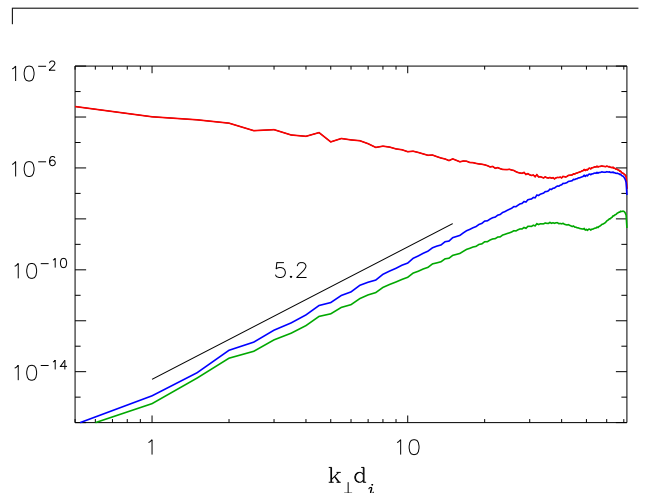


Figure 7. Spectral densities of the heating rate $D_L(k_{\perp})$ (red) and of the magnetic (blue) and kinetic (green) hyperdissipation as functions of the transverse wavenumber k_{\perp} for run LF3. A straight line of slope 5.2 is supplemented, for comparison with the scale-variation of the magnetic hyperdissipation.

The fact that Landau damping is present at all scales in the simulation can be seen by estimating the spectral density of total heating rate at a given wavenumber k_{\perp} , $D_L(k_{\perp}) = \int k_{\perp} H(\mathbf{k}) dk_z d\theta$, where $H(\mathbf{k})$ is the sum of the spectral densities given by equation (15) for both the ions and the electrons. This spectral density is represented in Fig. 7 along with the densities of hyperdissipation and hyperdiffusivity. One clearly sees that the heating rate due to the presence of heat fluxes dominates hyperdissipation over a broad range of scales due to the dissipation of KAWs and magnetosonic modes, the two becoming comparable only at the smallest scales (note that the magnetic hyperdissipation dominates at small scales over the kinetic one).

5.2. Dissipation due to Landau damping

The energy $\mathcal{E}_{\perp}(t)$ of the (quasi-incompressible) KAWs that cascade towards small scales, and which is the sub-

ject of our study, obeys

$$\frac{d}{dt}\mathcal{E}_\perp(t) = \mathcal{I}^C(t) - \mathcal{D}_L^C(t) - \mathcal{D}_h^C(t), \quad (16)$$

where \mathcal{I}^C is the part of the injection rate that contributes to the KAW cascade (the other part is transferred to magnetosonic modes which are dominantly dissipated at large scales), while \mathcal{D}_L^C and \mathcal{D}_h^C are the parts of the Landau and hyperviscous (and hyperdiffusive) dissipation that affect the cascading modes. Using cylindrical coordinates and assuming time stationarity, one can write the integrated energy balance at each Fourier mode as (adopting roman scripts for spectral densities):

$$\epsilon(k_\perp) = \int_0^{k_\perp} \{I^C(k'_\perp) - D_L^C(k'_\perp) - D_h^C(k'_\perp)\} dk'_\perp. \quad (17)$$

Considering two wavenumbers $k_{\perp 1}$ and $k_{\perp 2}$ large enough so that the forcing (which is concentrated at large scales) leads to $\int_0^{k_{\perp 1}} I^C(k'_\perp) dk'_\perp = \int_0^{k_{\perp 2}} I^C(k'_\perp) dk'_\perp = \mathcal{I}^C$, yet small enough for hyperviscous dissipation to be negligible, one obtains:

$$\epsilon(k_{\perp 1}) - \epsilon(k_{\perp 2}) = \int_{k_{\perp 1}}^{k_{\perp 2}} D_L^C(k'_\perp) dk'_\perp \lesssim \int_{k_{\perp 1}}^{k_{\perp 2}} D_L(k'_\perp) dk'_\perp. \quad (18)$$

$$\epsilon(k_\perp) = \mathcal{I}^C - \mathcal{D}_L^C + \int_{k_\perp}^\infty D_L^C(k'_\perp) dk'_\perp - \int_0^{k_\perp} D_h^C(k'_\perp) dk'_\perp = \int_{k_\perp}^\infty \{D_h^C(k'_\perp) + D_L^C(k'_\perp)\} dk'_\perp. \quad (19)$$

Equation (19) indicates that, as expected, the rate of energy transfer at the wavenumber k_\perp identifies with the sum of the rates of Landau and hyperdissipation beyond this wavenumber. One can compare the second right-hand-side term of this equation to the energy cascade rate $\epsilon(k_\perp)$ obtained from the IHMHD exact law, as displayed in Fig. 9. The difference between the two curves, which is especially significant at large scales, is due to the fact that the estimation of the dissipation includes the Landau damping of magnetosonic modes, whereas the cascade rate considers only incompressible modes. At smaller scales however, where magnetosonic modes have already been dissipated, the dissipation and cascade rates decreases parallel to each other: this indicates that, at scales not yet affected by hyperdissipation, the decay of $\epsilon(k_\perp)$ in a spectral interval identifies with Landau dissipation within this interval.

Figs. 8 and 9 clearly demonstrates that, through the cascade, the energy lost due to Landau damping is well

The inequality draws closer to an equality for values of k_\perp large enough so that all magnetosonic modes have been dissipated.

Equation (18) can be used to estimate a correction to the energy cascade rate which would take into account the energy lost due to Landau damping. We do so for run LF3: using this equation we add to the transfer rate the cumulative Landau dissipation between an arbitrary scale (chosen however to be not too large nor too small) and the running (smaller) scale l_\perp . Two of these resulting corrected rates ϵ^{corr} are shown in Fig. 8. They appear to be almost constant, and as such they behave very similarly to the transfer rate of run CGL3 (Fig. 5). The slight increase of ϵ^{corr} towards small scales probably reflects the (weak) contribution of some remaining magnetosonic waves to the calculated Landau damping. This clearly demonstrates that the energy lost along the cascade due to Landau damping is well captured by the decline of the (fluid) cascade rate at the corresponding scales.

A complementary estimate of energy dissipation can be done in Fourier space by also taking into account hyperdissipation. Indeed, assuming stationarity, one can also derive that

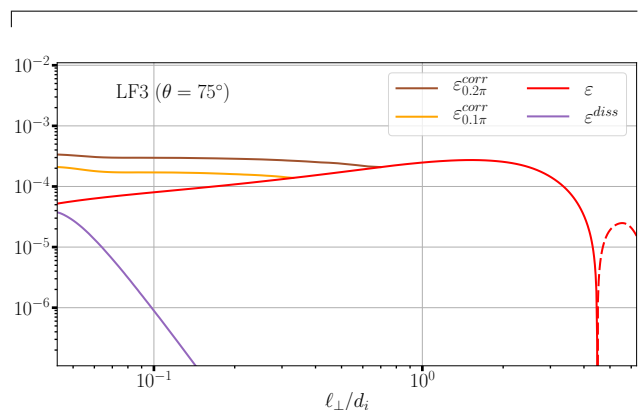


Figure 8. Energy cascade rate ϵ (red) and transverse hyperdissipation (violet) for run LF3. The orange and brown curves show the same ϵ corrected by Landau damping integrated between l_\perp and a reference scale $l_\perp = 0.1\pi d_i$ and $l_\perp = 0.2\pi d_i$ respectively.

captured by the decline of the (fluid) cascade rate at the corresponding scales. Note that a similar decline of the fluid cascade rate at kinetic scales was reported in 2D hybrid PIC simulations and spacecraft observations

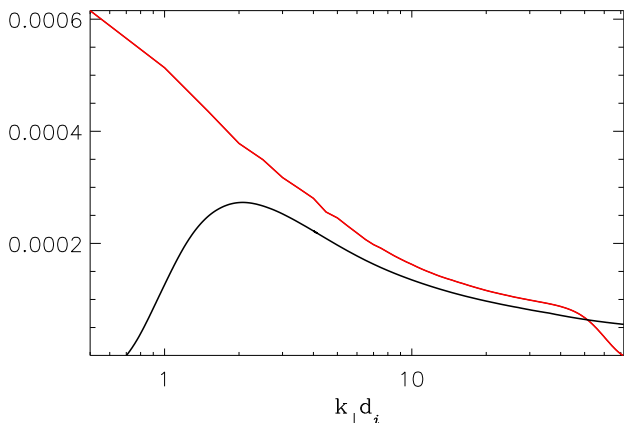


Figure 9. Energy cascade rate $\epsilon(k_{\perp})$ (black line) together with Landau and hyper-dissipation (red line) computed with equation (19) for run LF3.

in the SW and magnetosheath (Hellinger et al. 2018; Bandyopadhyay et al. 2020). Also, Sorriso-Valvo et al. (2019) found a correlation between enhancement of a proxy of the local cascade rate and the signatures of wave-particle interactions in MMS data.

6. CONCLUSION

In this study, we tackle a fundamental question about the ability of fluid exact laws to reflect the presence of kinetic (Landau) damping. By constructing multi-scale energy cascade and dissipation rates using the HMHD model on a variety of turbulence simulations bearing different intensities of Landau damping, we showed that the presence of Landau damping at small (kinetic) scales is reflected by the steady decline of the energy cascade

rate at the same scales, which was found to be comparable to the effective Landau dissipation at those scales. By demonstrating the ability of a fluid exact law to provide a correct estimate of kinetic dissipation in the sub-ion range of numerical simulations, this work provides a means to evaluate the amount of energy that is dissipated into particle heating in spacecraft data: the decline of the cascade rate allows one to evaluate the kinetic dissipation as a function of scale. This should help investigating (at least partially) a longstanding problem in astrophysical plasmas about energy partition between ions and electrons (Kawazura et al. 2019), which are generally heated at different scales.

The study presented in this paper only makes use of Landau damping. It would be interesting in future works to extend these conclusions to a broad variety of kinetic effects and to test them on more general simulations of the SW, featuring a plasma turbulence driven by other types of waves than slightly perturbed KAWs. It is also important to stress that, even if the oversimplified (yet fully nonlinear) fluid models of turbulence can provide good estimates of the amount of energy that is dissipated into particle heating, they do not specify how this dissipation occurs. The answer to this question and those related to the fate of energy when handed to the plasma particles requires a kinetic treatment.

7. ACKNOWLEDGEMENTS

This work was granted access to the HPC resources of CINES/IDRIS under the allocation A0060407042. Part of the computations have also been done on the “Mesocentre SIGAMM” machine, hosted by Observatoire de la Côte d’Azur.

REFERENCES

- Andrés, N., Galtier, S., & Sahraoui, F. 2018, *Phys. Rev. E*, 97, 013204
- Andrés, N., & Sahraoui, F. 2017, *Physical Review E*, 96, 053205
- Andrés, N., Sahraoui, F., Galtier, S., et al. 2019, *Phys. Rev. Lett.*, 123, 245101
- Antonia, R., Ould-Rouis, M., Anselmet, F., & Zhu, Y. 1997, *J. Fluid Mech.*, 332, 395
- Balbus, S. A., & Hawley, J. F. 1998, *Reviews of Modern Physics*, 70
- Bandyopadhyay, R., Sorriso-Valvo, L., Chasapis, A., et al. 2020, *Phys. Rev. Lett.*, 124, 225101
- Banerjee, S., & Galtier, S. 2013, *Phys. Rev. E*, 87, 013019
- Banerjee, S., Hadid, L., Sahraoui, F., & Galtier, S. 2016, *Astrophys. J. Lett.*, 829, L27
- Bruno, R., & Carbone, V. 2005, *Living Rev. Solar Phys.*, 2, 4
- Carbone, V., Marino, R., Sorriso-Valvo, L., Noullez, A., & Bruno, R. 2009, *Phys. Rev. Lett.*, 103, 061102
- Chen, C. H. K., Klein, K. G., & Howes, G. G. 2019, *Nat. Commun.*, 10, 740
- Chew, G. F., Goldberger, M. L., & Low, F. E. 1956, *Proc. R. Soc. London. A*, 236, 112
- Coburn, J., Forman, M., Smith, C., Vasquez, B., & Stawarz, J. 2015, *Phil. Trans. R. Soc. A*, 373, 20140150
- Diamond, P. H., Itoh, S. I., & Hahm, T. S. 2005, *Plasma Phys. Control. Fusion*, 47, R35
- Ferrand, R., Galtier, S., Sahraoui, F., et al. 2019, *Astrophys. J.*, 881, 50
- Fujisawa, A. 2021, *Proceedings of the Japan Academy, Series B*, 97, 103
- Galtier, S. 2008, *Phys. Rev. E*, 77, 015302
- Garbet, X. 2006, *Comptes Rendus Physique*, 7, 573, turbulent transport in fusion magnetised plasmas
- Goldstein, M. L., Roberts, D. A., & Matthaeus, W. 1995, *Annu. Rev. Astron. Astrophys.*, 33, 283
- Hadid, L., Sahraoui, F., & Galtier, S. 2017, *Astrophys. J.*, 838, 11

- Hadid, L. Z., Sahraoui, F., Galtier, S., & Huang, S. Y. 2018, *Phys. Rev. Lett.*, 120, 055102
- Hammett, G. W., & Perkins, F. W. 1990, *Phys. Rev. Lett.*, 64, 3019
- Hazeltine, R. D., Mahajan, S. M., & Morrison, P. J. 2013, *Phys. Plasmas*, 20, 022506
- He, J., Wang, L., Tu, C., Marsch, E., & Zong, Q. 2015, *Astrophys. J. Lett.*, 800, L31
- Hellinger, P., Verdini, A., Landi, S., Franci, L., & Matteini, L. 2018, *Astrophys. J.*, 857, L19
- Hunana, P., Tenerani, A., Zank, G. P., et al. 2019, *Journal of Plasma Physics*, 85, 205850603
- Kawazura, Y., Barnes, M., & Schekochihin, A. 2019, *PNAS*, 116, 771
- Kobayashi, S., Sahraoui, F., Passot, T., et al. 2017, *Astrophys. J.*, 839, 122
- Kolmogorov, A. 1941, *Dokl. Akad. Nauk SSSR*, 32, 16
- Leamon, R. J., Smith, C. W., Ness, N. F., Matthaeus, W. H., & Wong, H. K. 1998, *J. Geophys. Res.*, 103, 4775
- MacBride, B., Smith, C., & Forman, M. 2008, *Astrophys. J.*, 679, 1644
- Marino, R., Sorriso-Valvo, L., Carbone, V., et al. 2008, *Astrophys. J.*, 677, L71
- Matthaeus, W. H., & Velli, M. 2011, *Space Sci. Rev.*, 160, 145
- Matthaeus, W. H., Zank, G. P., Smith, C. W., & Oughton, S. 1999, *Phys. Rev. Lett.*, 82, 3444
- Monin, A. S. 1959, *Dokl. Akad. Nauk SSSR*, 125, 515
- Osman, K. T., Wan, M., Matthaeus, W. H., Weygand, J. M., & Dasso, S. 2011, *Phys. Rev. Lett.*, 107, 165001
- Passot, T., Henri, P., Laveder, D., & Sulem, P.-L. 2014, *The European Physical Journal D*, 68, doi:10.1140/epjd/e2014-50160-1
- Passot, T., & Sulem, P. L. 2007, *Phys. Plasmas*, 14, 082502
- Podesta, J. J., Forman, M. A., & Smith, C. W. 2007, *Phys. Plasmas*, 14, 092305
- Politano, H., & Pouquet, A. 1998, *Phys. Rev. E*, 57, 21
- Quataert, E., & Gruzinov, A. 1999, *Astrophys. J.*, 520, 248
- Richardson, J. D., Paularena, K. I., Lazarus, A. J., & Belcher, J. W. 1995, *Geophys. Res. Lett.*, 22, 325
- Sahraoui, F., Belmont, G., & Goldstein, M. L. 2012, *Astrophys. J.*, 748, 100
- Sahraoui, F., Goldstein, M. L., Belmont, G., Canu, P., & Rezeau, L. 2010, *Phys. Rev. Lett.*, 105, 131101
- Sahraoui, F., Goldstein, M. L., Robert, P., & Khotyaintsev, Y. V. 2009, *Phys. Rev. Lett.*, 102, 231102
- Sahraoui, F., Hadid, L., & Huang, S. 2020, *Rev. Mod. Plasmas Phys.*, 4, 4
- Schekochihin, A., Cowley, S. C., Dorland, W., et al. 2009, *Astrophys. J. Supp.*, 182, 310
- Smith, C. W., Hamilton, K., Vasquez, B. J., & Leamon, R. J. 2006, *Astrophys. J. Lett.*, 645, L85
- Smith, C. W., Stawarz, J. E., Vasquez, B. J., Forman, M. A., & MacBride, B. T. 2009, *Phys. Rev. Lett.*, 103, 201101
- Snyder, P. B., Hammett, G. W., & Dorland, W. 1997, *Phys. Plasmas*, 4, 3974
- Sorriso-Valvo, L., Marino, R., Carbone, V., et al. 2007, *Phys. Rev. Lett.*, 99, 115001
- Sorriso-Valvo, L., Catapano, F., Retinò, A., et al. 2019, *Phys. Rev. Lett.*, 122, 035102
- Stawarz, J. E., Smith, C. W., Vasquez, B. J., Forman, M. A., & MacBride, B. T. 2009, *Astrophys. J.*, 697, 1119
- Taylor, M. A., Kurien, S., & Eyink, G. L. 2003, *Phys. Rev. E*, 68, 026310
- TenBarge, J., Howes, G., Dorland, W., & Hammett, G. 2014, *Comp. Phys. Comm.*, 185, 578

AN IN-DEPTH NUMERICAL STUDY OF EXACT LAWS FOR COMPRESSIBLE HALL MAGNETOHYDRODYNAMIC TURBULENCE

R. FERRAND¹, F. SAHRAOUI¹, S. GALTIER^{1,2}, N. ANDRÉS³, P. MININNI³ AND P. DMITRUK³

¹ Laboratoire de Physique des Plasmas, CNRS, École polytechnique, Université Paris-Saclay, Sorbonne Université, Observatoire de Paris-Meudon, F-91128 Palaiseau Cedex, France

² Institut Universitaire de France (IUF)

and

³ University Buenos Aire, CONICET, Argentina

(Dated: October 26, 2021)

ABSTRACT

Various exact laws governing compressible magnetohydrodynamic (MHD) and Hall-MHD (CHMHD) turbulence have been derived in recent years. Other than their fundamental theoretical interest, these laws are generally used to estimate the energy dissipation rate from spacecraft observations in order to address diverse problems related, e.g., to heating of the solar wind (SW) and magnetospheric plasmas. Here we use various 1024³ direct numerical simulations (DNS) data of free-decay isothermal CHMHD turbulence obtained with the GHOST code to analyze two of the recently derived exact laws. The simulations reflect different intensities of the initial Mach number and the background magnetic field. The analysis demonstrates the equivalence of the two laws in the inertial range and relates the strength of the Hall effect to the amplitude of the cascade rate at sub-ion scales. When taken in their general form (i.e., not limited to the inertial range) some subtleties regarding the validity of the stationarity assumption or the absence of the forcing in the simulations are discussed. We show that the free-decay nature of the turbulence induces a shift from a large scale forcing towards the presence of a scale-dependent reservoir of energy fueling the cascade or dissipation. The reduced form of the exact laws (valid in the inertial range) ultimately holds even if the stationarity assumption is not fully verified.

1. INTRODUCTION

Understanding the dynamics of turbulent magnetized flows has been a longstanding problem in physics, and especially in astrophysics where turbulence is thought to play a leading role in various processes. Examples are the interstellar medium, the SW or planetary magnetospheres in which turbulence controls structures formation, energy whereabouts and particle heating or acceleration (Matthaeus et al. 1999; Bruno & Carbone 2013; Kritsuk et al. 2007; Arzoumanian et al. 2011; Sahraoui et al. 2020). Due to the chaotic nature of turbulence, such media are often studied thanks to the use of specific tools, which rely on statistical methods to uncover trends in the behavior of turbulent flows. A prime exam-

ple of such tools are exact laws: these equations, which can be obtained through the sole hypothesis of statistical homogeneity (and further refined by introducing time stationarity and infinite Reynolds number) express the rate of energy flowing towards the small/dissipative scales of a system as a function of two-point structure functions, without requiring the use of closure models. Initiated by the work of Kolmogorov and his four-fifths law for hydrodynamic turbulence (Kolmogorov 1941), the quest for exact laws has grown wider ever since with more and more elaborate models being derived. The first steps into studying plasma turbulence were taken by Politano & Pouquet (1998), who derived a law for incompressible MHD turbulence. This result paved the way for more precise studies of space plasmas (Sorriso-Valvo et al. 2007; MacBride et al. 2008; Marino et al. 2008; Stawarz et al. 2009; Osman et al. 2011; Galtier

2012). More general exact laws have been derived subsequently, by considering the influence of Hall physics (Galtier 2008; Banerjee & Galtier 2017; Hellinger et al. 2018; Ferrand et al. 2019), or the compression of the flow (Galtier & Banerjee 2011; Banerjee & Galtier 2013; Banerjee & Galtier 2014; Banerjee & Kritsuk 2017; Andrés & Sahaoui 2017; Andrés et al. 2018; Banerjee & Kritsuk 2018; Lindborg 2019; Ferrand et al. 2021a; Simon & Sahaoui 2021).

Thanks to those laws, several studies of astrophysical media have been made possible, either through direct numerical simulations (DNSs) (Mininni & Pouquet 2009; Kritsuk et al. 2013; Verdini et al. 2015; Ferrand et al. 2020) or *in situ* data analysis (Coburn et al. 2015; Banerjee et al. 2016; Hadid et al. 2017, 2018; Andrés et al. 2019; Sorriso-Valvo et al. 2019; Bandyopadhyay et al. 2020). These allowed testing the efficiency of the exact laws in practical situation in a variety of different systems. Studies specifically designed to test the validity of these exact laws were also conducted, allowing for a more in-depth understanding of how the constituents of these equations relate to each other (Hellinger et al. 2018; Andrés et al. 2018). This kind of work is especially important as the models are further refined, and exact laws grow even more complex, such as those derived for compressible Hall MHD. For this last plasma model, where two different exact laws have been derived, such a study has yet to be made. It is thus the aim of this paper to fill this gap by proposing, through the use of an ensemble of high-resolution DNSs for decaying compressible Hall MHD turbulence, a term-by-term analysis of exact laws derived by Andrés et al. (2018) and Ferrand et al. (2021a). The objective is not only to better comprehend the exact law by itself, but to test their more general expressions (valid beyond the inertial range and without time stationarity), which require the bare minimum of hypotheses, and unveil the relations between the energy cascade, the dissipation, and the dynamical variables that form these equations.

The structure of this paper is as follows: first we present the two models from Andrés et al. (2018) and Ferrand et al. (2021a), which will be referred to as A18 and F21 respectively, and provide compact and general expressions requiring only an assumption of statistical homogeneity to be obtained. We then describe the simulations and the numerical schemes used to compute all the terms forming both exact laws, and then present and discuss the results obtained. Finally, we give a conclusion on our work and on the behavior of the exact

laws.

2. THEORETICAL MODELS

Prior to presenting the theory of the two exact laws we introduce some notations and relations tied to the framework of both calculations. We introduce the spatial increment $\boldsymbol{\ell}$, connecting two points \mathbf{r} and \mathbf{r}' in the physical space as $\mathbf{r}' = \mathbf{r} + \boldsymbol{\ell}$, and define for any given field ξ : $\xi \equiv \xi(\mathbf{r})$ and $\xi' \equiv \xi(\mathbf{r}')$. We also define the notations $\delta\xi = \xi' - \xi$, $\bar{\delta}\xi = \frac{1}{2}(\xi' + \xi)$ and the differential operator in the direction $\boldsymbol{\ell}$ as $\nabla_{\boldsymbol{\ell}}$. This operator obeys the following relation on ensemble averages $\langle \cdot \rangle$: $\langle \nabla' \cdot \cdot \rangle = -\langle \nabla \cdot \cdot \rangle = \nabla_{\boldsymbol{\ell}} \cdot \langle \cdot \rangle$.

2.1. F21 model

The isothermal CHMHD exact law derived by Ferrand et al. (2021a) is obtained by considering the following three-dimensional compressible HMHD equations:

$$\partial_t \rho + \nabla \cdot (\rho \mathbf{v}) = 0, \quad (1)$$

$$\rho(\partial_t \mathbf{v} + \mathbf{v} \cdot \nabla \mathbf{v}) = -\nabla P + \mathbf{J} \times \mathbf{B} + \mathbf{d}_\nu + \mathbf{f}, \quad (2)$$

$$\partial_t \mathbf{B} = \nabla \times (\mathbf{v} \times \mathbf{B}) - \lambda \nabla \times (\mathbf{J}_c \times \mathbf{B}) + \mathbf{d}_\eta, \quad (3)$$

$$\nabla \cdot \mathbf{B} = 0, \quad (4)$$

where ρ is the mass density, \mathbf{v} the velocity, P the pressure, \mathbf{B} the magnetic field, $\mathbf{J} = (\nabla \times \mathbf{B})/\mu_0$ the current density, $\mathbf{J}_c = \mathbf{J}/\rho$ the normalized current, and $\lambda = m_i/q_e$ with m_i the ion mass and q_e the magnitude of the electron charge. The dissipation terms are:

$$\mathbf{d}_\nu = \nu \Delta \mathbf{v} + \frac{\nu}{3} \nabla \theta, \quad (5)$$

$$\mathbf{d}_\eta = \eta \Delta \mathbf{B}, \quad (6)$$

with $\theta = \nabla \cdot \mathbf{v}$ the dilatation, ν the dynamic viscosity and η the magnetic diffusivity. The isothermal closure writes $P = c_s^2 \rho$ with c_s the constant speed of sound. These equations are used to derive a dynamical equation for the modified second-order structure function

$$\langle S \rangle \equiv \left\langle \frac{1}{2} \bar{\delta}\rho |\delta \mathbf{v}|^2 + \frac{1}{2\mu_0} |\delta \mathbf{B}|^2 + \frac{1}{2} \delta \rho \delta e \right\rangle. \quad (7)$$

In the simulation code the internal energy follows the polytropic definition $e = \frac{c_s^2}{\gamma(\gamma-1)} ((\rho/\rho_0)^{\gamma-1} - 1)$ with a polytropic index $\gamma = 1.01$ close enough to unity so that the isothermal approximation remains valid. Note that under this approximation entropy is assumed to be constant, and thus the internal energy variation result only from the work of the pressure force (Simon & Sahaoui 2021).

Injecting equations (1)-(4) in the time derivative of

(7) leads, after a hefty amount of calculations, to the equation:

$$\begin{aligned}
\partial_t \langle S \rangle &= \partial_t \langle E^{tot} \rangle - \frac{1}{2} \nabla_{\boldsymbol{\ell}} \cdot \langle \bar{\delta} \rho |\delta \mathbf{v}|^2 \delta \mathbf{v} \rangle + \frac{1}{4} \langle (\rho \theta' + \rho' \theta) |\delta \mathbf{v}|^2 \rangle - \langle \delta \rho \delta \mathbf{v} \cdot \bar{\delta} (\mathbf{J}_c \times \mathbf{B}) \rangle + \lambda \langle \delta (\mathbf{J} \times \mathbf{B}) \cdot \delta \mathbf{J}_c \rangle \\
&- \frac{1}{2\mu_0} \nabla_{\boldsymbol{\ell}} \cdot \langle |\delta \mathbf{B}|^2 \delta \mathbf{v} - 2(\delta \mathbf{v} \cdot \delta \mathbf{B}) \delta \mathbf{B} - \lambda |\delta \mathbf{B}|^2 \delta \mathbf{J}_c + 2\lambda (\delta \mathbf{B} \cdot \delta \mathbf{J}_c) \delta \mathbf{B} \rangle \\
&- \frac{1}{2} \left\langle \left(1 + \frac{\rho'}{\rho}\right) \mathbf{v}' \cdot (\mathbf{d}_\nu + \mathbf{f}) + \left(1 + \frac{\rho}{\rho'}\right) \mathbf{v} \cdot (\mathbf{d}'_\nu + \mathbf{f}') \right\rangle \\
&+ \frac{1}{2} \left\langle \frac{\rho}{\rho'} \mathbf{v}' \cdot (\mathbf{d}'_\nu + \mathbf{f}') + \frac{\rho'}{\rho} \mathbf{v} \cdot (\mathbf{d}_\nu + \mathbf{f}) \right\rangle - \frac{1}{\mu_0} \langle \mathbf{B}' \cdot \mathbf{d}_\eta + \mathbf{B} \cdot \mathbf{d}'_\eta - \mathbf{B} \cdot \mathbf{d}_\eta \rangle, \tag{8}
\end{aligned}$$

with the total energy $E^{tot} = \rho u^2/2 + B^2/(2\mu_0) + \rho e$. Equation (8), already reported in Ferrand et al. (2021a) is the most general equation obtainable in this model under the sole assumption of statistical homogeneity. With

additional assumptions of time stationarity, forcing limited to the largest scales and infinite (magnetic and kinetic) Reynolds numbers one can then retrieve the exact law:

$$\begin{aligned}
-4\mathcal{E}_{F21} &= \nabla_{\boldsymbol{\ell}} \cdot \left\langle \bar{\delta} \rho |\delta \mathbf{v}|^2 \delta \mathbf{v} + \frac{1}{\mu_0} |\delta \mathbf{B}|^2 \delta \mathbf{v} - \frac{2}{\mu_0} (\delta \mathbf{v} \cdot \delta \mathbf{B}) \delta \mathbf{B} \right\rangle - \frac{1}{2} \langle (\rho \theta' + \rho' \theta) |\delta \mathbf{v}|^2 \rangle + 2 \langle \delta \rho \delta \mathbf{v} \cdot \bar{\delta} (\mathbf{J}_c \times \mathbf{B}) \rangle \\
&+ \frac{\lambda}{\mu_0} \nabla_{\boldsymbol{\ell}} \cdot \langle 2(\delta \mathbf{B} \cdot \delta \mathbf{J}_c) \delta \mathbf{B} - |\delta \mathbf{B}|^2 \delta \mathbf{J}_c \rangle - 2\lambda \langle \delta (\mathbf{J} \times \mathbf{B}) \cdot \delta \mathbf{J}_c \rangle. \tag{9}
\end{aligned}$$

Equation (9) (or similar ones obtained for other models) is generally the one that is used in numerical simulations and spacecraft data to infer the cascade rate (left-hand side) from measurable quantities (right-hand side) (Banerjee & Galtier 2016; Hadid et al. 2017, 2018; Andrés et al. 2018; Andrés et al. 2019). However, to be obtained, non-trivial approximations had to be made, about time stationarity and on the forcing and dissipative terms (Ferrand et al. 2021a). While these approximation are hard (if not impossible) to test on spacecraft

data, they can *a priori* be verified in direct numerical simulations, which is one of the goals of the present study. The specific point about time stationarity and the absence of driving is of a particular relevance in free-decay simulations as the ones we are using in this study. Therefore, we will consider in the following the more general equation (8), written in a more compact form:

$$2\mathcal{E}_{F21} + \partial_t \langle E^{tot} \rangle - \partial_t \langle S \rangle + \mathcal{D}_{F21} + \mathcal{D}_{F21}^{loc} + \mathcal{F}_{F21} + \mathcal{F}_{F21}^{loc} = 0 \tag{10}$$

where we define:

$$\mathcal{D}_{F21} \equiv -\frac{1}{2} \left\langle \left(1 + \frac{\rho'}{\rho}\right) \mathbf{v}' \cdot \mathbf{d}_\nu + \left(1 + \frac{\rho}{\rho'}\right) \mathbf{v} \cdot \mathbf{d}'_\nu \right\rangle - \frac{1}{\mu_0} \langle \mathbf{B}' \cdot \mathbf{d}_\eta + \mathbf{B} \cdot \mathbf{d}'_\eta \rangle, \tag{11}$$

$$\mathcal{D}_{F21}^{loc} \equiv +\frac{1}{2} \left\langle \frac{\rho}{\rho'} \mathbf{v}' \cdot \mathbf{d}'_\nu + \frac{\rho'}{\rho} \mathbf{v} \cdot \mathbf{d}_\nu \right\rangle + \frac{1}{2\mu_0} \langle \mathbf{B} \cdot \mathbf{d}_\eta + \mathbf{B}' \cdot \mathbf{d}'_\eta \rangle, \tag{12}$$

$$\mathcal{F}_{F21} \equiv -\frac{1}{2} \left\langle \left(1 + \frac{\rho'}{\rho}\right) \mathbf{v}' \cdot \mathbf{f} + \left(1 + \frac{\rho}{\rho'}\right) \mathbf{v} \cdot \mathbf{f}' \right\rangle, \tag{13}$$

$$\mathcal{F}_{F21}^{loc} \equiv +\frac{1}{2} \left\langle \frac{\rho}{\rho'} \mathbf{v}' \cdot \mathbf{f}' + \frac{\rho'}{\rho} \mathbf{v} \cdot \mathbf{f} \right\rangle. \tag{14}$$

Note that in equation (10) \mathcal{E}_{F21} is introduced by identifying it in equation (8) to its expression given by relation (9). It *does not* result from using the same assumptions that led to relation (9), and thus equation (10) remains very general. The superscript *loc* is used for the forcing and dissipation terms that result from the product of vectors taken locally (i.e., at the same position \mathbf{r} or \mathbf{r}'), assuming that $\rho \sim \rho'$ for the velocity field terms. This contrasts with the terms \mathcal{D}_{F21} and \mathcal{F}_{F21} that involve (distant) two-point correlations. Assuming that $\rho \sim \rho'$ in weakly compressible simulations as those of this study the terms \mathcal{D}_{F21} and \mathcal{F}_{F21} are likely to be scale-independent, however, as we will show below they still have significant impact on the energy balance. The same remark can be made about the term $\partial_t \langle E^{tot} \rangle$ in Eq. 10, which is clearly a local term (unlike $\partial_t \langle S \rangle$ since S is second order structure function).

2.2. A18 model

The other exact law derived by [Andrés et al. \(2018\)](#) relies on the same three-dimensional isothermal HMHD

equations, yet using the Alfvén speed $\mathbf{v}_A \equiv \mathbf{B}/\sqrt{\mu_0\rho}$ instead of the magnetic field:

$$\partial_t \rho = -\nabla \cdot (\rho \mathbf{v}), \quad (15)$$

$$\begin{aligned} \partial_t \mathbf{v} = & -\mathbf{v} \cdot \nabla \mathbf{v} + \mathbf{v}_A \cdot \nabla \mathbf{v}_A - \frac{1}{\rho} \nabla (P + P_M) \\ & - \mathbf{v}_A \cdot (\nabla \cdot \mathbf{v}_A) + \mathbf{d}_\nu + \mathbf{f}, \end{aligned} \quad (16)$$

$$\begin{aligned} \partial_t \mathbf{v}_A = & -(\mathbf{v} - \lambda \mathbf{J}_c) \cdot \nabla \mathbf{v}_A + \mathbf{v}_A \cdot \nabla (\mathbf{v} - \lambda \mathbf{J}_c) \\ & - \frac{\mathbf{v}_A}{2} (\nabla \cdot \mathbf{v} - \lambda \nabla \cdot \mathbf{J}_c) + \frac{\mathbf{d}_\eta}{\sqrt{\rho}}, \end{aligned} \quad (17)$$

$$\mathbf{v}_A \cdot \nabla \rho = -2\rho (\nabla \cdot \mathbf{v}_A), \quad (18)$$

$$\mathbf{J}_c \cdot \nabla \rho = -\rho (\nabla \cdot \mathbf{J}_c), \quad (19)$$

where $P_M \equiv \rho v_A^2/2$ is the magnetic pressure. The system is once again closed with an isothermal closure. These equations are used to compute the time derivative of the two point correlator $R_E \equiv \frac{\rho}{2} (\mathbf{v} \cdot \mathbf{v}' + \mathbf{v}_A \cdot \mathbf{v}'_A) + \rho e'$, which ultimately leads to the exact law:

$$\begin{aligned} -2\mathcal{E}_{A18} = & \frac{1}{2} \nabla_\ell \cdot \langle [(\delta(\rho \mathbf{v})) \cdot \delta \mathbf{v} + \delta(\rho \mathbf{v}_A) \cdot \delta \mathbf{v}_A + 2\delta e \delta \rho] \delta \mathbf{v} - [\delta(\rho \mathbf{v}) \cdot \delta \mathbf{v}_A + \delta \mathbf{v} \cdot \delta(\rho \mathbf{v}_A)] \delta \mathbf{v}_A \rangle \\ & + \left\langle [R'_E - \frac{1}{2}(R'_B + R_B) + \frac{P'_M - P'}{2} - E^{tot'}](\nabla \cdot \mathbf{v}) \right\rangle + \left\langle [R_E - \frac{1}{2}(R_B + R'_B) + \frac{P_M - P}{2} - E^{tot}](\nabla' \cdot \mathbf{v}') \right\rangle \\ & + \left\langle [(R_H - R'_H) - \bar{\rho}(\mathbf{v}' \cdot \mathbf{v}_A) + H' + \lambda \delta \rho \frac{\mathbf{J}_c \cdot \mathbf{v}'_A}{2}](\nabla \cdot \mathbf{v}_A) \right\rangle \\ & + \left\langle [(R'_H - R_H) - \bar{\rho}(\mathbf{v} \cdot \mathbf{v}'_A) + H - \lambda \delta \rho \frac{\mathbf{J}'_c \cdot \mathbf{v}_A}{2}](\nabla' \cdot \mathbf{v}'_A) \right\rangle \\ & + \frac{1}{2} \left\langle (e' + \frac{v_A'^2}{2}) [\nabla \cdot (\rho \mathbf{v})] + (e + \frac{v_A^2}{2}) [\nabla' \cdot (\rho' \mathbf{v}')] \right\rangle - \frac{1}{2} \left\langle \beta^{-1'} \nabla' \cdot (e' \rho \mathbf{v}) + \beta^{-1} \nabla \cdot (e \rho' \mathbf{v}') \right\rangle \\ & + \frac{1}{2} \nabla_\ell \cdot \langle 2\lambda [(\overline{\rho \mathbf{J}_c \times \mathbf{v}_A}) \times \delta \mathbf{v}_A - \delta(\mathbf{J}_c \times \mathbf{v}_A) \times \overline{\rho \mathbf{v}_A}] \rangle + \lambda \left\langle \frac{R_B - R'_B}{2} (\nabla \cdot \mathbf{J}_c) + \frac{R'_B - R_B}{2} (\nabla' \cdot \mathbf{J}'_c) \right\rangle, \end{aligned} \quad (20)$$

with the cross helicity $H \equiv \rho(\mathbf{v} \cdot \mathbf{v}_A)$, its two-points correlator $R_H \equiv \rho(\mathbf{v} \cdot \mathbf{v}'_A + \mathbf{v}_A \cdot \mathbf{v}')/2$, the correlator for magnetic energy $R_B \equiv \rho \mathbf{v}_A \cdot \mathbf{v}'_A/2$ and $\beta^{-1} \equiv v_A^2/2c_s^2$. Primed variables are obtained by inverting the positions of the primes in the definitions. Just like equation (9), this law is obtained under the assumptions of statistical homogeneity, forcing limited to large scales, time stationarity and infinite Reynolds number. The latter two can be dropped by using the general expression obtained directly from the dynamical equation of $\langle R_E + R'_E \rangle$:

$$2\mathcal{E}_{A18} + \partial_t \langle R_E + R'_E \rangle + \mathcal{D}_{A18} + \mathcal{F}_{A18} = 0. \quad (21)$$

Here again the same caution as above applies regarding the introduction of \mathcal{E}_{A18} , whose expression is given by (20). The dissipative and forcing terms \mathcal{D}_{A18} and \mathcal{F}_{A18} are not explicitly given in [Andrés et al. \(2018\)](#) but are easy to calculate. For the dissipation term, the component stemming from the velocity field and Navier-Stokes equation is the same as in (11), and the one originating from the magnetic field and induction equation stems from:

$$\partial_t \left\langle \frac{1}{2} (\rho + \rho') \mathbf{v}_A \cdot \mathbf{v}'_A \right\rangle, \quad (22)$$

and reads:

$$\begin{aligned} & \frac{1}{2} \left\langle \rho \mathbf{v}_A \cdot \frac{\mathbf{d}'_\eta}{\sqrt{\rho'}} + \rho \mathbf{v}'_A \cdot \frac{\mathbf{d}_\eta}{\sqrt{\rho}} + \rho' \mathbf{v}_A \cdot \frac{\mathbf{d}'_\eta}{\sqrt{\rho'}} + \rho' \mathbf{v}'_A \cdot \frac{\mathbf{d}_\eta}{\sqrt{\rho}} \right\rangle \\ &= \frac{1}{2\mu_0} \left\langle \left(\frac{\sqrt{\rho}}{\sqrt{\rho'}} + \frac{\sqrt{\rho'}}{\sqrt{\rho}} \right) (\mathbf{B} \cdot \mathbf{d}'_\eta + \mathbf{B}' \cdot \mathbf{d}_\eta) \right\rangle, \end{aligned} \quad (23)$$

which ultimately leads to

$$\begin{aligned} \mathcal{D}_{A18} &= -\frac{1}{2} \left\langle \left(1 + \frac{\rho'}{\rho} \right) \mathbf{v}' \cdot \mathbf{d}_\nu + \left(1 + \frac{\rho}{\rho'} \right) \mathbf{v} \cdot \mathbf{d}'_\nu \right\rangle \\ &\quad - \frac{1}{2\mu_0} \left\langle \left(\frac{\sqrt{\rho}}{\sqrt{\rho'}} + \frac{\sqrt{\rho'}}{\sqrt{\rho}} \right) (\mathbf{B} \cdot \mathbf{d}'_\eta + \mathbf{B}' \cdot \mathbf{d}_\eta) \right\rangle. \end{aligned} \quad (24)$$

The forcing term is identical to the one of law F21, and reads

$$\mathcal{F}_{A18} = -\frac{1}{2} \left\langle \left(1 + \frac{\rho'}{\rho} \right) \mathbf{v}' \cdot \mathbf{f} + \left(1 + \frac{\rho}{\rho'} \right) \mathbf{v} \cdot \mathbf{f}' \right\rangle. \quad (25)$$

3. NUMERICAL METHODS

3.1. Simulation data

The equations of CHMHD (1)-(4) are solved numerically using the pseudo-spectral code GHOST (Gómez et al. 2005; Mininni et al. 2011) along with a module for solving compressible HMHD flows with the eventual presence of a background magnetic field. Three simulations were run in a cubic periodic box of spatial resolution of $N = 1024$ grid points and size $L_0 = 2\pi$ in all three directions, and all simulations use dimensionless viscosity and magnetic diffusivity of $\nu = \eta = 3.0 \times 10^{-4}$. The ion inertial length d_i is set to $d_i = 0.02/L_0$ for the three Runs. These simulations do not feature any forcing: instead, they are set to an initial state built from a superposition of harmonic modes with random phases whose energy in Fourier space is put in a sphere between wave vectors k_{down} and k_{up} , following the idea of Pouquet & Patterson (1978). Then, the flow is left to evolve and decay. Varying the intensity of background magnetic field B_0 and the initial Mach number M_S allows us to evaluate the influence of these parameters on the dynamics of the system. All aforementioned parameters are reported in Table 1.

As these simulations are free-decay, instead of looking for a stationary regime, we wait for the simulations to reach a maximum of dissipation, indicating that turbulence has had enough time to fully develop, and lead our study on times selected around this moment. Around these times the sum of the kinetic and magnetic energies of the system, $E_k + E_m = \rho u^2/2 + B^2/(2\mu_0)$ is expected to be decreasing steadily. Figures 1 and 2 show

these dissipation and energy for Runs I and II (Run III exhibits an almost identical behavior to Run II). The steady decline of the energy is indeed observed for Run II, yet Run I shows oscillations on top of the general behavior. These oscillations, as shown in Fig. 1, match fluctuations of the internal energy and are thus thought to be a consequence of exchanges between the kinetic plus magnetic energy and internal energy, as was already reported in Yang et al. (2021), and initiated by the presence of waves. Using a linear fit, one can estimate the energy dissipation rate at the selected times: for Run I it is estimated at ~ -0.047 and for Runs II and III at ~ -0.087 . If the energy cascade rate is indeed representative of the energy transferred to and dissipated at small scales, its amplitude should match these estimates for the various simulations. We will return to this point in the next section.

3.2. Methods of calculation

To compute all terms from equations (10) and (21) with large-enough statistics we use two different numerical schemes depending on whether there is a background magnetic field in the simulation or not. Both originate from the discrete decomposition of space proposed by Taylor et al. (2003): increment vectors $\boldsymbol{\ell}$ are selected along 73 directions defined by base vectors connecting two points of the grid. Increments are taken as multiples of these base vectors so that both \mathbf{r} and $\mathbf{r}' = \mathbf{r} + \boldsymbol{\ell}$ lie on known grid points, allowing for a well mapping of space without having to interpolate the 3D data, which would be a very time-consuming process. Such a decomposition has already been successfully used to compute the two-point correlation functions in simulation data of compressible MHD turbulence (Andrés et al. 2018).

All source terms (i.e. terms that do not appear as divergences along the increment vector) can be computed directly as long as the increment vector is known. We only need to proceed to the ensemble average, which in our case is taken on the full simulation domain:

$$\langle \xi \rangle = \sum_{\mathbf{r}} \frac{\xi(\mathbf{r})}{N^3}, \quad (26)$$

where $N = 1024$ is the number of the grid points.

For flux terms (i.e. terms that appear as divergences along the increment vector, of the form $\nabla_{\boldsymbol{\ell}} \cdot \mathbf{F}$) we make the assumption that our system is isotropic. In this situation we naturally use spherical coordinates, in which $\boldsymbol{\ell}$ is defined as $\boldsymbol{\ell} = (\ell, \phi, \theta)$ and the derivative operator $\nabla_{\boldsymbol{\ell}}$ reduces to $\nabla_{\boldsymbol{\ell}} \cdot \langle \mathbf{F} \rangle = \frac{1}{\ell^2} \partial_{\ell} [\ell^2 \langle F_{\ell} \rangle (\ell)]$. Thus, for a given increment vector $\boldsymbol{\ell}$ we only have to compute the

Run	B_0	Resolution	$\nu = \eta$	d_i/L_0	M_S	k_{down}	k_{up}
I	2	1024^3	3.0×10^{-4}	0.02	0.25	1	3
II	0	1024^3	3.0×10^{-4}	0.02	0.25	1	3
III	0	1024^3	3.0×10^{-4}	0.02	0.5	1	3

Table 1. List of Runs and their relevant parameters.

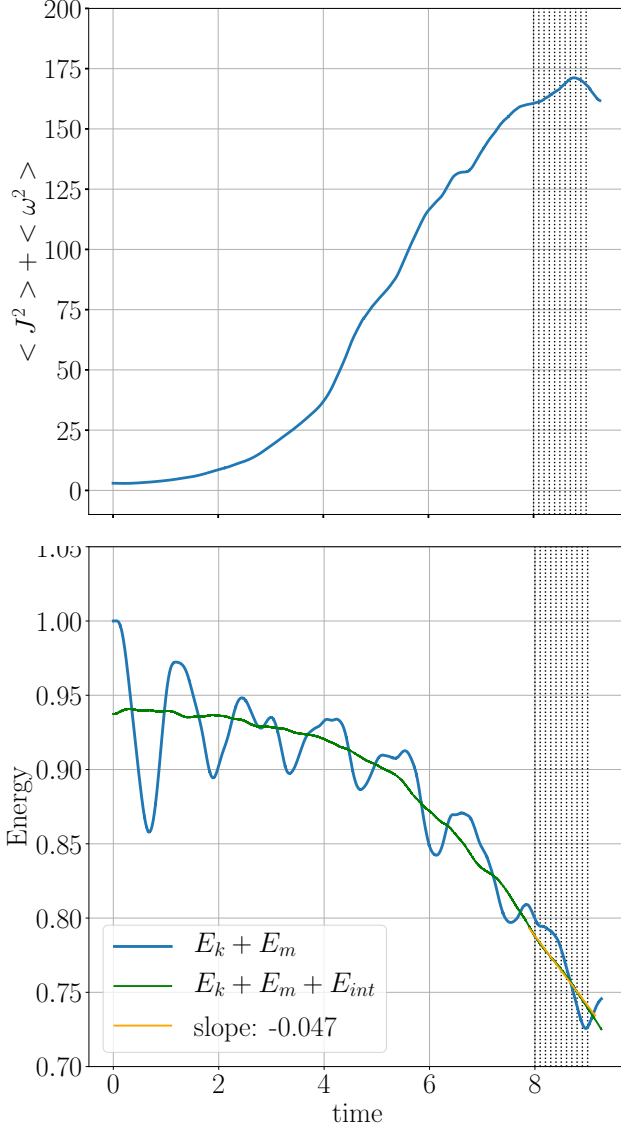


Figure 1. Top: Incompressible dissipation as a function of time for Run I. The vertical dotted lines represent the 11 times selected to compute the exact laws. Bottom: Fluctuations of kinetic, magnetic and internal energies (resp. E_k , E_m and E_{int}) as a function of time for Run I. The total energy (green curve) shows a continuous exchange between kinetic plus magnetic and internal energies. The narrow orange line is a linear fit of the times studied in this paper, and its slope represents the rate of energy loss at these times.

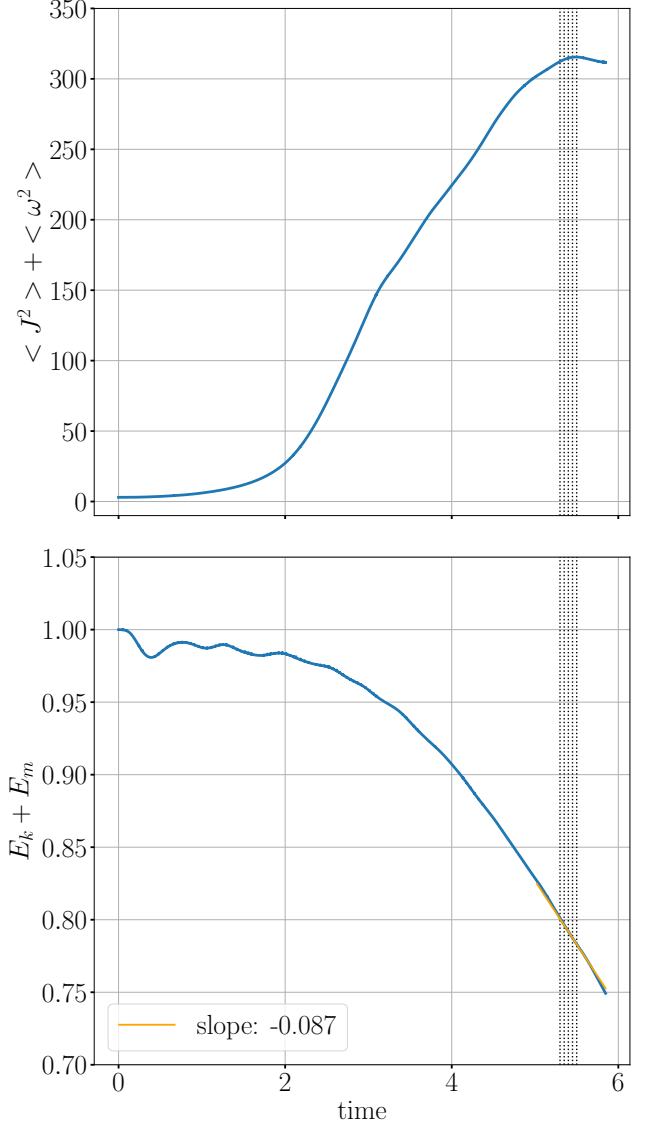


Figure 2. Top: Incompressible dissipation as a function of time for Run II. The vertical dotted lines represent the 5 times selected to compute the exact laws. Bottom: Fluctuations of kinetic plus magnetic energy as a function of time for Run II. The narrow orange line is a linear fit of the times studied in this paper, and its slope represents the rate of energy loss at these times.

projection of the vectorial flux \mathbf{F} on the direction of ℓ ,

which writes:

$$\langle F_\ell \rangle (\ell, \phi, \theta) = \langle \cos(\phi)\sin(\theta)F_x + \sin(\phi)\sin(\theta)F_y + \cos(\theta)F_z \rangle. \quad (27)$$

These projections are then averaged at fixed ℓ :

$$\langle F_\ell \rangle (\ell) = \sum_{\phi, \theta} \frac{\langle F_\ell \rangle (\ell, \phi, \theta)}{n_{dir}}, \quad (28)$$

where $n_{dir} = 73$ refers to the number of different directions taken for ℓ .

Note that, the isotropy assumption stands for Runs II and III in which $\mathbf{B}_0 = 0$. A similar method based on the assumption of a symmetry of revolution along the axis of \mathbf{B}_0 was also used to study Run I. While this method is *a priori* more suited for the study of simulations with $\mathbf{B}_0 \neq 0$, the isotropic method ultimately provided better results even on Run I, and is thus the only one used in this paper. A more detailed discussion on this point is given in the Appendix.

3.3. Applied calculation

Using the method described above we compute the various terms of equations (10) and (21). Note however that since the present simulations are free-decay the forcing terms appearing in those equations are identically zero. Therefore, the latter reduce to

$$2\mathcal{E}_{F21} + \partial_t \langle E^{tot} \rangle - \partial_t \langle S \rangle + \mathcal{D}_{F21} + \mathcal{D}_{F21}^{loc} = 0 \quad (29)$$

for the F21 model and to

$$2\mathcal{E}_{A18} + \partial_t \langle R_E + R'_E \rangle + \mathcal{D}_{A18} = 0. \quad (30)$$

for the A18 model.

To lead the calculations we retained a number of snapshots for each Run: 11 snapshots for Run I (that present fluctuations on the incompressible energy and thus require a time average) at turnover times [8,8.1,8.2,8.3,8.4,8.5,8.6,8.7,8.8,8.9,9], and 5 snapshots for Runs II and III at respective turnover times [5.3,5.35,5.4,5.45,5.5] and [5.6,5.65,5.7,5.75,5.8]. All time derivatives are obtained by using a five-points finite differences method:

$$f'(t) \approx \frac{f(t-2h) - 8f(t-h) + 8f(t+h) - f(t+2h)}{12h}, \quad (31)$$

where h represents the time step between two selected snapshots. For Run I, time derivatives (e.g. $\partial_t \langle S \rangle$) are calculated on all possible subsets of 5 consecutive snapshots among the initial 11, for a total of 7 calculations (one using times 8 to 8.4, one using times 8.1 to 8.5 etc.), then the resulting derivatives are averaged over

time. For all other terms (e.g. ε_{F21}) we compute the time average over all 11 snapshots. For Runs II and III, the derivatives are calculated on the 5 snapshots retained using the same derivation method and all other terms are calculated only on the central snapshot, respectively at times 5.4 and 5.7. Averaging these terms over the five snapshots was found to bring no change to the results (not shown).

4. CALCULATION OF THE ENERGY CASCADE RATE IN THE INERTIAL RANGE

We first study the energy cascade rates obtained for laws F21 and A18 classically obtained under the full assumptions of space homogeneity, time stationarity and infinite Reynolds number, i.e. equations (9) and (20) respectively. For both laws, energy cascade rates are broken down into a Hall component ε^{Hall} and a MHD component ε^{MHD} , which are made respectively of the terms in factor of λ and of all the remaining terms from equations (9) and (20). A comparison of the cascade rates provided by the two exact laws is shown in Fig. 3 for Runs I and II. One can observe that the two models yield closely similar components (MHD and Hall) of the cascade rate nearly at all scales. This validates numerically the equivalence of the two exact laws in the inertial range as anticipated in Ferrand et al. (2021a). Note that in both Run I and Run II the value of the cascade rate in the inertial range, centered around $\ell/d_i \simeq 2$, roughly matches the energy dissipation rate estimated through the linear fit on the energy (respectively ~ -0.047 and ~ -0.087 , see Figs. 1 and 2), suggesting that the energy cascade approximated in the inertial range is representative of the dissipation in the system. The difference in the cascade rate values between the two runs is due to differences in the initial/driving amplitude of fluctuations, which is the lowest for Run I with $B_0 = 2$.

Another question that can be addressed regarding the cascade rate in the inertial range is its sensitivity (or not) to the turbulent sonic Mach number. To do so we compare in Fig. 4 the results of Runs II and III that correspond to the initial Mach numbers $M_S = 0.25$ and $M_S = 0.5$, respectively. We observe that, overall, the cascade rate are very close to each other at all scale, and appear to be similar among all three Runs, indicating that the increase in the Mach number from $M_S = 0.25$ to $M_S = 0.5$ does not bring significant changes to the total dynamics of the system. This result agrees with the findings in Andrés et al. (2018) for compressible MHD turbulence who already reported that, for Mach num-

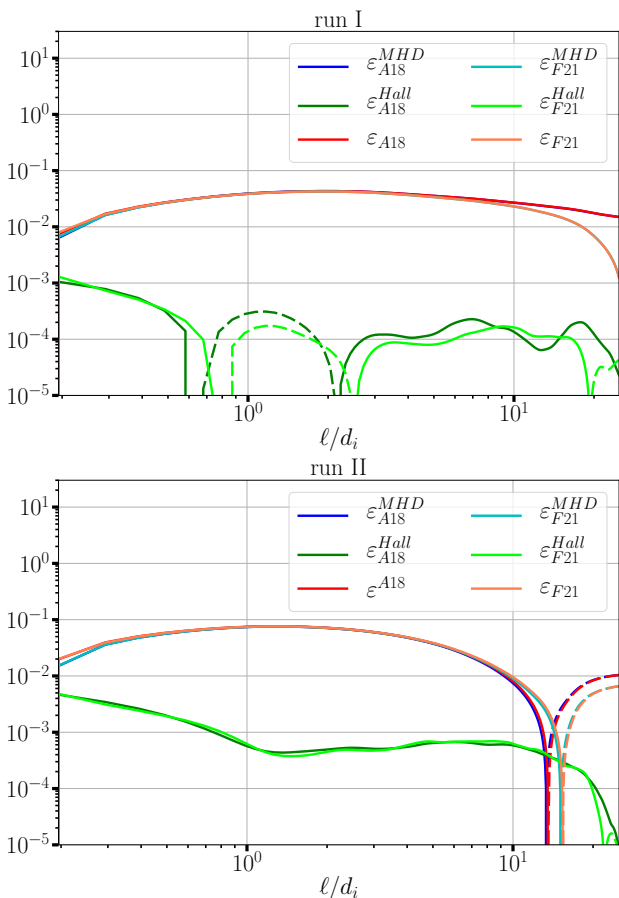


Figure 3. Comparison between the different components of the cascade rate given by the two models of Ferrand et al. (2021a) (Eq. 9) and Andrés et al. (2018) (Eq. 20) for Run I (top) and Run II (bottom). Plain lines represent positive values whereas dashed lines represent negative ones.

bers up to $M_S = 0.5$, purely compressible components of the exact law remain negligible in comparison to the flux terms, which only slightly deviate from their incompressible counterparts. Note that such conclusions only hold *a priori* for subsonic regimes: supersonic turbulent flows can develop a dominant compressible (source-like) component of the energy cascade over the traditional flux driven one (Ferrand et al. 2020).

At this point, an important remark can be made : all the energy cascade rates reported in Figs. 3 and 4 have a relatively low amplitude Hall component, which never becomes dominant with regard to the MHD component in contrast with results reported previously from 3D CGL simulations (Ferrand et al. 2021b) (i.e. simulations using a closure with an anisotropic pressure tensor). An explanation can be given: the Hall effect remains too weak in our simulations such that the dissipation inhibits the energy cascade before its Hall com-

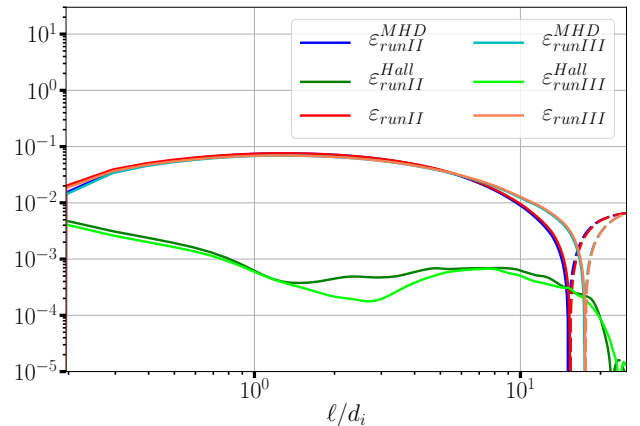


Figure 4. Comparison between the cascade rate given by model Ferrand et al. (2021a) (Eq. 9) for two different Mach numbers: $M_S = 0.25$ (Run II) and $M_S = 0.5$ (Run III)

ponent becomes dominant. To test this hypothesis we ran an additional simulation (Run I-512) that is akin to Run I but with a lower resolution $N = 512$, a slightly higher dissipation $\nu = \eta = 8.0 \times 10^{-4}$ and an ion inertial length $d_i = 0.05/L_0$. L_0 and M_S are kept unchanged. Reducing the resolution while increasing the value of d_i (despite the slight increase of the dissipation) allows for increasing the size of the sub-ion range, which should in turn increase the importance of the Hall effect at the smallest scales available. A first measure of this can be obtained by looking at the power spectrum of the electric field, defined by reduced Ohm's law as (omitting the resistive term):

$$\mathbf{E} = -\mathbf{v} \times \mathbf{B} + \frac{1}{nq_e} \mathbf{J} \times \mathbf{B}, \quad (32)$$

where n is the particle density. Fig. 5 shows the ratio of the power spectrum density (PSD) of the Hall to the ideal components of the electric field for Run I and the lower resolution Run I-512. As expected, we observe both an increase in the amplitude of the Hall electric field and its extension to smaller scales for Run I-512 in comparison with Run I.

We now look at how the increased Hall effect witnessed in Run I-512 is reflected on the energy cascade rate. The results, reported in Fig. 6, show little enhancement in the amplitude of the Hall component, but it still does not dominate the cascade at sub-ion scales despite the Hall effect being stronger. This suggests the need to further increase the potency of the Hall effect and/or to introduce hyperviscosity and hyperdiffusivity in the GHOST code, which would push the dissipation to the smallest possible scales. This solution was indeed used in CHMHD-CGL simulations where the Hall cas-

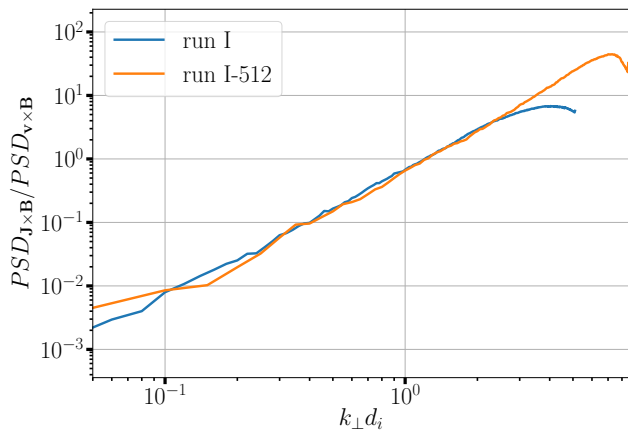


Figure 5. Ratio of the power spectrum density of the Hall to the ideal ($\mathbf{v} \times \mathbf{B}$) components of the electric field for Run I and the lower resolution Run I-512.

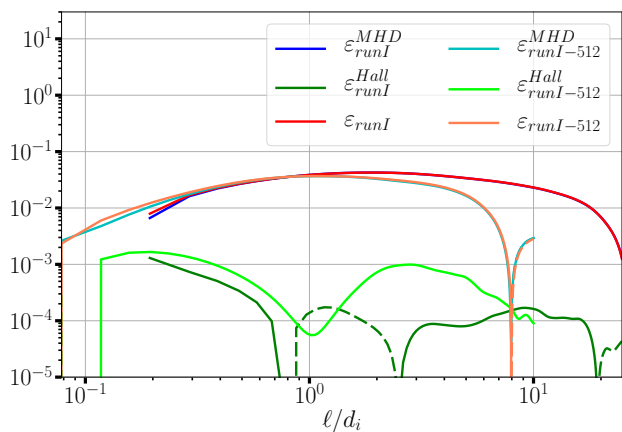


Figure 6. Comparison between the cascade rate given by model Ferrand et al. (2021a) (Eq. 9) for Run I and Run I-512.

cade was found to dominate below the ion inertial length (Ferrand et al. 2021b).

5. EXACT LAWS BEYOND THE INERTIAL RANGE AND TIME STATIONARITY

As we already stated, switching from a forced turbulence model to a free-decay model invalidates the stationarity hypothesis used to derive the final expression of the compressible exact laws, namely equations (9)-(20). Thus, we make use in this section of equations (29) and (30) describing the general exact laws F21 and A18, free from these hypotheses and of the presence of an external forcing. All the terms in those equations are computed for the three Runs and are displayed in figures 7 and 8, along with their sums that, according to the aforementioned equations, should amount to zero.

5.1. Full equation for law A18

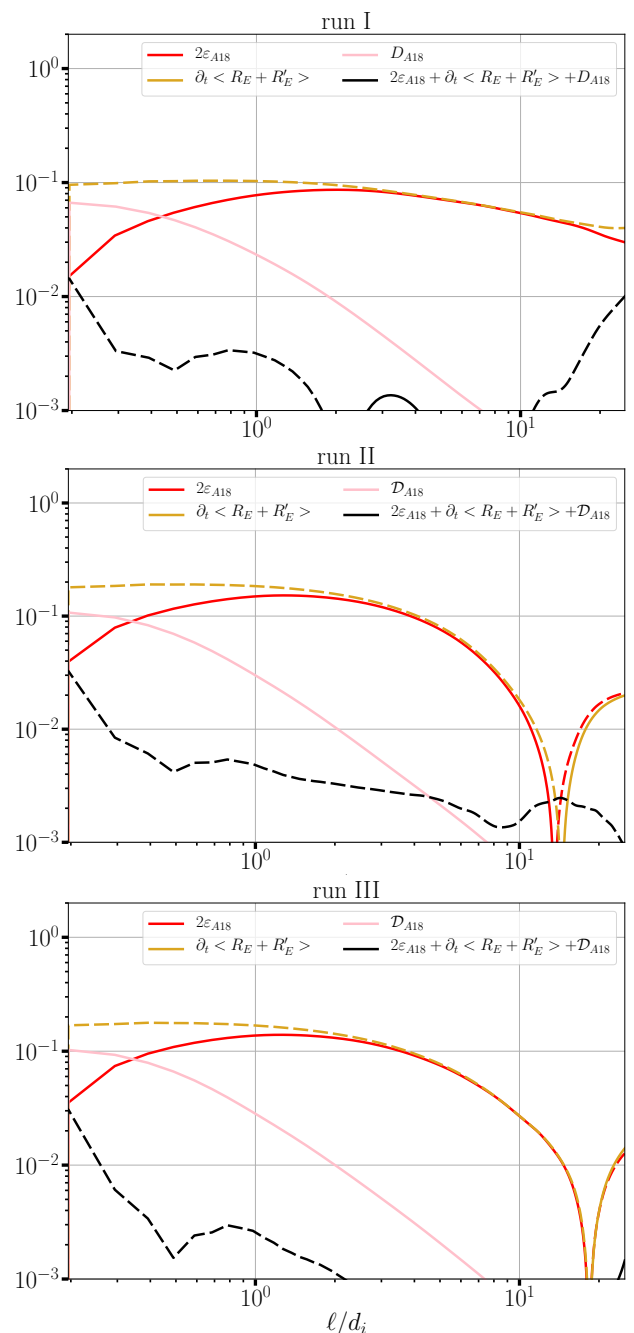


Figure 7. Calculation of equation (30) (black line) and its components for all three Runs.

Equation (30) gives a very similar behavior for all three Runs. The sum of all terms, which is supposed to be zero, lies around 1 to 1.5 orders of magnitude below all other terms, which is reasonable given the statistical and discrete nature of the numerical calculations led here. Theoretical limit cases can be easily evaluated here: at large and intermediate scales the dissipation term should be negligible as it represents a mean of un-

correlated terms, resulting in the equation:

$$2\mathcal{E}_{A18} + \partial_t \langle R_E + R'_E \rangle = 0. \quad (33)$$

This relation is overall well verified by Run II and III at large scales as reflected by the matching between the red and yellow curves in Fig. 7. This does not seem to be the case in Run I however, and the black curve rises at large scales as a result. The reason for this odd behavior is not fully understood yet. At small scales the dissipation is expected to kick in and take energy away from the cascade \mathcal{E}_{A18} . Also, at small scales we have $\mathbf{x} \rightarrow \mathbf{x}'$, and therefore $\partial_t \langle R_E + R'_E \rangle \rightarrow 2\partial_t \langle E^{tot} \rangle$, resulting in the equation:

$$2\mathcal{E}_{A18} + 2\partial_t \langle E^{tot} \rangle + \mathcal{D}_{A18} = 0. \quad (34)$$

This equation too is verified in all three Runs, since the black curve in Fig. 7 that represents a measure of any departure from the perfect fulfillment of the equation is at least 1 order of magnitude lower than the other components of the equation.

The physical interpretation of Eq. (30) is rather simple and can be summed up as follows: in free-decay simulations the term $\partial_t \langle R_E + R'_E \rangle$ in the A18 model plays the role of a “forcing”, i.e., $-\partial_t \langle R_E + R'_E \rangle \equiv \mathcal{F}_{F21}$ that inputs energy into the system at each time step. This reservoir of energy is then split into a cascade component with a rate \mathcal{E}_{A18} and a dissipation one with a rate \mathcal{D}_{A18} . At large scale, since $\mathcal{D}_{A18} \rightarrow 0$ all the energy is almost entirely injected in the cascade towards smaller scales. The sum of all terms, which should be equal to zero, can be seen as an estimation of the error induced in the calculations of time derivatives by the fluctuations of energy.

5.2. Full equation for law F21

Fig. 8 shows that, again, the results of equation (29) do not change much between the three Runs. The local terms (i.e., independent on the increment ℓ) \mathcal{D}_{F21}^{loc} and $\partial_t \langle E_{tot} \rangle$ are almost equal, which can be intuited by the fact that $\mathcal{D}_{F21}^{loc} \sim -\varepsilon_{F21}$ in the limit of $\rho \sim \rho'$. Note that in this case the model still perfectly hold for Run I, whereas with equation (30) the term $\partial_t \langle R_E + R'_E \rangle$ showed an irregular increase at large scale. This may suggest that the model depicted by equation (29) is more robust than the previous one.

Interpreting the balance between the terms of the non-stationary F21 law is more subtle than for A18 because of the presence of the local terms $\partial_t \langle E^{tot} \rangle$ and \mathcal{D}_{F21}^{loc} . Here it is the scale dependent term $-\partial_t \langle S \rangle$ that acts

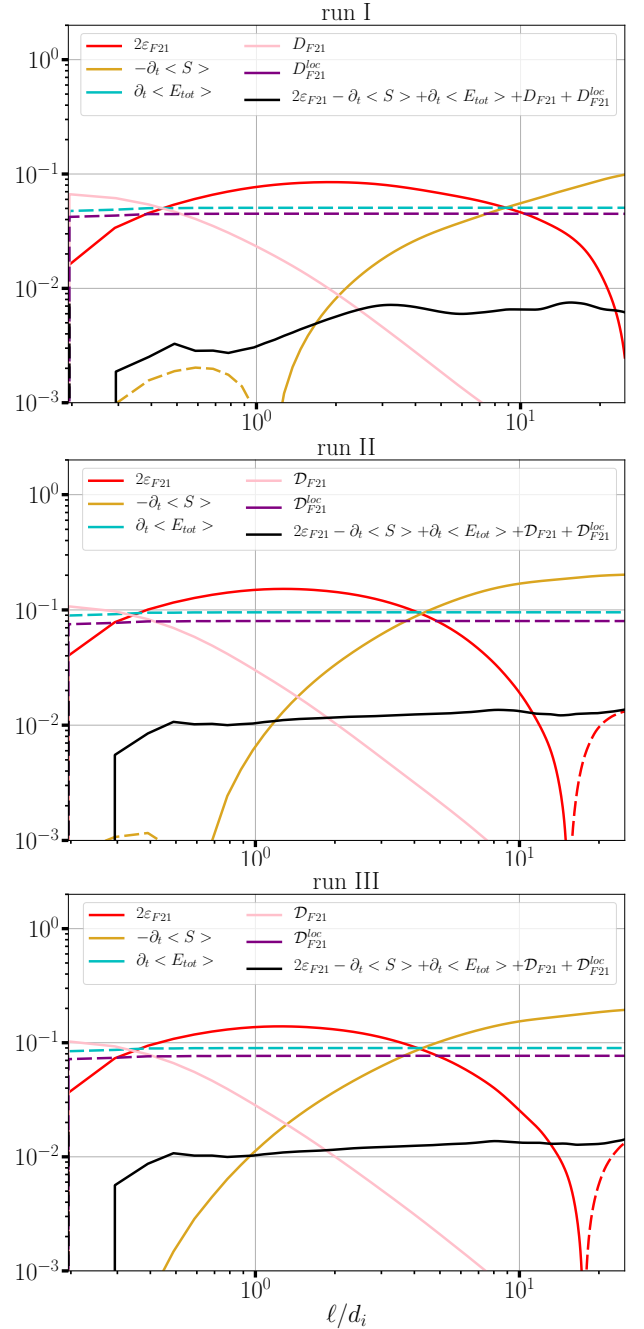


Figure 8. Calculation of equation (29) (black line) and its components for all three Runs.

as a “forcing” to input energy into the system, but this energy is diminished by the local (i.e., increment $\ell = 0$) energy variation term $\partial_t \langle E^{tot} \rangle$ and the local dissipation \mathcal{D}_{F21}^{loc} . Then, the resulting energy balance is split, similarly to the A18 model, between the cascading part to small scales and the dissipation (both being scale dependent quantities):

$$2\mathcal{E}_{F21} + \left[-\partial_t \langle S \rangle + \partial_t \langle E^{tot} \rangle + \mathcal{D}_{F21}^{loc} \right] + \mathcal{D}_{F21} = 0. \quad (35)$$

6. CONCLUSION

Similarly to the case of IHMHD, several exact laws exist for estimating the turbulence energy cascade rate in CHMHD. In this paper, making use of high resolution free-decay simulations of CHMHD turbulence, we showed that the two exact laws available for this model provide the same value of ε , as was already proven for IHMHD laws (Ferrand et al. 2019). In the absence of a direct mathematical proof of the equivalence between the two compressible laws, this paper brings evidence that they indeed describe the same turbulent cascade. The influence of the strength of Hall effect on the energy cascade was also investigated. It appears that the development of a Hall-driven energy cascade in numerical simulations may be much more hindered by the action of dissipation at near-ion scales than by the size of the sub-ionic range. This underlines the potential importance of a certain amount of hyperviscosity when running simulations of CHMHD.

The question as to how the exact laws behave in absence of an external forcing led us to investigate a more general form of compressible exact laws, dropping the usual assumption of time stationarity and considering otherwise neglected time derivatives. This study shows that a shift in the interpretation of both laws occurs: instead of the continuous (in time) large scale forcing, the laws point toward the existence of a scale dependent reservoir of energy, mainly described by the time derivative terms, from which either the turbulent cascade or the dissipation (depending on the considered scale) draws. This reservoir overall coincides with the energy dissipation rate, which suggests that the considered cascading energy is ultimately bound to be fully dissipated.

These results confirm the non-trivial assertion that the final, well-known form of exact laws, obtained with the assumption of stationarity, remain valid within the inertial range even for decaying turbulent flows in which the aforementioned assumption is not verified, as it is the case in some turbulent space plasmas such as the SW taken far away from the sun.

ACKNOWLEDGEMENTS

This work was granted access to the HPC resources of CINES under allocation 2021 A0090407714 made by GENCI.

APPENDIX
AXI-SYMMETRIC LAW CALCULATION

Throughout this paper, all terms of the generalized exact laws are computed using the isotropic model described in section 3.2. However, for simulations with $B_0 \neq 0$ the isotropy assumption should not *a priori* be used. Instead we thus propose an axi-symmetric scheme that may prove to be more suited for the analysis of such simulation data.

We assume a symmetry of revolution around \mathbf{B}_0 , which is here aligned with the \mathbf{z} -axis. In this case we adopt cylindrical coordinates: the increment vector is defined as $\boldsymbol{\ell} = (\ell_\perp, \phi, \ell_z)$ and the derivative operator becomes $\nabla_{\boldsymbol{\ell}} \cdot \langle \mathbf{F} \rangle = \frac{1}{\ell_\perp} \partial_{\ell_\perp} [\ell_\perp \langle F_{\ell_\perp} \rangle (\ell_\perp, \ell_z)] + \partial_{\ell_z} \langle F_{\ell_z} \rangle (\ell_\perp, \ell_z)$. However, the discrete decomposition adopted in this paper makes it impossible to effectively compute $\partial_{\ell_z} \langle F_{\ell_z} \rangle (\ell_\perp, \ell_z)$ at arbitrary values of (ℓ_\perp, ℓ_z) without resorting to multi-dimensional interpolation on irregular grids, bringing lots of additional calculations and more imprecision to the result. Consequently, we only consider the perpendicular component of the flux that is averaged over the parallel increments ℓ_z , thus the derivative operator : $\nabla_{\boldsymbol{\ell}} \cdot \langle \mathbf{F} \rangle = \frac{1}{\ell_\perp} \partial_{\ell_\perp} [\ell_\perp \langle F_{\ell_\perp} \rangle (\ell_\perp)]$. To do so we first compute the projection of \mathbf{F} on the direction of $\boldsymbol{\ell}_\perp$:

$$\langle F_{\ell_\perp} \rangle (\ell_\perp, \phi, \ell_z) = \langle \cos(\phi) F_x + \sin(\phi) F_y \rangle, \quad (36)$$

and then take the average over all directions (i.e., over ℓ_z and ϕ):

$$\langle F_{\ell_\perp} \rangle (\ell_\perp) = \sum_{\phi, \ell_z} \frac{\langle F_{\ell_\perp} \rangle (\ell_\perp, \phi, \ell_z)}{57}. \quad (37)$$

Here we only use 57 directions, corresponding to all directions of the isotropic model forming an angle of 45° or more with the parallel direction. This is done to obtain results pertaining to all values of ℓ_\perp while avoiding redundant calculations due to the periodicity of the data cubes.

This method presents two inconveniences: first, the

statistics are weaker than the isotropic model as we probe a smaller number of directions for the increment vector. This may lead to less precise calculations. Second, disregarding parallel fluxes may lead to miss a small portion of the cascade. Due to these limitations the isotropic decomposition may sometimes yield slightly better results even in presence of a background magnetic field. A good way to test the efficiency of this method is to compute the energy cascade rate of both exact laws A18 and F21 and see if they match as one would expect.

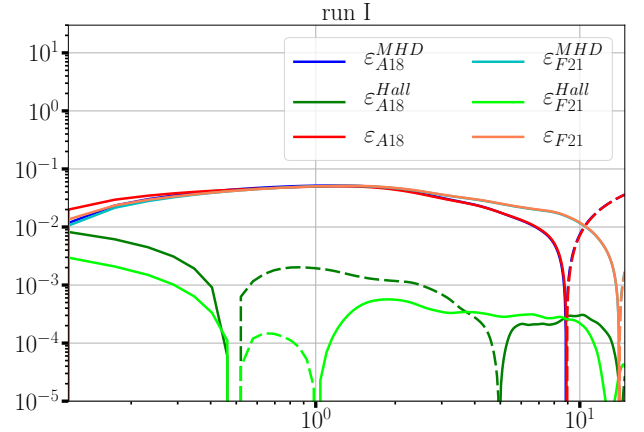


Figure 9. Energy cascade rate calculated with laws A18 and F21 for Run I, using the axi-symmetric method.

This test was used on Run I and the results are reported in Fig. 9. We immediately observe that the two laws, and especially the Hall components, do not match as well as they are with the isotropic model or for Run II (see Fig. 3), which may be a consequence of the aforementioned limitations. For this reason, we finally chose to keep using the isotropic model to study Run I in this paper.

Still, note that Run I remains a weakly anisotropic simulation, with a background magnetic field of only 2. Thus, the conclusion drawn in this appendix may not be true for simulations featuring a stronger background field, i.e. stronger anisotropies. Ultimately, checking which model is the most suited one to lead the study should be done on a case-by-case basis.

REFERENCES

- Andrés, N., Galtier, S., & Sahraoui, F. 2018, Phys. Rev. E, 97, 013204
- Andrés, N., & Sahraoui, F. 2017, Phys. Rev. E, 96, 053205
- Andrés, N., Sahraoui, F., Galtier, S., et al. 2018, J. Plasma Physics, 84, 1
- Andrés, N., Sahraoui, F., Galtier, S., et al. 2019, Phys. Rev. Lett., 123, 245101
- Arzoumanian, D., André, Ph., Didelon, P., et al. 2011, A&A, 529, L6
- Bandyopadhyay, R., Sorriso-Valvo, L., Chasapis, A., et al. 2020, Phys. Rev. Lett., 124, 225101
- Banerjee, S., & Galtier, S. 2013, Phys. Rev. E, 87, 013019
- Banerjee, S., & Galtier, S. 2014, J. Fluid Mech., 742, 230
- Banerjee, S., & Galtier, S. 2016, Phys. Rev. E, 93, 033120
- . 2017, J. Phys. A: Math. Theo., 50, 015501

- Banerjee, S., Hadid, L., Sahraoui, F., & Galtier, S. 2016, *Astrophys. J. Lett.*, 829, L27
- Banerjee, S., & Kritsuk, A. 2017, *Phys. Rev. E*, 96, 053116
- . 2018, *Phys. Rev. E*, 97, 023107
- Bruno, R., & Carbone, V. 2013, *Living Reviews in Solar Physics*, 10, 2
- Coburn, J., Forman, M., Smith, C., Vasquez, B., & Stawarz, J. 2015, *Phil. Trans. R. Soc. A*, 373, 20140150
- Ferrand, R., Galtier, S., & Sahraoui, F. 2021a, *Journal of Plasma Physics*, 87, 905870220
- Ferrand, R., Galtier, S., Sahraoui, F., & Federrath, C. 2020, *Astrophys. J.*, 904, 160
- Ferrand, R., Galtier, S., Sahraoui, F., et al. 2019, *Astrophys. J.*, 881, 50
- Ferrand, R., Sahraoui, F., Laveder, D., et al. 2021b, *ApJ* (accepted), arXiv:2109.03123
- Galtier, S. 2008, *Phys. Rev. E*, 77, 015302
- . 2012, *Astrophys. J.*, 746, 184
- Galtier, S., & Banerjee, S. 2011, *Phys. Rev. Lett.*, 107, 134501
- Gómez, D. O., Mininni, P. D., & Dmitruk, P. 2005, *Physica Scripta*, 123
- Hadid, L., Sahraoui, F., & Galtier, S. 2017, *Astrophys. J.*, 838, 11
- Hadid, L. Z., Sahraoui, F., Galtier, S., & Huang, S. Y. 2018, *Phys. Rev. Lett.*, 120, 055102
- Hellinger, P., Verdini, A., Landi, S., Franci, L., & Matteini, L. 2018, *Astrophys. J.*, 857, L19
- Kolmogorov, A. 1941, *Dokl. Akad. Nauk SSSR*, 32, 16
- Kritsuk, A. G., Norman, M. L., Padoan, P., & Wagner, R. 2007, *Astrophys. J.*, 665, 416
- Kritsuk, A. G., Wagner, R., & Norman, M. L. 2013, *J. Fluid Mech.*, 729, 1
- Lindborg, E. 2019, *JFM*, 874, R2
- MacBride, B., Smith, C., & Forman, M. 2008, *Astrophys. J.*, 679, 1644
- Marino, R., Sorriso-Valvo, L., Carbone, V., et al. 2008, *Astrophys. J.*, 677, L71
- Matthaeus, W. H., Zank, G. P., Smith, C. W., & Oughton, S. 1999, *Phys. Rev. Lett.*, 82, 3444
- Mininni, P. D., & Pouquet, A. 2009, *Phys. Rev. E*, 80, 025401
- Mininni, P. D., Rosenberg, D., Reddy, R., & Pouquet, A. 2011, *Parallel Computing*, 37, 316
- Osman, K. T., Wan, M., Matthaeus, W. H., Weygand, J. M., & Dasso, S. 2011, *Phys. Rev. Lett.*, 107, 165001
- Politano, H., & Pouquet, A. 1998, *Phys. Rev. E*, 57, 21
- Pouquet, A., & Patterson, G. S. 1978, *Journal of Fluid Mechanics*, 85, 305–323
- Sahraoui, F., Zafer Hadid, L., & Huang, S. 2020, *Reviews of Modern Plasma Physics*, 4, doi:10.1007/s41614-020-0040-2
- Simon, P., & Sahraoui, F. 2021, General exact law of compressible isentropic magnetohydrodynamic flows: theory and spacecraft observations in the solar wind, , , arXiv:2105.08011
- Sorriso-Valvo, L., Marino, R., Carbone, V., et al. 2007, *Phys. Rev. Lett.*, 99, 115001
- Sorriso-Valvo, L., Catapano, F., Retinò, A., et al. 2019, *Phys. Rev. Lett.*, 122, 035102
- Stawarz, J. E., Smith, C. W., Vasquez, B. J., Forman, M. A., & MacBride, B. T. 2009, *Astrophys. J.*, 697, 1119
- Taylor, M., Kurien, S., & Eyink, G. 2003, *Phys. Rev. E*, 68, 026310
- Verdini, A., Grappin, R., Hellinger, P., Landi, S., & Müller, W. C. 2015, *The Astrophysical Journal*, 804, 119
- Yang, Y., Wan, M., Matthaeus, W. H., & Chen, S. 2021, *Journal of Fluid Mechanics*, 916, A4

Titre: Turbulence multi-échelles compressible dans les plasmas astrophysiques: une approche théorique, numérique et observationnelle

Mots clés: Turbulence, Plasmas spatiaux, Lois exactes, Simulations, Observations

Résumé: Le vent solaire est un plasma turbulent dont la physique est largement étudiée depuis de nombreuses années grâce à des modèles théoriques, des simulations et des mesures *in situ* par satellite. Identifier les mécanismes de dissipation d'énergie turbulente à l'œuvre dans le vent solaire est une nécessité pour mieux comprendre la physique du vent dans son ensemble.

Dans cette thèse nous dérivons de nouvelles lois exactes pour la turbulence (in)compressible en MHD Hall, des équations permettant le calcul du taux de cascade d'énergie turbulente. Nous développons un programme à même de calculer ces lois sur des données de simulation 3D, que nous appliquons à un ensemble de simulations numériques directes effectuées pour des modèles de plasmas divers. D'une part, ce travail permet de confirmer l'équivalence entre les différentes lois exactes existant pour un modèle donné, et de mieux comprendre leur fonctionnement intrinsèque. D'autre part, ces simulations

permettent d'aboutir à d'importants résultats: elles montrent que la représentation fluide d'un plasma peut rendre compte de la dissipation d'énergie par des mécanismes cinétiques, et une étude de simulations fortement supersoniques précise le rôle que la turbulence joue dans la formation de filaments interstellaires.

À ces études séparées vient enfin s'ajouter l'analyse de données satellites mesurées par MMS dans la magnétogaine. L'utilisation des lois exactes compressibles révèle un comportement anormal de la méthode utilisée pour calculer les dérivées 3D des champs de vecteurs dans la formation MMS. Une étude plus poussée, menée sur la base de données réelles et de simulations (via l'utilisation de satellites virtuels), révèle que cette méthode induit parfois d'importantes erreurs dans le calcul des lois exactes. Ces révélations pourraient aider à mieux préparer de futures missions spatiales multi-points et multi-échelles à destination du vent solaire.

Title: Multi-scale compressible turbulence in astrophysical plasmas viewed through theoretical, numerical and observational methods

Keywords: Turbulence, Space plasmas, Exact laws, Simulations, Observations

Abstract: The Solar Wind is a turbulent plasma whose internal physics has been extensively studied for years through theoretical models, plasma simulations and *in situ* satellite observations. Understanding the mechanisms hidden behind turbulence energy dissipation is a key step in unraveling the mysteries of the solar wind.

In this thesis we first derive new Hall MHD turbulence exact laws, theoretical tools that allow for the calculation of the turbulence energy cascade rate. We develop a program able to compute these laws on 3D simulation datasets, and apply it to a variety of direct numerical simulations of different plasma models. On the one hand, these studies allow us to prove the consistency between the different exact laws existing for a same model and to better understand their detailed behavior. On the other hand, they yield important physical results: the study of Landau-fluid datasets allows us to partly reconcile

the fluid and kinetic description of plasmas, justifying the analysis of solar wind energy dissipation through fluid exact laws, and the study of strongly supersonic datasets hints at turbulence playing a key role on the formation of star-forming interstellar filaments.

These individual studies are then complemented by the analysis of *in situ* data measured by MMS in the magnetosheath. The application of the compressible exact laws to these data unveils the odd behavior of the methods used to compute 3D fields derivatives using MMS four satellites. An in-depth investigation of this method, both using MMS data and simulation data through the use of a virtual spacecraft, reveal important errors induced by this method in the calculation of exact laws. These new insights could help preparing future multipoint and multi-scale space missions targeting solar wind turbulence.